METAL IONS IN BIO-IMAGING TECHNIQUES

Edited by Astrid Sigel, Eva Freisinger and Roland K.O. Sigel
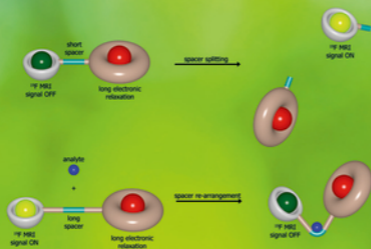
Astrid Sigel, Eva Freisinger, Roland K. O. Sigel
Metal Ions in Life Sciences 22

Metal Ions
in Life Sciences

———

Edited by
Astrid Sigel, Eva Freisinger and Roland K. O. Sigel

Volume 22

Metal Ions in Bio-Imaging Techniques

—

DE GRUYTER

Series Editors

Astrid Sigel
Department of Chemistry
Inorganic Chemistry
University of Basel
Spitalstrasse 51
CH-4056 Basel
Switzerland
<astrid.sigel@unibas.ch>

Eva Freisinger and Roland K. O. Sigel
Department of Chemistry
University of Zürich
Winterthurerstrasse 190
CH-8057 Zürich
Switzerland
<freisinger@chem.uzh.ch>
<roland.sigel@chem.uzh.ch>

About the Editors

Astrid Sigel has studied languages; she was an Editor of the *Metal Ions in Biological Systems* series (until Volume 44) and also of the "Handbook on Toxicity of Inorganic Compounds" (1988), the "Handbook on Metals in Clinical and Analytical Chemistry" (1994; both with H. G. Seiler and Helmut Sigel), and the "Handbook on Metalloproteins" (2001; with Ivano Bertini and Helmut Sigel). She is also an Editor of the *MILS* series from Volume 1 on, and she coauthored about 50 papers on topics in Bioinorgenic Chemistry.

Eva Freisinger is Associate Professor for Bioinorganic Chemistry and Chemical Biology (2018) at the Department of Chemistry at the University of Zürich, Switzerland. She obtained her doctoral degree (2000) from the University of Dortmund, Germany, working with Bernhard Lippert and spent three years as a postdoc at SUNY Stony Brook, USA, with Caroline Kisker. Since 2003, she performs independent research at the University of Zürich where she held a Förderungsprofessur of the Swiss National Science Foundation from 2008 to 2014. In 2014, she received her *Habilitation* in Bioinorganic Chemistry. Her research is focused on the study of plant metallothioneins with an additional interest in the sequence-specific modification of nucleic acids. Together with Roland Sigel she chaired the 12th European Bioinorganic Chemistry Conference (2014 in Zürich, Switzerland) and the 19th International Conference on Biological Inorganic Chemistry (2019 in Interlaken, Switzerland). She also serves on several Advisory Boards for international conference series; since 2014, she is the Secretary of the European Bioinorganic Chemistry Conferences (EuroBICs), and an Editorial Board Member of the *Journal of Inorganic Biochemistry*. She joined the group of editors of the *MILS* series from Volume 18 on.

Roland K. O. Sigel is Full Professor (2016) of Chemistry at the University of Zürich, Switzerland. In the same year he became Vice Dean of Studies (B.Sc./M.Sc.) and in 2017 he was elected Dean of the Faculty of Science. From 2003 to 2008 he was endowed with a Förderungsprofessur of the Swiss National Science Foundation, and he is the recipient of an ERC Starting Grant 2010. He received his doctoral degree summa cum laude (1999) from the University of Dortmund, Germany, working with Bernhard Lippert.

Thereafter, he spent nearly three years at Columbia University, New York, USA, with Anna Marie Pyle (now Yale University). During the six years abroad

he received several prestigious fellowships, and he was awarded the EuroBIC Medal in 2008 and the Alfred Werner Prize (SCS) in 2009. 2015–2019 he was the Secretary of the Society of Biological Inorganic Chemistry (SBIC) and since 2018 he is the Secretary of the International Conferences of Biological Inorganic Chemistry (ICBICs). His research focuses on the structural and functional role of metal ions in ribozymes, especially group II introns, regulatory RNAs, and on related topics. He is also an Editor of Volumes 43 and 44 of the *MIBS* series and of the *MILS* series from Volume 1 on.

Historical Development and Perspectives of the Series
Metal Ions in Life Sciences[*]

It is old wisdom that metals are indispensable for life. Indeed, several of them, like sodium, potassium, and calcium, are easily discovered in living matter. However, the role of metals and their impact on life remained largely hidden until inorganic chemistry and coordination chemistry experienced a pronounced revival in the 1950s. The experimental and theoretical tools created in this period and their application to biochemical problems led to the development of the field or discipline now known as *Bioinorganic Chemistry*, *Inorganic Biochemistry*, or more recently also often addressed as *Biological Inorganic Chemistry*.

By 1970 *Bioinorganic Chemistry* was established and further promoted by the book series *Metal Ions in Biological Systems* founded in 1973 (edited by H. S., who was soon joined by A. S.) and published by Marcel Dekker, Inc., New York, for more than 30 years. After this company ceased to be a family endeavor and its acquisition by another company, we decided, after having edited 44 volumes of the *MIBS* series (the last two together with R. K. O. S.) to launch a new and broader minded series to cover today's needs in the *Life Sciences*. Therefore, the Sigels' new series is entitled

Metal Ions in Life Sciences.

After publication of 16 volumes (since 2006) with various publishers during the past 10 years, we are happy to join forces now in this still growing endeavor with Walter de Gruyter GmbH, Berlin, Germany, a most experienced Publisher in the *Sciences*.

The development of *Biological Inorganic Chemistry* during the past 40 years was and still is driven by several factors; among these are (i) attempts to reveal the interplay between metal ions and hormones or vitamins, etc., (ii) efforts regarding the understanding of accumulation, transport, metabolism, and toxicity of metal ions, (iii) the development and application of metal-based drugs,

---

[*] Reproduced with some alterations by permission of John Wiley & Sons, Ltd., Chichester, UK (copyright 2006) from pages v and vi of Volume 1 of the series *Metal Ions in Life Sciences* (MILS-1).

(iv) biomimetic syntheses with the aim to understand biological processes as well as to create efficient catalysts, (v) the determination of high-resolution structures of proteins, nucleic acids, and other biomolecules, (vi) the utilization of powerful spectroscopic tools allowing studies of structures and dynamics, and (vii), more recently, the widespread use of macromolecular engineering to create new biologically relevant structures at will. All this and more is reflected in the volumes of the series *Metal Ions in Life Sciences*.

The importance of metal ions to the vital functions of living organisms, hence, to their health and well-being, is nowadays well accepted. However, in spite of all the progress made, we are still only at the brink of understanding these processes. Therefore, the series *Metal Ions in Life Sciences* links coordination chemistry and biochemistry in their widest sense. Despite the evident expectation that a great deal of future outstanding discoveries will be made in the interdisciplinary areas of science, there are still "language" barriers between the historically separate spheres of chemistry, biology, medicine, and physics. Thus, it is one of the aims of this series to catalyze mutual "understanding".

It is our hope that *Metal Ions in Life Sciences* continues to prove a stimulus for new activities in the fascinating "field" of *Biological Inorganic Chemistry*. If so, it will well serve its purpose and be a rewarding result for the efforts spent by the authors.

Astrid Sigel and Helmut Sigel
Department of Chemistry, Inorganic Chemistry
University of Basel, CH-4056 Basel, Switzerland

Roland K. O. Sigel
Department of Chemistry
University of Zürich, CH-8057 Zürich, Switzerland

October 2005
and September 2016

Preface to Volume 22

Metal Ions in Bio-Imaging Techniques

Endogenous metal ions play crucial roles in biological systems, ranging from transition metal cofactors in essential enzymes to calcium ions in bones and cartilages. The use of *exogenous* metal ions as tools dates back to the first half of the past century when barium sulfate was orally given to patients undergoing X-ray examination. Since then, molecular imaging has experienced remarkable changes due to the technical advances. The *Introductory Chapter* of the 22nd volume of the series *Metal Ions in Life Sciences* (MILS) is setting the scene by providing an overview of the metal ions and methods used today in the field of bio-imaging.

Gadolinium(III)-based Contrast Agents (GBCAs) have been extensively used in Magnetic Resonance Imaging (MRI) in clinical practice since 1988 because they improve the contrast between healthy and diseased tissues. This success story seemed to come to a halt in 2006 when Nephrogenic Systemic Fibrosis (NSF) was linked to the administration of linear GBCAs in a small subset of patients with poor kidney function. This and the observed deposition of Gd(III) in various tissues (brain, bone) raised concerns about the safety of GBCAs. The attempts to overcome these side effects and the re-appraisal of GBCAs are summarized in *Chapter 2*.

Manganese(II) is an essential element with 5 unpaired electrons, slow electron spin relaxation, and fast water exchange. Mn^{2+} is an excellent nuclear probe and the most promising alternative to replace Gd(III) in contrast agents (CAs) for MRI though there are handicaps due to the labile nature of Mn^{2+}. Yet, in the last decade much data has accumulated, which allows establishing relationships between the structure of Mn^{2+} complexes and their stability, inertness, and relaxation properties. Despite the endogenous nature of Mn^{2+}, in high concentrations it is neurotoxic and therefore, Mn^{2+} also needs to be protected like Gd(III) (Chapter 3). Finally, high-spin Mn^{3+} is also a good relaxation agent and indeed, Mn^{3+} complexes were investigated as MRI probes.

Chapter 4 deals with the Chemical Exchange Saturation Transfer (CEST), which is an emerging mechanism to provide contrast in clinical MRI. CEST agents are compounds that contain a pool of exchangeable or labile protons in exchange with the surrounding water molecules in tissues. Paramagnetic compounds (Fe^{3+}, Mn^{2+}, and Gd^{3+}) were soon proposed as contrast agents for MRI, as they can accelerate the relaxation times of water proton nuclei. Lanthanide complexes were the first to be considered as potential MRI paramagnetic CEST agents (paraCEST). Since then other transition metal ions like Fe^{2+}, Co^{2+}, Ni^{2+}, and Cu^{2+} were investigated.

As indicated, lanthanide complexes have been widely used in bioassays for over 40 years, but their usefulness in optical imaging is only now fully appreciated (*Chapter 5*). Their fundamental spectroscopic properties make them ideal as probes for optical imaging: Their large pseudo Stokes shift and long luminescent life times facilitate the elimination of background signals while the nature of the energy transfers involved in sensitizing lanthanide emission makes all of them amendable to perturbation by their surroundings.

The recent, more widespread clinical availability of stand-alone Positron Emission Tomography (PET) and PET/Computer Tomography (CT) in conjunction with cyclotron systems enable p,n and d,n nucleo transformations. These produce a variety of positron emissive isotopes (*Chapter 6*), which utilize two distinct nuclear imaging techniques, that is, Single Photon Emission Tomography (SPECT) and PET. Isotopes with unstable nuclei and a surplus of protons can undergo a nuclear transformation, where a proton in the nucleus is transformed to a neutron. This process liberates a positron which is emitted from the nucleus and which after encountering an electron results in the production of photons.

According to *Chapter 7* technetium has probably the most interesting and multifaceted chemistry amongst the metallic radionuclides in routine applications for radiopharmacy. The diversity of its possible oxidation states enables complexes to be formed with ligands covering any possible class. However, the plethora of compounds resulting from this broad chemistry did not translate into a comparable number of new imaging agents. The large majority of complexes concentrates on three cores: $[^{99m}TcV=O]^{3+}$, $[^{99m}TcV\equiv N]^{2+}$, and *fac*-$[^{99m}Tc(CO)_3)]^+$. Labeling strategies with these cores are indicated. Furthermore, cold rhenium is emphasized not only as a model for technetium, but also as an option for complementing imaging with ^{99m}Tc by radioactive $^{186/188}Re$, leading to a theranostic matched-pair situation.

The ^{19}F nuclide has nuclear magnetic properties similar to those of ^1H and can be used for MRI on common commercial scanners with only minor modifications. As there is no abundance of ^{19}F in a living body, ^{19}F MRI is presented as a hot-spot image and requires contrast agents containing fluorine atoms. In *Chapter 8* the current developments of ^{19}F MRI contrast agents are reviewed and how these are influenced by the utilization of paramagnetic metal ions as relaxation agents.

Iron oxide nanoparticles (IONPs) have been studied extensively for bio-imaging due to their strong MRI contrast enhancements, which brought them to clinical use. *Chapter 9* describes the main synthetic methodologies, the characteriza-

tion techniques, and the physico-chemical properties of IONPs. Further, the *in vivo* biodistribution of IONPs, their excretion, toxicity, and degradation processes are considered.

Sulfonated, metallated corroles have the potential for a contrast agent, in addition to therapeutic and diagnostic activities. Their delivery by targeted particles enables such corroles to be transported to specific sites in the body for multifunctional activities, including diagnosis, and therapy, thus acting as targeted theranostics. *Chapter 10* summarizes the work accumulated thus far on tumor-targeted particles delivering metallated corroles.

"Theranostics" is a relatively new field of nuclear medicine with the goal to lead to personalized cancer treatment. *Chapter 11* briefly describes the PET-based theranostics in cancer diagnosis and treatment, with a focus on metal-based agents. The thermodynamics, formation, and dissociation kinetics of metal ion-based radiopharmaceuticals are covered. It is the aim to select the optimal chelates for the complexation of radiometals and to develop novel cancer-specific theranostic agents.

Theranostics has been a booming field of research in the 21st century, as is also evidenced by preceding chapters. *Chapter 12* provides an overview of Gd(III)-based MRI theranostics, and evaluates both, small molecule and nanomaterial strategies. The nanomaterial platforms are divided into sub-categories: metal-based nanomaterials (metal oxides, sulfides, gold nanostructures, etc.), carbon nanomaterials, mesoporous silica nanoparticles, dendrimers and polymers, and biomolecular nanomaterials.

In vivo luminescence cell and animal imaging enables gathering of real-time data on physiological processes, thus increasing our understanding of cell growth and cell metabolism, and cell death and the underlying mechanisms. Bio-imaging agents range from emissive organic molecules to polymers and to systems containing metals. In *Chapter 13* recent advances in the development and use of metal-containing systems are highlighted; molecular, polymeric, and nanostructures for bio-imaging of cancer cells and tumors in animals, are also reviewed.

Fluorescence microscopic cell imaging is a very powerful tool in medicinal research and life sciences as it cannot only image subcellular organelles (nuclei, mitochondria, lysosomes, etc.) but also monitor metabolic species and cellular microenvironments (*Chapter 14*). Many organic fluorescence probes for optical imaging have been commercialized in the past few decades, but they have some disadvantages (self-quenching, small Stokes shift, etc.), which are overcome by emissive transition metal Ir(III) complexes with low-spin d^6 electronic structure. A brief overview on the progress of iridium complexes as anticancer agents is also given.

Bacteria play a two-part role in contrast-enhanced MRI: (i) pathogenic bacteria are an increasingly important biomedical imaging target, as cases of antibiotic-resistant bacteria and hospital infections increase. However, (ii) certain bacteria have characteristics that make them ideal for use as diagnostic and theranostic contrast agents as reviewed in *Chapter 15*.

Transition metals are not only important targets in studies of neurobiology and neurodegeneration, but are also useful agents for the detection and sensing of

molecules involved in the pathology and diagnosis of neurodegenerative diseases. In *Chapter 16* examples of fluorescence probes for imaging iron, copper, and zinc ions, small molecule neurotransmitters, and aggregated proteins are discussed.

"Heavy Elements for X-ray Contrast" is the topic of the terminating *Chapter 17*. X-ray imaging is the oldest, but most important ionizing radiation-based technique. It provides information on the structural features of the human body, thus contributing to the diagnosis and treatment of numerous diseases. Its success depends on the advances of diagnostic instruments (mammography, etc.) and the development of contrast agents. X-ray contrast agents are usually small molecules or nanoparticles that contain heavy elements with a high atomic number such as iodine, barium, gold, etc. The current clinically approved contrast agents for X-ray imaging are iodinated small molecules or barium sulfate suspensions despite the fact that adverse events can result. Therefore, the development of alternative heavy elements-based X-ray contrast agents has become a key focus.

As expressed in Chapter 1, since its inception in the middle of the 20th century, molecular imaging has developed into a vast interdisciplinary field, encompassing chemistry, material sciences, physics, biology, engineering, and computer sciences. Metal-based tracers are now widely used in various imaging modalities alone or in combination, enabling early diagnosis of most deadly diseases, thereby increasing the survival rate. The discovery of more specific biomarkers allows distinguishing between closely related pathological conditions, thus improving the efficacy of treatment. Eventually, this will revolutionize the landscape of clinical imaging, offering a patient-tailored diagnosis. To conclude, this volume, devoted to *Metal Ions in Bio-Imaging Techniques*, is rich on specific information. *MILS-22* updates our knowledge and provides deep insights on the new research frontiers in the fast growing field of bio-imaging. It is a *must* for all researchers working in medicinal chemistry and related fields and beyond. It is also an ideal source for teachers giving courses on bio-imaging and sensing or in analytical chemistry in a wider sense.

<div style="text-align: right;">

Astrid Sigel
Eva Freisinger
Roland K. O. Sigel

</div>

Contents

Contributors to Volume 22

Numbers in parentheses indicate the pages on which the authors' contributions begin.

Casey J. Adams   Department of Chemistry, Molecular Biosciences, Neurobiology, and Radiology, Northwestern University, 2145 Sheridan Road, Evanston, IL 60208, USA (425)

Shin Hye Ahn   Department of Chemistry, Stony Brook University, 100 Nicolls Road, Stony Brook, NY 11790, USA (157)

Roger Alberto   Department of Chemistry, University of Zürich, Winterthurerstrasse 190, CH-8057 Zürich, Switzerland <ariel@chem.uzh.ch> (195)

Goran Angelovski   MR Neuroimaging Agents, Max Planck Institute for Biological Cybernetics, Max-Planck-Ring 8–14, D-72076 Tübingen, Germany (101)

Ho Yu Au-Yeung   Department of Chemistry, The University of Hong Kong, Pokfulam Road, Chong Yuet Ming Chemistry Building, Room 503, Hong Kong, P. R. China <hoyuay@hku.hk> (437)

Zsolt Baranyai   Bracco Imaging S.p.a., Bracco Research Center, Via Ribes 5, I-10010 Colleretto Giacosa, Italy <zsolt.baranyai@bracco.com> (315)

Jan Blahut   NMR Laboratory, Faculty of Science, Charles University, Hlavova 2030/8, CZ-128 43 Prague 2, Czech Republic (239)

Eszter Boros   Department of Chemistry, Stony Brook University, 100 Nicolls Road, Stony Brook, NY 11790, USA <eszter.boros@stonybrook.edu> (157)

Richárd Botár   Department of Physical Chemistry, University of Debrecen, Egyetem tér 1, H-4032 Debrecen, Hungary (39)

Ernö Brücher   Department of Inorganic and Analytical Chemistry, University of Debrecen, Egyetem tér 1, H-4032 Debrecen, Hungary (39)

Peter Caravan   The Institute for Innovation in Imaging, A. A. Martinos Center for Biomedical Imaging, Massachusetts General Hospital, Harvard Medical School, Charlestown, MA 02129, USA <caravan@nmr.mgh.harvard.edu> (1)

David P. Cormode   Departments of Radiology and Bioingeneering, University of Pennsylvania, 3400 Spruce Street, 1 Silverstein, Philadelphia, PA 19104, USA <david.cormode@pennmedicine.upenn.edu> (457)

Alexia G. Cosby   Department of Chemistry, Stony Brook University, 100 Nicolls Road, Stony Brook, NY 11790, USA (157)

Tibor Csupász   Department of Physical Chemistry, University of Debrecen, Egyetem tér 1, H-4032 Debrecen, Hungary (39)

Ana de Bettencourt-Dias   Department of Chemistry, University of Nevada, Reno, NV 89557, USA <abd@unr.edu> (371)

Marie Hélène Delville   CNRS, Univ. Bordeaux, Bordeaux INP, ICMCB, UMR 5026, 87 avenue du Dr. A. Schweitzer, F-33608 Pessac, France <marie-helene.delville@icmcb.cnrs.fr> (271)

Yuxi C. Dong   Departments of Radiology and Bioingeneering, University of Pennsylvania, 3400 Spruce Street, 1 Silverstein, Philadelphia, PA 19104, USA <yuxidong@seas.upenn.edu> (457)

David Esteban-Gómez   Centro de Investigacións Científicas Avanzadas (CICA) and Departamento de Química, Facultade de Ciencias, Universidade da Coruña, CP-15071 A Coruña, Galicia, Spain (101)

Stephen Faulkner   Chemistry Research Laboratory, University of Oxford, Mansfield Road, Oxford, OX1 3TA, UK and Keble College, Oxford, OX1 3PG, UK <stephen.faulkner@chem.ox.ac.uk> (137)

Zoltán Garda   Department of Physical Chemistry, University of Debrecen, Egyetem tér 1, H-4032 Debrecen, Hungary (39)

Carlos F. G. C. Geraldes   Department of Life Sciences, Coimbra Chemistry Center and CIBIT/ICNAS, University of Coimbra, PT-3000-456 Coimbra, Portugal <geraldes@uc.pt> (271)

Giovanni B. Giovenzana   Dipartimento di Scienze del Farmaco, Università del Piemonte Orientale, Largo Donegani 2, I-28100 Novara, Italy (315)

Petr Hermann   Department of Inorganic Chemistry, Faculty of Science, Charles University, Hlavova 2030/8, CZ-128 43 Prague 2, Czech Republic <petr.hermann@natur.cuni.cz> (239)

Vít Herynek   NMR Laboratory, Faculty of Science, Charles University, Hlavova 2030/8, CZ-128 43 Prague 2, Czech Republic (239)

Liang-Nian Ji   MOE Key Laboratory of Bioinorganic and Synthetic Chemistry, School of Chemistry, Sun Yat-Sen University, 135 West Xingangxi Road, Guangzhou 510275, P. R. China (403)

Ferenc K. Kálmán   Department of Physical Chemistry, University of Debrecen, Egyetem tér 1, H-4032 Debrecen, Hungary (39)

Angus J. Koller Department of Chemistry, Stony Brook University, 100 Nicolls Road, Stony Brook, NY 11790, USA (157)

Jan Kotek Department of Inorganic Chemistry, Faculty of Science, Charles University, Hlavova 2030/8, CZ-128 43 Prague 2, Czech Republic (239)

Zoltán Kovács Advanced Imaging Research Center, University of Texas Southwestern Medical Center, 5323 Harry Hines Boulevard, Dallas, TX 75390, USA (39)

Sara Lacerda Centre de Biophysique Moléculaire, UPR 4301, CNRS, rue Charles Sadron, F-45071 Orléans, France (71)

Zong-Wan Mao MOE Key Laboratory of Bioinorganic and Synthetic Chemistry, School of Chemistry, Sun Yat-Sen University, 135 West Xingangxi Road, Guangzhou 510275, P. R. China <cesmzw@mail.sysu.edu.cn> (403)

Kirsten E. Martin Department of Chemistry, Stony Brook University, 100 Nicolls Road, Stony Brook, NY 11790, USA (157)

Shaunna M. McLeod Department of Chemistry, Molecular Biosciences, Neurobiology, and Radiology, Northwestern University, 2145 Sheridan Road, Evanston, IL 60208, USA (347)

Thomas J. Meade Department of Chemistry, Molecular Biosciences, Neurobiology, and Radiology, Northwestern University, 2145 Sheridan Road, Evanston, IL 60208, USA <tmeade@northwestern.edu> (347, 425)

Lali Medina Kauwe Department of Biomedical Sciences, Cedars-Sinai Medical Center, Los Angeles, CA 90048, USA <medinal@cshs.org> (299)

Enikö Molnár Department of Physical Chemistry, University of Debrecen, Egyetem tér 1, H-4032 Debrecen, Hungary (39)

Jorge H. S. K. Monteiro Department of Chemistry, Humboldt State University, Arcata, CA 90048, USA <jorge.monteiro@humboldt.edu> (371)

Qaisar Nadeem Department of Chemistry, University of Zürich, Winterthurerstrasse 190, CH-8057 Zürich, Switzerland (195)

Daouda Ndiaye Centre de Biophysique Moléculaire, UPR 4301, CNRS, rue Charles Sadron, F-45071 Orléans, France (71)

Apurva Pandey Department of Chemistry, Stony Brook University, 100 Nicolls Road, Stony Brook, NY 11790, USA (157)

Suresh Pandey Bracco Diagnostics Inc., Technology Scouting, Monroe Township, NJ 08831, USA (315)

Carlos Platas-Iglesias Centro de Investigacións Científicas Avanzadas (CICA) and Departamento de Química, Facultade de Ciencias, Universidade da Coruña, CP-15071 A Coruña, Galicia, Spain <carlos.platas.iglesias@udc.es> (101)

Aurora Rodríguez-Rodríguez   Centro de Investigacións Científicas Avanzadas (CICA) and Departamento de Química, Facultade de Ciencias, Universidade da Coruña, CP-15071 A Coruña, Galicia, Spain (101)

Sergey Shuvaev   The Institute for Innovation in Imaging, A. A. Martinos Center for Biomedical Imaging, Massachusetts General Hospital, Harvard Medical School, Charlestown, MA 02129, USA <sshuvaev@mgh.harvard.edu> (1)

Josiane A. Sobrinho   Department of Chemistry, University of Nevada, Reno, NV 89557, USA (371)

Thomas J. Sørensen   Nano-Science Center and Department of Chemistry, University of Copenhagen, Universitetsparken 5, DK-2100 København Ø, Denmark <tjs@chem.ku.dk> (137)

Dezsö Szikra   Department of Medical Imaging, University of Debrecen, Nagyerdei Krt. 98, H-4032 Debrecen, Hungary <szikra.dezso@med.unideb.hu> (315)

Cai-Ping Tan   MOE Key Laboratory of Bioinorganic and Synthetic Chemistry, School of Chemistry, Sun Yat-Sen University, 135 West Xingangxi Road, Guangzhou 510275, P. R. China <tancaip@mail.sysu.edu.cn> (403)

James Teh   Department of Biomedical Sciences, Cedars-Sinai Medical Center, Los Angeles, CA 90048, USA <james.teh@cshs.org> (299)

Gyula Tircsó   Department of Physical Chemistry, University of Debrecen, Egyetem tér 1, H-4032 Debrecen, Hungary (39)

Ka Yan Tong   Department of Chemistry, The University of Hong Kong, Pokfulam Road, Chong Yuet Ming Chemistry Building, Room 503, Hong Kong, P. R. China <hoyuay@hku.hk> (437)

Éva Tóth   Centre de Biophysique Moléculaire, UPR 4301, CNRS, rue Charles Sadron, F-45071 Orléans, France <eva.jakabtoth@cnrs-orleans.fr> (71)

Imre Tóth   Department of Physical Chemistry and Department of Inorganic and Analytical Chemistry, University of Debrecen, Egyetem tér 1, H-4032 Debrecen, Hungary <imre.toth@science.unideb.hu> (39)

Brett A. Vaughn   Department of Chemistry, Stony Brook University, 100 Nicolls Road, Stony Brook, NY 11790, USA (157)

Jie Wang   MOE Key Laboratory of Bioinorganic and Synthetic Chemistry, School of Chemistry, Sun Yat-Sen University, 135 West Xingangxi Road, Guangzhou 510275, P. R. China (403)

Moritz Zaiss   Department of Neuroradiology, University Clinic Erlangen, Friedrich-Alexander Universität Erlangen-Nürnberg (FAU), D-91054 Erlangen, Germany (101)

Titles of Volumes 1–44 in the
Metal Ions in Biological Systems Series

edited by the SIGELs
and published by Dekker/Taylor & Francis (1973–2005)
https://www.routledge.com/Metal-Ions-in-Biological-Systems/book-series/
IHCMEIOBISY

Contents of Volumes in the
Metal Ions in Life Sciences Series

edited by the SIGELs

Volumes 1–4

published by John Wiley & Sons, Ltd., Chichester, UK (2006–2008)
<http://www.Wiley.com/go/mils>
<http://www.wiley.com/WileyCDA/Section/id-300350.html>

Volumes 5–9

published by the Royal Society of Chemistry, Cambridge, UK (2009–2011)
since 2015 by Walter de Gruyter GmbH, Berlin, Germany
<http://www.bioinorganic-chemistry.org/mils>
<https://www.degruyter.com/serial/MILS-B/html>

Volumes 10–16

published by Springer Science & Business Media BV, Dordrecht,
The Netherlands (2012–2014; MILS-10 to MILS-14)
and by Springer International Publishing AG, Cham, Switzerland
(2015–2016; MILS-15 and MILS-16)
<http://www.bioinorganic-chemistry.org/mils>

and from Volume 17 on

published by Walter de Gruyter GmbH, Berlin, Germany
<https://www.degruyter.com/serial/MILS-B/html>

Volume 3: The Ubiquitous Roles of Cytochrome P450 Proteins

Volume 7:   Organometallics in Environment and Toxicology

**Volume 8:   Metal Ions in Toxicology:
                Effects, Interactions, Interdependencies**

Volume 20: Transition Metals and Sulfur: A Strong Relationship for Life
Guest Editors: Martha E. Sosa Torres and Peter M. H. Kroneck

Comments and suggestions with regard to contents, topics, and the like for future volumes of the series are welcome.

1

Metal Ions in Bio-Imaging Techniques: A Short Overview

Sergey Shuvaev and Peter Caravan

The Institute for Innovation in Imaging, A. A. Martinos Center for Biomedical Imaging,
Massachusetts General Hospital, Harvard Medical School,
Charlestown, Massachusetts 02129, USA
<caravan@nmr.mgh.harvard.edu>

Abstract: Endogenous metal ions play a pivotal role in many biological systems, ranging from transition metal cofactors in essential enzymes to calcium ions in bones and cartilages. The idea of using exogenous metal ions as a diagnostic tool dates back to the first half of the 20th century when barium salts were orally administered to patients undergoing X-ray examination. Since that time, the field of molecular imaging has experienced remarkable changes, driven by the technological advances offered by modern imaging techniques. Each year brings hundreds of new molecular probes that are reported in preclinical studies and a few dozen enter human clinical trials. Such a massive data flow requires an appropriate classification, both by the type of imaging modality and chemical structure of the molecular probe. In this introductory chapter, recent advances and challenges in metal-based molecular imaging are discussed in four individual sections, covering magnetic resonance imaging (MRI), the nuclear medicine techniques of positron emission tomography (PET) and single photon emission computed tomography (SPECT), X-ray computed tomography (CT), and luminescent imaging, while a final section is dedicated to multimodal imaging, encompassing probes that can simultaneously produce a diagnostic signal detected by more than one imaging mode. Each of these sections, in turn, is subdivided into several parts, each dealing with a particular class of molecular probes based on their chemical structure, as well as the combination of imaging with therapy. We highlight representative examples of the different types of probes.

Keywords: imaging · magnetic resonance imaging · molecular probe · positron emission tomography · radiotracer

1.   INTRODUCTION

The advent of modern-day clinical diagnostic tools has revolutionized the healthcare system. A wide range of imaging modalities, now routinely available to patients, allows rapid and accurate diagnosis and prognosis, significantly improving the quality of medical care. However, the full potential of imaging techniques would never be unleashed without the aid of the chemistry community, who have immensely contributed by developing various types of molecular probes administered to patients during a radiological procedure. As imaging instrumentation and technology advance, so do the molecular probes, pushing the limits of imaging modalities. Fresh insights into biochemical mechanisms help to identify new molecular targets for imaging probes with higher specificity towards a particular pathology.

2019 marked the 150th anniversary of the Periodic Table of the Elements, a construct that still remains by far the most convenient layout to group and analyze the elements for a specific application. Metals comprise the majority of known

elements, whose unique properties make them essential for virtually all biological systems, including the most advanced and sophisticated one – humankind – who eventually adapted metal ions to create molecular tools to study the biological processes behind their own existence. In the realm of molecular imaging, there are strong correlations between an exerted functional property and the element's position in the periodic table. Metal complexes of biologically endogenous first-row transition metal ions, such as $Mn^{2+/3+}$ and $Fe^{2+/3+}$, have been extensively studied as potential alternatives to gadolinium-based contrast agents, while their heavier cousins from the platinum-group are well known to form very stable and bright luminescent complexes used for cellular staining and photodynamic therapy. Externally shielded f orbitals in lanthanides engender truly unique optical and magnetic properties, prompting their use as magnetic resonance imaging (MRI) and fluorescent probes, while their remarkable chemical stability also sparked interest in the production of their radioisotopes suitable for positron emission tomography (PET) or single photon emission computed tomography (SPECT) imaging.

Despite continuing advances, each imaging modality has its own limitations, and these limitations have tempted researchers to create multimodal probes that can take advantage of several imaging techniques. Although still nascent, the field of multimodal imaging has experienced a rapid growth in the past few years and is expected to continue a steady rise, approaching clinical practice. At the same time, combining diagnostic and therapeutic modalities within a single molecule is of great value in the emerging era of personalized medicine.

2.   MAGNETIC RESONANCE IMAGING/MAGNETIC RESONANCE SPECTROSCOPY PROBES

2.1.   Recent Advances in Gadolinium-Based Probes

Gadolinium-based contrast agents (GBCAs) represent one of the most widely prescribed class of drugs and by far the largest administered metal-based drug with over 30 million administrations per year worldwide [1]. About 40 % of all MRI scans employ a GBCA which is required for diagnosis, staging, or monitoring treatment across a range of pathologies from cancer to cardiovascular disease to neurological disorders. There have been nine different GBCAs approved for clinical use, including 6 linear (acyclic) and 3 macrocyclic chelates (Figure 1), although some of these have been withdrawn from the market. Over the last decade, safety concerns have been mounting in connection to clear evidence that gadolinium can cause a devastating syndrome called nephrogenic systemic fibrosis in patients with impaired renal function [2], and that some Gd is retained in the body in all patients and that this retention is cumulative with cumulative dosing. Despite initial claims to the contrary, even the more kinetically inert macrocyclic GBCAs are clearly retained in patients, although likely to a lesser extent than the linear chelates [3]. These observations forced prompt reactions from regulatory agencies, resulting in suspension of three linear GBCAs and limitations on two others in
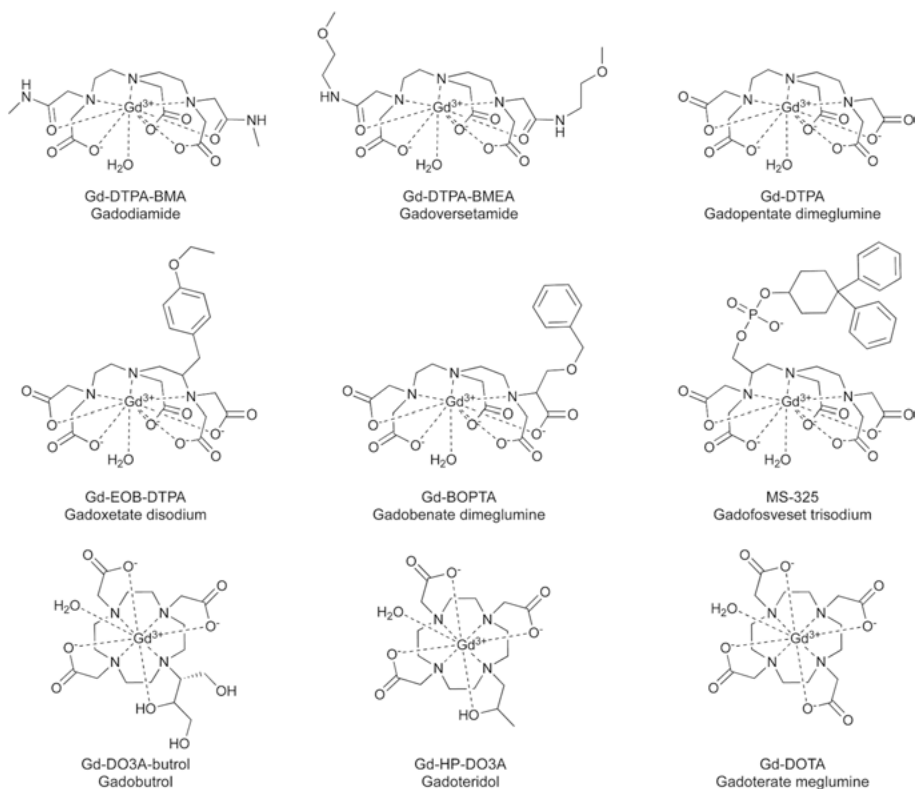
Figure 1. Structures of commercially available GBCAs. Top row: linear contrast agents. Middle row: specialty protein-binding GBCAs. Bottom row: macrocyclic contrast agents. Reproduced with permission from [2]; 2014, open access.

the EU and issuing warning labels for all GBCAs by the FDA to limit their concentration and frequency of administration [4, 5]. Given this new reality, multiple efforts have been made to (i) understand the human biodistribution and speciation of retained gadolinium in different tissues, (ii) estimate the long-term health implications of gadolinium retention in the body, (iii) design more kinetically inert gadolinium complexes, (iv) enhance longitudinal relaxivity to reduce the injected dose, and (v) suggest viable gadolinium-free alternatives. Although it is still prematurely to discuss the progress in the two first directions, the last three topics have been extensively discussed in the literature [6].

Due to its high kinetic inertness and thermodynamic stability, $[Gd(DOTA)(H_2O)]^-$ (Dotarem) is generally considered as a 'gold standard' in the chemistry of contrast agents and is widely used as a parent compound for derivatization. Despite its overall stability, the quest for even more kinetically inert GBCAs was boosted by reports that signs of Gd retention were observed in brains of children injected intravenously with Dotarem [7]. There are several strategies that have been utilized to improve kinetic inertness of gadolinium

complexes, such as conformational locking, reducing the basicity of the macrocycle, and rigidification of the structure [8]. Although the magnitude of the attained stability enhancement varies, each approach showed a potential to deliver a benefit that is even higher when these approaches are used synergistically, yielding remarkably stable gadolinium complexes [9, 10].

MRI contrast agents are not detected directly but are seen by the effect that they have on the relaxation times of nearby water molecules. Since water is detected, there is always a background signal and the contrast agent must be present at sufficient concentration to produce a measurable change in the water relaxation time to effect signal change. This requires low-to mid-micromolar concentrations per metal ion, depending on the tissue imaged and the properties of the contrast agent, i.e., its relaxivity. As a result, biological targets at the nano- and picomolar level generally cannot be detected with MRI, however, there are still numerous biologically relevant molecular targets that are present within this concentration range that can help to track abnormalities in metabolism associated with various diseases. Multiple examples of GBCAs devised for detection of metal ions (Ca^{2+}, Zn^{2+}, and Cu^{2+}), proteins, amino acids, redox-active molecules, pH, etc. [6] have been reported. Detection relies upon the probe either accumulating at the site of interest (targeting) and/or by modulation of the relaxivity value upon interaction with the desired molecule. Relaxivity modulation is usually achieved either by changing the hydration number, the solubility, the spin state, or restricting molecular tumbling upon interaction with the target (Figure 2).
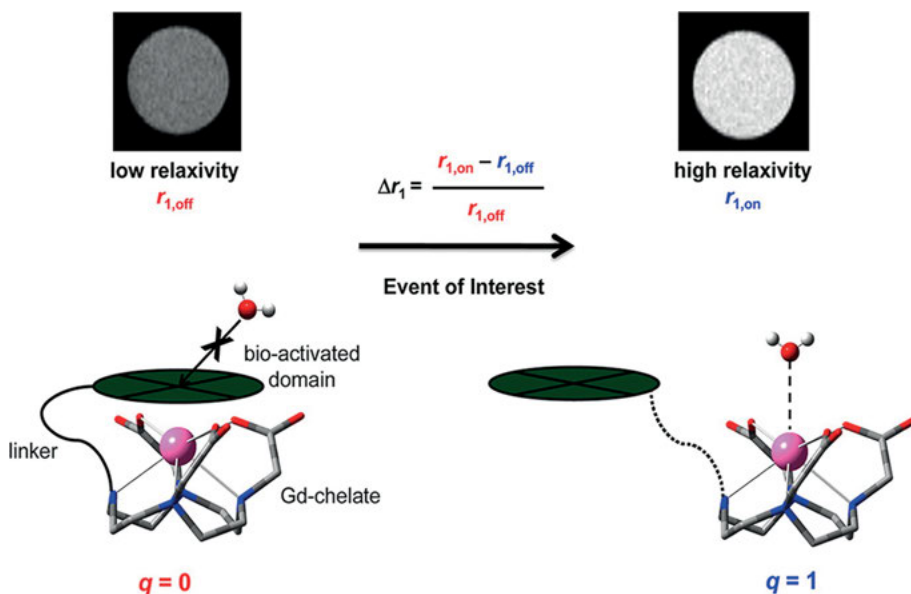
Figure 2. Hydration number (q) of GBCA can change in response to a biological event, modulating the relaxivity change. Reproduced with permission from [114]; copyright 2013, American Chemical Society.

This relaxivity modulation can be either reversible, where the probe returns to its original inactive state once the concentration of the targeted molecule falls below a certain threshold, or irreversible, when once activated the probe is in the "on state" until it has been metabolized or excreted. The former class allows for the detection of fluctuations in the concentration of the molecular target, as well as lighting up only the regions where it exceeds a threshold. On the other hand, irreversible probes produce a more intense signal and may be able to detect targets present at lower concentrations.

The signal change seen after probe administration depends on the probe's concentration and its relaxivity. One of the major drawbacks of responsive or activatable probes which change their relaxivity is that it is challenging to deconvolute the signal change arising from relaxivity or from concentration [11]. One approach to this problem is to design a multimodal probe. By co-injecting the GBCA with a surrogate that can provide a quantitative measure of concentration, such as $^{86}Y^{3+}$ for PET imaging [12] or $^{166}Ho^{3+}$ for SPECT imaging [13], the concentration of GBCA can be determined, allowing quantification of relaxivity and hence, the molecular target. On the other hand, the GBCA can be initially designed to incorporate additional modalities, as in the case of dual $Gd^{3+}/^{18}F$ MRI/PET [14] or dual $Gd^{3+}/^{19}F$ MRI/MRSI [15] probes. An alternate approach is to use a "matched" probe with similar pharmacokinetics to the responsive probe but that cannot undergo relaxivity change. Using a dual injection approach, each probe is administered and the signal change measured, and it is assumed that the difference in signal detected after their consequent injections is due to the difference in relaxivity in the area of interest, for example by using a pH-sensitive complex $[Gd(DOTP)]^{5-}$ and its pH non-responsive analogue $[Gd(DOTA-4AmP)]^{5-}$ (Figure 3) [16].
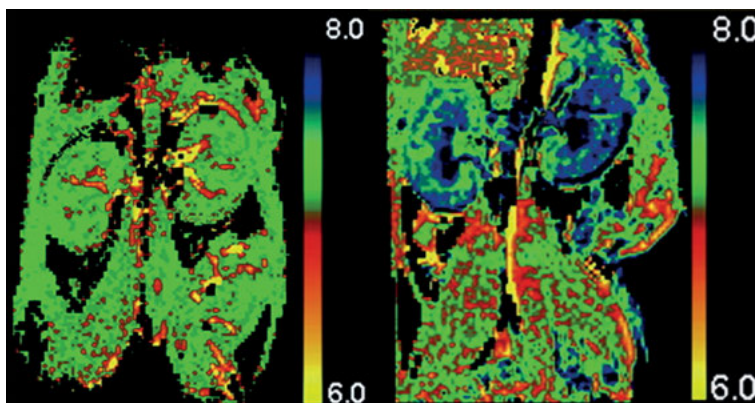
Figure 3. Calculated pH maps of mouse kidneys obtained using a dual injection approach with $[Gd(DOTP)]^{5-}$ (pH-sensitive) and $[Gd(DOTA-4AmP)]^{5-}$ (pH-insensitive) probes. pH values in the kidneys were higher after administration of acetazolamide (right) than before (left). Adapted with permission from [16]; copyright 2003, John Wiley and Sons.
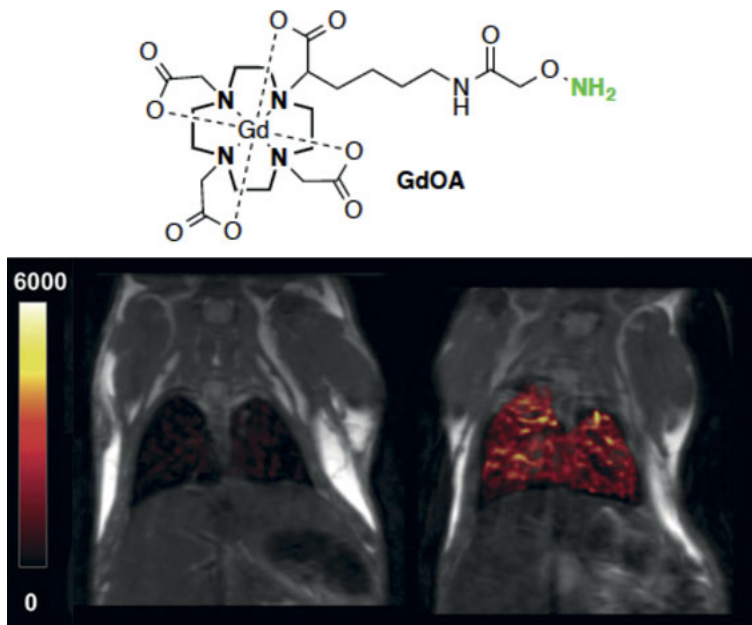
Figure 4. Coronal MR images of naïve (bottom left) and bleomycin-treated (bottom right) mice injected with a GdOA probe (top) for allysine binding. Reproduced with permission from [22]; copyright 2017, John Wiley and Sons.

Meanwhile, GBCAs binding to specific molecular targets have already demonstrated huge potential in tracking disease progression in preclinical and clinical studies. In particular, considerable progress has been made in developing probes for imaging fibrosis [17]. A few potential molecular targets present at micromolar concentration (fibrin [18], collagen [19], elastin [20], fibrin-fibronectin complex [21], allysine [22, 23]) have been imaged *in vivo* by probes comprising targeting vectors and one or several gadolinium-bearing chelates to increase the gadolinium payload per target, producing conspicuous contrast enhancement in disease areas. For instance, in active fibrosis, upregulated lysyl oxidase enzymes oxidize collagens and other matrix proteins to produce allysine at elevated concentrations that can be successfully detected by GBCAs bearing aldehyde-reactive moieties, clearly showing the areas of active fibrogenesis (Figure 4) [22, 23].

The pharmacokinetic properties of GBCAs significantly affect the signal enhancement in the desired region, as well as potential deposition of gadolinium in the body. For larger molecules bearing peptides or antibodies, the biological half-life and excretion pathways may be primarily dictated by these vectors rather than the nature of the gadolinium chelates. By varying the lipophilicity and charge of the probe, its excretion can shift between hepatobiliary and renal pathways, while also affecting the binding affinity to serum proteins and hence, the blood half-life of the probe. All these efforts aim at attaining an optimal interplay between rapid accumulation of the probe with concentration sufficient to

produce an adequate signal enhancement in the desired region with its fast elimination from the blood pool and adjacent tissues/organs. In the case of hard-to-reach regions, such as the brain, auxiliary moieties should be introduced to deliver GBCA to the desired destination.

2.2.   How Safe Are Gadolinium-Based Contrast Agents?

Following mounting evidence of *in vivo* deposition of gadolinium in various cohorts of patients, multiple efforts have been made to shed more light on molecular mechanisms promoting demetallation. In the wake of first reports linking nephrogenic systemic fibrosis (NSF) with administering GBCAs to patients with impaired renal function, first studies emerged addressing the speciation of gadolinium-containing compounds in the body, especially in subcutaneous areas [24]. The combination of various spectroscopic techniques soon revealed the presence of poorly soluble gadolinium phosphate, as well as various soluble species, including an intact GBCA (only for macrocyclic complexes) [25, 26]. The low glomerular filtration rate (GFR) in affected patients increases the biological half-life of GBCAs, increasing the rate of demetallation and subcutaneous gadolinium deposition. The incidence of NSF paralleled the lability of the administered probe, being the highest for neutral linear complexes. These findings caused the FDA to suspend administration of the three most labile GBCAs in patients with impaired renal function, whilst restricting the use of the others. Gadolinium (in some form) from all GBCAs is retained in most tissues, notably in the brain but in higher concentrations in kidney and bone. The half-life of GBCAs in patients with normal renal function is 60–90 min and it was long believed that gadolinium retention in the body in healthy individuals is negligible. However, the residual retention of gadolinium in the central nervous system (CNS), bones, and other tissues was observed in patients with normal kidney function who underwent multiple GBCA-enhanced MRI scans even years after their last GBCA dose [27, 28]. This cumulative gadolinium deposition also seems to strongly correlate with the lability of the GBCA in question, with the majority of cases reported in patients who were administered GBCAs with linear chelators (Figure 5) [29]. In healthy rats dosed repeatedly to build up a high level of Gd, the concentration of gadolinium in the brain experienced rapid decline within the first couple of weeks, followed by a plateau that was stable for at least a year [30]. On the other hand, the concentration of macrocyclic GBCAs was much lower at any given time point and was gradually decreasing within the year. These findings can be interpreted as an evidence of different gadolinium speciation in the brain for linear and macrocyclic GBCAs. The impaired excretion of linear GBCAs from the brain implies poor solubility of gadolinium-containing species, which are likely present in the form of inorganic salts, while slow but steady elimination of macrocyclic GBCAs suggests the presence of gadolinium in a soluble form, either as an intact probe, a complex with endogenous small molecules or an aggregate with a protein. However, these assumptions on gadolinium speciation require solid experimental evidence that should be produced in forthcoming studies.
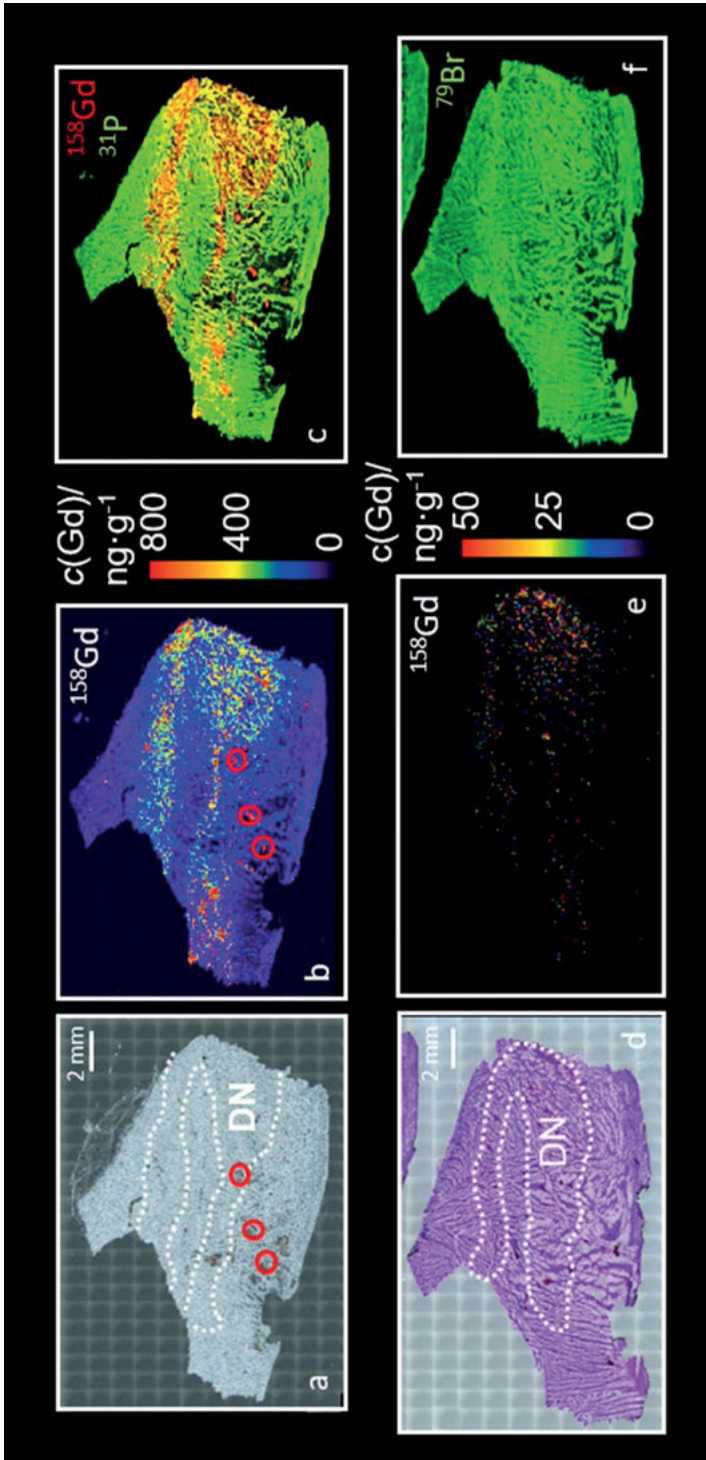
Figure 5. Post-mortem brain autopsy of a patient injected with Gd(DTPA-BMA) 726 days before death. Microscopic images of cerebellum before (**a**) and after H&E (hematoxylin and eosin) staining (**d**) with corresponding LA-ICP-MS mapping of gadolinium (**b**, **c**, **e**), and phosphorus (**c**) before H&E staining and bromine (**f**) after H&E staining. Three exemplary blood vessels are marked with red circles. Reproduced with permission from [115]; copyright 2015, Elsevier.

The initial reports on gadolinium deposition in the CNS were originally based on the residual signal in T_1-weighted scans of patients with a history of regular GBCA administration. However, it was later revealed that a similar signal enhancement was also observed in some patients who were never injected with GBCAs and is likely related to deposition of metals in the brain, other than gadolinium [31]. This finding shows the limitation of detecting gadolinium in patients based on T_1-weighted MRI scans alone and emphasizes the need to employ additional techniques as a cross-check.

2.3. Complexes of Transition Metals as a Potential Alternative to Gadolinium Probes

For a long time, GBCAs had been considered remarkably safe, and Gd(III) was seen as the preferred metal ion for contrast agents. Its 7 unpaired electrons, long electronic relaxation time, and fast water exchange kinetics make it a potent relaxation agent, while its high coordination number means that octadentate chelators can form extremely stable complexes with Gd(III) while still leaving a coordination site for an exchangeable water ligand. However, the long-standing consensus on the safety of GBCAs was challenged after their link to NSF had been established [4]. Although only linear GBCAs were initially scrutinized, more recent studies also argue that even significantly more stable macrocyclic GBCAs can be retained *in vivo* (especially in patients with compromised brain-blood barrier), leading to gadolinium deposition in various tissues. Notwithstanding these recent discoveries, it seems very unlikely that GBCAs will be discontinued in the short term, bearing in mind that acute GBCA toxicity has been reported only in a few patients [29]. Nevertheless, these controversies sparked interest in gadolinium-free contrast agents, particularly rekindling interest in manganese(II) and isoelectronic iron(III)-based contrast agents. Since Gd is not an essential element, there is no benefit to having retained Gd in the body, while for Fe or Mn, some retained metal ion may be incorporated into the body's pool of metal ion or regulated and eliminated through endogenous pathways.

There has been one Mn(II)-based contrast agent approved for human use. Mangafodipir (MnDPDP) was approved for liver imaging and was eventually discontinued [32]. This complex can be considered as a prodrug: the infused labile MnDPDP complex quickly releases free Mn^{2+} in the bloodstream and this is rapidly taken up by hepatocytes, giving rise to a strong signal enhancement in the liver [33]. Mn^{2+} is also taken up by the heart (cardiomyocytes), pancreas, and some glands via active transport through Ca^{2+} channels [34]. In fact, when MnDPDP was administered too rapidly, some acute cardiac effects were observed and so it was eventually administered as an infusion. The need for a slow infusion, the lack of a dynamic first pass effect, and a small overall market eventually resulted in MnDPDP being withdrawn for commercial reasons. However, its use did demonstrate that Mn^{2+}-based contrast agents, and even agents that release a large percentage of free Mn^{2+}, could be effective and safe.
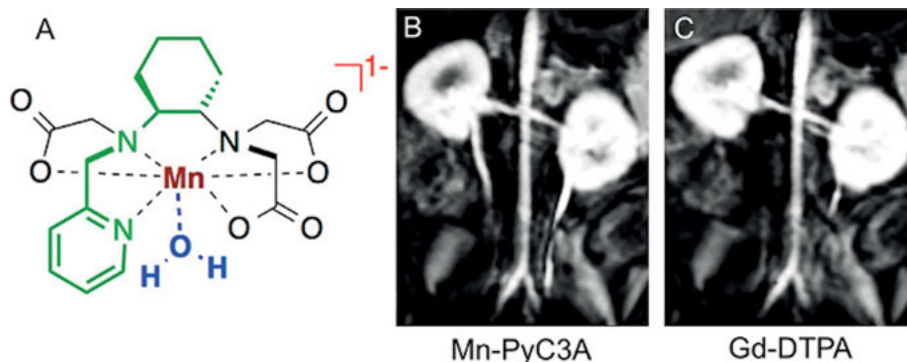
Figure 6. Structure of $[Mn(PyC3A)]^{1-}$ and comparison between T_{1w}-enhanced coronal MR images of baboon kidneys using $[Mn(PyC3A)]^{1-}$ and $[Gd(DTPA)]^{2-}$, showing abdominal aorta and arteries and renal arteries. Reproduced with permission from [116]; copyright 2016, John Wiley and Sons.

To avoid the myocardial toxicity associated with a high free Mn^{2+} concentration, highly stable manganese complexes that are excreted intact with a coordinated fast-exchanging water molecule for high relaxivity are needed. Thorough screening of both linear and macrocyclic chelators has yielded a number of kinetically inert Mn^{2+} complexes that are suitable for preclinical evaluation [35]. For instance, high *in vivo* stability of the $[Mn(PyC3A)]^{1-}$ complex showed equivalent imaging properties to FDA-approved $[Gd(DTPA)]^{2-}$ (Figure 6) [36]. Unlike MnDPDP, $[Mn(PyC3A)]^{1-}$ was excreted intact with no visible retention of manganese in the body, thereby minimizing the aforementioned risks associated with the toxicity of dissociated Mn^{2+}.

Also, a few examples of Mn^{3+}-based probes have been reported [37, 38], including metal sensors [39], where the lower magnetic moment of Mn(III) versus Mn(II) was compensated by a higher hydration number. Notably high relaxivities are observed with Mn(III) porphyrins [40].

Iron(III)-based contrast agents were proposed in the 1980s, but these were typically coordinatively saturated complexes with no exchangeable inner-sphere water ligand and their relaxivities were dwarfed by the Gd(III) complexes [41, 42]. While Fe(III) complexes can be extraordinarily stable with respect to Fe^{3+} dissociation, a number of other design factors must be considered. First, the potential for reduction followed by dissociation of Fe(II) must be considered. Second, the higher Lewis acidity of Fe(III) results in (1) slower water exchange of coordinated water ligands compared to Gd(III) and Mn(II); (2) the potential for deprotonation to a hydroxo ligand which undergoes very slow exchange; (3) potential for formation of μ-oxo-bridged dimers with no exchangeable water; (4) potential for reduction and generation of hydroxyl radicals, i.e. Fenton chemistry. However, we are now seeing innovative ligand design that is beginning to address these requirements [43, 44].

Since iron and manganese can access different oxidation states in biological systems, there exists opportunity for redox active probes which switch between low and high relaxivity states. For example, the judiciously designed redox active

[Mn(JED)]$^{-/2-}$ complex, featuring a ligand which supports both oxidation states of manganese (Mn^{2+} and Mn^{3+}) [45]. A recently unveiled redox-active [Fe(PyC3A)]$^{0/-}$ complex capable of detecting oxidative stress *in vivo* by switching from a spectroscopically silent ferrous state to a ferric state with a sufficiently high r$_1$, paves the way towards the new generation of iron-based activatable T$_1$ contrast agents.[46] Besides switching between Fe^{2+} and Fe^{3+} states, it is also possible to create a responsive T$_1$ probe based on the spin-crossover phenomenon in Fe^{3+} complexes. Although existing examples are limited to temperature, pressure, magnetic field, and light-responsive systems (none of them were tested *in vivo*), other more biologically relevant external stimuli, such as the presence of targeted molecules, can also be potentially used to trigger structural rearrangements in the coordination sphere of iron, thereby modulating a change in the spin state. The same spin-crossover phenomenon was also employed to build responsive Fe^{2+} probes, but low relaxivity values for the +2 oxidation state in both high- and low-spin configurations limit their clinical potential [47]. Alternately, a redox-active probe where the complex contains a redox active ligand, [Mn(H$_2$qtp1)]$^{+/2+}$, has been described [48].

There has also been great progress on europium(II) complexes from the Allen lab and others [49–51]. If not for a very short bench half-life, europium(II) would be an ideal candidate for use in contrast agents to complement an isoelectronic gadolinium(III). However, by turning vices into virtues, the high propensity for Eu(II) to oxidation was successfully utilized to image oxygen-deficient regions in the body – a hallmark of some malignant tumors (Figure 7) [49, 50]. As a complementary tool, a paraCEST signal for the T$_1$-silent Eu(III) species was acquired to track oxidized species in the body. However, extending the lifespan of Eu(II) species remains the major challenge for potential clinical translation [51, 52].
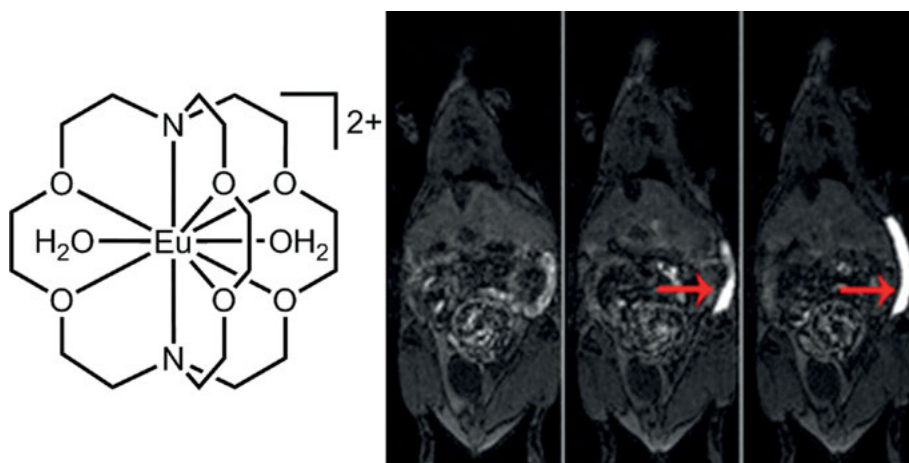
Figure 7. Structure of [Eu-222]$^{2+}$ and T$_{1w}$ MRI images of a mouse before subcutaneous injection (left), 3 min post-subcutaneous injection (middle), and 8 min post-subcutaneous injection (right). Red arrows indicate the areas of contrast enhancement. Reproduced with permission from [49]; copyright 2016, John Wiley and Sons.

2.4. Beyond Classic Magnetic Resonance Relaxation Probes: Direct Detection of Chemical Shift-Based Probes and Chemical Exchange Saturation Transfer (CEST)-Based Probes

Longitudinal and transverse relaxation rates are not the only read-outs available in MRI, although they are most likely to remain the most widely used in a foreseeable future since they provide the highest sensitivity for detection. Relaxation agents act on the high molar concentration of water in the body, giving rise to reasonably short acquisition times required for high-resolution images. Because of efficient relaxation and rapid water exchange, micromolar concentrations of T_1 relaxation agents are sufficient for contrast-enhanced MRI experiments. Another way to exploit the high signal of endogenous water for detection is chemical exchange. Fast exchange between protons of bulk water and labile protons in the molecular probe enable detection using a phenomenon called chemical exchange saturation transfer (CEST). These labile protons (e.g., of amines, amides, alcohols), whose chemical shift should be as far away as possible from the bulk water resonance, can be saturated by irradiating at their resonance frequency. Since these irradiated labile protons are being exchanged with protons from bulk water, the signal intensity of the latter decreases, giving rise to a meaningful signal.

For CEST to work, the slow exchange condition, $\omega\tau < 1$, must be met where ω is the chemical shift difference between bulk water and the exchangeable proton and τ is the mean time that this proton is bound to the probe (τ is the inverse of the exchange rate). In order to increase the CEST effect, chemical exchange should be as fast as possible while still meeting this slow exchange condition, and thus a larger ω value offers the potential for this. Paramagnetic ions can shift the resonance frequency of the labile proton further away from the water peak, therefore increasing the efficiency of saturation exchange as paraCEST probes. In responsive probes, external stimuli can modulate the magnitude of this chemical shift, with different species saturated at different frequencies [53]. For instance, an europium complex with a 4-hydroxybenzaldehyde moiety was used in a preclinical study to create a pH map in kidneys of healthy mice (Figure 8) [54]. Although CEST-based agents rely on detection of bulk water, the slower exchange rates involved relative to relaxation agents make them 1–2 orders of magnitude less sensitive. On the other hand, because the CEST effect is only detected when the appropriate saturation frequency is applied, the signal change due to CEST is very specific and does not require a reference, pre-injection image.

It should be noted that the paraCEST phenomenon is not limited to an exchange between bulk water and labile protons of the probe but can also be applied to any two exchanging pools that considerably differ in size and have concentrations sufficient to produce measurable and well-separated signals. For instance, fluorinated metal chelators when injected in a large excess compared to the concentration of endogenous metals, can be in fast exchange with the metal complex, shifting the ^{19}F resonance away from the signal produced by an unbound ligand [55–57].
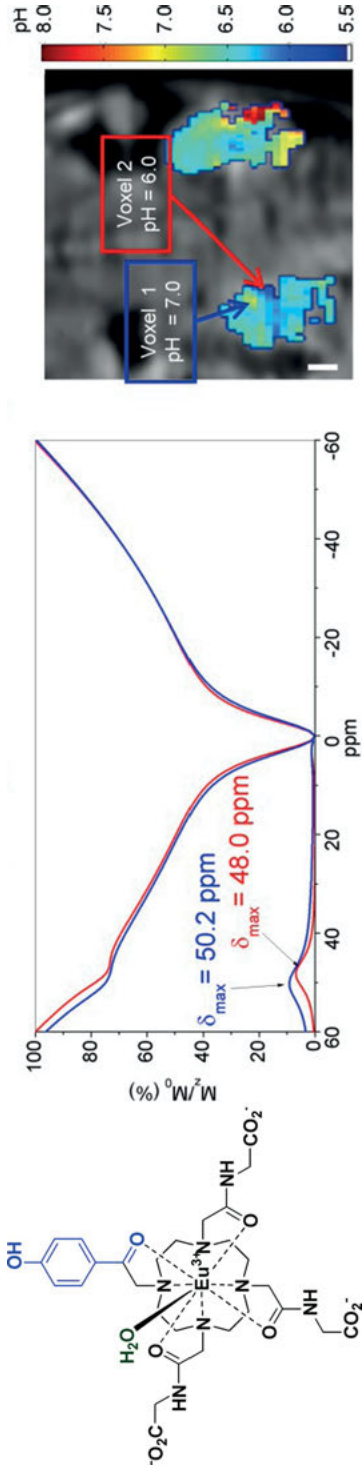
Figure 8.   Structure of the europium complex used for *in vivo* paraCEST imaging of pH in mouse lungs (left). Fitted CEST spectra and MTR$_{asym}$ profiles (middle) for two selected voxels in the left kidney (right). Adapted with permission from [54]; copyright 2015, John Wiley and Sons.
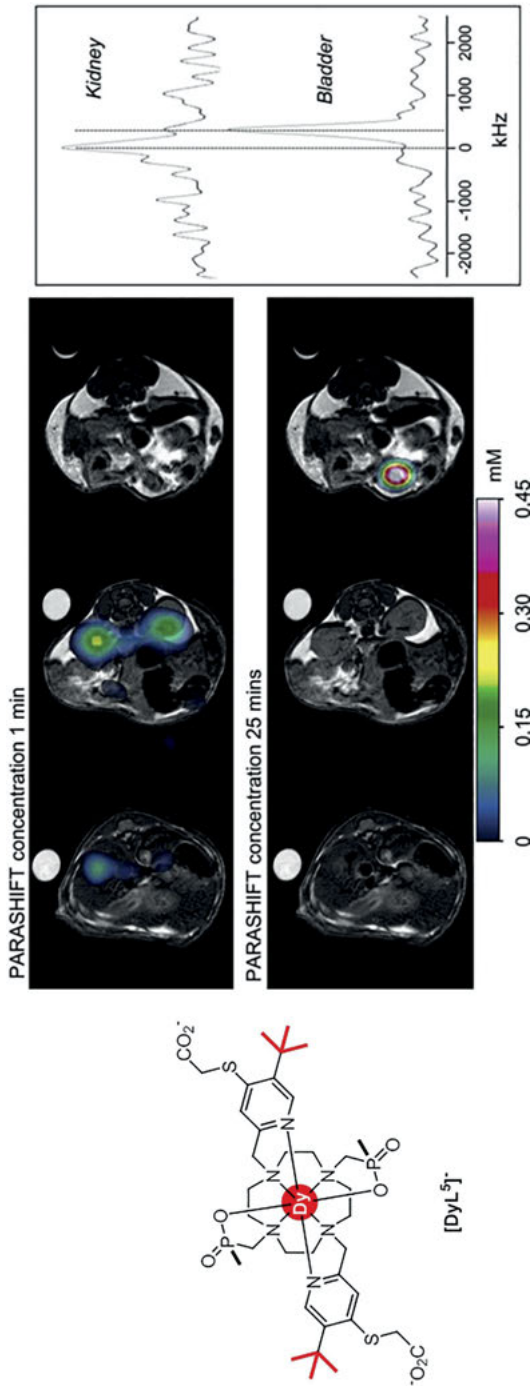
Figure 9. Structure of the dysprosium complex used for *in vivo* temperature measurement (left). Probe concentration contour map derived from MRSI signal of the probe overlaid with three slices of spin-echo images at 1 min (middle top) and 25 min (middle bottom) post-injection. Corresponding MRSI spectra acquired from the kidney (1 min post-injection) and bladder (25 min post-injection) showing a chemical shift, corresponding to 4.1K temperature decrease in the bladder. Adapted with permission from [58, 61]; copyright 2019, Elsevier and 2016, John Wiley and Sons, open access.

Besides imaging water, multiple attempts have been made to directly detect ^{1}H chemical shifts of endogenous molecules that are present at sufficiently high concentrations in the body, as well as exogenous tracers [58]. Magnetic resonance spectroscopic imaging (MRSI) is used clinically to detect metabolites like lactate and N-acetylaspartate that are present at high concentrations. However, for imaging, the much lower concentration compared to water requires sacrificing spatial resolution for signal. Overlap with very intense water and fat signals can also impede signal detection. The latter issue, however, might be completely overcome by detecting signals from other nuclei, such as ^{19}F or ^{31}P, but this would require the use of custom-built coils for detection and modification of the scanner for excitation. All other nuclei have a lower magnetogyric ratio compared to ^{1}H and are thus less sensitive for detection. Paramagnetic ions with very short electronic relaxation times, such as some lanthanides and first-row transition metals, can significantly shift resonances of NMR active nuclei without causing much line broadening. Stable metal complexes, dubbed as ParaSHIFT tracers, bearing a reporter group optimally positioned relative to the paramagnetic metal center to produce the biggest shift, have been proposed as temperature-, pH-, metal-, and anion-sensing probes [58].

By increasing the number of chemically equivalent protons in the reporter moiety (more signal) and placing them at an optimal distance to the lanthanide ion to reduce their T1 values (increased signal due to faster scanning and signal averaging) and move away their chemical shift, Parker and colleagues developed Dy^{3+} and Tm^{3+} complexes bearing two *tert*-butyl reporter groups responsible for considerably increased sensitivity, thereby reducing the concentration of the tracer needed in the injected dose to doses used with relaxation agents [59, 60]. An intrinsic quasi-linear temperature dependence of the chemical shift within the biologically relevant range in both lanthanide and transition metal Para-SHIFT probes was utilized in preclinical studies to map temperature in rats with millimeter resolution (Figure 9) [61]. Signal deconvolution is therefore required to detect external stimuli other than temperature and was implemented for pH-imaging of brain and liver tumors in rats using $[Tm(DOTP)]^{5-}$ complex [62, 63].

2.5.   Nanoparticle-Based Contrast Agents

Despite their many advantages, small-molecule-based probes require arduous structural modifications to tangibly change their pharmacokinetics, as well as switch between different imaging modalities. On the contrary, nanometer-sized particles show a great variation of blood circulation half-life as a function of size and shape, which can be easily and reproducibly synthesized with narrow size distributions. Furthermore, nanoparticles (NP) can contain multiple layers of different materials with precisely controlled thicknesses, thereby enabling detection with different imaging modalities, while their surface modification with a guiding vector enables their addressed delivery in the body [64, 65]. Regarding their structure, most of the NP-based MRI contrast agents fall into two major groups: (i) NPs with a para- or superparamagnetic core (e.g., Gd_2O_3, Mn_3O_4,
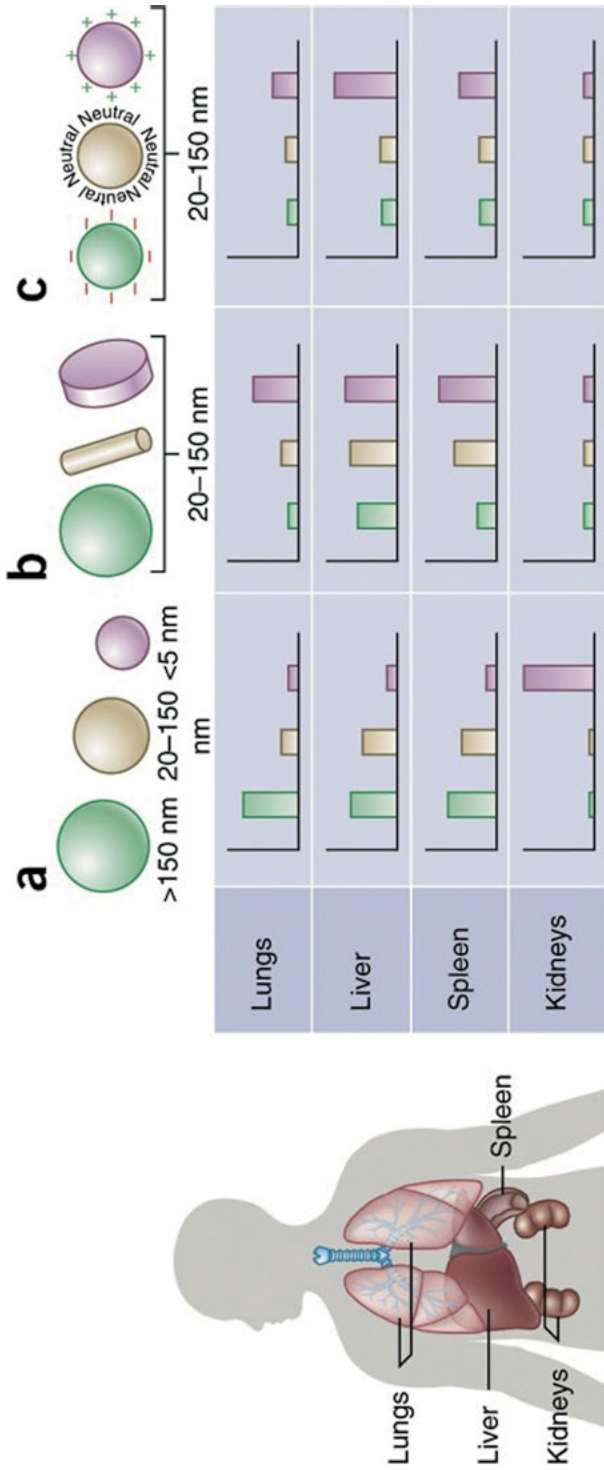
Figure 10. *In vivo* distribution and clearance of nanoparticles strongly depends on their size, shape, and surface charge. Reproduced with permission from [117]; copyright 2015, Springer Nature.

Fe_2O_3, Dy_2O_3, etc.) and (ii) NPs with a diamagnetic core/scaffold, which are superficially or internally anchored with paramagnetic complexes or can be directly detected, e.g., a perfluorocarbon core. Both classes have a significantly increased payload of imaging reporters compared to small-molecule GBCAs, thereby ensuing considerable relaxivity enhancement on a per-molecule basis [66].

Small nanoparticles (below 5 nm) can pass through the kidney via glomerular filtration giving rise to fast renal excretion, whereas larger and the most widely used nanoparticles are taken up by the liver and spleen through the action of macrophages in the reticuloendothelial system (RES, e.g., Kupffer cells in the liver) [67]. Depending on their size and surface modification, NPs can be taken up extremely rapidly by the RES or can evade the RES and have a long blood circulation (Figure 10). Compared to small molecules, NPs show poor extravasation into extravascular, interstitial spaces and so imaging targets outside the vascular system or liver usually takes hours to days and impacts the areas of their application as efficient contrast agents.

Applications include imaging the RES (liver and lymph nodes), the blood pool, cancerous lesions and inflammatory sites, tracking of stem cells, and implant labelling to name a few [65]. Despite a steadily growing number of NP-based contrast agents entering pre-clinical and clinical trials, only superparamagnetic iron oxide nanoparticles (SPIONs) as T_2 contrast agents have been approved by the FDA so far [68]. They were initially used to image hepatocellular carcinomas, as liver tumors generally lack Kupffer cells and therefore do not accumulate SPIONs and remain undarkened on MRI images. However, for similar reasons to MnDPDP described above, the approved SPIONs for liver imaging were discontinued for small market share. The only imaging nanoparticle now available is ferumoxytol, an intravenous iron replacement therapy that is sometimes used off-label for imaging in patients with impaired renal function [69]. Because NPs are in general not excreted from the body, care must be taken with respect to long term toxicity. The SPIOs that have been approved break down in the body and the iron is incorporated into the body's pool of iron. For non-endogenous metals, lack of elimination is a potential problem.

3. POSITRON EMISSION TOMOGRAPHY (PET) AND SINGLE PHOTON EMISSION COMPUTED TOMOGRAPHY (SPECT) PROBES

3.1. Overview of Positron Emission Tomography and Single Photon Emission Computed Tomography Probes

First reported studies using radiometals in humans date back to 1927, when ^{214}Bi was injected into patients to measure blood circulation between two arms [70]. However, the lack of adequate instrumentation at that time delayed the widespread use of radiometals in the clinic until the early 1960s, shortly after ^{99}Mo/^{99m}Tc generators were inaugurated [71]. The ^{99}Mo/^{99m}Tc generator is a device

that contains $^{99}MoO_4^{2-}$ adsorbed onto an alumina column. The $^{99}MoO_4^{2-}$ decays slowly to the metastable $^{99m}TcO_4^-$ ion which can be eluted off the column with saline while leaving the $^{99}MoO_4^{2-}$ on the column. Thus, each day the generator can be eluted to produce ^{99m}Tc for preparation of human doses. ^{99m}Tc has very favorable properties for imaging: a 6 hr half-life provides ample time for chemical synthesis and delivery of the dose, and a single gamma ray emitted at 140 keV is in the ideal range for detection by gamma cameras. Due to a relative ease of use and availability, these generators dominated the field for the next decades, largely expanding the radiochemistry of ^{99m}Tc compounds [72]. Other isotopes like ^{111}In, ^{201}Tl, and ^{67}Ga are used for SPECT imaging, albeit at a much smaller scale than ^{99m}Tc and this is mainly due to the more favorable imaging and half-life properties of ^{99m}Tc.

The last 20 years have seen a steady rise in the number of PET scanners available. PET has two major advantages over SPECT: first, PET, unlike SPECT, is a truly quantitative technique, and second, the spatial resolution of clinical (but not preclinical) PET scanners is 2–3 times higher than SPECT scanners. As PET became a part of routine clinical practice, the list of radiometals utilized for PET was expanded to include ^{64}Cu, ^{68}Ga, ^{82}Rb, and ^{89}Zr among others. This, in turn, prompted radiochemists to substantially expand their knowledge of coordination chemistry to search for compounds that are suitable for PET applications. The challenges faced were not as trivial as they might sound, since all chemical transformations occur in much more dilute solutions (in the pM-nM range) than usually studied by classic inorganic chemistry. Under these conditions, compounds may be more prone to dissociation and compete with trace metal impurities that can affect kinetics of radiolabeling and dissociation. Compared to other imaging modalities, low concentrations of the radioisotope in the injected dose greatly reduce the risk of chemical toxicity. As a rule of thumb, the decay half-life of the isotope used for PET imaging should match the biological half-life of the probe, to minimize the radiation exposure of patients. For example, rapidly excreted hydrophilic small molecules and peptides are usually labelled with ^{68}Ga ($t_{1/2}$ = 68 min), longer circulating antibody fragments with ^{64}Cu ($t_{1/2}$ = 12.7 h), while antibodies and nanoparticles usually bear ^{89}Zr ($t_{1/2}$ = 78.4 h) chelates.

The chemistry requirements vary with the isotope used. Different metals require different chelators depending on their fundamental chemical properties. In general, one requires rapid (minutes) and complete incorporation of the radiometal into the molecule. For antibodies and other heat sensitive compounds, labeling must be performed under mild conditions. Dissociation of the radiometal should be slow on the timescale of the imaging study. For antibody-based imaging applications where PET can be performed many days after injection, it is obviously critical that the radiometal remains associated with the antibody such that the image reflects the distribution of the antibody and not some metabolites.

The popularity of these aforementioned radionuclides rests on three major factors: (i) their well-established ability to form stable complexes, (ii) their optimal decay parameters, and (iii) their availability. Although the first two factors play an important role, easy access to sufficient quantities of a particular radiometal is key towards its widespread application in the clinic. There are dozens
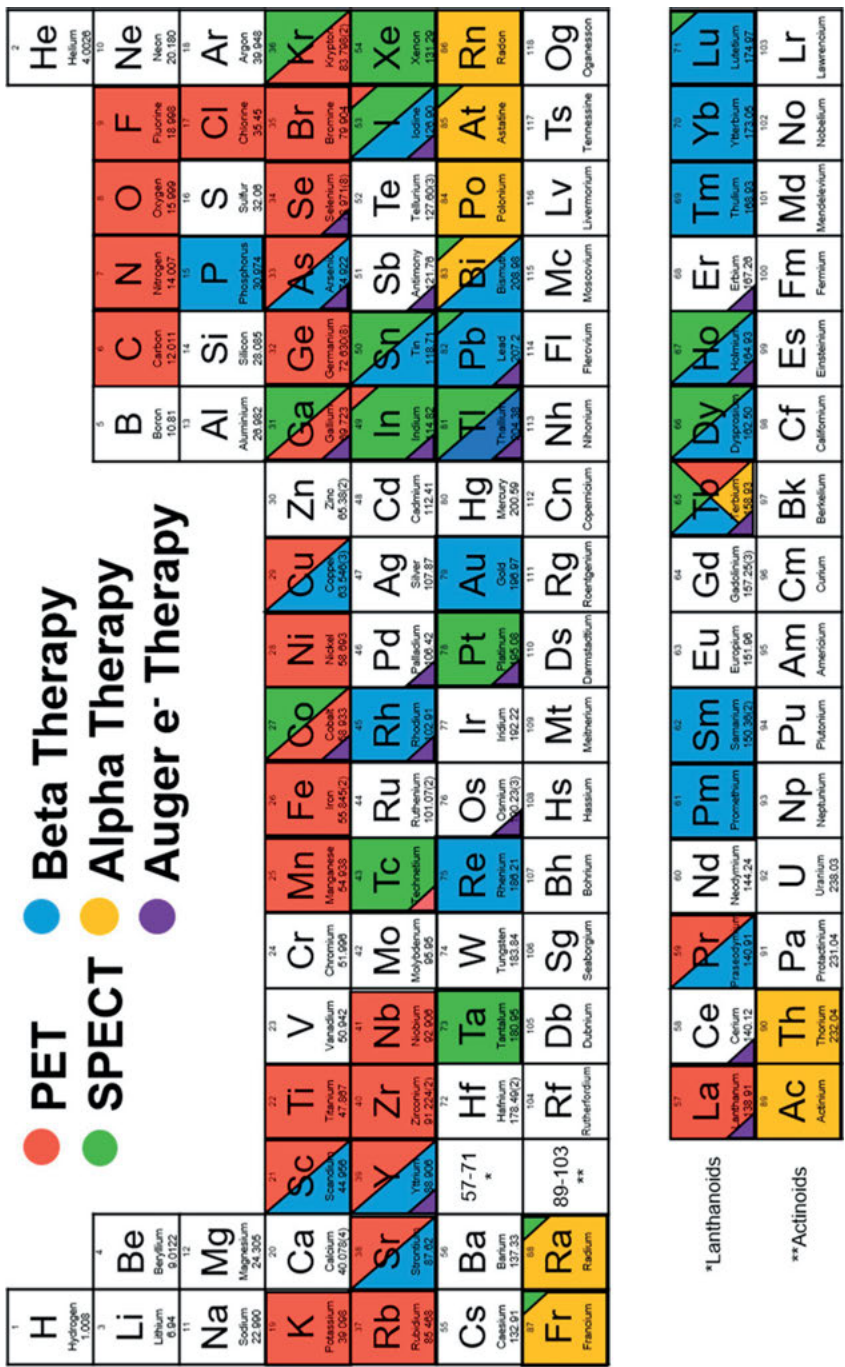
Figure 11. Color-coded periodic table denoting elements that are currently used or can be potentially used as radiopharmaceuticals for diagnostics and therapeutics. Reproduced with permission from [73]; copyright 2019, American Chemical Society.

of radiometal isotopes in the periodic table that combine a suitable half-life with an optimal decay profile but remained inaccessible in sufficient quantitates until very recently (Figure 11). However, this situation has been changing lately with many new isotopes now available for preclinical studies, while more radionuclides are expected to be within reach of radiochemists in the nearest future. This will, in turn, prompt the development of new chelators that form stable complexes with these emerging isotopes [73, 74].

3.2. Opportunities in Multimodal Imaging

The last decade marked the appearance of clinical simultaneous PET/MRI scanners that combine remarkable sensitivity of PET with high anatomical resolution and soft tissue contrast offered by MRI. Although the hardware combines both modalities, almost all studies rely on using PET-only and MRI-only imaging probes, and there is an opportunity to develop dual PET/MRI probes. In fact, co-injection of both an MRI tracer and its PET-active surrogate brings advantages, such as quantification of the MRI probe concentration, paving the way towards the use of responsive MRI probes *in vivo*.

However, only a few elements of common paramagnetic ions used for contrast-enhanced MRI imaging have isotopes suitable for PET imaging, such as ^{52}Mn and ^{55}Fe. However, the most obvious candidate – gadolinium – lacks any PET active isotopes, and therefore other ions such as ^{86}Y which have similar chemical and biological properties should be used instead [75]. Close chemical resemblance between Tc(I) and Re(I) complexes prompted the use of isostructural Tc(I)/Re(I) pairs that showed potential as SPECT/optical [76–77] dual probes, taking advantage of bright luminescence generated by rhenium complexes.

3.3 Combining PET Imaging and Radiotherapy: Theranostic Agents

Radiotherapeutic agents have a proven track record of successful treatment of disseminated diseases, where other therapeutic options are often inefficient. Currently, this field is dominated by two isotopes: ^{90}Y, emitting high-energy β^- particles, and ^{177}Lu, emitting low-energy β^- particles and γ-radiation [78]. However, the success of the field is spurring more research. Special emphasis has been placed on radiometals with a theranostic potential that either can combine PET with a therapeutic effect (e.g., ^{68}Ga PET with ^{177}Lu therapy) or that have a matched theranostic pair (e.g., ^{44}Sc/^{47}Sc, ^{161}Tb/^{155}Tb, ^{64}Cu/^{67}Cu, etc.) [79]. The idea is that PET can be used not only for disease detection and treatment monitoring, but because it is quantitative, the PET signal can be used to compute the optimum dose of the radiotherapy that provides killing power to the tumor while minimizing side effects from off-target accumulation. Ideally, this should be performed with metals that have an isotope for PET and an isotope for therapy to ensure that the pharmacokinetics are identical for imaging and therapy.

Along with developing economically viable routes to produce new isotopes on a large scale, their coordination chemistry has been widely explored as well. Even though DOTA-based chelators have been shown to form sufficiently stable complexes with most radiometals, a quest for more metal-specific ligands has never ceased. For instance, the majority of new radiometals entering preclinical and clinical trials are rare earths that share very similar chemical properties across the series, albeit slightly differ in ionic radii [80]. The latter gives rise to a variation of kinetic stability of the complex as a function of a metal ion used, requiring different chelators for smaller and larger rare earth ions [81, 82].

Once the radionuclide has decayed, daughter radiometals preferentially should be still bound to the same chelator to mitigate any toxic effect caused by a free metal. However, in the case of α-emitters, high recoil energy inevitably leads to dechelation of daughter ions, frequently leading to toxic side effects that significantly hamper clinical translation [83]. Multiple efforts have been focused on accelerating the delivery of a radiotherapeutic agent to the targeted region to minimize the release of the free metal outside the malignancy. Furthermore, various nano-sized carriers have been also reported that can efficiently confine the recoiled daughter isotopes inside.

4. COMPUTED TOMOGRAPHY CONTRAST AGENTS

4.1. Metal-Based Complexes

X-ray computed tomography (CT) remains the most frequently used diagnostic technique worldwide (ca. 70 million scans in the US alone), allowing visualization of pathological conditions in both soft tissues and bones [84]. To increase the contrast in CT images, various contrast agents containing barium and iodine are routinely used in the clinic, although common side effects observed at high concentrations required for injection prompted the search for alternatives [85].

Although the quest for new iodinated organic molecules with reduced adverse side effects still attracts a lot of attention, other elements that can absorb X-rays more efficiently than iodine or barium have been under scrutiny [86]. For instance, lanthanide ions have a higher mass attenuation coefficient than iodine and hence, should produce substantially higher contrast per atom. Furthermore, the widespread use of gadolinium contrast agents allowed their off-label use as dual MRI/CT contrast agents, although the dose required for CT contrast is much higher than for MRI. However, low molar loading of gadolinium at clinically approved concentrations of GBCAs produced suboptimal contrast enhancement, encouraging the development of contrast agents with higher molar loading. In particular, promising results were obtained by the Bayer company with their remarkably stable Bay-576 probe containing three Hf^{4+} ions per complex, allowing a significant reduction of the radiation dose as compared to commercially available iodinated agents in preclinical studies (Figure 12) [87, 88].
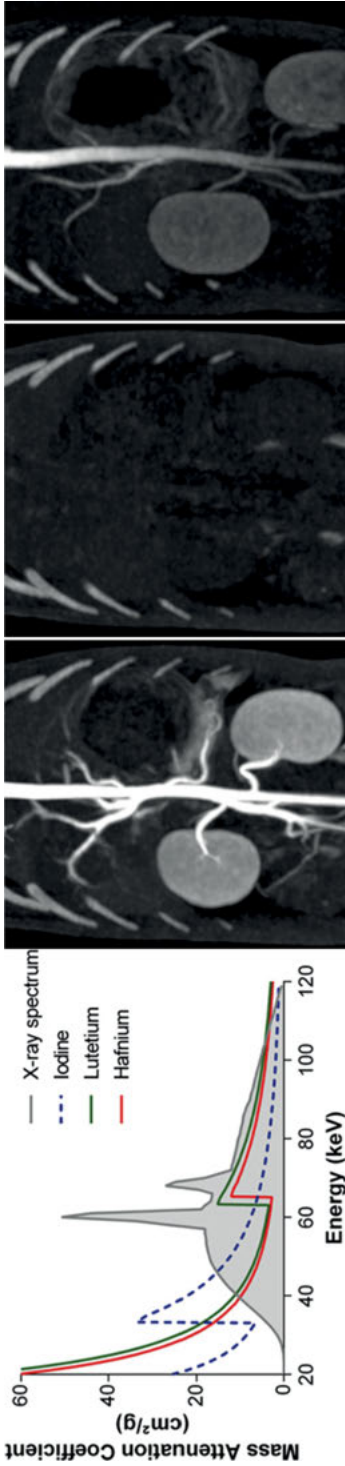
Figure 12. (**a**) Mass attenuation coefficients for iodine, lutetium, and hafnium, along with a typical emission spectrum of 120 kV X-ray sources used in CT. (**b**) CT angiography scans of a rabbit using Bay-576, (**c**) without contrast, and (**d**) with a clinically used iopromide. Adapted with permission from [87]; copyright 2017, American Chemical Society.
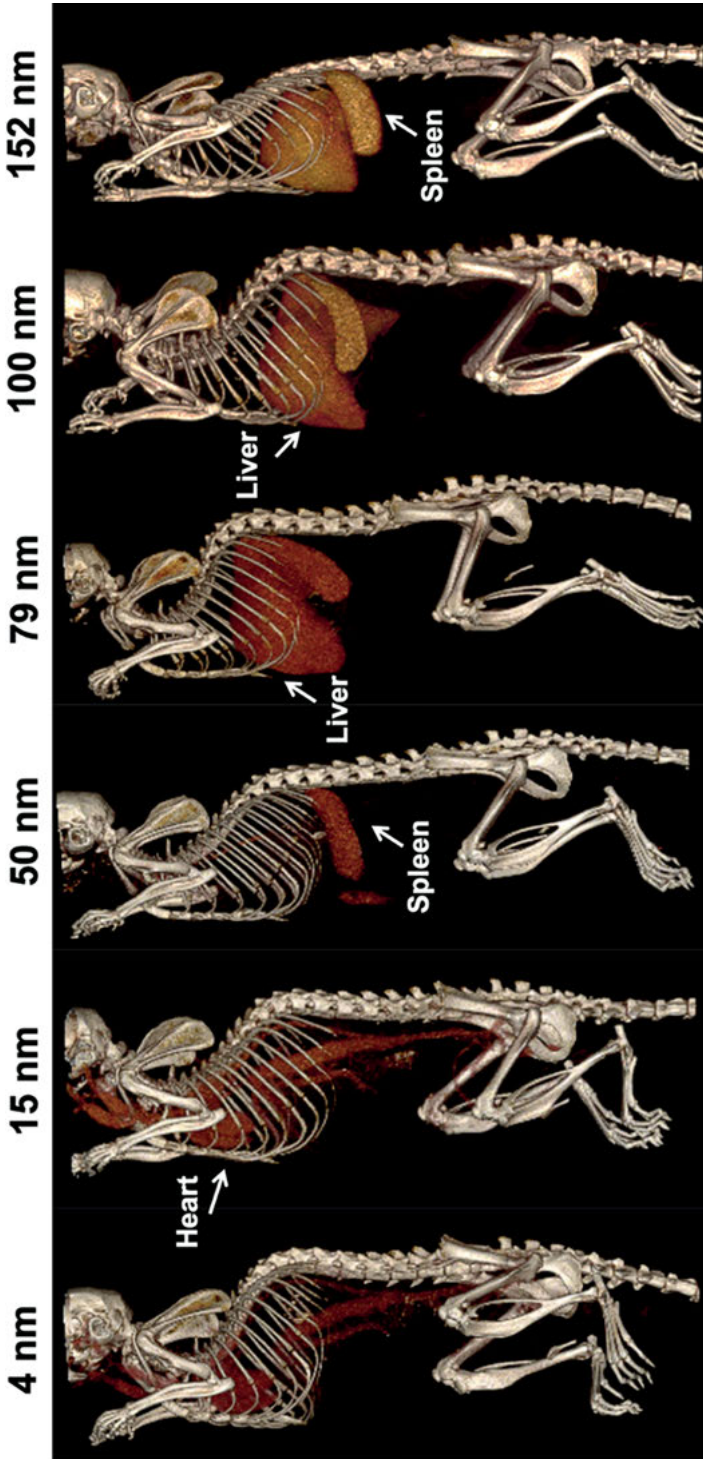
Figure 13. Three-dimensional CT images of mice injected with gold nanoparticles of different diameters show variability in biodistribution. Reproduced with permission from [93]; copyright 2019, Springer Nature, open access.

Following the same path, metal clusters with relatively high metal loadings have also been proposed as potential contrast agents, however, their likely toxicity at clinically relevant concentrations precluded their use in preclinical studies [89, 90].

4.2. Nanoparticles

In terms of metal loading, discrete complexes and clusters can hardly compete with nanoparticles, which also exhibit much longer circulation times in the blood, resulting in a higher uptake in targeted tissues and organs. With 2.7-times higher attenuation coefficient than iodine, relatively innocuous gold can form highly uniform nanoparticles with narrow size distribution, which have been extensively studied as prospective CT probes [91, 92]. Ease of surface functionalization allows facile tuning of pharmacokinetics and biodistribution (Figure 13). The surge in popularity of gold nanoparticles as antitumor therapeutic agents resulted in extensive preclinical and clinical trials, which may eventually facilitate the clinical translation of gold nanoparticles for imaging [93].

Nanoparticles containing other heavy metals have been also thoroughly investigated, including lanthanide nanoparticles. Their versatile physical properties enable multimodal imaging (MRI, CT, luminescence), and also make them suitable for molecular targeting. Unlike other imaging modalities (MRI, PET, SPECT), the low sensitivity of CT imaging makes it extremely hard to create targeted contrast agents, as there are only a few molecular targets that are expressed in sufficient concentrations to generate a detectable response. Calcium ions are one of the suitable candidates targeted by CT contrast agents to visualize bone defects [94]. A rapidly growing area of cell therapy can also benefit from CT-assisted *in vivo* tracking using nanoparticle-labelled cell strains [95].

Progress in devising new CT probes has been partially invigorated by advances in scanner design. For instance, recently inaugurated spectral CT instruments allow simultaneous detection of elements with different attenuation coefficients, providing a better contrast between the probe and surrounding tissues [96]. Such 'multi-color' imaging also enables concomitant tracking of several contrast agents with different elemental compositions – something that can greatly facilitate direct comparison with commercially available tracers in preclinical studies [97, 98].

5. OPTICAL PROBES

5.1. Novel Metal-Based Agents for Cellular Staining
and Therapy

Among many functional properties of metal complexes, photoluminescence is probably one of the most widely studied. Versatility of structural and electronic properties enables facile access to compounds with finely tuned photophysical properties, in many cases outperforming purely organic small molecules, in par-

ticular with regard to photophysical and chemical stability. This ensured their widespread use as cellular tracers, which are often exposed to harsh enzymatic conditions and extended signal acquisition times.

The advent of commercially available far-field super-resolution optical microscopy techniques enabled tracking chemical changes on a sub-cellular level and strengthened the interest in responsive fluorescent probes, while the progress in multi-photon imaging that allows deeper tissue penetration heralds the surge in subcutaneous diagnostic applications. However, there is a large variation in sensitization and emission mechanisms among different classes of metal complexes that markedly affect the photophysical properties (such as Stokes shift, lifetime of an excited state, width of emission bands, etc.), and therefore should be considered separately.

5.2.   First-Row Transition Metal Complexes

Despite the fact that first-row transition metal complexes attract much less attention than their heavier counterparts, there is still ongoing progress in devising new cellular stains utilizing these ions. The majority of publications solely focus on luminescent complexes with a spectroscopically silent Zn^{2+} ion that in most cases has very little impact on electronic structure of coordinated ligands and serves only as a structural pivot.

However, an unceasing inclination towards sustainable solutions in chemistry invigorated interest in other earth-abundant first-row transition metals that can at least partially replace less copious platinum-group metals [99]. Unlike widely used Ru(II) ($4d^6$) and Ir(III) ($5d^6$) emitters, low-lying d orbitals in $3d^6$ metal ions (Cr^0, Fe^{2+}, Co^{3+}) usually result in non-emissive depopulation of the metal-to-ligand charge transfer (MLCT) state, however multiple attempts to enhance ligand-field splitting have been made, which are primarily focused on increasing the symmetry and rigidity of the complex, as well as designing ligands with strongly donating binding groups [100].

Despite sizeable progress in this area, existing complexes possess lifetimes in the nano- to picosecond regime at best, precluding efficient time-gating of the emission signal and hence, their use in cellular imaging. More promising results have been attained for $3d^3$ complexes, particularly Cr^{3+}, that can emit in the biologically relevant near-IR window with long lifetimes and high quantum yields, although no cellular studies have been reported to date [101].

5.3.   Platinum Group Metal Complexes

Weaker binding between the nucleus and 4d/5d electrons in platinum group metals results in an unimpeded radiative decay of the MLCT state, giving rise to long-lived emission with high quantum yields. High sensitivity of the emission profile even to minor changes in the structure provides easy access to families of fine-tuned luminescent dyes [102]. The plethora of cellular stains based on

platinum metals has received scrutiny over the past two decades, ranging from organelle-specific tracers to sensors of messenger molecules and molecular thermometers. Along with detecting changes in the emission spectrum, long-lived excitation states in phosphorescent complexes enable efficient time-gating and therefore the ability to track changes in the lifetime of an excited state, allowing multimodal imaging. Although naturally broad, emission bands in platinum group metals may originate from various excited states that respond differently to external stimuli potentially giving rise to a ratiometric response with a quantitative readout.

One of the substantial benefits offered by many of these complexes is their therapeutic effect against cancer cells, including photoactivated chemotherapy [103]. Unlike the classic photodynamic therapy that relies on high oxygen content to generate a therapeutic effect, longer lived and lower lying electronic states in complexes of platinum group metals produce a cytotoxic effect even in hypoxic areas – a frequently encountered hallmark of cancerous tissues. The first and the only compound designed for photoactivated chemotherapy that has entered clinical trials so far is the Ru(II) complex TLD1433 that is believed to act as a 'supercatalyst' by generating more than one reactive species per every photon absorbed (Figure 14) [104]. A small cohort of patients with non-muscle-invasive bladder cancer was intravenously administered with TLD1433, which was excited by an optic fiber positioned in the bladder. After optimization of the therapeutic dose, two patients who received treatment showed no recurrence
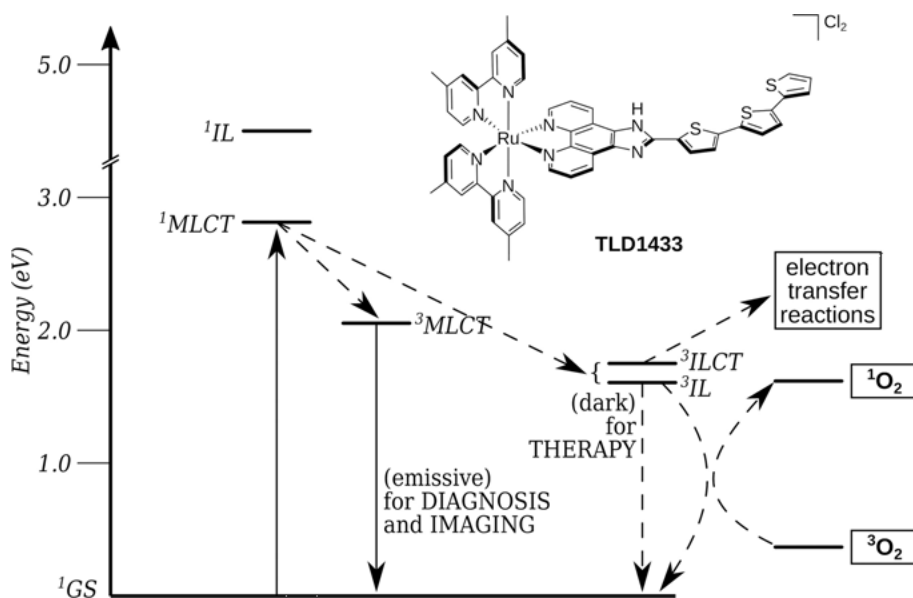
Figure 14. Structure of TLD1433 and the simplified electronic scheme depicting transitions responsible for diagnostic and therapeutic effects. Reproduced with permission from [104]; copyright 2019, American Chemical Society.

of the disease after 180 days post injection, giving a green light for a Phase II study with a much larger patient population. Notwithstanding these encouraging data, the need to deliver the excitation source close to the affected region remains the primary drawback of photoactivated chemotherapy. In some cases, this obstacle can be surpassed by developing compounds efficiently absorbing in the near-IR region, which can be excited by an external source.

5.4.   Lanthanide Complexes

Lanthanides also possess unique chemical and physical properties. Effectively shielded from outer 5s and 5p orbitals, 4f electrons experience very little impact from ligated atoms resulting in much larger spin-orbit coupling compared to ligand-field splitting. This results in very narrow emission bands and a very long-lived emission lifetime in lanthanide complexes, which along with very large 'pseudo-Stokes' shifts make them ideal candidates for cell imaging, as has been proved by a myriad of organelle-specific stains [105]. In addition, very intense circularly polarized luminescence (CPL) signals make it possible to probe chiral analytes and trace complexes of opposite helicities inside the cells using an emerging CPL microscopy [106]. Although the energies of f-f transitions in lanthanides are virtually unaffected by the changes in coordination environment, relative intensities of certain bands, called hypersensitive, may experience dramatic changes, as in the case of Eu^{3+} complexes.

Numerous reversible ratiometric probes based on the hypersensitivity of the emission spectrum have been devised to measure changes in pH, temperature, metal concentration, etc., although only a few have been actually used for cellular imaging of living cells [107]. The most recent advances in the field are associated with the emergence of IR-emitting discrete Yb^{3+} probes that have quantum yields sufficient for cellular and preclinical imaging use [108].

Higher photophysical and chemical stability of lanthanide-doped nanosized phosphors along with affinity of nanoparticles towards malignant tumors via the enhanced permeability and retention effect, makes them attractive candidates for fluorescence-guided surgery in cancer patients. In contrast to discrete metal complexes, lanthanide nanoparticles can have bright emission in the near-IR region that considerably minimizes autofluorescence from biological tissues, while alterations in their size and doping content allows for fine-tuning of the excitation wavelength to maximize the absorption with commercially available excitation sources [109].

6.   MULTIMODAL IMAGING PROBES

Incorporation of 2 or more imaging reporters into a probe is readily performed, although consideration should be given as to the need for such a probe. As discussed above, each modality has different limits of detection and thus a multi-
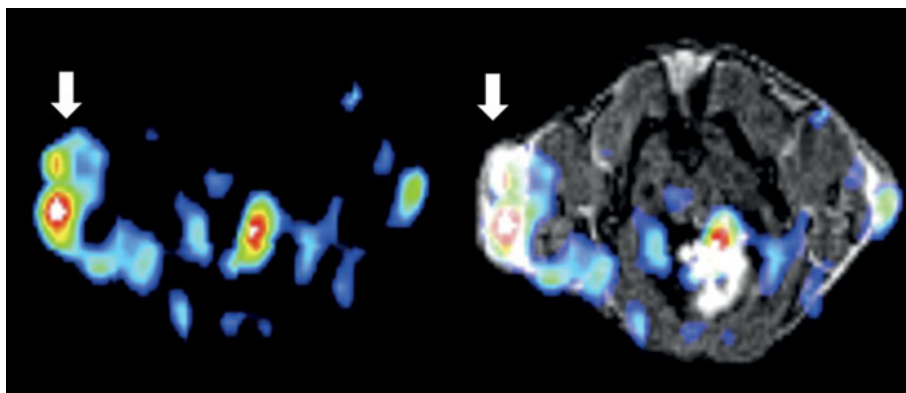
Figure 15. PET and overlaid PET/MRI scan in a tumor-bearing mouse using a dual ^{68}Ga/^{nat}Gd probe. The white arrow indicates the tumor site. Reproduced with permission from [110]; copyright 2015, American Chemical Society.

modal probe will only be as sensitive as the least sensitive detection modality. By combining multiple reporters in a single molecule, the chemistry is necessarily more complex, and the resultant molecule may have pharmacokinetic properties that suffer compared to the individual components. While the advent of commercial PET/MRI and PET/CT scanners make it possible to easily detect a dual probe with both modalities, it is not always obvious what the value would be in doing so. Rather would image one property with a PET probe and a second property with a separate MRI probe provide more information than a dual probe detectable by both modalities. Accepting these caveats, there are applications where multiple imaging readouts provide value, and these are discussed below.

As mentioned previously, the ability to use PET to quantify the *in vivo* concentration of an MRI contrast agent allows the determination of *in vivo* relaxivity. It also allows the detection of MRI probes at concentrations below detection limits of MRI. For instance, the close chemical resemblance of ^{nat}Gd and ^{86}Y complexes was successfully exploited to trace the fate of GBCAs in an animal model, exemplifying the huge potential of concomitant PET/MRI acquisition of similar pairs for assessing the safety of novel MRI tracers [12].

On the other hand, spiking the responsive MRI contrast agent with its PET-active surrogate potentially allows *in vivo* quantification of the signal [14]. Dual PET/MRI molecular probes have been proposed and assessed in preclinical studies (Figure 15) [110].

Fluorescence imaging (FLI) to guide surgery, e.g., to identify sentinel lymph nodes or to identify tumor margins, is a rapidly growing field. FLI also provides unprecedented spatial resolution with the ability to image subcellularly with high sensitivity. Dual FLI/MRI or FLI/PET (or SPECT) probes can thus be designed that are given systemically and the whole body imaged with MRI or PET, and then more directed FLI performed at regions where the probe localizes (Figure 16) [111]. Multiple dually labelled antibodies, peptides, small molecules and nanoparticles have been used in preclinical studies. Similarly, in the validation
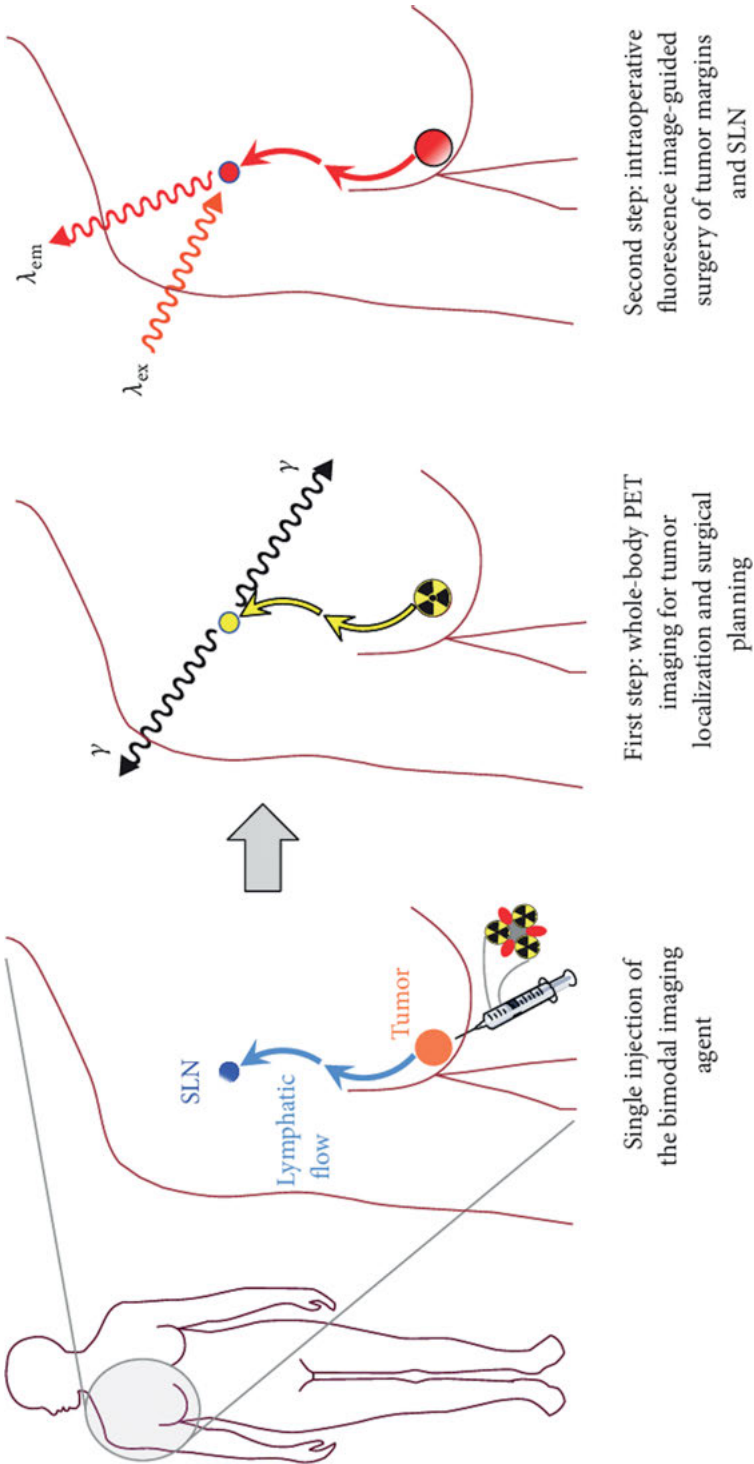
Figure 16. Schematic representation of the proposed use of dual PET/FLI probes for the preoperative diagnostic and subsequent intraoperative fluorescent imaging. Reproduced with permission from [111]; 2014, open access.

of molecular probes, FLI provides indispensable evidence *ex vivo* to show the microscopic distribution of the probe, e.g., is it extra- or intracellular, and if the latter were in the cell.

A major drawback of fluorescence imaging is low tissue penetration due to energy loss experienced by excitation and emission light beams that can be partially mitigated by employing the Cherenkov effect [112]. In a dual PET/FLI probe, when a positron emitted by a radioisotope exceeds the speed of light, a Cherenkov emission is generated that can be used as an excitation source for the fluorescent probe [113]. This can remove the need for an external excitation source for both imaging and guided surgery, although the latter would require the use of isotopes with longer half-lives, increasing the radiation burden on the surgeon and the patient.

7. CONCLUDING REMARKS AND FUTURE DIRECTIONS

Since its inception in the middle of the 20th century, molecular imaging has developed into a vast interdisciplinary field, encompassing chemistry, physics, biology, engineering, and computer sciences. Metal-based tracers are now widely used in various imaging modalities alone or in combination, delivering a positive change to early diagnosis of most deadly diseases, thereby increasing the survival rate. The discovery of more specific biomarkers facilitates the development of more selective molecular probes, allowing distinguishing between closely related pathological conditions, thus improving the efficacy of treatment. Eventually, this will revolutionize the landscape of modern clinical imaging, offering a patient-tailored diagnostic. The chapters of this volume provide a state-of-the-art account of metal-based imaging probes and theranostics across a range of modalities and provide a roadmap to future innovations.

In this book, readers will learn about recent advances in gadolinium-based contrast agents (Chapter 2), as well as substantial progress in the development of gadolinium-free alternatives, including manganese-containing probes (Chapter 3) and iron oxide nanoparticles (Chapter 9). Reflecting mounting interest beyond conventional T_1 contrast agents, separate chapters are dedicated to paraCEST (Chapter 4) and paramagnetic ^{19}F MRSI probes (Chapter 8).

Combining imaging with therapy, theranostic MRI probes, discussed in Chapters 10 and 12, allow tracking of a therapeutic load, thus offering potential benefits for personalized treatment plans. Thinking outside the synthetic chemistry box, intrinsically biocompatible endogenous paramagnetic biomolecules have been long considered as potential contrast agents and have been recently joined by magnetotactic bacteria, whose potential as MRI contrast agents is explored in Chapter 15.

Technetium radiotracers remain a cornerstone of modern SPECT imaging and despite their very long history, are still in an active development (Chapter 7). On the other hand, more chemically diverse tracers for PET imaging now include compounds with almost a dozen of different radiometals, all having distinctive radiochemical properties and diagnostic applications, as discussed in Chapter 6.

The exploration of new radiometals for PET imaging is largely driven by the availability of therapeutic radioisotopes of the same element, so they can form theranostic 'matched pairs' which have a large clinical potential (Chapter 11).

Although metal-based luminescent probes still have a very limited clinical application, various cellular probes have been developed and widely used for luminescent imaging. They proved to be especially useful for imaging cancer cells (Chapter 13) and staining particular organelles, such as mitochondria (Chapter 14). Selective visualization of molecular targets, such as metal ions and proteins, can be of particular interest for tracking down the processes underlying many pathological conditions, for instance neurodegenerative diseases (Chapter 16). Unique optical properties of lanthanides can greatly expand the potential of optical imaging, especially in terms of signal quantification (Chapter 5).

Recent technological advances in X-ray computed tomography rekindled the interest in developing new contrast agents, with significantly improved resolution and multichannel detection now allowing visualization of specific molecular targets (Chapter 17).

ABBREVIATIONS

4AmP	1,4,7,10-tetraazacyclododecane-1,4,7,10-tetrakis(acetamido-methylenephosphonic acid)
CEST	chemical exchange saturation transfer
CNS	central nervous system
CPL	circularly polarized luminescence
CT	computed tomography
DOTA	1,4,7,10-tetraazacyclododecane-1,4,7,10-tetraacetic acid
DOTP	1,4,7,10-tetraazacyclododecane-1,4,7,10-tetra(methylene phosphonic acid)
DPDP	dipyridoxyl diphosphate
DTPA	diethylenetriaminepentaacetic acid
FDA	Food and Drug Administration
FLI	fluorescence imaging
GBCA	gadolinium-based contrast agent
GdOA	2,2′,2″-(10-(5-(2-(aminooxy)acetamido)-1-carboxypentyl)-1,4,7,10-tetraazacyclododecane-1,4,7-triyl)triacetic acid gadolinium complex
GFR	glomerular filtration rate
H_2qtp1	N-(2,5-dihydroxybenzyl)-N,N′,N′-tris(2-pyr-idinylmethyl)-1,2-ethanediamine
IR	infrared
JED	2,2′-(ethane-1,2-diylbis(((2-hydroxyphenyl)(pyridin-2-yl)methyl)azanediyl))diacetic acid
MLCT	metal-to-ligand charge transfer
MnDPDP	Mangafodipir
MRI	magnetic resonance imaging

MRSI	magnetic resonance spectroscopic imaging
MTR	magnetization transfer ratio
NP	nanoparticle
NSF	nephrogenic system fibrosis
paraCEST	paramagnetic chemical exchange saturation transfer
PET	positron emission tomography
PyC3A	N-picolyl-N,N′,N′-trans-1,2-cyclohexenediaminetriacetate
RES	reticuloendothelial system
SPECT	single-photon emission computed tomography
(U)SPION	(ultra)small superparamagnetic iron oxide nanoparticle

REFERENCES

1. J. Lohrke, T. Frenzel, J. Endrikat, F. C. Alves, T. M. Grist, M. Law, J. M. Lee, T. Leiner, K. C. Li, K. Nikolaou, M. R. Prince, H. H. Schild, J. C. Weinreb, K. Yoshikawa, H. Pietsch, *Adv. Ther.* **2016**, *33*, 1–28.
2. M. Le Fur, P. Caravan, *Metallomics* **2019**, *11*, 240–254.
3. N. Murata, L. F. Gonzalez-Cuyar, K. Murata, C. Fligner, R. Dills, D. Hippe, K. R. Maravilla, *Invest. Radiol.* **2016**, *51*, 447–453.
4. R. J. McDonald, D. Levine, J. Weinreb, E. Kanal, M. S. Davenport, J. H. Ellis, P. M. Jacobs, R. E. Lenkinski, K. R. Maravilla, M. R. Prince, H. A. Rowley, M. F. Tweedle, H. Y. Kressel, *Radiology* **2018**, *289*, 517–534.
5. V. M. Runge, *Invest. Radiol.* **2018**, *53*, 571–578.
6. J. Wahsner, E. M. Gale, A. Rodriguez-Rodriguez, P. Caravan, *Chem. Rev.* **2019**, *119*, 957–1057.
7. M. C. Rossi Espagnet, B. Bernardi, L. Pasquini, L. Figa-Talamanca, P. Toma, A. Napolitano, *Pediatr. Radiol.* **2017**, *47*, 1345–1352.
8. T. J. Clough, L. Jiang, K. L. Wong, N. J. Long, *Nat. Commun.* **2019**, *10*, 1420.
9. C. Robic, M. Port, O. Rousseaux, S. Louguet, N. Fretellier, S. Catoen, C. Factor, S. Le Greneur, C. Medina, P. Bourrinet, I. Raynal, J. M. Idee, C. Corot, *Invest. Radiol.* **2019**, *54*, 475–484.
10. L. Dai, C. M. Jones, W. T. K. Chan, T. A. Pham, X. Ling, E. M. Gale, N. J. Rotile, W. C. Tai, C. J. Anderson, P. Caravan, G. L. Law, *Nat. Commun.* **2018**, *9*, 857.
11. L. A. Ekanger, M. J. Allen, *Metallomics* **2015**, *7*, 405–421.
12. M. Le Fur, N. J. Rotile, C. Correcher, V. Clavijo Jordan, A. W. Ross, C. Catana, P. Caravan, *Angew. Chem. Int. Ed. Engl.* **2020**, *59*, 1474–1478.
13. E. Gianolio, L. Maciocco, D. Imperio, G. B. Giovenzana, F. Simonelli, K. Abbas, G. Bisi, S. Aime, *Chem. Commun.* **2011**, *47*, 1539–1541.
14. L. Frullano, C. Catana, T. Benner, A. D. Sherry, P. Caravan, *Angew. Chem. Int. Ed. Engl.* **2010**, *49*, 2382–2384.
15. E. Gianolio, R. Napolitano, F. Fedeli, F. Arena, S. Aime, *Chem. Commun.* **2009**, 6044–6046.
16. N. Raghunand, C. Howison, A. D. Sherry, S. Zhang, R. J. Gillies, *Magn. Reson. Med.* **2003**, *49*, 249–257.
17. P. Desogere, S. B. Montesi, P. Caravan, *Chemistry* **2019**, *25*, 1128–1141.
18. K. Overoye-Chan, S. Koerner, R. J. Looby, A. F. Kolodziej, S. G. Zech, Q. Deng, J. M. Chasse, T. J. McMurry, P. Caravan, *J. Am. Chem. Soc.* **2008**, *130*, 6025–6039.
19. C. T. Farrar, E. M. Gale, R. Kennan, I. Ramsay, R. Masia, G. Arora, K. Looby, L. Wei, J. Kalpathy-Cramer, M. M. Bunzel, C. Zhang, Y. Zhu, T. E. Akiyama,

M. Klimas, S. Pinto, H. Diyabalanage, K. K. Tanabe, V. Humblet, B. C. Fuchs, P. Caravan, *Radiology* **2018**, *287*, 581–589.

20. M. R. Makowski, A. J. Wiethoff, U. Blume, F. Cuello, A. Warley, C. H. Jansen, E. Nagel, R. Razavi, D. C. Onthank, R. R. Cesati, M. S. Marber, T. Schaeffter, A. Smith, S. P. Robinson, R. M. Botnar, *Nat. Med.* **2011**, *17*, 383–388.

21. F. Ye, X. Wu, E. K. Jeong, Z. Jia, T. Yang, D. Parker, Z. R. Lu, *Bioconjug. Chem.* **2008**, *19*, 2300–2303.

22. P. A. Waghorn, C. M. Jones, N. J. Rotile, S. K. Koerner, D. S. Ferreira, H. H. Chen, C. K. Probst, A. M. Tager, P. Caravan, *Angew. Chem. Int. Ed. Engl.* **2017**, *56*, 9825–9828.

23. E. A. Akam, E. Abston, N. J. Rotile, H. R. Slattery, I. Y. Zhou, M. Lanuti, P. Caravan, *Chem. Sci.* **2020**, *11*, 224–231.

24. S. J. George, S. M. Webb, J. L. Abraham, S. P. Cramer, *Br. J. Dermatol.* **2010**, *163*, 1077–1081.

25. M. F. Tweedle, *Magn. Reson. Imaging* **2016**, *34*, 1377–1382.

26. M. Birka, K. S. Wentker, E. Lusmoller, B. Arheilger, C. A. Wehe, M. Sperling, R. Stadler, U. Karst, *Anal. Chem.* **2015**, *87*, 3321–3328.

27. D. R. Roberts, S. M. Lindhorst, C. T. Welsh, K. R. Maravilla, M. N. Herring, K. A. Braun, B. H. Thiers, W. C. Davis, *Invest. Radiol.* **2016**, *51*, 280–289.

28. M. L. Lord, D. R. Chettle, J. L. Grafe, M. D. Noseworthy, F. E. McNeill, *Radiology* **2018**, *287*, 96–103.

29. J. Garcia, S. Z. Liu, A. Y. Louie, *Philos. Trans. A Math. Phys. Eng. Sci.* **2017**, *375*.

30. G. Jost, T. Frenzel, J. Boyken, J. Lohrke, V. Nischwitz, H. Pietsch, *Radiology* **2019**, *290*, 340–348.

31. T. Kanda, Y. Nakai, S. Aoki, H. Oba, K. Toyoda, K. Kitajima, S. Furui, *Jpn. J. Radiol.* **2016**, *34*, 258–266.

32. M. P. Federle, J. L. Chezmar, D. L. Rubin, J. C. Weinreb, P. C. Freeny, R. C. Semelka, J. J. Brown, J. A. Borrello, J. K. T. Lee, R. Mattrey, A. H. Dachman, S. Saini, B. Harmon, M. Fenstermacher, R. E. Pelsang, S. E. Harms, D. G. Mitchell, H. H. Halford Iii, M. W. Anderson, C. D. Johnson, I. R. Francis, J. G. Bova, P. J. Kenney, D. L. Klippenstein, G. S. Foster, D. A. Turner, A. E. Stillman, R. C. Nelson, S. W. Young, R. H. Patt, M. Rifkin, S. E. Seltzer, S. B. Gay, R. O. Robison, P. F. Sherwin, R. Ballerini, *J. Magn. Res. Imag.* **2000**, *12*, 186–197.

33. J. Crossgrove, W. Zheng, *NMR Biomed.* **2004**, *17*, 544–553.

34. N. B. Spath, G. Thompson, A. H. Baker, M. R. Dweck, D. E. Newby, S. I. K. Semple, *Heart* **2019**, *105*, 1695–1700.

35. Z. Garda, E. Molnar, F. K. Kalman, R. Botar, V. Nagy, Z. Baranyai, E. Brucher, Z. Kovacs, I. Toth, G. Tircso, *Front. Chem.* **2018**, *6*, 232.

36. E. M. Gale, H. Y. Wey, I. Ramsay, Y. F. Yen, D. E. Sosnovik, P. Caravan, *Radiology* **2018**, *286*, 865–872.

37. A. Barandov, B. B. Bartelle, B. A. Gonzalez, W. L. White, S. J. Lippard, A. Jasanoff, *J. Am. Chem. Soc.* **2016**, *138*, 5483–5486.

38. W. Cheng, I. E. Haedicke, J. Nofiele, F. Martinez, K. Beera, T. J. Scholl, H. L. Cheng, X. A. Zhang, *J. Med. Chem.* **2014**, *57*, 516–520.

39. A. Barandov, B. B. Bartelle, C. G. Williamson, E. S. Loucks, S. J. Lippard, A. Jasanoff, *Nat. Commun.* **2019**, *10*, 897.

40. T. Lee, X. A. Zhang, S. Dhar, H. Faas, S. J. Lippard, A. Jasanoff, *Chem. Biol.* **2010**, *17*, 665–673.

41. J. A. Davies, S. G. Dutremez, C. M. Hockensmith, R. Keck, N. Richardson, S. Selman, D. A. Smith, C. W. Ulmer, L. S. Wheatley, J. Zeiss, *Academic Radiology* **1996**, *3*, 936–945.

42. M. F. Tweedle, *Radiology* **2018**, *286*, 409–411.

43. P. Boehm-Sturm, A. Haeckel, R. Hauptmann, S. Mueller, C. K. Kuhl, E. A. Schellenberger, *Radiology* **2018**, *286*, 537–546.

44. E. M. Snyder, D. Asik, S. M. Abozeid, A. Burgio, G. Bateman, S. G. Turowski, J. A. Spernyak, J. R. Morrow, *Angew. Chem. Int. Ed. Engl.* **2020**, *59*, 2414–2419.

45. E. M. Gale, C. M. Jones, I. Ramsay, C. T. Farrar, P. Caravan, *J. Am. Chem. Soc.* **2016**, *138*, 15861–15864.

46. H. Wang, V. C. Jordan, I. A. Ramsay, M. Sojoodi, B. C. Fuchs, K. K. Tanabe, P. Caravan, E. M. Gale, *J. Am. Chem. Soc.* **2019**, *141*, 5916–5925.

47. J. Wang, C. Gondrand, F. Touti, J. Hasserodt, *Dalton Trans.* **2015**, *44*, 15391–15395.

48. M. Yu, S. L. Ambrose, Z. L. Whaley, S. Fan, J. D. Gorden, R. J. Beyers, D. D. Schwartz, C. R. Goldsmith, *J. Am. Chem. Soc.* **2014**, *136*, 12836–12839.

49. L. A. Ekanger, L. A. Polin, Y. Shen, E. M. Haacke, M. J. Allen, *Contrast Media Mol. Imaging* **2016**, *11*, 299–303.

50. L. A. Ekanger, L. A. Polin, Y. Shen, E. M. Haacke, P. D. Martin, M. J. Allen, *Angew. Chem. Int. Ed. Engl.* **2015**, *54*, 14398–14401.

51. A. M. Funk, V. Clavijo Jordan, A. D. Sherry, S. J. Ratnakar, Z. Kovacs, *Angew. Chem. Int. Ed. Engl.* **2016**, *55*, 5024–5027.

52. L. A. Basal, Y. Yan, Y. Shen, E. M. Haacke, M. Mehrmohammadi, M. J. Allen, *ACS Omega* **2017**, *2*, 800–805.

53. É. Tóth, C. S. Bonnet, *Inorganics* **2019**, *7*.

54. Y. Wu, S. Zhang, T. C. Soesbe, J. Yu, E. Vinogradov, R. E. Lenkinski, A. D. Sherry, *Magn. Reson. Med.* **2016**, *75*, 2432–2441.

55. Y. Yuan, Z. Wei, C. Chu, J. Zhang, X. Song, P. Walczak, J. W. M. Bulte, *Angew. Chem. Int. Ed. Engl.* **2019**, *58*, 15512–15517.

56. A. Bar-Shir, N. N. Yadav, A. A. Gilad, P. C. van Zijl, M. T. McMahon, J. W. Bulte, *J. Am. Chem. Soc.* **2015**, *137*, 78–81.

57. A. Bar-Shir, A. A. Gilad, K. W. Chan, G. Liu, P. C. van Zijl, J. W. Bulte, M. T. McMahon, *J. Am. Chem. Soc.* **2013**, *135*, 12164–12167.

58. A. C. Harnden, D. Parker, N. J. Rogers, *Coord. Chem. Rev.* **2019**, *383*, 30–42.

59. P. Harvey, A. M. Blamire, J. I. Wilson, K.-L. N. A. Finney, A. M. Funk, P. K. Senanayake, D. Parker, *Chem. Sci.* **2013**, *4*, 4251–4258.

60. A. M. Funk, K. N. A. Finney, P. Harvey, A. M. Kenwright, E. R. Neil, N. J. Rogers, P. Kanthi Senanayake, D. Parker, *Chem. Sci.* **2015**, *6*, 1655–1662.

61. P. K. Senanayake, N. J. Rogers, K. N. Finney, P. Harvey, A. M. Funk, J. I. Wilson, D. O'Hogain, R. Maxwell, D. Parker, A. M. Blamire, *Magn. Reson. Med.* **2017**, *77*, 1307–1317.

62. D. Coman, Y. Huang, J. U. Rao, H. M. De Feyter, D. L. Rothman, C. Juchem, F. Hyder, *NMR Biomed.* **2016**, *29*, 309–319.

63. D. Coman, D. C. Peters, J. J. Walsh, L. J. Savic, S. Huber, A. J. Sinusas, M. Lin, J. Chapiro, R. T. Constable, D. L. Rothman, J. S. Duncan, F. Hyder, *Magn. Reson. Med.* **2020**, *83*, 1553–1564.

64. J. Pellico, C. M. Ellis, J. J. Davis, *Contrast Media Mol Imaging* **2019**, *2019*, 1845637.

65. X. Mao, J. Xu, H. Cui, *Wiley Interdiscip. Rev. Nanomed. Nanobiotechnol.* **2016**, *8*, 814–841.

66. Z. Zhou, L. Yang, J. Gao, X. Chen, *Adv. Mater.* **2019**, *31*, e1804567.

67. F. Kiessling, M. E. Mertens, J. Grimm, T. Lammers, *Radiology* **2014**, *273*, 10–28.

68. A. S. Thakor, J. V. Jokerst, P. Ghanouni, J. L. Campbell, E. Mittra, S. S. Gambhir, *J. Nucl. Med.* **2016**, *57*, 1833–1837.

69. N. Singh, G. J. Jenkins, R. Asadi, S. H. Doak, *Nano Rev.* **2010**, *1*.

70. S. Carlsson, *Acta Oncol.* **1995**, *34*, 1095–1102.

71. P. Richards, W. D. Tucker, S. C. Srivastava, *Int. J. Appl. Rad. Isot.* **1982**, *33*, 793–799.

72. A. U. Alberto R., in *Handbook of Nuclear Chemistry*, 2 ed., Eds. N. S. A.Vértes, Z. Klencsár, R. G. Lovas, F. Rösch, Springer, Boston **2011**, pp. 2073–2120.

73. T. I. Kostelnik, C. Orvig, *Chem. Rev.* **2019**, *119*, 902–956.

74. E. Boros, A. B. Packard, *Chem. Re.v* **2019**, *119*, 870–901.

75. M. A. Synowiecki, L. R. Perk, J. F. W. Nijsen, *EJNMMI Radiopharm. Chem.* **2018**, *3*, 3.

76. A. Yazdani, N. Janzen, S. Czorny, J. F. Valliant, *Inorg. Chem.* **2017**, *56*, 2958–2965.

77. A. H. Day, J. Domarkas, S. Nigam, I. Renard, C. Cawthorne, B. P. Burke, G. S. Bahra, P. C. F. Oyston, I. A. Fallis, S. J. Archibald, S. J. A. Pope, *Dalton Trans.* **2020**, *49*, 511–523.

78. C. Muller, N. P. van der Meulen, M. Benesova, R. Schibli, *J. Nucl. Med.* **2017**, *58*, 91S–96S.

79. K. Herrmann, S. M. Larson, W. A. Weber, *J. Nucl. Med.* **2017**, *58*, 1S–2S.

80. K. Mishiro, H. Hanaoka, A. Yamaguchi, K. Ogawa, *Coord. Chem. Rev.* **2019**, *383*, 104–131.

81. B. A. Vaughn, S. H. Ahn, E. Aluicio-Sarduy, J. Devaraj, A. P. Olson, J. Engle, E. Boros, *Chem. Sci.* **2020**, *11*, 333–342.

82. E. Aluicio-Sarduy, N. A. Thiele, K. E. Martin, B. A. Vaughn, J. Devaraj, A. P. Olson, T. E. Barnhart, J. J. Wilson, E. Boros, J. W. Engle, *Chemistry* **2020**, *26*, 1238–1242.

83. R. M. de Kruijff, H. T. Wolterbeek, A. G. Denkova, *Pharmaceuticals (Basel)* **2015**, *8*, 321–336.

84. M. Bosch de Basea, J. A. Salotti, M. S. Pearce, J. Muchart, L. Riera, I. Barber, S. Pedraza, M. Pardina, A. Capdevila, A. Espinosa, E. Cardis, *Pediatr. Radiol.* **2016**, *46*, 119–129.

85. A. Michele, F. Teresa, D. S. Giovanbattista, M. Ashour, S. Yu, *J. Nephrol. Adv.* **2017**, *1*, 6–41.

86. H. Lusic, M. W. Grinstaff, *Chem. Rev.* **2013**, *113*, 1641–1666.

87. M. Berger, M. Bauser, T. Frenzel, C. S. Hilger, G. Jost, S. Lauria, B. Morgenstern, C. Neis, H. Pietsch, D. Sulzle, K. Hegetschweiler, *Inorg. Chem.* **2017**, *56*, 5757–5761.

88. T. Frenzel, M. Bauser, M. Berger, C. S. Hilger, C. Hegele-Hartung, G. Jost, C. Neis, K. Hegetschweiler, B. Riefke, D. Suelzle, H. Pietsch, *Invest. Radiol.* **2016**, *51*, 776–785.

89. S. B. Yu, M. Droege, S. Downey, B. Segal, W. Newcomb, T. Sanderson, S. Crofts, S. Suravajjala, E. Bacon, W. Earley, D. Delecki, A. D. Watson, *Inorg. Chem.* **2001**, *40*, 1576–1581.

90. A. A. Krasilnikova, M. A. Shestopalov, K. A. Brylev, I. A. Kirilova, O. P. Khripko, K. E. Zubareva, Y. I. Khripko, V. T. Podorognaya, L. V. Shestopalova, V. E. Fedorov, Y. V. Mironov, *J. Inorg. Biochem.* **2015**, *144*, 13–17.

91. A. Silvestri, V. Zambelli, A. M. Ferretti, D. Salerno, G. Bellani, L. Polito, *Contrast Media Mol. Imaging* **2016**, *11*, 405–414.

92. L. E. Cole, R. D. Ross, J. M. Tilley, T. Vargo-Gogola, R. K. Roeder, *Nanomedicine (Lond)* **2015**, *10*, 321–341.

93. Y. C. Dong, M. Hajfathalian, P. S. N. Maidment, J. C. Hsu, P. C. Naha, S. Si-Mohamed, M. Breuilly, J. Kim, P. Chhour, P. Douek, H. I. Litt, D. P. Cormode, *Sci. Rep.* **2019**, *9*, 14912.

94. Y. Wang, C. Jiang, W. He, K. Ai, X. Ren, L. Liu, M. Zhang, L. Lu, *ACS Nano* **2016**, *10*, 4164–4172.

95. J. Kim, P. Chhour, J. Hsu, H. I. Litt, V. A. Ferrari, R. Popovtzer, D. P. Cormode, *Bioconjug. Chem.* **2017**, *28*, 1581–1597.

96. C. H. McCollough, in *Computed Tomography: Approaches, Applications, and Operations*, Eds. E. Samei, N. J. Pelc, Springer International Publishing, Cham, **2020**, pp. 223–242.

97. D. Pan, C. O. Schirra, A. Senpan, A. H. Schmieder, A. J. Stacy, E. Roessl, A. Thran, S. A. Wickline, R. Proska, G. M. Lanza, *ACS Nano* **2012**, *6*, 3364–3370.

98. F. Ostadhossein, I. Tripathi, L. Benig, D. LoBato, M. Moghiseh, C. Lowe, A. Raja, A. Butler, R. Panta, M. Anjomrouz, A. Chernoglazov, D. Pan, *Advanced Functional Materials* **2019**, *30,* 1904936.
99. O. S. Wenger, *J. Am. Chem. Soc.* **2018**, *140*, 13522–13533.
100. C. Forster, K. Heinze, *Chem. Soc. Rev.* **2020**, *49*, 1057–1070.
101. L. A. Buldt, O. S. Wenger, *Chem. Sci.* **2017**, *8*, 7359–7367.
102. K. K. W. Lo, in *Advances in Inorganic Chemistry*, Vol. 68 of *Insights from Imaging in Bioinorganic Chemistry*, Eds. R. van Eldik, C. D. Hubbard, Elsevier Academic Press Inc, San Diego **2016**, pp. 97–140.
103. L. K. McKenzie, H. E. Bryant, J. A. Weinstein, *Coord. Chem. Rev.* **2019**, *379*, 2–29.
104. S. Monro, K. L. Colon, H. Yin, J. Roque, 3rd, P. Konda, S. Gujar, R. P. Thummel, L. Lilge, C. G. Cameron, S. A. McFarland, *Chem. Rev.* **2019**, *119*, 797–828.
105. S. Shuvaev, M. Starck, D. Parker, *Chemistry* **2017**, *23*, 9974–9989.
106. A. T. Frawley, R. Pal, D. Parker, *Chem. Commun.* **2016**, *52*, 13349–13352.
107. D. G. Smith, B. K. McMahon, R. Pal, D. Parker, *Chem. Commun.* **2012**, *48*, 8520–8522.
108. Y. Ning, M. Zhu, J.-L. Zhang, *Coord. Chem. Rev.* **2019**, *399*, 213028.
109. P. Wang, Y. Fan, L. Lu, L. Liu, L. Fan, M. Zhao, Y. Xie, C. Xu, F. Zhang, *Nat. Commun.* **2018**, *9*, 2898.
110. A. Kumar, S. Zhang, G. Hao, G. Hassan, S. Ramezani, K. Sagiyama, S. T. Lo, M. Takahashi, A. D. Sherry, O. K. Oz, Z. Kovacs, X. Sun, *Bioconjug. Chem.* **2015**, *26*, 549–558.
111. U. Seibold, B. Wangler, R. Schirrmacher, C. Wangler, *Biomed. Res. Int.* **2014**, *2014*, 153741.
112. E. Ciarrocchi, N. Belcari, *EJNMMI Phys.* **2017**, *4*, 14.
113. A. G. Cosby, S. H. Ahn, E. Boros, *Angew. Chem. Int. Ed. Engl.* **2018**, *57*, 15496–15499.
114. L. M. Matosziuk, J. H. Leibowitz, M. C. Heffern, K. W. MacRenaris, M. A. Ratner, T. J. Meade, *Inorg. Chem.* **2013**, *52*, 12250–12261.
115. S. Fingerhut, A. C. Niehoff, M. Sperling, A. Jeibmann, W. Paulus, T. Niederstadt, T. Allkemper, W. Heindel, M. Holling, U. Karst, *J. Trace Elem. Med. Biol.* **2018**, *45*, 125–130.
116. E. M. Gale, P. Caravan, *ACS Chem. Neurosci.* **2018**, *9*, 395–397.
117. E. Blanco, H. Shen, M. Ferrari, *Nat. Biotechnol.* **2015**, *33*, 941–951.

2

Gadolinium(III)-Based Contrast Agents for Magnetic Resonance Imaging. A Re-Appraisal*

Gyula Tircsó,[1] *Enikő Molnár,*[1] *Tibor Csupász,*[1] *Zoltán Garda,*[1]
Richárd Botár,[1] *Ferenc K. Kálmán,*[1] *Zoltán Kovács,*[2]
Ernő Brücher,[3*] *and Imre Tóth* [1,3*]

[1]Department of Physical Chemistry, University of Debrecen,
Egyetem tér 1, H-4032 Debrecen, Hungary
<imre.toth@science.unideb.hu>

[2]Advanced Imaging Research Center, University of Texas Southwestern Medical Center,
5323 Harry Hines Boulevard, Dallas, TX 75390, USA

[3]Department of Inorganic and Analytical Chemistry, University of Debrecen,
Egyetem tér 1, H-4032 Debrecen, Hungary

*E. B. and I. T. dedicate this paper to the memory of their friend, Ingmar Grenthe,
who passed away in January 2020.

Abstract: Gadolinium(III)-based contrast agents (GBCAs) have been extensively used in magnetic resonance imaging (MRI) in clinical practice since 1988, largely because they can dramatically improve contrast between healthy and diseased tissues. GBCAs are complexes of Gd(III) in which the metal ion is encapsulated in a cavity of linear (open-chain) or macrocyclic ligands. Although the safety statistics of GBCAs are in general excellent, nephrogenic systemic fibrosis (NSF) observed in a small subset of patients with poor kidney function after the administration of linear GBCAs and more recently, gadolinium deposition in various tissues (e.g., brain, bone) raised safety concerns. In this review we briefly describe the physical principles of MRI, the background of NSF, environmental concerns of gadolinium as well as related regulatory actions. The robustness of commercial GBCAs in terms of stability and inertness and innovative research to develop safer and more effective new GBCAs, as well as smart/responsive contrast agents (SCAs) (pH-, hypoxia-sensitive CAs, enzyme activated systems) will also be discussed.

Keywords: alternative MRI contrast agents · gadolinium-based contrast agents (GBCAs) · gadolinium retention · improving the safety profile · magnetic resonance imaging (MRI) · nephrogenic systemic fibrosis (NSF) · positive gadolinium anomaly

1. INTRODUCTION

Before 1988, i.e., in the pre-MRI era, the coordination chemistry of lanthanide elements (Ln) was mainly driven by some interest of ion exchange separation of nuclear fission products and macroscopic amounts of lanthanide compounds from rare earth minerals. The advent of magnetic resonance imaging (MRI) and the suggestion that Gd complexes could be used to enhance MR image contrast

revolutionized this field attracting many researchers around the world. At the same time, the use of open-chain and macrocyclic amino-polycarboxylate (APC) ligands as binders of Gd(III) in clinically approved gadolinium(III)-based contrast agents (GBCAs) led to the higher appreciation of research on Ln(III) APC complexes [1–6].

In the following decades GBCAs have become one of the most successful metal-containing drugs beside the technetium-99m diagnostic agents and the platinum-based anticancer therapeutics. The success of GBCAs can be attributed to the valuable diagnostic/prognostic information and the outstanding safety statistics compared to other diagnostic agents. Although MRI images can be generated without contrast agents (CAs), approximately 40–60 % of all exams are GBCA-enhanced, which represents about 40 million/year administrations globally [7, 8]. The market of GBCAs is currently over 1 billion USD per year and it is projected to increase because of longer life expectancy.

The above success story seemed to come to a halt in 2006 when nephrogenic systemic fibrosis (NSF), a destructive disease linked to GBCAs was described in some renally impaired patients [9, 10]. The mechanism of NSF is not fully understood, but the Gd-toxicity is attributed to the release of Gd(III) from GBCAs. The risk of NSF is significantly higher in patients with impaired renal function and repeated and/or multiple dosing [11–13]. Although the actual clinical guidelines and warnings issued by the regulatory agencies (especially for linear GBCAs) have eliminated new NSF cases, the confidence in GBCAs has not been completely restored yet. The safety concerns re-emerged again a few years later when seemingly irreversible Gd retentions were detected in brain [14] and bone [15] tissues of patients receiving multiple doses of GBCAs. In addition, we should not ignore the "positive gadolinium anomaly" found in surface waters close to large MRI centers [16] caused by scattered Gd(III) from CAs.

The aim of our review is to provide a brief re-appraisal on the current state of research on GDBCs within the scope of this book. The development of the field, both advantages and the negative effects, are well documented in the literature [17–19]. In a recent review Caravan and his coauthors [7] give a comprehensive overview of the actual chemistry of MRI CAs including GBCAs offering detailed discussions of the biophysical and medical/biochemical aspects and applications. Here, we will summarize the current understanding of the mechanism of *in vivo* Gd(III) release and deposition in tissues and describe some innovative efforts to develop better and safer GBCAs. In line with the contents of related chapters of this book we only deal with selected aspects of "smart" imaging agents.

2. MAGNETIC RESONANCE IMAGING IN MEDICAL IMAGING

2.1. Physical Principles of Magnetic Resonance Imaging

Since several publications and books are available on the basic principles of MRI, only a brief overview of the physical background of the technique is provided here [18].

The nuclear magnetic resonance (NMR) signal originates from the Zeeman-splitting of the spin states of nuclei with non-zero spin in an external magnetic field (B_0). In the clinical routine, MRI (based on the same physical phenomena as NMR) in fact is using the proton (^1H) signal of water since it is present in fairly high concentration (~60 %) in the human body. After the radio frequency (RF) excitation in the B_0 field the system returns to the thermal equilibrium by spin-lattice (longitudinal) and spin-spin (transversal) relaxation. The exponential time constants T_1 and T_2 characterize changes of longitudinal and transversal magnetization, respectively.

The most frequently used pulse-sequence in MRI is based on the spin echo (SE) [20]. The signal intensity (SI) in SE can be given as

$$\text{SI} = N(H)[1 - e^{-TR/T1}]e^{-TE/T2} \tag{1}$$

where $N(H)$ is the proton density, T_1 and T_2 are the relaxation times, TE and TR are the echo and repetition time. The TE is the time between the 90° RF pulse and the echo (180° RF excitation occurs at $TE/2$) and TR is the interval between two successive excitations. Based on Equation (1), one can conclude that shortening of T_1 increases while that of T_2 decreases the SI.

The raw data are stored as a data matrix in the k-space which is used to generate the image. Each pixel in the 2D image with a given slice thickness corresponds to volume elements (voxel) of space in reality. The gradients (G_x, G_y, and G_z, generated by small coils positioned along the electromagnet) are used to distinguish the voxels with respect to positions. The k-space data points and the image pixels are related to each other by Fourier transform.

The contrast of the MR images can be enhanced by paramagnetic materials accelerating both T_1 and T_2 relaxation. Currently, complexes of the Gd(III) ion are used for this purpose. The relaxivity (r_{1p}, $mM^{-1}s^{-1}$) of GBCAs [the enhancement of the relaxation rates ($1/T_1$ and $1/T_2$) of the water protons relative to the diamagnetic media caused by the paramagnetic substance present at 1 mM concentration] is determined by several factors (Figure 1A).

The relaxivity of a complex is directly proportional to the number of water molecules coordinated to the paramagnetic metal ion (q). The paramagnetic effect from the metal to the bulk water k_{ex} ($\tau_M = 1/k_{ex}$) is transmitted via water exchange that has to be in the optimal range. If the exchange is too fast (relative to the value of the electron relaxation time, $T_{1,2e}$), the excited protons will not have enough time to relax (in connection to the value of the electron relaxation time, $T_{1,2e}$), while in slow exchange fewer water molecules participate and the
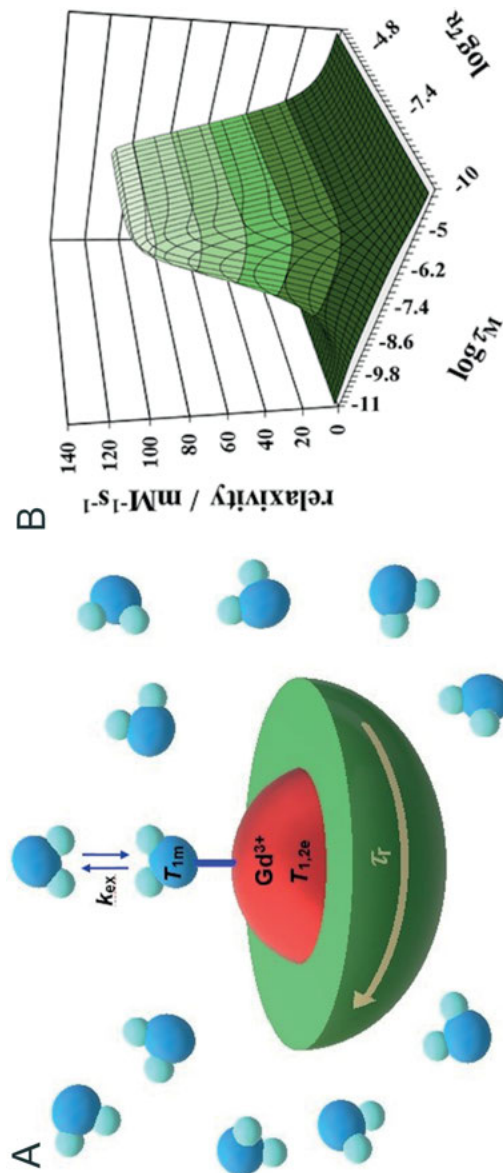
Figure 1. (**A**) Schematic illustration of a Gd(III) complex with one coordinated water molecule, surrounded by bulk water. τ_r is the rotational correlation time, k_{ex} is the rate of the water/proton exchange. T_{1m} is the longitudinal relaxation time of the protons of the metal bound water molecule and $T_{1,2e}$ refers to the electronic relaxation times of Gd(III). (**B**) Dependence of the r_1 relaxivity on the rotational correlation time τ_r and the water residence time τ_M. The electronic relaxation times ($T_{1,2e}$) of Gd(III) were set to 1 ns. The calculations were performed at $B_0 = 0.47$ T external magnetic field strength.

relaxation effect is less efficient. The third parameter is the τ_R rotational correlation time, which describes the rotation (tumbling rate) of the molecule. Figure 1B shows the correlation between the relaxivity, τ_M and τ_R [21].

The longer τ_R, the higher the relaxivity of the complex (at least at lower fields). The relaxivity of contrast agents used in the clinical practice is limited by τ_R. However, to attain maximum relaxivity (around $100 \, \text{mM}^{-1}\text{s}^{-1}$), the water exchange rate ($k_{ex} = 1/\tau_M$) must also be tuned close to the optimal value (log τ_M ~ –8).

2.2. Commercial Gadolinium(III) Complexes

The first approved agent for human examinations in 1988 was the Gd(DTPA) (gadopentetate, Magnevist) which was followed very soon by the macrocyclic Gd(DOTA) (gadoterate, Dotarem) (the charges of the complexes are ommitted for clarity). Later, to avoid the drawback of negatively charged CAs (high osmotic concentration can cause pain at injection), neutral contrast agents were also developed such as Gd(HP-DO3A) (gadoteridol, ProHance), Gd(DTPA-BMA) (gadodiamide, Omniscan), Gd(BT-DO3A) (gadobutrol, Gadovist), and Gd(DTPA-BMEA) (gadoversetamide, Optimark) [7]. All CAs listed above are distributed rapidly in the extracellular space of the body following intravenous administration, and mostly excrete through the kidneys via glomerular filtration thanks to their hydrophilic character. However, CAs containing lipophilic groups just like in Gd(EOB-DTPA) (gadoxetate, Primovist) and Gd(BOPTA) (gadobenate, Multihance) show specificity to the blood pool or the liver. The complex Gd(MS-325) (gadofosveset, Ablavar) possessing high binding affinity to the human serum albumin (HSA) is designed to visualize the vascular system (MR angiography). However, Ablavar is no longer available because of the low market demand [7]. The structures of the GBCAs mentioned in the text are shown in Figure 2.

The most important consideration is safety [22]. The next key property of CAs for MRI is the relaxivity. Obviously, high relaxivity is preferred because it translates into lower dose and consequently, reduced side effects. The gadolinium toxicity is generally attributed to free Gd(III) released from the agent. The higher the stability, the lower the free Gd concentration expected to form in a (time-dependent) equilibrium reaction, but the free Gd-concentration is largely determined by the inertness of the agent (i.e., the rates of decomplexation). To prevent the *in vivo* decomplexation in living systems, the GBCAs must have high kinetic inertness [19]. The half-life of CA excretion is about 1.5 h [23] through (healthy) kidneys, i.e., the GBCAs must not be (substantially) decomplexed in the body within a time period of 8–10 hours. The commercial GBCAs fulfill these requirements to different extents. The outstanding kinetic inertness of macrocyclic GBCAs seems to be the key parameter in safety issues. The most important physicochemical data of GBCAs are summarized in Table 1 [23, 24, 46].

log K_{cond} was calculated at pH = 7.4 using the protonation constants (K_i^H) of the ligand, $t_{1/2} = \ln2/k_d$; k_d [s^{-1}] = k_1 [H$^+$] at [H$^+$] = 3.98·10^{-8} M (pH = 7.4) using k_1 [M^{-1}s^{-1}] values of proton-assisted decomplexation from [19], except **bold**
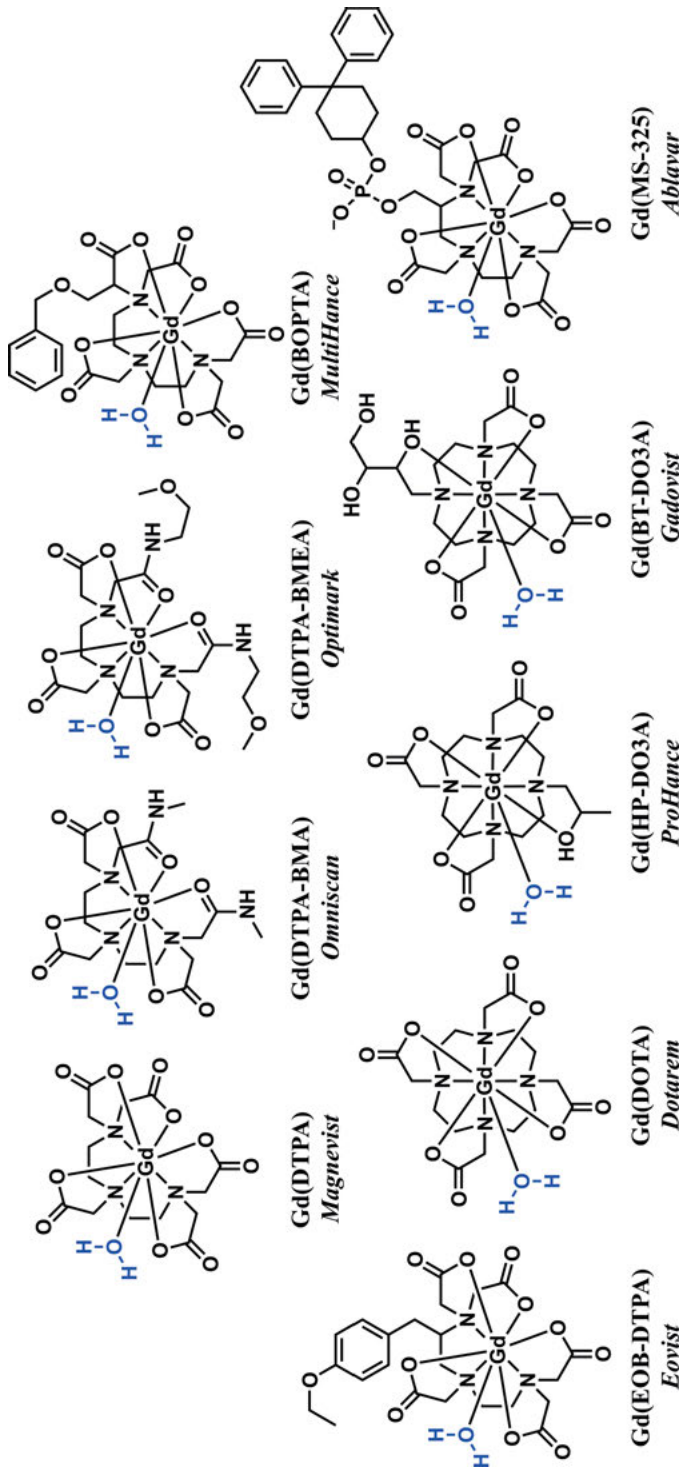
Figure 2. Gd(III)-based commercial GBCAs.

Table 1.   The thermodynamic ($\log K$) and conditional ($\log K_{\text{cond}}$) stability constants [46] and the decomplexation half times ($t_{1/2}$) calculated at pH = 7.4 of commercial GBCAs [23, 24].

GBCA	$\log K$	$\log K_{\text{cond}}$	$t_{1/2}$ [h]
Gd(DTPA)	22.03	18.48	$1.2 \cdot 10^4$ / **$3.1 \cdot 10^2$**
Gd(BOPTA)	21.91	18.83	$1.7 \cdot 10^4$
Gd(EOB-DTPA)	23.6	18.70	$4.36 \cdot 10^4$
Gd(DTPA-BMA)	16.64	15.05	$3.81 \cdot 10^2$/**9.3**
Gd(DTPA-BMEA)	16.85	14.98	$5.62 \cdot 10^2$
Gd(DOTA)	24.7	20.98	$5.76 \cdot 10^8$
Gd(HP-DO3A)	23.8	17.21	$7.56 \cdot 10^6$
Gd(BT-DO3A)	20.8	14.61	$1.73 \cdot 10^8$

values for Gd(DTPA) [24] at 25 °C and Gd(DTPA-BMA) at 37 °C [23], where k_d [s^{-1}] is the rate constant of decomplexation at physiological concentration of citrate, carbonate, and phosphate, pH = 7.4. Similar data have not been published for the other three linear GBCAs.

3.   NEGATIVE EFFECTS OF MASS APPLICATION OF GADOLINIUM(III)-BASED CONTRAST AGENTS

3.1.   Gadolinium Accumulation in Human Tissues

In 2000 NSF was described as an independent disease entity. The clinicopathological diagnosis is based on presentation and histological findings [25]. NSF was observed in patients with impaired kidney function and it took six years to prove the direct connection of NSF to GBCAs in 2006 [26, 27]. The retrospective analysis of NSF cases (estimations on the number of cases span between 600–2000 globally) proved not only the role of gadolinium, but clearly showed that linear CAs derived from DTPA, especially gadodiamide (Omniscan), were the ones associated with Gd(III) toxicity. After tightening the regulations (see Section 4.1), the restricted use of linear agents for patients with impaired renal function practically eliminated the risk of NSF. However, there is no widely accepted model for NSF so far.

A new concern emerged in 2010, when Gd(III) retention was observed in the central nervous system (CNS) of patients with normal kidney function. Xia et al. reported gadolinium accumulation in human brain tumors [28]. The level of concern was significantly increased when hyperintensity regions in the normal brain were observed in MRI images of patients who earlier received repeated doses of GBCAs [29]. However, unlike NSF, Gd(III) deposition in the brain has not been associated with any adverse biological effect by scientific investigation so far. The mounting evidence (mainly published by radiologists working with human patients) strongly suggests that Gd(III) retention in the CNS can appear in

patients with intact blood-brain barrier (BBB) after multi-dose GBCAs adminstration [30]. A remarkable similarity between Gd retention in the brain and NSF is the role of linear GBCAs while macrocyclic GBCAs seem to be less involved [31]. The mechanism of Gd(III) retention and chemical speciation of Gd(III) in the tissues remain unknown. In summary, GBCAs provide clinical information that is not available by other diagnostic methods, and in most cases the benefit of a contrast-enhanced MR exam far outweighs the risk associated with GBCA administration, especially with macrocylic agents.

3.2. Positive Gadolinium Anomaly

Until 2018, over 450 million GBCA doses have been administered worldwide [30]. Considering 1 g Gd(III)/dose the cumulative mass of gadolinium is 4500 tons, which has been mobilized in GBCAs and drained to the waste water systems after excretion from patients. Just a few years after the introduction of GDCAs it was shown that the Gd(III) concentration in river and lake waters in the vicinity of densely populated and industrialized regions was elevated (this is termed as the positive gadolinium anomaly), and could be attributed to the application of GBCAs (mostly Gd(DTPA)) at that time [16]. The robust GBCAs likely go through the standard waste water plants and end up in surface water. [32] Although no severe adverse biological effect has been reported so far, the emerging environmental concern is obvious [33].

4. ACTIONS IN THE "POST-NEPHROGENIC SYSTEMIC FIBROSIS AGE"

4.1. Actions of Regulatory Agencies in the EU and the USA

In 2006 the Food and Drug Administration (FDA) alerted the public about NSF. In 2007 the addition of a boxed warning about the risk of NSF to the labelling of GBCA drugs was required by the agency. In 2010 the FDA prohibited the use of the three less inert linear GBCAs (Gd(DTPA), Gd(DTPA-BMA), and Gd(DTPABMEA)) in patients with severe kidney disease. Finally, FDA issued another safety announcement on December 19, 2017, requiring a new class warning and other safety measures for all GBCAs. In 2017 the European Medicines Agency (EMA) declared that the marketing authorization of the above mentioned linear GBCAs would be suspended while Gd(EOB-DTPA) and Gd(BOP-TA) could only be used for liver imaging [34, 35]. Recently, two linear GBCAs were voluntarily withdrawn from the US market by their manufacturers. We have no information about other governmental regulations worldwide, but the organisations of radiologists seem to be aware of these new recommendations [36, 37, 42].

4.2. Research on the Connections between Nephrogenic Systemic Fibrosis, Gadolinium Deposition in Living Systems, and Gadolinium(III)-Based Contrast Agents

The direct connection of NSF to GBCAs has been understood since 2006 [38]. Although the mechanism of toxicity has not been fully explored, the toxicity of free Gd(III) as Ca(II) antagonist can be rationalized [39].

Retrospective analysis of chemical literature clearly shows that a substantial body of equilibrium and kinetic data had been published before 2006, describing relevant differences between linear and macrocyclic agents. As in 2018 some of us reviewed this issue in detail [19], here we only summarize the main points (one may note: "It is easy to be wise after the event").

The stability constants of the approved GBCAs are well known and reliable (Table 1). It should be noted that the higher thermodynamic stability (higher log K_{GdL}) of macrocyclic complexes compared to the open chain ones does not translate into higher stability at pH = 7.4 as shown by the respective conditional stability constants (log K_{cond}), which take into account the different basicities of the ligands (see definitions in Section 5.1). Kinetic studies on the decomplexation of LnAPCs also have a long history. [4, 19] The importance of kinetic inertness had been recognised years before the first reports of NSF [40]. Long-term (14 days) Gd(III) deposition was studied after intravenous administration of various linear and macrocyclic ^{153}Gd(III)-labeled GBCAs in rats, giving values between 0.01–1 %. The data clearly demonstrated the higher *in vivo* stability of the macrocyclic agents as these had the lowest residual Gd(III). Early studies on the decomplexation kinetics of GBCAs were carried out in 0.1 M HCl giving first order constants characterizing the dissociation rate of the complexes (k_d; s^{-1}). The half-lives of dissociation ($t_{1/2} = \ln2/k_d$) calculated from k_d values were 338 h, 43 h, 3.9 h, and < 5 s for Gd(DOTA), Gd(BT-DO3A), Gd(HP-DO3A), and Gd(DTPA), respectively. The lability (i.e., low inertness) of the linear Gd(DTPA) was obvious [41].

However, *in vitro* model systems closer to the milieu of bio-fluids have also been used for kinetic studies. Conditions that drive to the decomplexation could be generated by adding competing metal ions (such as the endogenous Zn(II), Cu(II), Ca(II), and Fe(II)/Fe(III) ions) and H$^+$ for transmetalation, or organic ligands (citrate, phosphate, large biomolecules, proteins such as transferrin) for trans-chelation.

Figure 3 summarizes the possible kinetic pathways for decomplexation of lanthanide chelates Ln(L): 1. spontaneous (**black**, k_0; s^{-1}), 2. H$^+$-assisted (**red**, k_H and k_H^H; M^{-1} s^{-1}), 3. metal ion assisted (**green**, k_M and k_M^H M^{-1} s^{-1}), 4. hydroxide-ion assisted (**brown**, k_{OH} and k_M^{OH}; M^{-1} s^{-1}), 5. ligand assisted (**blue**, k_L and k_L^H; M^{-1} s^{-1}) dissociations. Rate constants with subscript characters and superscript H or OH mean that both the competing agent (subscript) and H$^+$ or OH$^-$ (superscript) are involved in the reaction [17–19]. The large body of kinetic data allows the classification of the Ln(L) complexes into two groups: (i) Macrocyclic Ln(III) complexes; these are usually extremely inert, and their decomplexation occurs only via the proton-assisted dissociation pathway (Figure 3, **red** path-
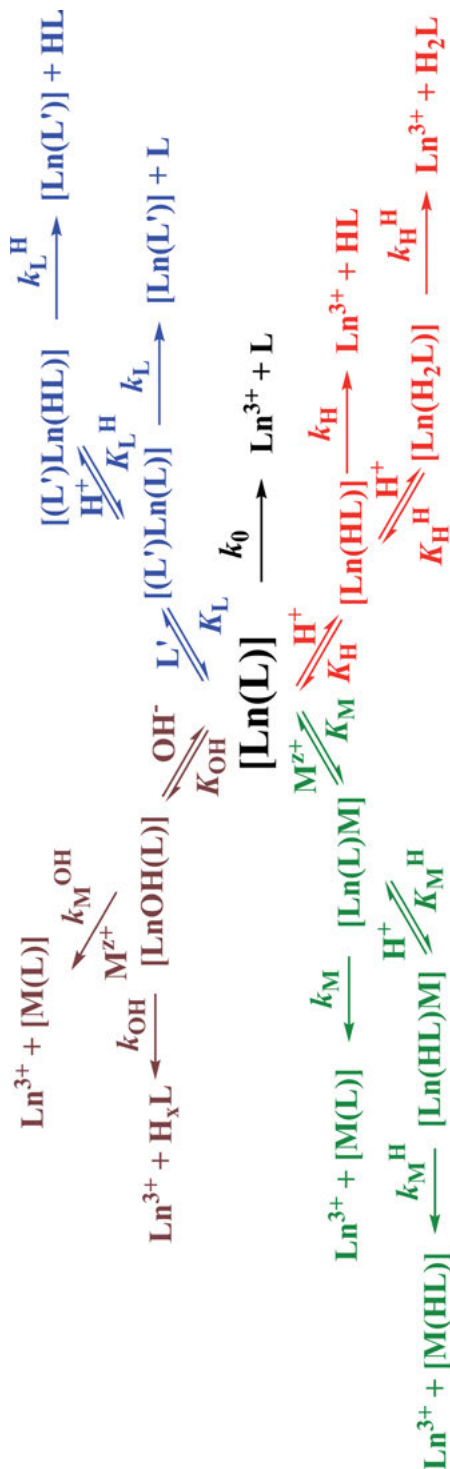
Figure 3. Assumed reaction paths of the dissociation of Ln(L) complexes (charges are omitted for clarity).

way(s)). The rate-determining step is always the release of free Ln(III) ion, which will then react with an accessible ligand in a fast(er) reaction. On the other hand, the released protonated ligand can react with metal ions present in the milieu. (ii) Open-chain Ln(III) complexes; they are generally much less inert. The rate of spontaneous dissociation could be 2–3 orders of magnitude faster than that of DOTA-type complexes, although the dominating pathway here is again the proton-assisted dissociation. The contribution of the ligand exchange reactions (Figure 3, **blue** pathway(s)) is less studied, but it also appears to be less substantial. For the majority of these complexes, decomplexation involving the direct attack of exchanging metal ions (Cu(II) or Zn(II)) on the complex is also pronounced. The role of small bioligands (citrate, carbonate, phosphate) in the decomplexation has been recognized only recently (see Table 1) as it notably affects the rate of dissociation of Gd(DTPA-BMA).

Baranyai et al. [24] studied the kinetics of metal exchange reactions between Cu(II) ions and the open-chain Gd(DTPA) and Gd(DTPA-BMA) as well as the macrocyclic Gd(DOTA) and Gd(HP-DO3A) complexes in 2012. Citrate, HCO_3^-/CO_3^{2-} and $H_2PO_4^-$ ions can catalyze the dissociation of the open-chain complexes. The dissociation rates of Gd(DTPA-BMA) are about two orders of magnitude higher than those of Gd(DTPA). The much slower exchange reactions of macrocyclic complexes occur through proton-assisted dissociation and the endogenous ligands do not influence the rates [24]. Equilibrium and dissociation kinetics of Gd(DTPA-BMA) were further studied in 2015 at near physiological conditions [23]. The extent of dissociation of Omniscan (0.35 mM Gd(DTPA-BMA)) in a simplified plasma model at equilibrium was calculated to be 17 % with the formation of Gd(PO$_4$). The formation of Ca(DTPA-BMA) was detected by capillary electrophoresis in human serum. At physiological concentrations the dissociation half-life of Gd(DTPA-BMA) is 9.3 h at pH = 7.4. Considering the rates of distribution and dissociation of Gd(DTPA-BMA) in the extracellular space of the human body, an open two-compartment model has been developed [23]. The fraction of dissociated Omniscan predicted by this model strongly depends on the excretion rate, i.e., on kidney function, in accordance with literature data [42].

In conclusion, a closer look at the kinetic properties of the commercial GBCAs (including the restricted ones) in Table 1 (Section 2.2) shows that the order of inertness according to the half-lives of dissociation is as follows: Gd(DOTA) > Gd(BT-DO3A) > Gd(HP-DO3A) > Gd(MS-325) > Gd(EOB-DTPA) > Gd(BOPTA) > Gd(DTPA) > Gd(DTPA-BMEA) ≥ Gd(DTPA-BMA). The very poor inertness of Gd(DTPA-BMA) can obviously be connected to the NSF cases. At the same time, the conditional stability of these GBCAs does not follow a similar trend (see Table 1) indicating the dominant role of kinetic inertness over the thermodynamic stability in determining the *in vivo* safety of the complex.

Substantial effort has been devoted to study the retention of GBCAs in human tissues in connection to NSF, e.g., analysis of post-mortem brain slices [43] and skin samples [44, 45]. Bone samples from patients receiving hip replacement surgery and examined previously by MRI using Gd(DTPA-BMA) or Gd(HP-DO3A) [15] were analyzed by ICP-AES or ICP-MS in 2004. The data revealed

a reverse and positive correlation of Gd(III) retention (i.e., the total concentration of Gd(III)) with inertness and cumulative dose of GBCAs, respectively. Extended X-ray fine structure (EXAFS) analysis [44] and sampling by laser ablation ICP-MS [45] were used to gather information about the chemical environment of the deposited Gd(III). In the case of Gd(DTPA-BMA), the retained Gd(III) appears to be in the form of $GdPO_4$ which is insoluble in bio-fluids.

The Gd(III) retention in the CNS stimulated new research on the mechanism and long-term consequences of Gd(III) deposition. The quantity of the retained Gd(III) in brain tissues is usually less than 0.001 % of the dose. Current studies focus on the following issues: (i) speciation of retained Gd(III) (classification as intact complex, insoluble or resoluble deposits); (ii) detecting the mechanism by which GBCAs cross biological barriers such as the BBB; and (iii) relaxivity–Gd(III) speciation relations in various brain regions [46]. Resolving these issues requires interdisciplinary research including state-of-the-art analytical, structural, separation, microscopic, etc., techniques to trace the fate of "free" Gd(III) and/or "free" ligand in living systems or *ex vivo* samples [47]. The outcome of this research may pave the way for the construction of a (common) model that could account for both NSF and Gd(III) retention in the brain. This model should be based on the experimental observation that NSF and *in vivo* Gd(III) depositions are associated with linear GBCAs but not with the macrocyclic ones.

5. INNOVATIVE RESEARCH FOR IMPROVING GADOLINIUM(III)-BASED CONTRAST AGENTS

5.1. Synthesis of New Ligands with the Aim of Improving the Physicochemical Properties of Gd(III) Complexes

An essential contribution of chemistry to the safety and performance of GBCAs is the design and synthesis of ligands that form complexes with improved properties. However, the diverse requirements (high thermodynamic stability, selectivity, relaxivity, inertness, solubility, etc.) are often difficult to be satisfied simultaneously. Increasing the number of donor atoms may improve stability on the expense of relaxivity due to the lowered number of inner sphere waters. Inertness can decrease as a result of increased reactivity of GBCAs against H^+ and/or endogenous cations at the donor atoms as well as against anions that can replace the Gd(III)-bound water molecules, which also diminishes the relaxivity.

The stability of the complexes is usually expressed by their thermodynamic stability constant defined by (Equation 2)

$$K_{ML} = \frac{[ML]}{[M][L]} \tag{2}$$

where [ML], [M], and [L] are the equilibrium concentrations of the complex, the metal ion, and the ligand, respectively. The ML complex can be protonated or a hydroxo mixed complex might be formed (Equation 3)

$$K_{ML}^{H} = \frac{[MLH]}{[ML][H^+]} \qquad K_{ML}^{OH} = \frac{[MLOH]}{[ML][OH^-]} \qquad (3)$$

In some cases the formation of mixed ligand and binuclear complexes are also possible, which can be expressed by the following Equation (4)

$$K_{MLL'} = \frac{[MLL']}{[ML][L']} \qquad K_{MLM'} = \frac{[MLM']}{[ML][M']} \qquad (4)$$

where $[MLL']$, $[L']$, $[MLM']$, and $[M']$ are the equilibrium concentrations of the mixed ligand complex, the additional ligand, the binuclear complex, and the additional metal ion, respectively. The protonation constants of the ligand itself (Eq. 5) must also be known to calculate the stability and protonation constants of the complexes:

$$K_i^H = \frac{[H_iL]}{[H_{i-1}L][H^+]} \qquad (5)$$

In biological systems, endogenous metal ions (Ca(II), Zn(II), Cu(II), etc.) and ligands (phosphate, citrate, carbonate, etc.) can have an impact on the equilibria. Therefore, conditional stability constants are used to take into account the influence of these metal ions and ligands present in multicomponent systems (Equation 6)

$$K_{cond} = \frac{[ML]_t}{[M]_t[L]_t} = \frac{[ML]}{[M][L]} \frac{\alpha_{ML}}{\alpha_M \alpha_L} = K_{ML} \frac{\alpha_{ML}}{\alpha_M \alpha_L} \qquad (6)$$

where

$[M]_t = [M] + [MA] + [MB] + \dots;$

$[L]_t = [L] + [HL] + [H_2L] + \dots + [HnL] + [CaL] + [CaHL] + \dots + [ZnL]$
$\quad + [ZnHL] + \dots;$

$[ML]_t = [ML] + [MHL] + \dots + [MLA] + [MLB] + \dots;$

$\alpha_M = 1 + K_{MA}[A] + K_{MB}[B] + \dots;$

$\alpha_L = 1 + K_1[H^+] + K_1K_2[H^+]^2 + \dots + K_1K_2\dots K_n[H^+]^n + K_{CaL}[Ca^{2+}] +$
$\quad K_{CaHL}[H^+] + \dots;$

$\alpha_{ML} = 1 + K_{MHL}[H^+] + K_{MLA}[A] + K_{MLB}[B] + \dots$

Since the toxicity of the contrast agents is often correlated to the elevated concentration of the free metal ion, pM values are widely used to compare the stability of different complexes (Equation 7):

$$pM = -\log [M^{z+}]_{free} \tag{7}$$

pGd values are calculated according to the method suggested by Raymond et al., which recommends total concentrations, $[Gd]_t = 10^{-6}$ M, $[L]_t = 10^{-5}$ M and pH = 7.4 as specific conditions [48]. However, the defined condition, ($[L]_t$ is ten times higher than $[Gd]_t$), is not realistic for biological applications because contrast agents are never formulated this way. Equilibrium models can also be visualized with speciation diagrams generated by sophisticated computer programs [49] to show the species distributions (including $[M^{z+}]_{free}$) in biological systems. However, these calculations need expertise in aqueous equilibrium chemistry and a solid background in biochemistry to avoid misinterpretation of data. Moreover, thermodynamic equilibrium is an idealized concept, which cannot be applied directly for the description of GBCAs in bio-fluids, especially the highly inert ones [23].

Among the huge collection of newly synthesized ligands, only a few have been characterized physicochemically, providing high quality data for comparison of the stability and kinetics. Selected examples are given below.

5.1.1.   *Improving the Stability*

The increase in stability is often observed for the complexes of rigidified ligands, which is usually achieved by incorporating a cyclohexane unit in the ligand backbone. For instance, the cyclohexyl derivative of the DTPA, CHXDTPA, forms a Gd(III) complex with log K = 22.83, which is somewhat higher than that of the Gd(DTPA) (log K = 22.03) [50]. By applying the same modification to the OCTAPA ligand, bearing two picolinate and two acetate pendants connected with an ethylene linker a moderate increase in the stability of its Gd(III) complex was observed (log K = 20.39 and log K = 20.68 for Gd(OCTAPA) and Gd(CDDADPA), respectively) [51, 52]. However, there are counter examples in the literature when the incorporation of a cyclohexane ring resulted in a decrease in the stability. The Gd(III) complex of the heptadentate AAZTA ligand has high thermodynamic stability (log K = 20.24) [53] whereas, Gd(CyAAZTA) is less stable (log K = 18.26) (Figure 4) [54]. (The lowered stability might be attributed to the less flexible cavity of CyAAZTA.) This is a trade off between better kinetic inertness and lower thermodynamic stability (see Section 5.2.2).

The fusion of the pyridine ring with the tetraaza macrocycle increases the rigidity of the ligand, and thus their complexes are kinetically more inert than the parent DO3A complexes. However, Gd(PCTA) has lower thermodynamic stability (log K = 18.28) [55] than Gd(DO3A) (log K = 21.0) [56] since the overall basicity of the PCTA ligand is lower. The replacement of acetate pendant arms by picolinates or phosphonates can be a good strategy to improve the stability of the Gd(III) complexes. For example, PC2AP possesses notably higher stability (log K = 23.4) than the acetate (PCTA) analogue [57]. Substituting (one or two) bidentate picolinic acid moieties for the acetate group(s) also significantly raises the stability as it was shown by Le Fur et al. [58, 59] The arrangement of the
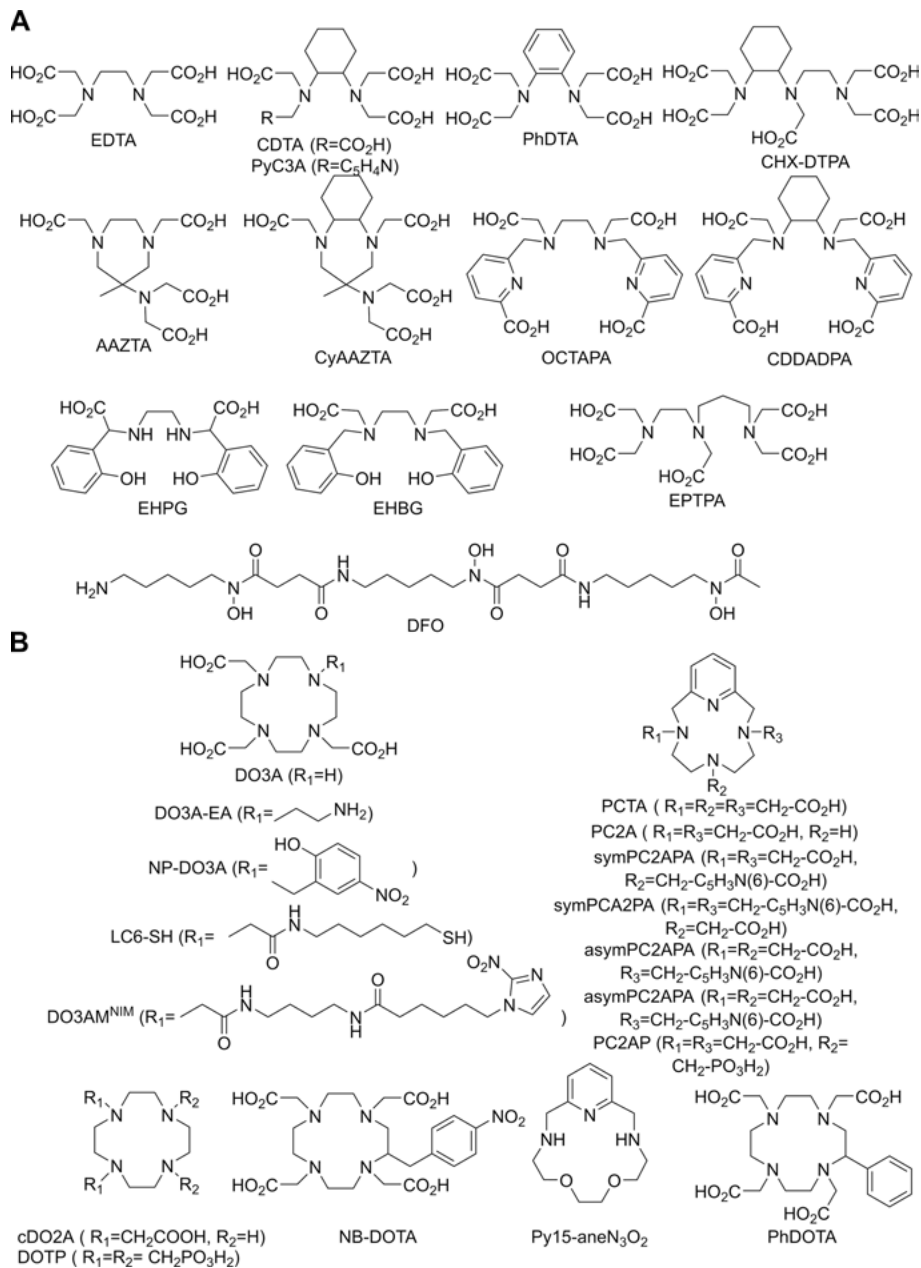
Figure 4. Linear/AAZTA derivate (A) and macrocyclic (B) ligands mentioned in the text.

pendant arms can also have a significant effect on the properties as illustrated by the log K values of the monopicolinate derivatives (referred to as symPC2A-PA and asymPC2APA): 20.49 and 22.37 for the symmetric and asymmetric ligands, respectively.

5.1.2. Complexes with Enhanced Inertness

Inertness can be enhanced by rigidifying the ligand structure described in Section 5.1.1. Incorporating a cyclohexane moiety into the ligand backbone of OC-TAPA (Figure 4) can significantly increase the inertness. The Gd(CDDADPA) has inertness comparable to that of Gd(DO3A) [51, 52]. The Gd(AAZTA) complex was found to be more inert than the commercially available, linear Gd(DTPA) at near physiological conditions. [53] However, the incorporation of the cyclohexane ring into the parent ligand CyAAZTA leads to an additional increase in the inertness ($t_{1/2} = 8.0 \cdot 10^5$ hours) [54].

The dissociation kinetics of pyclen-based complexes has been investigated in detail. Gd(PCTA) showed high inertness, which was further increased by substitution of the acetate pendants with picolinate arms [58, 59]. Enhanced inertness could also be achieved with cyclam-based ligands containing an ethylene cross-bridge. This extremely rigid structure has a tight binding cavity for the metal ion, but unfortunately, does not accommodate an inner sphere water molecule ($q = 0$) [60, 61].

The inertness of DOTA-based complexes could also be enhanced by introducing steric hindrance to the cyclene ring [62, 63] Bulky substituents block the conformational rearrangements during dissociation as demonstrated for PhDOTA [64] and for NB-DOTA [65].

5.1.3. Pursuing High Relaxivity

The relaxivity is determined by several factors. The basic considerations have been discussed in Section 2.2. The r_1 relaxivity values of commercially available contrast agents range from 3.6 to 6.3 mM^{-1}s^{-1} [7], which is considerably lower than the theoretically attainable maximum value (see Figure 1B) [66].

Omitting one of the acetate pendant arms of DOTA results in the ligand DO3A, which forms a bishydrated complex with Gd(III) ($r_1 = 6.0$ mM^{-1}s^{-1} at 20 MHz, 25 °C) [67]. Gd(DO3A) forms ternary complexes with phosphate or bicarbonate ions, which reduces the relaxivity. [68] The heptadentate, but more rigid PCTA (Figure 4) also forms a bishydrated ($q = 2$) Gd(III) complex ($r_1 = 6.9$ mM^{-1}s^{-1} at 20 MHz, 25 °C) [67], but anions do not alter its relaxivity. Due to the favorable properties of PCTA, one of its derivatives (P03277, Gadopiclenol, $r_1 = 12.2$ mM^{-1}s^{-1} in water at 1.41 T, 37 °C) [69] is currently in phase 2 clinical trials [7]. Another complex in clinical trials [70] consists of four Gd(DO3A)-monoamide "units" connected to a central carbon atom via dipeptide linkers (BAY 1747846, $r_1 = 11.8$ mM^{-1}s^{-1}/Gd(III), in human plasma at 1.5 T, 37 °C) [71].

The rotational correlation time as well as the r_1 relaxivity often show a reasonably good linear correlation between the molecular weight of gadolinium complexes, but the effect usually levels off at a certain value. However, a more convenient approach involves the non-covalent binding of the CA to macromolecules via van der Waals forces [19]. Bifunctional ligands, usually based on DOTA or DTPA, are widely used for the attachment of the complex to macromolecular platforms. A classic example of this concept is the non-covalent binding of the Gd(DTPA)-based blood pool agent (Gadofosveset or Vasovist) with a diphenylcyclohexyl group to HSA. Linking multiple Gd(III) centers together is another way to increase the relaxivity of complexes. Higher relaxivity can be achieved when a spherical shape (dendrimer) rather than a linear oligomer is formed [7, 71].

The optimal water residence time at low field for slowly tumbling complexes is between 10 and 30 ns (see Figure 1B), while at higher field this optimal range broadens. The τ_M of most Gd APCs is longer than the optimal value at clinically relevant fields (1.5 to 3 T). Since the water exchange on monohydrated Gd complexes proceeds by a dissociative mechanism, the most reliable way of speeding up the exchange is increasing the steric compression around the water coordination site, which lengthens the metal ion–water distance. This can be accomplished by incorporating an additional methylene group into the polyamine backbone (macrocycle) or acetate sidearm, or by replacing the carboxylate with a bulkier coordinating group [72]. For example, Gd(DTPA) and Gd(EPTPA) (Figure 4A) can be modified to achieve faster water exchange, however, the thermodynamic stability of these complexes is lower than that of the parent chelates [73–75]. The water exchange can also be modulated by the electron donating properties of the donor atoms. The τ_M increases in the following order: phosphonates ~ phenolates < alpha-substituted acetates < acetate < hydroxamates ~ sulphonamides ~ acetamides ~ pyridyl ~ imidazole, i.e., the water exchange rate is faster for negatively charged donor groups than for neutral ones [76].

5.2.   Responsive/Activatable Contrast Agents

Several excellent reviews were published on this field in the last decade [7, 77–79]. Moreover, Chapter 12 of this book deals with responsive MRI agents. We provide only a short overview of Gd(III)-based responsive agents with some selected examples focusing on the coordination chemistry aspects.

How ligand design can improve the relaxivity of GBCAs is discussed in Section 5.1.3. Changes in relaxivity can also be generated via modulating q, τ_r, and τ_M by different stimuli, such as changes in pH, redox potential, concentration of endogenous cations, anions, metabolic products, enzyme activity, etc., in living systems. These molecular devices are named as "smart", responsible or activatable CAs (i.e., SCAs).

A simple model for pH-sensors based on the alteration of the number of inner sphere water molecule(s) (q) in GBCAs is shown in Equation (8):

$$\begin{array}{c} L \\ | \\ L' \end{array} Gd_{aq} + H^+ \rightleftharpoons HL' - L - Gd(H_2O) \qquad (8)$$

$$\quad\text{OFF} \qquad\qquad\qquad\qquad \text{ON}$$
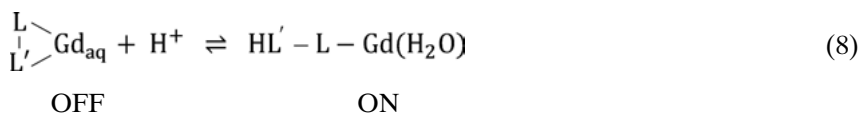
The $q = 0$ for the Gd(III) center at low concentration of H^+ (or metal ion in case of metal ion-responsive probes) (OFF state, low relaxivity), while at higher concentration of H^+ or M(II) the equilibrium is shifted to the right due to the protonation or metal binding of a suitable pendant arm (L'). As this sidearm leaves the inner sphere of Gd(III), a water molecule enters, which results in a substantial increase of the inner sphere relaxivity (ON state, high relaxivity). The analogy to acid-base indicators and metal indicators used in complexometric titrations is obvious in terms of pK or pM of the indicator. The higher the change in relaxivity, the better the sensitivity of the probe. If the equilibrium is fast and reversible, then the reverse reaction can also be observed. (The effect of anion coordination on relaxivity is opposite as the q and r_1 are decreasing, but the equilibrium considerations are similar and will not be discussed here.)

However, irreversible responsive probes do not return to their original state in the absence of their specific biomarker, i.e., alteration in the concentration of the biomarker cannot be detected. Nevertheless, the large-scale conversion of the SCA into the activated form can improve the sensitivity (see Figure 5 in Section 5.2.1). A linkage between the GBCA and the biomolecule can be generated by a stimulus. For instance, the reduction of an $-NO_2$ group of the nitroimidazole moiety in hypoxic tissues allows for its covalent binding to intracellular macromolecules. Accumulation of the GBCA in hypoxic regions results in substantial increase in the relaxation rate of the tissue water protons [80]. Enzyme-activity can be detected the other way around. The irreversible enzymatic cleavage of a bulky pendant arm of the agent results in decreased relaxivity due to faster tumbling (shorter rotational correlation time) of the product [81].

The heptadentate ligand DO3A is a widely used design platform for "smart" GBCAs. The unsubstituted N atom can easily be functionalized with a responsible pendant arm. In case of pH probes, the pK value should be slightly lower than the normal physiological pH (7.4), around pK = 6.4–6.8, to be able to measure pH in the range of 6.0–7.2. The pK can be fine-tuned by the nature of the donor atom(s) and/or by using electronic effects (see below [82]).

The measured relaxation effect *in vivo* depends on both the relaxivity of the "smart" GBCA used and the concentration of this agent in the studied biological compartment. For quantitative measurements the distribution of the "smart" agent has to be measured. This crucial requirement is challenging, and it is a serious limitation for the application of responsive agents. Several methods have been proposed to overcome this problem:

(1) Ratiometric approaches where the observed effect is independent of the concentration of the probe (e.g., by measuring the ratio between the transverse (R_2) and the longitudinal paramagnetic (R_1) relaxation rates of the bulk water protons) [83].

(2) The "cocktail" approach includes parallel injection of two complexes (responsive and nonresponsive) of similar (or the same) structures and presumably identical pharmacokinetics. The nonresponsive agent is used to estimate the local concentration of the probe while based on the known ratio of the two the concentration of the responsive agent can be assessed [108].

(3) The concentration of the probe can also be determined with a bimodal agent, where the other imaging modality, like PET or SPECT [84, 85], can be used to follow the biodistribution of the agent. The biodistribution data is used for the de-convolution of the MRI signals and to quantify the degree of activation (i.e., applying the mixture of ^{18}F labeled and stable ^{19}F-containing Gd(DOTA-4AmP) to simultaneous MRI-PET investigation) [86]. In the following we briefly review some recently published SCAs.

5.2.1. pH-Sensitive Contrast Agents

Measurement of the extracellular pH has an important role in cancer diagnosis, guided anticancer therapies, kidney diseases, etc. [7]. Tumor pH typically ranges between 5.7–7.8, depending on the histology and the volume of the tumor [87].

The first selected example uses an increase of q from 1 to 2 as the pH is lowered [88]. The Gd(NP-DO3A) (Figure 4B) is a DO3A derivative functionalized with a p-nitrophenolate pendant arm. As the pH decreases, the protonation and simultaneous decoordination of the phenolate oxygen atom occurs, resulting in a 71 % enhancement in the r_1 value (from 4.1 to 7.0 mM^{-1}s^{-1}) in the pH range of 9–5. A similar principle is used for the pH-sensing in the Gd(DO3A-EA) complex having an amino-ethyl group attached to DO3A [82]. Gd(DO3A-EA) shows an increase in its relaxivity in the physiologically relevant pH range, and the pH range can be fine-tuned by the substitution of at least one of the H atoms on the –NH$_2$ moiety.

An elegant example of bimodal agents is a heteroditopic complex containing Gd(III) for MRI and ^{68}Ga(III) as PET reporter (Figure 5A) [89]. The dimeric ligand consists of two chelating units. The DO3A sulfonamide "bucket" binds Gd(III), while the AAZTA moiety is designed for ^{68}Ga(III) chelation. The sulfonamide pendant ensures the pH sensitivity of the Gd(III) center while PET imaging (independent of the biochemical stimulus) allows for the calculation of the local concentration of the CA, which is essential to generate a pH map.

Acidification of a pH-sensitive liposome loaded with a paramagnetic complex (e.g., the clinically approved Gadoteridol) causes the release of the paramagnetic chelate resulting in a decrease in the T_1 relaxation time [90]. Polymeric micelles were also used as SCAs for *in vivo* pH imaging [91].

Alteration of the tumbling rate as a result of protonation can also change the relaxivity via morphological changes. It suppresses the flexibility of the Gd(III) chelate followed by a relaxivity response [92].
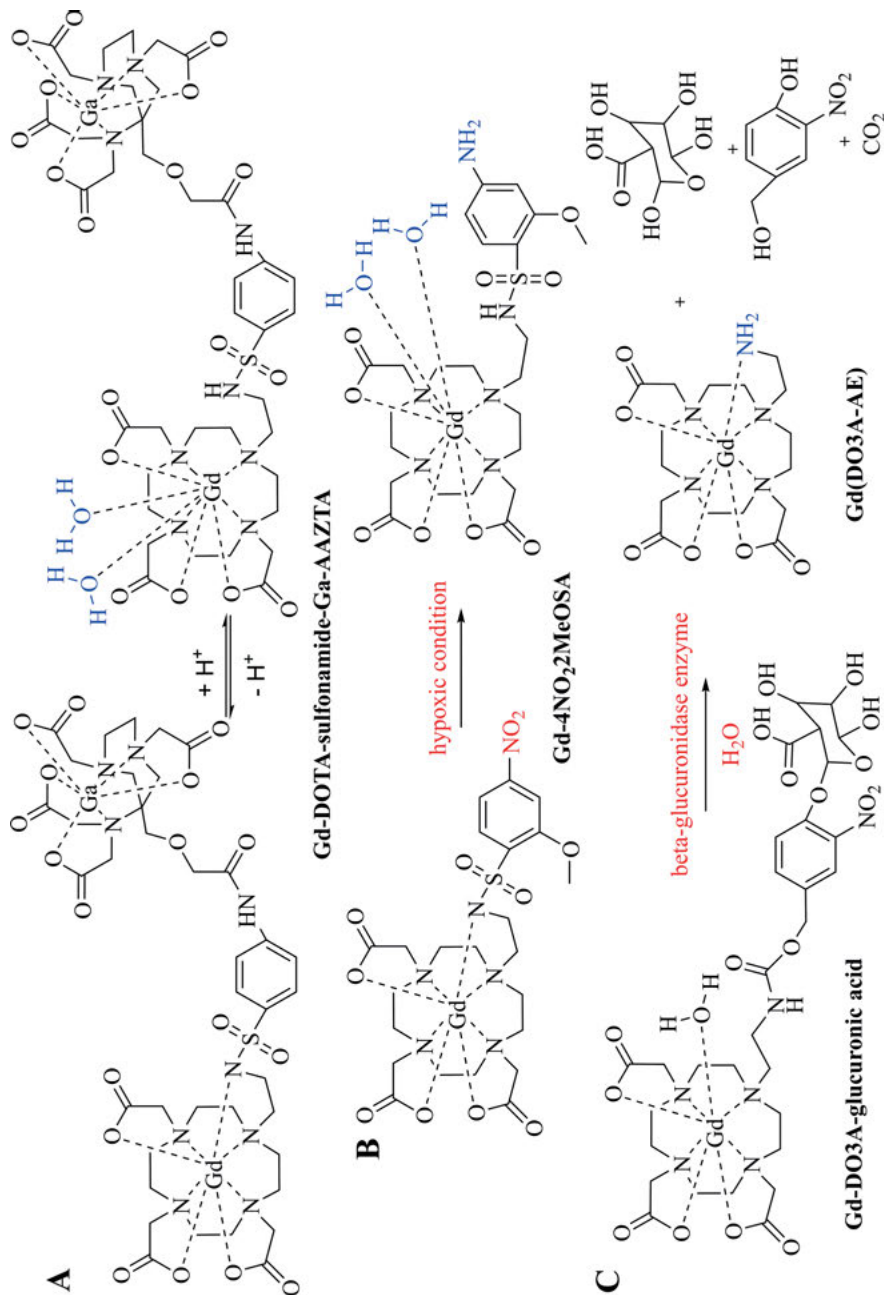
Figure 5. Representative examples of (**A**) some pH-responsive, (**B**) hypoxia- and (**C**) enzyme-activated SCAs.

5.2.2. Redox Responsive Contrast Agent Candidates

In order to maintain the normal biological processes, the intra- and extracellular redox environment is highly regulated [93]. Redox SCAs in which the oxidation state of the Gd(III) center changes cannot be designed. This can only be achieved by incorporating redox sensitive moieties/ligand fragments in the GBCAs [93, 94].

The reduction of the nitro group in the Gd(4NO$_2$MeOSA) complex bearing a nitrobenzene-sulfonamide side chain (Figure 5B) can selectively indicate hypoxic conditions with a 1.8-fold increase in the r_1 relaxivity in rats [95]. The reduction of the nitro group increases the pK value of the sulfonamide nitrogen from 5.2 to 6.7 resulting in the protonation and dissociation of the nitrogen from the Gd(III) ion (meanwhile q rises from 0 to 2). A DOTA-monoamide-based ligand bearing a 2-nitroimidazole side chain Gd(DO3AM^{NIM}) (Figure 4B) is another example of a redox SCA. Following the reduction of the nitro group under hypoxic conditions the molecule is trapped in hypoxic cells and the accumulation of the Gd complex results in contrast enhancement [80].

Another approach to sense the redox potential by using Gd(III)-based CAs is the reversible or irreversible binding of low molecular weight probes to macromolecules in order to increase the τ_R [93, 94]. An example is a series of Gd(DO3A) and Gd(DOTA-monoamides) bearing alkyl linkers with terminal thiol groups that can react with the Cys-34 residue of HSA via the formation of an S—S bond resulting in increased τ_R [96–98]. For example, Gd(LC6-SH) (Figure 4B) binds to HSA in this manner. However, reducing environment cleaves the S—S bond, which lowers the relaxivity by 55 % [99].

5.2.3. Reporters of Enzyme Activity

Enzymes such as esterases, β-galactosidase, peroxidases, caspases, etc., are very important biomarkers for biological or pathological processes. Enzymes are initially expressed in an inactive form as zymogens and become activated when the cells or tissues need them. Therefore, the detection of the presence of an inactive enzyme could be a source of error. To avoid this problem, responsive probes should detect the activity level of the enzyme rather than the presence of the enzyme [7].

An often cited example of the enzyme-responsive agents by the modulation of the hydration state is a Gd(DO3A) derivative with a pendant β-glucuronic acid attached to the macrocycle through the self-immolative linker Gd(DO3A-glucuronic acid) (Figure 5C) [100]. Bovine liver β-glucuronidase enzymatically cleaved off the β-D-glucuronic acid moiety followed by the self-immolation of the intermediary complex into Gd(DO3A-EA) and 4-hydroxy-3-nitrobenzyl alcohol. The enzyme activation resulted in a 17 % increase in relaxivity in a buffer, while a 27 % decrease was observed in blood serum.

Enzymatic cleavage can also lengthen the rotational correlation time by removing a blocking group and thereby allowing the complex to interact with a high molecular weight molecule (e.g., HSA) [81, 101, 102]. Enzyme-catalyzed

breakdown of polymers that contain covalently linked Gd(III) complexes was also utilized to detect enzyme activity. Hyaluronidase activity was visualized by the enhanced relaxivity of the Gd(DTPA)-hyaluronan conjugate after the enzymatic break-down of the hyaluronan network [103].

A dual ^{1}H MRI/^{19}F NMR probe was developed to detect the activity of the protease caspase-3, which cleaves tetrapeptide sequences after aspartic acid residues. The probe Gd(DOTA)-DEVD-Tfb consisted of three parts, the Gd complex, the caspase-3 substrate sequence and the ^{19}F-containing moiety by incorporating ^{19}F nuclei into the molecule [104, 105]. The ^{19}F T_2 is dramatically shortened by the presence of Gd(III) when the two atoms are intramolecularly bound. However, the T_2-shortening effect was significantly diminished after cleavage of the tetrapeptide sequence by the enzyme. The activity of other enzymes such as β-galactosidase or β-lactamase can also be detected [106, 107].

6. CONCLUDING REMARKS AND FUTURE PERSPECTIVES

6.1. Non-Lanthanide-Based Alternative Magnetic Resonance Imaging Contrast Agents and New Technologies

The primary importance of MRI in clinical practice together with safety concerns related to GBCAs strongly motivates the search for alternative MRI CAs. Paramagnetic transition metal complexes (Mn(II), Fe(III) as T_1 agents) have been considered since the introduction of MRI, while recent directions also involve other approaches as quadrupolar relaxation agents (QRE, ^{209}Bi or ^{14}N compounds) [108, 109] or (metal ion-free) organic radical-based contrast agents (ORCAs) [110, 111]. A related technology, magnetic resonance spectroscopy (MRS) and spectroscopic imaging, escpecially when combined with hyperpolarization techniques, is an emerging MR-based molecular imaging modality. Some of these methods are discussed in detail in other chapters of this book; therefore we only briefly mention Mn-based agents and do not discuss paraCEST agents (see Chapter 4).

6.1.1. Manganese-Based Probes

In Chapter 3 Eva Jakab-Tóth et al. describe the massive research on Mn(II/III)-based probes. Here, we briefly summarize the outcome of our own work over the last decade (Figure 4). In our view the best open-chain candidates for manganese chelation (as far as stability/inertness/relaxation enhancement properties are concerned) are the rigid *trans*-1,2-diaminocyclohexane (*trans*CDTA or PyC3A) or *ortho*-phenylenediamine derivates [112–114]. Among the macrocyclic platforms the most promising structures include the *c*DO2A (and its bisamide derivatives) [115], the 15-Py-ane-N$_3$O$_2$ macrocycle, and the PC2A ligand [116, 117]. Furthermore, the easy functionalization of the macrocyclic pyclen N-atoms pro-

vides convenient access to PC2A-based smart probes that respond to external stimuli (pH, Zn(II), etc.) [117].

6.1.2. Fe(III)-Based Contrast Agents

Certain high-spin (S = 5/2) Fe(III) complexes have also been considered as GBCAs alternatives. A recent review by Kuźnik and Wyskocka gives a nice overview of the research on small molecule-based Fe(III)-containing CAs [118]. The complexation of Fe(III) ion is usually achieved by ligands derived from Tiron, EHPG, EHBG, catecholate or aminophenolate-type ligands possessing O,O and N,O donor atoms, respectively, as well as traditional APC-type ligands such as EDTA, *trans*CDTA, PhDTA, etc. or even DFO (desferrioxamine) (see Figure 4A). The group of potential Fe(III)-binding chelators was lately expanded by Morrow et al. by proposing 1,4,7-triazacyclononane-based (TACN) ligands possessing 2-hydroxypropyl, 2-methylimidazole or 1-methyl-2-methylimidazole moieties [119, 120]. Recently Caravan et al. have demonstrated that the Fe(II/III) complex of the PyC3A chelator (proposed originally for Mn(II) complexation) is a highly effective redox RCA candidate [121].

6.1.3. Hyperpolarized Probes

In conventional NMR, the signal intensity is proportional to the difference in the nuclear spin population (spin polarization) of the Zeeman levels as determined by the Boltzmann distribution at thermal equilibrium. MRI has inherently low sensitivity because these levels are almost equally populated at room temperature. The spin polarization increases with the B_0 magnetic field (proportional to B_0/T) and the gyromagnetic ratio (γ) of the nucleus. The observed nucleus in conventional MRI experiments is almost exclusively ^1H since it has the second highest γ of all nuclei after ^3H and the ^1H concentration (spin density) is also the highest *in vivo*. Dramatic NMR signal enhancements (5 orders of magnitude or more) can be achieved by hyperpolarization (HP). This can be performed by various experimental methods including dynamic nuclear polarization (DNP), spin-exchange optical pumping, and parahydrogen induced polarization [122]. Currently, DNP, which involves the microwave-driven transfer of electron spin polarization to coupled nuclear spins, is the most commonly used technique because it is generally applicable to a wide range of nuclei (^1H, ^{19}F, ^{13}C, ^{15}N, ^{31}P, ^{29}Si, ^{89}Y, and $^{107,109}Ag$) [123–129]. Such increases in sensitivity make it possible to perform molecular/functional MR imaging of nuclei other than ^1H. The hyperpolarized spin state is not persistent and decays to thermodynamic equilibrium by T_1 relaxation. This limits the detectable HP-NMR signal for ~5 T_1. Therefore, long T_1 values are highly desirable [128]. The most commonly used HP agents are ^{13}C-based for obvious reasons. HP-^{13}C labeled tracers provide a very convenient way of determining fluxes through specific enzyme-catalyzed steps by ^{13}C MRS/MRI allowing the real-time monitoring of biochemical pathways in various

organs. HP[1-^{13}C]pyruvate is currently in clinical trials at several sites for grading prostate cancer, evaluating heart disease, and liver metabolism [122, 130–133].

Among other spin ½ NMR active nuclei, ^{89}Y (100 % natural abundance) has extremely long T_1 relaxation times. $T_1 = 499$ s was measured for Y(DOTA) at 9.4 T [134], and the NMR signal is sharp (3–5 Hz). HP-^{89}Y is particularly relevant for the topic of this chapter as Y(III) is often considered as the diamagnetic analogue of Gd(III). Ligand systems developed for Gd(III) and Eu(III), can directly be used with Y(III) [134–136].

The sensitivity of the chemical shift of ^{89}Y(III) to its chemical environment can be exploited in the design of responsive probes to image and map biomarkers such as pH *in vivo* by HP-^{89}Y MRS/MRI. The ^{89}Y chemical shift of the hyperpolarized ^{89}Y(DOTP) gradually decreases from 150 to 140 ppm between pH 5 and 8 with decreasing electronic shielding of the ^{89}Y nucleus due to the protonation of the non-coordinating phosphonate oxygens [137].

6.2. The Future Role of Chemical Research in the Development of Magnetic Resonance Imaging Contrast Agents

The 450 millions contrast enhanced MRI exams indicate the importance of gadolinium-based diagnostic agents. Yet, the future of GBCAs is uncertain. Their role very likely will not be suppressed or taken over by other agents in the foreseeable future despite the active research on alternative CAs. New high relaxivity and/or targeted GBCAs may also enter to the market [70, 71]. Dual probes (e.g., PET-MRI) and theranostic applications (see Chapters 11 and 12) are under progress. The chemical research of SCAs is in high gear, and one may expect a breakthrough human application in the next decade.

The chemist's role is obvious in the synthesis of new ligands and the physicochemical characterization of their metal complexes, as it is in the analytical studies (ICP-MS) of Gd-retention in tissue samples. Biodistribution and/or Gd-retention studies require multi-disciplinary teams [47]. The Gd speciation in such a complex matrix as brain tissue might be addressed by using molecular spectroscopy/microscopy techniques (IR, Raman spectroscopy) [138, 139] together with emerging new methods to evaluate experimental data (artificial intelligence, machine learning, etc.).

ACKNOWLEDGMENTS

ABBREVIATIONS AND DEFINITIONS

For the commercial names of the gadolinium-based contrast agents see Section 2.2. and Figure 2.

APC	amino-polycarboxylate
BBB	blood brain barrier
CA	contrast agent
CNS	central nervous system
DNP	dynamic nuclear polarization
EMA	European Medicines Agency
EXAFS	extended X-ray fine structure
FDA	Food and Drug Administration
GBCAs	gadolinium-based contrast agents
HP	hyperpolarized
HSA	human serum albumin
ICP-AES	inductively coupled plasma atomic emission
ICP-MS	inductively coupled plasma mass spectrometry
MRI	magnetic resonance imaging
MRS	magnetic resonance spectroscopy
NMR	nuclear magnetic resonance
NSF	nephrogenic systemic fibrosis
ORCAs	organic radical-based contrast agents
PET	positron emission tomography
QRE	quadrupolar relaxation enhancement
RF	radio frequency
SCA	"smart" contrast agent
SE	spin echo
SI	signal intensity
SPECT	single photon emission tomography

REFERENCES

1. I. Grenthe, G. Gardhammar, *Acta Chem. Scand.* **1972**, *26*, 3207–3214.
2. K. B. Yatsimirskii, N. A. Kostromina, Z. A. Shcheka, N. K. Davidenko, E. E. Kriss, V. I. Ermolenko, *Khimiya Kompleksnykh Soedinenii Redkozemeľnykh Elementov (Chemistry of Complex Compounds of Rare Earth Elements)*, Naukova Dumka, Kiev, **1966**.
3. G. R. Choppin, M. P. Goedken, T. F. Gritmon, *J. Inorg. Nucl. Chem.* **1977**, *39*, 2025–2030.

4. E. Brücher, G. Laurenczy, *J. Inorg. Nucl. Chem.* **1981**, *41*, 2089–2096.

5. W. D. Horrocks, V. K. Arkle, F. J. Liotta, D. R. Sudnick, *J. Am. Chem. Soc.* **1983**, *105*, 3455–3459.

6. C. Cossy, L. Helm, A. E. Merbach, *Inorg. Chem.* **1988**, *27*, 1973–1979.

7. J. Wahsner, E. M. Gale, A. Rodríguez-Rodríguez, P. Caravan, *Chem. Rev.* **2019**, *119*, 957–1057.

8. V. M. Runge, *Invest. Radiol.* **2017**, *52*, 317–323.

9. T. Grobner, *Nephrol. Dial. Transplant.* **2006**, *21*, 1104–1108.

10. P. Marckmann, L. Skov, K. Rossen, A. Dupont, M. B. Damholt, J. G. Heaf, H. S. Thomsen, *J. Am. Soc. Nephrol.* **2006**, *17*, 2359–2362.

11. G. Schuhmann-Giampieri, G. Krestin, *Invest. Radiol.* **1991**, *26*, 975–979.

12. P. Joffe, H. S. Thomsen, M. Meusel, *Acad. Radiol.* **1998**, *5*, 491–502.

13. B. Tombach, C. Bremer, P. Reimer, R. M. Schaefer, W. Ebert, V. Geens, W. Heindel, *Invest. Radiol.* **2000**, *35*, 35–40.

14. T. Kanda, T. Fukusato, M. Matsuda, K. Toyoda, H. Oba, J. Kotoku, T. Haruyama, K. Kitajima, S. Furui, *Radiology* **2015**, *276*, 228–232.

15. W. A. Gibby MD, K. A. Gibby, W. A. Gibby, *Invest. Radiol.* **2004**, *39*, 138–142.

16. M. Bau, P. Dulski, *Earth Planet. Sci. Lett.* **1996**, *143*, 245–255.

17. E. Brücher, Z. Baranyai, G. Tircsó, *The Future of Biomedical Imaging: Synthesis and Chemical Prioerties of the DTPA and DOTA Derivate Ligands and Their Complexes*, in *Biomedical Imaging: The Chemistry of Labels, Probes and Contrast Agents*, Ed. M. Braddock, Royal Society of Chemistry, **2012**, 208–206.

18. E. Brücher, Gy. Tircsó, Zs. Baranyai, Z. Kovács, A. D. Sherry, *Stability and Toxicity of Contrast Agents*, in *The Chemistry of Contrast Agents in Medical Magnetic Resonance Imaging*, 2nd ed., Eds. A. S. Merbach, L. Helm, É. Tóth, Wiley, Chichester, UK, **2013**, 157–208.

19. Q. N. Do, J. S. Ratnakar, Z. Kovács, G. Tircsó, F. K. Kálmán, Z. Baranyai, E. Brücher, I. Tóth, *General Synthetic and Physical Methods*, in *Contrast Agents for MRI: Experimental Methods*, Eds. V. C. Pierre, M. J. Allen, Royal Society of Chemistry, **2018**, 1–120.

20. H. Y. Carr, E. M. Purcell, *Phys. Rev.* **1954**, *94*, 630–638.

21. G. E. Hagberg, K. Scheffler, *Contrast Media Mol. Imaging* **2013**, *8*, 456–465.

22. R. Shah, F. D'arco, B. Soares, J. Cooper, J. Brierley, *Br. J. Radiol.* **2019**, *92*, 20180746.

23. Z. Baranyai, E. Brücher, F. Uggeri, A. Maiocchi, I. Tóth, M. Andrási, A. Gáspár, L. Zékány, S. Aime, *Chem. Eur. J.* **2015**, *21*, 4789–4799.

24. Z. Baranyai, Z. Pálinkás, F. Uggeri, A. Maiocchi, S. Aime, E. Brücher, *Chem. Eur. J.* **2012**, *18*, 16426–16435.

25. B. L. Daftari, S. Aran, K. Shaqdan, J. Kay, H. Abujudeh, *Clin. Radiol.* **2014**, *69*, 661–668.

26. M. R. Prince, H. L. Zhang, Z. T. Zou, R. B. Staron, P. W. Brill, *Am. J. Roentgenol.* **2011**, *196*, W138–W143.

27. B. Wagner, V. Drel, Y. Gorin, *Am. J. Physiol. Renal Physiol.* **2016**, *311*, 1–11.

28. D. Xia, R. L. Davis, J. A. Crawford, J. L. Abraham, *Acta Radiol.* **2010**, *51*, 1126–1136.

29. T. Kanda, K. Ishii, H. Kawaguchi, K. Kitajima, D. Takenaka, *Radiology* **2014**, *270*, 834–841.

30. R. J. McDonald, D. Levine, J. Weinreb, E. Kanal, M. S. Davenport, J. H. Ellis, P. M. Jacobs, R. E. Lenkinski, K. R. Maravilla, M. R. Prince, H. A. Rowley, M. F. Tweedle, H. Y. Kressel, *Radiology* **2018**, *289*, 517–534.

31. J. W. Choi, W. J. Moon, *Korean J. Radiol.* **2019**, *20*, 134–147.

32. M. Braun, G. Zavanyi, A. Laczovics, E. Berényi, S. Szabó, *Water Research* **2018**, *135*, 104–111.

33. P. Ebrahimi, M. Barbieri, *Geosciences* **2019**, *9*, 93.

34. Food and Drug Administration Advisory Committee, *Gadolinium-Based Contrast Agents & Nephrogenic Systemic Fibrosis, FDA Briefing Document*, **2015**.

35. P. Désogère, L. F. Tapias, L. P. Hariri, N. J. Rotile, T. A. Rietz, C. K. Probst, F. Blasi, H. Day, M. Mino-Kenudson, P. Weinreb, S. M. Violette, B. C. Fuchs, A. M. Tager, M. Lanuti, P. Caravan, *Sci. Transl. Med.* **2017**, *9*, eaaf4696.

36. Japan Pharmaceuticals and Medicals Devices Agency, *Report on the Investigation Results − Gadolinium-based contrast agents*, **2017**. https://www.pmda.go.jp/files/000221379.pdf. Accessed May 2, 2020.

37. A. D. Elster, *Does gadolinium accumulate in tissues after repeated doses?*, **2019**. http://mriquestions.com/gd-accumulation.html. Accessed May 2, 2020.

38. B. J. Edwards, A. E. Laumann, B. Nardone, F. H. Miller, J. Restaino, D. W. Raisch, J. M. McKoy, J. A. Hammel, K. Bhatt, K. Bauer, A. T. Samaras, M. J. Fisher, C. Bull, E. Saddleton, S. M. Belknap, H. S. Thomsen, E. Kanal, S. E. Cowper, A. K. Abu Alfa, D. P. West, *Br. J. Radiol.* **2014**, *87*, 20140307.

39. C. H. Evens, *Biochemistry of the Lanthanides*, Plenum Press, New York, **1990**.

40. P. Wedeking, K. Kumar, M. F. Tweedle, *Magn. Reson. Imaging* **1992**, *10*, 641–648.

41. M. Port, J. M. Idée, C. Medina, C. Robic, M. Sabatou, C. Corot, *Biometals* **2008**, *21*, 469–490.

42. M. Van Wagoner, M. O'toole, D. Worah, P. T. Leese, S. C. Quay, *Invest. Radiol.* **1991**, *26*, 980–986.

43. K. A. Layne, P. I. Dargan, J. R. H. Archer, D. M. Wood, *Br. J. Clin. Pharmacol.* **2018**, *84*, 2522–2534.

44. S. J. George, S. M. Webb, J. L. Abraham, S. P. Cramer, *Br. J. Dermatol.* **2010**, *163*, 1077–1081.

45. M. Birka, K. S. Wentker, E. Lusmöller, B. Arheilger, C. A. Wehe, M. Sperling, R. Stadler, U. Karst, *Anal. Chem.* **2015**, *87*, 3321–3328.

46. E. Gianolio, E. D. Gregorio, S. Aime, *Eur. J. Inorg. Chem.* **2019**, *2019*, 137–151.

47. M. L. Fur, P. Caravan, *Metallomics* **2019**, *11*, 240–254.

48. J. Xu, S. J. Franklin, D. W. Whisenhunt, K. N. Raymond, *J. Am. Chem. Soc.* **1995**, *117*, 7245–7246.

49. I. Puigdomenech, *Chemical Equilibrium Diagrams: Medusa and Hydra*, The Royal Institute of Technology, Stockholm, Sweden, **2020**, https://www.kth.se/che/medusa/. Accessed May 2, 2020.

50. Z. Baranyai, Z. Pálinkás, F. Uggeri, E. Brücher, *Eur. J. Inorg. Chem.* **2010**, *2010*, 1948–1956.

51. F. K. Kálmán, A. Végh, M. Regueiro-Figueroa, É. Tóth, C. Platas-Iglesias, G. Tircsó, *Inorg. Chem.* **2015**, *54*, 2345–2356.

52. G. Tircsó, M. Regueiro-Figueroa, V. Nagy, Z. Garda, T. Garai, F. K. Kálmán, D. Esteban-Gómez, É. Tóth, C. Platas-Iglesias, *Chem. Eur. J.* **2016**, *22*, 896–901.

53. Z. Baranyai, F. Uggeri, G. B. Giovenzana, A. Bényei, E. Brücher, S. Aime, *Chem. Eur. J.* **2009**, *15*, 1696–1705.

54. A. Vágner, E. Gianolio, S. Aime, A. Maiocchi, I. Tóth, Z. Baranyai, L. Tei, *Chem. Commun.* **2016**, *52*, 11235–11238.

55. K. Kumar, M. F. Tweedle, M. F. Malley, J. Z. Gougoutas, *Inorg. Chem.* **1995**, *34*, 6472–6480.

56. G. Tircsó, Z. Kovács, A. D. Sherry, *Inorg. Chem.* **2006**, *45*, 9269–9280.

57. S. Aime, M. Botta, L. Frullano, S. G. Crich, G. Giovenzana, R. Pagliarin, G. Palmisano, F. R. Sirtori, M. Sisti, *J. Med. Chem.* **2000**, *43*, 4017–4024.

58. M. L. Fur, E. Molnár, M. Beyler, F. K. Kálmán, O. Fougère, D. Esteban-Gómez, O. Rousseaux, R. Tripier, G. Tircsó, C. Platas-Iglesias, *Chem. Eur. J.* **2018**, *24*, 3127–3131.

59. M. L. Fur, E. Molnár, M. Beyler, O. Fougère, D. Esteban-Gómez, O. Rousseaux, R. Tripier, G. Tircsó, C. Platas-Iglesias, *Inorg. Chem.* **2018**, *57*, 6932–6945.

60. A. Rodríguez-Rodríguez, D. Esteban-Gómez, R. Tripier, G. Tircsó, Z. Garda, I. Tóth, A. de Blas, T. Rodríguez-Blas, C. Platas-Iglesias, *J. Am. Chem. Soc.* **2014**, *136*, 17954–17957.

61. A. Rodríguez-Rodríguez, M. Regueiro-Figueroa, D. Esteban-Gómez, R. Tripier, G. Tircsó, F. K. Kálmán, A. Bényei, I. Tóth, A. de Blas, T. Rodríguez-Blas, C. Platas-Iglesias, *Inorg. Chem.* **2016**, *55*, 2227–2239.

62. T. J. Clough, L. Jiang, K. Wong, N. J. Long, *Nat. Comm.* **2019**, *10*, 1420.

63. H. Wan, J. Yue, S. Zhu, T. Uno, X. Zhang, Q. Yang, K. Yu, G. Hong, J. Wang, L. Li, Z. Ma, H. Gao, Y. Zhong, J. Su, A. L. Antaris, Y. Xia, J. Luo, Y Liang, H. Dai, *Nat. Comm.* **2018**, *9*, 1–10.

64. C. D. Edlin, S. Fauner, D. Parker, M. P. Wilkinson, M. Woods, J. Lin, E. Lasri, F. Neth, M. Port, *New J. Chem.* **1998**, *22*, 1359–1364.

65. K. M. Payne, M. Woods, *Bioconjug. Chem.* **2015**, *26*, 338–344.

66. E. J. Werner, A. Datta, C. J. Jocher, K. N. Raymond, *Angew. Chem. Int. Ed.* **2008**, *47*, 8568–8580.

67. S. Aime, M. Botta, S. G. Crich, G. Giovenzana, R. Pagliarin, M. Sisti, E. Terreno, *Magn. Reson. Chem.* **1998**, *36*, 200–208.

68. R. M. Supkowski, W. DeW. Horrocks, *Inorg. Chem.* **1999**, *38*, 5616–5619.

69. C. Robic, M. Port, O. Rousseaux, S. Louguet, N. Fretellier, S. Catoen, C. Factor, S. Le Greneur, C. Medina, P. Bourrinet, I. Raynal, J. Idée, C. Corot, *Investig. Radiol.* **2019**, *54*, 475–484.

70. Bayer Clinical Trials Contact, *Study to Find the Appropriate Dose of a New Gadolinium-based Contrast Agent (GBCA) for Adults Undergoing Magnetic Resonance Imaging (MRI) for Known or Highly Suspected Brain and/or Spinal Cord Conditions*, **2020**. https://clinicaltrials.gov/ct2/show/study/NCT04307186. Accessed May 2, 2020.

71. M. Beger, J. Lohrke, J. Lohrke, C. Hilger, G. Jost, T. Frenzel, O. Panknin, H. Pietsch, *High Relaxivity Gadolinium Chelate Compounds for Use in Magnetic Resonance Imaging*, Bayer Pharma AG, Berlin, **2018**, *PCT/EP2017/080306, WO/2018/096082*.

72. L. Helm, A. E. Merbach, *Chem. Rev.* **2005**, *105*, 1923–1960.

73. É. Tóth, L. Burai, E. Brücher, A. E. Merbach, *Dalton Trans.* **1997**, 1587–1594.

74. S. Laus, R. Ruloff, É. Tóth, A. E. Merbach, *Chem. Eur. J.* **2003**, *9*, 3555–3566.

75. Z. Jászberényi, A. Sour, A. Sour, É. Tóth, M. Benmelouka, A. E. Merbach, *Dalton Trans.* **2005**, 2713–2719.

76. S. Dumas, V. Jacques, W. C. Sun, J. S. Troughton, J. T. Welch, J. M. Chasse, H. Schmitt-Willich, P. Caravan, *Investig. Radiol.* **2010**, *45*, 600–612.

77. D. V. Hingorani, B. Yoo, A. S. Bernstein, M. D. Pagel, *Chem. Eur. J.* **2015**, *20*, 9840–9850.

78. D. V. Hingorani, A. S. Bernstein, M. D. Pagel, *Contrast Media Mol. Imaging* **2015**, *10*, 245–265.

79. Q. N. Do, J. S. Ratnakar, Z. Kovács, A. D. Sherry, *ChemMedChem* **2014**, *9*, 1116–1129.

80. F. A. Rojas-Quijano, G. Tircsó, E. Tircsóné Benyó, Z. Baranyai, H. T. Hoang, F. K. Kálmán, P. K. Gulaka, V. D. Kodibagkar, S. Aime, Z. Kovács, A. D. Sherry, *Chem. Eur. J.* **2012**, *18*, 9669–9676.

81. A. L. Nivorozhkin, A. F. Kolodziej, P. Caravan, M. T. Greenfield, R. B. Lauffer, T. J. McMurry, *Angew. Chem. Int. Ed.* **2001**, *40*, 2903–2906.

82. G. B. Giovenzana, R. Negri, G. A. Rolla, L. Tei, *Eur. J. Inorg. Chem.* **2012**, 2035–2039.

83. S. Aime, F. Fedeli, A. Sanino, E. Terreno, *J. Am. Chem. Soc.* **2006**, *128*, 11326–11327.

84. E. Gianolioa, L. Maciocco, D. Imperio, G. B. Giovenzana, F. Simonelli, K. Abbas, G. Bisie, S. Aime, *Chem. Commun.* **2011**, *47*, 1539–1541.
85. K. P. Malikidogo, I. D. Silva, J. Morfin, S. Lacerda, L. Barantin, T. Sauvage, J. Sobilo, S. Lerondel, É. Tóth, C. S. Bonnet, *Chem. Commun.* **2018**, *54*, 7597–7600.
86. L. Frullano, C. Catana, T. Benner, A. D. Sherry, P. Caravan, *Angew. Chem. Int. Ed.* **2010**, *49*, 2382–2384.
87. K. Engin, D. B. Leeper, J. R. Cater, A. J. Thistlethwaite, L. Tupchong, D. McFarlane, *Int. J. Hyperth.* **1995**, *11*, 211–216.
88. M. Woods, G. E. Kiefer, S. Bott, A. Castillo-Muzquiz, C. Eshelbrenner, L. Michaudet, K. McMillan, S. D. K. Mudigunda, D. Ogrin, G. Tircsó, S. Zhang, P. Zhao, A. D. Sherry, *J. Am. Chem. Soc.* **2004**, *126*, 9248–9256.
89. N. Vologdin, G. A. Roll, M. Bott, L. Tei, *Org. Biomol. Chem.* **2013**, *11*, 1683–1690.
90. E. Gianolio, S. Porto, R. Napolitano, S. Baroni, G. B. Giovenzana, S. Aime, *Inorg. Chem.* **2012**, *51*, 7210–7217.
91. K. Sub Kim, W. Park, J. Hu, Y. Han Bae, K. Na, *Biomaterials* **2014**, *35*, 337–343.
92. S. Okada, S. Mizukami, K. Kikuchi, *Bioorg. Med. Chem.* **2012**, *20*, 769–774.
93. S. M.Pinto, V. Tomé, M. J. F. Calvete, M. Margarida, C. A. Castro, É. Tóth, C. F. G. C. Geraldes, *Coord. Chem. Rev.* **2019**, *390*, 1–31.
94. S. Guo, X. Xiao, X. Wang, Q. Luo, H. Zhu, H. Zhang, H. Li, Q. Gonga, K. Luo, *Biomater. Sci.* **2019**, *7*, 1919–1932.
95. S. Iwaki, K. Hanaoka, W. Piao, T. Komatsu, T. Ueno, T. Terai, T. Nagano, *Bioorg. Med. Chem. Lett.* **2012**, *22*, 2798–2802.
96. C. Carrera, G. Digilio, S. Baroni, D. Burgio, S. Consol, F. Fedeli, D. Longo, A. Mortillaro, S. Aime, *Dalton Trans.* **2007**, 4980–4987.
97. N. Raghunand, G. P. Guntle, V. Gokhale, G. S. Nichol, E. A. Mash, B. Jagadish, *J. Med. Chem.* **2010**, *53*, 6747–6757.
98. T. H. Landowski, G. P.Guntle, D. Zhao, B. Jagadish, E. A. Mash, R. T. Dorr, N. Raghunand, *Transl. Oncol.* **2016**, *9*, 228–235.
99. G. P. Guntle, B. Jagadish, E. A. Mash, G. Powis, R. T. Dorr, N. Raghunand, *Transl. Oncol.* **2012**, *5*, 190–199.
100. J. A. Duimstra, F. J. Femia, T. J. Meade, *J. Am. Chem. Soc.* **2005**, *127*, 12847–12855.
101. Y. Chang, C. Cheng, Y. Su, W. Lee, J. Hsu, G. Liu, T. Cheng, Y. Wang, *Bioconjug. Chem.* **2007**, *18*, 1716–1727.
102. Y. Chen, S. Wu, C. Chen, S. Tzou, T. Cheng, Y. Huang, S. Yuan, Y. Wang, *Biomaterials* **2014**, *35*, 304–315.
103. L. Shiftan, T. Israely, M. Cohen, V. Frydman, H. Dafni, R. Stern, M. Neeman, *Cancer Res.* **2005**, *65*, 10316−10323.
104. S. Mizukami, R. Takikawa, F. Sugihara, Y. Hori, H. Tochio, M. Wälchli, M. Shirakawa, K. Kikuchi, *J. Am. Chem. Soc.* **2008**, *130*, 794–795.
105. S. Mizukami, R. Takikawa, F. Sugihara, M. Shirakawa, K. Kikuchi, *Angew. Chem. Int. Ed.* **2009**, *48*, 3641–3643.
106. S. Mizukami, H. Matsushita, R. Takikawa, F. Sugihara, M. Shirakawad, K. Kikuchi, *Chem. Sci.* **2011**, *2*, 1151–1155.
107. H. Matsushita, S. Mizukami, Y. Mori, F. Sugihara, M. Shirakawa, Y. Yoshioka, K. Kikuchi, *ChemBioChem* **2012**, *13*, 1579–1583.
108. C. Gösweiner, P. Lantto, R. Fischer, C. Sampl, E. Umut, P. Westlund, D. Kruk, M. Bödenler, S. Spirk, A. Petrovič, H. Scharfetter, *Phys. Rev.* **2018**, *8*, 021076.
109. D. Kruk, E. Umut, E. Masiewicz, C. Sampl, R. Fischer, S. Spirk, C. Goesweiner, H. Scharfetter, *Phys. Chem. Chem. Phys.* **2018**, *20*, 12710–12718.
110. A. Rajca, Y. Wang, M. Boska, J. T. Paletta, A. Olankitwanit, M. A. Swanson, D. G. Mitchell, S. S. Eaton, G. R. Eaton, S. Rajca, *J. Am. Chem. Soc.* **2012**, *134*, 15724–15727.

111. H. V.-T. Nguyen, Q. Chen, J. T. Paletta, P. Harvey, Y. Jiang, H. Zhang, M. D. Boska, F. Ottaviani, A. Jasanoff, A. Rajca, J. A. Johnson, *ACS Cent. Sci.* **2017**, *3*, 800–811.

112. K. Póta, Z. Garda, F. K. Kálmán, J. L. Barriada, D. Esteban-Gómez, C. Platas-Iglesias, I. Tóth, E. Brücher, G. Tircsó, *New J. Chem.* **2018**, *42*, 8001–8011.

113. F. K. Kálmán, G. Tircsó, *Inorg. Chem.* **2012**, *51*, 10065–10067.

114. E. M. Gale, I. P. Atanasova, F. BlasiI, I. Ay, P. Caravan, *J. Am. Chem. Soc.* **2015**, *137*, 15548–15557.

115. M. Botta, F. Carniato, D. Esteban-Gómez, C. Platas-Iglesias, L. Tei, *Future Sci.* **2019**, *11*, 1461–1483.

116. B. Drahoš, J. Kotek, P. Hermann, I. Lukeš, É. Tóth, *Inorg. Chem.* **2010**, *49*, 3224–3238.

117. R. Botár, E. Molnár, Gy. Trencsényi, J. Kiss, F. K. Kálmán, G. Tircsó, *J. Am. Chem. Soc.* **2020**, *142*, 1662–1666.

118. N. Kuźnik, M. Wyskocka, *Eur. J. Inorg. Chem.* **2016**, *2016*, 445–458.

119. E. M. Snyder, D. Asik, S. M. Abozeid, A. Burgio, G. Bateman, S. G. Turowski, J. A. Spernyak, J. R. Morrow, *Angew. Chem. Int. Ed.* **2020**, *59*, 2414–2419.

120. P. B. Tsitovich, F. Gendron, A. Y. Nazarenko, B. N. Livesay, A. P. Lopez, M. P. Shores, J. Autschbach, J. R. Morrow, *Inorg. Chem.* **2018**, *57*, 8364–8374.

121. H. Wang, V. C. Jordan, I. A. Ramsay, M. Sojoodi, B. C. Fuchs, K. K. Tanabe, P. Caravan, E. M. Gale, *J. Am. Chem. Soc.* **2019**, *141*, 5916–5925.

122. P. Nikolaou, B. M. Goodson, E. Y. Chekmenev, *Chem. Eur. J.* **2015**, *21*, 3156–3166.

123. J. H. Ardenkjær-Larsen, B. Fridlund, A. Gram, G. Hansson, L. Hansson, M. H. Lerche, R. Servin, M. Thaning, K. Golman, *Proc. Natl. Acad. Sci. USA* **2003**, *100*, 10158–10163.

124. K. R. Keshari, D. M. Wilson, *Chem. Soc. Rev.* **2014**, *43*, 1627–1659.

125. P. Dutta, G. V. Martinez, R. J. Gillies, *Biophys. Rev.* **2013**, *5*, 271–281.

126. Y. Lee, H. Zeng, S. Ruedisser, A. D. Gossert, C. Hilty, *J. Am. Chem. Soc.* **2012**, *134*, 17448–17451.

127. A. Nardi-Schreiber, A. Gamliel, T. Harris, G. Sapir, J. Sosna, J. M. Gomori, R. Katz-Brull, *Nat. Comm.* **2017**, *8*, 1–7.

128. L. Lumata, S. J. Ratnakar, A. Jindal, M. Merritt, A. Comment, C. Malloy, A. D. Sherry, Z. Kovacs, *Chem. Eur. J.* **2011**, *17*, 10825–10827.

129. L. Lumata, M. E. Merritt, Z. Hashami, S. J. Ratnakar, Z. Kovacs, *Angew. Chem. Int. Ed.* **2012**, *51*, 525–527.

130. J. Kurhanewicz, D. B. Vigneron, J. H. Ardenkjaer-Larsen, J. A. Bankson, K. Brindle, C. H. Cunningham, F. A. Gallagher, K. R. Keshari, A. Kjaer, C. Laustsen, D. A. Mankoff, M. E. Merritt., S. J. Nelson, J. M. Pauly, P. Lee, S. Ronen, D. J. Tyler, S. S. Rajan, D. M. Spielman, L. Wald, X. Zhang, C. R. Malloy, R. Rizi, *Neoplasia* **2019**, *21*, 1–16.

131. K. M. Brindle, S. E. Bohndiek, F. A. Gallagher, M. I. Kettunen, *Magn. Reson. Med.* **2011**, *66*, 505–519.

132. A. Comment, M. E. Merritt, *Biochemistry* **2014**, *53*, 7333–7357.

133. J. Singh, E. H. Suh, G. Sharma, C. Khemtong, A. D. Sherry, Z. Kovacs, *NMR Biomed.* **2019**, *32*, e4018.

134. M. E. Merritt, C. Harrison, Z. Kovacs, P. Kshirsagar, C. R. Malloy, A. D. Sherry, *J. Am. Chem. Soc.* **2007**, *129*, 12942–12943.

135. L. Lumata, A. K. Jindal, M. E. Merritt, C. R. Malloy, A. D. Sherry, Z. Kovacs, *J. Am. Chem. Soc.* **2011**, *133*, 8673–8680.

136. P. Miéville, S. Jannin, L. Helm, G. Bodenhausen, *J. Am. Chem. Soc.* **2010**, *132*, 5006–5007.

137. A. K. Jindal, M. E. Merritt, E. H. Suh, C. R. Malloy, A. D. Sherry, Z. Kovács, *J. Am. Chem. Soc.* **2010**, *132*, 1784–1785.

138. C. Nord, M. Eriksson, A. Dicker, A. Eriksson, E. Grong, E. Ilegems, R. Mårvik, B. Kulseng, P. Berggren, A. Gorzsás, U. Ahlgren, *Sci. Rep.* **2017**, *7*, 6646.
139. J. Felten, H. Hall, J. Jaumot, R. Tauler, A. de Juan, A. Gorzsás, *Nat. Protoc.* **2019**, *14*, 3032.

3

Manganese Complexes as Contrast Agents for Magnetic Resonance Imaging

Sara Lacerda, Daouda Ndiaye, and Éva Tóth

Centre de Biophysique Moléculaire, CNRS UPR 4301, Université d'Orléans,
rue Charles Sadron, F-45071 Orléans, France
<eva.jakabtoth@cnrs-orleans.fr>

Abstract: Manganese is an essential element. With five unpaired electrons, slow electron spin relaxation and fast water exchange, Mn^{2+} is an excellent nuclear relaxation probe and the most promising alternative to replace Gd^{3+} in contrast agents for magnetic resonance imaging (MRI). Given the labile nature of the Mn^{2+} ion, its complexation in thermodynamically stable and kinetically inert complexes is difficult. Moreover, the complexes also need to contain inner sphere water to maintain good relaxivity. In the last decade, a large body of data has been gathered including linear and macrocyclic complexes as well as cage molecules which allow now to establish relationships between the structure of the Mn^{2+} complexes and their stability, inertness and relaxation properties, and this constitutes the basis for a rational design of more stable and efficient probes. In addition, high spin Mn^{3+} is also a good relaxation agent and Mn^{3+} complexes, in particular porphyrins, have been investigated as MRI probes. Chelates of both Mn^{2+} and Mn^{3+} have been explored to derive smart MRI agents with a specific response to various biomarkers, such as pH, enzymes or redox indicators. This chapter surveys shortly these different fields where manganese-based complexes are exploited in relation to MRI.

Keywords: manganese(II) · manganese(III) · MRI · contrast agents · responsive probes

1. INTRODUCTION

Magnetic resonance imaging (MRI) is an indispensable tool in modern diagnostic medicine. In a non-invasive way, it provides three-dimensional images with excellent spatial and temporal resolution without the need for ionizing radiation. The clinical progress of MRI has been largely promoted by the use of contrast enhancing agents [1, 2] which provide essential diagnostic information, not accessible otherwise. MR images depend on the density and on the longitudinal (T_1) and transverse (T_2) relaxation times of water proton nuclei in the tissue. Paramagnetic or superparamagnetic substances accelerate water proton relaxation *via* dipolar interactions, thus substantially enhance tissue contrast and improve image quality.

Complexes of Gd^{3+} have dominated the contrast agent (CA) market. Gd^{3+} has been the metal ion of choice since it has the highest electron spin among all metal ions (S = 7/2), accompanied by a slow electron spin relaxation. Gd^{3+} complexes were long regarded as very safe drugs, and this led to repeated and multiple-dose injections in patients. Starting from 2006, the view on their safety changed drastically. A new disease, nephrogenic systemic fibrosis, was identified first in renally impaired patients and linked to gadolinium-complex injections [3]. As commercial Gd^{3+} agents undergo mostly renal excretion, kidney insufficiency leads to slower elimination and longer gadolinium exposure. The toxicity risk is directly related to the potential release of free Gd^{3+} from the complex, thus to the kinetic inertness of the chelates with respect to dissociation.

Independently of renal impairment, brain and bone accumulation of small, but detectable quantities of gadolinium were also evidenced, although without associated toxic effects. These safety concerns generated regulatory measures in-

volving withdrawal of some linear Gd^{3+} chelates from the clinics. In parallel, research to identify safe and more biocompatible alternatives has gained considerable momentum. In this respect, Mn^{2+} chelates attract increasing attention and are generally considered as the most promising class of compounds to replace Gd^{3+}. High spin Mn^{2+} has five unpaired electrons ($S = 5/2$), slow electron relaxation and fast water exchange, which make it an efficient relaxing agent. To a lesser extent, high spin Mn^{3+} ($S = 2$) has been also investigated in the context of MRI.

Manganese is an essential element. Mn^{2+} is involved in enzymes, such as superoxide dismutase. Mn^{2+} and Ca^{2+} have similar size, and Mn^{2+} displays a certain affinity to Ca^{2+} binding sites in proteins and nucleic acids. Despite the endogenous nature of Mn^{2+}, in high concentrations it causes neurotoxicity ($LD_{50} = 0.22$ mmol/kg for rat) [4] and overexposure leads to Parkinson-like symptoms [5]. Hence, Mn^{2+} also needs to be protected, such as Gd^{3+}, in thermodynamically stable and kinetically inert complexes. Nevertheless, one can expect that with respect to Gd^{3+}, the body can better handle free Mn^{2+}.

Mn^{2+} is relatively difficult to chelate in a stable and inert form. The lack of ligand-field stabilization energy for the high spin d^5 electron configuration implies that Mn^{2+} forms less stable complexes than the endogenously available Zn^{2+}. The complex must contain at least one inner sphere water molecule as well, important for the transfer of the paramagnetic effect to bulk water *via* the water exchange process. Due to the lower charge and the smaller size of Mn^{2+} which limits the number of donor atoms it can accommodate, the thermodynamic stability of Mn^{2+} complexes is lower than that of Gd^{3+} chelates. Mn^{2+} typically forms hexa- or hepta-coordinated complexes, meaning that penta- or hexa-dentate ligands can allow for inner sphere water. The Mn^{2+} complex should show high resistance to dissociation to avoid transmetallation with endogenous metal ions, such as Zn^{2+} or Cu^{2+}. Recent years have seen important progress in understanding the structural features that can lead to inert Mn^{2+} complexes and ligand rigidity is identified as a major element to prevent fast dissociation.

Mn^{2+} is not new to MRI. $MnCl_2$ was the first CA used by Lauterbur [6]. Later, manganese-enhanced MRI using $MnCl_2$ injections has been developed for *in vivo* brain activity measurements and neuronal tract tracing [7, 8]. As a Ca^{2+} analog, Mn^{2+} enters excitable cells such as neurons and cardiac cells *via* voltage-gated Ca^{2+} channels and can be transported along axons and cross synapses to neighboring neurons. Manganese-enhanced MRI requires elevated Mn^{2+} concentrations which restricts it to animal experiments. Mn^{2+} has been also present in clinical MRI. A liposome-formulation of $MnCl_2$ (Lumenhance) was commercialized as an oral, gastrointestinal agent and a Mn^{2+} complex (Teslascan®, MnDPDP) was approved for liver, kidney, and cardiac imaging, now both withdrawn from the market.

In this chapter we will discuss the major classes of Mn^{2+} complexes explored for potential MRI applications, with specific attention to their relaxation properties, thermodynamic stabilities, and kinetic inertness. We will also present examples of Mn^{3+} chelates and demonstrate how Mn-complexes have been exploited to design responsive MRI probes. Several reviews are available in the literature [1, 9–12].

2.   MANGANESE(II) CHELATES

2.1.   Relaxation Properties

The MRI efficiency of a paramagnetic complex is expressed by its relaxivity, r_1, the paramagnetic enhancement of the longitudinal water proton relaxation rate induced by 1 mM concentration of the probe (r_2 refers to transverse relaxation). In Equation (1), $1/T_{1obs}$ and $1/T_{1dia}$ are the relaxation rates in the presence and in the absence of the paramagnetic agent, $[Mn^{2+}]$ is the millimolar concentration and r_1 is the relaxivity.

$$\frac{1}{T_{1obs}} = \frac{1}{T_{1dia}} + r_1 \times [Mn^{2+}] \tag{1}$$

Relaxivity can be decomposed into inner and outer sphere contributions, related to different relaxation mechanisms. They are both linearly proportional to $S(S+1)$, thus directly impacted by the lower electron spin of Mn^{2+} ($S = 5/2$) with respect to Gd^{3+} (7/2). The outer sphere term originates from long-range dipolar interactions between the electron spin and the proton nuclear spins of diffusing water molecules. Provided that the diffusion coefficient and the distance of the closest approach between the diffusing water and the electron spin are identical, the dependence on the electron spin implies that the outer sphere relaxivity is 1.8 times lower for Mn^{2+} than for Gd^{3+} [11].

The inner sphere relaxation mechanism is related to the dipolar interaction of Mn^{2+} with protons of the metal-coordinated water molecule(s). This term is dependent on the number of inner sphere water molecules, q, their exchange rate with bulk water, k_{ex}, the rotational correlation time, τ_R, of the complex, the electronic relaxation rates, and the distance between Mn^{2+} and the water protons. The relaxivity of Mn^{2+} is well described in most cases by the Solomon-Bloembergen-Morgan theory of paramagnetic relaxation [13]. For Mn^{2+}, a scalar relaxation mechanism might also add up to the dipole-dipole contribution. It is important only at low field and when water exchange and electronic relaxation are slow. As a result, a second, low-field dispersion appears on the nuclear magnetic relaxation dispersion (NMRD) profiles, like for the Mn^{2+} aqua ion but rarely observed for Mn^{2+} chelates [9].

To assess the hydration number, q, of Mn^{2+} complexes, Caravan et al. [14] proposed a method based on the temperature-dependent ^{17}O transverse relaxation rates, provided they show a maximum. Using the plausible hypothesis that the ^{17}O scalar coupling constant is independent of the nature of the complex, q is estimated with an uncertainty of ± 0.2 water molecules [14]. Peters and Geraldes derived an empirical equation to estimate q (± 0.4) using low field relaxivities and the molecular weight of the chelate [15].

The distance between the Mn^{2+} electron spin and the coordinated water protons, r_{MnH}, enters on the inverse 6th power in the equation describing inner sphere relaxivity, thus its small variations lead to important relaxivity changes. No proton electron nuclear double resonance (^1H ENDOR) spectroscopy data

are available so far for Mn^{2+} to directly assess Mn-H distances in solution; they are known from solid state X-ray structures or DFT calculations [16]. r_{MnH} is typically 5–10 % shorter than r_{GdH} in Gd^{3+} chelates (~2.8 versus 3.1 Å) and this can partially compensate the relaxivity decrease related to the lower electron spin of Mn^{2+}.

Concerning water exchange, the rate and the mechanism are inherently related to the charge and the inner sphere structure of the complexes. In contrast to Gd^{3+} chelates, the structural factors that govern water exchange are less understood. The difficulty is also related to the flexible nature of Mn^{2+} which can accommodate 6 as well as 7 donor atoms, and it is often difficult to predict the coordination number. Although the water exchange mechanism was directly assessed for few complexes by determining the activation volume by variable pressure ^{17}O NMR [9], generally one can say that seven-coordinate complexes tend to undergo dissociatively activated water exchange, while six-coordinate complexes tend to have associatively activated exchange process. Structural elements that accelerate dissociative water exchange on metal complexes by facilitating the leaving of the coordinated water molecule, such as higher negative charge or increased steric crowding in the inner sphere, will also operate for Mn^{2+} chelates. On the other hand, an associative exchange can be accelerated by higher positive charge which facilitates the approach of the entering water in the rate determining step. In general, water exchange is faster on Mn^{2+} than on Gd^{3+} complexes and is not a limiting factor for relaxivity even for slowly rotating systems. Relaxivity is solely limited by rotation.

Finally, the same approaches that have been used to improve the relaxivity of Gd^{3+} chelates are applicable for Mn^{2+} as well. For instance, strategies based on slowing down rotation by macromolecular constructs have been explored [11], but are obviously limited to intermediate frequencies (20–60 MHz) [13].

2.2. Linear Ligands

2.2.1. EDTA Derivatives

MnEDTA and its derivatives were among the first Mn^{2+} complexes studied with respect to their relaxation properties, starting from the 1970s. In MnEDTA, Mn^{2+} has a total coordination number of seven including one inner sphere water. Water exchange rates were determined by ^{17}O NMR first on MnEDTA, and then on PhDTA and CDTA derivatives, and were one order of magnitude higher than that on the $Mn(H_2O)_6^{2+}$ aqua ion (Scheme 1, Table 1) [17–20]. The positive activation volumes measured by variable pressure ^{17}O NMR ($\Delta V^{\neq} = +3.0$ and $+9.4$ cm^3mol^{-1} for MnEDTA and MnCDTA, respectively), indicated dissociatively activated water exchange for these seven-coordinate complexes, in contrast to an associative mechanism for the six-coordinate aqua ion ($\Delta V^{\neq} = –5.4$ cm^3mol^{-1}) [21]. NMRD profiles of MnEDTA show a single dispersion, in contrast to $Mn(H_2O)_6^{2+}$ which has a second dispersion at low frequencies, attributed to the scalar relaxation mechanism operating for the aqua ion but not for typical Mn^{2+} chelates [22].
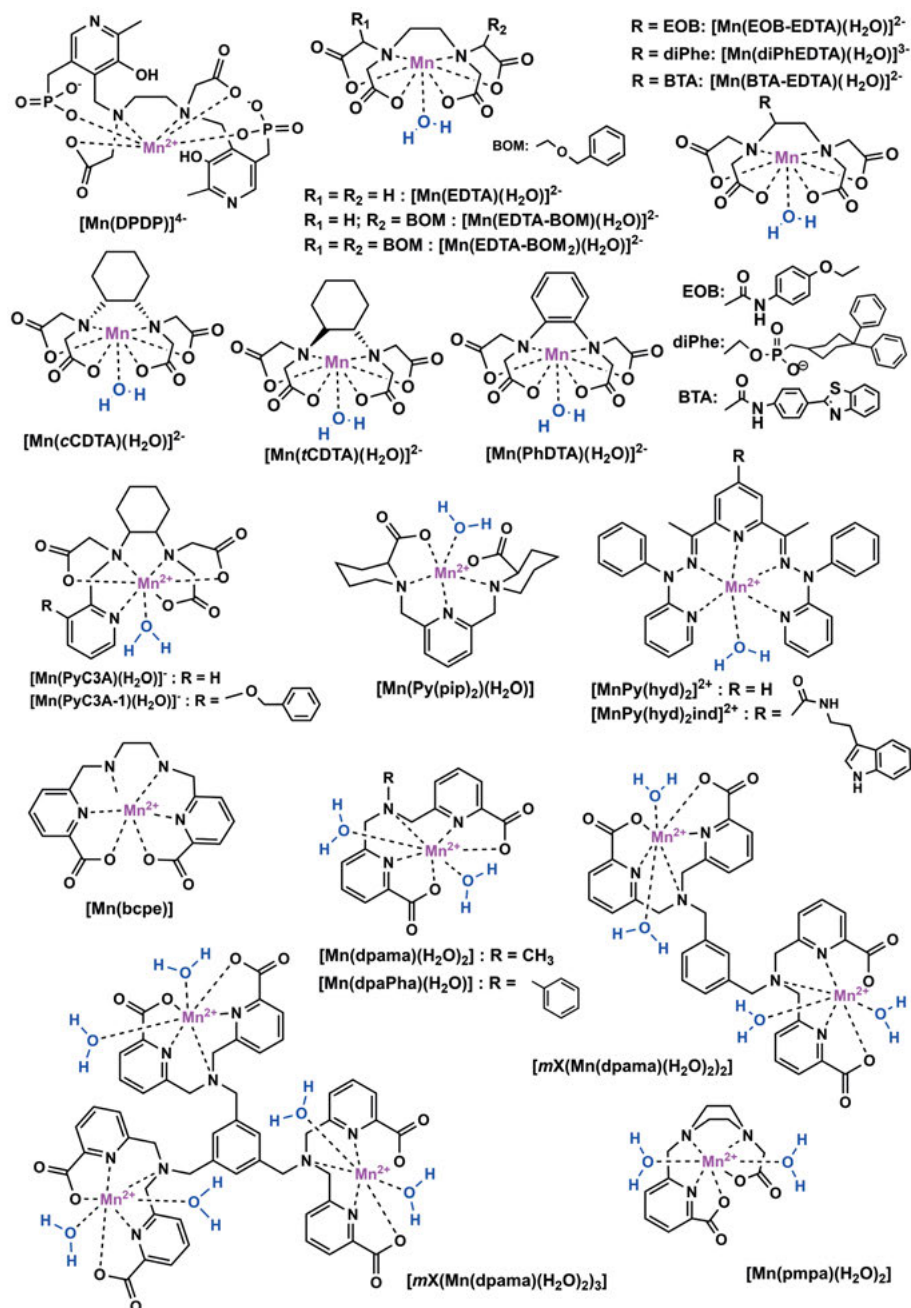
Scheme 1.

Table 1. Coordination (CN) and hydration numbers (q), water exchange rates (k_{ex}^{298}), rotational correlation times (τ_R^{298}) and proton relaxivities (r_1) for selected Mn^{2+} complexes.

	CN / q	k_{ex}^{298} (10^6 s^{-1})	τ_R^{298} (ps)	r_1 (mM^{-1}s^{-1}) 20 MHz, 25 °C
linear ligands				
EDTA [24]	7 / 1	440	57	3.00 [23]
tCDTA	7 / 1	140	74	3.62
cCDTA [27]	7 / 1	225	–	3.79
PhDTA	7 / 1	350 [17]	–	3.72[29]
EDTA-BOM [23]	7 / 1	93	84	3.60
EDTA-BOM$_2$ [23]	7 / 1	130	111	4.30
diPhEDTA [24]	7 / 1	230	–	5.8 (37 °C)
PyC3A[35]	7 / 1	100 (310K)	–	3.30
dpama [40]	7 / 2	306	48	5.3
mX(dpama)$_2$[40]	7 / 2	306	96	8.6
mX(dpama)$_3$[40]	7 / 2	306	136	11.4
dpaPha [118]	7 / 2	56	81	6.6
macrocyclic ligands				
ENOTA [43]	6 / 1	55	85	3.39
BzNO2A [45]	6 / 1	44	53	3.40
MeBzNO2A [45]	6 / 1	26.0	67	3.50
NOTA-EB [46]	7(?) / 1	–	–	4.78 (300 MHz, 37 °C)
1,4DO2A[50]	6–7 / 0.87	1134	46	2.1
1,7DO2A[50]	6 / 0	–	–	1.5
DO1A [50]	6 / 1	5957	22	2.4
PC2A [56]	7 / 1	152	–	-
PC2A-EA [56]	7 / 1	40	–	3.52
PC1A [55]	6 / 1	3030	23	2.39
PC1P [55]	6 / 1	1770	39	2.84
15-pyN$_5$ [58]	7 / 2	6.9	–	3.56
15-pyN$_3$O$_2$ [58]	7 / 2	3.8	–	4.48
9-aneN$_2$O-2A [48]	6–7 / 1.46	1.19×10^3	–	2.83
9-aneN$_2$O-2P [48]	6 / 1	12.0	–	5.08
other ligands				
AAZTA [60]	7 / 0	–	–	1.57
AAZ3A [60]	6–7 / 0.64	47	50	2.49
MeAAZ3A [60]	6–7 / 0.32	126	50	2.01
AAZ3MA [60]	6–7 / 0.24	133	51	1.90
Bisp1 [61]	6 / 1	51.0	100	4.28

Later, in the objective of developing Mn^{2+}-based angiographic agents, EDTA was modified with functions that promote binding to human serum albumin (HSA). Aime et al. introduced one or two benzyloxymethyl (BOM) substituents [23], while Caravan et al. used the diphenylcyclohexyl-phosphate moiety (di-PhEDTA) [24], analogously to the HSA-targeted Gd^{3+} complex MS-325

(Scheme 1). In both cases, a significant relaxivity enhancement was obtained in the presence of serum albumin, resulting from the slow rotational motion of the protein-bound chelates.

Chang et al. derivatized MnEDTA for liver targeting. In order to increase lipophilicity and obtain a hepatobiliary probe, they attached a benzothiazole aniline (BTA) [25] or an ethoxybenzyl (EOB) [26] moiety to the ligand backbone, the latter being the same as in the commercial CA Gd(EOB-DTPA) (Scheme 1). The log P value changed from –2.72 for MnEDTA to –2.33 for Mn(EOB-EDTA) and –1.84 for Mn(BTA-EDTA). Both complexes showed moderate HSA binding (K_a = 95 and 655 M^{-1} for the BTA- and the EOB-derivative, respectively) with the relaxivity increasing from 3.5 to 15.1 in the case of Mn(BTA-EDTA) and from 2.3 to 6.3 $mM^{-1}s^{-1}$ for Mn(EOB-EDTA), in the presence of 0.67 mM HSA (64 MHz, 24 °C). *In vivo* MRI biodistribution confirmed hepatobiliary and renal excretion for both compounds, and they were successfully used to highlight tumors in a mouse liver tumor model.

2.2.2. Rigidified Linear Ligands

The investigation of EDTA analogues that contain a rigidified ligand backbone to provide better kinetic inertness while retaining one hydration water has been a major research direction. The ethylenediamine bridge was replaced with less flexible moieties, such as a diaminocyclohexane, a benzene or a pyridine ring. The *trans* isomer of CDTA was a previously well-known complexing agent. Tircsó et al. [27] compared the complexation properties of the *cis* (*c*) and the *trans* (*t*) isomers (Scheme 1). They provide coordination cages of different size, as the maximum distance between the two N-donor atoms is 4 versus 3.1 Å in *t*- and *c*CDTA, respectively. A combined experimental and DFT study evidenced similar geometry in solution. The *trans* isomer has nevertheless better conditional stability (pMn = 8.68 for Mn-*t*CDTA versus 7.82 for Mn-*c*CDTA, c_{MnL} = 10 μM; pH 7.4) and 250 times higher kinetic inertness. While their relaxivities are similar, (3.62 (*trans*) and 3.79 mM^{-1} s^{-1} (*cis*); 20 MHz, 25 °C), Mn-*c*CDTA has a ~60 % faster water exchange, likely related to the higher steric constraints in the coordination sphere, which accelerates the rate-determining dissociation step in a dissociatively activated process. A bifunctional derivative adapted to biological targeting has been also reported [28].

In PhDTA, the ligand skeleton is rigidified with an aromatic ring (Scheme 1). The conditional stability (pMn = 8.16) and the relaxivity (3.72 mM^{-1} s^{-1}; 20 MHz, 25 °C) of MnPhDTA are comparable to those of Mn-*t*CDTA, while its kinetic inertness is slightly higher with a dissociation half-life estimated to be 19 h at pH 7.4 [29]. A pyridine ring has been also incorporated in the ligand backbone [30]. Two additional piperidine rings can be found in the ligand Py(pip)$_2$ (Scheme 1) which forms a monohydrated complex with a relaxivity of 3.6 mM^{-1} s^{-1} (20 °C, 1.5 T) [31, 32]. This complex was conjugated to PEG chains of different length [32] or to an amphiphilic dextran [33], and the conjugates were evaluated for MR angiography. The dextran derivative forms micelles in aqueous solution resulting in improved relaxivity (13.3 $mM^{-1}s^{-1}$). Both the PEG and the dextran

Table 2. Thermodynamic stability constants, log K_{ML}, pM values ($c_{Mn} = c_{lig} = 10^{-5}$ M, pH 7.4) and dissociation half-lives, $t_{1/2}$, (estimated for pH 7.4, 10^{-5} M Zn^{2+} or 10^{-6} M Cu^{2+} concentrations) for selected Mn^{2+} complexes.

	CN / q	logK_{ML}	pMn	$t_{1/2}$ (hours)
linear ligands				
EDTA [62]	7 / 1	12.46[a]	7.83[a]	0.076
*t*CDTA	7 / 1	14.32[a]	8.68[a]	12
*c*CDTA [27]	7 / 1	14.19[a]	7.82[a]	0.47
PhDTA [29]	7 / 1	11.79[a]	8.38[a]	19.1
EDTA-BOM [23]	7 / 1	13.50[b]	7.82[b]	–
EDTA-BOM$_2$ [23]	7 / 1	13.80[b]	8.12[b]	–
PyC3A [35]	7 / 1	14.14[a]	8.17[a]	0.285[c]
macrocyclic ligands				
NOTA [44]	6 / 0	14.90	11.80	74 [48]
ENOTA [43]	6 / 1	24.06 (for Mn$_2$L)		–
DOTA [119]	6 / 0	19.44	9.02	1037 [48]
DO3A [63]	6 / 0	16.55	8.66	11000
ODO3A [63]	6 / 0	13.88	8.57	180
1,4DO2A [52]	6–7 / 0.87	15.68	7.27	48.3
1,7DO2A [52]	6 / 0	14.64	6.52	56.8
PC2A [56]	7 / 1	17.09	8.64	–
PC2A-EA [56]	7 / 1	19.01	9.27	54.4[c]
PC1A	6 / 1	11.54[d]		–
PC1P	6 / 1	14.06[d]		2.4
15-pyN$_5$ [58]	7 / 2	10.89[d]	6.37[d]	11.40
15-pyN$_3$O$_2$ [58]	7 / 2	14.06[d]	6.19[d]	–
9-aneN$_2$O-2A [48]	6–7 / 1.46	7.43[d]	5.23[d]	–
9-aneN$_2$O-2P [48]	6 / 1	10.61[d]	5.06[d]	–
other ligands				
AAZTA [60]	7 / 0	14.19	8.15	
AAZ3A [60]	6–7 / 0.64	11.00	6.58	0.7 [62]
MeAAZ3A [60]	6–7 / 0.32	11.43	6.47	–
AAZ3MA [60]	6–7 / 0.24	10.67	6.39	–
Bisp1 [61]	6 / 1	12.21	6.65	> 140 days[c]

[a] 0.1 M NaCl; 25 °C.
[b] 1 M KCl; 20 °C.
[c] pH 6, 37 °C 25 eq. Zn^{2+}.
[d] 0.1 M (CH$_3$)$_4$NCl; 25 °C.

derivatives could highlight blood vessels in rats with a long-lasting vascular enhancement at a low dose (0.1 Mn mmol kg^{-1} body weight for the dextran micelles). Hydrazine functions were incorporated in Py(hyd)$_2$ (Scheme 1). X-ray crystal structure evidenced seven coordinate complexes including one inner sphere water. Py(hyd)$_2$ind was specifically designed to bind the amyloid Aβ$_{1-42}$ peptide thanks to the indole function [34].
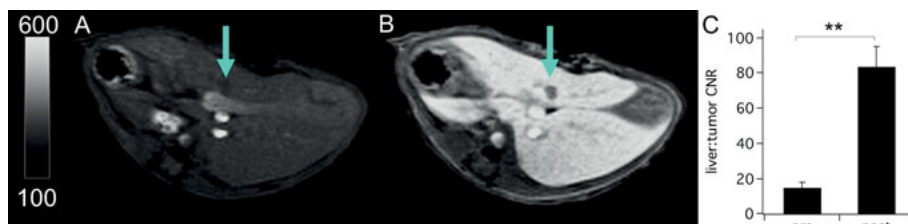
Figure 1. Liver imaging of an orthotopic mouse model of colorectal liver metastasis with MnPyC3A-1 at 4.7 T. (**A**, **B**) T_1-weighted axial images of the liver at the level of the tumor (arrow) prior to and during the hepatocellular phase after injection of MnPyC3A-1, respectively. (**C**) Liver parenchyma versus tumor contrast to noise ratios (CNR) prior to and following treatment with MnPyC3A-1 are 14.8 ± 3.1 and 83.8 ± 11.5, respectively. Reproduced with permission from [38]; copyright 2018, American Chemical Society.

So far the Mn^{2+} complex which has been taken the farthest in the validation process towards MRI applications is based on the pyridine-substituted CDTA chelator PyC3A (Scheme 1), developed by the group of Caravan. MnPyC3A is a monohydrated complex, proposed as an alternative to the commercial extracellular Gd-based agents [35]. The chelate has good thermodynamic stability and kinetic inertness (Table 2). Indeed, in a comparative dissociation kinetics experiment when challenged with 25-fold excess of Zn^{2+} (pH 6, 37 °C), MnPyC3A proved to be 20 times more inert than the clinically used GdDTPA. Its relaxivity is slightly increased in serum indicating modest protein binding. The slightly lipophilic character of the complex leads to excretion *via* both hepatobiliary and renal pathways, without detectable *in vivo* degradation. The *in vivo* MR contrast-enhancing capability of MnPyC3A has been similar to that of GdDTPA in a non-human primate model [36]. The capacity of MnPyC3A to detect tumors in mouse models of breast or liver cancer was comparable to that of commercial agents. In addition, at equal doses, less Mn is retained in the body following MnPyC3A injection than Gd after GdDOTA injection [37]. A family of liver-specific derivatives of MnPyC3A has been also reported, and structure−activity relationships governing protein binding, relaxivity, pharmacokinetics, biodistribution, and elimination of the chelates have been established. The lead compound (PyC3A-1, Scheme 1) showed rapid blood clearance, good relaxivity, and hepatocellular targeting and successfully detected liver tumors in a mouse model (Figure 1) [38].

2.2.3. Picolinate Derivatives

Botta, Platas-Iglesias et al. reported ligands containing one, two or three penta-dentate 6,6′-((methylazanediyl)bis(methylene))dipicolinic acid units that form mono- (H_2dpama, H_2dpaPha), di- (mX(H_2dpama)$_2$), and trinuclear (mX(H_2dpama)$_3$) Mn^{2+} complexes (Scheme 1) [39–40]. In contrast to the hexadentate bcpe which forms a non-hydrated Mn^{2+} complex, dpama deriva-

tives contain two coordinated water molecules per metal. The relaxivities for dpaPha^{2-} and dpama^{2-} complexes are comparable to bishydrated Gd^{3+} chelates, evidencing that the lower magnetic moment of Mn^{2+} is compensated by a shorter Mn–H$_w$ distance of the bound water molecule(s).

The dpama derivatives bind HSA with association constants in the 10^3 M^{-1} range. The binding of the mononuclear Mn^{2+} chelate leads to the replacement of both coordinated water molecules by donor atoms from the protein. Interestingly, the dinuclear and the trinuclear analogues bind HSA *via* the involvement of a single Mndpama which implies the replacement of its hydration water molecules, but the remaining Mndpama moieties retain their water coordination. This results in high relaxivities for the protein-bound complexes, in the order of 40 mM^{-1}s^{-1} (20 MHz; 37 °C).

A single picolinate moiety and an additional carboxylate were appended to a piperazine backbone in pmpa (Scheme 1). Mnpmpa has pentagonal bipyramidal geometry where the axial positions are occupied by two water molecules and the equatorial plane is constituted by the ligand ON3O donor set. Thermodynamic stability was relatively high for a bishydrated chelate with log K_{MnL} = 14.3 and pM = 8.06 (pH = 7.4; [M] = [L] = 10 μM). Thanks to the two inner sphere water molecules, it has high relaxivity (5.88 mM^{-1} s^{-1} at 1.41 T, 25 °C, pH 7.4) [41].

2.3. Macrocyclic Chelators

2.3.1. 9-Membered Macrocycles

Within the triazacyclononane family, it was early established that the triacetate NOTA forms a non-hydrated complex with Mn^{2+}, with accordingly low relaxivity [42]. Therefore, different structural modifications have been made to NOTA to derive ligands which allow for hydrated Mn^{2+} chelates. The dimeric ENOTA was the first example [43] of the replacement of one carboxylate by non-coordinating pending arms, followed by other monomeric, dimeric or macromolecular structures [16, 44, 45] (Scheme 2). For Mn$_2$ENOTA, hexacoordination including five donor atoms from the ligand and one inner sphere water was proved by X-ray crystallography in the solid state and by ^{17}O NMR and NMRD data in solution. The water exchange was twice as fast as that on the aqua ion and the high negative activation volume ($\Delta V^{\neq}$ = –10.7 cm^{3}mol^{-1} versus –5.4 cm^{3}mol^{-1} for Mn(H$_2$O)$_6^{2+}$) evidenced a strongly associative water exchange mechanism. In an ^{17}O NMR, NMRD, and DFT study on NO2A derivatives (MeNO2A, BzNO2A, MeBzNO2A, and *m*Bz(NO2A)$_2$; Scheme 2), Platas-Iglesias et al. showed that the steric crowding induced by the non-coordinating pending arm around the first sphere has an important influence on the water exchange rate [45]. In such associatively activated water exchange processes, a bulky group limits the approach of the incoming water molecule, thus slows down water exchange: one order of magnitude diminution was found in k_{ex}^{298} when substituting the methyl to a benzyl substituent on NO2A. Sterically very demanding groups even restrict the number of coordinated water molecules which drops to 0.5 in [*m*Bz(MnNO2A)$_2$].
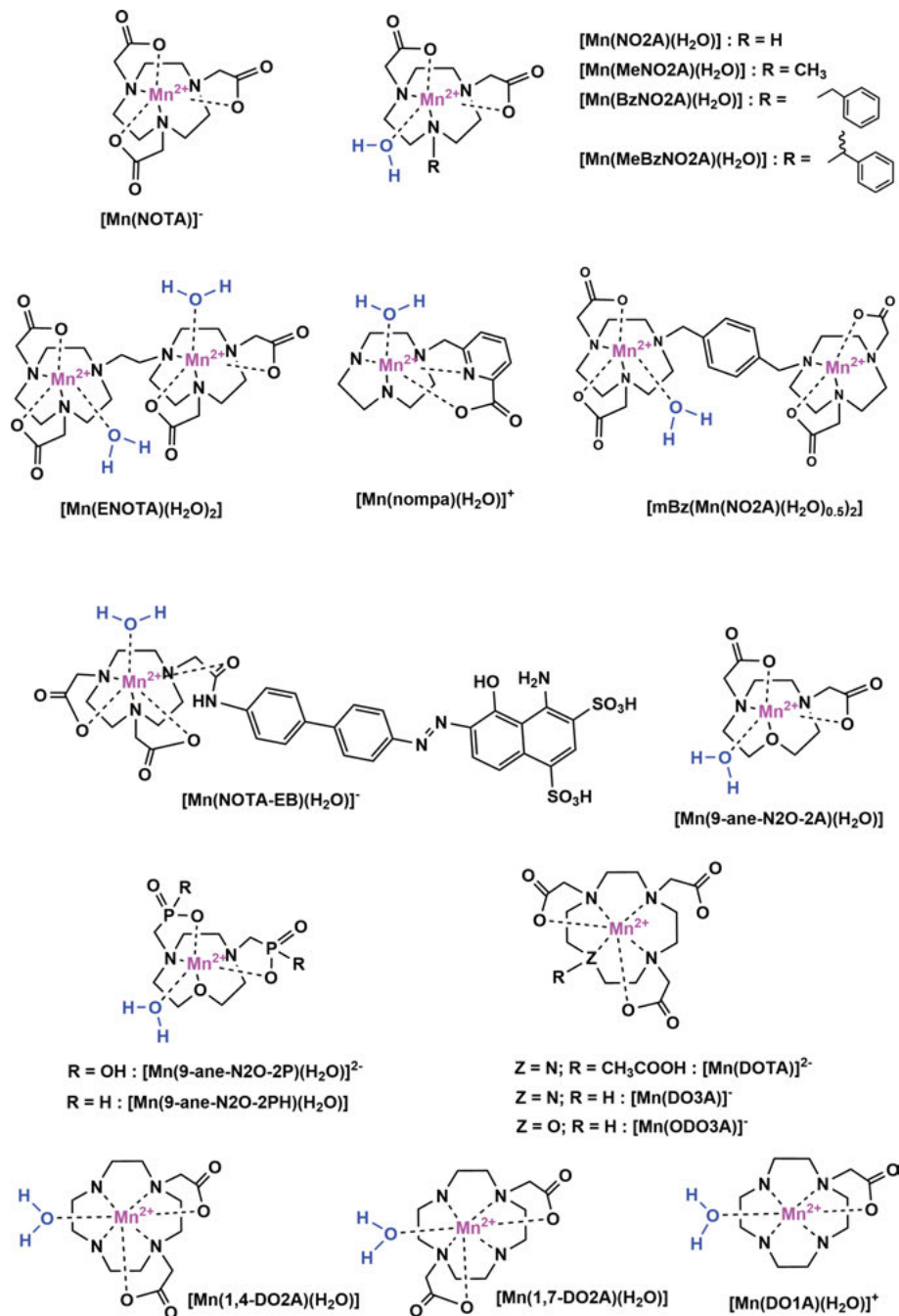
Scheme 2.

The NO2A-monoamide was conjugated to a truncated Evans blue (EB) moiety that promotes HSA binding and the Mn^{2+} complex was evaluated as dual T_1 and T_2 agent for the visualization of subcutaneous and orthotopic brain tumors in mice (Scheme 2) [46]. For this complex, the coordination of the amide function, thus the absence of an inner sphere water molecule would be expected. Even if the hydration number of the complex was not assessed, the relaxivity and its strong increase (from ~6 to ~28 $mM^{-1}s^{-1}$ at 20 MHz) in the presence of serum albumin, point to a contribution of inner sphere relaxation, thus the presence of a hydration water.

Platas-Iglesias et al. appended a picolinate function on one nitrogen of the triazacyclononane macrocycle to obtain nompa (Scheme 2). Mnnompa is monohydrated, but its kinetic inertness is unsatisfactory for practical application as MRI CA, which is related to a fast spontaneous dissociation at pH 7.4 [47].

In a different approach, Drahoš et al. replaced one nitrogen in the triazacyclononane ring by an oxygen and investigated the Mn^{2+} complexes of this 9-$aneN_2O$ macrocycle bearing acetate, phosphonate, phosphinate or phenylphosphinate pending groups (Scheme 2) [48]. A combined NMRD and ^{17}O NMR study allowed to conclude that the diacetate $Mn(9\text{-}aneN_2O\text{-}2A)$ exists in equilibrium between mono- and bishydrated species, with an extremely fast water exchange ($k_{ex}^{298} = 1.2 \times 10^9$ s^{-1}) while the phosphonate derivative $Mn(9\text{-}aneN_2O\text{-}2P)$ has one inner sphere water and two orders of magnitude lower water exchange ($k_{ex}^{298} = 1.2 \times 10^7$ s^{-1}). Unfortunately, the thermodynamic stability of the Mn^{2+} complexes, especially of the phosphinates is rather low and their dissociation was instantaneous at pH 6 and in the presence of 5 equivalents of Zn^{2+}, which obviously prevents any consideration for *in vivo* use.

2.3.2. 12-Membered Macrocycles

Among cyclen-based ligands, DOTA forms a very stable and inert Mn^{2+} complex [49]. As expected with octa- or heptadentate ligands, neither MnDOTA, nor MnDO3A or its derivatives contain inner sphere water [50, 51]. For the *trans* (Mn(1,7-DO2A)) and *cis* (Mn(1,4-DO2A)) diacetate derivatives (Scheme 3), as well as for Mn(DO1A), the hydration state and the water exchange properties have been assessed in a combined ^{17}O NMR, NMRD, and DFT work [50]. In contrast to the EDTA family, there is no clear predominance of seven-coordination in aqueous solution. Mn(DO1A) has one inner sphere water and a total coordination number of 6, while for the diacetates, non-hydrated and monohydrated species co-exist with an average q of 0.9 for Mn(1,4-DO2A) and close to 0 for Mn(1,7-DO2A). Accordingly, the relaxivity drops from ~2.1 $mM^{-1}s^{-1}$ for Mn(1,4-DO2A) to 1.5 $mM^{-1}s^{-1}$ for Mn(1,7-DO2A) (25 °C, 30 MHz). Mn(1,4-DO2A) has very fast water exchange ($k_{ex}^{298} = 1.1 \times 10^9$ s^{-1}), attributed to the small energy difference between the two differently hydrated species facilitating the transition from the starting seven-coordinate complex to the six-coordinate transition state in a dissociatively activated water exchange. Mn(1,4-DO2A) has slightly higher thermodynamic stability and pM value than the *trans* isomer (pMn = 7.27 versus 6.52; pH = 7.4, $c_{MnL} = 10^{-5}$ M, 0.15 M NaCl). Their kinetic

Z = N; R = CH$_3$COOH : [Mn(DOTA)]$^{2-}$

Z = N; R = H : [Mn(DO3A)]$^-$

Z = O; R = H : [Mn(ODO3A)]$^-$

[Mn(1,4-DO2A)(H$_2$O)]

[Mn(1,7-DO2A)]

[Mn(DO1A)(H$_2$O)]$^+$

[Mn(PC1A)(H$_2$O)]$^+$

[Mn(PC1P)(H$_2$O)]

R = H : [Mn(PC2A)(H$_2$O)]

R = CH$_2$CH$_2$NH$_3^+$: [Mn(HPC2A-EA)(H$_2$O)]

Z = N : [Mn(15-PyN$_5$)(H$_2$O)$_2$]$^{2+}$
Z = O : [Mn(15-PyN$_3$O$_2$)(H$_2$O)$_2$]$^{2+}$

[M400401(H$_2$O)$_2$]$^{2+}$

[Mn(AAZTA)]$^{2-}$

R = H: [Mn(AAZ3A)(H$_2$O)$_x$]$^-$
R = CH$_3$: [Mn(MeAAZ3A)(H$_2$O)$_x$]$^-$

[Mn(AAZ3MA)(H$_2$O)$_x$]$^-$

[Mn(Bisp1)(H$_2$O)]
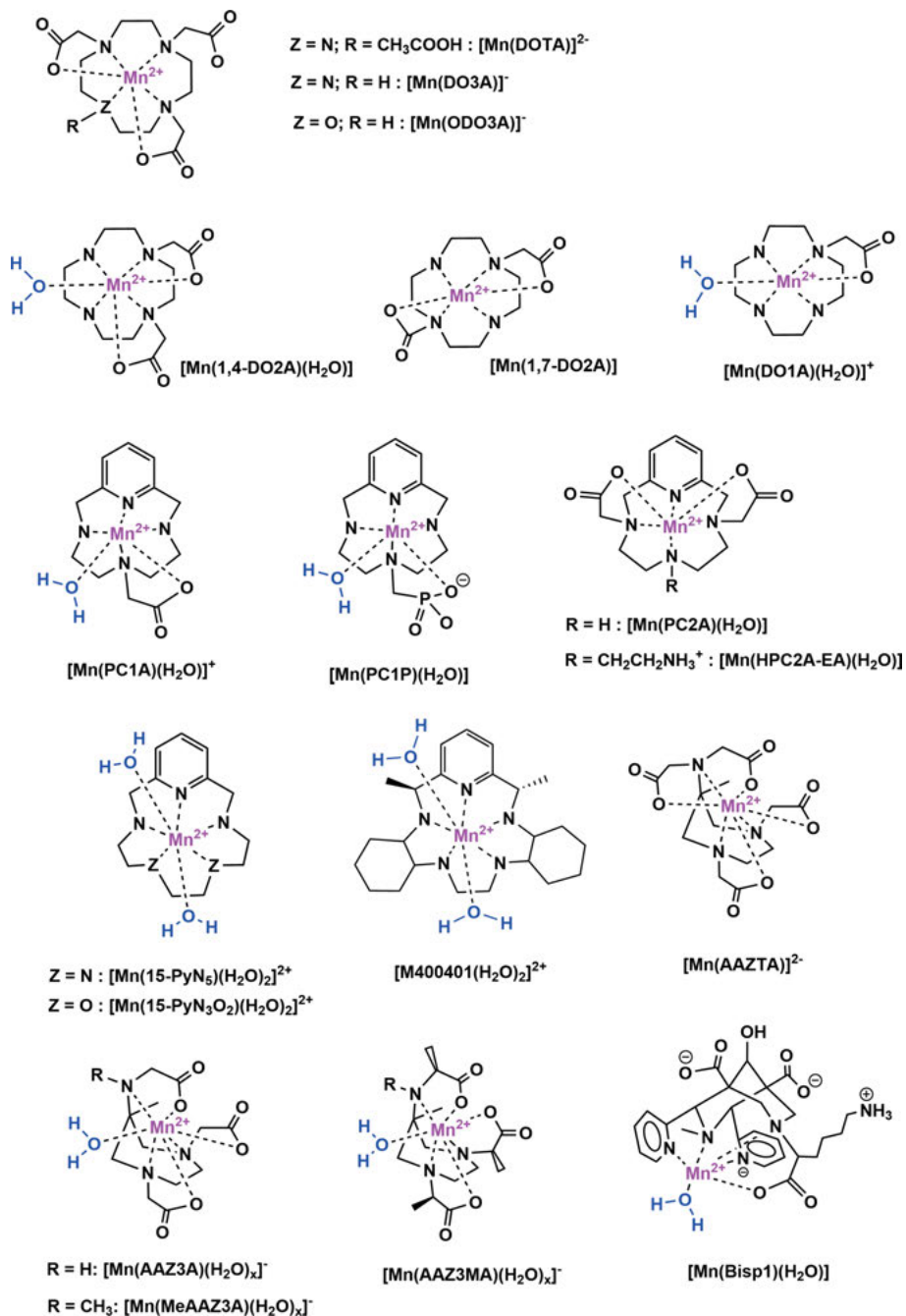
Scheme 3.

inertness is similar, with dissociation half-lives ($t_{1/2}$) estimated to 48 and 57 h, respectively, for Mn(1,4-DO2A) and Mn(1,7-DO2A) under physiologically relevant conditions [52]. Nevertheless, these complexes remain about twenty times more labile than MnDOTA ($t_{1/2}$ = 1061 h) [48]. 1,4-DO2A was further functionalized on the secondary amines with C12 or C16 hydrophobic chains which promote micelle formation and efficient HSA binding, both resulting in a substantial relaxivity increase (~6 to 7-fold increase for the micellar form and ~15-fold for the HSA-bound form; 25 °C, 30 MHz) [53]. Ligands bearing phosphonate or phosphinate groups in 1,4 positions of the cyclen form six-coordinate, non-hydrated Mn^{2+} complexes with r_1 ~2 mM^{-1}s^{-1} (37 °C, 20 MHz) [54].

The 12-membered pyclen containing a pyridine ring is a rigidified macrocycle expected to provide better inertness for the complexes. Derivatives containing one acetic or one methylphosphonic acid pendant arm were first investigated for Mn^{2+} complexation (Scheme 3) [55]. The MnPC1A and MnPC1P complexes are six-coordinate, including one inner sphere water. The chelates have moderate thermodynamic stability and kinetic inertness, and are not sufficiently resistant to oxidation under air. The ligand bearing two acetate functions on the opposite macrocycle nitrogens (PC2A) and derivatives with additional non-coordinating pending arms on the third amine such as PC2A-EA (Scheme 3) form monohydrated Mn^{2+} complexes with excellent thermodynamic stability and kinetic inertness. The pMn value decreases only slightly from MnPCTA to Mn(PC2A-EA) and to MnPC2A (respectively 9.74, 9.27 and 8.64, at pH 7.4, 10^{-5} M MnL) and in a comparative study, Mn(HPC2A-EA) (at pH 6 the amine is protonated) was found to be 190 more inert than MnPyC3A [56].

2.3.3. Larger Macrocycles

Numerous aza- or aza-oxa crown ethers were investigated for Mn^{2+} complexation, often with respect to their superoxide dismutase activity [57]. Typically, the macrocyclic donor atoms form an equatorial plane around the metal ion, and water molecules occupy the two axial positions in a pentagonal-bipyramidal geometry with an overall coordination number of 7. The 15-membered 15-pyN$_3$O$_2$ and 15-pyN$_5$ integrate a pyridine ring (Scheme 3) [58]. The coordination of two inner sphere water molecules was evidenced in the solid state by crystal structures, but also in solution by the relaxivity values. Interestingly, very slow water exchange was found for Mn(15-pyN$_3$O$_2$) (k_{ex}^{298} = 3.8 × 10^6 s^{-1}), explained by strong H-bonds between the coordinated water and the macrocycle oxygens.

Bogdanov et al. used the Mn^{2+} chelate M400401 as a theranostic agent to combine MRI and superoxide dismutase activity (Scheme 3). Encapsulated in a liposome, it entered the brain and was proposed as MRI-trackable neuroprotective agent to counteract damaging levels of superoxide produced during cerebral ischemia [59].

2.4. Other Chelators

AAZTA-like chelators based on the 6-amino-6-methylperhydro-1,4-diazepine scaffold and possessing pendant carboxylates were reported by Botta et al. (Scheme 3) [60]. The relaxivities of the Mn^{2+} complexes of the hexadentate ligands AAZ3A, MeAAZ3A, and AAZ3MA are 2.49, 2.01, and 1.90 mM^{-1}s^{-1} (20 MHz, 25 °C) and ^{17}O NMR and NMRD data pointed to the presence of a hydration equilibrium between mono- and non-hydrated complexes for each of them, with average hydration numbers of 0.64, 0.32, and 0.24 for AAZ3A, MeAAZ3A, and AAZ3MA, respectively. MnAAZTA has no inner sphere water. As expected, the removal of one carboxylate from AAZTA also leads to a decreased thermodynamic stability for the complexes.

Very recently, the bispidine derivative bisp1 was described to provide extreme resistance to dissociation (Scheme 3) [61]. Bispidines are a versatile platform in coordination chemistry. The chair-chair conformer is best suited for stable metal coordination and its exceptionally preorganized structure favors high kinetic inertness. Indeed, at 37 °C, pH 6.0 and in the presence of up to 50 equivalents of Zn^{2+}, Mnbisp1 remained intact and did not show any relaxivity change for at least 140 days. Under similar conditions, a dissociation half-life of 54.4 h has been reported for MnPC2A-EA, considered as the most inert Mn^{2+} chelate so far. The ligand coordinates in a five-dentate manner, involving two pyridine and two bispidine nitrogens and the methylene carboxylate. This leaves one coordination site for hydration water. The two non-coordinating pending carboxylates create a second sphere contribution and increase proton relaxivity. *In vivo* MRI experiments performed in mice indicated quick renal clearance, which was also supported by *ex vivo* ICP determination of the Mn tissue content in different organs. Bisp1 can be readily functionalized for biological targeting *via* the lysine terminal amine.

2.5. Stability and Kinetic Inertness

Even if the use of MnDPDP, once commercialized and known to partially dissociate *in vivo*, did not raise toxicity problems, today it is generally accepted that only a stable and inert Mn^{2+} chelate which efficiently prevents Mn^{2+} release could be approved for clinical application. Mn^{2+} is a labile cation and to ensure very high kinetic inertness for a hydrated Mn^{2+} chelate, comparable to the reference agent GdDOTA for instance, seems a difficult task. Nevertheless, as more dissociation kinetic data are available, some general trends become visible.

To assess kinetic inertness, typically transmetalation reactions with Zn^{2+} or Cu^{2+} are followed under pseudo-first order conditions, at different pHs. The dissociation mechanisms of Mn^{2+} chelates do not differ substantially from that of the Gd^{3+} complexes and involve spontaneous, acid-catalyzed and metal-assisted decomplexation. The first detailed dissociation kinetic study concerned the non-hydrated MnNOTA and MnDOTA and proved that spontaneous and proton-assisted pathways are important at pH 3.5–5.5 [48].

In a comparative study on Mn^{2+} complexes of EDTA derivatives and AAZTA, Kálmán and Tircsó evidenced the superior kinetic inertness of MnCDTA, with a dissociation half-life of 12 h (pH 7.4 and 10^{-5} M Cu^{2+}), two orders of magnitude higher than the next most inert MnAAZTA [62]. This was related to the rigid structure of CDTA providing a compact and preorganized coordination cavity. Interestingly, the non-hydrated MnDTPA undergoes instantaneous dissociation under the same conditions. The reason is likely the high basicity of the central amine, but the non-coordinating donor atoms which can promote the formation of protonated and dinuclear intermediates likely contribute also to the fast dissociation.

A large series of 12-membered macrocyclic ligands was investigated in order to assess the relationship between ligand rigidity, the nature of the donor atoms in the macrocycle (pyridine N, amine N, ether O) and in the pendant arms (carboxylates, phosphonates, primary, secondary, and tertiary amides), and the thermodynamic stability and the kinetic inertness of the Mn^{2+} complexes [63]. Although many of these complexes were non-hydrated, they allowed identifying structure–stability relationships. As expected, decreasing the denticity and the basicity of the DOTA by removing carboxylates results in decreased stability, which can be partially compensated by incorporating a pyridine ring (PCTA) or an ether oxygen (ODO3A) in the macrocycle (Scheme 3). Ligands with amide functions form thermodynamically less stable complexes than carboxylate analogues and primary amides are less stable than secondary and tertiary amides, but they promote higher kinetic inertness. The same tendency was also observed in comparing Mn(1,4-DO2A) and its bismethylamide derivative [64]. Phosphonates lead to poor conditional stability and kinetic inertness. The rigidity of the macrocycle was again identified as an important feature for high resistance to dissociation. The importance of ligand preorganization was further confirmed by the exceptional kinetic inertness of Mnbisp1 [61].

3.   MANGANESE(III) CHELATES

The Mn^{3+} oxidation state is also accessible under biologically relevant conditions. Mn^{3+} ($3d^4$ configuration) is paramagnetic, typically giving rise to high spin $S = 2$ complexes. Water exchange was reported to be fast on Mn^{3+} [65, 66], but the longitudinal electronic relaxation times are short (~10 ps or below [67]) and this limits their nuclear relaxation efficiency.

Water-soluble and air-stable porphyrin complexes of Mn^{3+} were investigated early on in the context of MRI. Mn^{3+} porphyrins combine several interesting features. Their bishydration contributes to good relaxivity. In an octahedral coordination geometry, the porphyrin nitrogens provide a planar coordination environment and two water molecules occupy the apical positions. Porphyrin complexes show high thermodynamic stability and kinetic inertness. Porphyrins are naturally targeted to tumor cells and can offer additional imaging or therapeutic options as well such as fluorescence imaging, photodynamic or photothermal therapy. For all these reasons, Mn^{3+} prophyrins will likely gain increasing interest in the future.

R1 = [benzene]-SO_3^{-2}

R2 = [fluorinated phenyl]-$O(CH_2CH_2O)_n CH_3$

R = R1 : $[Mn^{2+/3+}(tpps)(H_2O)_2]^{-4/-3}$
R = R2 : $[Mn^{2+/3+}(tpfpp(PEG)_4)(H_2O)_2]^{-4/-3}$
R = 3 R1 +1 R3 : $[Mn^{3+}((DPA-C_2)_2-tpps_3)(H_2O)_2]^{-3}$

R3 = [structure]

$X_1 = X_2 = H_2O$, solvent or buffer molecules

[MnPDA1]$^{+1}$

[MnPDA2]$^{+1}$

[MnPDA3]$^{+2}$

R_2 = H : $[Mn^{2+/3+}(HBET)(H_2O)]^{-2/-1}$
R_2 = OCH_3 : $[Mn^{2+/3+}(HBET-OMe)(H_2O)]^{-2/-1}$
R_2 = NO_2 : $[Mn^{2+/3+}(HBET-NO_2)(H_2O)]^{-2/-1}$

R_2 = H : $[Mn^{2+/3+}(CyHBET)(H_2O)]^{-2/-1}$
R_2 = OCH_3 : $[Mn^{2+/3+}(CyHBET-OMe)(H_2O)]^{-2/-1}$
R_2 = NO_2 : $[Mn^{2+/3+}(CyHBET-NO_2)(H_2O)]^{-2/-1}$

$[Mn^{2+}(JED)(H_2O)]$

$[Mn^{3+}(JED)]^{-1}$

$[Mn^{2+}(HBED)]^{-2}$

$[Mn(ptp1)(H_2O)]^{2+}$

$[Mn(qtp1)(H_2O)]^{2+}$

$[Mn(qtp2)(H_2O)]^{2+}$

Scheme 4.

It was shown in the 1980s that the meso-tetra(4-sulfonatophenyl)porphine derivative, Mntpps, (Scheme 4) is stable in human plasma for hours. Upon intravenous injection into athymic mice bearing subcutaneous human colon carcinoma xenografts, Mntpps provided enhanced water proton relaxation in excised mouse tissues, such as kidney, liver, and tumor [68].

Anomalously elevated relaxivities were reported for Mntpps [69]. It has also been shown that their NMRD curve cannot be appropriately fitted within the frame of the Solomon-Bloembergen-Morgan theory assuming reasonable distances between the Mn^{3+} electron spin and the coordinated water proton. This was attributed to the anisotropy of the electron density at the metal center, which brings the Mn^{3+} spin density closer to those protons. Another interesting feature is that the field dependency of the relaxivities is different for Mn^{3+} than for Mn^{2+} or Gd^{3+}. In contrast to classical MRI agents, relaxivity increases with increasing magnetic field above 1 MHz, which could be interesting for clinical applications, but has been largely underexploited.

Zhang et al. appended carboxylate functions on the porphyrin to accelerate the *in vivo* clearance rate and minimize the retention of the Mn^{3+} complex [70]. Their results suggest that the size, geometry, and polarity of complexes can be systematically modified to optimize their relaxivities and pharmacokinetic properties, including tissue specificity, diffusion rate, metabolic pathway, and clearance rate. They also created dimers to slow down rotation and increase relaxivity, and the linker between the two porphyrin rings was also exploited for HSA binding aiming to the development of a vascular imaging agent [71]. Porphyrins were linked to dextran polymers [72], virus-like particles [73] or incorporated in metal-organic frameworks [74].

Phthalocyanines have been also investigated. Following early work on a tetrasulfonated manganese(II) phthalocyanine which showed preferential retention and contrast in tumor [75], new water-soluble manganese(III) phthalocyanines bearing four PEG500 or four choline substituents, to promote water solubility, were reported [76]. Unfortunately, these Mn^{3+} complexes still displayed low solubility and relatively low r_1 relaxivities, due to their tendency to aggregate in aqueous solution. The ^{1}H NMRD profiles of the PEG500- and choline-substituted Mn^{3+}-phthalocyanine complexes are typical of self-aggregated Mn^{3+} systems with r_1 of 4.0 and 5.7 mM^{-1} s^{-1} at 20 MHz and 25 °C. The Mn^{3+} oxidation state is stabilized by the electron-donating substituents at the periphery of the phthalocyanines.

Jasanoff et al. reported ligands based on the 1,2-phenylenediamido (PDA) backbone (Scheme 4), in the objective of obtaining MRI probes to visualize in-cell targets [77]. Indeed, the combination of a lipophilic aryl backbone with a hydrophilic metal-binding site affords a good balance that facilitates crossing of cell membranes. Mn^{3+}-PDA complexes are bishydrated and display relaxivities comparable to that of small-molecular Gd^{3+} agents (4.1, 5.4, and 5.1 $mM^{-1}s^{-1}$ for MnPDA1, MnPDA2 and MnPDA3, respectively, 7 T, 22 °C). They spontaneously localize in the cytosol. Derivatives incorporating enzyme-cleavable acetomethoxy ester groups were also investigated [77]; they are processed by intracellular esterases and accumulate in cells.

4. RESPONSIVE PROBES

The relatively easy modulation of the relaxivity of MRI probes, thus of the consequent MRI signal by the environment of the CA enables the design of responsive molecular probes for the detection of many pertinent *in vivo* biomarkers. A number of *in vivo* parameters, such as overexpression of a specific protein, redox or pH variations, are intrinsically related to certain diseases and can be useful biomarkers for their early detection. The design of appropriate probes to detect those parameters and their variations has been the focus of extended research. New classes of probes, namely "smart" responsive and specific "targeted" CAs have emerged and slowly make their way through *in vivo* application and subsequent clinical use [1, 78–82]. In the case of Mn-based CA, a change in the metal redox state can also lead to an MRI signal variation, yielding alternative mechanisms to design responsive probes, in addition to the usual relaxivity modulation *via* the ligand structure (see below).

4.1. Redox Sensing Based on the Manganese(II)/ Manganese(III) Couple

Tissue redox is an important biomarker. Tight regulation of the intra- and extracellular redox environment is primordial to normal organism function. Modifications in the redox balance are linked to many cellular events and diseases, mainly associated to the generation of reactive oxygen species and consequent oxidative stress. The main actors in redox homeostasis are cysteine, glutathione, hydrogen peroxide, or nicotinamide adenine dinucleotide (NADH), whose concentrations and reduction potential vary depending on the biological status of the cell (e.g., proliferation, differentiation or apoptosis) and in disease states. These are therefore optimal biomarkers [83, 84]. Mn^{2+} and Mn^{3+} are both efficient paramagnetic relaxation agents, but with different relaxation mechanisms and different relaxivities.

4.1.1.   *Porphyrins*

The first redox-sensitive Mn-porphyrin-based agent has been reported by Aime et al. [85]. Their aim was to follow levels of partial oxygen pressure, $p(O_2)$, pertinent of a number of pathological conditions, and to obtain probes which enable a good separation of arterial and venous blood oxygenation levels by MRI. The porphyrin tpps (Scheme 4) forms stable complexes with both Mn^{2+} and Mn^{3+}. The complexes have a high r_1 relaxivity difference, but unfortunately only at low magnetic fields (~21 and ~6 mM^{-1}s^{-1} for Mn^{2+} and Mn^{3+}, respectively at 0.1 MHz, 25 °C). At clinical fields (1.5–3 T) the difference drops to ~1.2-fold. The analysis of the parameters influencing the relaxation pathways for $Mn^{2+/3+}$tpps showed that the r_1 of Mn^{3+}tpps depends mostly on the electronic relaxation, while that of Mn^{2+}tpps is controlled by the rotational motion (τ_R). To circumvent the low relaxivity difference between the two oxidation states, they incorporated

these tpps ligands in cyclodextrin. By using a poly-β-cyclodextrin with 3–9 units and a global molecular weight of 6 kDa, they reached a 4-fold enhancement of the relaxivity of the Mn^{2+} versus the Mn^{3+} state (20 MHz, 25 °C). Mn^{2+}tpps was then exposed to different oxygen levels, with complete oxidation to Mn^{3+} at 40 mmHg O_2, but the best discrimination in relaxivity occurs in values lower than this pressure, and therefore this probe is not fully adapted for *in vivo* applications. Nevertheless, it has opened the way for the design of other probes for differentiation of arterial *versus* venous blood vessels.

Tóth, Geraldes et al. have reported on more soluble and stable porphyrins, which would be very important for *in vivo* applications [86]. They have proposed a more biocompatible and water-soluble fluorinated porphyrin conjugated to polyethylene glycol (PEG) chains, tpfpp(PEG)$_4$ (Scheme 4). This novel probe stabilizes both $Mn^{2+/3+}$ in the relevant biological redox range. A reversible redox response to ascorbic acid/oxygen is observed, but Mn^{3+} reduction does not occur in the presence of glutathione or cysteine and this probe is specific for ascorbic acid. It has fast reduction and slow re-oxidation kinetics and low toxicity at concentrations relevant for MRI. Mn^{2+}- and Mn^{3+}tpfpp(PEG)$_4$ relaxivities are 24 mM^{-1}s^{-1} and 10 mM^{-1}s^{-1} at 20 MHz and 25 °C, a 2.4-fold difference at clinically relevant magnetic field.

4.1.2. EDTA-Phenolate Derivatives

Caravan et al. have reported EDTA and CDTA derivative families functionalized with phenolate groups (Scheme 4) [87]. The HBET and the more rigid CyHBET scaffolds bear substituents at the 5-position of the aromatic phenyl ring (–H, –OMe, and –NO$_2$) with different electronic properties. Complexes of these

Table 3. Main properties of $Mn^{2+/3+}$ complexes of HBET and CyHBET ligand families, HBED and JED: pMn^{2+}, r_1 and r_2 relaxivities, hydration number (q) and observed rate constant for conversion of Mn^{3+} to Mn^{2+} in the presence of L-cysteine.

	pMn^{2+a}	Mn^{2+b}		Mn^{3+b}		q	k_{obs} (s^{-1}) [d]	Refs.
		r_1	r_2	r_1	r_2			
HBET	6.62	2.8	9.4	1.1	2.7	1	0.042	[87, 120]
HBET-OMe	6.48	3.1	11.1	[c]	[c]	1		[87]
HBET-NO$_2$	7.01	2.3	4.8	0.5	1.0	0.5	0.732	[87]
CyHBET	6.68	3.3	6.0	0.4	0.9	1	0.063	[87]
CyHBET-OMe	6.24	3.3	5.8	[c]	[c]	1		[87]
CyHBET-NO$_2$	7.55	2.3	3.7	0.5	0.9	1	0.563	[87]
HBED	5.72							[88]
JED		3.3		0.5				[88]

[a] pH 7.4 and [M] = [L] = 10 μM.
[b] In mM^{-1}s^{-1}, at pH 7.4, 37 °C, 1.4 T.
[c] Complexes of Mn^{3+} with –OMe derivatives were not possible to isolate.
[d] [Mn^{3+}] = 0.5 mM, [L-cysteine] = 10 mM.

6 novel ligands with Mn^{3+} and Mn^{2+} were studied yielding thermodynamic, redox, and relaxivity data and a structure-activity analysis (Table 3).

There was no particular increase in complex stability by rigidifying the ligand, but the increased kinetic inertness is in favor of the CDTA scaffold. The thermodynamic stability of the complexes follows the electronic nature of the substituent groups, increasing in the order of –OMe < –H < –NO₂. Both r_1 and r_2 are higher for the Mn^{2+} than for the Mn^{3+} complexes. The highest difference was observed for CyHBET: 8.3-fold in r_1 and 6.6-fold in r_2. Within each series, r_1 and r_2 increase with the pK_a of the phenolate donor. The reduction of Mn^{3+} to Mn^{2+} with L-cysteine is also dependent on the electronic nature of the substituent; it is an order of magnitude slower for the –H than for the –NO₂ derivative. The redox reversibility of $Mn^{2+/3+}$ can be tuned by changing the ligand structure.

A more adapted structure to stabilize both Mn^{2+} and Mn^{3+} is the JED ligand (Scheme 4), an ethylenediamine scaffold bearing two sets of donor groups stabilizing Mn^{2+} and Mn^{3+}, respectively [88]. This strategy resulted in a 7-fold higher r_1 relaxivity for the Mn^{2+} than for the Mn^{3+} complexes (Table 3). Mn^{2+} has an inner sphere water molecule while the smaller Mn^{3+} is coordinatively saturated by 6 donor atoms (2 N from the scaffold and 4 O), with no room for water. The Mn^{3+} complex is rapidly reduced in the presence of L-cysteine (k_{obs} of 3.6 s⁻¹), and the peroxidase-mediated oxidation of Mn^{2+} guaranties its reversibility. Such improvement in terms of r_1 variation and fast interconversion of the stable forms $Mn^{2+/3+}$ JED represented real progress in the rational design of redox-responsive probes.

4.2. pH-Responsive Probes

Most Mn-based pH-responsive probes are based on the release of Mn^{2+} (see below). Recently, a promising probe whose signal change is based on the variation of the hydration number was reported [56]. This PC2A derivative PC2A-EA bears an ethylamine pH-sensing moiety (Scheme 3). This chelate is thermodynamically very stable and kinetically inert (see Table 2 in Section 2.2.2). At 0.49 T, 25 °C and in the pH range 3.7−5.8, r_1 is 3.5 mM⁻¹s⁻¹ and corresponds to the monoaquated and protonated Mn(HPC2A-EA). Below pH = 3.5, r_1 increases owing to the formation of a diprotonated chelate followed by dissociation. Above pH 5.8, a decrease to 2.1 mM⁻¹s⁻¹ at pH > 8.4 is observed, indicating the deprotonation and coordination of the ethylamine pendant to the Mn^{2+} (q = 0). MRI phantoms at 3 T in the presence of human serum revealed a good signal change on T_1 and an even higher pH discrimination in T_2-weighted images, with r_2 changing from 1.71 mM⁻¹s⁻¹ at pH 7.5 to 8.34 mM⁻¹s⁻¹ at pH 6.7.

4.3. Other Responsive Probes

Mn complexes have been used for the detection of redox biomarkers, such as reactive oxygen species (e.g., H_2O_2) or superoxide dismutase (SOD) [89–91], but also Zn^{2+} [92, 93] and Ca^{2+} [94].
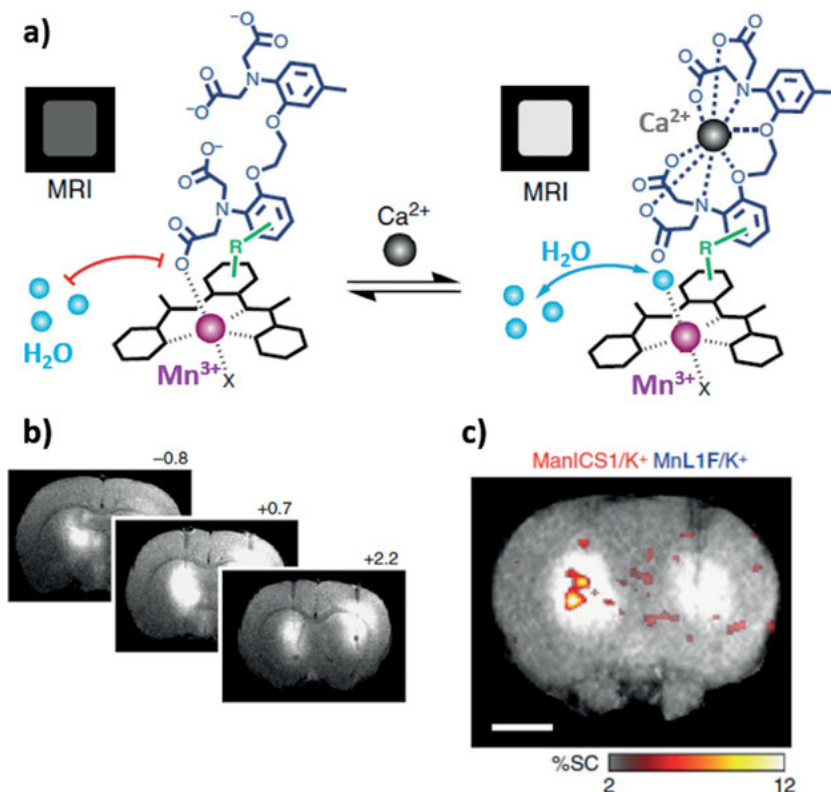
Figure 2. Calcium-responsive probe ManICS1-AM: (**a**) schematic presentation of the MRI signal with T_1-weighted MRI phantom images acquired at 7 T. (**b**) *In vivo* T_1-weighted MRI (7 T) showing broad contrast enhancement after infusion of ManICS-1 (left) or calcium-insensitive control agent (MnL1F, right) into rat striatum; (**c**) T_1-weighted MRI signal increase upon K^+ infusion in the presence of preinjected ManICS1-AM (left) but not of MnL1F (right). Adapted with permission from [94].

Goldsmith and coworkers have reported on three redox-active ligands prone to oxidation in the presence of H_2O_2 (Scheme 4): ptp1 [89]; the substitution of the methyl by a hydroxyl group yielded ligand qtp1 [90]; and the further substitution of the pyridine group by a second quinol led to ligand qtp2 [91]. While oxidation of ptq1 yields a binuclear species and the deprotonation of at least one of the phenols, for the other two ligands, the quinol groups are oxidized to *para*-quinone. The presence of H_2O_2 led to r_1 variation 3-fold better than for the ones obtained for ptp1 and qtp1 (5.46 to 7.17 mM^{-1}s^{-1}, 3 T). EPR studies confirmed that the Mn^{2+} oxidation state does not change and this increased relaxivity is attributed to a higher number of water molecules coordinated to the metal. The qtp2 complex is more susceptible to transmetalation, with a pMn^{2+} of 5.36 (pH 7.4), but is less cytotoxic than qtp1. All three complexes also work as potent antioxidants, suggesting a potential to simultaneously visualize and improve oxidative stress.

Jasanoff and collaborators have studied both Zn^{2+} and Ca^{2+} sensing probes. The Zn^{2+} probes are based on Mn-$(DPA$-$C_2)_2$-$TPPS_3$, a tpps3 porphyrin functionalized with two dipicolylamine (DPA) groups [92, 93]. In the presence of Zn^{2+}, DPA binding functions flip from Mn^{3+} to Zn^{2+}, thus leaving place for two water molecules in the Mn^{3+} coordination sphere. Surprisingly, r_1 of this water-soluble and membrane-permeable probe decreases 1.3-fold in the presence of Zn^{2+} (4.7 T), a phenomenon dependent on pH and the ionic force. As the probe is cell-penetrable, intracellular Zn^{2+} detection was possible in HEK-293 cells both in T_1 and T_2-weighted MRI. *In vivo* studies were reported in living brain by intracranial injection in rats. A T_1-weighted contrast enhancement at 9.4 T was more distinct in the hippocampus, a zinc-rich brain region, than in the caudate nucleus, which contains relatively little labile Zn^{2+}, revealing the interest of these porphyrin-DPA derivatives.

Intracellular Ca^{2+} probes were later described [94]. They are based on fluorescent dyes and consist of two parts: a selective Ca^{2+}-binding moiety derived from BAPTA modified with acetomethoxy (AM) ester groups (which undergo esterase cleavage following cell penetration), and a cell-permeable phenylenediamido(PDA)-based Mn^{3+} complex (ManICS1-AM). Relaxivity studies in the presence of Ca^{2+} were encouraging and studies in cells showed cell penetration, with conversion of the ethyl ester AM groups to carboxylates. The cells were stimulated with pharmacological agents that elevate cytosolic calcium levels and yielded satisfactory results, leading to further *in vivo* tests in rat brain (Figure 2). Intracranial infusion of ManICS1-AM into the rat striatum results in T_1-weighted MRI signal enhancement upon stimulation of the brain with K^+ ions. A Ca^{2+}-insensitive agent MnL1F was injected for control.

4.4. Magnetic Resonance Imaging Response Based on Mn^{2+} Release

MRI intensity changes resulting from the release of "free" Mn^{2+} from complexes have been exploited to develop strategies and detect the redox state *via* Mn^{3+} reduction [95], pH [96, 97], enzymes [98], Ca^{2+} [99] or Zn^{2+} [100]. Botta et al. have reported 3 Mn^{2+} chelates based on EDTA, DTPA, and DTTA scaffolds, where an *L*-tyrosine residue replaces one aminoacetate unit [98]. These probes are responsive to tyrosinase, overexpressed in melanoma cells. Upon enzymatic action, the complex is destabilized causing controlled release of Mn^{2+}, eventually taken up by biological macromolecules, thus yielding a remarkable relaxivity increase, 350 % for the DTTA derivative.

Jasanoff et al. [99] showed that labile Mn^{2+} complexes of EGTA, BAPTA, and calmodulin (a Ca^{2+}-binding protein), all three selective for Ca^{2+}, promote Mn^{2+} displacement in the presence of extracellular Ca^{2+}. A T_1-weighted MRI (4.7 T) signal increase was observed for EGTA (3-fold) and BAPTA (4.7-fold), whereas Mn^{2+} displacement from calmodulin results in a signal decrease (2-fold). The MRI signal increase is related to the higher number of first sphere water molecules for the aqua-ion ($q = 6$) than for complexed Mn^{2+}, $q = 0 – 2$. However, in the

case of calmodulin, the long τ_R probably compensates the reduced q. A bimodal fluorescence/MRI Zn^{2+} responsive probe was also reported [100], based on a dinuclear Mn^{2+} complex of the zinc-responsive fluorescent indicator Zinpyr-1, [$ZP1Mn_2$]. The probe is selective for Zn^{2+} over endogenous metals. In the presence of Zn^{2+}, the fluorescence signal increases 25-fold. In parallel, a 1.7-fold r_2 relaxivity increase is observed, while r_1 remains unchanged within the measurement error.

5. GENERAL CONCLUSIONS

Manganese is a versatile element for the creation of MRI contrast-enhancing substances. Mn^{2+} was the first CA ever used, though later replaced by Gd^{3+} agents. Following recent toxicity concerns associated to Gd^{3+}, the design of stable, inert, and highly relaxing Mn^{2+} complexes has been an active field and by today, we gained good understanding of the structural factors that govern these properties. Some Mn^{2+} complexes are successfully progressing towards clinical tests. Mn^{3+} has been less investigated, though its relaxation mechanism allowing for elevated relaxivities at high magnetic fields can be interesting to exploit. Based on the recent spectacular progress in these fields, manganese will likely gain increased importance in both preclinical and clinical applications.

ABBREVIATIONS

BAPTA	1,2-bis(o-aminophenoxy)ethane tetraacetic acid
bcpe	6,6′-((ethane-1,2-diylbis-(azanediyl))bis(methylene))dipicolinic acid
BOM	benzyloxomethyl
BTA	benzothiazole aniline
CA	contrast agent
CDTA	1,2-cyclohexylenedinitrilotetraacetic acid
DOTA	1,4,7,10-Tetraazacyclododecane-1,4,7,10-tetraacetic acid
DPA	dipicolylamine
DTA	1,3-diamino-2-hydroxypropane tetraacetic acid
DTTA	di-p-toluoyl-D-tartaric acid
EDTA	ethylenediamine tetraacetic acid
EGTA	(ethylene glycol-bis(β-aminoethyl ether) tetraacetic acid
ENOTA	dimeric triazacyclononane tetraacetic acid
EOB	ethoxybenzyl
HSA	human serum albumin
ICP	inductively coupled plasma
ManICS1-AM	phenylenediamido(PDA)-based Mn^{3+} complex
MRI	magnetic resonance imaging
NADH	nicotinamide adenine dinucleotide, reduced

NMRD   nuclear magnetic relaxation dispersion
NOTA   1,4,7-triazacyclononane-1,4,7-triacetic acid
PDA   1,2-phenylenediamido
PEG   polyethylene glycol
SOD   superoxide dismutase

REFERENCES

1. J. Wahsner, E. M. Gale, A. Rodríguez-Rodríguez, P. Caravan, *Chem. Rev.* **2019**, *119*, 957–1057.
2. A. E. Merbach, L. Helm, E. Tóth, *The Chemistry of Contrast Agents in Medical Magnetic Resonance Imaging*, John Wiley & Sons, Chichester, **2013**.
3. T. Grobner, *Nephrol. Dial. Transplant.* **2006**, *21*, 1104–1108.
4. M. Aschner, K. M. Erikson, D. C. Dorman, *Crit. Rev. Toxicol.* **2005**, *35*, 1–32.
5. M. G. Cersosimo, W. C. Koller, *Neurotoxicology* **2006**, *27*, 340–346.
6. P. G. Lauterbur, *Nature* **1973**, *242*, 190–191.
7. *Special Issue: "Manganese Enhanced Magnetic Resonance Imaging (MEMRI)*, *NMR Biomed.* **2004**, *17*, p. 527–634.
8. C. A. Massaad, R. G. Pautler, *Methods Mol. Biol.* **2011**, *711*, 145–174.
9. B. Drahos, I. Lukes, E. Tóth, *Eur. J. Inorg. Chem.* **2012**, 1975–1986.
10. D. Pan, A. H. Schmieder, S. A. Wickline, G. M. Lanza, *Tetrahedron* **2011**, *67*, 8431–8444.
11. M. Botta, F. Carniato, D. Esteban-Gomez, C. Platas-Iglesias, L. Tei, *Future Med. Chem.* **2019**, *11*, 1461–1483.
12. M. Kueny-Stotz, A. Garofalo, D. Felder-Flesch, *Eur. J. Inorg. Chem.* **2012**, 1987–2005.
13. E. Tóth, L. Helm, A. Merbach, in *Relaxivity of Gd(III) Complexes: Theory and Mechanism*, Ch. 2 in *The Chemistry of Contrast Agents in Medical Magnetic Resonance Imaging*, Eds. A. Merbach, L. Helm, E. Tóth, John Wiley & Sons, Chichester, **2013**, pp. 25–81.
14. E. M. Gale, J. Zhu, P. Caravan, *J. Am. Chem. Soc.* **2013**, *135*, 18600–18608.
15. J. A. Peters, C. E. G. C. Geraldes, *Inorganics* **2018**, *6*, 116.
16. V. Patinec, G. A. Rolla, M. Botta, R. Tripier, D. Esteban-Gomez, C. Platas-Iglesias, *Inorg. Chem.* **2013**, *52*, 11173–11184.
17. G. Liu, H. W. Dodgen, J. P. Hunt, *Inorg. Chem.* **1977**, *16*, 2652–2653.
18. M. S. Zetter, E. J. Wood, J. P. Hunt, H. W. Dodgen, M. W. Grant, *Inorg. Chem.* **1972**, *11*, 2701–2706.
19. J. Maigut, R. Meier, A. Zahl, R. van Eldik, *Inorg. Chem.* **2008**, *47*, 5702–5719.
20. J. Maigut, R. Meier, A. Zahl, R. van Eldik, *J. Am. Chem. Soc.* **2008**, *130*, 14556–14569.
21. Y. Ducommun, K. E. Newman, A. E. Merbach, *Inorg. Chem.* **1980**, *19*, 3696–3703.
22. S. H. Koenig, C. Baglin, R. D. Brown, *Magn. Reson. Med.* **1984**, *1*, 496–501.
23. S. Aime, P. L. Anelli, M. Botta, M. Brocchetta, S. Canton, F. Fedeli, E. Gianolio, E. Terreno, *J. Biol. Inorg. Chem.* **2002**, *7*, 58–67.
24. J. S. Troughton, M. T. Greenfield, J. M. Greenwood, S. Dumas, A. J. Wiethoff, J. Wang, M. Spiller, T. McMurry, P. Caravan, *Inorg. Chem.* **2004**, *43*, 6313–6323.
25. M. K. Islam, S. Kim, H.-K. Kim, S. Park, G.-H. Lee, H. J. Kang, J.-C. Jung, J.-S. Park, T.-J. Kim, Y. Chan, *J. Med. Chem.* **2017**, *60*, 2993–3001.

26. M. K. Islam, S. Kim, H. K. Kim, Y. H. Kim, Y. M. Lee, G. Choi, A. R. Baek, B. K. Sung, M. Kim, A. E. Cho, H. Kang, G. H. Lee, S. H. Choi, T. Lee, J. A. Park, Y. Chang, *Bioconjug. Chem.* **2018**, *29*, 3614–3625.

27. E. Molnár, B. Varadi, Z. Garda, R. Botar, F. K. Kálmán, E. Tóth, C. Platas-Iglesias, I. Tóth, E. Brücher, G. Tircsó, *Inorg. Chim. Acta* **2018**, *472*, 254–263.

28. C. Vanasschen, E. Molnár, G. Tircsó, F. K. Kálmán, E. Tóth, M. Brandt, H. H. Coenen, B. Neumaier, *Inorg. Chem.* **2017**, *56*, 7746–7760.

29. K. Pota, Z. Garda, F. K. Kálmán, J. L. Barriada, D. Esteban-Gomez, C. Platas-Iglesias, I. Tóth, E. Brücher, G. Tircsó, *New J. Chem.* **2018**, *42*, 8001–8011.

30. S. Laine, C. S. Bonnet, F. K. Kálmán, Z. Garda, A. Pallier, F. Caille, F. Suzenet, G. Tircsó, E. Tóth, *New J. Chem.* **2018**, *42*, 8012–8020.

31. H. Su, C. Wu, J. Zhu, T. Miao, D. Wang, C. Xia, X. Zhao, Q. Gong, B. Song, H. Ai, *Dalton Trans.* **2012**, *41*, 14480–14483.

32. C. Wu, L. Yang, Z. Chen, H. Zhang, D. Li, B. Lin, J. Zhu, H. Ai, X. Zhang, *RSC Adv.* **2017**, *7*, 54603–54609.

33. C. Wu, D. Li, L. Yang, B. Lin, H. Zhang, Y. Xu, Z. Cheng, C. Xia, Q. Gong, B. Song, H. Ai, *J. Mater. Chem. B* **2015**, *3*, 1470–1473.

34. N. Rastogi, N. Tyagi, O. Singh, B. S. Hemanth Kumar, U. P. Singh, K. Ghosh, R. Roy, *J. Inorg. Biochem.* **2017**, *177*, 76–81.

35. E. M. Gale, I. P. Atanasova, F. Blasi, I. Ay, P. Caravan, *J. Am. Chem. Soc.* **2015**, *137*, 15548–15557.

36. E. M. Gale, H.-Y. Wey, I. Ramsay, Y.-F. Yen, D. E. Sosnovik, P. Caravan, *Radiology* **2018**, *286*, 877–884.

37. D. J. Erstad, I. A. Ramsay, V. C. Jordan, M. Sojoodi, B. C. Fuchs, K. K. Tanabe, P. Caravan, E. M. Gale, *Invest. Radiol.* **2019**, *54*, 697–703.

38. J. Wang, H. Wang, I. A. Ramsay, D. J. Erstad, B. C. Fuchs, K. K. Tanabe, P. Caravan, E. M. Gale, *J. Med. Chem.* **2018**, *61*, 8811–8824.

39. M. Regueiro-Figueroa, G. A. Rolla, D. Esteban-Gomez, A. de Blas, T. Rodriguez-Blas, M. Botta, C. Platas-Iglesias, *Chem. Eur. J.* **2014**, *20*, 17300–17305.

40. A. Forgacs, M. Regueiro-Figueroa, J. L. Barriada, D. Esteban-Gomez, A. de Blas, T. Rodriguez-Blas, M. Botta, C. Platas-Iglesias, *Inorg. Chem.* **2015**, *54*, 9576–9587.

41. B. Phukan, C. Mukherjee, U. Goswami, A. Sarmah, S. Mukherjee, S. K. Sahoo, S. C. Moi, *Inorg. Chem.* **2018**, *57*, 2631–2638.

42. C. F. G. C. Geraldes, A. D. Sherry, R. D. Brown, III, S. H. Koenig, *Magn. Reson. Med.* **1986**, *3*, 242–250.

43. E. Balogh, Z. He, W. Hsieh, S. Liu, E. Tóth, *Inorg. Chem.* **2007**, *46*, 238–250.

44. A. de Sa, C. S. Bonnet, C. Geraldes, E. Tóth, P. M. T. Ferreira, J. P. Andre, *Dalton Trans.* **2013**, *42*, 4522–4532.

45. R. Pujales-Paradela, F. Carniato, D. Esteban-Gomez, M. Botta, C. Platas-Iglesias, *Dalton Trans.* **2019**, *48*, 3962–3972.

46. Z. Zhou, R. Bai, Z. Wang, H. Bryant, L. Lang, H. Merkle, J. Munasinghe, L. Tang, W. Tang, R. Tian, G. Yu, Y. Ma, G. Niu, J. Gao, X. Chen, *Bioconjug. Chem.* **2019**, *30*, 1821–1829.

47. E. Molnár, N. Camus, V. Patinec, G. A. Rolla, M. Botta, G. Tircsó, F. K. Kálmán, T. Fodor, R. Tripier, C. Platas-Iglesias, *Inorg. Chem.* **2014**, *53*, 5136–5149.

48. B. Drahos, M. Pniok, J. Havlickova, J. Kotek, I. Cisarova, P. Hermann, I. Lukes, E. Tóth, *Dalton Trans.* **2011**, *40*, 10131–10146.

49. B. Drahos, V. Kubicek, C. S. Bonnet, P. Hermann, I. Lukes, E. Tóth, *Dalton Trans.* **2011**, *40*, 1945–1951.

50. G. A. Rolla, C. Platas-Iglesias, M. Botta, L. Tei, L. Helm, *Inorg. Chem.* **2013**, *52*, 3268–3279.

51. R. Artali, Z. Baranyai, M. Botta, G. B. Giovenzana, A. Maspero, R. Negri, G. Palmisano, M. Sisti, S. Tollari, *New J. Chem.* **2015**, *39*, 539–547.

52. Z. Garda, A. Forgacs, Q. N. Do, F. K. Kálmán, S. Timari, Z. Baranyai, L. Tei, I. Tóth, Z. Kovács, G. Tircsó, *J. Inorg. Biochem.* **2016**, *163*, 206–213.

53. G. Rolla, V. De Biasio, G. B. Giovenzana, M. Botta, L. Tei, *Dalton Trans.* **2018**, *47*, 10660–10670.

54. J. Barta, P. Hermann, J. Kotek, *Molecules* **2019**, *24*, 3324.

55. B. Drahos, J. Kotek, I. Cisarova, P. Hermann, L. Helm, I. Lukes, E. Tóth, *Inorg. Chem.* **2011**, *50*, 12785–12801.

56. R. Botár, E. Molnár, G. Trencsényi, J. Kiss, F. K. Kálmán, G. Tircsó, *J. Am. Chem. Soc.* **2020**, *142*, 1662–1666.

57. D. Lieb, F. C. Friedel, M. Yawer, A. Zahl, M. M. Khusniyarov, F. W. Heinemann, I. Ivanovic-Burmazovic, *Inorg. Chem.* **2013**, *52*, 222–236.

58. B. Drahos, J. Kotek, P. Hermann, I. Lukes, E. Tóth, *Inorg. Chem.* **2010**, *49*, 3224–3238.

59. M. S. Shazeeb, G. Feula, A. Bogdanov, Jr., *Contrast Media Mol. Imaging* **2014**, *9*, 221–228.

60. L. Tei, G. Gugliotta, M. Fekete, F. K. Kálmán, M. Botta, *Dalton Trans.* **2011**, *40*, 2025–2032.

61. D. Ndiaye, M. Sy, A. Pallier, S. Meme, I. de Silva, S. Lacerda, A. M. Nonat, L. J. Charbonniere, E. Tóth, *Angew. Chem. Int. Ed.* **2020**, *59*, 11958–11963.

62. F. K. Kálmán, G. Tircsó, *Inorg. Chem.* **2012**, *51*, 10065–10067.

63. Z. Garda, E. Molnár, F. K. Kálmán, R. Botár, V. Nagy, Z. Baranyai, E. Brücher, Z. Kovács, I. Tóth, G. Tircsó, *Front. Chem.* **2018**, *6*, 232.

64. A. Forgacs, L. Tei, Z. Baranyai, I. Tóth, L. Zekany, M. Botta, *Eur. J. Inorg. Chem.* **2016**, 1165–1174.

65. D. Lieb, A. Zahl, T. E. Shubina, I. Ivanovic-Burmazovic, *J. Am. Chem. Soc.* **2010**, *132*, 7282–7284.

66. A. Budimir, K. Jozsef, F. Istvan, G. Lente, B. Istvan, I. Batinic-Haberle, M. Birus, *Dalton Trans.* **2010**, *39*, 4405–4410.

67. I. Bertini, C. Luchinat, G. Parigi, E. Ravera, *NMR of Paramagnetic Molecules-Applications to Metallobiomolecules and Models*, Elsevier, Amsterdam, **2017**.

68. R. C. Lyon, P. J. Faustino, J. S. Cohen, A. Katz, F. Mornex, D. Colcher, C. Baglin, S. H. Koenig, P. Hambright, *Magn. Reson. Med.* **1987**, *4*, 24–33.

69. S. H. Koenig, R. D. Brown, III, M. Spiller, *Magn. Reson. Med.* **1987**, *4*, 252–260.

70. W. Cheng, I. E. Haedicke, J. Nofiele, F. Martinez, K. Beera, T. J. Scholl, H.-L. M. Cheng, X.-a. Zhang, *J. Med. Chem.* **2014**, *57*, 516–520.

71. W. Cheng, T. Ganesh, F. Martinez-Santiesteban, J. Lam, H. Yoon, R. Macgregor, T. Scholl, H.-L. Cheng, X.-A. Zhang, *J. Biol. Inorg. Chem.* **2014**, *19*, 229–235.

72. Z. Zhang, R. He, K. Yan, Q.-n. Guo, Y.-g. Lu, X.-x. Wang, H. Lei, Z.-y. Li, *Bioorg. Med. Chem. Lett.* **2009**, *19*, 6675–6678.

73. S. Qazi, M. Uchida, R. Usselman, R. Shearer, E. Edwards, T. Douglas, *J. Biol. Inorg. Chem.* **2014**, *19*, 237–246.

74. M. E. He, Y. A. Chen, C. Tao, Q. Q. Tian, L. An, J. M. Lin, Q. W. Tian, H. Yang, S. P. Yang, *ACS Appl. Mater. Interfaces* **2019**, *11*, 41946–41956.

75. S. K. Saini, A. Jena, J. Dey, A. K. Sharma, R. Singh, *Magn. Reson. Imaging* **1995**, *13*, 985–990.

76. S. M. A. Pinto, V. A. Tomé, M. J. F. Calvete, M. M. Pereira, H. D. Burrows, A. M. S. Cardoso, A. Pallier, M. M. C. A. Castro, É. Tóth, C. F. G. C. Geraldes, *J. Inorg. Biochem.* **2016**, *154*, 50–59.

77. A. Barandov, B. B. Bartelle, B. A. Gonzalez, W. L. White, S. J. Lippard, A. Jasanoff, *J. Am. Chem. Soc.* **2016**, *138*, 5483–5486.

78. D. V. Hingorani, A. S. Bernstein, M. D. Pagel, *Contrast Media Mol. Imaging* **2015**, *10*, 245–265.

79. C. S. Bonnet, L. Tei, M. Botta, E. Tóth, in *Responsive Probes*, Ch. 8 in *The Chemistry of Contrast Agents in Medical Magnetic Resonance Imaging*, Eds. A. E. Merbach, L. Helm, E. Tóth, John Wiley & Sons, Chichester, **2013**, pp. 343–385.

80. S. M. Pinto, V. Tomé, M. J. F. Calvete, M. M. C. A. Castro, É. Tóth, C. F. G. C. Geraldes, *Coord. Chem. Rev.* **2019**, *390*, 1–31.

81. S. Lacerda, *Inorganics* **2018**, *6*, 129.

82. É. Tóth, S. C. Bonnet, *Inorganics* **2019**, *7*, 68.

83. R. Zhang, J. Yong, J. Yuan, Z. Ping Xu, *Coord. Chem. Rev.* **2020**, *408*, 213182.

84. F. Q. Schafer, G. R. Buettner, *Free Radic. Biol. Med.* **2001**, *30*, 1191–1212.

85. S. Aime, M. Botta, E. Gianolio, E. Terreno, *Angew. Chem. Int. Ed.* **2000**, *39*, 747–750.

86. S. M. A. Pinto, M. J. F. Calvete, M. E. Ghica, S. Soler, I. Gallardo, A. Pallier, M. B. Laranjo, A. M. S. Cardoso, M. M. C. A. Castro, C. M. A. Brett, M. M. Pereira, É. Tóth, C. F. G. C. Geraldes, *Dalton Trans.* **2019**, *48*, 3249–3262.

87. E. M. Gale, S. Mukherjee, C. Liu, G. S. Loving, P. Caravan, *Inorg. Chem.* **2014**, *53*, 10748–10761.

88. E. M. Gale, C. M. Jones, I. Ramsay, C. T. Farrar, P. Caravan, *J. Am. Chem. Soc.* **2016**, *138*, 15861–15864.

89. M. Yu, R. J. Beyers, J. D. Gorden, J. N. Cross, C. R. Goldsmith, *Inorg. Chem.* **2012**, *51*, 9153–9155.

90. M. Yu, S. L. Ambrose, Z. L. Whaley, S. Fan, J. D. Gorden, R. J. Beyers, D. D. Schwartz, C. R. Goldsmith, *J. Am. Chem. Soc.* **2014**, *136*, 12836–12839.

91. M. Yu, M. B. Ward, A. Franke, S. L. Ambrose, Z. L. Whaley, T. M. Bradford, J. D. Gorden, R. J. Beyers, R. C. Cattley, I. Ivanović-Burmazović, D. D. Schwartz, C. R. Goldsmith, *Inorg. Chem.* **2017**, *56*, 2812–2826.

92. T. Lee, X.-a. Zhang, S. Dhar, H. Faas, S. J. Lippard, A. Jasanoff, *Chemistry & Biology* **2010**, *17*, 665–673.

93. X.-a. Zhang, K. S. Lovejoy, A. Jasanoff, S. J. Lippard, *Proc. Nat. Acad. Sci. USA* **2007**, *104*, 10780.

94. A. Barandov, B. B. Bartelle, C. G. Williamson, E. S. Loucks, S. J. Lippard, A. Jasanoff, *Nature Commun.* **2019**, *10*, 897.

95. S.-S. Wan, Q. Cheng, X. Zeng, X.-Z. Zhang, *ACS Nano* **2019**, *13*, 6561–6571.

96. J. Chen, W.-J. Zhang, Z. Guo, H.-B. Wang, D.-D. Wang, J.-J. Zhou, Q.-W. Chen, *ACS Appl. Mater. Interfaces* **2015**, *7*, 5373–5383.

97. P. Mi, D. Kokuryo, H. Cabral, H. Wu, Y. Terada, T. Saga, I. Aoki, N. Nishiyama, K. Kataoka, *Nat. Nanotech.* **2016**, *11*, 724–730.

98. G. A. Rolla, L. Tei, M. Fekete, F. Arena, E. Gianolio, M. Botta, *Bioorg. Med. Chem.* **2011**, *19*, 1115–1122.

99. T. Atanasijevic, X.-a. Zhang, S. J. Lippard, A. Jasanoff, *Inorg. Chem.* **2010**, *49*, 2589–2591.

100. Y. You, E. Tomat, K. Hwang, T. Atanasijevic, W. Nam, A. P. Jasanoff, S. J. Lippard, *Chem. Commun.* **2010**, *46*, 4139–4141.

4

Metal Ion Complexes in Paramagnetic Chemical Exchange Saturation Transfer (ParaCEST)

Aurora Rodríguez-Rodríguez,[1] *Moritz Zaiss,*[2] *David Esteban-Gómez,*[1]
Goran Angelovski,[3] *and Carlos Platas-Iglesias*[1]

[1]Centro de Investigacións Científicas Avanzadas (CICA) and Departamento de Química,
Facultade de Ciencias, Universidade da Coruña, CP-15071 A Coruña, Galicia, Spain
<carlos.platas.iglesias@udc.es>

[2]Department of Neuroradiology, University Clinic Erlangen,
Friedrich-Alexander Universität Erlangen-Nürnberg (FAU), D-91054 Erlangen, Germany

[3]MR Neuroimaging Agents, Max Planck Institute for Biological Cybernetics,
Tübingen, Max-Planck-Ring 8–14, D-72076 Tübingen, Germany

Abstract: Chemical exchange saturation transfer (CEST) is an emerging mechanism to provide contrast in clinical magnetic resonance imaging (MRI). CEST agents are compounds that contain a pool of exchangeable or labile protons involved in exchange with the surrounding

water molecules in tissues. Application of a radio frequency pulse at the frequency of the labile protons results in some saturation being transferred to bulk water due to chemical exchange. This attenuates the intensity of the bulk water signal, thus generating image contrast. Both diamagnetic and paramagnetic compounds can be used as CEST agents. In this chapter, the use of paramagnetic probes based on both lanthanide and transition metal ions as CEST agents is reviewed. The most promising agents reported in the literature are presented, including several probes that respond to the environment and some successful *in vivo* applications.

Keywords: lanthanides · MRI · metal ions · transition metals · complexes

1. INTRODUCTION

The advent of magnetic resonance imaging (MRI) at the end of the 1970s and beginning of the 1980s represented a major advance for medical diagnosis, as this technique allows recording high-resolution images of the body with unlimited tissue penetration and without use of ionizing radiation [1]. MRI uses the ^{1}H resonances of water and tissues (i.e., fat), generating contrast on the basis of differences in nuclear spin densities and relaxation times. Paramagnetic compounds (Fe^{3+}, Mn^{2+}, and Gd^{3+}) were soon proposed as contrast agents for MRI, as they can accelerate the relaxation times of water proton nuclei (see Chapter 2) [2–4]. These contrast agents enhance image contrast by shortening the longitudinal relaxation times (T_1) of water protons, and are thus often denoted as T_1 agents. Several Gd^{3+} complexes developed by different pharmaceutical companies entered the market by the end of the 1980s and early 1990s, and since then they have been routinely applied in millions of MRI scans. These T_1 agents are non-specific, distribute in the extracellular space, and are rapidly excreted from the body, mostly through the kidneys [5, 6].

Some toxicity issues associated to the administration of Gd^{3+}-based agents, as well as additional limitations associated to certain MRI applications, triggered a renewed interest in finding alternatives to the classical paramagnetic T_1 agents [7–9]. For instance, quantification of contrast agent concentration is extremely difficult, as these agents affect the relaxation times of an already existing signal (the bulk water signal). Indeed, the signal changes induced by the contrast agent, in response to a change in the environment, are concentration-dependent. Thus, while many Gd^{3+} agents with response to different biomarkers have been developed (pH, concentration of metal ions, redox potential, enzymatic activity, etc.), quantification of the observed changes is very challenging due to the difficulties in determining the exact concentration of the probe [10, 11]. Thus, alternative contrast agents are required for molecular imaging applications, which aim at obtaining not only anatomical but also functional information [12, 13].

Chemical exchange saturation transfer (CEST) contrast agents represent a very attractive alternative to the classical T_1 agents [14]. The CEST effect or magnetization transfer (MT) effect was first introduced by Forsén and Hoffman and later demonstrated *in vivo* by Wolff and Balaban [15, 16]. Shortly after this initial report, exogenous compounds (i.e., barbituric acid) were proposed as CEST MRI contrast agents [17]. CEST agents rely on the presence of a pool of
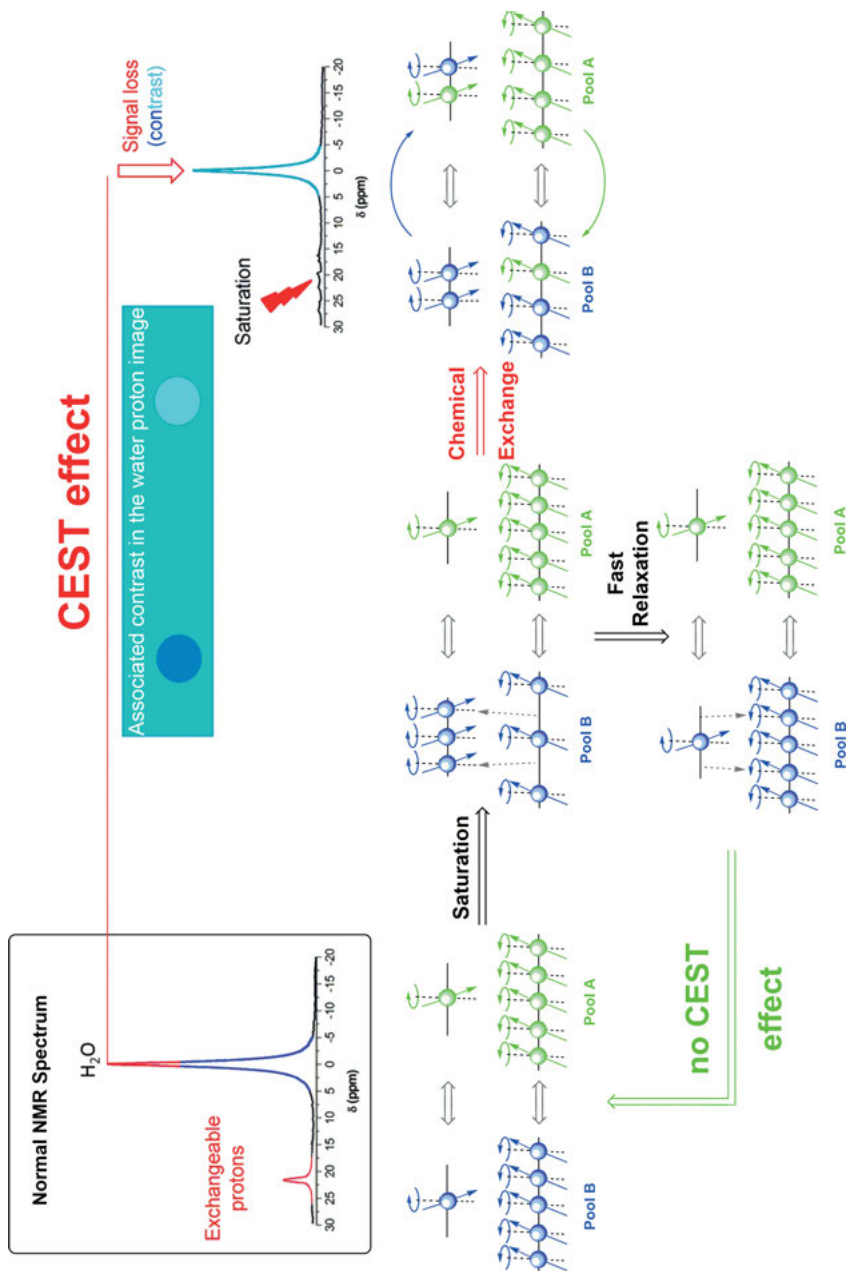
Figure 1. Schematic representation of the CEST effect. Saturation of a pool of exchangeable protons (pool B) with a radio frequency pulse may result in transferring some saturation to the bulk water pool A causing a decrease in the intensity of pool A.

protons (pool B, Figure 1) involved in chemical exchange with the bulk water signal (pool A). In the presence of an external magnetic field, the population of nuclear spins orientated in the same direction as the magnetic field is slightly higher than those with opposite orientation, as determined by the Boltzmann distribution. Application of a radio frequency (RF) pulse at the resonance frequency of the exchangeable protons increases the population of nuclei aligned against the magnetic field, the two populations becoming equal if enough energy is provided. The nuclear spin population of pool B can return to the equilibrium situation through spin-lattice relaxation (T_{1B}). However, if the exchange rate characterizing the movement of protons from pool B to pool A (k_B) is faster than the relaxation of pool B (R_1^B), some magnetization can be transferred from pool B to pool A. If the relaxation rate of pool A (R_1^A) is long enough, the acquisition of an NMR spectrum (using a $\pi/2$ pulse on pool A) will result in a reduced intensity of the signal of pool A (bulk water) due to the exchange with pool B, generating image contrast. A remarkable difference with T_1 agents is that CEST probes allow switching contrast on and off at will, by applying an RF saturation pulse at the frequency of protons in exchange with bulk water. Additionally, CEST probes may also contain two or more pools of exchangeable protons with different resonance frequencies, so that ratiometric analyses are possible [10]. This provides a straightforward strategy to develop responsive agents allowing quantification of the CEST effect [18].

The pool of exchangeable protons in CEST agents must be in the slow-to-intermediate exchange regime with bulk water, that is, $k_B \leq \Delta\omega$, where $\Delta\omega$ is the frequency difference between the two pools. It was soon realized that the use of paramagnetic complexes can generate larger chemical shift differences between the two pools, so that the slow-to-exchange condition can be achieved with faster k_B values [19–21]. Additionally, enlarging the frequency separation between the two pools allows using higher saturation power without direct saturation of the bulk water signal. This enhances the CEST effect and can potentially increase detection sensitivity, one of the main limitations of MRI [22, 23]. Last but not least, a large paramagnetic shift is expected to minimize the problems associated to semi-solid macromolecular MT, a non-selective effect observed in tissues attributed to the saturation of exchangeable protons at the surface of macromolecules, as well as water molecules trapped in the macromolecular matrix. This results in an intrinsic background saturation transfer signal of this so-called semi-solid MT (ssMT) spanning a large frequency range (~100 kHz), which makes the detection of the CEST effect more difficult, particularly for low $\Delta\omega$ values [24, 25].

Some lanthanide ions induce large chemical shifts in the NMR signals of ligand nuclei in the vicinity of the paramagnetic center, without causing extreme line-broadening [26, 27]. Thus, lanthanide complexes were the first class of paramagnetic complexes considered as potential MRI paramagnetic CEST agents (paraCEST). Since then, a variety of other paramagnetic metal complexes were investigated in this context, including those based on the transition metal ions Fe^{2+}, Co^{2+}, Ni^{2+}, and Cu^{2+} [28, 29].

The CEST effect is often measured by recording the so-called Z-spectrum or CEST spectrum, defined according to Equation (1)

$$\text{Z-spectrum} = \frac{M_z^A\left(\Delta\omega_A\right)}{M_0^A} \tag{1}$$

Here, $M_z^A\left(\Delta\omega_A\right)$ represents the magnetization of pool A (bulk water) upon saturation at a frequency $\Delta\omega_A = \omega_A - \omega$, which is expressed in Hz, or most commonly in ppm. Thus, a Z-spectrum is a plot of the magnetization of bulk water (M_z^A or simply M_z) normalized by the signal without saturation (M_0^A or simply M_0) as a function of the saturation frequency (Figure 2 left). Z-spectra are generally plotted by assigning a chemical shift of $\delta = 0$ ppm to the bulk water signal. They are therefore dominated by a central peak at $\delta = 0$ ppm that reaches a value of $M_z/M_0 = 0$, as a result of the full saturation of the bulk water signal upon direct irradiation. CEST effects due to exchangeable protons are characterized by peaks with $0 < M_z/M_0 < 1$ at the resonance frequency of the exchangeable protons of the CEST agent. Saturation at frequencies sufficiently away from those of bulk water or exchangeable protons does not affect the intensity of the bulk water signal, and thus $M_z/M_0 = 1$, providing that direct saturation of bulk water is negligible. Z-spectra are therefore expressed in terms of a reduction of the bulk water signal (i.e., a stronger effect corresponds to lower M_z/M_0 values).

Alternatively, the CEST effect can be analyzed using the magnetization transfer asymmetry spectra (MTR$_{asym}$ spectra, Figure 2 right), which plots the difference in magnetization of bulk water upon saturation at a frequency $\Delta\omega_A$ and its mirror frequency with respect to bulk water $-\Delta\omega_A$, a relation defined by Equation (2):

$$\text{MTR}_{asym} = \frac{M_z^A\left(-\Delta\omega_A\right) - M_z^A\left(+\Delta\omega_A\right)}{M_0^A} \tag{2}$$
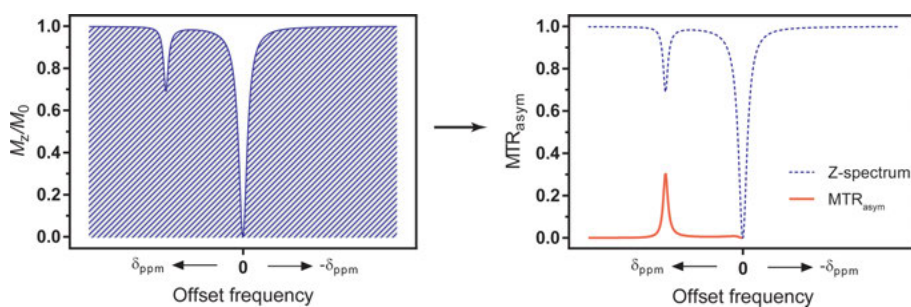
Figure 2. Schematic presentations of the CEST effect through the Z-spectrum and MTR effect. **Left**: Z-spectrum showing the decrease in magnetization due to saturation pulses at the frequency of exchangeable protons (small peak) or bulk water (large peak); the shaded area indicates magnetization levels. **Right**: the plot of MTR$_{asym}$ (red line), obtained by subtracting the signals at $-\Delta\omega$ from $\Delta\omega$ frequencies from the Z-spectrum (dashed line).

The application of an RF pulse at the resonance frequency of pool B ($+\Delta\omega_A$) decreases the magnetization of bulk water protons (pool A) thanks to chemical exchange. However, application of an RF pulse at $-\Delta\omega_A$ does not provoke attenuation of the bulk water signal, as there are no exchangeable protons resonating at this frequency. As a result, MTR$_{asym}$ spectra reflect only the effects caused by the contrast agent, removing other effects such as direct saturation of the bulk water signal.

In this chapter an overview of the progress in the design of metal complexes as paraCEST agents is presented. The first part reviews the progress made in the use of paramagnetic lanthanide complexes as paraCEST agents, including the design of responsive probes. A separate section is devoted to transition metal-based paraCEST agents, with emphasis in the development of redox-responsive systems. Finally, the chapter is concluded by providing the authors' perspective on the future directions of this exciting interdisciplinary field that encompasses NMR spectroscopy and imaging, coordination chemistry and *in vitro* and *in vivo* applications.

2. LANTHANIDE COMPLEXES AS ParaCEST AGENTS

2.1. Lanthanide-Induced Shifts and Relaxation Rate Enhancements

Some paramagnetic metal ions induce relatively large paramagnetic shifts in ^{1}H nuclei situated in their vicinity, without causing extensive line broadening due to fast relaxation. To this end, different paramagnetic lanthanide ions (Ln^{3+}) were introduced in the early times of NMR as shift reagents, as the lanthanide shifts induced by these ions aided spectral assignment [30]. The paramagnetic shifts induced by the Ln^{3+} ions are generally dominated by the pseudocontact mechanism, which is the result of a dipolar interaction between the electron and nuclear spins, as expressed by Equations (3)–(5) [31]:

$$\Delta_{pc} = \frac{10^6}{12\pi r^3}\left[\Delta\chi_{ax}\left(3\cos^2\theta - 1\right) + \frac{3}{2}\Delta\chi_{rh}\left(\sin^2\theta\cos 2\varphi\right)\right] \tag{3}$$

$$\Delta\chi_{ax} = \chi_{zz} - \frac{\chi_{xx} + \chi_{yy}}{2} \tag{4}$$

$$\chi_{rh} = \chi_{xx} - \chi_{yy} \tag{5}$$

Here, r, θ, and φ define the spherical coordinates of the observed nuclei with the paramagnetic metal ion placed at the origin, and $\Delta\chi_{ax}$ and $\Delta\chi_{rh}$ are the axial and the rhombic parts of the magnetic susceptibility tensor. In the specific case of systems with axial symmetry ($C_n \geq 3$), the rhombic contribution is zero. Bleaney showed that the pseudocontact shifts in Ln^{3+} complexes are proportional to the so-called Bleaney factors, which have the values shown in Table 1 [32]. In the case
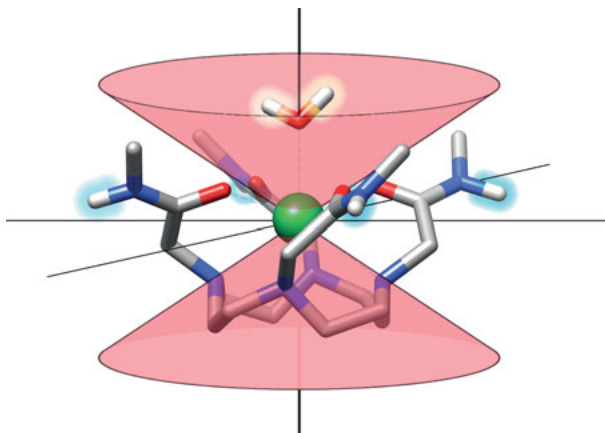
Figure 3. Representation of the double cone surface generated by the pseudocontact shift in a Ln^{3+} DOTA-tetraamide complex. The surface of the cone signals is characterized by a θ value of 54.7° that results in zero pseudocontact shift. Nuclei placed inside and outside the double cone are shifted in opposite directions.

of Gd^{3+}, the symmetrical $^8S_{7/2}$ electronic ground state is isotropic, and thus the pseudocontact shift is zero under first order conditions. Recent results evidenced limitations of Bleaney's theory to predict quantitatively the paramagnetic shifts induced by Ln^{3+} ions, but still qualitative trends are predicted correctly in most cases [33, 34]. For axially symmetric systems, Equation (3) generates a double cone surface characterized by an angle θ = 54.7° for which the pseudocontact shift is zero. As a result, nuclei lying inside the double cone surface experience pseudocontact shifts of opposite sign with respect to those placed outside.

The maximum pseudocontact shift is expected for nuclei situated along the principal magnetic axis (θ = 0°). This effect can be demonstrated by representing the surface of the double cone generated by the magic angle of θ = 54.7° on the structure of a EuDOTA-tetraamide complex, a class of paraCEST agents that has been extensively investigated in the literature (see Section 3.2) (Figure 3). The water molecule coordinated to the metal ion lies on the principal magnetic axis of the complex, which coincides with the C_4 symmetry axis of the molecule. As a result, the proton nuclei of coordinated water molecules experience a rather large paramagnetic shift, being observed at ca. 50 ppm. Amide protons lie outside the double cone and are placed rather close to its surface, which results in small negative paramagnetic shifts (~3 ppm).

Proton nuclei close to the paramagnetic center in terms of number of bonds can also experience significant contact shifts, which are related to the spin density at the observed nuclei originated by the paramagnetic metal ion through spin delocalization and spin polarization effects [35, 36]. This is expressed with Equation (6),

$$\Delta_{con} = \langle S_z \rangle \, \frac{\mu_B}{3kT\gamma_I} \, \frac{A}{\hbar} \, 10^6 \qquad (6)$$

where μ_B and k are the Bohr magneton and the Boltzmann constant, respectively, γ_I is the magnetogyric ratio of the nucleus and $A/\hbar$ is the scalar hyperfine coupling constant expressed in rad s^{-1}. The reduced values of the average spin polarization $\langle S_z \rangle$ have been calculated for the different Ln^{3+} ions, and are negative for Ce^{3+}, Pr^{3+}, and Nd^{3+}, and positive for the remaining Ln^{3+} ions (Table 1) [37].

Table 1. Bleaney constants (C_j), reduced values of the average spin polarization ($\langle S_z \rangle$), effective magnetic moments (μ_{eff}), electron spin relaxation times (T_{1e}) and estimated Ln···H distances for optimal paraCEST properties.

	C_j[a]	$\langle S_z \rangle$[b]	(μ_{eff}) (BM)	T_{1e} ($\times 10^{-13}$ s)[c]	Ln···H (Å)
Ce	−6.3	−0.974	2.56	0.9	2.7−4.5
Pr	−11	−2.956	3.62	0.57	3.2−5.4
Nd	−4.2	−4.452	3.68	1.15	3.3−4.0
Sm	−0.7	0.224	1.55−1.65	0.45	1.9−2.2
Eu	4.0	7.569	3.40−3.51	0.09	3.0−3.9
Tb	−86	31.853	9.7	2.03	6.1−7.6
Dy	−100	28.565	10.6	2.99	6.5−8.1
Ho	−39	22.642	10.6	1.94	6.4−8.1
Er	33	15.382	9.6	2.38	6.0−7.6
Tm	53	8.21	7.6	3.69	5.3−6.7
Yb	22	2.589	4.5	1.37	3.7−4.7

[a] Data taken from [32].
[b] Data taken from [37].
[c] Data from reference [42].

The paramagnetism of the Ln^{3+} ions also enhances the longitudinal (R_1) and transverse (R_2) relaxation rates of proton nuclei in their vicinity. The relaxation rates induced by Ln^{3+} ions other than Gd^{3+} are dominated by the dipolar ($R_{i,dip}$) and the Curie susceptibility mechanisms ($R_{i,Curie}$), as expressed in Equations (7)–(10) [38−41]:

$$R_{1,dip} = \frac{2}{15} \left(\frac{\mu_0}{4\pi} \right)^2 \frac{\gamma_I^2 \mu_{eff}^2}{r^6} \left(\frac{3\tau_c}{1 + \omega_I^2 \tau_c^2} + \frac{7\tau_c}{1 + \omega_S^2 \tau_c^2} \right) \tag{7}$$

$$R_{2,dip} = \frac{1}{15} \left(\frac{\mu_0}{4\pi} \right)^2 \frac{\gamma_I^2 \mu_{eff}^2}{r^6} \left(4\tau_c + \frac{3\tau_c}{1 + \omega_I^2 \tau_c^2} + \frac{13\tau_c}{1 + \omega_S^2 \tau_c^2} \right) \tag{8}$$

$$R_{1,Curie} = \frac{6}{5} \left(\frac{\mu_0}{4\pi} \right)^2 \frac{\omega_I^2 \mu_{eff}^4}{(3kT)^2 r^6} \left(\frac{\tau_R}{1 + \omega_I^2 \tau_R^2} \right) \tag{9}$$

$$R_{2,Curie} = \frac{1}{5} \left(\frac{\mu_0}{4\pi} \right)^2 \frac{\omega_I^2 \mu_{eff}^4}{(3kT)^2 r^6} \left(4\tau_R + \frac{3\tau_R}{1 + \omega_I^2 \tau_R^2} \right) \tag{10}$$

In these equations τ_C is the correlation time given by $\tau_C^{-1} = \tau_R^{-1} + \tau_M^{-1} + T_{ie}^{-1}$ ($i = 1, 2$), τ_M is the residence time of the nucleus in the first coordination sphere of the Ln^{3+} ion ($\tau_M = 1/k_B$), τ_R is the rotational correlation time, T_{ie} are the longitudinal ($i = 1$) or transverse ($i = 2$) relaxation times of the electron spin, r is the distance between the observed nucleus and the paramagnetic ion, while other symbols have been previously defined (see above). T_{1e} of Ln^{3+} ions other than Gd^{3+} take values of a few ps or less, while τ_R for small complexes are > 50 ps. Thus, in the absence of exchange $\tau_C^{-1} \sim T_{ie}^{-1}$ [42]. The Curie mechanism scales with the square of the applied magnetic field (ω_I^2), and may dominate paramagnetic relaxation at high fields, particularly for Ln^{3+} ions with high effective magnetic moments (μ_{eff}) like Tb^{3+}, Dy^{3+}, Ho^{3+}, Er^{3+}, and Tm^{3+} (Table 1). The relaxation rates induced by paramagnetic Ln^{3+} ions present a $1/r^6$ dependence with the distance from the observed nuclei to the paramagnetic center, while pseudocontact shifts present a $1/r^3$ dependence. Thus, relaxation rate enhancements drop much quickly on increasing the distance than pseudocontact shifts.

The design of a Ln^{3+}-based contrast agent requires attaining an optimal balance to allow a large paramagnetic shift without increasing too much relaxation. Thus, a critical parameter for the design of a paraCEST agent is the distance between the pool of exchangeable protons and the lanthanide ion. A simulation of Δ_{pc} for the different Ln^{3+} ions assuming axial symmetry ($\Delta\chi_{rh} = 0$ in Equation (3)) and longitudinal relaxation rates (Equations (7) and (9)) provides some hints on the range of Ln···H distances that should result in optimal paraCEST properties for each Ln^{3+} ion (Figure 4). The optimal Ln···H distances for inducing large chemical shift values can be estimated by calculating the $\Delta\chi_{ax}$ value for
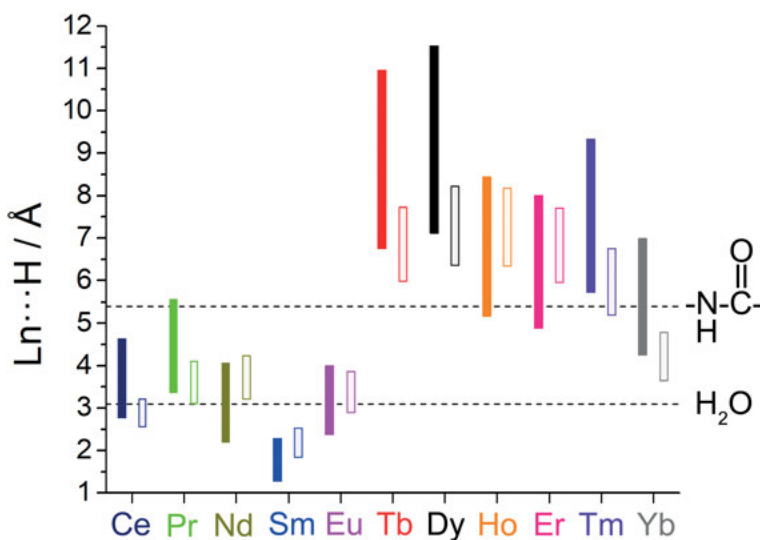
Figure 4. Optimal distances between the metal ion and labile protons in paraCEST agents for the different Ln^{3+} ions. The solid bars indicate the optimal ranges to generate pseudocontact shifts, and the open bars the lower limit to avoid excessive relaxation.

an Eu^{3+} tetraamide complex, considering a paramagnetic shift of 50 ppm, with $\theta = 0°$ and $r = 3.1$ Å [43]. The $\Delta\chi_{ax}$ values for other Ln^{3+} ions were then obtained by assuming that they are proportional to the Bleaney factors (Table 1).

Furthermore, the range of appropriate Ln···H distances was considered to induce paramagnetic shifts in the range 25–100 ppm. Obviously the pseudocontact shift depends not only on the distance, but also on the position of the observed nucleus with respect to the magnetic axes, and thus the obtained distance ranges should be taken only as rough estimates (see Figure 4). Concerning relaxation, a T_1 value of 25 ms for the exchangeable protons was taken in this simulation as a lower limit value to allow comparing the relaxation ability of the different Ln^{3+} ions across the series. The corresponding Ln···H distances were calculated with the T_{ie} and μ_{eff} values listed in Table 1, and a τ_R value of 100 ps, which is typical of low molecular weight complexes [44]. The simulation shows that Sm^{3+} fails to provide significant paramagnetic shifts at reasonable Ln···H distances. Indeed, the Ln···H distance of 3.1 Å characteristic of protons of coordinated water molecules can be considered as the lower limit that can be attained in a paraCEST agent, with the protons being placed two bonds away from the metal ion. Interestingly, this distance lies above the lower limit value estimated to avoid excessive relaxation for Ce^{3+}, Pr^{3+}, and Eu^{3+}, while generating large pseudocontact shifts. Thus, it is not surprising that the coordinated water molecule in Eu^{3+} and Pr^{3+} complexes was widely exploited to generate a paraCEST affect. Among the first half of the lanthanide series, these three Ln^{3+} ions appear to be the best suited for paraCEST applications using exchangeable protons two bonds away from the metal center. However, Nd^{3+} is more efficient in inducing relaxation than chemical shifts, as reflected by the fact that the optimal Ln···H range to generate large chemical shifts is below the range for optimal relaxation. A similar situation is observed for Ho^{3+} and Er^{3+}, which therefore are not well suited to design paraCEST effects. Metal ions such as Yb^{3+} and particularly Tm^{3+} appear to be very adequate to generate a paraCEST effect using amide protons, which lie ~5.4 Å away from the paramagnetic metal ion [45]. Finally, Tb^{3+} and Dy^{3+} should be the paramagnetic ions of choice if the exchangeable protons are placed at distances > 6.1 and 6.5 Å, respectively.

2.2. Cyclen-Based Complexes

Lanthanide complexes with cyclen-based ligands functionalized with four pendant arms have been the subject of intense research efforts during the last two decades, mainly due to the successful application of some of these Gd^{3+} complexes as T_1 MRI contrast agents (Chapter 2) and complexes with other Ln^{3+} ions as paraCEST agents. Ever since the initial reports, it became obvious that the stereochemistry of these complexes is essential for defining their physicochemical features and hence, their performance as contrast agents. Therefore, the stereochemistry of the cyclen-based complexes has been studied in detail and it is well understood [46−48].

$SSSS\text{-}\Delta(\lambda\lambda\lambda\lambda)$, SAP $SSSS\text{-}\Lambda(\lambda\lambda\lambda\lambda)$, TSAP

$SSSS\text{-}\Delta(\delta\delta\delta\delta)$, TSAP $SSSS\text{-}\Lambda(\delta\delta\delta\delta)$, SAP
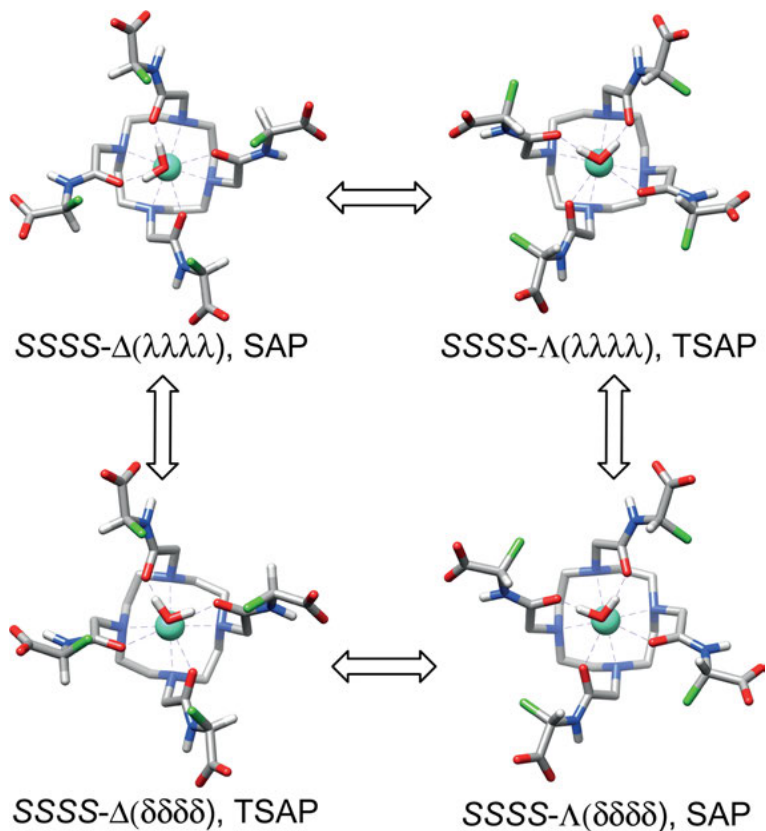
Figure 5. Representation of the four diastereoisomers with square-antiprismatic (SAP) and twisted square-antiprismatic (TSAP) coordination environments that are formed upon Ln^{3+} complexation with a chiral ligand. The methyl groups at the chiral centers of the ligand are highlighted in green.

These compounds are generally present in solution as two diasteroisomeric pairs of enantiomers with either square-antiprismatic (SAP) or twisted square-antiprismatic (TSAP) geometries. However, these four stereoisomers become diastereoisomers if the ligand is chiral, as illustrated for Ln^{3+} complexes that contain chiral centers in the amide side chains (Figure 5) [49]. The obtained isomers differ in the orientation of the four pendant arms of the ligand (Δ or Λ) and the conformation of the macrocyclic fragment, which adopts either a ($\delta\delta\delta\delta$) or a ($\lambda\lambda\lambda\lambda$) conformation [50, 51].

To get further insights in the geometry and behavior of these isomer species, the ^{1}H NMR signals of the coordinated water molecule in **Eu(1)** (Figure 6) were detected in CD_3CN solution at room temperature [52]. This signal in the SAP isomer was found at 84.1 ppm, while that of the TSAP isomer was observed at $\delta = 19.0$ ppm. The larger paramagnetic shift observed for the SAP isomer is related to a larger magnetic anisotropy and thus a larger pseudocontact shift
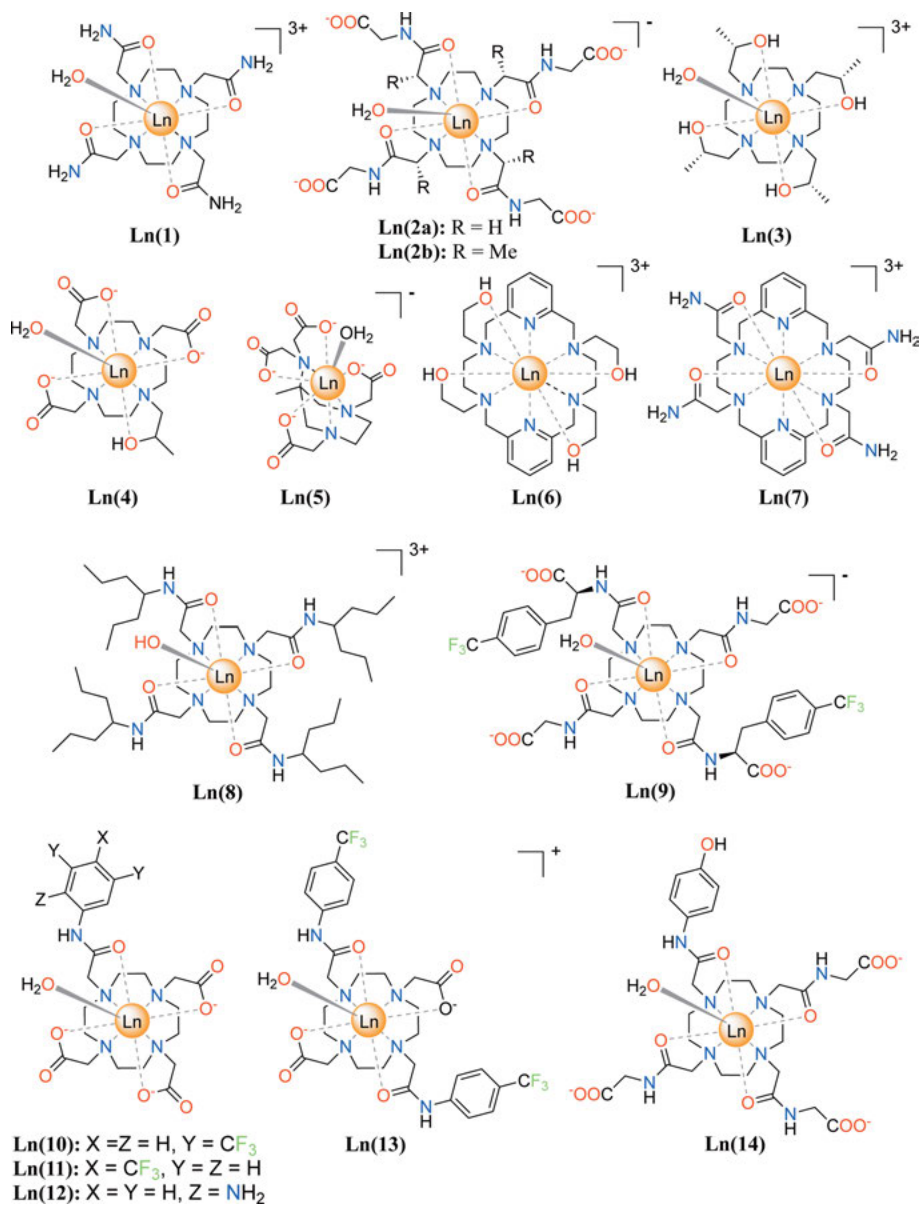
Figure 6. Lanthanide-based paraCEST agents discussed in the text.

(Equation 3) [53, 54]. This allowed determining the water exchange rates of the coordinated water molecule individually for the two isomers, which revealed that water exchange in the TSAP isomer was ~50 times faster than in the SAP isomers [55]. Subsequently, it was shown that the ¹H signal of the coordinated water molecule in the SAP isomers of different DOTA-tetraamide complexes can be

observed in pure water at room temperature at about 50 ppm, and that this signal could be used to generate a CEST effect [56]. This discovery triggered intense research in Ln^{3+} DOTA-tetraamide complexes as potential paraCEST candidates for MRI applications. However, tri-cationic DOTA-tetraamide complexes were found to be toxic at the high doses that are required for MRI applications; this particular issue can be solved by incorporating negatively charged groups in the ligand structure [57].

The amide protons in Eu^{3+} complexes with DOTA-tetraamide ligands experience relatively small paramagnetic shifts, as they lay closer to the double cone surface that signals a zero pseudocontact shift (θ ~86°) and present rather large $Eu\cdots H$ distances (Figures 3 and 4). As a result, the signals of amide protons are hidden by the huge bulk water signal, and they are not observed in CEST spectra. The pseudocontact shifts induced by Yb^{3+} are expected to be ~5 times larger than those of Eu^{3+}, considering the ratio of the corresponding Bleaney constants (Table 1). Indeed, the ^1H NMR signals of the **Yb(1)** complex are shifted well away from the bulk water signal (~15 ppm), and in opposite direction with respect to the protons of the coordinated water molecule [58]. These amide protons can also act as a source of MT to bulk water, generating contrast through the CEST mechanism. Furthermore, a mixture of **Eu(2)** and **Yb(2)** was shown to present CEST signals due to both the water molecule coordinated to Eu^{3+} and the amide protons of the Yb^{3+} derivative. The ratio of the two signals can be used to remove the concentration dependence, and can be correlated to the pH of the solution [21].

Besides the coordinated water molecule or amide protons in Ln^{3+} DOTA-tetraamide complexes, other groups containing exchangeable protons such as amines were investigated in the context of paraCEST agents [59]. Perhaps the most widely explored alternatives are hydroxyl protons, which have been incorporated into a variety of cyclen derivatives such as **Ln(3)** and related derivatives [60–63]. The hydroxyl protons of these complexes showed relatively small shifts with respect to the bulk water signal, as a result of the position of these nuclei close to the surface of the double cone that defines a zero pseudocontact shift. Furthermore, the optimal CEST effect is achieved in most cases at rather low pH values, presumably due to a fast proton exchange rate at neutral pH that becomes slower under more acidic conditions. Other complexes containing hydroxyl exchangeable protons that were investigated as potential paraCEST candidates include **Eu(4)** and **Yb(4)**, the Eu^{3+} and Yb^{3+} analogues of the commercially available contrast agent GdHP-DO3A [64, 65].

2.3. Other Complexes

An additional challenge that is faced when developing paraCEST agents (besides the desire to designing a potent agent with affirmative CEST properties) is to achieve a high kinetic inertness of the complexes, i.e., to avoid the release of the toxic free metal ion. Lanthanide complexes with DOTA-tetraamide ligands are extremely inert, even more than the commercially available T_1 agent $GdDOTA^-$

[66]. However, some cyclen-based systems with structures similar to DOTA were found to be labile, and thus a macrocyclic DOTA-like structure does not necessarily ensure a high kinetic inertness [67].

A few kinetically inert Ln^{3+}-based paraCEST agents alternative to DOTA-tetraamide derivatives have been proposed so far. In a recent work, it has been shown that the $[Yb(AAZTA)]^-$ (**Yb(5)**) complex (AAZTA = 1,4-bis(carboxymethyl)-6-[bis(carboxymethyl)]amino-6-methylperhydro-1,4-diazepine) provides a sizeable CEST effect thanks to the presence of a water molecule coordinated to the metal ion observed at 83 ppm (Figure 6) [68]. The number of coordinated water molecules in $LnAAZTA^-$ complexes changes from $q = 2$ for Gd^{3+} to $q = 1$ by the end of the lanthanide series, as the overall water exchange rates decrease from 1.1×10^6 for Gd^{3+} to 6.7×10^3 s^{-1} for Yb^{3+} (at 278 K) [69, 70]. This unexpected trend paves the way for the design of paraCEST agents based on the AAZTA framework, as the $LnAAZTA^-$ complexes are considerably stable and inert with respect to complex dissociation [71].

Another family of Eu^{3+} paraCEST agents that were proved to be extremely inert is based on an 18-membered macrocycle containing two pyridyl head units, which was functionalized with hydroxyethyl and acetamide pendant arms. Indeed, the **Eu(6)** and **Eu(7)** complexes do not experience dissociation under very harsh conditions such as HCl 1 M, or in the presence of competing anions and cations. The four magnetically equivalent hydroxide protons in **Eu(6)** are observed at 21.6 ppm with respect to bulk water at 25 °C, and provide a rather strong CEST effect. The corresponding Pr^{3+} and Yb^{3+} complexes also give a CEST effect upon saturation of the hydroxyl protons at 25.2 and 42.0 ppm, respectively [72]. The eight amide protons of **Eu(7)** give rise to two signals at 15.0 and 9.5 ppm that present different exchange rates, which allows pH mapping *in vitro* using ratiometric analysis [73]. Besides providing a set of four magnetically equivalent protons, these complexes have the advantage that they lack coordinated water molecules that could potentially contribute to shorten T_1 of bulk water protons.

2.4.   Chemical Shift and Proton Exchange Optimization

A large amount of research has been carried out over the last 15 years to optimize several properties of Ln^{3+}-based paraCEST agents, particularly to tune proton exchange to maximize the effect and shift the pool of exchangeable protons far from the bulk water resonance. The chemical shift of both the coordinated water molecule and amide protons in LnDOTA-tetraamide complexes can be modulated by changing the nature of the Ln^{3+} ion (Table 2). The chemical shifts of both pools of protons determined from CEST spectra follow rather well the trend predicted by Bleaney's theory. A comparison of the chemical shifts observed for **Ln(2a)** and Ln(**2b**) complexes suggests that modification in the ligand scaffold has little influence in the shifts of amide protons, while those of water molecules present larger variations [45].

The chemical shift of amide protons in YbDOTA-monoamide complexes (–10 ppm) is somewhat smaller than in **Yb(2a)** (–16 ppm), which suggests that

Table 2. Chemical shifts of the coordinated water molecule and amide protons in **Ln(2a)** and **Ln(2b)** complexes obtained from CEST spectra.[a]

	Water		Amide	
	Ln(2a)	**Ln(2b)**	**Ln(2a)**	**Ln(2b)**
Pr	−60	−85	13	15
Nd	−32	−50	11	10
Sm	−4	−13		6
Eu	50	66	−4	−4
Tb	−600	−752	62	
Dy	−720		77	
Ho	−360		39	
Er	200		−22	
Tm	500		−51	−64
Yb	200		−16	−20

[a] Data taken from [45].

changes in the symmetry and/or bond distances of the metal coordination environment affect significantly the crystal field produced by the ligand, and thus the pseudocontact shifts [74–76]. This effect appears to be more pronounced for Tm^{3+} complexes, for which chemical shifts of amide protons in the range –20 to –100 ppm have been reported [75–79]. The different chemical shifts are in some cases related to changes in the point group of the molecule (i.e., mono- versus bis-amide DOTA derivatives) or variations of the substituents of the amide groups. These subtle modifications appear to have a profound effect in the magnetic anisotropy of the complexes, and thus in their pseudocontact shifts. A different point group of the molecule may result in a different orientation of the magnetic axes, and thus different pseudocontact shifts. Recent work has demonstrated that pseudocontact shifts are very sensitive to small structural changes of the metal coordination environment [79–81]. TmDOTA-tetraamide complexes inducing large paramagnetic shifts (–100 ppm) provide a CEST effect beyond the frequency of macromolecular MT [82].

Regarding the proton exchange optimization, one needs to consider the intrinsic nature of groups that provide exchangeable protons, as well as their environment. For instance, amide exchange at pH values > 5 is considered to be a base-catalyzed process, and thus the rate of proton exchange is expressed as $k_B = k_b[OH^-]$, where k_b is the rate constant characterizing the base-catalyzed process. The contribution of the non-catalyzed exchange mechanism is negligible [83]. Thus, the exchange rates of amide protons are strongly pH-dependent, which allowed the design of different paraCEST pH sensors [84]. The exchange rate of amide protons generally becomes faster on increasing their acidity. However, comparing k_B values reported for different agents is not straightforward, given the sensitivity of the process not only to pH but also to ionic strength. Still, exchange rates determined under the same conditions provide some hints on how to control amide exchange. For instance, the exchange rate determined for

Tm(10) at 25 °C and pH 7.4 (12.9 kHz) is considerably faster than that determined for **Tm(11)** under the same conditions (1.4 kHz), which was ascribed to an increasing acidity of the amide protons in the former due to the combined electron withdrawing effect of two –CF$_3$ groups. The faster amide proton exchange in **Tm(13)** (4.6 kHz) compared to **Tm(11)** (1.4 kHz) can be also related to an increased acidity of amide protons on increasing the positive charge of the complex, as a result of a stronger Tm-O$_{amide}$ interaction [76]. The amide exchange rates measured for Tm^{3+} tetraamide complexes containing benzyl (8 kHz) and *tert*-butyl (3.7 kHz) substituents on the amide groups are also in line with a higher electron withdrawing effect of the benzyl group [85].

The chemical shifts of the coordinated water molecule in Ln^{3+} DOTA-tetraamides and related complexes can be modulated to a certain extent by modifying the substituents of the amide groups. This offers the possibility of using multifrequency paraCEST agents, if related probes can be activated selectively by changing the frequency of the saturation pulse [86]. Furthermore, chemical shifts can be modulated by changing the Ln^{3+} ion and the groups that provide exchangeable protons. For instance, the CEST effect of the coordinated water molecule in a Tb^{3+} derivative was observed at –550 ppm, well beyond the MT window. The chemical shift of this resonance is strongly pH-dependent, providing a straightforward approach for pH-sensing purposes [87]. The water exchange rate of the coordinated water molecule is extremely sensitive to different factors, as described in detail in several review articles [88–90]. These factors include: (i) the nature of the Ln^{3+} ion, as water exchange can change dramatically across the series [91]; (ii) the isomer present in solution, as TSAP isomers show faster water exchange rates than SAP isomers (see above) [55]; (iii) the presence of hydrophobic side chains appended to the amide groups, which slow down water exchange [92, 93]; (iv) electronic effects originated by remote substituents at the amide groups [94]; (v) The configuration of chiral centers in the amide side chains [49, 95]; (vi) the position of the coordinated water molecule in the metal coordination environment (labile capping bond effect) [96, 97].

2.5. Responsive Agents

ParaCEST agents offer advantageous properties for the design of probes with response to different biomarkers, an issue of great importance to understand different biochemical processes and to obtain valuable diagnostic information relying on physicochemical rather than anatomical properties [98, 99]. For instance, pH is an important biomarker of different diseases including inflammation and cancer, and thus a number of pH-sensitive paraCEST agents have been reported and a few were tested successfully *in vivo* [59, 74]. The practical determination of pH *in vivo* often requires specific approaches in the signal acquisition and detection, as the CEST response depends not only on pH but also on the concentration of the agent. The most common way of neglecting the agent concentration as essential parameter is engaging the ratiometric approach, i.e., the strategy employing the measurement of two signals were at least one of them, or their

ratio, depends solely on the behavior of the monitored target (e.g., pH) [10]. In the case of **Ln(2a)** complexes (Ln = Pr^{3+}, Nd^{3+} or Eu^{3+}), this was successfully achieved by using the ratio of the CEST effects provided by amide protons and the coordinated water molecule, as the latter does not change with pH [84]. Alternatively, the two pools of protons may arise from amide and amine groups, whose CEST effects are both pH-dependent. Amine proton exchange in a Yb^{3+} DO3A complex containing an *N*-(2-aminophenyl)acetamide pendant arm (**Yb(12)**, Figure 6) is influenced by contributions of both acid and base-catalyzed mechanisms close to physiological pH, and presents a different trend with respect to amide protons. The ratio of the effects provided by the two pools was used successfully to measure pH *in vivo* using a single agent [59, 74].

The ratiometric approach was also successfully applied to determine extracellular pH in murine melanoma using **Yb(4)**. This was achieved due to the presence of two CEST signals shifted 99 and 71 ppm from bulk water, arising from two isomers of this complex [100, 101]. In the case of **Eu(7)**, the two CEST signals that allow for ratiometric analysis correspond to two pools of amide protons that provide signals at 8 and 14 ppm at 37 °C [73]. An alternative approach to generate a pH dependency is to incorporate a group that deprotonates close to physiological pH, causing a shift of the CEST peak. An example of this strategy is **Eu(14)**, which contains a phenol group that induces a shift of ~5 ppm in the CEST peak of water upon deprotonation. This allowed ratiometric pH mapping *in vitro* and *in vivo* [102, 103]. In a completely different approach, extracellular pH was determined *in vivo* measuring the linewidth of the amide proton CEST signal in a TmDOTA-tetraamide complex [77].

ParaCEST agents were also designed to respond to other important biomarkers, for instance endogenous cations or anions, enzyme activity or the redox environment. The CEST agents designed for cation recognition generally contain a CEST-responsive unit linked to a cation recognition moiety, for instance the iminodiacetate, thioether or dipicolylamine groups of **Ln(15)** (Ln = Eu, Yb), **Tm(16)**, and **Eu(17)**, which were designed for sensing Ca^{2+}, Zn^{2+} and Cu^+, Cu^{2+}, and Zn^{2+}, respectively (Figure 7) [104–106]. In all cases cation addition diminished or eliminated the CEST effect, which for **Ln(15)** and **Tm(16)** was attributed to a reduction of the amide proton exchange rates upon cation binding. For **Eu(17)**, the CEST effect is provided by the coordinated water molecule, and Zn^{2+} addition likely accelerates water exchange. Some attempts to obtain Ca^{2+}-sensitive paraCEST probes, based on design that provided successful T_1 agents, failed to provide any response due to strict prerequisites for generation of CEST signals that obviously do not overlap with the analogous requirements valid for Gd-based complexes [107].

Several paraCEST agents that respond to the redox environment have been developed. For instance **Yb(12)** can be oxidized in the presence of nitric oxide (NO) and O_2 to give a binuclear structure with a triazene bridge, causing the disappearance of the CEST effect of both amine and amide protons [108]. Complex **Eu(18)** was designed as a potentially biocompatible redox-active CEST agent with response to the nicotinamide adenine dinucleotide (NAD^+/NADH) coenzyme system. The quinolinium units are reduced by addition of β-NADH,
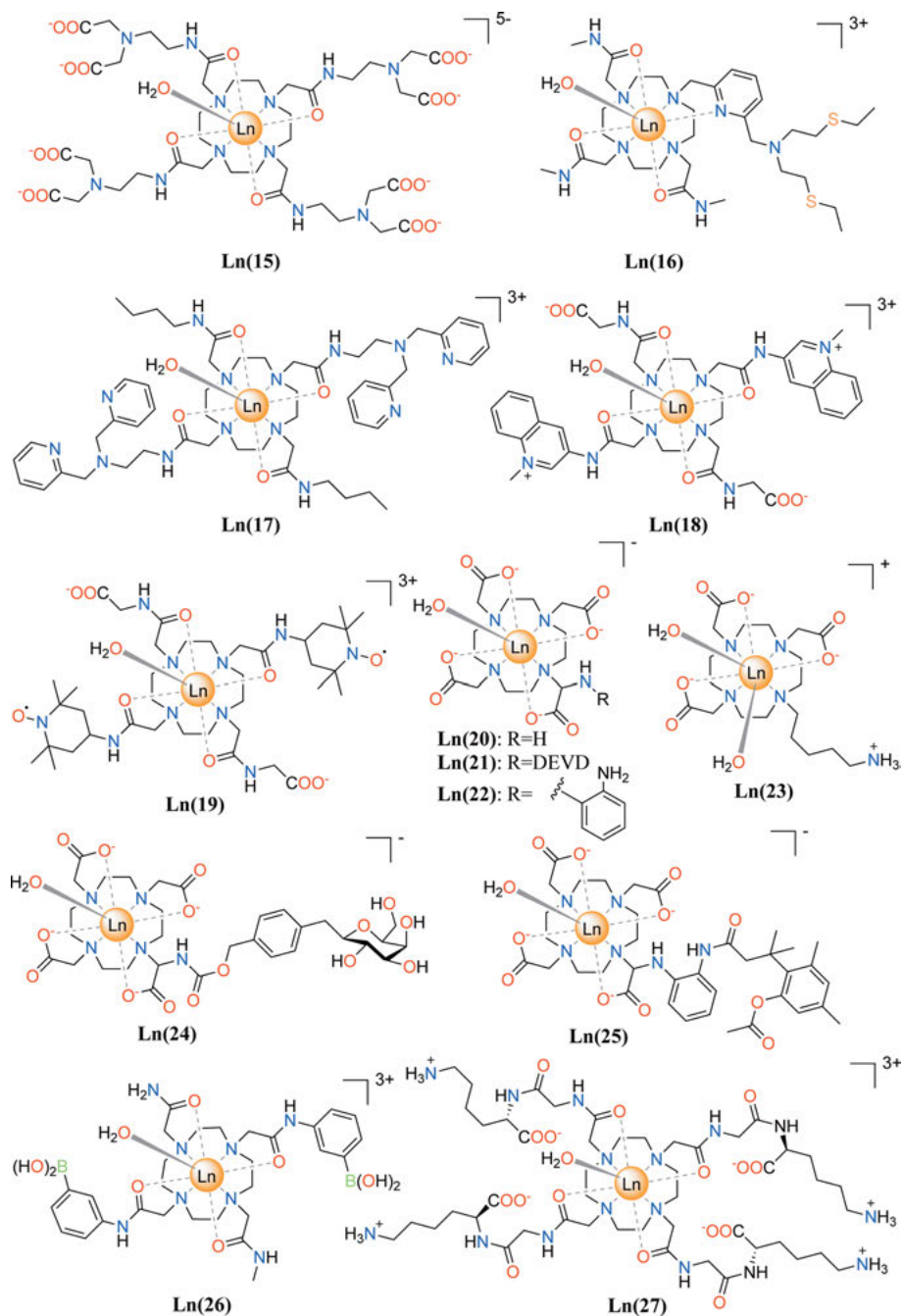
Figure 7. Responsive lanthanide-based paraCEST agents discussed in the text.

which triggers an "on" response of the CEST effect due to the coordinated water molecule *in vitro* [109]. A few examples of redox-responsive probes were tested successfully *in vivo*. This includes **Eu(19)**, which incorporates two nitroxide moieties into a DOTA-tetraamide complex. The nitroxide radicals act as rather efficient relaxation agents, so the T_1 of bulk water is reduced, resulting in a very weak CEST effect due to the coordinated water molecule. Reduction of the nitroxide groups to hydroxylamine by addition of ascorbic acid produces a diamagnetic ligand that yields a long T_1 of bulk water, activating the CEST effect. *In vivo* experiments demonstrated that **Eu(19)** can be activated by addition of L-ascorbic acid in the bladder [110]. More recently, it was shown that **Eu(2a)** behaves as an efficient T_1 contrast agent *in vivo* when reduced to Eu^{2+}, though the reduction potential is quite negative (–903 mV versus Ag/AgCl). Oxidation of the complex takes place in a period of minutes, generating the Eu^{3+} complex that was detected by CEST in an animal model [111, 112].

A number of paraCEST agents responsive to enzymatic activity were designed inspired by the pioneering work of Meade on T_1 agents [113]. The design of these so-called 'smart' contrast agents is generally composed of a Ln^{3+} chelating unit and a functional group that reacts with a specific enzyme, which triggers either an "on" or an "off" paraCEST response. Thus, these agents aim at detecting catalytic enzymatic activity, rather than the enzyme itself, which is likely impossible due to the intrinsic low sensitivity of paraCEST MRI. An early example reported by Pagel et al. used the TmDO3A derivative **Ln(21)** functionalized with an amide pendant attached to a DEVD unit (Asp-Glu-Val-Asp) (Figure 7) to target caspase-3 activity. The enzyme reduced the CEST signal of the amide proton at –51 ppm *in vitro*, while a weak CEST signal at 8 ppm due to the amine protons was generated upon cleavage of the amide by caspase-3 [114, 115]. The same system functionalized with a ZGGR (Cbz-Gly-Gly-Arg) peptide was used to monitor urokinase plasminogen activator (uPA), a protease biomarker for pancreatic tumor invasion [116]. A TmDOTA-monoamide complex was also functionalized with optical reporter groups connected to a cell-penetrating peptide by an aspartyl protease cathepsin D cleavable sequence. Overexpression of this enzyme was associated with certain cancers and also Alzheimer's disease. Intracellular cell deposition of the agent occurs in the presence of overexpressed cathepsin D, as demonstrated by optical imaging and MRI using the paraCEST effect of the amide resonance [117]. The **Tm(23)** complex was used to monitor the formation of an amide bond with a glutamine residue of albumin facilitated by the catalytic activity of transglutaminase in the presence of glutathione. The amide proton was detected at –9.2 ppm by CEST experiments, suggesting that the amide unit generated by enzyme activity coordinates to the paramagnetic ion [118].

Different types of agents that have been developed contain an enzyme-specific, self-immolative group linked to a Ln^{3+} complex. Following an enzyme activity, the self-immolative group is transformed into another function that is CEST-active. For instance, this is the case of the benzyl carbamate function such as that in **Yb(24)**, which is transformed into an amine function in **Yb(20)** by β-galactosidase after cleavage of the β-D-galactopyranoside moiety. The newly

formed amine group of **Yb(20)** yields CEST effects at –16.7 and –20.5 ppm that are pH-sensitive [119,120]. The benzyl carbamate function can be also linked to a pyridine group attached to a DO3A platform, giving Ln^{3+} complexes suitable to follow enzymatic activities using luminescence, paraCEST, and T_1-MRI by selecting the appropriate metal ion [121]. A similar concept was applied for the complex **Yb(25)**, which contains a trimethyl lock spacer functionalized with an ester group. Once the ester is cleaved by an esterase, the strain generated by the methyl groups triggers lactonization to form a hydrocoumarin and compound **Yb(22)**, which displays paraCEST response thanks to both the amine and the amide groups at 12.23 and 10.3 ppm, respectively [122]. Similarly, a quinone functional group responded to the DT-diaphorase enzyme, which reduces the quinone to a hydroquinone, triggering lactonization and eventually generating **Yb(22)** [123].

Several paramagnetic Ln^{3+} complexes showed paraCEST response to biologically relevant anions. For instance **Ln(3)** complexes (Ln = Ce, Eu, Yb) give CEST response to different anions such as phosphate esters, lactate, citrate, and acetate [61, 63, 124]. The formation of outersphere complexes with these anions slows proton exchange, so that k_B is more suitable for paraCEST at neutral pH than in the absence of anion.

The coordinatively unsaturated nature of complexes such as EuDO3A, which are able to bind different anions that replace one or two of the inner sphere water molecules, were also exploited for paraCEST anion sensing. For instance, lactate binding to EuDO3A provokes a CEST signal at 47 ppm due to the hydroxyl group of lactate coordinated to the metal ion [125]. Subsequently, chiral YbDO3A-triamide derivatives were used to discriminate D- and L-lactate by using CEST [126]. A binuclear Nd^{3+} complex containing two DO3A-triamide units linked by a xylyl spacer showed weak CEST changes upon binding to certain anions and hairpin DNA [127]. However, the challenge for these anion binding agents is to design systems with selectivity for specific anions.

Finally, a very successful example of a responsive paraCEST agent is **Eu(26)**, which binds glucose with a reasonably high association constant, causing changes in the CEST effect due to the coordinated water molecule at 50 ppm. This effect could be detected *in vivo* and used to image tissue distribution of glucose in the liver in mice [128–130].

2.6.   Macromolecular Agents

Low-molecular-weight paraCEST agents possess detection limits typically one order of magnitude higher than the T_1 agents currently used in clinical practice. Thus, different strategies have been developed to tackle the sensitivity problem associated to the CEST mechanism. An obvious possibility is to incorporate molecular paraCEST agents into nanometric structures to deliver a high payload of the probe to the site of interest [131, 132]. However, this approach is not straightforward, as the immobilization of the paramagnetic agent may increase dramatically T_2 relaxation of the labile protons, which can compete with CEST

or even quench the effect completely. This has been shown recently upon loading reverse nano-assembled capsules with **Dy(1)**. The CEST effect due to the amide protons of the molecular agent at about $+80$ ppm was completely quenched in the nanostructures. This is likely related to a very strong contribution to T_2 of the Curie-spin mechanism associated to a very long $\tau_{\mathbf{R}}$ and the high μ_{eff} of Dy^{3+} (Equation (10)) [133]. In another study, the CEST effect of **Eu(2a)** was completely quenched when attached to silica nanoparticles containing amine surface groups. This effect was ascribed to an acceleration of the exchange rate of the coordinated water molecule due to excess of positively charged amino groups on the surface of the nanoparticles [134].

Among the macromolecular agents that have been developed as paraCEST agents are also PAMAM dendrimers functionalized with **Eu(2a)** or **Yb(2a)**, which can be activated upon saturation at $+55$ and $–16$ ppm, respectively. The sensitivity of these multimeric agents per paramagnetic ion was essentially the same as for the monomeric ones [135]. However, this dendrimer-based agent was found to accumulate in the tumor using a mouse model of MCF-7 mammary carcinoma [136]. PAMAM dendrimers were subsequently functionalized with **Eu(2a)** tagged with a fluorescent dye, and detected using *in vivo* CEST MRI in a glioma model [137].

Eu(2a) was also functionalized with a single acrylamide side chain and copolymerized using classical free radical chain polymerization chemistry. The random linear polymers obtained showed an improved sensitivity compared to the monomer, with a detection limit of 20 μM [138]. An Eu^{3+} DOTA-tetraamide complex was also attached covalently to monoclonal antibody as a model targeting vector for diagnostic and therapeutic applications and to human serum albumin. The exchange lifetime of the coordinated water molecule was little affected by the mode of attachment of the agent, through one of the amide groups or a benzyl thiourea group attached to the macrocyclic framework [139]. Other nanometric paraCEST agents reported in the literature include perfluorocarbon and adenovirus particles loaded with Ln^{3+} DOTA-tetraamide complexes attached to their surfaces [140–142].

A very elegant and successful alternative to macromolecular paraCEST agents is the use of liposomes loaded with paramagnetic complexes (lipoCEST). Liposomes contain a phospholipid bilayer enveloping an aqueous core that can trap different payloads. The phospholipid bilayer allows the exchange of the water molecules placed in the core and bulk water, and the permeability can be tuned by modifying liposome composition [143]. The first generation of lipoCEST agents consisted of spherical liposomes loaded with a paramagnetic chelate that shifts the resonance due to water molecules in the core of the particle away from the bulk water signal (Figure 8). Saturation of the water molecules inside the core of the liposome provides the CEST affect. The shift reagent confined in the interior of the liposome is generally a complex of the DOTA family, as the presence of the coordinated water molecule along the principal magnetic axis ensures that the $(3cos^2\text{-}1)$ term of the pseudocontact shift reaches a maximal value (Equation 3, see also Figure 3) [144]. The Ln^{3+} ions of choice are often
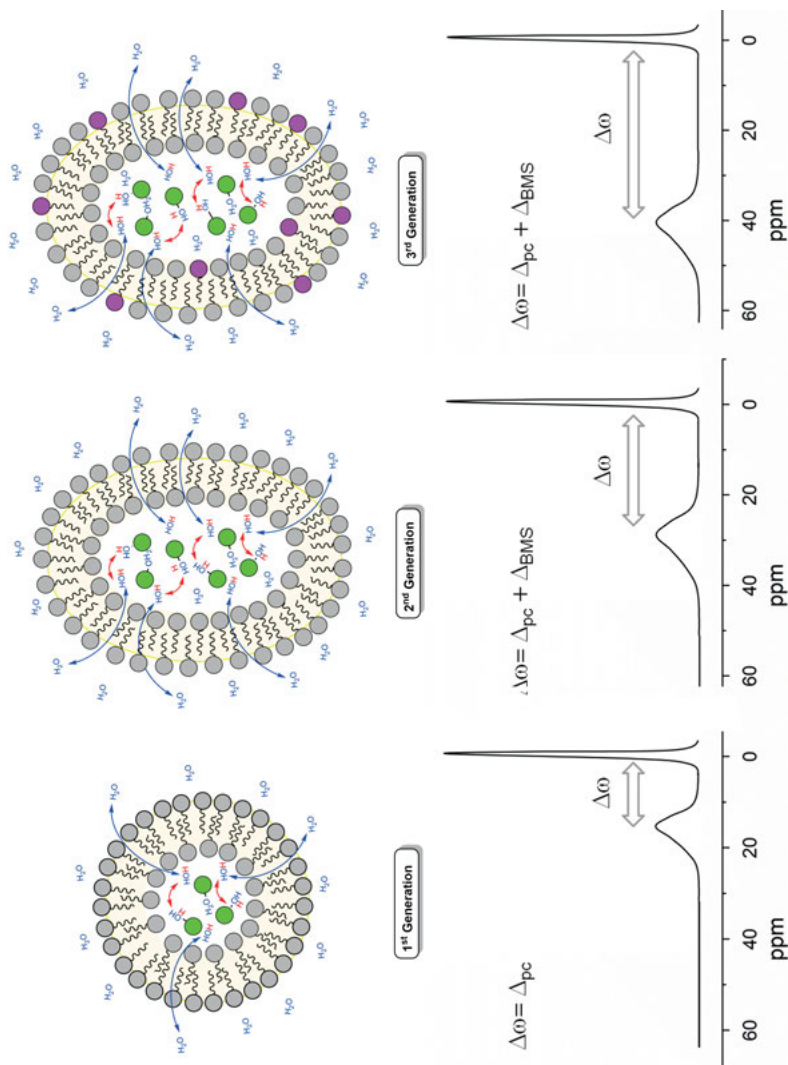
Figure 8. Schematic representation of the lipoCEST approach. A paramagnetic chelate loaded in the liposome shifts the ^{1}H NMR signal of water inside the liposome with respect to bulk water through the pseudocontact mechanism (1st generation). Non-spherical liposomes present a second contribution to the paramagnetic shift due to the BMS mechanism (2nd generation), which is enhanced when an amphiphilic complex is incorporated to the membrane (3rd generation).

Dy^{3+} and Tm^{3+}, which induce large pseudocontact shifts. A generation of improved lipoCEST agents was obtained with nonspherical osmotically shrunken nanoparticles. Incorporation of a paramagnetic amphiphilic agent in the membrane of the non-spherical liposomes causes a larger paramagnetic shift due to the bulk magnetic susceptibility (BMS) shift. This can be expressed with Equation (11), where c is the molar concentration and s is a factor that depends on the sample where the paramagnetic agent is confined ($s = 0$, 1/3 and –1/6 for a sphere, a cylinder parallel to the main field, and a cylinder perpendicular to it, respectively).

$$\Delta_{BMS} = \frac{4\pi cs}{T}\left(\frac{\mu_{eff}}{2.84}\right) \times 10^3 \tag{11}$$

Thus, spherical liposomes loaded with paramagnetic agents are characterized by a $\Delta_{BMS} = 0$; however, non-spherical liposomes loaded with paramagnetic chelates provide larger shifts thanks to the BMS mechanism (2nd generation, Figure 8). Furthermore, liposomes loaded with amphiphilic paramagnetic complexes in their membranes and a hydrophilic paramagnetic complex in the core result in even larger shifts of the inner-core water resonance of up to 45 ppm (3rd generation, Figure 8) [145, 146]. The sign of the shift can be manipulated by changing the lanthanide ion, as it depends on the sign of Bleaney's constant (i.e., Dy^{3+} and Tm^{3+} provoke shifts in opposite directions, Table 1). Interestingly, non-spherical liposomes loaded with **Gd(4)** can be used as dual T_1 and paraCEST agents [147]. Since Gd^{3+} is characterized by a Bleaney constant of $C_j = 0$, the shift of the in-core water is associated to the BMS effect only. Paramagnetic liposomes containing **Dy(4)** in their core were attached electrostatically to red blood cells, providing CEST response due to both liposomal water protons and cytoplasmatic water protons [148].

3. TRANSITION METAL COMPLEXES

3.1. Ligands, Metal Ions, and Exchangeable Protons

ParaCEST agents based on transition metals represent an attractive alternative to those containing lanthanide ions due to several reasons. First, some transition metal ions potentially useful to design paraCEST agents, such as Fe^{2+}, Co^{2+}, and Cu^{2+}, are biogenic elements, and thus, living organisms are adapted to manage small excess amounts of the free metal ions [149]. As a result, these metal ions are expected to have lower toxicity than the lanthanide ions [150]. A second property of transition metals is their ability to adopt different oxidation states and the possibility to tune their magnetic properties by changing the metal coordination environment. This interesting feature is paving the way for the design of responsive probes that cannot be obtained with the lanthanides. However, paraCEST agents based on transition metals have been by far less studied than

those of the Ln^{3+} ions. Among the transition metal ions of the first row Fe^{2+}, Co^{2+}, and Ni^{2+} are the obvious choices to design paraCEST agents, as these ions induce relatively large paramagnetic shifts and do not cause excessive relaxation. High-spin complexes of metal ions with $3d^5$ configurations possess electronic ground states that derive from a symmetrical ^6S term for the free ion, and are very efficient relaxation agents (i.e., Mn^{2+}, Fe^{3+}). As a result, these metal ions are useful for the design of T_1 contrast agents [7, 9, 151].

The use of transition metal complexes as paraCEST agents was first proposed by Morrow et al., who discovered that some high-spin Fe^{2+} complexes based on triazamacrocycles (**Fe(30)** and **Fe(36)**, Figure 9) display CEST effect upon saturation of their labile amide or amine protons [152]. In subsequent works, Ni^{2+} and Co^{2+} complexes were also introduced, with ligands containing amide groups as paraCEST agents [153, 154]. Following this pioneering work, a relatively large number of paraCEST agents based on transition metal complexes were synthesized and investigated *in vitro* (Figure 9). Most of the investigated complexes contain macrocyclic platforms like 1,4,7,10-tetraazacyclodocecane (cyclen), 1,4,8,11-tetraazacyclododecane (cyclam) or 1,4,7-triazacyclononane, though some complexes with acyclic ligands were also investigated. Concerning the nature of the metal ions, Fe^{2+}, Co^{2+}, and Ni^{2+} are the most extensively investigated, although Cu^{2+} was also found suitable for paraCEST due to magnetic exchange interactions in binuclear complexes [155]. Different types of labile protons were explored to provide saturation transfer, most frequently amide, hydroxyl, imidazole, or amine protons (Figure 9). Water molecules coordinated to Co^{2+} in macrocyclic complexes based on 1,4,7-triazacyclononane did not provide CEST effect due to fast water exchange [156].

The paramagnetic shifts induced by transition metal ions like Ni^{2+}, Co^{2+}, and Fe^{2+} have been far less studied than those of the Ln^{3+} ions, although it is likely that they are dominated by the contact mechanism. For some Ni^{2+} six-coordinate complexes, ^1H and ^{13}C chemical shifts were predicted accurately from the values of the hyperfine coupling constants $A/\hbar$ obtained with DFT calculations (see Equation (6) above) [157, 158]. Octahedral Ni^{2+} complexes possess an orbitally non-degenerate $^3A_{2g}$ ground state, and thus, magnetic anisotropy and pseudocontact shifts are expected to be small (Equation (3)). The pseudocontact shift might not be negligible for Co^{2+} and Fe^{2+} complexes, still the contact contribution likely dominates the paramagnetic shifts of nuclei that are 3–5 bonds away from the paramagnetic center [159, 160]. Most of the complexes studied so far contain amide groups, so the exchangeable protons are four bonds away from the paramagnetic center (Table 3). The two protons of primary amide groups are not magnetically equivalent, and thus provide two different signals, one showing a rather large paramagnetic shift: $+39$ to $+92$ ppm (Fe^{2+}), $+32$ to $+125$ (Co^{2+}), and $+50$ to $+91$ (Ni^{2+}). The second amide resonance presents a smaller shift with respect to bulk water and is often hidden below the huge water signal. DFT calculations performed on the **Ni(34)** complex allowed to assign the most paramagnetic signal at 91.5 ppm to the amide protons in the *trans* position with respect to the C=O amide bond, and the peak at 22.2 ppm to the *cis* amide NH protons [158]. Imidazol and benzimidazol protons, which lie also four bonds away from the paramagnetic center, show large shifts with respect to bulk water
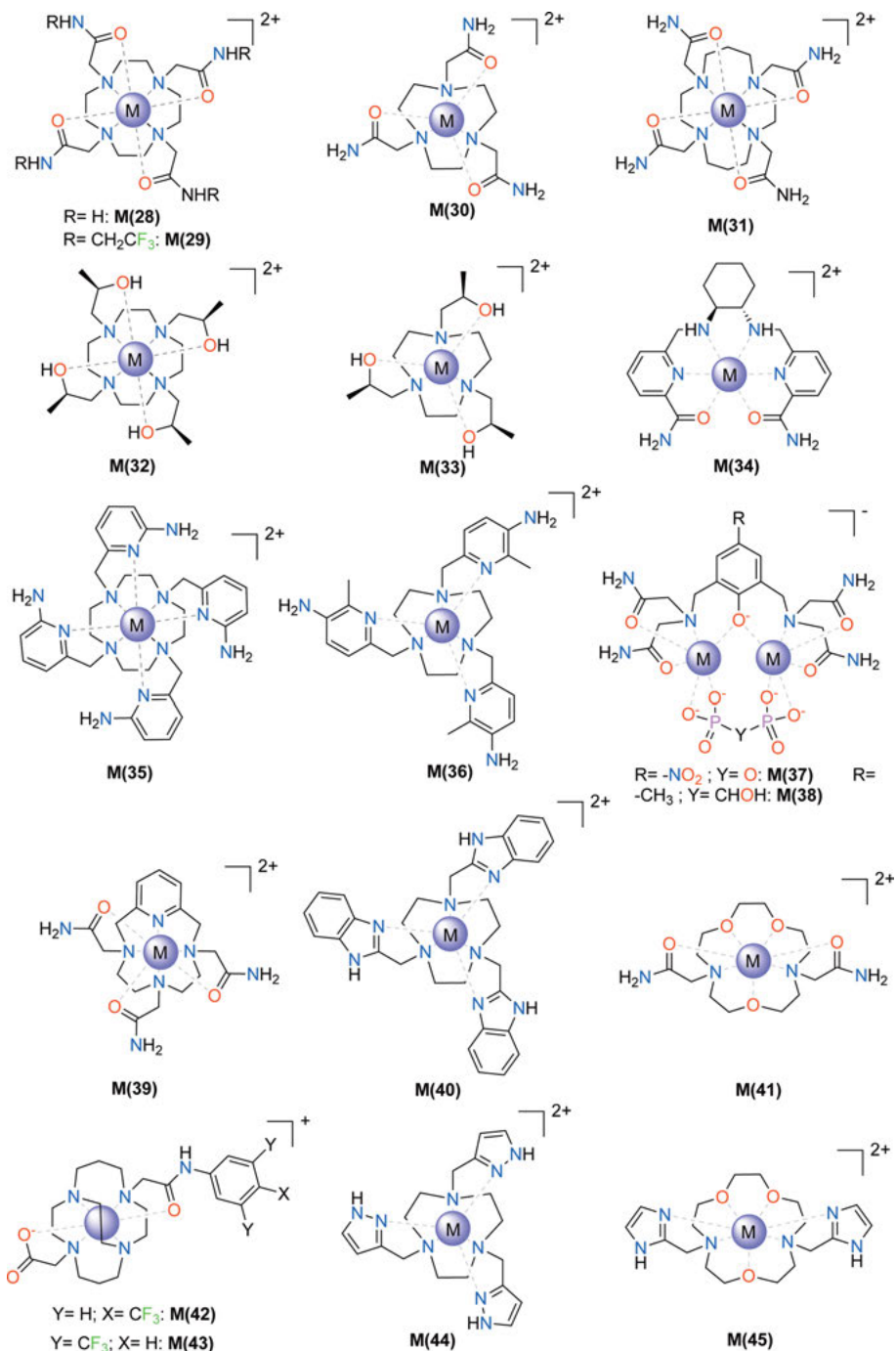
Figure 9. Transition metal-based paraCEST agents discussed in the text.

Table 3. Chemical shifts, exchange rates and number of bonds to the metal ion in transition metal paraCEST agents. All data at 37 °C.

	Group	δ_H (ppm)	k_B (s^{-1})	Bonds	pH	Reference
Fe(28)	Amide	50	330/400	4	7.4	[163,171]
Co(28)	Amide	45	300	4	7.4	[154,171]
Ni(28)	Amide	76/69	364	4	7.4	[171]
Fe(29)[a]	Amide	39	7692	4	7.4	[167]
Fe(30)	Amide	69	240	4		[28]
Co(30)	Amide	32	890	4	7.4	[154]
Ni(30)	Amide	76/72	364	4	7.4	[153]
Fe(31)	Amide	64/78	–	4		[172]
1,8-Co(31)	Amide	124/45	600/900	4	7.4	[171]
Ni(31)	Amide	76	328	4	7.4	[153,171]
Fe(32)	Hydroxyl	54	3000	2	7.3	[163]
Co(33)	Hydroxyl	140	5000	2	7.5	[156]
Ni(34)	Amide	91/22	7400/5000	4	7.2	[158]
Fe(35)	Amine	–74	1800	4	7.7	[164]
Co(35)	Amine	–114/14	–	4	6.0	[164]
Fe(36)	Amine	6.5	–	5	7.0	[28]
Co(37)	Amide	102/66	350/270	4	8.62	[170]
Cu(38)	Amide	29	420	4	7.0	[155]
Co(39)	Amide	57	3691	4	7.4	[166]
Ni(39)	Amide	70	5096	4	7.4	[166]
Fe(40)	Benzim.	53	–	4		[28]
Fe(41)	Amide	92/24	500	4	7.4	[165]
Co(41)	Amide	59/–19	240	4	7.4	[254,165]
Ni(41)	Amide	72/11	240	4	7.4	[153,165]
Ni(42)	Amide	52	7100	4	7.0	[168]
Ni(43)	Amide	52	10900	4	7.0	[168]
Co(44)	Pyrazole	135	9200	3	6.9	[162]
Co(45)	Imidazole	32	1600	4	7.4	[161]
Ni(45)	Imidazole	55	1630	4	7.4	[161]

[a] Data at 21 °C.

too (about +30 to +55 ppm) [28, 161]. The CEST signal due to the pyrazol protons in the **Co(44)** complex shows a larger shift (135 ppm), presumably because of the reduced distance with respect to the paramagnetic ion in terms of number of bonds [162].

Hydroxyl protons at a two-bond distance from the metal ion have been also been exploited to obtain a CEST effect in Fe^{2+} and Co^{2+} complexes (**Fe(32)** and **Co(33)**, Figure 9) [156, 163]. Amine protons placed five bonds away from the metal ion were detected in the CEST spectrum at only 6.5 ppm from bulk water [28]. Amine groups at four bonds were however found to experience shifts of up to 114 ppm (**Fe(35)** and **Co(35)**), and remain the only type of labile protons that are shifted upfield with respect to bulk water [164]. A DFT study suggested that this negative shift in **Fe(35)** is related to a dative $O_{amide} \rightarrow Fe$ interaction that transfers β spin density only [160].

The proton exchange rates of primary amide groups are rather low, in the range of a few hundred s^{-1} (Table 3). The nature of the metal ion does not affect much the k_B values, as evidenced by the data reported for the **M(28)**, **M(30)**, and **M(41)** complexes (M = Fe, Co or Ni), though **Co(30)** presents a somewhat higher exchange rate [28, 153, 154, 163, 165]. It is also worth noting that **Co(39)** and **Ni(39)** present exchange rates one order of magnitude faster than other complexes containing primary amide groups [166]. Incorporating electron-withdrawing groups to the amide function results in a dramatic increase of the proton exchange rate, as evidenced by the k_B values determined for **Fe(29)**, **Ni(42)**, and **Ni(43)** [167,1 68]. This trend is consistent with the base-catalyzed mechanism expected for amide protons around neutral pH, which results in faster k_B values on increasing proton acidity. Due to the same reason, the picolylamide protons of **Ni(34)** also present fast proton exchange rates [158]. The limited set of k_B data reported so far suggest that hydroxyl and amine protons are endowed with faster exchange rates than acetamide protons (Table 3) [156, 163, 164].

3.2.   Responsive Agents Based on Transition Metal Complexes

Similarly to the lanthanide analogues, transition metal complexes exhibited paraCEST response towards temperature, redox potential or more commonly pH, although the number of their examples is substantially smaller. For instance, the chemical shift of the CEST peak of the **Fe(35)** complex at ca. –78 ppm varies monotonically with pH below 6.7 due to protonation of the amine groups. However, imaging experiments on tube phantoms suggested that the chemical shift changes induced by pH were not large enough to be detected on low-field instruments [164]. Additionally, some transition metal paraCEST agents present two CEST features that allow using ratiometric approaches for monitoring a pH response. To this end, the **Co(31)** complex forms two different isomers resulting from the coordination of two pendant arms in positions 1,4 or 1,8, the latter being the thermodynamically stable form. This **1,8Co(31)** complex presents two pairs of overlapping CEST features at 124 and 45 ppm whose relative intensity varies with pH [169]. Similarly, the binuclear complex **Co(37)** presents two CEST signals at 102 and 66 ppm that allow a concentration-independent ratiometric measure of solution pH over a biologically relevant range [170].

Regarding transition metal systems responsive to other targets, the **M(27)** and **M(31)** complexes (M = Fe, Co or Ni) were proposed as paraCEST temperature sensors, as they present paraCEST signals with chemical shifts that vary significantly with temperature. The **Co(31)** complex shows a temperature coefficient of –0.66 ppm °C^{-1}, which is 60-fold higher than that of bulk water [171]. The **Co(44)** complex displays a CEST signal at 135 ppm and a Co^{2+}/Co^{3+} couple with a reduction potential within the biologically relevant range, which opens avenues to develop redox-activated paraCEST agents [172, 173].

4.   CONCLUDING REMARKS AND FUTURE DIRECTIONS

The appearance of paramagnetic chelates as potential MRI contrast agents that take advantage of the CEST mechanism triggered a great deal of fundamental research along different directions in the past two decades. This allowed a detailed understanding of the factors that influence the CEST effects both *in vitro* and in tissues; consequently, compounds with optimized properties could be designed and tested.

Complexes with the Ln^{3+} ions have intensively been explored as paraCEST agents using different types of labile protons (coordinated water molecules, amide, hydroxyl, etc.) and molecular architectures, most often based on DOTA-tetraamide scaffolds. Different systems were also tested successfully *in vivo* using animal models. These initial studies indicated that paraCEST agents can be of great help for a better understanding of different pathologies by providing a more specific response to various biomarkers, an application of great potential in biomedical research. However, the main challenge associated to the application of Ln^{3+}-based paraCEST agents both in biomedical research and in clinical practice is to overcome sensitivity limitations. Besides developing complexes based on different types of lanthanide metals or macrocyclic chelates, this problem has been also tackled by preparing different macromolecular agents. Nevertheless, further developments are still necessary, particularly additional fundamental advances in probe design and a better understanding of the behavior of paraCEST agents in tissues.

The development of paraCEST agents based on transition metal ions has started more recently, but the *in vitro* studies reported so far already demonstrate their great potential. The rich coordination chemistry of transition metals and their ability to stabilize different oxidation states make them ideal candidates for development of redox-sensitive probes. Importantly, these agents may also have a lower toxicity than analogous Ln^{3+}-based probes. The detection of transition metal-based paraCEST agents *in vivo* is still to be demonstrated, and will likely require designing new probes or modifying the existing ones to ensure a good toxicity profile. One of the possible ways might be focusing on macromolecular systems that contain transition metals, as an attempt to develop more efficient systems. However, many key advances in the application of paramagnetic complexes as CEST agents have been accomplished during the last two decades. In parallel to these significant advances on the probe design and understanding the physicochemical aspects of their behavior, the upcoming period should bring substantial progress on their *in vivo* application for biomedical research and potentially clinical purposes. This will lead to improved MRI routines and subsequently great benefit for molecular imaging in general.

ACKNOWLEDGMENTS

ABBREVIATIONS AND DEFINITIONS

AAZTA	6-amino-6-methylperhydro-1,4-diazepine tetraacetate
BMS	bulk magnetic susceptibility
CEST	chemical exchange saturation transfer
DFT	density-functional theory
DO3A	1,4,7,10-tetraazacyclododecane-1,4,7-triacetate
DOTA	1,4,7,10-tetraazacyclododecane-1,4,7,10-tetraacetate
HP-DO3A	10-(2-hydroxypropyl)-1,4,7,10-tetraazacyclododecane-1,4,7,10-tetraacetate
MRI	magnetic resonance imaging
MT	magnetization transfer
MTR_{asym}	magnetization transfer asymmetry
NAD	nicotinamide adenine dinucleotide
NMR	nuclear magnetic resonance
PAMAM	polyamidoamine
paraCEST	paramagnetic chemical exchange saturation transfer
RF	radio frequency
SAP	square antiprismatic
TSAP	twisted-square antiprismatic
RF	radio frequency
ssMT	semi-solid magnetization transfer
uPA	urokinase plasminogen activator

REFERENCES

1. R. G. Henderson, *J. R. Soc. Med.* **1983**, *76*, 206–212.
2. P. C. Lauterbur, M. H. Mendoça-Dias, A. A. Rudin, *Front. Biol. Energ.* **1978**, *1*, 752–759.
3. T. J. Brady, M. R. Goldman, I. L. Pykett, F. S. Buonanno, J. P. Kistler, J. H. Newhouse, C. T. Burt, W. S. Hinshaw, G. M. Pohost, *Radiology* **1982**, *144*, 549; M. R. Goldman, T. J. Brady, I. L. Pykett, C. T. Burt, F. S. Buonanno, J. P. Kistler, J. H. Newhouse, W. S. Hinshaw, G. M. Pohost, *Circulation* **1982**, *66*, 1012–1016.
4. D. H. Carr, J. Brown, G. M. Bydder, H. J. Weinmann, U. Speck, D. J. Thomas, I. R. Young, *Lancet* **1984**, *1*, 484–486.
5. J. Wahsner, E. M. Gale, A. Rodríguez-Rodríguez, P. Caravan, *Chem. Rev.* **2019**, *119*, 957–1057.
6. *The Chemistry of Contrast Agents in Medical Magnetic Resonance Imaging*, Eds. A. Merbach, L. Helm, E. Tóth, John Wiley & Sons, Chichester, **2013**.
7. M. Botta, F. Carniato, D. Esteban-Gómez, C. Platas-Iglesias, L. Tei, *Fut. Med. Chem.* **2019**, *11*, 1461–1483.
8. J. R. Morrow, E. Tóth, *Inorg. Chem.* **2017**, *56*, 6029–6034.
9. A. Gupta, P. Caravan, W. S. Price, C. Platas-Iglesias, E. M. Gale, *Inorg. Chem.* **2020**, *59*, 6648–6678.
10. L. A. Ekanger, M. J. Allen, *Metallomics* **2015**, *7*, 405–421.
11. E. L. Que, C. J. Chang, *Chem Soc. Rev.* **2010**, *39*, 51–60.
12. R. Weissleder, U. Mahmood, *Radiology* **2001**, *219*, 316–333.

13. E. Terreno, D. Delli Castelli, A. Viale, S. Aime, *Chem. Rev.* **2010**, *110*, 3019–3042.

14. P. C. M. van Zijl, N. N. Yadav, *Magn. Reson. Med.* **2011**, *65*, 927–948.

15. S. Forsén, R. A. Hoffman, *J. Chem. Phys.* **1963**, *39*, 2892–2901.

16. S. D. Wolff, R. S. Balaban, *Magn. Reson. Med.* **1989**, *10*, 135–144.

17. K. M. Ward, R. S. Balaban, *J. Magn. Reson.* **2000**, *143*, 79–87.

18. E. Terreno, D. Delli Castelli, S. Aime, *Contrast Media Mol. Imaging* **2010**, *5*, 78–98.

19. S. Zhang, P. Winter, K. Wu, A. D. Sherry, *J. Am. Chem. Soc.* **2001**, *123*, 1517–1518.

20. S. Zhang, M. Merritt, D. E. Woessner, R. E. Lenkinski, A. D. Sherry, *Acc. Chem. Res.* **2003**, *36*, 783–790.

21. S. Aime, A. Barge, D. Delli Castelli, D. Fedeli, A. Mortillaro, F. U. Nielsen, E. Terreno, *Magn. Reson. Med.* **2002**, *47*, 639–648.

22. S. Aime, S. Geninatti-Crich, E. Gianolio, G. B. Giovenzana, L. Tei, E. Terreno, *Coord. Chem. Rev.* **2006**, *250*, 1562–1579.

23. S. Aime, D. Delli Castelli, S. G. Crich, E. Gianolio, E. Terreno, *Acc. Chem. Res.* **2009**, *42*, 822–831.

24. R. M. Henkelman, X. Huang, Q. S. Xiang, G. J. Stanisz, S. D. Swanson, M. J. Bronskill, *Magn. Reson. Med.* **1993**, *29*, 759–766.

25. M. Zaiss, A. Anemone, S. Goerke, D. L. Longo, K. Herz, R. Pohmann, S. Aime, M. Rivlin, G. Navon, X. Golay, K. Scheffler, *NMR Biomed.* **2019**, *32*, e4113.

26. J. A. Peters, J. Huskens, D. J. Raber, *Prog. Nucl. Magn. Reson. Spectrosc.* **1996**, *28*, 283–350.

27. J. A. Peters, K. Djanashvili, C. F. G. C. Geraldes, C. Platas-Iglesias, *Coord. Chem. Rev.* **2020**, *406*, 213146.

28. S. J. Dorazio, A. O. Olatunde, P. B. Tsitovich, J. R. Morrow, *J. Biol. Inorg. Chem.* **2014**, *19*, 191–205.

29. S. J. Dorazio, J. R. Morrow, *Eur. J. Inorg. Chem.* **2012**, 2006–2014.

30. W. D. Horrocks, J. P. Sipe, *J. Am. Chem. Soc.* **1971**, *93*, 6800−6804.

31. I. Bertini, C. Luchinat, G. Parigi, *Prog. Nucl. Magn. Reson. Spectrosc.* **2002**, *40*, 249−273.

32. B. Bleaney, *J. Magn. Reson.* **1972**, *8*, 91−100.

33. A. M. Funk, K. L. N. A. Finney, P. Harvey, A. M. Kenwright, E. R. Neil, N. J. Rogers, P. K. Senanayake, D. Parker, *Chem. Sci.* **2015**, *6*, 1655−1662.

34. G. Castro, M. Regueiro-Figueroa, D. Esteban-Gómez, P. Pérez-Lourido, C. Platas-Iglesias, L. Valencia, *Inorg. Chem.* **2016**, *55*, 3490−3497.

35. A. A. Pinkerton, M. Rossier, S. Spiliadis, *J. Magn. Reson.* **1985**, *64*, 420–425.

36. A. Rodríguez-Rodríguez, D. Esteban-Gómez, A. de Blas, T. Rodríguez-Blas, M. Botta, R. Tripier, C. Platas-Iglesias, *Inorg. Chem.* **2012**, *51*, 13419−13429.

37. R. M. Golding, M. P. Halton, *Aust. J. Chem.* **1972**, *25*, 2577−2581.

38. I. Solomon, *Phys. Rev.* **1955**, *99*, 559−565.

39. N. Bloembergen, L. O. Morgan, *J. Chem. Phys.* **1961**, *34*, 842−850.

40. N. Bloembergen, *J. Chem. Phys.* **1957**, *27*, 572−573.

41. M. Gueron, *J. Magn. Reson.* **1975**, *19*, 58−66.

42. B. M. Alsaadi, F. J. C. Rossotti, R. J. P. Williams, *J. Chem. Soc., Dalton Trans.* **1980**, 2147−2150.

43. A. V. Astashkin, A. M. Raitsimring, P. Caravan, *J. Phys. Chem. A* **2004**, *108*, 1990−2001.

44. P. Caravan, J. J. Ellison, T. J. McMurry, R. B. Lauffer, *Chem. Rev.* **1999**, *99*, 2293–2352.

45. C. Kumas, W. S. Fernando, P. Zhao, M. Regueiro-Figueroa, G. E. Kiefer, A. E. Martins, C. Platas-Iglesias, A. D. Sherry, *Inorg. Chem.* **2016**, *55*, 9297−9305.

46. S. Aime, M. Botta, M. Fasano, M. P. M. Marques, C. F. G. C. Geraldes, D. Pubanz, A. E. Merbach, *Inorg. Chem.* **1997**, *36*, 2059–2068.

47. C. Platas-Iglesias, *Eur. J. Inorg. Chem.* **2012**, 2023–2033.
48. D. Parker, R. S. Dickins, H. Puschmann, C. Crossland, J. A. K. Howard, *Chem. Rev.* **2002**, *102*, 1977–2010.
49. T. Mani, A. C. L. Opina, P. Zhao, O. M. Evbuomwan, N. Milburn, G. Tircso, C. Kumas, A. D. Sherry, *J. Biol. Inorg. Chem.* **2014**, *19*, 161–171.
50. J. Blahut, P. Hermann, Z. Tosner, C. Platas-Iglesias, *Phys. Chem. Chem. Phys.* **2017**, *19*, 26662–26671.
51. M. Purgel, Z. Baranyai, A. de Blas, T. Rodríguez-Blas, I. Banyai, C. Platas-Iglesias, I. Tóth, *Inorg. Chem.* **2010**, *49*, 4370–4383.
52. S. Aime, A. Barge, M. Botta, A. S. De Sousa, D. Parker, *Angew. Chem. Int. Ed.* **1998**, *37*, 2673–2675.
53. S. Aime, M. Botta, G. Ermondi, *Inorg. Chem.* **1992**, *31*, 4291–4299.
54. M. P. M. Marques, C. F. G. C. Geraldes, A. D. Sherry, A. E. Merbach, H. Powell, D. Pubanz, S. Aime, M. Botta, *J. Alloys Comp.* **1995**, *225*, 303–307.
55. F. A. Dunand, R. S. Dickins, D. Parker, A. E. Merbach, *Chem. Eur. J.* **2001**, *7*, 5160–5167.
56. S. Zhang, K. Wu, M. C. Biewer, A. D. Sherry, *Inorg. Chem.* **2001**, *40*, 4284–4290.
57. M. Woods, P. Caravan, C. F. G. C. Geraldes, M. T. Greenfield, G. E. Kiefer, M. Lin, K. McMillan, M. I. M. Prata, A. C. Santos, X. Sun, J. Wang, S. Zhang, P. Zhao, A. D. Sherry, *Invest. Radiol.* **2008**, *43*, 861–870.
58. S. Zhang, L. Michaudet, S. Burgess, A. D. Sherry, *Angew. Chem. Int. Ed.* **2002**, *41*, 1919–1921.
59. G. Liu, Y. Li, V. R. Sheth, M. D. Pagel, *Mol. Imaging* **2012**, *11*, 47–57.
60. M. Woods, D. E. Woessner, P. Zhao, A. Pasha, M.-Y. Yang, C.-H. Huang, O. Vasalitiy, J. R. Morrow, A. D. Sherry, *J. Am. Chem. Soc.* **2006**, *128*, 10155–10162.
61. C.-H. Huang, J. R. Morrow, *J. Am. Chem. Soc.* **2009**, *131*, 4206–4207.
62. C.-H. Huang, J. R. Morrow, *Inorg. Chem.* **2009**, *48*, 7237–7243.
63. J. Hammell, L. Buttarazzi, C.-H. Huang, J. R. Morrow, *Inorg. Chem.* **2011**, *50*, 4857–4867.
64. D. Delli Castelli, E. Terreno, S. Aime, *Angew. Chem. Int. Ed.* **2011**, *18*, 1798–1800.
65. G. Ferrauto, D. Delli Castelli, E. Terreno, S. Aime, *Magn. Reson. Med.* **2013**, *69*, 1703–1711.
66. A. Pasha, G. Tircso, E. T. Benyó, E. Brücher, A. D. Sherry, *Eur. J. Inorg. Chem.* **2007**, 4340–4349.
67. M. Polasek, P. Caravan, *Inorg. Chem.* **2013**, *52*, 4084–4096.
68. D. Delli Castelli, L. Tei, F. Carniato, S. Aime, M. Botta, *Chem. Commun.* **2018**, *54*, 2004–2007.
69. S. Aime, L. Calabi, C. Cavallotti, E. Gianolio, G. B. Giovenzana, P. Losi, A. Maiocchi, G. Palmisano, M. Sisti, *Inorg. Chem.* **2004**, *43*, 7588–7590.
70. Z. Baranyai, D. Delli Castelli, C. Platas-Iglesias, D. Esteban-Gómez, A. Bényei, L. Tei, M. Botta, *Inorg. Chem. Front.* **2020**, *7*, 795–803.
71. Z. Baranyai, F. Uggeri, G. B. Giovenzana, A. Bényei, E. Brücher, S. Aime, *Chem. Eur. J.* **2009**, *15*, 1696–1705.
72. G. Castro, M. Regueiro-Figueroa, D. Esteban-Gómez, R. Bastida, A. Macías, P. Pérez-Lourido, C. Platas-Iglesias, L. Valencia, *Chem. Eur. J.* **2015**, *21*, 18662–18670.
73. T. Gambino, L. Valencia, P. Perez-Lourido, D. Esteban-Gómez, M. Zaiss, C. Platas-Iglesias, G. Angelovski, *Inorg. Chem. Front.* **2020**, *7*, 2274–2286.
74. C. R. Sheth, Y. Li, L. Q. Chen, C. M. Howison, C. A. Flask, M. D. Pagel, *Magn. Reson. Med.* **2012**, *67*, 760–768.
75. A. C. L. Opina, Y. Wu, P. Zhao, G. Kiefer, A. D. Sherry, *Contrast Media Mol. Imaging* **2011**, *6*, 459–464.

76. R. Pujales-Paradela, T. Savic, P. Pérez-Lourido, D. Esteban-Gómez, G. Angelovski, M. Botta, C. Platas-Iglesias, *Inorg. Chem.* **2019**, *58*, 7571–7583.

77. N. McVicar, A. X. Li, M. Suchý, R. H. E. Hudson, R. S. Menon, R. Bartha, *Magn. Reson. Med.* **2013**, *70*, 1016–1025.

78. M. Suchý, M. Milne, A. A. H. Elmehriki, N. McVicar, A. X. Li, R. Bartha, R. H. E. Hudson, *J. Med. Chem.* **2015**, *58*, 6516–6532.

79. D. Esteban-Gómez, L. A. Büldt, P. Pérez-Lourido, L. Valencia, M. Seitz, C. Platas-Iglesias, *Inorg. Chem.* **2019**, *58*, 3732−3743.

80. M. Vonci, K. Mason, E. A. Suturina, A. T. Frawley, S. G. Worswick, I. Kuprov, D. Parker, E. J. L. McInnes, N. F. Chilton, *J. Am. Chem. Soc.* **2017**, *139*, 14166−14172.

81. K. Mason, A. C. Harnden, C. W. Patrick, A. W. J. Poh, A. S. Batsanov, E. A. Suturina, M. Vonci, E. J. L. McInnes, N. F. Chilton, D. Parker, *Chem. Commun.* **2018**, *54*, 8486−8489.

82. T. K. Stevens, M. Milne, A. A. H. Elmehriki, M. Suchy, R. Bartha, R. H. E. Hudson, *Contrast Media Mol. Imaging* **2013**, *8*, 289−292.

83. M. A. Eriksson, T. Härd, L. Nilsson, *Biophys. J.* **1995**, *69*, 329−339.

84. S. Aime, D. Delli Castelli, E. Terreno, *Angew. Chem. Int. Ed.* **2002**, *41*, 4334–4336.

85. M. Suchý, A. X. Li, M. Milne, R. Bartha, R. H. E. Hudson, *RSC Adv.* **2016**, *6*, 62647−62655.

86. S. Viswanathan, S. J. Ratnalar, K. N. Green, Z. Kovacs, L. M. De León-Rodríguez, A. D. Sherry, *Angew. Chem. Int. Ed.* **2009**, *48*, 9330−9333.

87. X. Wang, Y. Wu, T. C. Soesbe, J. Yu, P. Zhao, G. E. Kiefer, A. D. Sherry, *Angew. Chem. Int. Ed.* **2015**, *54*, 8662–8664.

88. P. Caravan, D. Esteban-Gómez, A. Rodríguez-Rodríguez, C. Platas-Iglesias, *Dalton Trans.* **2019**, *48*, 11161–11180.

89. N. B. Siriwardena-Mahanama, M. J. Allen, *Molecules* **2013**, *18*, 9352–9381.

90. A. D. Sherry, Y. Wu, *Curr. Opin. Chem. Biol.* **2013**, *17*, 167–174.

91. S. Zhang, K. Wu, A. D. Sherry, *J. Am. Chem. Soc.* **2002**, *124*, 4226–4227.

92. T. Mani, G. Tircso, O. Togao, P. Zhao, T. C. Soesbe, M. Takahashi, A. D. Sherry, *Contrast Media Mol. Imaging* **2009**, *4*, 183–191.

93. W. S. Fernando, A. F. Martins, P. Zhao, Y. Wu, G. E. Kiefer, C. Platas-Iglesias, A. D. Sherry, *Inorg. Chem.* **2016**, *55*, 3007–3014.

94. S. J. Ratnakar, M. Woods, A. J. M. Lubag, Z. Kovacs, A. D. Sherry, *J. Am. Chem. Soc.* **2008**, *130*, 6–7.

95. N. Cakic, B. Tickner, M. Zaiss, D. Esteban-Gómez, C. Platas-Iglesias, G. Angelovski, *Inorg. Chem.* **2017**, *56*, 7737–7745.

96. A. Rodríguez-Rodríguez, M. Regueiro-Figueroa, D. Esteban-Gómez, T. Rodríguez-Blas, V. Patinec, R. Tripier, G. Tircso, F. Carniato, M. Botta, C. Platas-Iglesias, *Chem. Eur. J.* **2017**, *23*, 1110–1117.

97. Z. Garda, V. Nagy, A. Rodríguez-Rodríguez, R. Pujales-Paradela, V. Patinec, G. Angelovski, É. Tóth, F. K. Kálmán, D. Esteban-Gómez, R. Tripier, C. Platas Iglesias, G. Tircsó, **2020**, *Inorg. Chem.* **2020**, *59*, 8184–8195.

98. E. Toth, C. S. Bonnet, *Inorganics* **2019**, *7*, 68.

99. D. V. Hingorani, A. S. Bernstein, M. D. Pagel, *Contrast Media Mol. Imaging* **2015**, *10*, 245–265.

100. D. Delli Castelli, E. Terreno, S. Aime, *Angew. Chem. Int. Ed.* **2011**, *50*, 1798–1800.

101. D. Delli Castelli, G. Ferrauto, J. C. Cutrin, E. Terreno, S. Aime, *Magn. Reson. Med.* **2014**, *71*, 326–332.

102. Y. Wu, T. C. Soesbe, G. E. Kiefer, P. Zhao, A. D. Sherry, *J. Am. Chem. Soc.* **2010**, *132*, 14002–14003.

103. Y. Wu, S. Zhang, T. C. Soesbe, J. Yu, E. Vinogradov, R. E. Lenkinski, A. D. Sherry, *Magn. Reson. Med.* **2016**, *75*, 2432–2441.

104. G. Angelovski, T. Chauvin, R. Pohmann, N. K. Logothetis, É. Tóth, *Bioorg. Med. Chem.* **2011**, *19*, 1097–1105.

105. K. Srivastava, G. Ferrauto, S. M. Harris, D. L. Longo, M. Botta, S. Aime, V. C. Pierre, *Dalton Trans.* **2018**, *47*, 11346–11357.

106. R. Trokowski, J. Ren, F. K. Kálmán, A. D. Sherry, *Angew. Chem. Int. Ed.* **2005**, *44*, 6920–6923.

107. N. Cakić, T. Ž. Verbić, R. M. Jelić, C. Platas-Iglesias, G. Angelovski, *Dalton Trans.* **2016**, *45*, 6555–6565.

108. G. Liu, Y. Li, M. D. Pagel, *Magn. Reson. Med.* **2007**, *58*, 1249–1256.

109. S. J. Ratnakar, S. Viswanathan, Z. Kovacs, A. K. Jindal, K. N. Green, A. D. Sherry, *J. Am. Chem. Soc.* **2012**, *134*, 5798–5800.

110. S. J. Ratnakar, T. C. Soesbe, L. L. Lumata, Q. N. Do, S. Viswanathan, C.-Y. Lin, A. D. Sherry, Z. Kovacs, *J. Am. Chem. Soc.* **2013**, *135*, 14904–14907.

111. A. M. Funk, V. C. Jordan, A. D. Sherry, S. J. Ratnakar, Z. Kovacs, *Angew. Chem. Int. Ed.* **2016**, *55*, 5024–5027.

112. M. E. Burnettt, B. Adebesin, A. M. Funk, Z. Kovacs, A. D. Sherry, L. A. Ekanger, M. J. Allen, K. N. Green, S. J. Ratnakar, *Eur. J. Inorg. Chem.* **2017**, 5001–5005.

113. R. A. Moats, S. E. Fraser, T. J. Meade, *Angew. Chem. Int. Ed.* **1997**, *36*, 726–728.

114. B. Yoo, M. D. Pagel, *J. Am. Chem. Soc.* **2006**, *128*, 14032–14033.

115. B. Yoo, M. S. Raam, R. M. Rosenblum, M. D. Pagel, *Contrast Media Mol. Imaging* **2007**, *2*, 189–198.

116. B. Yoo, V. R. Sheth, C. M. Howison, M. J. K. Douglas, C. T. Pineda, E. A. Maine, A. F. Baker, M. D. Pagel, *Magn. Reson. Med.* **2014**, *71*, 1221–1221.

117. M. Suchý, R. Ta, A. X. Li, F. Wojciechowski, S. H. Pasternak, R. Bartha, R. H. E. Hudson, *Org. Biomol. Chem.* **2010**, *8*, 2560–2566.

118. D. V. Hingorani, E. A. Randtke, M. D. Pagel, *J. Am. Chem. Soc.* **2013**, *135*, 6396–6398.

119. T. Chauvin, P. Durand, M. Bernier, H. Meudal, B.-T. Doan, F. Noury, B. Badet, J.-C. Beloeil, É. Tóth, *Angew. Chem. Int. Ed.* **2008**, *47*, 4370–4373.

120. T. Chauvin, S. Torres, R. Rosseto, J. Kotek, B. Badet, P. Durand, É. Tóth, *Chem. Eur. J.* **2012**, *18*, 1408–1418.

121. J. He, C. S. Bonnet, S. V. Eliseeva, S. Lacerda, T. Chauvin, P. Retailleau, F. Szeremeta, B. Badet, S. Petoud, E. Tóth, P. Durand, *J. Am. Chem. Soc.* **2016**, *138*, 2913–2916.

122. Y. Li, V. R. Sheth, G. Liu, M. D. Pagel, *Contrast Media Mol. Imaging* **2011**, *6*, 219–228.

123. I. Daryaei, K. M. Jones, M. D. Pagel, *Chem. Eur. J.* **2017**, *23*, 6514–6517.

124. C.-H. Huang, J. Hammell, S. J. Ratnakar, A. D. Sherry, J. R. Morrow, *Inorg. Chem.* **2010**, *49*, 5963–5970.

125. L. Zhang, A. F. Martins, Y. Mai, P. Zhao, A. M. Funk, M. V. C. Jordan, S. Zhang, W. Chen, Y. Wu, A. D. Sherry, *Chem. Eur. J.* **2017**, *23*, 1752–1756.

126. L. Zhang, A. F. Martins, P. Zhao, M. Tieu, D. Esteban-Gómez, G. T. McCandless, C. Platas-Iglesias, A. D. Sherry, *J. Am. Chem. Soc.* **2017**, *139*, 17431–17437.

127. K. New, C. M. Andolina, C.-H. Huang, J. R. Morrow, *Bioconjugate Chem.* **2009**, *20*, 1375–1382.

128. S. Zhang, R. Trokowski, A. D. Sherry, *J. Am. Chem. Soc.* **2003**, *125*, 15288–15289.

129. R. Trokowski, S. Zhang, A. D. Sherry, *Bioconjugate Chem.* **2004**, *15*, 1431–1440.

130. J. Ren, R. Trokowski, S. Zhang, C. R. Malloy, A. D. Sherry, *Magn. Reson. Med.* **2008**, *60*, 1047–1055.

131. P. M. Winter, *WIREs Nanomed. Nanobiotechnol.* **2012**, *4*, 389–398.

132. D. Delli Castelli, E. Terreno, D. Longo, S. Aime, *NMR Biomed.* **2013**, *26*, 839–849.

133. A. Farashishiko, J. R. Slack, M. Botta, M. Woods, *Front. Chem.* **2018**, *6*, 96.

134. O. M. Evbuomwan, M. E. Merritt, G. E. Kiefer, A. D. Sherry, *Contrast Media Mol. Imaging* **2012**, *7*, 19–25.

135. J. A. Pikkemaat, R. T. Wegh R. Lamerichs, R. A. van de Molengraaf, S. Langereis, D. Burdinski, A. Y. F. Raymond, H. M. Janssen, B. F. M. de Waal, N. P. Willard, E. W. Meijer, H. Grüll, *Contrast Media Mol. Imaging* **2007**, *2*, 229–239.

136. M. M. Ali, B. Yoo, M. D. Pagel, *Mol. Pharm.* **2009**, *6*, 1409–1416.

137. M. M. Ali, M. P. Bhuiyan, B. Janic, N. R. Varma, T. Mikkelsen, J. R. Ewing, R. A. Knight, M. D. Pagel, A. S. Arbab, *Fut. Med. Chem.* **2012**, *7*, 1827–1837.

138. Y. Wu, P. Zhao, G. E. Kiefer, A. D. Sherry, *Macromolecules* **2010**, *43*, 6616–6624.

139. O. Vasalatiy, P. Zhao, M. Woods, A. Marconescu, A. Castillo-Muzquiz, P. Thorpe, G. E. Kiefer, A. D. Sherry, *Bioorg. Med. Chem.* **2011**, *19*, 1106–1114.

140. P. M. Winter, K. Cai, J. Chen, C. R. Adair, G. E. Kiefer, P. S. Athey, P. J. Gaffney, C. E. Buff, J. D. Robertson, S. D. Caruthers, S. A. Wickline, G. M. Lanza, *Magn. Reson. Med.* **2006**, *56*, 1384–1388.

141. K. Cai, G. E. Kiefer, S. D. Caruthers, S. A. Wicklinea G. M. Lanza, P. M. Winter, *NMR Biomed.* **2012**, *25*, 279–285.

142. O. Vasalatiy, R. D. Gerard, P. Zhao, X. Sun, A. D. Sherry, *Bioconj. Chem.* **2008**, *19*, 598–606.

143. E. Terreno, A. Sanino, C. Carrera, D. Delli Castelli, G. B. Giovenzana, A. Lombardi, R. Mazzon, L. Milone, M. Visigalli, S. Aime, *J. Inorg. Biochem.* **2008**, *102*, 1112–1119.

144. S. Aime, D. Delli Castelli, E. Terreno, *Angew. Chem. Int. Ed.* **2005**, *44*, 5513–5515.

145. E. Terreno, C. Cabella, C. Carrera, D. Delli Castelli, R. Mazzon, S. Rollet, J. Stancanello, M. Visigalli, S. Aime, *Angew. Chem. Int. Ed.* **2007**, *46*, 966–968.

146. D. Delli Castelli, E. Terreno, C. Carrera, G. B. Giovenzana, R. Mazzon, S. Rollet, M. Visigalli, S. Aime, *Inorg. Chem.* **2008**, *47*, 2928–2930.

147. S. Aime, D. Delli Castelli, D. Lawson, E. Terreno, *J. Am. Chem. Soc.* **2007**, *129*, 2430–2431.

148. G. Ferrauto, E. Di Gregorio, S. Baroni, S. Aime, *Nano Lett.* **2014**, *14*, 6857–6862.

149. P. Chellan, P. J. Sadler, *Phil. Trans. R. Soc. A* **2015**, *373*, 20140182.

150. K. Nesmerak, *Lanthanide/Actinide Toxicity*, in *Encyclopedia of Metalloproteins*, Eds. R. H. Kretsinger, V. N. Uversky, E. A. Permyakov, Springer, New York, **2013**, pp. 1–391.

151. H. Wang, V. Clavijo Jordan, I. A. Ramsay, M. Sojoodi, B. C. Fuchs, K. K. Tanabe, P. Caravan, E. M. Gale, *J. Am. Chem. Soc.* **2019**, *141*, 5916–5925.

152. S. J. Dorazio, P. B. Tsitovich, K. E. Siters, J. A. Spernyak, J. R. Morrow, *J. Am. Chem. Soc.* **2011**, *133*, 14154–14156.

153. A. O. Olatunde, S. J. Dorazio, J. A. Spernyak, J. R. Morrow, *J. Am. Chem. Soc.* **2012**, *134*, 18503–18505.

154. S. J. Dorazio, A. O. Olatunde, J. A. Spernyak, J. R. Morrow, *Chem. Commun.* **2013**, *49*, 10025–10027.

155. K. Du, T. D. Harris, *J. Am. Chem. Soc.* **2016**, *138*, 7804–7807.

156. S. M. Abozeid, E. M. Snyder, T. Y. Tittiris, C. M. Steuerwald, A. Y. Nazarenko, J. R. Morrow, *Inorg. Chem.* **2018**, *57*, 2085−2095.

157. R. Meier, C. Platas-Iglesias, F. W. Heinemann, G. Linti, J. Shulte, S. K. Srivastava, *Inorg. Chem.* **2014**, *53*, 6684–6697.

158. L. Caneda-Martínez, L. Valencia, I. Fernández-Pérez, M. Regueiro-Figueroa, G. Angelovski, I. Brandariz, D. Esteban-Gómez, C. Platas-Iglesias, *Dalton Trans.* **2017**, *46*, 15095–15106.

159. I. Bertini, C. Luchinat, G. Parigi, E. Ravera, *Coord. Chem. Rev.* **1996**, *150*, 29–75.

160. B. Martin, J. Autschbach, *Phys. Chem. Chem. Phys.* **2016**, *18*, 21051−21068.

161. P. J. Burns, J. M. Cox, J. R. Morrow, *Inorg. Chem.* **2017**, *56*, 4545−4554.

162. P. B. Tsitovich, J. A. Spernyak, J. R. Morrow, *Angew. Chem. Int. Ed.* **2013**, *52*, 13997−14000.

163. S. J. Dorazio, J. R. Morrow, *Inorg. Chem.* **2012**, *51*, 7448−7450.

164. P. B. Tsitovich, J. M. Cox, J. A. Spernyak, J. R. Morrow, *Inorg. Chem.* **2016**, *55*, 12001−12010.

165. A. O. Olatunde, J. M. Cox, M. D. Daddario, J. A. Spernyak, J. B. Benedict, J. R. Morrow, *Inorg. Chem.* **2014**, *53*, 8311−8321.

166. R. N. Pradhan, S. Chakraborty, P. Bharti, J. Kumar, A. Ghosh, A. K. Singh, *Dalton Trans.* **2019**, *48*, 8899−8910.

167. K. Srivastava, G. Ferrauto, V. G. Young, S. Aime, V. C. Pierre, *Inorg. Chem.* **2017**, *56*, 12206−12213.

168. R. Pujales-Paradela, T. Savic, I. Brandariz, P. Pérez-Lourido, G. Angelovski, D. Esteban-Gómez, C. Platas-Iglesias, *Chem. Commun.* **2019**, *55*, 4115−4118.

169. C. J. Bond, R. Cineus, A. Y. Nazarenko, J. A. Spernyak, J. R. Morrow, *Dalton Trans.* **2020**, *49*, 279−284.

170. A. E. Thorarinsdottir, K. Du, J. H. P. Collins, T. D. Harris, *J. Am. Chem. Soc.* **2017**, *139*, 15836−15847.

171. A. O. Olatunde, C. J. Bond, S. J. Dorazio, J. M. Cox, J. B. Benedict, M. D. Daddario, J. A. Spernyak, J. R. Morrow, *Chem. Eur. J.* **2015**, *21*, 18290−18300.

172. P. B. Tsitovich, J. A. Spernyak, J. N. Morrow, *Angew. Chem. Int. Ed.* **2013**, *52*, 13997−14000.

173. P. B. Tsitovich, P. J. Burns, A. M. McKay, J. R. Morrow, *J. Inorg. Biochem.* **2014**, *133*, 143−154.

5

Lanthanide Complexes Used for Optical Imaging

Thomas Just Sørensen[1] *and Stephen Faulkner*[2]

[1]Nano-Science Center & Department of Chemistry, University of Copenhagen,
Universitetsparken 5, DK-2100 København Ø, Denmark
<tjs@chem.ku.dk>

[2]Chemistry Research Laboratory, University of Oxford, Mansfield Road, Oxford OX1 3TA, UK
<stephen.faulkner@chem.ox.ac.uk>

Abstract: Lanthanide complexes have been widely used in bioassay for over forty years, but their usefulness in optical imaging is only now beginning to be appreciated fully. In this chapter, we explore the fundamental spectroscopic properties of lanthanide ions that make them ideal as components in probes for optical imaging: their large pseudo Stokes' shift and long luminescence lifetimes facilitate the elimination of background signals, while the nature of the energy transfer pathways involved in sensitizing lanthanide emission makes all of them amenable to perturbation by their surroundings. We explore the use of lanthanide tags and labels in cellular imaging,

focusing on potential issues with localization and control, and using the Eurotracker® dyes as examples of controlling cellular localization. Moving from these to the use of responsive probes, we define and exemplify the ways in which sensitized emission can be controlled by perturbing the sensitization pathway, and explore the issues inherent to developing responsive probes for cations, anions and oxygen. Finally, we outline the prospects for quantitative imaging and the issues with multiplexing while studying different analytes.

1.   INTRODUCTION

The potential of using lanthanide complexes in optical bioimaging has yet to be realized [1]. Since the seminal paper by Selvin showing that lanthanide(III) ions could be used as contrast agents for optical imaging [2, 3], the potential advantages of using lanthanide complexes in optical bioimaging has been repeatedly demonstrated [4–15]. Although the biological applications are yet to emerge, research into optical bioimaging using lanthanide luminescence and the development of lanthanide-based molecular probes has been extensively reviewed [16–22].

While the potential use of nanophosphors containing lanthanides was recognized early on [23, 24], we will focus our attention on molecular probes – lanthanide complexes – exclusively. Many lanthanide(III) ions have been used [25–30], but europium(III) and terbium(III) are best suited due to the much higher quantum yield of luminescence of these two ions.
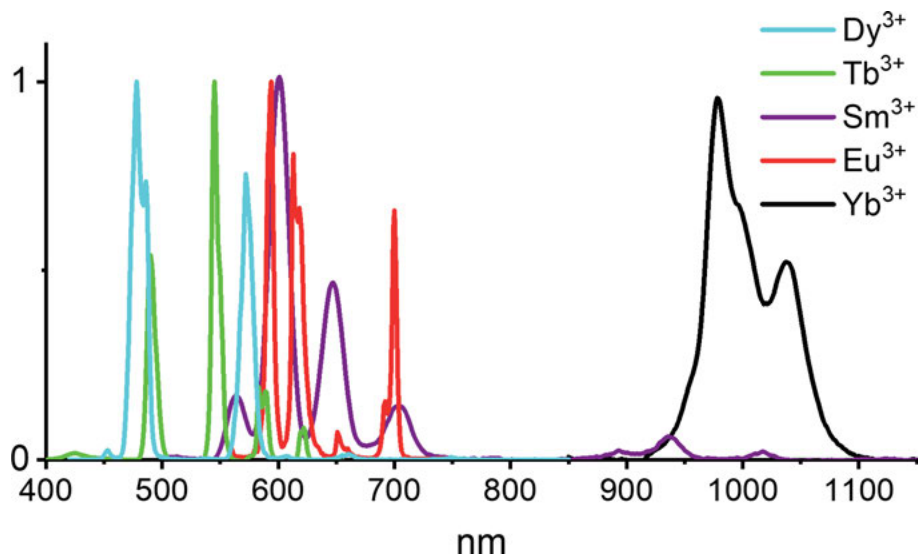
Figure 1.   Steady state luminescence spectrum of selected lanthanide(III) complexes with emssion in the visible and near infrared part of the electromagnetic spectrum.

The potential advantages of using lanthanide luminescence to generate contract in optical bioimaging are obvious. Since the early reports of imaging using lanthanide luminescence in the visible and the first detection of lanthanide luminescence in the near-infrared part of the spectrum [2, 4, 31, 32], it is a natural extension to envision highly selective and spectrally resolved images based on lanthanide luminescence [2, 4, 5, 33]. Figure 1 shows the narrow emission lines of trivalent lanthanide ions found across the visible and infrared part of the electromagnetic spectrum. Further, due to the invention of the time-gated microscope [23, 34], the diverse range of luminescence lifetimes of the lanthanides allow for both time-gated imaging and other interesting optical imaging modalities [10, 11, 13, 35–38].

The chemical properties of lanthanide(III) complexes, their bioavailability, and the stability of lanthanide-based dyes have been fully documented due to the use of lanthanide complexes in MRI [39, 40]. Thus, the application of kinetically inert lanthanide complexes in optical bioimaging is straight forward [41]. The major draw-back is the very low absorption coefficients of the lanthanide ions [15]. Although direct excitation is possible, the resulting emission intensity is low. A manifold improvement is achieved by exploiting the antenna principle [20, 21, 42, 43]. The antenna principle exploits that energy transfer from a strongly absorbing antenna chromophore to the lanthanide(III) ion populates the lanthanide-centered excited state, with an overall efficiency thousands times higher than that achieved by direct excitation. Thus, we have design principles for creating efficient lanthanide(III)-based dyes [17, 44–47], yet we are still to see widespread use of these in optical bioimaging.

2. CONTEXT AND CHALLENGES

The acceptance of lanthanide complexes as a standard tool in optical bioimaging faces several challenges that are not related to the physicochemistry of the molecular probes in question. Commercial or general availability is mandatory. As developing imaging protocols and developing new methods based on a particular molecular probe is labor-intensive, the scientists involved will demand that the supply of the molecular probe is secure. Further, even though clear advantages can be seen in adopting a new probe, there is a large inertia in the bioimaging community. If a traditional fluorophore, sourced from a reliable supplier, can be used, the drive towards using new and untested molecular probes is small. And with a 100-year history, the field of optical bioimaging has a strong, established tradition for using organic dyes.

2.1. Fluorescent Probes

Molecular probes for optical bioimaging were initially based on fluorescein and rhodamines, dyes discovered at the end of the 19th century. The work of Drexhage and others – aimed at producing better laser dyes – resulted in highly

fluorescent dyes of several classes including coumarines and oxazines [48]. With the work of Tsien and Haugland and their coworkers, both biological and synthetic fluorophores became assessable for optical bioimaging [49–53]. The Alexa dyes and green fluorescent protein were instrumental in the transformation of optical bioimaging from a specialist tool to one of the most commonly used techniques. The work is continued by Lavis, Grimm and coworkers with the open source Janelia Fluores [54–56], and by Nagano, Urano et al. [57–59]. The focus of the fluorophore development has been photostability and brightness [60], the latter has become less relevant, with the advance in optical imaging systems capable of single photon detection [61]. Nevertheless, a high brightness probe is always an advantage when considering the sample background, in particular with excitation in the blue part of the visible spectrum [62]. The commonly used fluorescent dyes for optical bioimaging have a brightness (the molar absorption coefficient at the point of excitation times the fluorescence quantum yield in the relevant medium) in the range from 20,000 to 100,000 $M^{-1}cm^{-1}$. The most popular Alexa dyes,
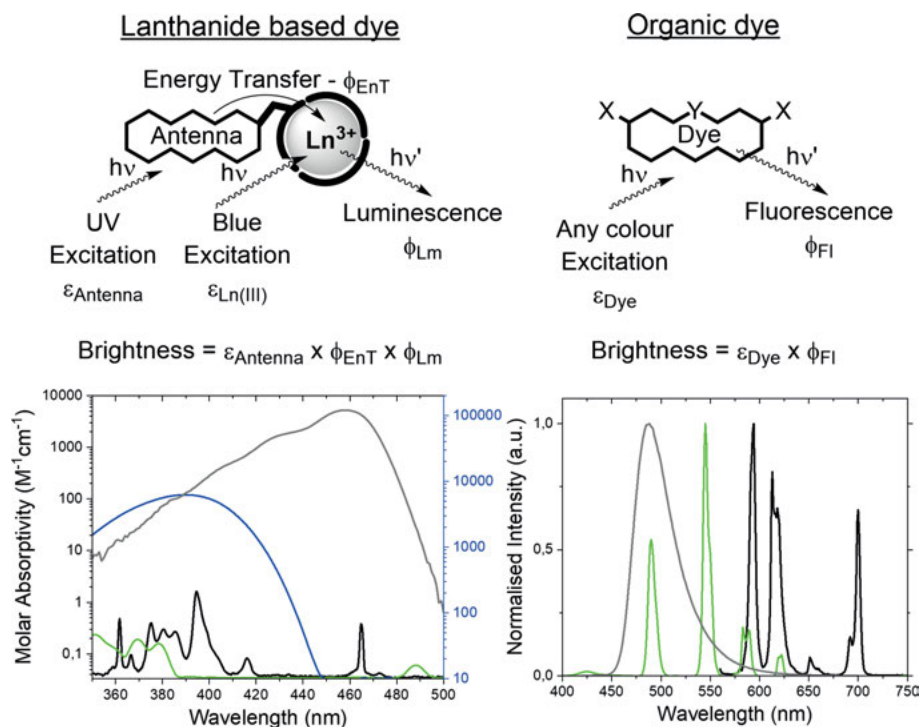
Figure 2. **Top**: the complexity of a dye using lanthanide luminescence as a signal, contrasted to simplicity of organic dyes that consist of a single subunit. **Bottom left**: Comparison of light absorption by europium(III) ions (black, left y-axis), terbium(III) ions (green, left y-axis), a thioxanthone antenna chromophore (blue, right y-axis), and fluorescein (gray, right y-axis). **Bottom right**: Comparison of light emission by europium(III) ions (black), terbium(III) ions (green), and fluorescein (gray).

cyanines, and fluoresceins have a brightness in the higher end of this range [62]. For lanthanide complexes, achieving a high brightness combined with an excitation wavelength in the visible part of the spectrum is problematic. This is one of the main reasons that the unique features of lanthanide luminescence are not widely used in molecular probes for optical bioimaging – yet.

Figure 2 shows a comparison between the lanthanide-based molecular probes and a conventional fluorescent probe. The lanthanide-based probe is based on the antenna principle and the photophysics is thus more complicated than in the organic fluorophore. To build a bright lanthanide complex, it is required that the system has a robust solution structure with an antenna dye coordinated to the lanthanide center [44, 63]. Where the fluorescence of an organic dye only requires one stimulated absorption and one spontaneous emission event, the lanthanide luminescence is a result of a three-step process: stimulated absorption, excited state energy transfer from antenna dye to lanthanide center, and spontaneous emission. This introduces additional design considerations that can be exploited, see below, but in all cases it also reduces the brightness of the lanthanide-based dye compared to the organic dye. Further, it also poses a requirement that the excited states of the antenna dye have to be higher in energy than the lanthanide centered electronic energy levels. Thus, only antenna dyes with absorption in the UV, violet and blue part of the spectrum can be used in dyes based on europium(III) and terbium(III) luminescence [44, 64].

2.2. Lanthanide Labels for Use in Imaging Cells

Cell imaging presents a key challenge, that is, getting the complex into a cell. The cellular uptake of metal complexes is poorly understood, and requires further study: however, Parker and coworkers carried out a systematic study on a library of lanthanide complexes and concluded that aspects of the ligand structure (such as the chromophore) can control the uptake pathway to a greater extent than the charge on the complex or the structure of the system as a whole [22]. For many systems, they found that micropinocytosis dominates the available uptake pathways: such mechanisms result from inclusion of the complex as part of a vesicle which then dissociates inside the cell.

Parker's Eurotracker$^®$ dyes, shown in Figure 3, exploit intrinsic uptake to deliver luminescent complexes to the mitochondria [65], endoplasmic reticulum or cytoplasm depending on structure and charge. Thus, $Eu.L^M$ targets the mitochondria, while the anionic complex $[Eu.L^L]^{3-}$ localizes in lysosomes and the cationic complex $[Eu.L^E]^{6+}$ localizes in the endoplasmic reticulum.

Directed uptake using a targeting vector offers an alternative to intrinsic uptake. For instance, in our own work we have employed tuftsin-targeting vectors to define specific uptake towards macrophage cell lines [66, 67]. This complex is internalized by active uptake, meaning that it is cell-specific, since the tuftsin sequence is specific to activating macrophages.
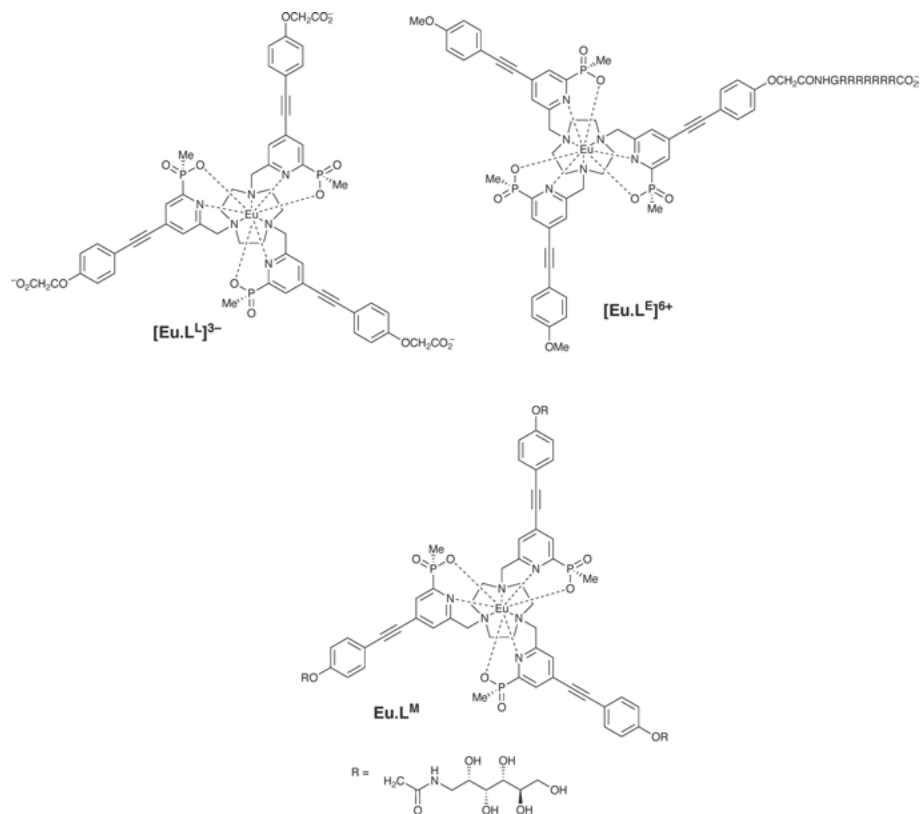
Figure 3. Three examples of the europium(III) based Eurotracker® dyes from the lab of David Parker. G = Glycine.

2.3. Challenges for Luminescent Lanthanide Ions in Bioimaging

Up to now, we have focused on agents that are effective tags, meaning that their photophysical properties are unchanged by their environment. However, there are limitations to this approach, particularly when interferents are present.

Perhaps the greatest concern is in the stability of the complexes themselves: labile complexes in which the metal ion dissociates (and is likely to be sequestered) will obviously not perform as consistently as stable ones [39, 41, 68]. It is important to note that this concern applies regardless of the affinity constant of the metal for the ligand – it is the rate constant for dissociation that really matters [41].

That the dyes do not change in the sample medium is critical for all dyes, as no secondary measurement is performed on the samples to ensure dye integrity. In some modern microscopes luminescence spectra and luminescence lifetimes can be recorded, which can give some support to the origin of the photons used

to create the images coming of the microscope, but we must be able to rely on that the dyes do not change during an imaging experiment. In addition to this universal challenge, the current lanthanide-based dyes have to rely on either two-photon or UV excitation. In essence, a specialized microscope is still needed to make use of lanthanide-based dyes [2, 6, 38, 69, 70].

Interferent ions can also pose a problem. Of these, the quenching of singlet excited states by chloride ions represents a particular issue, since variations in chloride concentration will result in changes in emission intensity as a consequence of quenching intermediate states in the energy transfer pathway. Such problems can be turned to advantage when developing responsive probes, as will be seen in the next section.

3.   RESPONSIVE LANTHANIDE COMPLEXES

In this section, we will exemplify how the spectroscopic behavior of lanthanide ions can be influenced by ionic and molecular analytes.

3.1.   Overview

Two energy transfer pathways, see Figure 4, dominate the sensitization of emission from a lanthanide ion (for a review see [71]). In most cases, the triplet state mediates energy transfer, though for ytterbium complexes a double charge transfer pathway applies where it is feasible (and particularly where spectral overlap between the triplet state and lanthanide manifolds is limited). Perturbation of the intermediate states in these pathways can result in modulation of the emission intensity, while perturbation to the lanthanide emissive state (for instance by changing the local coordination environment) can also alter the luminescence lifetime. These phenomena can be exploited to monitor changes in the surroundings of a complex.

3.2.   Probes of pH and Cations

Perhaps the simplest kind of response to consider is the response to changes in pH, and chemists have been using colorimetric indicators of pH for well over a century.

In the case of lanthanide-containing systems, the key point to note is that protons exhibit affinity for Lewis bases, resulting in the protonation of lone pairs on a ligand skeleton. In extreme cases, protons can compete with lanthanide ions for a ligand binding site, resulting in undesirable consequences in terms of complex lability. However, while all complexes exhibit a pH-dependent component to their dissociation rate [72], the pH-assisted dissociation of complexes derived from DOTA and DO3A is very slow and can usually be neglected [41]. Protonation of individual lone pairs can however be exploited to the fullest.
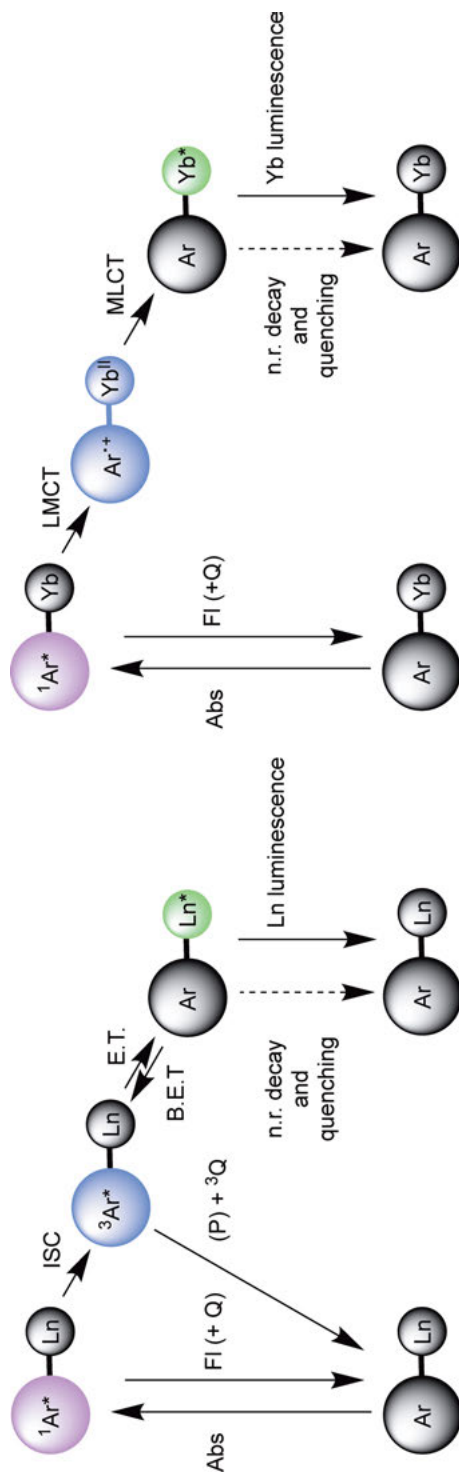
Figure 4. The two possible excited state energy transfer pathways required for efficient generation of lanthanide(III)-centered excited states and subsequent luminescence. **Left:** energy transfer between electronic energy levels of the antenna chromophore and lanthanide(III) ion. **Right:** electron transfer between the excited antenna chromophore and the lanthanide(III) ion. This pathway is only possible if the lanthanide(II) redox state is accessible, i.e., for europium and ytterbium. The energy transfer mechanism is explained by the Dexter and Förster theory and must be between isoenergetic states. The electron transfer mechanism follows the Marcus theory, which allows energy to be dissipated along the reaction coordinate. Abbreviations used in the figure: Abs: light absorption; Fl + Q: fluorescence, internal conversion and quenching; ISC: inter-system crossing; (P) + Q: phosphorescence, ISC and quenching of the triplet state; E. T.: energy transfer; B. E. T.: back energy transfer; n.r. decay: non-radiative decay; LMCT: ligand-to-metal charge transfer; MLCT: metal-to-ligand charge transfer.
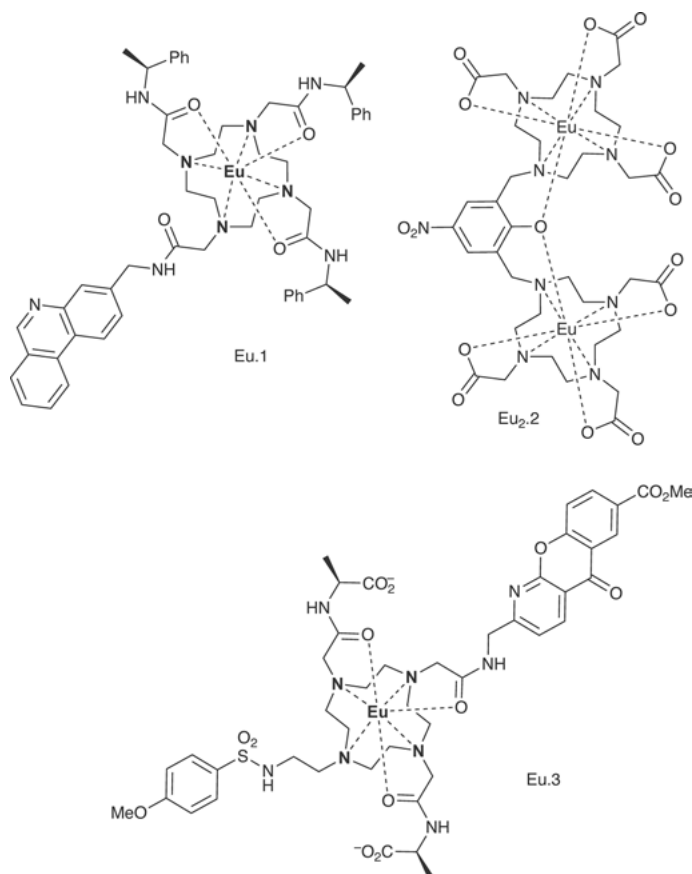
Figure 5. Examples of lanthanide(III) complexes with a luminescence spectrum that is responsive to pH.

Early approaches made use of remote lone pairs such as those on pendent phenanthridine or quinoline chromophores (see Ln.1 in Figure 5) [73]. Such protonation events change the energies of the chromophore-centered excited states and the redox potential of the chromophore itself. For the energy change to influence the behavior of the complex to a significant degree, the donor triplet must be close enough in energy to the lanthanide emissive state to permit reversible energy transfer, and energy transfer fast enough to allow pre-equilibration of the triplet state and the lanthanide state. In such circumstances (e.g., with Tb.1), collisional quenching of the triplet state by oxygen results in a reduced emission intensity and lifetime in the protonated form of the complex [74]. In such circumstances, both pH and oxygen concentration will influence the intensity of the observed luminescence. By contrast, Eu.1 and Yb.1 exhibit pH-dependent luminescence that is independent of oxygen concentration [75], but do so for different reasons. In both cases, protonation of the phenanthridine nitrogen atom
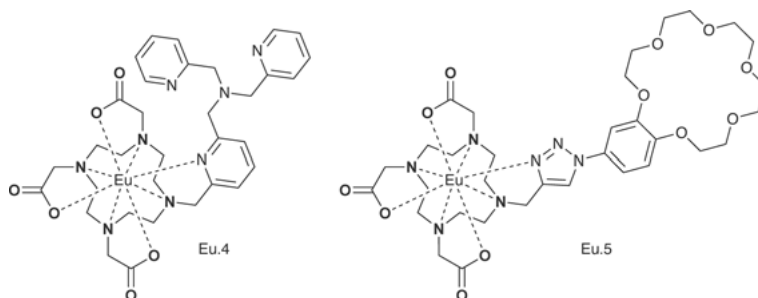
Figure 6. Examples of lanthanide(III) complexes with a luminescence spectrum that is responsive to transition and alkaline metal ions.

inhibits photoelectron transfer from the chromophore to the lanthanide, but the outcomes are different. In the case of Eu.1, the resulting ligand-to-metal charge transfer state lies lower in energy than the emissive $^5D_0$ state, meaning that luminescence is quenched at high pH. By contrast, in Yb.1 the spectral overlap between the chromophore triplet state and the $^2F_{5/2}$ emissive state is negligible (meaning that energy transfer is rate-determining and ineffective). Deprotonation enables the charge transfer mechanism, and switches the luminescence on.

Charge transfer can also be exploited in other ways to exploit pH-dependent behavior. For instance, in $Eu_2.2$ (Figure 5) coordination of both europium ions to a bridging phenolate inhibits charge transfer [76], resulting in intense luminescence. However, at low pH, where protonation of the chromophore inhibits binding of a second lanthanide ion, electron transfer is not inhibited, and luminescence is quenched.

Alternative approaches may involve changes to coordination at the metal center. For instance, in Eu.3 (Figure 5) [77], coordination of a deprotonated sulfonamide group results in displacement of water from the lanthanide center, giving rise in turn to an increase in metal centered luminescence (since vibrational harmonics of local O-H oscillators can assist non-radiative deactivation of the metal center).

While protons are ubiquitous in aqueous media, the recognition of other cations adds a new dimension to the problem; the structure must incorporate a binding site which displays sufficient selectivity for the target anion over other competitor cations (including protons). This has been addressed in detail for a number of ions, notably zinc and the alkali metals (e.g., in Eu.4 and Eu.5, Figure 6) [78, 79]. Such systems employ the same general approaches to perturbing the excited state manifold to modulate luminescence.

3.3.   Probes of Anion Concentration

The development of probes for anions presents a different set of challenges, but lanthanides offer one significant advantage over organic molecules in that their charge can attract anions, resulting in inner sphere coordination provided that the attraction can overcome hydration of the ion and the metal center.
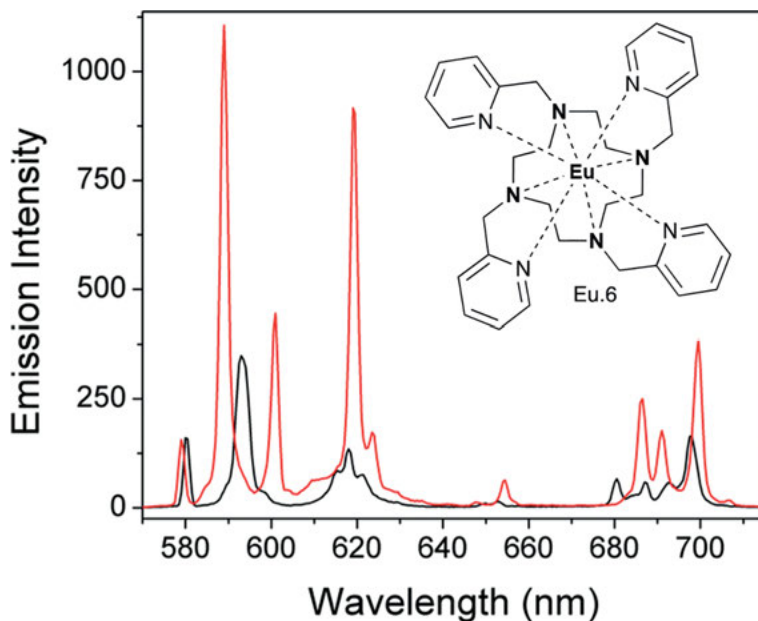
Figure 7. Luminescence spectra of Eu.6 in the presence (red line) and absence (black line) of fluoride ions.

We have already mentioned that chloride ions quench the luminescence from lanthanide emissive states by collisional deactivation. This process occurs via photoelectron transfer in the encounter complex. As such, it is not specific to any single complex (though pCl can be inferred in systems where it is known that the complex does not interact with other interferent analytes) [80].

By contrast, fluoride ions displace water from positively charged lanthanide complexes, giving rise to changes in luminescence intensity and lifetime [81–83]. Notably, such changes also influence the form of the spectrum, since changes in the local ligand field alter the splitting of the mJ states in the lanthanide ground state and excited state manifolds (for an example, see Figure 7, which shows the differences in the emission spectrum for Eu.6).

Other ions can also be used to modulate lanthanide luminescence. Perhaps phosphate offers the best-known example; coordination of phosphate by complexes such as Eu.7 (Figure 8) displaces solvent from the lanthanide center [84, 85], and enhances the luminescence intensity and lifetime. Other anionic species such as hydrogen carbonate act as potential interferents in such systems; selectivity for one ion over another can be achieved through ligand design [86].

Chemical reactivity can also be exploited in probes for ions. At their simplest, such probes can only monitor a single event; as in the hydrogensulfide-mediated reduction of an azide to an amine in the case of Eu.8 (Figure 8) [87]. Reversible reactions can also be used to sense changes in analyte concentration. For instance, Eu.9 (Figure 8) reacts reversibly with cyanide ions to form cyanohydrins [88],
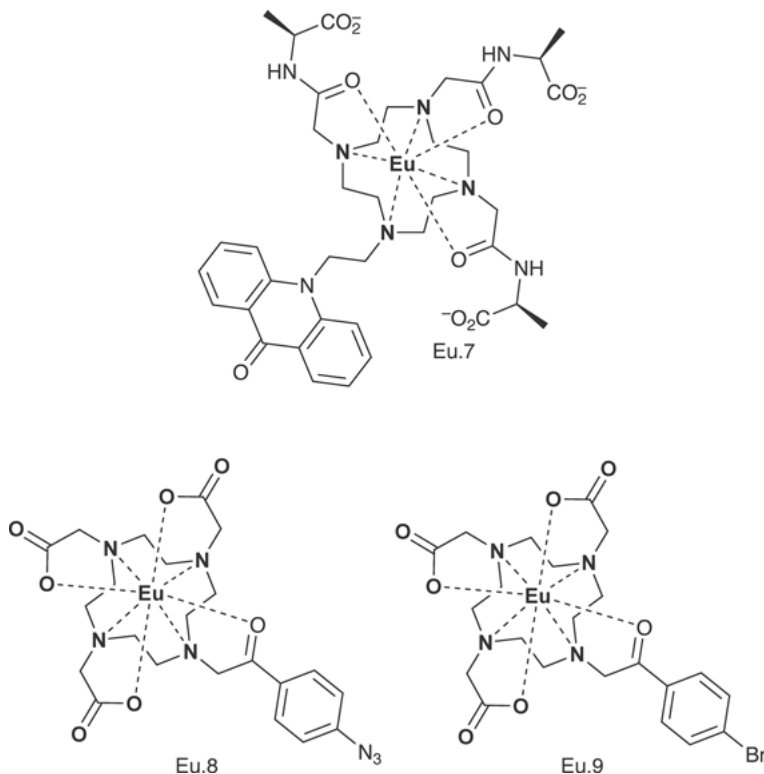
Figure 8. Selected anion-responsive and reactivity-based probes based on lanthanide ions.

inhibiting energy transfer from a chromophore to the metal by removing the possibility of through bond energy transfer by Dexter exchange and enforcing less-efficient through space (Förster) energy transfer processes [89–91].

3.4. Detection of Oxygen

Oxygen plays a vital and obvious role in biology, and is unusual in existing as a diatomic molecule with a triplet ground state. This triplet state can quench excited state triplets very effectively, and we have already seen that it can provide a pathway for non-radiative deactivation of intermediate triplet states in the sensitization cascade. In such cases, collisional deactivation is observed via the triplet state: collisional interactions with oxygen can mediate intersystem crossing from the singlet state to the triplet and quench the triplet.

We have already mentioned quenching of lanthanide luminescence by oxygen in systems where fast energy transfer from the triplet is reversible by thermal repopulation of the triplet state from the lanthanide emissive state. In such sys-
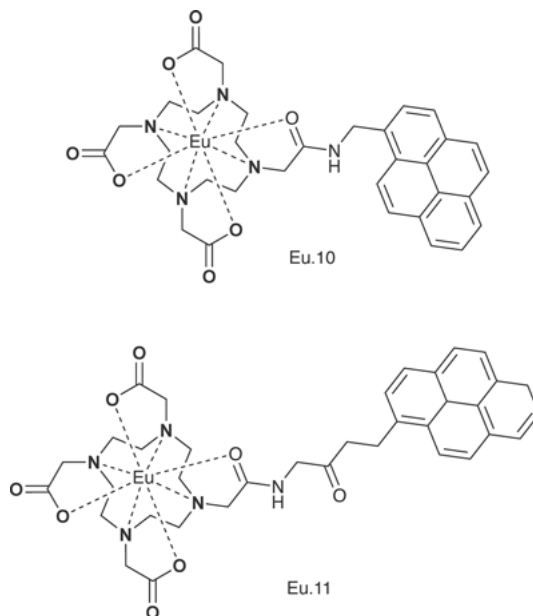
Figure 9. Oxygen-responsive lanthanide(III) complexes with the response to the oxygen concentration modulated by the distance between lanthanide ion and pyrene antenna chromophore.

tems (e.g., Tb.1, Figure 5) [92, 93], pre-equilibration of the excited state with the ground state means that quenching of the triplet state by oxygen changes both the luminescence lifetime and the luminescence intensity.

Alternatively, controlling the rate of energy transfer can be used to control the response to oxygen. In systems where energy transfer occurs through space (i.e., where an aliphatic spacer separates a chromophore from the coordinating group), the rate of energy transfer diminishes as the separation between donor and acceptor increases. This is possible for the same chromophore-lanthanide pair. For instance, in Eu.10 (Figure 9), pre-equilibration of the triplet and lanthanide emissive state results in oxygen quenching the luminescence intensity and lifetime in the commonplace way; however, Eu.11 (Figure 9, which has an extended spacer) exhibits slow energy transfer, and emission intensity is reduced by oxygen without changing the observed luminescence lifetime [94].

4. QUANTIFIABLE LANTHANIDE PROBES

The use of responsive probes presents a challenge in that the behavior of the complexes in biology is always going to be influenced by other factors, particularly the kinetics associated with their transport and removal from cells, but also their metabolism.

For a probe whose signal is merely switched on and off by an external stimulus, it is impossible to define whether a given signal arises from (for instance) a small quantity of probe in the "on" state, or a large quantity of probe in the "off" state. While this does not matter for qualitative measurements on relatively short timescales – where the essence of the experiment is to observe change – it is certainly important for systems in which a more definitive answer is required.

Quantification is possible in a number of ways. The simplest way for systems in which a change in lifetime is observed is to measure the intensity of the emission in a number of different windows after an excitation pulse. These can then be used to define the balance between emissive species with known lifetimes [10, 13, 95, 96].

However, in systems where the lifetime does not change, this approach is obviously invalid. Europium complexes offer an alternative, in that the $^5D_0$-$^7F_2$ transition in their emission spectra is hypersensitive to local coordination environment, meaning that the ratio of the intensity of this transition to others in the spectrum can be used to quantify the balance between species. Where there is a direct change to the local coordination environment (e.g., for Eu.6 (Figure 7) or Eu.7 (Figure 8)), these changes can be used in ratiometric measurements of concentration. This strategy has been exploited to the full by Parker and coworkers in the quantification of citrate in assays for the early detection of prostate cancer [97].

Once again, hypersensitive transitions are not a panacea. In many systems, the perturbation to the lanthanide coordination environment is small, meaning that it is very difficult to measure ratios with certainty. This is particularly true when considering ligand-centered processes. This difficulty can, however, be overcome by observing more than one signal. At the simplest, this can involve looking at other molecules in the process; Yb.12 (Figure 10) exhibits slow energy transfer from the chromophore to ytterbium, meaning that the intensity of the ytterbium-centered emission at 980 nm is modulated by oxygen [98]. Collisional deactivation of the chromophore triplet state results in formation of singlet oxygen,

Yb.12
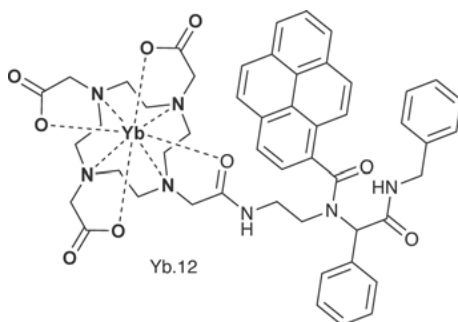
Figure 10. Ytterbium(III) complex where the ratio between the ytterbium(III)-centered emission and singlet oxygen emission can be used to determine the oxygen concentration of a sample.
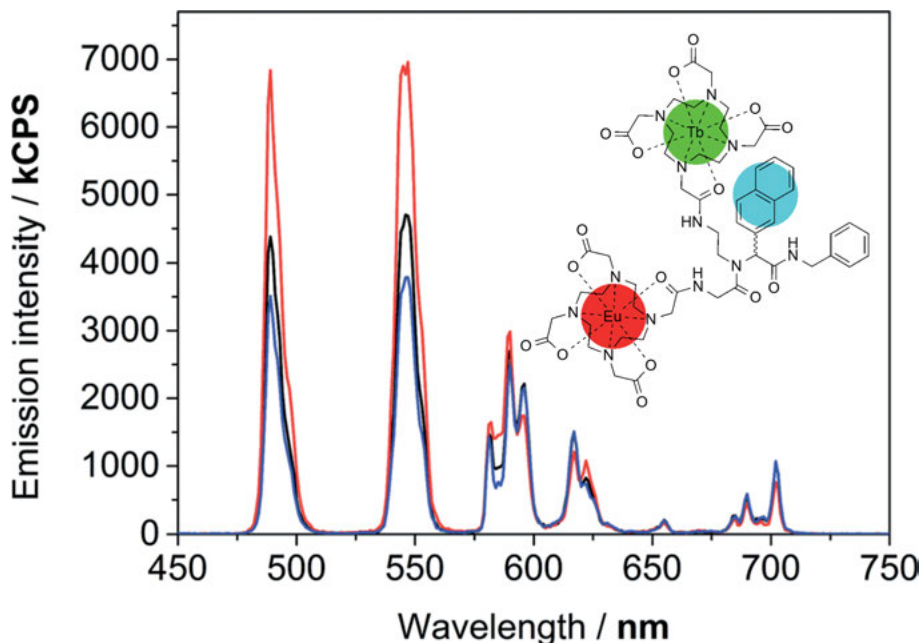
Figure 11. Bimetallic lanthanide(III) complex Eu.L^{O2}.Tb that has a luminescence spectrum that shows a ratiometric change proportional to the oxygen concentration. The intensity is measured in kilocounts per second (kCPS), and the emission spectra are shown as recorded in an atmosphere with no oxygen (red), with ambient oxygen (black), and saturated with oxygen (blue).

which is itself luminescent at 1270 nm. Thus, collisional quenching diminishes the intensity at 980 nm but increases intensity at 1270 nm, and the ratio of these two signals can be used to quantify oxygen concentrations.

Bimetallic complexes may offer a more general solution to the problem of quantification – exploiting the luminescence from one metal center that does not respond to its surroundings to provide a "reference channel" that can be compared to the intensity of emission from a second center that provides an analyte-dependent "signal". The ratio of the two provides a calibration curve that can be used to quantify the analyte. We have used this approach to quantify oxygen concentrations using Eu.L^{O2}.Tb (see Figure 11) [99]. In this complex, through space energy transfer to europium from the naphthyl triplet state is rapid, while energy transfer to terbium occurs much more slowly. As a consequence, oxygen modulates the intensity of terbium emission without significantly altering the intensity of the europium emission, and the ratio of emission intensities can provide a calibration curve to measure oxygen.

5. GENERAL CONCLUSIONS

Lanthanide complexes offer many advantages in optical imaging, including facile time-gating to eliminate background noise, low detection limits and considerable possibilities for lifetime- or wavelength-based approaches to multiplexing.

Challenges remain before the lanthanides can fulfil their full potential as imaging agents. While their role as tags and stains is now well established, responsive probes create new challenges. Chief among this is the issue of selectivity when multiple analytes are being considered. True specificity is very hard to achieve, though we have seen how chloride ions can be detected collisionally by complexes that do not interact with other analytes. For other analytes, it is important to appreciate that complexes are selective rather than specific, and that interferents may alter signal intensity or lifetime. Accordingly, the results from a multiplexed approach will always need to be considered as a whole: if we consider a system with n probe complexes and m analytes, it is clear that there must be at least as many probes as analytes under study. Furthermore, all probes may respond to some degree to all the analytes, but their responses will differ as a consequence of individual complexes having different selectivities for different species. In such circumstances, the use of neural network analysis (or the solution of multiple simultaneous equations) can yield direct information about change [13, 80, 95].

For the future, we expect to see increased use of quantifiable probes in imaging. The development of bimetallic complexes has opened up the field beyond the niche of europium complexes, and stands ready to provide valuable information about many species. There is much to be done, but the potential for success is great.

ACKNOWLEDGMENTS

ABBREVIATIONS

DO3A   1,4,7,10-tetraazacyclododecane-1,4,7-triacetate
DOTA   1,4,7,10-tetraazacyclododecane-1,4,7,10-tetraacetate

REFERENCES

1. Searching the Web of Science for records using lanthanides (Eu and Tb) in imaging outside the field of chemistry returns 88 (76) of 108,356 records. Search terms used ALL=(XX AND imaging) AND SU=(biology NOT chemistry) 20/01/2020 10:47.
2. G. Vereb, E. Jares-Erijman, P. R. Selvin, T. M. Jovin, *Biophys. J.* **1998**, *74*, 2210–2222.

3. P. R. Selvin, *Annu. Rev. Biophys. Biomol. Struct.* **2002**, *31*, 275–302.

4. A. Beeby, S. W. Botchway, I. M. Clarkson, S. Faulkner, A. W. Parker, D. Parker, J. A. G. Williams, *J. Photochem. Photobio. B-Biology* **2000**, *57*, 83–89.

5. L. Charbonniere, R. Ziessel, M. Guardigli, A. Roda, N. Sabbatini, M. Cesario, *J. Am. Chem. Soc.* **2001**, *123*, 2436–2437.

6. J. H. Yu, D. Parker, R. Pal, R. A. Poole, M. J. Cann, *J. Am. Chem. Soc.* **2006**, *128*, 2294–2299.

7. B. Song, C. D. Vandevyver, A. S. Chauvin, J.-C. G. Bünzli, *Org. Biomol. Chem.* **2008**, *6*, 4125–4133.

8. N. Gahlaut, L. W. Miller, *Cytometry. Part A* **2010**, *77*, 1113–1125.

9. A. D'Aleo, A. Bourdolle, S. Brüstlein, T. Fauquier, A. Grichine, A. Duperray, P. L. Baldeck, C. Andraud, S. Brasselet, O. Maury, *Angew. Chem.* **2012**, *51*, 6622–6625.

10. Z. Liao, M. Tropiano, S. Faulkner, T. Vosch, T. J. Sørensen, *RSC Adv.* **2015**, 70282–70286.

11. Z. Liao, M. Tropiano, K. Mantulnikovs, S. Faulkner, T. Vosch, T. J. Sørensen, *Chem. Commun.* **2015**, *51*, 2372–2375.

12. A. T. Frawley, R. Pal, D. Parker, *Chem. Commun.* **2016**, *52*, 13349–13352.

13. M. R. Carro-Temboury, R. Arppe, C. Hempel, T. Vosch, T. J. Sørensen, *Plos One* **2017**, *12*, e0189529.

14. U. Cho, D. P. Riordan, P. Ciepla, K. S. Kocherlakota, J. K. Chen, P. B. Harbury, *Nature Chem. Biol.* **2018**, *14*, 15–21.

15. R. Arppe-Tabbara, M. R. Carro-Temboury, C. Hempel, T. Vosch, T. J. Sørensen, *Chem. Eur. J.* **2018**, *24*, 11885–11889.

16. J.-C. G. Bünzli, in *Luminescence of Lanthanide Ions in Coordination Compounds and Nanomaterials*, John Wiley & Sons Ltd, **2014**, pp. 125–196.

17. M. C. Heffern, L. M. Matosziuk, T. J. Meade, *Chem. Rev.* **2014**, *114*, 4496–4539.

18. J. M. Zwier, H. Bazin, L. Lamarque, G. Mathis, *Inorg. Chem.* **2014**, *53*, 1854–1866.

19. M. Cardoso Dos Santos, J. Goetz, H. Bartenlian, K. L. Wong, L. J. Charbonnière, N. Hildebrandt, *Bioconj. Chem.* **2018**, *29*, 1327–1334.

20. M. Latva, H. Takalo, V.-M. Mukkala, C. Matachescu, J. C. Rodriguez-Ubis, J. Kankare, *J. Luminesc.* **1997**, *75*, 149–169.

21. E. G. Moore, A. P. Samuel, K. N. Raymond, *Acc. Chem. Res.* **2009**, *42*, 542–552.

22. C. P. Montgomery, B. S. Murray, E. J. New, R. Pal, D. Parker, *Acc. Chem. Res.* **2009**, *42*, 925–937.

23. H. B. Beverloo, A. v. Schadewijk, S. v. Gelderen-Boele, H. J. Tanke, *Cytometry* **1990**, *11*, 784–792.

24. H. S. Afsari, M. Cardoso Dos Santos, S. Lindén, T. Chen, X. Qiu, P. M. P. van Bergen en Henegouwen, T. L. Jennings, K. Susumu, I. L. Medintz, N. Hildebrandt, L. W. Miller, *Science Advances* **2016**, *2*, e1600265.

25. A. Foucault-Collet, C. M. Shade, I. Nazarenko, S. Petoud, S. V. Eliseeva, *Angew. Chem. Int. Ed.* **2014**, *53*, 2927–2930.

26. A. T. Bui, M. Beyler, A. Grichine, A. Duperray, J. C. Mulatier, Y. Guyot, C. Andraud, R. Tripier, S. Brasselet, O. Maury, *Chem. Commun.* **2017**, *53*, 6005–6008.

27. N. Hamon, M. Galland, M. Le Fur, A. Roux, A. Duperray, A. Grichine, C. Andraud, B. Le Guennic, M. Beyler, O. Maury, R. Tripier, *Chem. Commun.* **2018**, *54*, 6173–6176.

28. A. T. Bui, A. Grichine, S. Brasselet, A. Duperray, C. Andraud, O. Maury, *Chem. Eur. J.* **2015**, *21*, 17757–17761.

29. A. Foucault-Collet, K. A. Gogick, K. A. White, S. Villette, A. Pallier, G. Collet, C. Kieda, T. Li, S. J. Geib, N. L. Rosi, S. Petoud, *Proc. Nat. Ac. Sci. USA* **2013**, *110*, 17199–17204.

30. I. Martinić, S. V. Eliseeva, T. N. Nguyen, F. Foucher, D. Gosset, F. Westall, V. L. Pecoraro, S. Petoud, *Chem. Sci.* **2017**, *8*, 6042–6050.

31. A. Beeby, R. S. Dickins, S. Faulkner, D. Parker, J. A. Gareth Williams, *Chem. Commun.* **1997**, 1401–1402.

32. A. Beeby, S. Faulkner, *Chem. Phys. Lett.* **1997**, *266*, 116–122.

33. N. Weibel, L. J. Charbonniere, M. Guardigli, A. Roda, R. Ziessel, *J. Am. Chem. Soc.* **2004**, *126*, 4888–4896.

34. G. Marriott, R. M. Clegg, D. J. Arndt-Jovin, T. M. Jovin, *Biophys. J.* **1991**, *60*, 1374–1387.

35. L. J. Charbonniere, N. Hildebrandt, R. F. Ziessel, H. G. Lohmannsroben, *J. Am. Chem. Soc.* **2006**, *128*, 12800–12809.

36. S. Faulkner, S. J. A. Pope, B. P. Burton-Pye, *Appl. Spec. Rev.* **2005**, *40*, 1–31.

37. A. D'Aleo, G. Pompidor, B. Elena, J. Vicat, P. L. Baldeck, L. Toupet, R. Kahn, C. Andraud, O. Maury, *ChemPhysChem* **2007**, *8*, 2125–2132.

38. A. Picot, A. D'Aléo, P. L. Baldeck, A. Grichine, A. Duperray, C. Andraud, O. Maury, *J. Am. Chem. Soc.* **2008**, *130*, 1532–1533.

39. P. Caravan, J. J. Ellison, T. J. McMurry, R. B. Lauffer, *Chem. Rev.* **1999**, *99*, 2293–2352.

40. J. Wahsner, E. M. Gale, A. Rodríguez-Rodríguez, P. Caravan, *Chem. Rev.* **2019**, *119*, 957–1057.

41. T. J. Sørensen, S. Faulkner, *Acc. Chem. Res.* **2018**, *51*, 2493–2501.

42. B. Alpha, R. Ballardini, V. Balzani, J. M. Lehn, S. Perathoner, N. Sabbatini, *Photochem. Photobiol.* **1990**, *52*, 299–306.

43. A. Dadabhoy, S. Faulkner, P. G. Sammes, *J. Chem. Soc., Perkin Trans. 2* **2000**, 2359–2360.

44. L. G. Nielsen, A. K. R. Junker, T. J. Sørensen, *Dalton Trans.* **2018**, *47*, 10360–10376.

45. J.-C. G. Bünzli, C. Piguet, *Chem. Soc. Rev.* **2005**, *34*, 1048–1077.

46. L. Armelao, S. Quici, F. Barigelletti, G. Accorsi, G. Bottaro, M. Cavazzini, E. Tondello, *Coord. Chem. Rev.* **2010**, *254*, 487–505.

47. J.-C. G. Bünzli, *Coord. Chem. Rev.* **2015**, *293*, 19–47.

48. K. H. Drexhage, *Top. Appl. Phys.* **1973**, *1*, 144–193.

49. A. Minta, J. P. Y. Kao, R. Y. Tsien, *J. Biol. Chem.* **1989**, *264*, 8171–8178.

50. B. N. G. Giepmans, S. R. Adams, M. H. Ellisman, R. Y. Tsien, *Science* **2006**, *312*, 217–224.

51. R. P. Haugland, *Handbook of Fluorescent Probes and Research Chemicals*, 11th ed., Molecular Probes, Eugene, Oregon, **2010**.

52. J. E. Berlier, A. Rothe, G. Buller, J. Bradford, D. R. Gray, B. J. Filanoski, W. G. Telford, S. Yue, J. X. Liu, C. Y. Cheung, W. Chang, J. D. Hirsch, J. M. Beechem, R. P. Haugland, *J. Histochem. Cytochem.* **2003**, *51*, 1699–1712.

53. N. Panchuk-Voloshina, R. P. Haugland, J. Bishop-Stewart, M. K. Bhalgat, P. J. Millard, F. Mao, W. Y. Leung, *J. Histochem. Cytochem.* **1999**, *47*, 1179–1188.

54. L. M. Wysocki, L. D. Lavis, *Current Op. Chem. Biol.* **2011**, *15*, 752–759.

55. J. B. Grimm, B. P. English, J. Chen, J. P. Slaughter, Z. Zhang, A. Revyakin, R. Patel, J. J. Macklin, D. Normanno, R. H. Singer, T. Lionnet, L. D. Lavis, *Nat. Methods* **2015**, *12*, 244–250.

56. J. B. Grimm, A. K. Muthusamy, Y. Liang, T. A. Brown, W. C. Lemon, R. Patel, R. Lu, J. J. Macklin, P. J. Keller, N. Ji, L. D. Lavis, *Nat. Methods* **2017**, *14*, 987.

57. T. Myochin, K. Hanaoka, S. Iwaki, T. Ueno, T. Komatsu, T. Terai, T. Nagano, Y. Urano, *J. Am. Chem. Soc.* **2015**, *137*, 4759–4765.

58. T. Ueno, Y. Urano, K. Setsukinai, H. Takakusa, H. Kojima, K. Kikuchi, K. Ohkubo, S. Fukuzumi, T. Nagano, *J. Am. Chem. Soc.* **2004**, *126*, 14079–14085.

59. Y. Urano, M. Kamiya, K. Kanda, T. Ueno, K. Hirose, T. Nagano, *J. Am. Chem. Soc.* **2005**, *127*, 4888–4894.

60. C. R. Benson, L. Kacenauskaite, K. L. VanDenburgh, W. Zhao, B. Qiao, T. Sadhukhan, M. Pink, J. Chen, S. Borgi, C.-H. Chen, B. J. Davis, Y. C. Simon, K. Raghavachari, B. W. Laursen, A. H. Flood, *Chem.* **2020**, *6*, 1978–1997.

61. R. Arppe, M. R. Carro-Temboury, C. Hempel, T. Vosch, T. J. Sørensen, *Plos One* **2017**, *12*, e0188359.

62. L. D. Lavis, R. T. Raines, *ACS Chem. Biol.* **2008**, *3*, 142–155.

63. L. G. Nielsen, T. J. Sørensen, *Inorg. Chem.* **2019**, *59*, 94–105.

64. *Lanthanide Luminescence*, Eds. P. Hänninen, H. Härmä, *Springer Series on Fluorescence*, *Vol. 7*, Springer, Heidelberg, **2011**, pp. 1–388.

65. S. J. Butler, L. Lamarque, R. Pal, D. Parker, *Chem. Sci.* **2014**, *5*, 1750–1756.

66. R. J. Aarons, J. K. Notta, M. M. Meloni, J. Feng, R. Vidyasagar, J. Narvainen, S. Allan, N. Spencer, R. A. Kauppinen, J. S. Snaith, S. Faulkner, *Chem. Commun.* **2006**, 909–911.

67. J. Feng, M. M. Meloni, S. M. Allan, S. Faulkner, J. Narvainen, R. Vidyasagar, R. Kauppinen, *Contrast Media & Molecular Imaging* **2010**, *5*, 223–230.

68. E. M. Gale, P. Caravan, A. G. Rao, R. J. McDonald, M. Winfeld, R. J. Fleck, M. S. Gee, *Pediatric Radiology* **2017**, *47*, 507–521.

69. R. Pal, A. Beeby, *Meth. Appl. Fluoresc.* **2014**, *2*, 037001.

70. L. Zhang, X. Zheng, W. Deng, Y. Lu, S. Lechevallier, Z. Ye, E. M. Goldys, J. M. Dawes, J. A. Piper, J. Yuan, M. Verelst, D. Jin, *Sci. Rep.* **2014**, *4*, 6597.

71. S. Faulkner, L. S. Natrajan, W. S. Perry, D. Sykes, *Dalton Trans.* **2009**, 3890–3899.

72. É. Tóth, R. Király, J. Platzek, B. Radüchel, E. Brücher, *Inorg. Chim. Acta* **1996**, *249*, 191–199.

73. D. Parker, *Coord. Chem. Rev.* **2000**, *205*, 109–130.

74. D. Parker, P. Kanthi Senanayake, J. A. Gareth Williams, *J. Chem. Soc., Perkin Trans. 2* **1998**, 2129–2140.

75. A. Beeby, S. Faulkner, J. A. G. Williams, *J. Chem. Soc., Dalton Trans.* **2002**, 1918–1922.

76. O. A. Blackburn, M. Tropiano, L. S. Natrajan, A. M. Kenwright, S. Faulkner, *Chem. Commun.* **2016**, *52*, 6111–6114.

77. D. G. Smith, B. K. McMahon, R. Pal, D. Parker, *Chem. Commun.* **2012**, *48*, 8520–8522.

78. A. K. R. Junker, M. Tropiano, S. Faulkner, T. J. Sørensen, *Inorg. Chem.* **2016**, *55*, 12299–12308.

79. S. J. A. Pope, R. H. Laye, *Dalton Trans.* **2006**, 3108–3113.

80. S. Faulkner, D. Parker, J. A. G. Williams, in *Supramolecular Science: Where It Is and Where It Is Going*, Eds. R. Ungaro, E. Dalcanale, *Nato Science Series C* **1999**, pp. 53–66.

81. O. A. Blackburn, N. F. Chilton, K. Keller, C. E. Tait, W. K. Myers, E. J. McInnes, A. M. Kenwright, P. D. Beer, C. R. Timmel, S. Faulkner, *Angew. Chem. Int. Ed.* **2015**, *54*, 10783–10786.

82. O. A. Blackburn, A. M. Kenwright, P. D. Beer, S. Faulkner, *Dalton Trans.* **2015**, *44*, 19509–19517.

83. O. A. Blackburn, A. M. Kenwright, A. R. Jupp, J. M. Goicoechea, P. D. Beer, S. Faulkner, *Chem. Eur. J.* **2016**, *22*, 8929–8936.

84. P. Atkinson, Y. Bretonniere, D. Parker, *Chem. Commun.* **2004**, 438–439.

85. L. Bridou, L. G. Nielsen, T. J. Sørensen, *J. Rare Earths* **2020**, *38*, 498–505.

86. J. I. Bruce, R. S. Dickins, L. J. Govenlock, T. Gunnlaugsson, S. Lopinski, M. P. Lowe, D. Parker, R. D. Peacock, J. J. B. Perry, S. Aime, M. Botta, *J. Am. Chem. Soc.* **2000**, *122*, 9674–9684.

87. M. Tropiano, S. Faulkner, *Chem. Commun.* **2014**, *50*, 4696–4698.

88. J. D. Routledge, X. Zhang, M. Connolly, M. Tropiano, O. A. Blackburn, A. M. Kenwright, P. D. Beer, S. Aldridge, S. Faulkner, *Angew. Chem. Int. Ed.* **2017**, *56*, 7783–7786.

89. D. L. Dexter, *J. Chem. Phys.* **1953**, *21*, 836–850.

90. T. Forster, *Ann. Phys. (Berlin)* **1948**, *2*, 55–75.

91. G. J. Kavarnos, *Fundamentals of Photoinduced Electron Transfer*, *Vol. 1*, VCH, New York, **1993**, pp. 1–359.

92. A. Beeby, S. Faulkner, D. Parker, J. A. G. Williams, *J. Chem. Soc., Perkin Trans. 2* **2001**, 1268–1273.

93. A. Beeby, D. Parker, J. A. G. Williams, *J. Chem. Soc., Perkin Trans. 2* **1996**, 1565–1579.

94. R. Hueting, M. Tropiano, S. Faulkner, *RSC Adv.* **2014**, *4*, 44162–44165.

95. M. R. Carro-Temboury, R. Arppe, T. Vosch, T. J. Sørensen, *Science Advances* **2018**, *4*, e1701384.

96. J. R. Lakowicz, *Principles of Fluorescence Spectroscopy*, 3rd ed., Springer-Verlag, New York, **2006**, pp. 1–954.

97. R. Pal, D. Parker, L. C. Costello, *Org. Biomol. Chem.* **2009**, *7*, 1525–1528.

98. A. Watkis, R. Hueting, T. J. Sørensen, M. Tropiano, S. Faulkner, *Chem. Commun.* **2015**, *51*, 15633–15636.

99. T. J. Sørensen, A. M. Kenwright, S. Faulkner, *Chem. Sci.* **2015**, *6*, 2054–2059.

6

Radiometals for Positron Emission Tomography (PET) Imaging

Shin Hye Ahn, Alexia G. Cosby, Angus J. Koller, Kirsten E. Martin, Apurva Pandey, Brett A. Vaughn, and Eszter Boros

Department of Chemistry, Stony Brook University, Stony Brook, NY 11794, USA

<eszter.boros@stonybrook.edu>

Abstract: The recent, more widespread clinical availability of standalone PET and PET/CT clinical scanners in conjunction with the commercialization of 16 MeV cyclotron systems that enable p,n and d,n nuclear transformations to produce a variety of positron emissive isotopes continues to revolutionize nuclear medicine. Paired with advances in solid targetry and rekindled interest in radionuclide therapy, metallic PET radioisotopes are experiencing a resurgence in the field of radiotracer development. Radiometals provide a broad range of radioactive half-lives and are readily compatible with temperature- and solvent-sensitive biologics – a stark contrast with low-yielding ^{18}F or ^{11}C radiochemistry. Herein, we provide the reader with a timely review on recent developments in radiometal isotope synthesis, ideal separation and subsequent chelation strategies, followed by illustrative examples of applications for preclinical and clinical imaging.

1. INTRODUCTION

Nuclear medicine utilizes two distinct nuclear imaging techniques, specifically single photon emission computed tomography (SPECT) and positron emission tomography (PET). Isotopes with unstable nuclei and a surplus of protons can undergo a nuclear transformation, where a proton in the nucleus is transformed to a neutron. This process liberates a positron, which is emitted from the nucleus. Following ejection, the positron eventually encounters an electron which results in an annihilation event that produces two 511 keV photons which are emitted at a 180° angle to each other. These photons can be detected using a circular detector ring comprised of lead collimators and allow for a construction of a three-dimensional "heatmap" of the location of the positron-emitting isotope within the scanner field of view. Modern PET imaging provides an intrinsic resolution of 2–4 mm and a reconstructed resolution of 5–8 mm in human PET scanners [1].

Consequently, the incorporation of PET nuclides into molecules that enable the detection and monitoring of disease-specific biochemical processes has the potential to have immense clinical impact. The focus of developmental radiochemistry and radiotracer design has long been dictated by the availability and broad accessibility of corresponding radionuclides. As a consequence of the availability of the SPECT nuclide ^{99m}Tc from a portable ^{99}Mo generator in the second half of the 20th century, a series of ^{99m}Tc tracers were developed, entered the clinic and remain important diagnostic nuclear medicine tracers until today [2]. However, the last two decades have seen a distinct shift and notably increased interest in positron emissive nuclides. This has been catalyzed by the successful and widespread application of ^{18}F-labeled fluorodeoxyglucose (^{18}FDG) as a pluripotent oncological, neurological, and inflammation tracer. This has accelerated a more widespread clinical availability of standalone PET and PET/CT clinical scanners and motivated the development and commercialization 16 MeV cyclotron systems that enable p,n and d,n nuclear transformations to produce a variety of positron emissive isotopes [3, 4].

The more wide-spread access to cyclotrons has also led to advances in solid targetry to produce metallic radioisotopes. In contrast with ^{18}F ($t_{1/2}$ = 1.82 h) and ^{11}C ($t_{1/2}$ = 0.3 h), the two most popular, yet exceedingly short-lived main group PET isotopes, PET metal ions provide a broad range of radioactive half-lives. An additional advantage of radiometals are the relatively mild, aqueous radiolabeling conditions required to achieve high radiochemical yields, which are readily compatible with temperature and solvent sensitive biologics – a stark contrast with low-yielding ^{18}F or ^{11}C radiochemistry which often demands anhydrous conditions and high reaction temperatures of 120–140 °C and the need for large quantities of radioactivity at the onset of radiotracer synthesis to compensate for comparatively low radiochemical yields at the end of the respective tracer synthesis [5, 6].

Figure 1 summarizes the PET radiometals and their respective half-lives discussed in this chapter and illustrates that radiometals enable matching of isotope according to half-life with the pharmacokinetics of the corresponding targeting
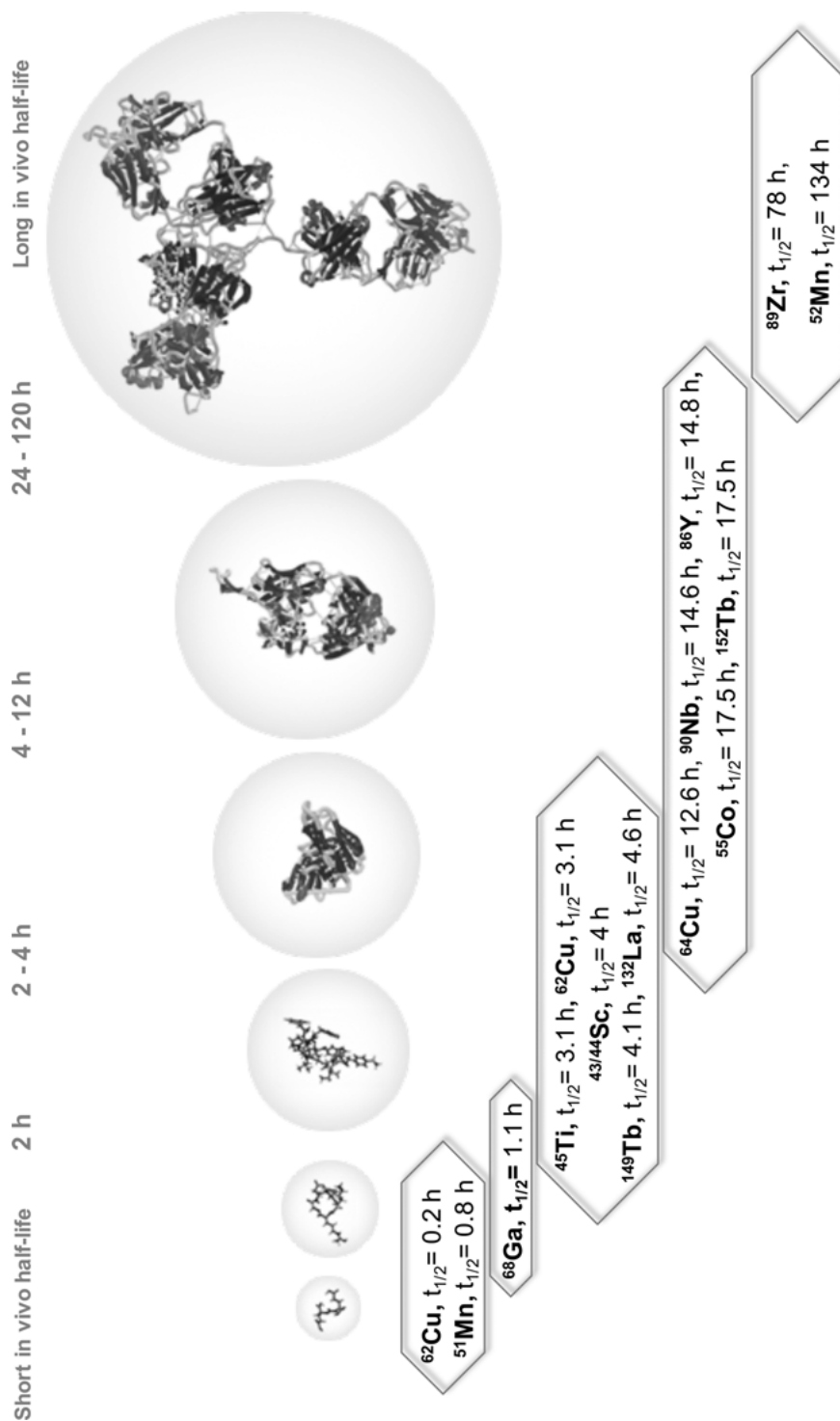
Figure 1. Summary of PET radiometal isotopes discussed in this chapter in the context of typical *in vivo* half-lives of biomolecules.

Table 1. Isotope half-lives, emission properties, and production routes.

Isotope	Half-Life	Primary Emission Energies	Production Route	Proton Energy Required for Production
Sc-43	3.89 h	$Emax(\beta^+) = 1.19$ MeV	$^{43}Ca(p,n)^{43}Sc$ $^{nat}Ca(\alpha, p)^{43}Sc$	8–16 MeV 24–27 MeV
Sc-44g	4.04 h	$Emax(\beta^+) = 2.63$ MeV	$^{45}Sc(p, 2n)^{44}Ti > {}^{44g}Sc$ $^{44}Ca(p,n)^{44}Sc$	8–16 MeV 25 MeV
Ti-45	3.09 h	$Emax(\beta^+) = 1.04$ MeV	$^{45}Sc(p,n)^{45}Ti$ $^{45}Sc(d,2n)^{45}Ti$	8–15 MeV
Mn-51	46 min	$Emax(\beta^+) = 2.18$ MeV	$^{52}Cr(p,2n)^{51}Mn$	8–16 MeV
Mn-52m	21 min	$Emax(\beta^+) = 2.63$ MeV	$^{52}Cr(p,n)^{52m}Mn$	8–16 MeV
Mn-52g	5.6 d	$Emax(\beta^+) = 3.69$ MeV	$^{52}Cr(p,n)^{52g}Mn$	8–16 MeV
Co-55	17.5 h	$Emax(\beta^+) = 2.43$ MeV	$^{58}Ni(p, a)^{55}Co$ $^{54}Fe(d,n)^{55}Co$	16 MeV 20 MeV
Cu-60	23 min	$Emax(\beta^+) = 5.11$ MeV	$^{60}Ni(p,n)^{60}Cu$	14.7 MeV
Cu-61	3.3 h	$Emax(\beta^+) = 1.22$ MeV	$^{61}Ni(d,n)^{61}Cu$	8.1 MeV
Cu-62	10 min	$Emax(\beta^+) = 2.92$ MeV	$^{62}Ni(p,n)^{62}Cu$ $^{62}Zn/^{62}Cu$ generator	8–12/30MeV 26 MeV
Cu-64	12.7 h	$Emax(\beta^+) = 653$ keV, $Emax(\beta^-) = 580$ keV	$^{64}Ni(p,n)^{64}Cu$	12 MeV
Ga-68	1.14 h	$Emax(\beta^+) = 1.89$ MeV	$^{69}Ga(p,2n)^{68}Ge > {}^{68}Ga$ $^{68}Zn(p,n)^{68}Ga$	40 MeV 12 MeV
Y-86	14.7 h	$Emax(\beta^+) = 4.21$ MeV	$^{86}Sr(p,n)^{86}Y$ $^{89}Y(p, 4n)^{86}Zr > {}^{86}Y$	7–14 MeV 40–75 MeV
Zr-89	78.41 h	$Emax(\beta^+) = 1.81$ keV $E\gamma = 908.97$ keV	$^{89}Y(p,n)^{89}Zr$	15–16.5 MeV 14 MeV
Nb-90	14.6 h	$Emax(\beta^+) = 5.08$ MeV	$^{90}Zr(p,n)^{90}Nb$	20 MeV
La-132	4.59 h	$Emax(\beta^+) = 3.67$ MeV	$^{nat}Ba(p,n)^{132}La$	16 MeV
Tb-149	4.12 h	$Emax(\beta^+) = 2.61$ keV, $Emax(\alpha) = 4.08$ MeV	spallation on tantalum	1.4 GeV
Tb-152	17.5 h	$Emax(\beta^+) = 2.98$ MeV	spallation on tantalum $^{155}Gd(p,4n)^{152}Tb$ $^{152}Gd(p,n)^{152}Tb$	1.4 GeV

vector. While initial production routes may have been established decades ago, the PET radiometal isotopes discussed herein (Table 1) are experiencing a resurgence in interest and applications. We aim to provide the reader with a timely review that serves as a compendium on isotope synthesis, ideal separation and subsequent chelation strategies (Table 2), followed by illustrative examples of applications for preclinical and clinical imaging.

Table 2. Chelator and isotope compatibility chart.

Chelator	Metal ion										
	Ga^{3+}	Cu^{2+}	Mn^{2+}	Co^{2+}	Sc^{3+}	Y^{3+}	La^{3+}	Tb^{3+}	Ti^{4+}	Zr^{4+}	Nb^{4+}
DOTA	l, h	l, rt	st, rt	st, rt	st, h	st, h	st, h	st, h	–	st, h	–
DOTAGA	l, h	l, rt	st, rt	st, rt	st, h	st, h	st, h	st, h	–	–	–
DO3A	st, h	l, rt	st, rt	st, rt	st, h	st, h	–	st, h	–	–	–
NOTA	st, rt	st, rt	l, rt	st, rt	l, rt	–	–	–	–	–	–
NOTP	st, rt	–	–	–	–	–	–	–	–	–	–
TRAP	st, rt	st, rt	–	–	–	–	–	–	–	–	–
HBED	st, rt	–	–	–	–	–	–	–	–	–	–
THP	st, rt	–	–	–	–	–	–	–	–	–	–
DFO	l, rt	–	–	–	–	–	–	–	st, rt	st, rt	st, rt
TETA	–	l, rt	–	–	–	–	–	–	–	–	–
CB-DO2A	–	st, h	–	–	–	–	–	–	–	–	–
CB-TE2A	–	st, h	–	–	–	–	–	–	–	–	–
SAR	–	st, rt	–	–	–	–	–	–	–	–	–
ATSM	–	l, rt	–	–	–	–	–	–	–	–	–
BAT	–	l, rt	–	–	–	–	–	–	–	–	–
CDTA	l, rt	–	–	–	l, rt	–	–	–	–	–	–
EDTA	l, rt	–	–	–	l, rt	–	–	–	l, rt	–	–
DTPA	l, rt	–	–	–	l, rt	l, rt	–	l, rt	l, rt	–	–
CHX-DTPA	l, rt	–	–	–	l, rt	l, rt	–	l, rt	–	–	–
AAZTA	–	–	–	–	st, rt	–	–	–	–	–	–
Picaga-R	–	–	–	–	st, rt	–	–	–	–	–	–
Pypa	–	–	–	–	st, rt	–	–	–	–	–	–
DO3Apic	–	–	–	–	–	–	st, h	–	–	–	–
Macropa	–	–	–	–	–	–	st, rt	–	–	–	–
DFO*	–	–	–	–	–	–	–	–	–	st, rt	–
DFO-sq	–	–	–	–	–	–	–	–	–	st, rt	–
HOPO	–	–	–	–	–	–	–	–	–	st, rt	–
2,3-HOPO	–	–	–	–	–	–	–	–	–	st, rt	–

st, h – stable, heating required; st, rt – stable, room temperature labeling; l, h – diminished stability, heating required; l, rt – diminished stability, room temperature labeling; – no data;

2. GALLIUM AND FIRST ROW TRANSITION METALS: COPPER, MANGANESE, COBALT

2.1. Gallium

2.1.1. Production and Speciation

^{68}Ga is a positron-emitting isotope with a half-life ($t_{1/2}$) of 67.6 min. It decays dominantly via positron emission (89 %, 1.92 MeV) and electron capture (11 %). ^{68}Ga is a decay product of ^{68}Ge and is conveniently generated using the ^{68}Ge/^{68}Ga generator system [7, 8]. The long half-life of the parent nuclide ^{68}Ge ($t_{1/2}$ = 271 d) guarantees ongoing supply of ^{68}Ga for hospitals and clinics for several months. ^{68}Ge is immobilized on TiO_2- or SnO_2-based ion exchange columns, where it decays to a shorter-lived daughter ^{68}Ga by electron capture. Subsequently, ^{68}Ga is eluted using a hydrochloric acid mobile phase, specifically, 0.05 M, 0.1 M or 1.0 M HCl. Currently, the most common commercially available generators are provided with ^{68}Ge activities of up to 3.7 GBq and the overall breakthrough of ^{68}Ge in chromatographic generators is not more than 0.005 % [7].

The increasing clinical demand of ^{68}Ga has also motivated the evaluation of cyclotron-based production methods of ^{68}Ga, for instance the ^{68}Zn(p,n)^{68}Ga reaction [9]. This production method can yield 4.3 GBq in a typical production run at 46 µA for 32 mins, providing a competitive alternative to the current ^{68}Ge/^{68}Ga generator [10].

2.1.2. Common Chelators of Gallium

Although some low valent gallium complexes are known, all the relevant radiopharmaceutical gallium chemistry occurs with Ga(III). Gallium is a hard acid. As a result, gallium's chelate chemistry is dominated by ligands with Lewis basic oxygen and nitrogen donors [11], forming complexes with a range of macrocyclic and acyclic chelators under different pH, temperature, and varying chelator concentrations [12]. The coordination- and radiochemistry of gallium has been well established with polyazamacrocycle-type chelators such as 1,4,7,10-tetraazacyclododecane-1,4,7,10-tetraacetic acid (DOTA), 1,4,7-triazacyclononane-1,4,7-triacetic acid (NOTA), 1,4,7-triazacyclononane-1,4,7-tri(methylene phosphonic acid (NOTP) and triazacyclononane phosphinic acid (TRAP) groups but catecholate and hydroxamate-based systems, such as N,N-bis(2-hydroxybenzyl)ethylenediamine-N,N-diacetic acid (HBED), tris(hydroxypyridinone) (THP) and desferrioxamine (DFO) have also been successfully utilized, and provide biomolecule-compatible room temperature radiolabeling conditions (Figure 2) [13].

2.1.3. Preclinical and Clinical Applications of ^{68}Ga

With the availability and accessibility of the ^{68}Ga generator, gallium has been used extensively for preclinical, and more recently for clinical PET imaging. The
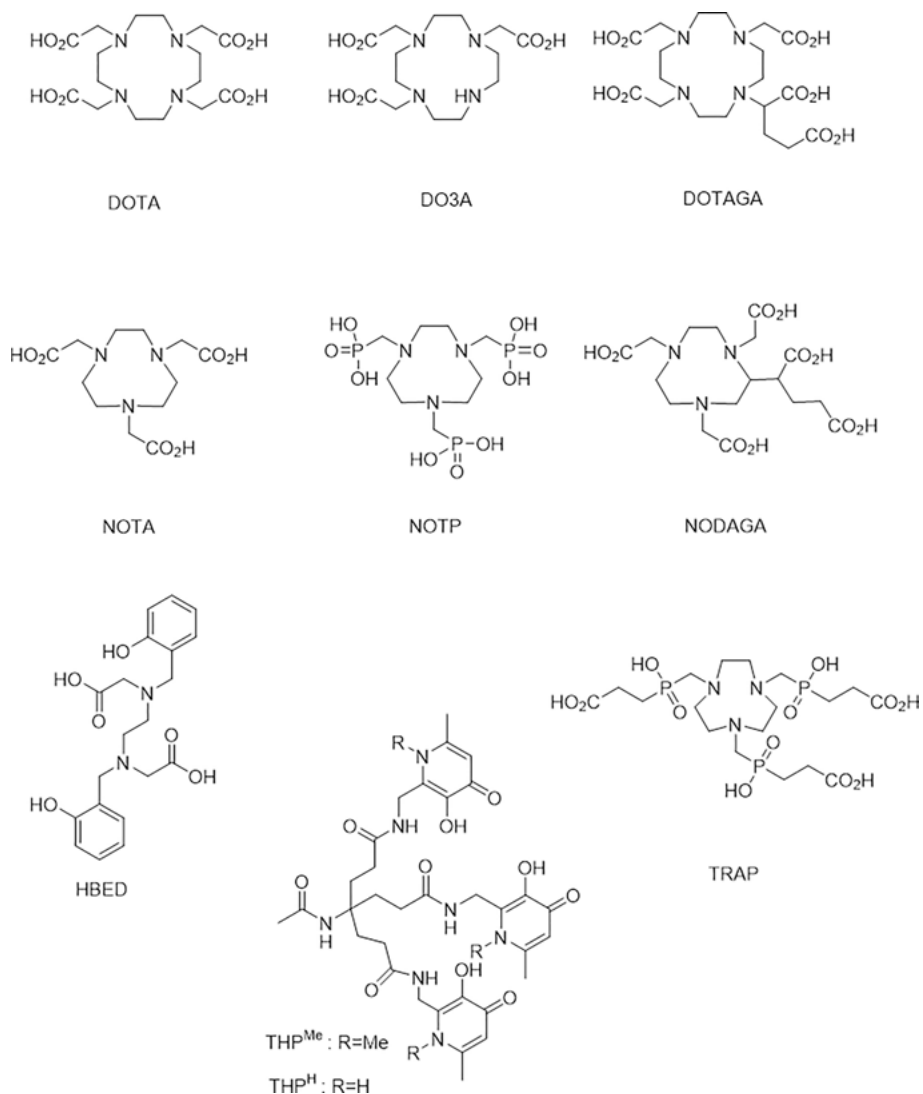
Figure 2.   Commonly employed chelators for gallium isotopes.

short half-life of ^{68}Ga enables repeat imaging for the monitoring of disease or treatment progression, making the isotope ideal for clinical use. Most recent work has focused on peptides as targeting vectors, as their typical *in vivo* pharmacokinetics are well-matched with the isotope's short half-life. Two ^{68}Ga-based, peptide conjugates have already been successfully clinically translated [14].

The first example is ^{68}Ga-PSMA-11 (Figure 3), which targets the prostate-specific membrane antigen (PSMA) using a dipeptide-based Glu-urea-Lys inhibitor of the bis-zinc active site. Nearly all prostate cancers express PSMA, with increased expression in metastasized carcinomas [15]. Overexpression of PSMA
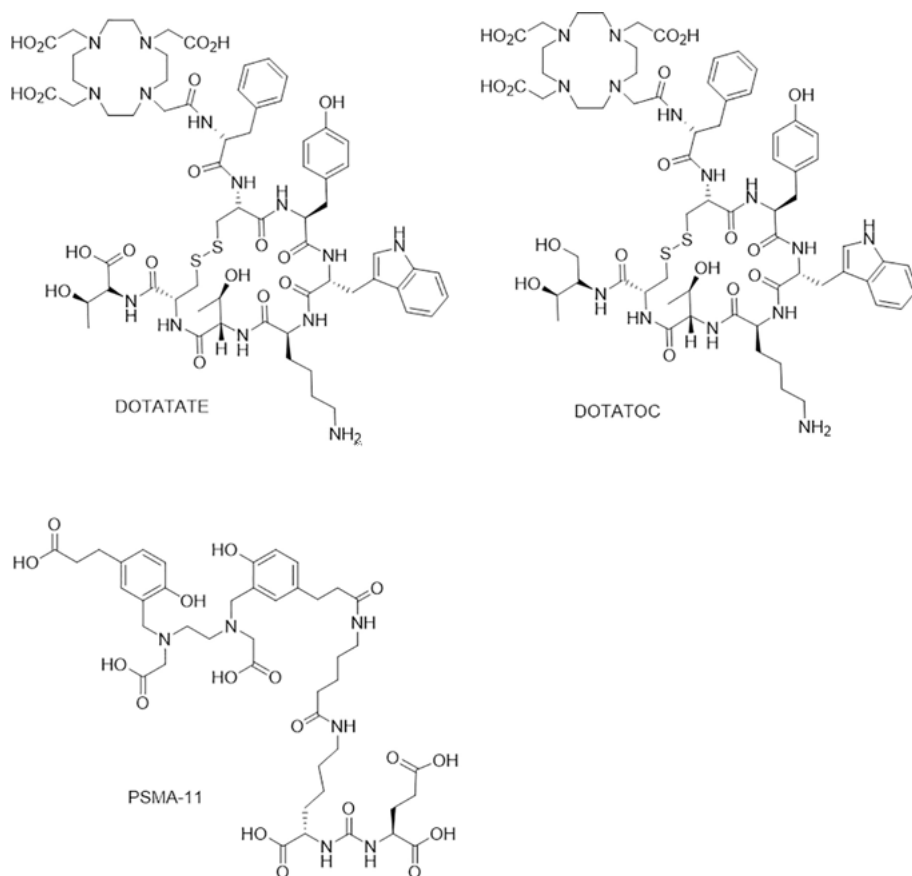
Figure 3. Structures of chelator-targeting vector constructs for preclinical and clinical imaging with [68]Ga.

is primarily restricted to the prostate with low levels of expression in the salivary gland and kidney [16–18].

^{68}Ga-PSMA-11 comprises the HBED chelator appended to Glu-urea-Lys with an alkyl linker [19]. Apart from its favorable Ga-complexing properties, HBED was selected because of its lipophilicity that provides enhanced binding affinity of the tracer to the lipophilic pocket of PSMA [20]. Approaches to improve ^{68}Ga-PSMA-11 have resulted in moderate success. ^{68}Ga-PSMA-617, which incorporates DOTA as the metal chelator, exhibited lower tumor uptake relative to HBED-chelated conjugates [19]. The lower tumor affinity of DOTA-conjugated compounds led to the development of 1,4,7,10-tetraazacyclododecane,1-(glutaric acid)-4,7,10-triacetic acid, DOTAGA-conjugated compounds, including PSMA for imaging and therapy (PSMA-I&T), a construct with a lipophilic linker to enhance affinity to PSMA [21]. The clinical efficacy of ^{68}Ga-PSMA-I&T appears equivalent to ^{68}Ga-PSMA-HBED though the target to background contrast appears slightly better for the latter [13].

Another successfully clinically translated tracer is ^{68}Ga-DOTA-(tyrosine[3])-octreotate (DOTATATE), targeting neuroendocrine tumors (Figure 3). Neuroendocrine tumors (NETs) are malignant and benign tumors in the hormone-producing endocrine system of the body [22]. These tumors overexpress the somatostatin receptor (SSR), a hormone that regulates the endocrine system. In 2016, the FDA approved the use of ^{68}Ga-DOTATATE for PET imaging for diagnosis, staging, and treatment management of neuroendocrine tumors [23]. ^{68}Ga-DOTATATE consists of tyrosine[3]-octreotate (TATE), a somatostatin analogue, radiolabeled with ^{68}Ga via the macrocyclic chelator DOTA [24]. ^{68}Ga-DOTATATE provides increased sensitivity to detect neuroendocrine tumors and specificity of metastatic uptake when compared to ^{18}F-FDG and ^{111}In-penetreotide [25, 26]. Its combination with the radiotherapeutic ^{177}Lu-DOTATATE is particularly attractive because it provides a curative option for patients with NETs [26, 27].

In addition to cancer imaging, an emerging area of interest for the application of ^{68}Ga is the imaging of bacterial infections, specifically using siderophores, low-molecular-weight chelators produced by bacteria to scavenge essential iron [28]. Decristoforo and coworkers have successfully imaged *Pseudomonas aeruginosa* (PA01) infections in rats with ^{68}Ga labeled pyoverdine, a siderophore produced by pseudomonas. [68]Ga efficiently coordinates pyoverdine (PVD) in lieu of iron and utilizes active siderophore-mediated trans-membrane transport for bacterial uptake. The complex more efficiently localized in bacterial infections *in vivo* than ^{18}F-FDG and ^{68}Ga-citrate thus, making ^{68}Ga-PVD-PA01 a promising new PET agent for specific *P. aeruginosa* imaging. The concept of radiolabeled siderophores for specific infection imaging is also transferable to different pathogens [29].

2.2. Copper

2.2.1. *Production and Speciation*

Copper-64 is the most widely utilized copper PET radionuclide, and the most commonly used synthetic route is the [64]Ni(p,n)[64]Cu reaction, which can be conducted on low-energy biomedical cyclotrons [30]. A solution target method has also been developed which removes the need for target dissolution post-irradiation [31]. Additional PET isotopes of copper accessible by proton or deuteron bombardment are [60]Cu, [61]Cu, [62]Cu, and [67]Cu. [60]Cu and [61]Cu have short half-lives of 23 min and 3.3 h, respectively, and must be produced at end user sites using the following production methods: [60]Ni(p,n)[60]Cu, [61]Ni(p,n)[61]Cu, and [60]Ni(d,n)[61]Cu. [62]Cu can be produced by the [62]Zn/[62]Cu generator. This generator requires the production of the [62]Zn parent, which has a relatively short half-life of 9.2 h [32].

2.2.2. *Common Chelators of Copper*

The most common oxidation states of copper are Cu(I) and Cu(II). Both of these states are easily accessible; however, Cu(II) is the more stable and primary

oxidation state used for radiochemistry applications. For applications of ^{64}Cu-labeled complexes for PET imaging *in vivo*, high kinetic inertness of the complex is paramount. As there are a variety of endogenous copper chelators and copper-scavenging proteins present *in vivo*, there is the potential for the copper ion to be displaced from the chelator [33]. Many of these copper chelators employ the reduction of Cu(II) to Cu(I), which is readily accessible under physiological conditions. Copper that has been scavenged typically accumulates in the liver.

Most stable configurations of copper complexes exhibit trigonal bipyramidal and square pyramidal geometries when 5-coordinate and square planar, distorted square planar, and distorted octahedral structure when 6-coordinate. Cu(II) exhibits Jahn-Teller distortion when hexacoordinated. The most common chelators are tetraaza-macrocycle-based to provide preorganization and enhanced structural rigidity to stabilize Cu(II) [33]. Polyazamacrocycles with pendant acetate arms, such as DOTA, TETA (1,4,8,11-tetraazacyclotetradecane-1,4,8,11-tetraacetic acid) (Figure 4) and NOTA (Figure 2) have been extensively explored. However, ^{64}Cu-complexes of DOTA and TETA exhibit high hepatic uptake, which is indicative of release of free ^{64}Cu from the complex. To improve *in vivo* stability of these chelators, cross-bridged chelators have been developed [34, 35]. The corresponding ^{64}Cu-CB-DO2A (4,10-bis(carboxymethyl)-1,4,7,10-tetraazabicyclo[5.5.2]tetradecane) and ^{64}Cu-CB-TE2A (4,11-bis(carboxymethyl)-1,4,8,11-tetraazabicyclo[6.6.2]hexadecane) complexes showed improved stability of
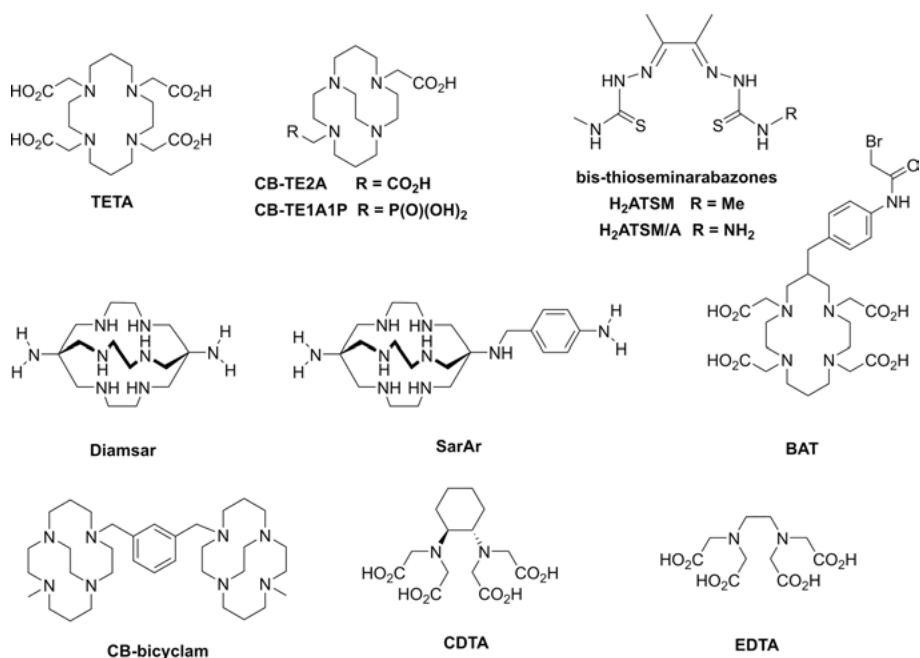
Figure 4. Commonly employed chelators for copper and manganese isotopes discussed herein.

[64]Cu-CB-TE2A and rapid clearance from the blood, liver and kidneys as compared to the corresponding, non-bridged complexes ^{64}Cu-TETA and ^{64}Cu-DOTA. However, the formation of ^{64}Cu-complexes with enhanced stability *in vivo* also requires high temperature for efficient radiolabeling, which is not ideal for targeting vectors such as antibodies. Sarcophagine (SAR) chelators like Diamsar (1,8-diamino-3,6,10,13,16,19-hexaazabicyclo[6,6,6]-eicosane) and SarAr (1-N-(4-aminobenzyl)-3,6,10,13,16,19-hexaazabicyclo[6,6,6]-eicosane-1,8-diamine) (Figure 4) and NOTA-type chelators provide a suitable alternative, as they have been shown to efficiently radiolabel at room temperature and also form complexes of high *in vivo* stability [36, 37]. In conclusion, a variety of copper chelators and targeting vector combinations have been explored successfully, with no single chelator superseding in performance for all, but rather enabling the careful matching of the chelator with the targeting vector of interest to produce ideal PET imaging outcomes with [64]Cu.

2.2.3.   *Preclinical and Clinical Applications of Cu-PET Isotopes*

The first clinical studies of ^{64}Cu-labeled conjugates focused on [60/64]Cu(ATSM) (copper (II) diacetylbis(N(4)-methylthiosemicarbazonato)) in lung cancer patients for the imaging of hypoxic cancer cells. Hypoxia is a well established hallmark for certain cancers, and therefore hypoxia-specific tracers can facilitate early diagnosis and improve treatment plans. ATSM is an acyclic chelator that coordinates Cu^{2+} in a square planar fashion (Figure 4) [38]. Under reducing conditions, the ATSM-bound Cu^{2+} can be reduced to Cu^+, which dissociates from the chelator and is trapped in the hypoxic cell [39, 40]. [64]Cu(ATSM) has also been used to assess ischemic regions of the heart [41]. While some studies have demonstrated the imaging of hypoxia with [64]Cu(ATSM) *in vivo*, this imaging probe has not produced long-term clinical success: many cancer subtypes show little to no [64]Cu(ATSM) uptake, necessitating the development of alternative, more specific imaging probes.

Due to the intermediate half-life of copper-64, small peptides, and proteins, which possess intermediate *in vivo* half-lives, can be used as targeting moieties. Some examples include Glu-urea-Lys (targeting PSMA in prostate cancer) [42–46], bombesin (targeting GRPr (gastrin-releasing peptide receptor) in lung and colon cancers) [47–53], RGD (targeting human $\alpha v\beta_3$ integrin in glioblastoma) [54–57], and octreotide [58–61] appended to a variety of ^{64}Cu chelators.

Recent clinical trials have been conducted with ^{64}Cu-MeCOSar-tyrosine[3]-octreotrate   (^{64}Cu-SARTATE)   (5-(8-methyl-3,6,10,13,16,19-hexaaza-bicyclo[6.6.6]icosan-1-ylamino)-5-oxopentanoic acid) in patients with neuroendocrine neoplasia. Imaging with ^{64}Cu-SARTATE, a conjugate comprised of MeCO-Sar, which is based on a cage amine ligand called Sar, linked to octreotate through a tyrosine[3] linker, was compared to the commercially available ^{68}Ga-DOTATATE (Figure 3). High uptake and retention in tumors were observed for ^{64}Cu-SARTATE and high contrast PET images were achieved until 24 h post-injection [62]. PET images acquired for ^{64}Cu-SARTATE at 4 h were judged to be comparable or superior to images acquired for ^{68}Ga-DOTATATE at 1 h. The

longer half-life of ^{64}Cu relative to ^{68}Ga allows for imaging at later time points which resulted in improved image quality due to improved target-to-background uptake. Ongoing studies include the imaging of patients with ^{64}Cu-SARTATE followed by treatment with the radiotherapy analogue ^{67}Cu-SARTATE.

Recently, Archibald et al. have demonstrated the potential of ^{64}Cu-CuCB-bicyclam as clinical diagnostic PET imaging agent of the CXCR4 (C-X-C chemokine receptor type 4), which is overexpressed in multiple cancer types, specifically leukemia, breast cancer, and prostate cancer [63]. The bicyclam complex, AMD3100 (Plerixafor), which acts as an antagonist against the CXCR4, has been approved by the US Food and Drug Administration for human used in HIV therapy [64]. Attempts towards PET imaging with the ^{64}Cu-labeled complex led to high non-specific hepatic uptake due to complex instability. To address this instability, Archibald et al. employed the CB-bicyclam chelator [63]. This complex features a structurally restricted chelator which confers higher kinetic stability [65], enabling the successful imaging of human CXCR4 in U87.CXCR4 xenograft-bearing mice.

Due to the thermal instability of antibodies above 40 °C, ^{64}Cu chelators that require heating to achieve high radiolabeling yields are not compatible for use with antibodies. Alternatively, chelators that form less stable complexes with ^{64}Cu such as DOTA, BAT (6-(p-bromoacetamidobenzyl)-1,4,8,11-tetraazacyclotetradecane-1,4,8,11-tetraacetic acid), and TETA have been used (Figure 4). BAT conjugates have been utilized with the immunoconjugate ^{64}Cu-BAT-1A3 to image colorectal cancer [66], and ^{67}Cu-BAT-2IT-Lym-1 was evaluated for radioimmunotherapy in patients with non-Hodgkin's lymphoma [67]. Lewis and coworkers substituted BAT with TETA, which resulted in improved *in vivo* performance [66]. Similarly, NOTA-derived chelators have also been successfully employed for the room temperature radiolabeling of ^{64}Cu with antibodies [68, 69].

2.3. Manganese

2.3.1. *Production and Speciation*

Some manganese PET isotopes can be readily produced using accelerators: ^{51}Mn, ^{52m}Mn, and ^{52g}Mn [70]. ^{51}Mn has a half-life of $t_{1/2}$ = 46 mins, which makes it applicable to image fast biological processes. However, the shorter half-life also restricts efficient target separation and radiolabeling with ^{51}Mn. Furthermore, the β^+ energy is relatively high (2.19 MeV) in comparison with the standard PET nuclide ^{18}F (0.6 MeV), which leads to diminished spatial resolution in PET images. ^{51}Mn can be produced by irradiation of isotopically enriched ^{50}Cr with 3–14 MeV deuterons (^{50}Cr(d,n)^{51}Mn) or using a natural ^{52}Cr target in ^{52}Cr(p,2n)^{51}Mn reaction [71]. The ^{52m}Mn isotope has a half-life of $t_{1/2}$ = 21.2 mins, comparable with the half-life of ^{11}C ($t_{1/2}$ = 20 mins), which renders its radiochemical handling even more challenging. Furthermore, ^{52m}Mn also results in lower PET resolution due to the high β^+ energy of ^{52m}Mn (2.6 MeV) [72, 73]. The most broadly applicable manganese PET isotope is ^{52g}Mn, with a half-life

of 5.6 days. The long half-life enables better target separation, radiochemical handling and applications with slowly clearing targeting vectors. ^{52g}Mn emits a relatively low energy β^+ (0.57 MeV) which corresponds to better resolution in PET images. One major disadvantage of the isotope is the additional emission of three high energy gamma rays which represents a dosimetry concern for the patient [73]. ^{52g}Mn and ^{52m}Mn can be produced by the irradiation of natural chromium targets with 8–16 MeV protons using the ^{nat}Cr(p,xn)^{52}Mn reaction. The two isotopes are always coproduced because of similar energy thresholds, but pure ^{52g}Mn can be isolated following decay of the short-lived ^{52m}Mn [74].

2.3.2.   *Common Chelators of Manganese*

Manganese is a first-row transition metal that exists in various oxidation states. It exhibits oxidation states from $+2$ to $+7$, with $+2$ as the most stable oxidation state and a preferred coordination number of 6 or 7. Mn(II) is considered a hard to borderline Lewis acid and prefers hard Lewis-basic donors such as nitrogen or carbonyl oxygen. Well characterized chelators of ^{52}Mn are DOTA, NOTA, ethylenediaminetetraacetic acid (EDTA) and its derivatives like cyclohexanedi-aminetetraacetic acid (CDTA, Figure 4) [73, 75]. The radiolabeling conditions are pH 4–6 at room temperature to 50 °C [6].

2.3.3.   *Preclinical Applications of ^{52g}Mn*

A number of studies have been carried out with non-chelated ^{52g}MnCl$_2$ to study exogenous manganese distribution following different administration paths, specifically via intravenous injection or inhalation. Rapid blood clearance, followed by retention of ^{52}Mn in the brain, thyroid, and thymus was observed [76]. ^{52}Mn is also significantly taken up by the pancreas [76], possibly by mimicking Ca^{2+} in pancreatic metabolic pathways. Hernandez et al. utilized ^{52g}MnCl$_2$ to monitor β-cell mass using imaging and biodistribution in type 1 and type 2 diabetes mouse models [77]. The non-invasive measurement of functional β-cell mass is clinically valuable for monitoring the progression of type 1 and type 2 diabetes as well as the viability of transplanted insulin-producing cells. Previous work using manganese-enhanced magnetic resonance imaging (MEMRI) showed that the utility of this method was limited by the toxicity of free Mn^{2+} ions, which is not a concern with small quantities used in nuclear imaging studies with ^{52g}Mn and the shorter lived ^{51}Mn [78, 79].

   More recently, ^{52g}Mn-chelate complexes have been successfully utilized for the preclinical imaging of antibodies. The favorable half-life of ^{52g}Mn (t$_{1/2}$ = 5.4 d), and its low β^+ energy paired with the lack of high-energy gammas render this isotope a promising alternative to ^{89}Zr. The first *in vivo* study with a ^{52g}Mn-labeled antibody utilized a DOTA chelator conjugated to the AT1-targeting antibody TRC105 with subsequent *in vivo* evaluation in a breast cancer xenograft mouse model. The results showed favorable biodistribution and PET imaging comparable to the ^{89}Zr analogue, with ^{52g}Mn-DOTA-TRC105 exhibiting slower

clearance from the blood pool. [52]Mn represents an attractive new option in addition to other long-lived imaging PET and SPECT nuclides, especially for multimodal applications in combination with Mn-based MRI [75].

2.4.   [55]Cobalt

2.4.1.   *Production and Speciation*

[55]Co ($t_{1/2}$ = 17.5 h, $E_{\beta+}$ = 570 keV (77 %), EC (23 %)) [80] is an emerging radioisotope with decay properties ideal for targeted PET imaging applications. The positron abundance of [55]Co is > 4 times higher than that of ^{64}Cu; however, this advantage is partially offset by the higher average β^+ energy of 570 keV relative to the 278 keV of ^{64}Cu, which can decrease image quality. [55]Co is primarily produced by the [54]Fe(d,n)[55]Co, [56]Fe(p,2n)[55]Co, and [58]Ni(p,α)[55]Co reactions [81]. The [58]Ni(p,α)[55]Co reaction is well suited for production on low-energy biomedical cyclotrons (15 MeV). A major disadvantage of this method is the production of long-lived [57]Co which is produced concomitantly if the proton energy increases during production. The [54]Fe(d,n)[55]Co reaction requires an enriched target, while the [56]Fe(p,2n)[55]Co reaction can produce large amounts of [56]Co [82]. Separation and isolation involves the elution of [55]CoCl$_2$ from an anion-exchange resin with 4–9 M HCl, evaporation and reconstitution of [55]CoCl$_2$ in 0.04 M HCl for further use [82, 83].

2.4.2.   *Common Chelators of Cobalt*

The most commonly observed oxidation states of cobalt are Co(II) and Co(III) where oxidation to Co(III) is promoted at high pH. For *in vivo* PET imaging applications, it is preferred that the oxidation state of the metal ion remains constant, typically in the Co(II) form.

Chelation radiochemistry of Co(II) remained underexplored until recently, when Dam and coworkers evaluated a [55]Co-labeled bombesin antagonist, PEG2-RM26 using several tri- and tetra-aza macrocyclic chelators (DOTA, NODAGA (1,4,7-triazacyclononane,1-glutaric acid-4,7-acetic acid), NOTA, and DOTAGA; see Figure 2). Chelation was achieved for all conjugates by dynamic microwave heating to 90 °C for up to 3 min [84–85]. Superior PET imaging in a PC-3 xenograft mouse model was seen with [55]Co-DOTA-PEG2-RM26 and [55]Co-NOTA-PEG2-RM26 at 24 hours post-injection [84].

2.4.3.   *Preclinical Applications of [55]Co*

[55]Co has an intermediate half-life of 17.5 h which allows for applications with targeting vectors with longer *in vivo* half-lives such as peptides, proteins, and affibodies [81] and shipment to remote user sites without cyclotrons. Several preclinical studies of [55]Co appended to peptides and antibodies for targeted PET

imaging have been conducted. Thisgaard and coworkers have used [55]Co-labeled PSMA-617 for *in vivo* PET imaging of mice with PSMA-expressing xenografts. Imaging with [55]Co at delayed timepoints resulted in improved target to background ratios (24 h p.i.) when compared with early timepoint PET imaging using ^{68}Ga-PSMA-11 [86]. A similar study by the same group was conducted with a bombesin derivative, [55]Co-NOTA-AMBA (NOTA-Gly-4-ABz-Gln-Trp-Ala-Val-Gly-His-Leu-Met-NH$_2$) [87]. Superior tumor accumulation and hepatic clearance *in vivo* was also observed with [55]Co-DOTA-Z$_{EGFR:2377}$, as compared to the ^{68}Ga-labeled conjugate [88] to image the overexpression of epidermal growth factor receptor (EGRF). [55]Co-DOTATOC (DOTA-D-Phe[1]-Tyrosine[3]-octreotide) is well suited for PET imaging of somatostatin receptor-expressing tumors [89]. Thisgaard and coworkers observed high levels of receptor-specific uptake for [55]Co-DOTATOC (Figure 3) when compared to the [68]Ga- and ^{64}Cu-labeled-derivatives with respect to target-to-background ratios, leading to improved image contrast [90].

3. LANTHANIDES AND PSEUDOLANTHANIDES: SCANDIUM, YTTRIUM, LANTHANUM, TERBIUM

3.1. Scandium

3.1.1. Production and Speciation

Two isotopes of scandium are of imminent interest for PET imaging applications: [43]Sc and [44]Sc. [43]Sc has a half-life 3.9 h and a positron branching ratio of 88.1 %. However, production of [43]Sc requires an enriched [43]Ca target on medical cyclotrons. The absence of the 1.157 MeV high probability (99.9 %) gamma means a lower radiation dose to patients [91]. Scandium-44 has an ideal positron branching ratio (94 %), average positron energy (Eβ^+ = 632 KeV), and half-life (t$_{1/2}$ = 4.04 h) [92], with PET imaging characteristics of scandium-44 comparing favorably to gallium-68. [44]Sc is the daughter of [44]Ti, which can be produced by the [45]Sc(p, 2n)[44]Ti reaction. The long half-life [44]Ti (t$_{1/2}$ = 59.2 $\pm$ 0.6 y) [93] means the [44]Ti/[44]Sc generator system is an attractive, portable long-term source of [44]Sc in the absence of a cyclotron. Separation of [44]Ti from the scandium target is achieved by target dissolution in concentrated HCl, followed by sequential anion and cation exchange column chromatography [94]. To date, numerous generators with > 3 mCi activity have been prepared, with one generator having produced [44]Sc for PET imaging of patients [95].

   Challenges associated with the development of the [44]Ti/[44]Sc generator system include elution volume, acid concentration, and [44]Ti breakthrough [96–101]. Separation of [44]Ti and [44]Sc on resin was explored using branched diglycolamide (BDGA) resin and hydroxamate-based ZR resin. ZR resin showed the most potential as a solid support to date loaded with 6 M HCl media and eluted with 0.05 M HCl for [44]Ti/[44]Sc with low [44]Ti breakthrough ($\sim$15 Bq per 2 elutions) [97]. Roesch describes processing and concentration of the [44]Sc eluate by adsorp-

tion of the [44]Sc on a cation exchange resin (AG 50W-X4 [200–400 mesh, H^{+}-form] resulted in 89 % retention of [44]Sc on the resin). Recovery of 90 % of the captured [44]Sc was achieved using 3 mL of 0.25 M ammonium acetate buffer at pH 4.0 which is well suited to direct labeling [98]. [44]Sc can also be directly produced by proton irradiation of a solid calcium target, either $CaCO_3$ or calcium metal via the [44]Ca(p,n)[44]Sc reaction. This production method can be used to produce up to 2 GBq [44]Sc after purification [99]. Production via proton bombardment of a liquid target containing $(Ca(NO_3)_2 \cdot 4 \, H_2O)$ has also been demonstrated [100]. Separation from the calcium target has been effectively achieved using a variety of methods including filtration using HCl and ammonium hydroxide [101], and dipentyl pentylphosphonate [102], nobias resin [103], DGA resin, SCX cation exchange resin [99], and chelex 100 resin [104].

3.1.2. Common Chelators of Scandium

Scandium is present as a trivalent cation in aqueous media and despite its presence in the top row of transition metals, it shares characteristics with the lanthanide series. The hydrolysis reaction of Sc^{3+} occurs to form $[Sc(OH)]^{2+}$ and $[Sc(OH_2)]^+$ at low pH (pH 3.0–4.5) and the formation of the poorly soluble ($[Sc(OH_3)]$ ($K_{sp} = 1.9 \times 10^{-28}$) begins at pH 4.9 [105]. These properties place
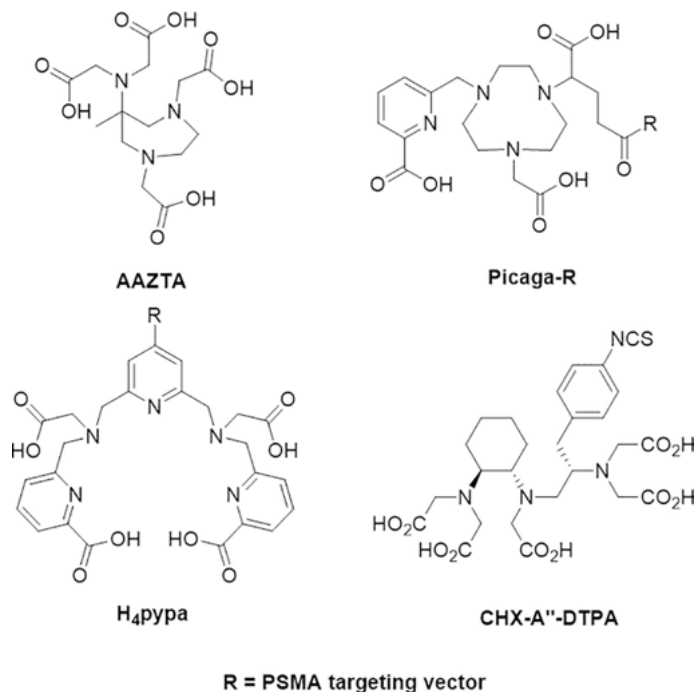
Figure 5. Commonly employed chelators for scandium and yttrium isotopes discussed herein.

some constraints on the corresponding radiochemistry. Scandium prefers a 6–8 coordinate environment and hard donors. Roesch and coworkers have explored a number of DOTA-based chelators bearing one methylenephosphonic (DO3AP) or methylenephosphinic (DO3AP(PrA) and DO3AP(ABn)) acid pendant arms [106]. None of the cyclen-derived structures label at room temperature, which limits the application of these chelators to peptidic and small molecule targeting vectors. Approaches to enable the room temperature chelation of [44]Sc include small-cavity macrocycles and acyclic chelators. AAZTA (AAZTA = 1,4-bis(carboxymethyl)-6-[bis(carboxymethyl)]amino-6-methylperhydro-1,4-diazepine) demonstrates rapid and quantitative labeling with [44]Sc under mild conditions (Figure 5) [107, 108]. Similarly, with the ligand Picaga-R (Figure 5), Boros and coworkers have employed a 7-coordinate triazamacrocyclic chelator bearing a picolinic acid pendant arm [109] and Orvig and coworkers have labeled the acyclic, 9-coordinate chelator H$_4$pypa with [44]Sc [110]. Both approaches enable radiolabeling at room temperature and perform well in a PSMA-expressing animal model.

3.1.3. *Preclinical and Clinical Applications of [44]Sc*

The half-life of [44]Sc is well-matched to small molecules, peptides or antibody fragments (Fab), with PET image acquisition feasible up to 24 h post injection. As the dipeptide-based PSMA-targeting moiety has pharmacokinetics well-matched to the half-life of [44]Sc, this has been an area of active research. In addition to the above examples employed in proof-of-concept chelator studies, the DOTA conjugate PSMA-617 was labeled with generator-produced [44]Sc for clinical imaging in a first-in-human study of PSMA-617 (Figure 6). [44]Sc-PSMA-617 showed lower kidney uptake and demonstrated statistically similar uptake values when compared to ^{68}Ga-PSMA-11 [111]. [44]Sc-DOTATOC (Figure 3) was administered to humans, the first clinical PET imaging using cyclotron-produced [44]Sc targeting neuroendocrine neoplasms as a proof-of-concept [112]. A [44]Sc-DOTA folate conjugate has been used to image in mice with folate receptor positive KB tumor xenografts [113]. This study was followed up with [47]Sc-DOTA folate for therapy demonstrating the suitability of the theranostic pair [114]. Cai and coworkers linked the Fab fragment Cetuximab, which targets EGFR, with N-[(R)-2-amino-3-(para-isothiocyanato-phenyl)propyl]-*trans*-(S,S)-cyclohexane-1,2-diamine-N,N,N′,N″,N″-pentaacetic acid (CHX-A″-DTPA) and labeled at room temperature with [44]Sc for PET imaging [115]. However, enhanced hepatic uptake of this derivative indicates that DTPA-derived chelators represent a non-ideal chelator match for Sc. The short half-life of [44]Sc also opens up possibilities for pre-targeting applications. [44]Sc-labeled tetrazine DOTA complexes and a *trans*-cyclooctene-functionalized bisphosphonate-targeting vector were used to evaluate pre-targeted PET imaging with [44]Sc using the inverse electron demand Diels-Alder reaction (IEDDA) by Edem et al. [116].
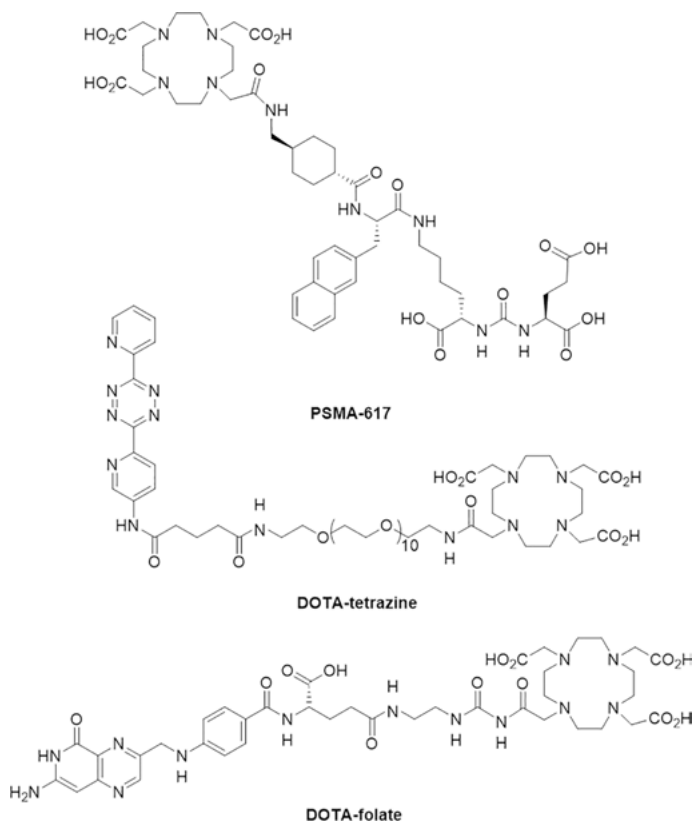
Figure 6. Structures of chelator-targeting vector constructs utilized for preclinical and clinical imaging with [44]Sc and [86]Y.

3.2. Yttrium

3.2.1. Production and Speciation

Y-86 is the only PET isotope of interest of yttrium and serves as a convenient imaging congener to [90]Y. Considered a pseudolanthanide, the chemical behavior of yttrium compares well with that of small lanthanides such as ytterbium and lutetium. The only relevant redox state for radiochemical applications is Y(III). [86]Y can be produced on small biomedical cyclotrons using a solid, enriched [86]Sr in the form [86]SrCO$_3$ or [86]SrCl$_2$ or liquid [86]Sr(NO$_3$)$_2$ solution targets [117–119]. The [86]Sr(p,n)[86]Y reaction can be accomplished using low energy cyclotrons (7-14 MeV). An alternative method of production has been demonstrated using [86]Zr as the parent isotope in a generator system. Baimukhanova et al. used a natural yttrium target and a medium energy bombardment (40–70 MeV) to produce [86]Zr which upon processing provided high radiochemical yield ($\geq 98\,\%$) [86]Zr. The generator systems explored used ZR resin and resulted in 70–95 % elution yield of [86]Y with low breakthrough of the parent [86]Zr ($\leq$10–3 %) [120].

3.2.2. *Common Chelators and Applications of Yttrium*

Due to the similarity to lanthanides, ligands based on the DOTA and DTPA-based chelators are well suited for [86]Y. The cyclohexane modified CHX-A″-DTPA showed improved thermodynamic stability over DTPA [121]. There are numerous examples of the use of [86]Y for PET imaging. Chen and coworkers have used the [86]Y/^{90}Y theranostic pair with a DOTA-octreotate conjugate modified with Evans Blue moiety (EB-octreotate) for improved pharmacokinetics delay excretion [122]. This study illustrates the usefulness of [86]Y as the half-life was well-matched to this application maximum uptake was observed at the 24 h time-point and ^{90}Y was subsequently used therapeutically against SSTR2-positive tumors xenografted in mice [122]. Pomper and coworkers have radiolabeled PSMA targeting small molecules with [86]Y for PET imaging [123]. [86]Y has also been used to radiolabel antibodies. Examples include [86]Y-1B4M-DTPA-trastuzamab targeting LS-174T tumor xenografts in mice [124] and [86]Y-CHX-A″-DTPA-panitumumab targeting the HER1 receptor [125].

3.3. Lanthanum

3.3.1. *Production and Speciation*

Recent efforts to optimize the production of the lanthanum radioisotopes toward targeted theranostic pharmaceuticals were conducted by Engle and coworkers [126]. A major incentive to working with [132]La is the availability [135]La ($t_{1/2}$ = 18.9 h), which decays 100 % by electron capture, and is therefore useful for Auger therapy. The chemical similarity of the lanthanum(III) and actinium(III) ions also offers potential opportunities to employ [132]La as a diagnostic partner to therapeutic isotope [225]Ac. Lanthanum-132 ($t_{1/2}$ = 4.59 h, 42.1 % β^+) is produced by proton irradiation using a small 16 MeV biomedical cyclotron by way of the $^{nat}Ba(p,x)^{13x}La$ reaction which co-produces La-135 [127]. Radiochemical isolation of $^{132/135}La^{3+}$ was achieved by removal of the precipitated, residual target material $Ba(NO_3)_2$ by centrifugation, followed by ion separation with BDGA resin to elute $^{132/135}La^{3+}$ in 0.1 M HCl.

3.3.2. *Common Chelators of Lanthanum*

Lanthanum is a large lanthanide, therefore 8-coordinate chelators like DOTA work well to complex La^{3+}, however nona- or deca-dentate ligands such as DO3Apic (9-coordinate) or macropa (10-coordinate) can further enhance kinetic inertness (Figure 7) [128, 129].

3.3.3. *Preclinical and Clinical Applications of ^{132}La*

The first *in vivo* application of the $^{132/135}La^{3+}$ isotopes used small-molecular chelator-peptide conjugates to image PSMA-expressing tumors [130]. The che-

X = -OH   DO3Apic
X = -DUPA   DO2Apic-DUPA

Y = -H   macropa
Y = —NH(S)DUPA   macropa-DUPA

DUPA
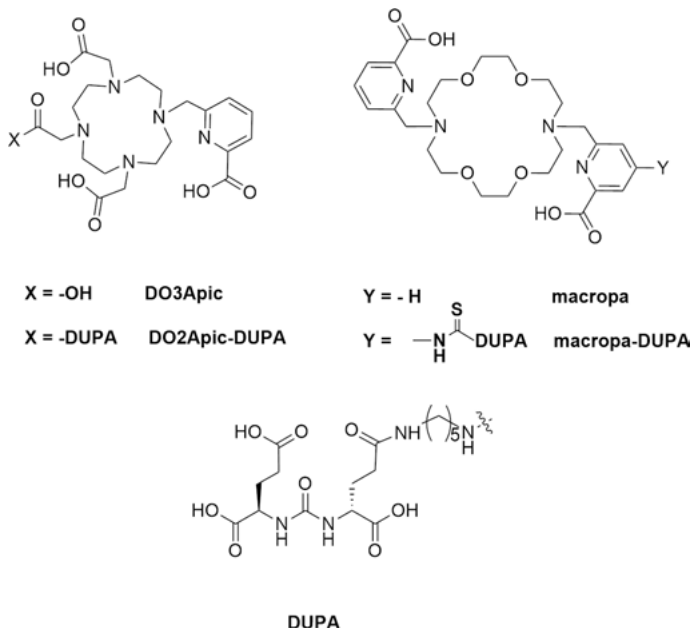
Figure 7.   Recently explored chelators and bioconjugates for lanthanum isotopes discussed herein.

lators DO3Apic and macropa appended to a Glu-urea-Glu PSMA-targeting dipeptide were radiolabeled successfully with $^{132/135}$La^{3+}. While macropa exhibited radiolabeling at room temperature, sensitivity to radiolysis diminished complex stability of the corresponding bioconjugate. Both conjugates showed rapid uptake in PSMA-expressing tumors, with low off-target organ uptake, specifically in the liver and marrow, indicating no significant release of La^{3+} *in vivo*.

3.4.   Terbium

3.4.1.   *Production and Speciation*

Terbium has four clinically relevant radioisotopes, enabling possible theranostic applications in nuclear medicine. Two PET isotopes of interest exist: terbium-152 ($t_{1/2}$ = 17.4 h) and terbium-149 ($t_{1/2}$ = 4.12 h), decaying by 20 % and 7 % β^+ emission respectively [131]. Terbium provides intrinsic theranostic pairs, as terbium-161 ($t_{1/2}$ = 17.4 h) emits therapeutic Auger electrons as well as gamma rays suitable for SPECT imaging. Terbium-155 ($t_{1/2}$ = 128 h) is a γ emitter, suitable for SPECT imaging. The $^{149/152}$Tb radioisotopes are most commonly produced by proton-induced spallation of tantalum targets using 1.4 GeV protons, and products isolated through an online mass-to-charge separation process at ISOLDE/CERN [132]. Terbium-152 can also be produced by proton irradiation,

specifically the ^{155}Gd(p,4n)^{152}Tb and ^{152}Gd(p,n)^{152}Tb reactions [132, 133]. Purification of ^{152}Tb is carried out by slow elution of ^{152}Tb/^{152}Dy combined products using ion exchange chromatography, followed by removal of ^{152}Dy by decay to ^{152}Tb. The pure ^{152}Tb solution is concentrated in 0.05 M HCl to be used for radiolabeling [134].

3.4.2.   Common Chelators of Terbium

Terbium generally favors 8- or 9-coordinate environments and is most commonly chelated by DOTA-based scaffolds, which generally afford robust at high temperature radiolabeling conditions [135–136]. Alternatively, DTPA can also be used, as radiolabeling of Tb isotopes with this chelator proceeds at room temperature [135].

3.4.3.   Preclinical and Clinical Applications of Tb-PET Isotopes

Müller et al. were the first to demonstrate the targeted, *in vivo* imaging with terbium radioisotopes [137]. The proof-of-concept study was carried out with the folate-targeting conjugate cm09, which incorporates a DOTA-macrocycle chelator for complexation of radioactive terbium. Phantom PET images of ^{152}Tb demonstrated poor spatial resolution, which the authors attribute to the high positron energy of ^{152}Tb (Eβ^+ average = 1140 keV, 20.3 %). *In vivo* PET scans of ^{152}Tb-cm09 show good tumor conspicuity and enhanced kidney uptake.

Terbium-149 is a low-energy alpha-emitter (E$_\alpha$ = 3970 keV, 17 %), though it also emits positrons (E$_{\beta+}$ average = 730 keV, 7.1 %) for PET imaging which could facilitate its use as a theranostic [131, 138–142]. Müller and coworkers also demonstrated alpha-PET with ^{149}Tb-DOTANOC *in vivo* evaluation using a mouse xenograft model expressing the somatostatin receptor target [138]: PET images of ^{149}Tb-DOTANOC showed accumulation in the corresponding AR42J tumor xenografts. The disadvantages of the alpha-PET approach thus far, is the requirement for increased quantities of radiation and increased specific activity in order to completely eradicate tumors. Of note, the terbium radioisotopes allow for comparison of α (^{149}Tb) and β$^-$ (^{161}Tb) therapies and are considered interchangeable with ^{152}Tb as well as ^{177}Lu without significantly altering pharmacokinetics [143]. Recently, a first in-human trial has been successfully completed with ^{152}Tb-DOTANOC. Small tumor metastases were successfully detected using clinical PET/CT [134]. Other targeted preclinical and clinical applications of ^{152}Tb include the imaging of the prostate-specific membrane antigen with ^{152}Tb-PSMA-617, in a preclinical and clinical setting. ^{152}Tb-PSMA-617 successfully imaged metastatic prostate cancer in a patient, revealing comparable uptake to ^{68}Ga-PSMA-11, although diminished PET image quality [137]. While terbium may be considered the "Swiss knife of nuclear medicine", its limited availability and low production yields is a major issue that currently limits use [135, 137, 139].

4. TETRA- AND PENTAVALENT METALS: TITANIUM, ZIRCONIUM, NIOBIUM

4.1. Titanium

4.1.1. Production and Speciation

Titanium-45 is an ideal potential PET imaging isotope due to its 3.09 h half-life, 85 % positron branching ratio (15 % electron capture), low maximum positron energy of 1040 keV [144, 145], and minimal release of concurrent gamma rays (< 1 %) [145]. ^{45}Ti is commonly produced via proton bombardment on standard medical cyclotrons, at about 13–14.5 MeV [146, 147] via the ^{45}Sc(p,n)^{45}Ti reaction, or by deuteron bombardment via the ^{45}Sc(d,2n)^{45}Ti reaction [145]. Ti(IV) is a hard Lewis acid, and is highly oxophilic [148], thus it typically prefers hard, Lewis basic oxygen-containing ligand donors. Hydrolysis of titanium in solution happens readily, with aqueous solutions as low as pH 0 forming exclusively $[Ti(OH)_2]^{2+}$ [149, 150], solutions at pH 3–11 forming $Ti(OH)_4$, and $[Ti(OH)_5]^-$ forming above pH 11 [150]. ^{45}Ti is isolated by target dissolution in 6 M HCl, followed by separation with a hydroxamate resin. The ^{45}Ti product is eluted using several fractions of 1 M oxalic acid [151, 152].

4.1.2. Common Chelators of Titanium

Titanium is readily coordinated by carboxylates, catecholates, tyrosinates, hydroxamates, and salicylates among many others (Figure 8) [149]. Ti(IV) also forms strong complexes with Fe(III)-sequestering siderophores such as DFO [153], and enterobactin [154], even outcompeting Fe(III) in these particular cases with respect to the magnitude of the formation constants, and in the case of enterobactin, kinetically displacing the Fe(III) for Ti(IV).

4.1.3. Preclinical Applications of ^{45}Ti

The first example of *in vivo* imaging of ^{45}Ti-labeled compounds dates back to 1981. Ishiwata and coworkers labeled and conducted imaging and biodistribution studies of ^{45}Ti-DTPA and phytate [155, 156]. Imaging and biodistribution showed increased uptake of free ^{45}Ti and ^{45}Ti-phytate in the liver and spleen, whereas ^{45}Ti-DTPA was found at increased levels in the blood. Additional *in vivo* studies of ^{45}TiOCl$_2$, ^{45}TiO-phytate, ^{45}TiO-DTPA, ^{45}TiO-citrate, and ^{45}TiO-human serum albumin (HSA) were published by the same group ten years later. The ^{45}TiOCl$_2$ and ^{45}TiO-phytate showed increased liver uptake, likely due to colloid formation, whereas ^{45}TiO-DTPA, ^{45}TiO-citrate, and ^{45}TiO-HSA were found to remain circulating in the blood pool. ^{45}TiO-DTPA likely trans-chelates with transferrin to form a ^{45}Ti-transferrin complex which remains highly stable in serum (> 99 % binding). *In vivo* studies in mice with EMT-6 tumors showed high blood uptake
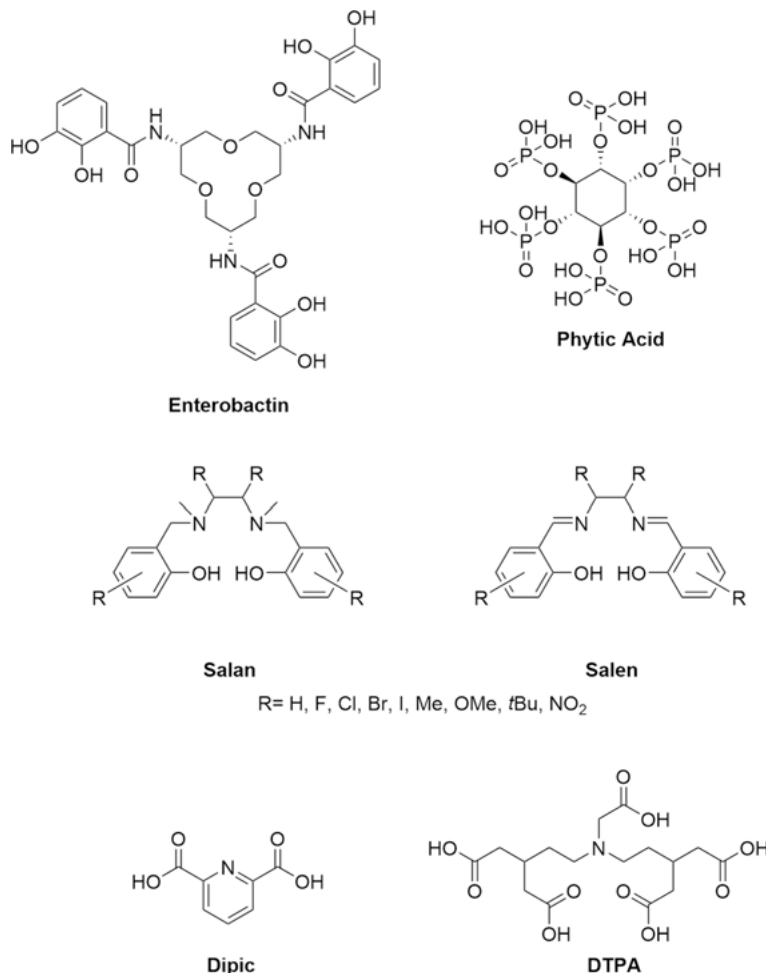
Figure 8. Commonly employed chelators for titanium isotopes discussed herein.

and retention, as well as nearly a 60 % increase in tumor uptake compared to non-target tissue [157].

Titanium(IV) complexes with salan or salen (Figure 8) have shown potential for use as anticancer agents *in vitro* [158–161] with some even outperforming cisplatin. Additionally, several *in vivo* experiments of various Ti-salan derivatives have proved promising, showing significantly reduced tumor growth over the course of treatment [162–164]. This renders Ti-salan and salen derivatives appropriate for theranostic applications with [45]Ti. In a study by Severin and coworkers [152], one such salan derivative, (salan)Ti(dipic), was labeled with [45]Ti, using a novel solid-state synthesis. A symmetric 1,3-diol functionalized resin, was used to immobilize the [45]Ti, followed by step-wise coordination of the salan and dipic ligands to afford (salan)[45]Ti(dipic) with high radiochemical purity and 15 %

yield. Imaging and *ex vivo* biodistribution were conducted with mice bearing HT-29 tumors, but no significant tumor uptake was observed, while liver and intestinal uptake were enhanced, indicating poor tumor specificity of the (salan)[45]Ti(dipic) complex [147].

4.2.   Zirconium

4.2.1.   *Production and Speciation*

The long half-life and relatively low energy of the emitted positrons make Zr-89 ($t_{1/2} = 78.41$ h, $E_{\beta+} = 395$ keV, 22 %) an especially favorable isotope for immuno-PET imaging. Production of [89]Zr occurs primarily via the [89]Y(p,n)[89]Zr transmutation reaction. Radioactive [89]Zr is separated from the yttrium target with a hydroxamate-functionalized resin, and [89]Zr is eluted with oxalic acid in high specific activity (45 GBq/μmol) and purity (> 99.99 %) [165–168].

4.2.2.   *Common Chelators of Zirconium*

Zirconium is a second-row transition metal that exists primarily in the Lewis acidic, +4 oxidation state. Due to its high charge and oxophilicity, it binds strongly to hard donors such as hydroxamates [11]. The tris-hydroxamate siderophore DFO is the most often-used ligand for chelating zirconium. The DFO binds [89]Zr more efficiently than EDTA or DTPA [169]. To date, DFO-appended antibody tracers have been reported extensively and applied in preclinical and clinical PET imaging studies [168, 170–183].

Even though [89]Zr-DFO displays high stability *in vitro* with minimal demetallation [184], concerns regarding [89]Zr release from the chelator, evidenced by bone uptake in mouse models, remain [185]. Crystal structures of Zr-EDTA [186] and Zr-DTPA [187] have shown that zirconium will coordinate readily in octacoordinate fashion, thus research efforts have focused on developing an octadentate chelator that would provide greater stability *in vivo* than DFO. One approach is DFO*, a DFO derivative that incorporates four hydroxamate functional groups to coordinatively saturate the zirconium metal (Figure 9) [188, 189]. Similarly, Donnelly and coworkers have reported [89]Zr radiolabeling of DFO-Sq, a squaramide derivative of DFO with two additional carbonyls available to coordinate the zirconium ion [190]. Both DFO* and DFO-Sq display similar or improved radiolabeling efficiency compared to DFO, and result in decreased bone uptake in mouse models compared to DFO. However, these constructs also have diminished solubility in water, which complicates their conjugation to biomolecules. Alternatively, octadentate chelators with hydroxypyridinone donors have been studied, including HOPO and 2,3-HOPO (Figure 9) [191, 192]. Despite the increased stability of [89]Zr-HOPO and significantly lower bone uptake in comparison to [89]Zr-DFO, the complicated synthesis of preparing bifunctional HOPO ligands for conjugation to antibody has impeded further applications of this chelator to date [191].
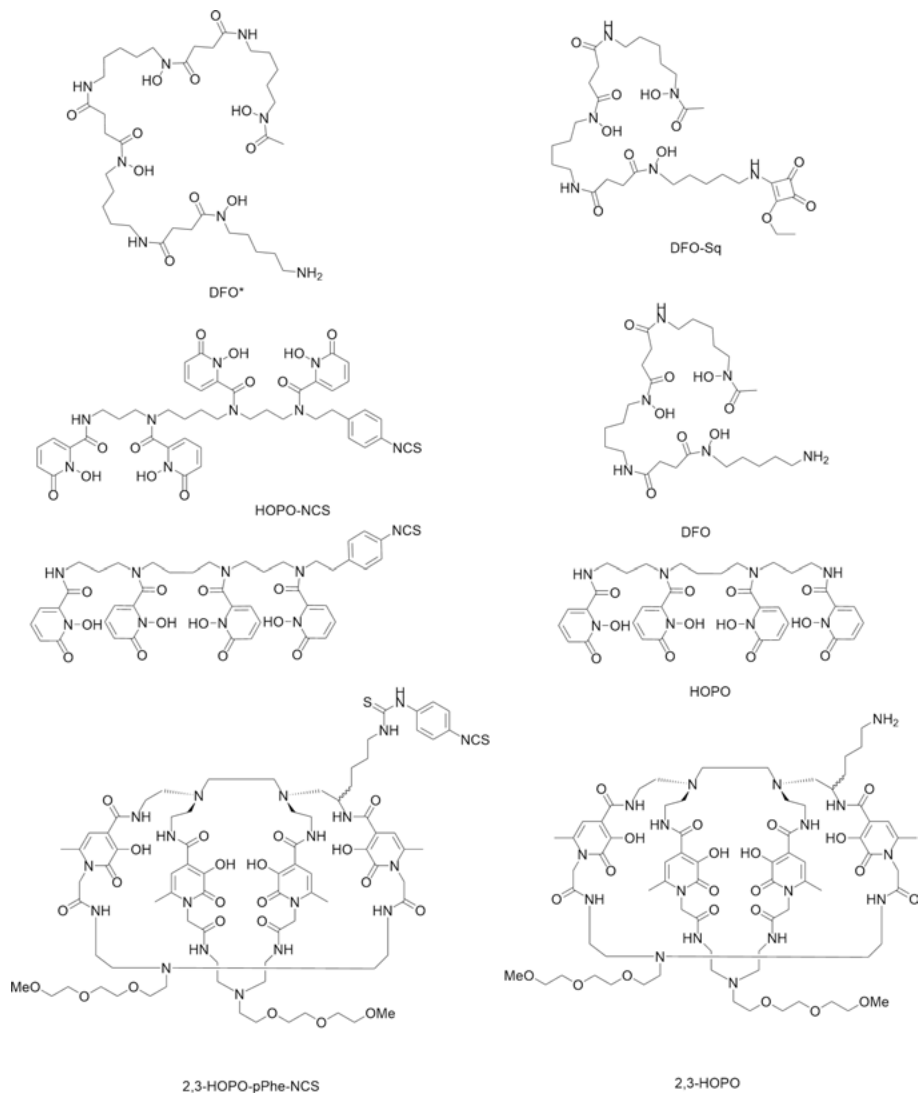
Figure 9. Commonly employed chelators for zirconium isotopes discussed herein.

4.2.3. Preclinical and Clinical Applications of ^{89}Zr

The first preclinical immunoPET imaging with ^{89}Zr was reported by Meijs et al. in 1997, in which ^{89}Zr-labeled anti-EpCam antibody 323/A3 was used to image mice with human OVCAR-3 xenografts [171]. In 2006, the first clinical imaging was performed with ^{89}Zr-labeled anti-CD44v6 antibody U36 in 20 patients with head and neck squamous carcinoma [193]. The patients were imaged 144 h after receiving ^{89}Zr-cmAb-U36; all primary tumors and 18 of 25 lymph node metasta-

ses were detected, demonstrating the better sensitivity of PET (72 %) over CT/ MRI (60 %).

Similarly, clinical imaging has been performed with [89]Zr-trastuzumab on patients with HER2-positive metastatic breast cancer to detect lesions in lung, liver, bone, and brain, and PET images helped reveal brain lesions that had previously been undetected [194]. In addition to detecting primary tumors and sites of metastases, [89]Zr-immunoPET can be used to accurately predict patient response to immunotherapy. PET imaging with [89]Zr-trastuzumab in tandem with [18]FDG scans helped to stratify patients that would show response to treatment with trastuzumab emtansine (T-DM1) by determining the level of tumor heterogeneity and level of HER2 expression [195].

Clinical PET imaging studies with [89]Zr-ibritumomab tiuxetan (commercial name Zevalin) have also been performed to predict response of patients with relapsed B-cell non-Hodgkin's lymphoma towards treatment with ^{90}Y-labeled ibritumomab tiuxetan [196–197]. Preclinical studies have shown that [89]Zr-bevacizumab PET can be used to monitor early antiangiogenic tumor response of patients with ovarian cancer to treatment with protein inhibition therapy (NVP-AUY922) [198, 199].

4.3.   Niobium

4.3.1.   *Production and Speciation*

Nb-90 ($t_{1/2}$ = 14.6 h, β^+, E_{mean} = 0.35 MeV, 53 %) is produced by irradiating natural zirconium foils (20 MeV) in the ^{90}Zr (p,n) ^{90}Nb reaction. The target is then dissolved with HF under reduced temperature, and following the addition of HCl and boric acid, ^{90}Nb is extracted with N-benzoyl-N-phenylhydroxylamine in $CHCl_3$. For complete removal of trace levels of zirconium, necessary because of the similarity in radiolabeling chemistries of niobium and zirconium, further purification by ion exchange chromatography is performed [200–202].

4.3.2.   *Radiolabeling and Preclinical Imaging with ^{90}Nb*

Rösch and coworkers demonstrated successful quantitative radiolabeling of DFO ligand with ^{90}Nb [201]. Furthermore, rituximab and bevacizumab coupled with the DFO chelator have been labeled with ^{90}Nb in radiochemical yields of > 90 %. Preclinical PET imaging of ^{90}Nb-bevacizumab in a mouse xenograft model at 4 h post-injection indicated visible uptake of the radiolabeled antibody in the tumor and liver [200, 202].

5.   CONCLUSIONS

As part of the recent resurgence of PET radionuclides, radiometals continue to take on an increasingly prominent role in developmental and clinical nuclear

medicine. Historically, most of the early PET metal work was focused on ^{64}Cu and its early successes with hypoxia imaging. The advent of the $^{68}Ge/^{68}Ga$ generator and convenient access to large quantities of ^{89}Zr due to the naturally abundant target material and production methods accessible with low-energy biomedical cyclotrons has moved those two isotopes to the foreground and among the currently most heavily investigated isotopes in nuclear medicine related clinical trials. The recent (2016) FDA approval of ^{68}Ga-DOTATATE for PET imaging for diagnosis, staging, and treatment management of neuroendocrine tumors, followed by the 2018 approval of the therapeutic analogue ^{177}Lu-DOTATATE has further spurred the development of theranostic isotopes: scandium, yttrium, lanthanum, and terbium isotopes are all interest in this regard and have recently begun to produce literature entries that detail their successful production, efficient chelation, and application.

The access to isotopes with more convenient, intermediate half-lives also enables imaging at time-points that fall between those accessible by ^{68}Ga and ^{89}Zr, and are also becoming of increasing interest such as ^{45}Ti, ^{52}Mn, ^{55}Co, and ^{90}Nb. ^{45}Ti and ^{90}Nb can be considered shorter-lived congeners to the already widely applied ^{89}Zr, but still require extensive development, especially with respect to efficient and robust chelation. The intermediate half-life of ^{55}Co provides opportunities for targeted imaging with larger peptides, rapidly circulating antibodies and antibody fragments. In addition to providing an alternative long-lived PET isotope to ^{89}Zr, ^{52}Mn may also open opportunities for multimodal applications in conjunction with ^{nat}Mn-based contrast agents and therefore add value to a growing PET-MR scanner base.

Conclusively, the field of PET radiometals is growing quickly and provides opportunities for medical physicists, coordination chemists, organic chemists, biochemists, and imaging scientists alike. However, the close collaboration of these groups of scientists is required to successfully transition these nuclides from radiochemical curiosity and exploratory preliminary studies to clinically relevant and viable products that will be able to improve patient outcomes.

ACKNOWLEDGMENTS

ABBREVIATIONS

AMBA	Gly-4-ABz-Gln-Trp-Ala-Val-Gly-His-Leu-Met-NH$_2$
ATSM	diacetylbis(N(4)-methylthiosemicarbazonato
BAT	6-(p-bromoacetamidobenzyl)-1,4,8,11-tetraazacyclotetradecane-1,4,8,11-tetraacetic acid

BDGA	branched diglycolamide
CB	cross-bridged
CDTA	cyclohexanediaminetetraacetic acid
CT	computed tomography
CB-DO2A	4,10-bis(carboxymethyl)-1,4,7,10-tetraazabicyclo[5.5.2]tetradecane
CB-TE2A	4,11-bis(carboxymethyl)-1,4,8,11-tetraazabicyclo[6.6.2]hexadecane
CXCR4	C-X-C chemokine receptor type 4
DFO	desferrioxamine
DFO-sq	desferrioxamine squaramide ester
Diamsar	1,8-diamino-3,6,10,13,16,19-hexaazabicyclo[6,6,6]-eicosane
DO3A	1,4,7,10-tetraazacyclododecane-1,4,7-triacetic acid trisodium salt
DO3Apic	2,2′,2″-(10-((6-carboxypyridin-2-yl)methyl)-1,4,7,10-tetraazacyclododecane-1,4,7-triyl)triacetic acid
DOTA	1,4,7,10-tetraazacyclododecane-1,4,7,10-tetraacetic acid
DOTAGA	1,4,7,10-tetraazacyclododececane,1-(glutaric acid)-4,7,10-triacetic acid
DOTANOC	DOTA-1-Nal^3-octreotide
DOTATATE	DOTA-(tyrosine^3)-octreotate
DOTATOC	DOTA-D-Phe^1-tyrosine^3-octreotide
DTPA	diethylenetriaminepentaacetic acid
EDTA	ethylenediaminetetraacetic acid
EGRF	epidermal growth factor receptor
FDA	Food and Drug Administration
^{18}FDG	fluorodeoxyglucose
GRPr	gastrin-releasing peptide receptor
HBED	N, N-bis(2-hydroxybenzyl)ethylenediamine-N,N-diacetic acid
HOPO	N,N′-1,4-Butanediylbis(N-(3-(((1,6-dihydro-1-hydroxy-6-oxo-2-pyridinyl)carbonyl)amino)propyl)-1,6-dihydro-1-hydroxy-6-oxo-2-pyridinecarboxamide
HSA	human serum albumin
MeCOSAR	5-(8-methyl-3,6,10,13,16,19-hexaaza-bicyclo[6.6.6]icosan-1-ylamino)-5-oxopentanoic acid
MEMRI	manganese-enhanced magnetic resonance imaging
NETs	neuroendocrine tumors
NODAGA	1,4,7-triazacyclononane,1-glutaric acid-4,7-acetic acid
NOTA	1,4,7-triazacyclononane-1,4,7-triacetic acid
NOTP	1,4,7-triazacyclononane-1,4,7-tri(methylene phosphonic acid)
PA01	*Pseudomonas aeruginosa* 01
PET	positron emission tomography
PSMA	prostate specific membrane antigen
PSMA-I&T	PSMA for imaging and therapy
PVD	pyoverdine
RGD	Arg-Gly-Asp
SAR	sarcophagine

SarAr	1-N-(4-aminobenzyl)-3,6,10,13,16,19-hexaazabicyclo[6,6,6]-eicosane-1,8-diamine
SARTATE	MeCOSar-tyrosine[3]-octreotate
SPECT	single-photon emission computed tomography
SSR	somatostatin receptors
TATE	(tyrosine[3])-octreotate
TETA	1,4,8,11-tetraazacyclotetradecane-1,4,8,11-tetraacetic acid
THP	tris(hydroxypyridinone)
TRAP	triazacyclononane phosphinic acid

REFERENCES

1. B. J. Pichler, H. F. Wehrl, M. S. Judenhofer, *J. Nucl. Med.* **2008**, *49*, 5S.
2. M. Morais, A. Paulo, L. Gano, I. Santos, J. D. Correia, *J. Organomet. Chem.* **2013**, *744*, 125–139.
3. M. Jensen, *Nucl. Med. Rev.* **2012**, *15*, 9–12.
4. H. Thisgaard, M. Jensen, D. R. Elema, *App. Rad. Isot.* **2011**, *69*, 1–7.
5. T. I. Kostelnik, C. Orvig, *Chem. Rev.* **2019**, *119*, 902–956.
6. E. Boros, A. B. Packard, *Chem. Rev.* **2019**, *119*, 870–901.
7. I. A. E. Agency, *Production of Long Lived Parent Radionuclides for Generators : 68Ge, 82Sr, 90Sr and 188W*, **2010**.
8. I. Velikyan, *Theranostics* **2014**, *4*, 47–80.
9. M. K. Pandey, J. F. Byrne, H. Jiang, A. B. Packard, T. R. DeGrado, *Am. J. Nucl. Med. Mol. Imaging* **2014**, *4*, 303–310.
10. S. Riga, G. Cicoria, D. Pancaldi, F. Zagni, S. Vichi, M. Dassenno, L. Mora, F. Lodi, M. P. Morigi, M. Marengo, *Phys. Med.* **2018**, *55*, 116–126.
11. T. J. Wadas, E. H. Wong, G. R. Weisman, C. J. Anderson, *Chem. Rev.* **2010**, *110*, 2858–2902.
12. M. I. Tsionou, C. E. Knapp, C. A. Foley, C. R. Munteanu, A. Cakebread, C. Imberti, T. R. Eykyn, J. D. Young, B. M. Paterson, P. J. Blower, M. T. Ma, *RSC Adv.* **2017**, *7*, 49586–49599.
13. M. McCarthy, T. Langton, D. Kumar, A. Campbell, *Eur. J. Nucl. Med. Mol. Imaging* **2017**, *44*, 1455–1462.
14. J. Yang, Y. Kan, B. H. Ge, L. Yuan, C. Li, W. Zhao, *Acta Radiol.* **2014**, *55*, 389–398.
15. D. A. Silver, I. Pellicer, W. R. Fair, W. D. W. Heston, C. Cordon-Cardo, *Clin. Cancer Res.* **1997**, *3*, 81–85.
16. N. Schülke, O. A. Varlamova, G. P. Donovan, D. Ma, J. P. Gardner, D. M. Morrissey, R. R. Arrigale, C. Zhan, A. J. Chodera, K. G. Surowitz, P. J. Maddon, W. D. W. Heston, W. C. Olson, *Proc. Natl. Acad. Sci. USA* **2003**, *100*, 12590–12595.
17. N. J. Rupp, C. A. Umbricht, D. A. Pizzuto, D. Lenggenhager, A. Töpfer, J. Müller, U. J. Muehlematter, D. A. Ferraro, M. Messerli, G. B. Morand, G. F. Huber, D. Eberli, R. Schibli, C. Müller, I. A. Burger, *J. Nucl. Med.* **2019**, *60*, 1270–1276.
18. T. J. W. Klein Nulent, M. H. Valstar, B. de Keizer, S. M. Willems, L. A. Smit, A. Al–Mamgani, L. E. Smeele, R. J. J. van Es, R. de Bree, W. V. Vogel, *Oral Surg. Oral Med. Oral Pathol. Oral Radiol.* **2018**, *125*, 478–486.
19. M. Eder, O. Neels, M. Müller, U. Bauder-Wüst, Y. Remde, M. Schäfer, U. Hennrich, M. Eisenhut, A. Afshar-Oromieh, U. Haberkorn, K. Kopka, *Pharmaceuticals* **2014**, *7*, 779–796.

20. M. Eder, M. Schäfer, U. Bauder-Wüst, W. E. Hull, C. Wängler, W. Mier, U. Haberkorn, M. Eisenhut, *Bioconjugate Chem.* **2012**, *23*, 688–697.

21. S. Lutje, T. D. Poeppel, S. Rosenbaum-Krumme, A. Bockisch, S. Heskamp, A. S. Cornelissen, M. Gotthardt, M. Rijpkema, O. C. Boerman, S. A. M. W. van den Broek, *Theranostics* **2015**, *5*, 1388–1408.

22. M. Cives, J. R. Strosberg, *CA Cancer J. Clin.* **2018**, *68*, 471–487.

23. S. A. Deppen, E. Liu, J. D. Blume, J. Clanton, C. Shi, L. B. Jones-Jackson, V. Lakhani, R. P. Baum, J. Berlin, G. T. Smith, M. Graham, M. P. Sandler, D. Delbeke, R. C. Walker, *J. Nucl. Med.* **2016**, *57*, 708–714.

24. M. Fani, G. P. Nicolas, D. Wild, *J. Nucl. Med.* **2017**, *58*, 61S–66S.

25. S. A. Deppen, J. Blume, A. J. Bobbey, C. Shah, M. M. Graham, P. Lee, D. Delbeke, R. C. Walker, *J. Nucl. Med.* **2016**, *57*, 872–878.

26. J. Strosberg, G. El-Haddad, E. Wolin, A. Hendifar, J. Yao, B. Chasen, E. Mittra, P. L. Kunz, M. H. Kulke, H. Jacene, D. Bushnell, T. M. O'Dorisio, R. P. Baum, H. R. Kulkarni, M. Caplin, R. Lebtahi, T. Hobday, E. Delpassand, E. Van Cutsem, A. Benson, R. Srirajaskanthan, M. Pavel, J. Mora, J. Berlin, E. Grande, N. Reed, E. Seregni, K. Öberg, M. L. Sierra, P. Santoro, T. Thevenet, J. L. Erion, P. Ruszniewski, D. Kwekkeboom, E. Krenning, *N. Engl. J. Med.* **2017**, *376*, 125–135.

27. B. L. R. Kam, J. J. M. Teunissen, E. P. Krenning, W. W. De Herder, S. Khan, E. I. Van Vliet, D. J. Kwekkeboom, *Eur. J. Nucl. Med. Mol. Imaging* **2012**, *39*, 103–112.

28. M. Petrik, C. Zhai, H. Haas, C. Decristoforo, *Clin. Transl. Imaging* **2017**, *5*, 15–27.

29. M. Petrik, E. Umlaufova, V. Raclavsky, A. Palyzova, V. Havlicek, H. Haas, Z. Novy, D. Dolezal, M. Hajduch, C. Decristoforo, *Sci Rep.* **2018**, *8*, 15698.

30. D. W. McCarthy, R. E. Shefer, R. E. Klinkowstien, L. A. Bass, W. H. Margeneau, C. S. Cutler, C. J. Anderson, M. J. Welch, *Nucl. Med. Biol.* **1997**, *24*, 35–43.

31. F. Alves, V. H. P. Alves, S. J. C. Do Carmo, A. C. B. Neves, M. Silva, A. J. Abrunhosa, *Mod. Phys. Lett. A* **2017**, *32*, 1740013–1740013.

32. Y. Fujibayashi, K. Matsumoto, Y. Yonekura, K. Junji, A. Yokoyama, *J. Nucl. Med.* **1989**, *30*, 1838–1842.

33. Z. Cai, C. J. Anderson, *J. Labelled Compd. Radiopharm.* **2014**, *57*, 224–230.

34. R. Ferdani, D. J. Stigers, A. L. Fiamengo, L. Wei, B. T. Y. Li, J. A. Golen, A. L. Rheingold, G. R. Weisman, E. H. Wong, C. J. Anderson, *Dalton Trans.* **2012**, *41*, 1938–1950.

35. E. H. Wong, G. R. Weisman, D. C. Hill, D. P. Reed, M. E. Rogers, J. S. Condon, M. A. Fagan, J. C. Calabrese, K. C. Lam, I. A. Guzei, A. L. Rheingold, *J. Amer. Chem. Soc.* **2000**, *122*, 10561–10572.

36. M. S. Cooper, M. T. Ma, K. Sunassee, K. P. Shaw, J. D. Williams, R. L. Paul, P. S. Donnelly, P. J. Blower, *Bioconjugate Chem.* **2012**, *23*, 1029–1039.

37. N. M. Di Bartolo, A. M. Sargeson, T. M. Donlevy, S. V. Smith, *Dalton Trans.* **2001**, 2303–2309.

38. P. J. Blower, J. S. Lewis, J. Zweit, *Nucl. Med. Biol.* **1996**, *23*, 957–980.

39. J. R. Ballinger, *Semin. Nucl. Med.* **2001**, *31*, 321–329.

40. A. L. Vavere, J. S. Lewis, *Dalton Trans.* **2007**, 4893–4902.

41. Y. Fujibayashi, H. Taniuchi, Y. Yonekura, H. Ohtani, J. Konishi, A. Yokoyama, *J. Nucl. Med.* **1997**, *38*, 1155–1160.

42. M. L. Lepage, H. T. Kuo, Á. Roxin, S. Huh, Z. Zhang, R. Kandasamy, H. Merkens, J. O. Kumlin, A. Limoges, S. K. Zeisler, K. S. Lin, F. Bénard, D. M. Perrin, *ChemBioChem* **2019**, *20*, 943–947.

43. N. A. Zia, C. Cullinane, J. K. Van Zuylekom, K. Waldeck, L. E. McInnes, G. Buncic, M. B. Haskali, P. D. Roselt, R. J. Hicks, P. S. Donnelly, *Angew. Chem. Int. Ed.* **2019**, *58*, 14991–14994.

44. B. Grubmüller, R. P. Baum, E. Capasso, A. Singh, Y. Ahmadi, P. Knoll, A. Floth, S. Righi, S. Zandieh, C. Meleddu, S. F. Shariat, H. C. Klingler, S. Mirzaei, *Cancer Biother. Radiopharm.* **2016**, *31*, 277–286.

45. R. P. Bandari, Z. Jiang, T. S. Reynolds, N. E. Bernskoetter, A. F. Szczodroski, K. J. Bassuner, D. L. Kirkpatrick, T. L. Rold, G. L. Sieckman, T. J. Hoffman, J. P. Connors, C. J. Smith, *Nucl. Med. Biol.* **2014**, *41*, 355–363.

46. S. R. Banerjee, M. Pullambhatla, C. A. Foss, S. Nimmagadda, R. Ferdani, C. J. Anderson, R. C. Mease, M. G. Pomper, *J. Med. Chem.* **2014**, *57*, 2657–2669.

47. A. F. Prasanphanich, P. K. Nanda, T. L. Rold, L. Ma, M. R. Lewis, J. C. Garrison, T. J. Hoffman, G. L. Sieckman, S. D. Figueroa, C. J. Smith, *Proc. Natl. Acad. Sci. USA* **2007**, *104*, 12462–12467.

48. A. F. Prasanphanich, L. Retzloff, S. R. Lane, P. K. Nanda, G. L. Sieckman, T. L. Rold, L. Ma, S. D. Figueroa, S. V. Sublett, T. J. Hoffman, C. J. Smith, *Nucl. Med. Biol.* **2009**, *36*, 171–181.

49. R. P. Bandari, Z. Jiang, T. S. Reynolds, N. E. Bernskoetter, A. F. Szczodroski, K. J. Bassuner, D. L. Kirkpatrick, T. L. Rold, G. L. Sieckman, T. J. Hoffman, J. P. Connors, C. J. Smith, *Nucl. Med. Biol.* **2014**, *41*, 355–363.

50. J. J. Parry, T. S. Kelly, R. Andrews, B. E. Rogers, *Bioconjugate Chem.* **2007**, *18*, 1110–1117.

51. M. T. Ma, J. A. Karas, J. M. White, D. Scanlon, P. S. Donnelly, *Chem. Commun.* **2009**, 3237–3239.

52. P. K. Nanda, U. Pandey, B. N. Bottenus, T. L. Rold, G. L. Sieckman, A. F. Szczodroski, T. J. Hoffman, C. J. Smith, *Nucl. Med. Biol.* **2012**, *39*, 461–471.

53. J. M. Craft, R. A. De Silva, K. A. Lears, R. Andrews, K. Liang, S. Achilefu, B. E. Rogers, *Nucl. Med. Biol.* **2012**, *39*, 609–616.

54. K. Durkan, Z. Jiang, T. L. Rold, G. L. Sieckman, T. J. Hoffman, R. P. Bandari, A. F. Szczodroski, L. Liu, Y. Miao, T. S. Reynolds, C. J. Smith, *Nucl. Med. Biol.* **2014**, *41*, 133–139.

55. S. Sarkar, N. Bhatt, Y. S. Ha, P. T. Huynh, N. Soni, W. Lee, Y. J. Lee, J. Y. Kim, D. N. Pandya, G. I. An, K. C. Lee, Y. Chang, J. Yoo, *J. Med. Chem.* **2018**, *61*, 385–395.

56. E. Gourni, L. Del Pozzo, E. Kheirallah, C. Smerling, B. Waser, J.-C. Reubi, B. M. Paterson, P. S. Donnelly, P. T. Meyer, H. R. Maecke, *Mol. Pharm.* **2015**, *12*, 2781–2790.

57. R. Hernandez, A. Czerwinski, R. Chakravarty, S. A. Graves, Y. Yang, C. G. England, R. J. Nickles, F. Valenzuela, W. Cai, *Eur. J. Nucl. Med. Mol. Imaging* **2015**, *42*, 1859–1868.

58. C. J. Anderson, F. Dehdashti, P. D. Cutler, S. W. Schwarz, R. Laforest, L. A. Bass, J. S. Lewis, D. W. McCarthy, *J. Nucl. Med.* **2001**, *42*, 213–221.

59. A. Pfeifer, U. Knigge, T. Binderup, J. Mortensen, P. Oturai, A. Loft, A. K. Berthelsen, S. W. Langer, P. Rasmussen, D. Elema, E. Von Benzon, L. Hjgaard, A. Kjaer, *J. Nucl. Med.* **2015**, *56*, 847–854.

60. A. Pfeifer, U. Knigge, J. Mortensen, P. Oturai, A. K. Berthelsen, A. Loft, T. Binderup, P. Rasmussen, D. Elema, T. L. Klausen, S. Holm, E. Von Benzon, L. Højgaard, A. Kjaer, *J. Nucl. Med.* **2012**, *53*, 1207–1215.

61. C. B. Johnbeck, U. Knigge, A. Loft, A. K. Berthelsen, J. Mortensen, P. Oturai, S. W. Langer, D. R. Elema, A. Kjaer, *J. Nucl. Med.* **2017**, *58*, 451–457.

62. R. J. Hicks, P. Jackson, G. Kong, R. E. Ware, M. S. Hofman, D. A. Pattison, T. A. Akhurst, E. Drummond, P. Roselt, J. Callahan, R. Price, C. M. Jeffery, E. Hong, W. Noonan, A. Herschtal, L. J. Hicks, A. Hedt, M. Harris, B. M. Paterson, P. S. Donnelly, *J. Nucl. Med.* **2019**, *60*, 777–785.

63. B. Burke, C. Miranda, R. Lee, I. Renard, S. Nigam, G. Clemente, T. D'Huys, T. Ruest, J. Domarkas, J. Thompson, D. Schols, T. Hubin, C. Cawthorne, S. Archibald, *J. Nucl. Med.* **2019**, *61*, 123–128.

64. A. M. E. Walenkamp, C. Lapa, K. Herrmann, H. J. Wester, *J. Nucl. Med.* **2017**, *58*, 77S–82S.

65. B. Burke, C. Miranda, R. Lee, I. Renard, S. Nigam, G. Clemente, T. D'Huys, T. Ruest, J. Domarkas, J. Thompson, D. Schols, T. Hubin, C. Cawthorne, S. Archibald, *Journal of Nuclear Medicine* **2019**, doi: 10.2967/jnumed.118.218008.

66. M. R. Lewis, C. A. Boswell, R. Laforest, T. L. Buettner, D. Ye, J. M. Connett, C. J. Anderson, *Cancer Biother. Radiopharm.* **2001**, *16*, 483–494.

67. S. J. DeNardo, G. L. DeNardo, D. L. Kukis, S. Shen, L. A. Kroger, D. A. DeNardo, D. S. Goldstein, G. R. Mirick, Q. Salako, L. F. Mausner, S. C. Srivastava, C. F. Meares, *J. Nucl. Med.* **1999**, *40*, 302–310.

68. J. L. J. Dearling, S. D. Voss, P. Dunning, E. Snay, F. Fahey, S. V. Smith, J. S. Huston, C. F. Meares, S. T. Treves, A. B. Packard, *Nucl. Med. Biol.* **2011**, *38*, 29–38.

69. J. H. Lee, H. Kim, Z. Yao, S. J. Lee, L. P. Szajek, L. Grasso, I. Pastan, C. H. Paik, *Nucl. Med. Biol.* **2015**, *42*, 880–886.

70. M. Brandt, J. Cardinale, I. Rausch, T. L. Mindt, *J. Labelled Compd. Radiopharm.* **2019**, *62*, 541–551.

71. A. Sánchez-Crespo, P. Andreo, S. A. Larsson, *Eur. J. Nucl. Med. Mol. Imaging* **2004**, *31*, 44–51.

72. R. W. Atcher, A. M. Friedman, J. R. Huizenga, G. V. Rayudu, E. A. Silverstein, D. A. Turner, *J. Nucl. Med.* **1980**, *21*, 566–569.

73. C. Vanasschen, M. Brandt, J. Ermert, H. H. Coenen, *Dalton Trans.* **2016**, *45*, 1315–1321.

74. A. T. J. Klein, F. Rosch, S. M. Qaim, *Radiochim. Acta* **2000**, *88*, 253–264.

75. S. A. Graves, R. Hernandez, J. Fonslet, C. G. England, H. F. Valdovinos, P. A. Ellison, T. E. Barnhart, D. R. Elema, C. P. Theuer, W. Cai, R. J. Nickles, G. W. Severin, *Bioconjugate Chem.* **2015**, *26*, 2118–2124.

76. A. L. Wooten, T. A. Aweda, B. C. Lewis, R. B. Gross, S. E. Lapi, *PLoS One* **2017**, *12*, 1–14.

77. R. Hernandez, S. A. Graves, T. Gregg, H. R. VanDeusen, R. J. Fenske, H. N. Wienkes, C. G. England, H. F. Valdovinos, J. J. Jeffery, T. E. Barnhart, G. W. Severin, R. J. Nickles, M. E. Kimple, M. J. Merrins, W. Cai, *Diabetes* **2017**, *66*, 2163–2174.

78. A. Meyer, K. Stolz, W. Dreher, J. Bergemann, V. H. Thimmashetty, N. Lueschen, Z. Azizi, V. Khobragade, K. Maedler, E. Kuestermann, *Diabetes* **2015**, *64*, 2138–2147.

79. S. A. Graves, R. Hernandez, H. F. Valdovinos, P. A. Ellison, J. W. Engle, T. E. Barnhart, W. Cai, R. J. Nickles, *Sci. Rep.* **2017**, *7*, 1–14.

80. M. Uddin Khandaker, S. K. I. Ali, H. Abu Kassim, N. Yusof, *Radiat. Phys. Chem.* **2017**, *140*, 511–520.

81. N. Amjed, M. Hussain, M. N. Aslam, F. Tárkányi, S. M. Qaim, *Appl. Radiat. Isot.* **2016**, *108*, 38–48.

82. T. Mastren, B. V. Marquez, D. E. Sultan, E. Bollinger, P. Eisenbeis, T. Voller, S. E. Lapi, *Mol. Imaging* **2015**, *15*, 526–532.

83. H. Thisgaard, M. L. Olesen, J. H. Dam, *J. Labelled Compd. Radiopharm.* **2011**, *54*, 758–762.

84. B. Mitran, H. Thisgaard, U. Rosenström, J. H. Dam, M. Larhed, V. Tolmachev, A. Orlova, *Contrast Media Mol. Imaging* **2017**, *2017*, 1–10.

85. B. Mitran, H. Thisgaard, S. Rinne, J. H. Dam, F. Azami, V. Tolmachev, A. Orlova, U. Rosenström, *Sci. Rep.* **2019**, *9*, 1–11.

86. J. H. Dam, B. B. Olsen, C. Baun, P. F. Høilund-Carlsen, H. Thisgaard, *Mol. Imag. Biol.* **2017**, *19*, 915–922.

87. J. H. Dam, B. B. Olsen, C. Baun, P.-F. Høilund-Carlsen, H. Thisgaard, *Mol. Imag. Biol.* **2016**, *18*, 368–376.

88. J. Garousi, K. G. Andersson, J. H. Dam, B. B. Olsen, B. Mitran, A. Orlova, J. Buijs, S. Ståhl, J. Löfblom, H. Thisgaard, V. Tolmachev, *Sci. Rep.* **2017**, *7*, 1–10.

89. A. Heppeler, J. P. André, I. Buschmann, X. Wang, J. C. Reubi, M. Hennig, T. A. Kaden, H. R. Maecke, *Chem. Eur. J.* **2008**, *14*, 3026–3034.

90. T. L. Andersen, C. Baun, B. B. Olsen, J. H. Dam, H. Thisgaard, *J. Nucl. Med.* **2019**, 1–17.

91. C. Duchemin, A. Guertin, F. Haddad, N. Michel, V. Metivier, *Phys. Med. Biol.* **2015**, *60*, 6847–6864.

92. E. Garcia-Torano, V. Peyres, M. Roteta, A. I. Sanchez-Cabezudo, E. Romero, A. Martinez Ortega, *Appl. Radiat. Isot.* **2016**, *109*, 314–318.

93. I. Ahmad, G. Bonino, G. C. Castagnoli, S. M. Fischer, W. Kutschera, M. Paul, *Phys. Rev. Lett.* **1998**, *80*, 2550–2553.

94. V. Radchenko, J. W. Engle, D. G. Medvedev, J. M. Maassen, C. M. Naranjo, G. A. Unc, C. A. L. Meyer, T. Mastren, M. Brugh, L. Mausner, C. S. Cutler, E. R. Birnbaum, K. D. John, F. M. Nortier, M. E. Fassbender, *Nucl. Med. Biol.* **2017**, *50*, 25–32.

95. E. Eppard, A. de la Fuente, M. Benesova, A. Khawar, R. A. Bundschuh, F. C. Gaertner, B. Kreppel, K. Kopka, M. Essler, F. Roesch, *Theranostics* **2017**, *7*, 4359–4369.

96. F. Roesch, *Curr. Radiopharm.* **2012**, *5*, 187–201.

97. V. Radchenko, C. A. L. Meyer, J. W. Engle, C. M. Naranjo, G. A. Unc, T. Mastren, M. Brugh, E. R. Birnbaum, K. D. John, F. M. Nortier, M. E. Fassbender, *J. Chromatogr. A* **2016**, *1477*, 39–46.

98. D. Wittwer, R. Dressler, R. Eichler, H. W. Gaggeler, D. Piguet, A. Serov, A. Turler, A. Vogele, *Radiochim. Acta* **2011**, *99*, 193–196.

99. N. P. van der Meulen, M. Bunka, K. A. Domnanich, C. Muller, S. Haller, C. Vermeulen, A. Turler, R. Schibli, *Nucl. Med. Biol.* **2015**, *42*, 745–751.

100. C. Hoehr, E. Oehlke, C. J. Lee, B. Badesso, S. Ferguson, Q. Miao, H. Yang, K. Buckley, V. Hanemaayer, S. Zeisler, F. Benard, X. Hou, A. Celler, T. Ruth, P. Schaffer, *Nucl. Med. Biol* **2014**, *41*, 401–406.

101. G. W. Severin, J. W. Engle, H. F. Valdovinos, T. E. Barnhart, R. J. Nickles, *Appl. Radiat. Isot.* **2012**, *70*, 1526–1530.

102. W. Wojdowska, D. Pawlak, I. Cieszykowska, M. Zoltowska, T. Janiak, T. Barcikowski, J. Parus, P. Garnuszek, R. Mikolajczak, A. Stolarz, J. Choinski, *Nucl. Med. Rev. Cent. East. Eur.* **2019**, *22*, 56–59.

103. K. Kilian, M. Sitarz, J. Choinski, A. Stolarz, L. Cheda, M. Sitarz, K. Szkliniarz, *Molecules* **2018**, *23*, E1787, doi: 10.3390/molecules23071787.

104. S. Krajewski, I. Cydzik, K. Abbas, A. Bulgheroni, F. Simonelli, U. Holzwarth, A. Bilewicz, *Radiochim. Acta* **2013**, *101*, 333–338.

105. *Scandium: Its Occurrence, Chemistry, Physics, Metallurgy, Biology, and Technology*, Ed. C. T. Horovitz, Academic Press, London, New York, San Francisco, **1975**.

106. R. Kerdjoudj, S. Huclier-Markai, M. Pniok, V. Kubicek, J. Havlickova, P. Hermann, C. Alliot, F. Roesch, *Dalton Trans.* **2016**, *45*, 1398–1409.

107. G. Nagy, D. Szikra, G. Trencsenyi, A. Fekete, I. Garai, A. M. Giani, R. Negri, N. Masciocchi, A. Maiocchi, F. Uggeri, I. Toth, S. Aime, G. B. Giovenzana, Z. Baranyai, *Angew. Chem. Int. Ed.* **2017**, *56*, 2118–2122.

108. J.-P. Sinnes, J. Nagel, F. Rösch, *EJNMMI Radiopharm. Chem.* **2019**, *4*, 18.

109. B. A. Vaughn, S. H. Ahn, E. Aluicio-Sarduy, J. Devaraj, A. P. Olson, J. Engle, E. Boros, *Chem. Sci.* **2020**, *11*, 333–342.

110. L. Li, M. d. G. Jaraquemada-Pelaez, E. Aluicio-Sarduy, X. Wang, D. Jiang, M. Sakheie, H.-T. Kuo, T. E. Barnhart, W. Cai, V. Radchenko, P. Schaffer, K.-S. Lin, J. W. Engle, F. Benard, C. Orvig, *Inorg. Chem.* **2020**, *59*, 1985–1995.

111. A. Khawar, E. Eppard, J. P. Sinnes, F. Roesch, H. Ahmadzadehfar, S. Kurpig, M. Meisenheimer, F. C. Gaertner, M. Essler, R. A. Bundschuh, *Clin. Nucl. Med.* **2018**, *43*, 323–330.

112. A. Singh, N. M. van der Meulen, C. Müller, I. Klette, H. R. Kulkarni, A. Türler, R. Schibli, R. P. Baum, *Cancer Biother. Radiopharm.* **2017**, *32*, 124–132.

113. C. Müller, *Molecules* **2013**, *18*, 5005–5031.

114. C. Müller, M. Bunka, S. Haller, U. Koester, V. Groehn, P. Bernhardt, N. van der Meulen, A. Tuerler, R. Schibli, *J. Nucl. Med.* **2014**, *55*, 1658–1664.

115. R. Chakravarty, S. Goel, H. F. Valdovinos, R. Hernandez, H. Hong, R. J. Nickles, W. Cai, *Bioconjugate Chem.* **2014**, *25*, 2197–2204.

116. P. E. Edem, A. Kjaer, M. M. Herth, P. E. Edem, A. Kjaer, P. E. Edem, M. M. Herth, J.-P. Sinnes, F. Rösch, S. Pektor, N. Bausbacher, M. Miederer, R. Rossin, M. S. Robillard, A. Yazdani, J. F. Valliant, A. Yazdani, *EJNMMI Res.* **2019**, *9*, 49.

117. E. Oehlke, C. Hoehr, X. Hou, V. Hanemaayer, S. Zeisler, M. J. Adam, T. J. Ruth, A. Celler, K. Buckley, F. Benard, P. Schaffer, *Nucl. Med. Biol.* **2015**, *42*, 842–849.

118. F. Roesch, H. Herzog, S. M. Qaim, *Pharmaceuticals* **2017**, *10*, 56/51–56/28.

119. M. A. Avila-Rodriguez, J. A. Nye, R. J. Nickles, *Appl. Radiat. Isot.* **2008**, *66*, 9–13.

120. A. Baimukhanova, V. Radchenko, J. Kozempel, A. Marinova, V. Brown, V. Karandashev, D. Karaivanov, P. Schaffer, D. Filosofov, *J. Radioanal. Nucl. Chem.* **2018**, *316*, 191–199.

121. L. Camera, S. Kinuya, K. Garmestani, C. Wu, M. W. Brechbiel, L. H. Pai, T. J. McMurry, O. A. Gansow, I. Pastan, C. H. Paik, J. A. Carrasquillo, *J. Nucl. Med.* **1994**, *35*, 882–889.

122. R. Tian, O. Jacobson, G. Niu, D. O. Kiesewetter, Z. Wang, G. Zhu, Y. Ma, G. Liu, X. Chen, *Theranostics* **2018**, *8*, 735–745.

123. S. R. Banerjee, C. A. Foss, M. Pullambhatla, Y. Wang, S. Srinivasan, R. F. Hobbs, K. E. Baidoo, M. W. Brechbiel, S. Nimmagadda, R. C. Mease, G. Sgouros, M. G. Pomper, *J. Nucl. Med.* **2015**, *56*, 628–634.

124. K. Garmestani, D. E. Milenic, P. S. Plascjak, M. W. Brechbiel, *Nucl. Med. Biol.* **2002**, *29*, 599–606.

125. T. K. Nayak, K. Garmestani, K. E. Baidoo, D. E. Milenic, M. W. Brechbiel, *J. Nucl. Med.* **2010**, *51*, 942–950.

126. E. Aluicio-Sarduy, R. Hernandez, A. P. Olson, T. E. Barnhart, W. Cai, P. A. Ellison, J. W. Engle, *Scientific Reports* **2019**, *9*, 1–6.

127. E. P. Abel, H. K. Clause, J. Fonslet, R. J. Nickles, G. W. Severin, *Phys. Rev. C* **2018**, *97*, 1–5.

128. M. Regueiro-Figueroa, B. Bensenane, E. Ruscsák, D. Esteban-Gómez, L. J. Charbonnière, G. Tircsó, I. Tóth, A. De Blas, T. Rodríguez-Blas, C. Platas-Iglesias, *Inorg. Chem.* **2011**, *50*, 4125–4141.

129. N. A. Thiele, V. Brown, J. M. Kelly, A. Amor-Coarasa, U. Jermilova, S. N. MacMillan, A. Nikolopoulou, S. Ponnala, C. F. Ramogida, A. K. H. Robertson, C. Rodriguez-Rodriguez, P. Schaffer, C. Williams, Jr., J. W. Babich, V. Radchenko, J. J. Wilson, *Angew. Chem. Int. Ed. Engl.* **2017**, *56*, 14712–14717.

130. E. Aluicio-Sarduy, N. A. Thiele, K. E. Martin, B. A. Vaughn, J. Devaraj, A. P. Olson, T. E. Barnhart, J. J. Wilson, E. Boros, J. W. Engle, *Chemistry-A European Journal* **2019**, *26*, 1238–1242.

131. B. J. Allen, G. Goozee, S. Sarkar, G. Beyer, C. Morel, A. P. Byrne, *Appl. Rad. Isotopes* **2001**, *54*, 53–58.

132. C. Müller, K. Zhernosekov, U. Köster, K. Johnston, H. Dorrer, A. Hohn, N. T. Van Der Walt, A. Türler, R. Schibli, *J. Nucl. Med.* **2012**, *53*, 1951–1959.

133. C. Vermeulen, G. F. Steyn, F. Szelecsényi, Z. Kovács, K. Suzuki, K. Nagatsu, T. Fukumura, A. Hohn, T. N. Van Der Walt, *Nuclear Instruments and Methods in Physics Research, Section B: Beam Interactions with Materials and Atoms* **2012**, *275*, 24–32.

134. R. P. Baum, A. Singh, M. Benešová, C. Vermeulen, S. Gnesin, U. Köster, K. Johnston, D. Müller, S. Senftleben, H. R. Kulkarni, A. Türler, R. Schibli, J. O. Prior, N. P. Van Der Meulen, C. Müller, *Dalton Trans.* **2017**, *46*, 14638–14646.

135. T. I. Kostelnik, C. Orvig, *Chem. Rev.* **2019**, *119*, 902–956.

136. J. Byegård, G. Skarnemark, M. Skålberg, *J. Radioanal. Nucl. Chem.* **1999**, *241*, 281–290.

137. C. Müller, K. Zhernosekov, U. Köster, K. Johnston, H. Dorrer, A. Hohn, N. T. Van Der Walt, A. Türler, R. Schibli, *J. Nucl. Med.* **2012**, *53*, 1951–1959.

138. C. Müller, C. Vermeulen, U. Köster, K. Johnston, A. Türler, R. Schibli, N. P. van der Meulen, *EJNMMI Radiopharmacy and Chemistry* **2017**, *1*, 2–6.

139. C. Müller, A. Singh, C. A. Umbricht, H. R. Kulkarni, K. Johnston, M. Benešová, S. Senftleben, D. Müller, C. Vermeulen, R. Schibli, U. Köster, N. P. van der Meulen, R. P. Baum, *EJNMMI Research* **2019**, *9*, 1–10.

140. R. P. Baum, A. Singh, M. Benešová, C. Vermeulen, S. Gnesin, U. Köster, K. Johnston, D. Müller, S. Senftleben, H. R. Kulkarni, A. Türler, R. Schibli, J. O. Prior, N. P. Van Der Meulen, C. Müller, *Dalton Trans.* **2017**, *46*, 14638–14646.

141. C. A. Umbricht, U. Köster, P. Bernhardt, N. Gracheva, K. Johnston, R. Schibli, N. P. van der Meulen, C. Müller, *Sci. Rep.* **2019**, *9*, 1–10.

142. C. A. Umbricht, U. Köster, P. Bernhardt, N. Gracheva, K. Johnston, R. Schibli, N. P. van der Meulen, C. Müller, *Sci. Rep.* **2019**, *9*, 1–10.

143. C. Müller, J. Reber, S. Haller, H. Dorrer, P. Bernhardt, K. Zhernosekov, A. Türler, R. Schibli, *E. J. Nucl. Med. Mol. Imaging* **2014**, *41*, 476–485.

144. J. C. Merrill, R. M. Lambrecht, A. P. Wolf, *Int. J. Appl. Radiat. Isot.* **1978**, *29*, 115–116.

145. M. Sadeghi, M. Enferadi, H. Nadi, *Radiochemistry* **2011**, *53*, 411–414.

146. A. L. Vavere, R. Laforest, M. J. Welch, *Nucl. Med. Biol.* **2005**, *32*, 117–122.

147. G. W. Severin, C. H. Nielsen, A. I. Jensen, J. Fonslet, A. Kjaer, F. Zhuravlev, *J. Med. Chem.* **2015**, *58*, 7591–7595.

148. K. P. Kepp, *Inorg. Chem.* **2016**, *55*, 9461–9470.

149. M. Saxena, S. A. Loza-Rosas, K. Gaur, S. Sharma, S. C. Perez Otero, A. D. Tinoco, *Coord. Chem. Rev.* **2018**, *363*, 109–125.

150. J. Schmidt, W. Vogelsberger, *J. Solution Chem.* **2009**, *38*, 1267–1282.

151. K. Gagnon, G. W. Severin, T. E. Barnhart, J. W. Engle, H. F. Valdovinos, R. J. Nickles, in *14th International Workshop on Targetry and Target Chemistry, Vol. 1509*, AIP Conf. Proc, Playa Del Carmen, Mexico, **2012**, pp. 211–214.

152. F. Chen, H. F. Valdovinos, R. Hernandez, S. Goel, T. E. Barnhart, W. Cai, *Acta Pharmacol. Sin.* **2017**, *38*, 907–913.

153. K. E. Jones, K. L. Batchler, C. Zalouk, A. M. Valentine, *Inorg. Chem.* **2017**, *56*, 1264–1272.

154. T. Baramov, K. Keijzer, E. Irran, E. Mosker, M. H. Baik, R. Sussmuth, *Chem. Eur. J.* **2013**, *19*, 10536–10542.

155. P. Costa, L. Metello, F. Alves, M. Duarte Naia, *Instruments* **2018**, *2*.

156. K. Ishiwata, T. Ido, M. Monma, M. Murakami, H. Fukuda, K. Yamada, S. Endo, S. Yoshioka, T. Sato, T. Matsuzawa, in *CYRIC Annual Report*, **1981**.

157. K. Ishiwata, T. Ido, M. Monma, M. Murakami, H. Fukuda, M. Kameyama, K. Yamada, S. Endo, S. Yoshioka, T. Sato, T. Matsuzawa, *Int. J. Radiat. Appl. Instrum. Part A Appl. Radiat. Isot.* **1991**, *42*, 707–712.

158. A. Tzubery, E. Y. Tshuva, *Inorg. Chem.* **2012**, *51*, 1796–1804.

159. H. Glasner, E. Y. Tshuva, *Inorg. Chem.* **2014**, *53*, 3170–3176.

160. T. A. Immel, M. Grutzke, E. Batroff, U. Groth, T. Huhn, *J. Inorg. Biochem.* **2012**, *106*, 68–75.

161. A. Tzubery, E. Y. Tshuva, *Eur. J. Inorg. Chem.* **2017**, *2017*, 1695–1705.

162. T. A. Immel, M. Grutzke, A. K. Spate, U. Groth, P. Ohlschlager, T. Huhn, *Chem. Commun.* **2012**, *48*, 5790–5792.

163. T. A. Immel, U. Groth, T. Huhn, P. Ohlschlager, *PLoS One* **2011**, *6*, e17869.

164. M. Miller, O. Braitbard, J. Hochman, E. Y. Tshuva, *J. Inorg. Biochem.* **2016**, *163*, 250–257.

165. E. Aluicio-Sarduy, P. A. Ellison, T. E. Barnhart, W. Cai, R. J. Nickles, J. W. Engle, *J. Labelled Compd. Radiopharm.* **2018**, *61*, 636–651.

166. J. P. Holland, Y. Sheh, J. S. Lewis, *Nucl. Med. Biol.* **2009**, *36*, 729–739.

167. P. A. Ellison, H. F. Valdovinos, S. A. Graves, T. E. Barnhart, R. J. Nickles, *Appl. Radiat. Isot.* **2016**, *118*, 350–353.

168. M. A. Deri, B. M. Zeglis, L. C. Francesconi, J. S. Lewis, *Nucl. Med. Biol.* **2013**, *40*, 3–14.

169. M. T. Friend, N. A. Wall, *Inorg. Chim. Acta* **2019**, *484*, 357–367.

170. Y. W. S. Jauw, C. W. Menke-van der Houven van Oordt, O. S. Hoekstra, N. H. Hendrikse, D. J. Vugts, J. M. Zijlstra, M. C. Huisman, G. A. M. S. van Dongen, *Front. Pharmacol.* **2016**, *7*.

171. W. E. Meijs, H. J. Haisma, R. P. Klok, F. B. Van Gog, E. Kievit, H. M. Pinedo, J. D. Herscheid, *J. Nucl. Med.* **1997**, *38*, 112–118.

172. G. Fischer, U. Seibold, R. Schirrmacher, B. Wängler, C. Wängler, *Molecules* **2013**, *18*, 6469–6490.

173. I. Verel, G. W. Visser, R. Boellaard, M. Stigter-van Walsum, G. B. Snow, G. A. van Dongen, *J. Nucl. Med.* **2003**, *44*, 1271–1281.

174. L. R. Perk, M. J. Vosjan, G. W. Visser, M. Budde, P. Jurek, G. E. Kiefer, G. A. van Dongen, *Eur. J. Nucl. Med. Mol. Imaging* **2010**, *37*, 250–259.

175. N. J. Sijbrandi, E. Merkul, J. A. Muns, D. C. Waalboer, K. Adamzek, M. Bolijn, V. Montserrat, G. W. Somsen, R. Haselberg, P. J. Steverink, *Cancer Res.* **2017**, *77*, 257–267.

176. B. M. Zeglis, P. Mohindra, G. I. Weissmann, V. Divilov, S. A. Hilderbrand, R. Weissleder, J. S. Lewis, *Bioconjugate Chem.* **2011**, *22*, 2048–2059.

177. D. J. Vugts, A. Vervoort, M. Stigter-van Walsum, G. W. Visser, M. S. Robillard, R. M. Versteegen, R. C. Vulders, J. D. Herscheid, G. A. Van Dongen, *Bioconjugate Chem.* **2011**, *22*, 2072–2081.

178. J. N. Tinianow, H. S. Gill, A. Ogasawara, J. E. Flores, A. N. Vanderbilt, E. Luis, R. Vandlen, M. Darwish, J. R. Junutula, S.-P. Williams, *Nucl. Med. Biol.* **2010**, *37*, 289–297.

179. M. T. Ma, L. K. Meszaros, B. M. Paterson, D. J. Berry, M. S. Cooper, Y. Ma, R. C. Hider, P. J. Blower, *Dalton Trans.* **2015**, *44*, 4884–4900.

180. B. M. Zeglis, C. B. Davis, R. Aggeler, H. C. Kang, A. Chen, B. J. Agnew, J. S. Lewis, *Bioconjugate chem.* **2013**, *24*, 1057–1067.

181. M. J. Vosjan, L. R. Perk, G. W. Visser, M. Budde, P. Jurek, G. E. Kiefer, G. A. Van Dongen, *Nat. Protoc.* **2010**, *5*, 739–743.

182. J.-P. Meyer, P. Adumeau, J. S. Lewis, B. M. Zeglis, *Bioconjugate Chem.* **2016**, *27*, 2791–2807.

183. B. M. Zeglis, C. B. Davis, D. Abdel-Atti, S. D. Carlin, A. Chen, R. Aggeler, B. J. Agnew, J. S. Lewis, *Bioconjugate Chem.* **2014**, *25*, 2123–2128.

184. J. P. Holland, V. Divilov, N. H. Bander, P. M. Smith-Jones, S. M. Larson, J. S. Lewis, *J. Nucl. Med.* **2010**, *51*, 1293–1300.

185. S. Heskamp, R. Raavé, O. Boerman, M. Rijpkema, V. Goncalves, F. Denat, *Bioconjugate Chem.* **2017**, *28*, 2211–2223.

186. A. I. Pozhidaev, M. A. Porai-Koshits, T. N. Polynova, *J. Struct. Chem.* **1974**, *15*, 548–553.

187. A. Ilyukhin, R. Davidovich, I. Samsonova, L. Teplukhina, *Crystallogr. Rep.* **2000**, *45*, 39–43.

188. M. Patra, A. Bauman, C. Mari, C. A. Fischer, O. Blacque, D. Häussinger, G. Gasser, T. L. Mindt, *Chem. Commun.* **2014**, *50*, 11523–11525.

189. D. J. Vugts, C. Klaver, C. Sewing, A. J. Poot, K. Adamzek, S. Huegli, C. Mari, G. W. Visser, I. E. Valverde, G. Gasser, *Eur. J. Nucl. Med. Mol. Imaging* **2017**, *44*, 286–295.

190. S. E. Rudd, P. Roselt, C. Cullinane, R. J. Hicks, P. S. Donnelly, *Chem. Commun.* **2016**, *52*, 11889–11892.

191. M. A. Deri, S. Ponnala, P. Kozlowski, B. P. Burton-Pye, H. T. Cicek, C. Hu, J. S. Lewis, L. C. Francesconi, *Bioconjugate Chem.* **2015**, *26*, 2579–2591.

192. J. N. Tinianow, D. N. Pandya, S. L. Pailloux, A. Ogasawara, A. N. Vanderbilt, H. S. Gill, S.-P. Williams, T. J. Wadas, D. Magda, J. Marik, *Theranostics* **2016**, *6*, 511–521.

193. P. K. Börjesson, Y. W. Jauw, R. Boellaard, R. De Bree, E. F. Comans, J. C. Roos, J. A. Castelijns, M. J. Vosjan, J. A. Kummer, C. R. Leemans, *Clin. Cancer Res.* **2006**, *12*, 2133–2140.

194. E. Dijkers, T. Oude Munnink, J. Kosterink, A. Brouwers, P. Jager, J. De Jong, G. Van Dongen, C. Schröder, M. Lub-de Hooge, E. De Vries, *Clin. Pharmacol. Ther.* **2010**, *87*, 586–592.

195. G. Gebhart, L. Lamberts, Z. Wimana, C. Garcia, P. Emonts, L. Ameye, S. Stroobants, M. Huizing, P. Aftimos, J. Tol, *Ann. Oncol.* **2016**, *27*, 619–624.

196. L. R. Perk, O. J. Visser, M. Stigter-van Walsum, M. J. Vosjan, G. W. Visser, J. M. Zijlstra, P. C. Huijgens, G. A. Van Dongen, *Eur. J. Nucl. Med. Mol. Imaging* **2006**, *33*, 1337–1345.

197. S. N. Rizvi, O. J. Visser, M. J. Vosjan, A. van Lingen, O. S. Hoekstra, J. M. Zijlstra, P. C. Huijgens, G. A. van Dongen, M. Lubberink, *Eur. J. Nucl. Med. Mol. Imaging* **2012**, *39*, 512–520.

198. T. H. O. Munnink, M. A. de Korte, W. B. Nagengast, H. Timmer-Bosscha, C. P. Schröder, J. R. de Jong, G. A. van Dongen, M. R. Jensen, C. Quadt, M. N. Lub-de Hooge, *Eur. J. Cancer* **2010**, *46*, 678–684.

199. W. B. Nagengast, M. A. de Korte, T. H. O. Munnink, H. Timmer-Bosscha, W. F. den Dunnen, H. Hollema, J. R. de Jong, M. R. Jensen, C. Quadt, C. Garcia-Echeverria, *J. Nucl. Med.* **2010**, *51*, 761–767.

200. V. Radchenko, H. Hauser, M. Eisenhut, D. Vugts, G. Van Dongen, F. Roesch, *Radiochim. Acta* **2012**, *100*, 857–864.

201. S. Busse, J. Brockmann, F. Rösch, *Radiochim. Acta* **2002**, *90*, 411–415.

202. V. Radchenko, P. Bouziotis, T. Tsotakos, M. Paravatou-Petsotas, A. de la Fuente, G. Loudos, A. L. Harris, S. Xanthopoulos, D. Filosofov, H. Hauser, *Nucl. Med. Biol.* **2016**, *43*, 280–287.

7

^{99m}Technetium-Based Imaging Agents and Developments in ^{99}Tc Chemistry

Roger Alberto and Qaisar Nadeem

Department of Chemistry, University of Zurich,
Winterthurerstr. 190, CH-8057 Zurich, Switzerland
<ariel@chem.uzh.ch>

Abstract: Technetium has probably the most interesting and multifaceted chemistry amongst the metallic radionuclides in routine applications for radiopharmacy or molecular imaging. Being situated in the middle of the periodic table, the diversity of its possible oxidation states enables complexes with ligands covering any possible class of coordinating organic molecules and ions. However, the plethora of compounds resulting from this broad chemistry did not translate into a comparable number of new imaging agents. Reasons for this fact are discussed and practical requirements to which new potential radiopharmaceuticals have to comply with are outlined. Despite the chemical diversity of feasible complexes, the large majority of complexes concentrates on the three cores $[^{99m}Tc^V=O]^{3+}$, $[^{99m}Tc^V\equiv N]^{2+}$, and fac-$[^{99m}Tc^I(CO)_3]^+$. Labelling strategies with these cores and classes of imaging agents are discussed and scrutinized. The more recent coordination chemistry of these cores is highlighted with a focus on new complexes, which are either fundamentally new or carry targeting functions for receptor binding with the known cores. Many of them have been subjected to *in vitro* and *in vivo* studies, important in the context of this chapter. It covers about the last ten years but references to earlier studies are given where necessary. Very few of these complexes proceeded to preclinical or even clinical studies. These are presented together with already market-introduced examples in Section 4. Throughout the chapter, the chemistry of rhenium plays a pivotal role for the one of technetium. This feature of rhenium is emphasized not only as a model for technetium using cold rhenium but also as an option for complementing imaging with ^{99m}Tc with therapy by radioactive $^{186/188}$Re, leading to a theranostic matched-pair situation as a perspective. As a scope for the future of fundamental technetium and rhenium chemistry, novel building blocks and strategies such as the integrated concept are introduced. It will corroborate the relevance of fundamental ^{99}Tc chemistry for keeping ^{99m}Tc as a core imaging radionuclide at the forefront of nuclear medicine.

Keywords: bioorganometallic chemistry · labelling · molecular imaging · radiopharmaceuticals · receptor targeting · rhenium · technetium · theranostic

1.   INTRODUCTION

Since its commercial availability in the Sixties, technetium-99m or ^{99m}Tc is an established radionuclide in nuclear medicine for the radioimaging of many diseases and malfunctions. Hundreds of thousands of ^{99}Mo/^{99m}Tc generators are produced and still nowadays about 11 million patients per year are imaged with single photon emission computed tomography (SPECT), the nuclear medicine diagnostic procedures with one or the other radiopharmaceutical, in the USA alone. A representative analysis of the use of radiopharmaceuticals for nuclear medicine procedures including not only ^{99m}Tc but supporting its indispensable role has been published a couple of years ago [1]. This strong role of ^{99m}Tc is due to its easy availability from relatively cheap generators and its excellent decay characteristics, which almost perfectly match clinical requirements (see Section 2).

The development of new ^{99m}Tc radiopharmaceuticals is on the other hand impeded by its relatively complex chemistry. Technetium has a total of nine oxidations states (from −I to +VII), six of which are chemically accessible under aqueous conditions. Each of these oxidations states demands appropriate ligands, which are able to stabilize the corresponding complex under physiological conditions. Over the years of discovery and development of ^{99m}Tc-based radiopharmaceuticals, a few cores and complexes emerged as suitable for application in nuclear medicine. These cores, together with suitable ligands, have been brought to routine clinical application. They represent most of the diagnostic procedures in clinics (see Sections 3 and 4). To get into application, the preparation of a ^{99m}Tc complex must fulfil very strong conditions such as quantitative yields, synthesis in water, and readiness to be administered and all in a relatively short time. The chemistry together with these constraints resulted in very few new radiopharmaceuticals entering clinical trials or routine application since the Nineties. This may also be one of the reasons, why companies do scarcely invest in further ^{99m}Tc chemistry for radiopharmaceutical applications. Competitors like ^{68}Ga for positron emission tomography (PET) has one single oxidation state, namely +III, and can easily be stabilized with multidentate chelators. [68]Ga is also available in the form of a [68]Ge/^{68}Ga generator. Although not as convenient as the [99]Mo/^{99m}Tc generator, ^{68}Ga is readily available on site in clinics [2–4].

The essential lack of novel block-busting ^{99m}Tc radiopharmaceuticals over the past decades, together with missing interests from industry lead to a steep decrease in fundamental ^{99}Tc and applied ^{99m}Tc chemistry. Chemistry with the long-lived radionuclide [99]Tc ($t_{1/2} = 2.111 \times 10^5$ y) serves as model for chemistry with the short-lived [99m]Tc ($t_{1/2} = 6$ h) and is the driving force behind application in nuclear medicine [5, 6]. Whereas dozens of groups did fundamental ^{99}Tc research in the Nineties, only a handful of groups is left today. Still, important fundamental results emerge from these groups, which may ultimately have an impact in SPECT radiopharmacy with [99m]Tc (see Section 5).

Since model chemistry with ^{99}Tc has diminished, many groups perform rhenium chemistry instead. Especially low valent [99m]Tc[I] and Re[I] complexes are structurally very close and their respective stabilities comparable. Thus, rhenium serves as a good model for technetium and the chemistry related to radiopharmaceuticals is covered throughout. The radionuclides [188]Re and [186]Re are considered as very appropriate for radionuclide therapy and a [188]W/[188]Re generator in support of these endeavors is available [7]. This opens in addition the opportunity of stepping into a new form of theranostics; namely, diagnosis with ^{99m}Tc and therapy with identical compounds but comprising [186/188]Re. Aspects of these synergisms will be covered as well.

Many reviews about ^{99}Tc/^{99m}Tc appeared over the years, some with a focus on fundamental chemistry [5], some on application [3, 8–16]. Since it is not the intention to cover all the years of ^{99}Tc/^{99m}Tc chemistry, this chapter will focus on newer developments in chemistry and radiopharmacy, covering about the last decade with references to publications that appeared earlier where adequate [17–20].

2. LABELLING STRATEGIES WITH ^{99m}Tc

2.1. The ^{99}Mo/^{99m}Tc Generator

The radionuclide ^{99m}Tc is readily available from a so-called generator system. ^{99}Mo is produced upon fission of ^{235}U in a yield of about 6.1 %. The radionuclide ^{99}Mo is a β^--emitter and has a half-life time $t_{1/2}$ of 67 h. It decays to ^{99m}Tc, which is thus the daughter of ^{99}Mo. The parent/daughter pair ^{99}Mo – ^{99m}Tc is in a transient equilibrium with the daughter, approaching the absolute activity of the parent ^{99}Mo after about 4–5 half-life times. This makes the convenience of this generator, it can be eluted every 24 h or even less with a high activity. Since the parent decays with 67 h, the eluted activity decreases accordingly. For research purposes, a generator can be used as long as four weeks or even longer. In hospitals, where more activity is needed, generators are typically replaced after one week. From irradiated highly enriched ^{235}U, the ^{99}Mo is isolated from a modified Purex process. It is therefore present as $[^{99}MoO_4]^{2-}$ in an aqueous solution. In this form, it is loaded on an Al_2O_3 Alox column on which it is strongly adsorbed (Figure 1a). When
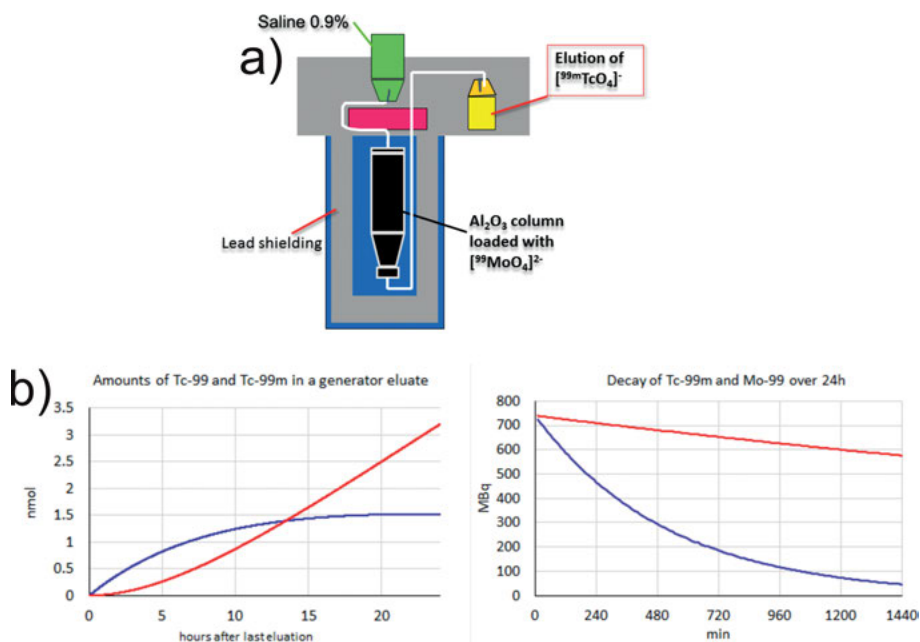
Figure 1. **(a)** Principle of a ^{99}Mo/^{99m}Tc generator; $[^{99}MoO_4]^{2-}$ is loaded on an Alox column (black), $[^{99m}TcO_4]^-$ is formed upon decay of ^{99}Mo and is eluted into an evacuated vial (yellow). **(b)** Amounts of ^{99m}Tc and ^{99}Tc (blue and red lines) as a function of time. More "cold" ^{99}Tc is in the eluted saline solution (left) at later time points. The decay of ^{99m}Tc over 24 h for a start activity of 740 MBq (20 mCi) (blue), and the decay of ^{99}Mo over the same time (red, right).

$[^{99}MoO_4]^{2-}$ decays to ^{99m}Tc, the technetium is present as mono-anionic pertechnetate $[^{99m}TcO_4]^-$ which binds much weaker to Alox and is eluted with saline (0.9 % NaCl in water) in a kind of anion-exchange process. This solution is the starting material for any subsequent reaction and for the preparation of radiopharmaceuticals. It is clear that chemistry in saline makes these reactions demanding since many components may not be soluble or stable in this solvent. Still, as shown below, surprisingly uncommon compounds from water as a solvent are still accessible [21–23].

In the generator and in the eluted solution, ^{99m}Tc decays continuously to ^{99}Tc. Therefore, solutions coming from the generator contain always ^{99}Tc in amounts depending on the time passed since the last elution. What has been said for $[^{99m}TcO_4]^-$ holds also true for its higher homologue. The principle of the $^{188}W/^{188}Re$ generator is the same, i.e., $[^{188}WO_4]^{2-}$ is adsorbed on Alox and $[^{188}ReO_4]^-$ is eluted with saline. Since the half-life time of ^{188}W is about 70 d, these generators are much longer in use (> 6 months) than the ^{99}Mo generators. However, ^{188}W has to be prepared in a (2n,2γ) reaction from highly enriched ^{186}W in high flux reactors and corresponding generators are much more expensive and difficult to obtain. Not many reactors worldwide have neutron fluxes for allowing this nuclear reaction. The half-life time of ^{188}Re is 17 h and thus very appropriate for radionuclide therapy [24, 25].

Typical $^{99}Mo/^{99m}Tc$ commercial generators have activities up to 37 GBq (1 Ci) or even higher. Eluted saline solutions have a typical volume of 7–10 mL, from which adequate smaller volumes are taken for the preparation of radiopharmaceuticals or for research purposes. Since the $t_{1/2}$ of ^{99m}Tc is only 6 h, the absolute amounts of materials are minuscule, despite their apparent high activities. They are typically in the pico- to nanograms range. Characterizations with "normal" chemical methods are thus essentially impossible. Table 1 gives some concentrations and amounts after elutions and dilutions. ^{99m}Tc is a long-lived excited nucle-

Table 1. Activity, concentrations, and absolute amounts of ^{99m}Tc and ^{99}Tc for 5 mL elution directly from generator (A and B), and for diluted solution of A, (C and D, 1 mL each), corresponding to a typical preparation of ^{99m}Tc complexes or radiopharmaceuticals.

Generator eluted and diluted solutions	(A) Generator elution 5 mL after 24 h	(B) Generator elution 5 mL after 12 h	(C) 0.2 mL of A + H₂O/ saline dilution (up to 1 mL)	(D) 0.1 mL of A + H₂O/ saline dilution (up to 1 mL)
activity ^{99m}Tc	18.5 GBq (500 mCi)	15 GBq (400 mCi)	740 MBq (20 mCi)	370 MBq (10 mCi)
mass ^{99}Tc	288 ng	140 ng	12 ng	6 ng
mass ^{99m}Tc	98 ng	79 ng	4 ng	2 ng
mol ^{99}Tc	2.9 nmol	1.4 nmol	120 pmol	60 pmol
mol ^{99m}Tc	1 nmol	0.8 nmol	40 pmol	20 pmol
conc. ^{99}Tc	582 nM	288 nM	116 nM	58 nM
conc. ^{99m}Tc	198 nM	160 nM	40 nM	32 nM
$^{99}Tc/^{99m}Tc$	2.9	1.8	2.9	1.8

ar state (comparable to phosphorescence in the electron shell) which decays to ^{99}Tc. Due to the long half-life time of ^{99}Tc, it does not decay over the time until all ^{99m}Tc is gone (about 60 h) (Figure 1b).

Since about ten years, concerns rose about the future availability of ^{99m}Tc in general and ^{99}Mo/^{99m}Tc generators in particular. These concerns emerged because many of the reactors producing ^{99}Mo will reach their ends of function soon. In addition, expected or unexpected shutdowns led to a shortage of ^{99}Mo supply in 2009, 2012, and 2013, which affected the nuclear medicine community to some extent. The reactors producing the largest amounts of ^{99}Mo are available in Chalk River, Canada, and in Petten, The Netherlands have been shut down for medical radionuclide production. In part, they were replaced by sites in South Africa, Belgium, Poland, and the Czech Republic, but the continuity of production remains fragile [22, 26].

Due to these shortages, alternative production methods have been sought for ^{99}Mo but also directly for ^{99m}Tc [27]. Different nuclear reaction methods have been proposed, which should ideally not depend on the availability of reactors. Therefore, cyclotrons or linear accelerators are alternatives, which are widely available but often not designed for medical radionuclide production. Although many nuclear reactions have been studied quietly in detail, they suffer partly from the fact that unwanted nuclides of the same or different elements are obtained at the same time [28]. Possible routes without the need for enriched ^{235}U are neutron-producing accelerators via e.g., the classical ^{98}Mo(n,γ)^{99}Mo path or by accelerators producing high energy photons ^{100}Mo(γ,n)^{99}Mo [29, 30]. The nuclear reaction in cyclotrons, ^{100}Mo(p,pn)^{99}Mo, is an alternative, but all these methods would lead to low specific activities of ^{99}Mo since parent and daughter are the same elements. They are thus not very well suited for the preparation of generators.

A more promising approach which is currently practiced is the direct production of ^{99m}Tc without the bypass over ^{99}Mo. The reaction ^{100}Mo(p,2n)^{99m}Tc in cyclotrons with medium-energy protons has become a true option [31, 32]. Along this nuclear reaction, ^{99m}Tc is produced in TBq quantities. This may ensure the demand for this radionuclide in the future [22, 33–36]. Although ^{99m}Tc can be delivered even to remote clinics if an appropriate cyclotron is not available on site, still, the immediate availability, which is one of the most convenient advantages of ^{99m}Tc, is lost and costs may rise. Different studies comparing imaging with generator- and cyclotron-produced ^{99m}Tc with a special focus on dose burden to the patients have been published [37, 38].

The challenges for ^{188}Re and ^{186}Re are similar. Since the numbers of high-flux reactors as needed for the preparation of ^{188}W are decreasing, alternative approaches are urgent. ^{186}Re would be even more suited for nuclear medicine procedures (radionuclide therapy) but the direct production from natural ^{185}Re via the (n,γ) reaction does not yield sufficiently high specific activities. Therefore, studies with cyclotrons for the direct production of ^{186}Re at the no-carrier-added level have been undertaken. Alternative routes towards high specific activity ^{186}Re are through the ^{186}W(p,n)^{186}Re or the ^{186}W(d,2n)^{186}Re path [39, 40]. The disadvantage of these reaction pathways is the concomitant production of low levels of other rhenium radionuclides.

2.2. Labelling Chemistry and Bifunctional Chelators

Since $[^{99m}TcO_4]^-$ as eluted from the generator is not very useful as a radiopharmaceutical, it has to be converted into a chemical form or a new complex, which is either a radiopharmaceutical by itself (*de novo* radiopharmaceutical, 1st generation) or being coordinated to a ligand conjugated to a targeting molecule (targeting radiopharmaceutical or 2nd generation). Indeed, the majority of routinely applied radiopharmaceuticals belongs to the first class and only a very limited number of targeting radiopharmaceuticals have been introduced in the market (see Section 4). A more recent labelling strategy is mimicking an existing pharmaceutical without attaching a ligand but using coordinating sites in the lead structure directly (Scheme 1). This strategy though has not yet led to a new radiopharmaceutical although some compounds showed high affinities to their targets [41, 42] but it is more explorative at this stage.
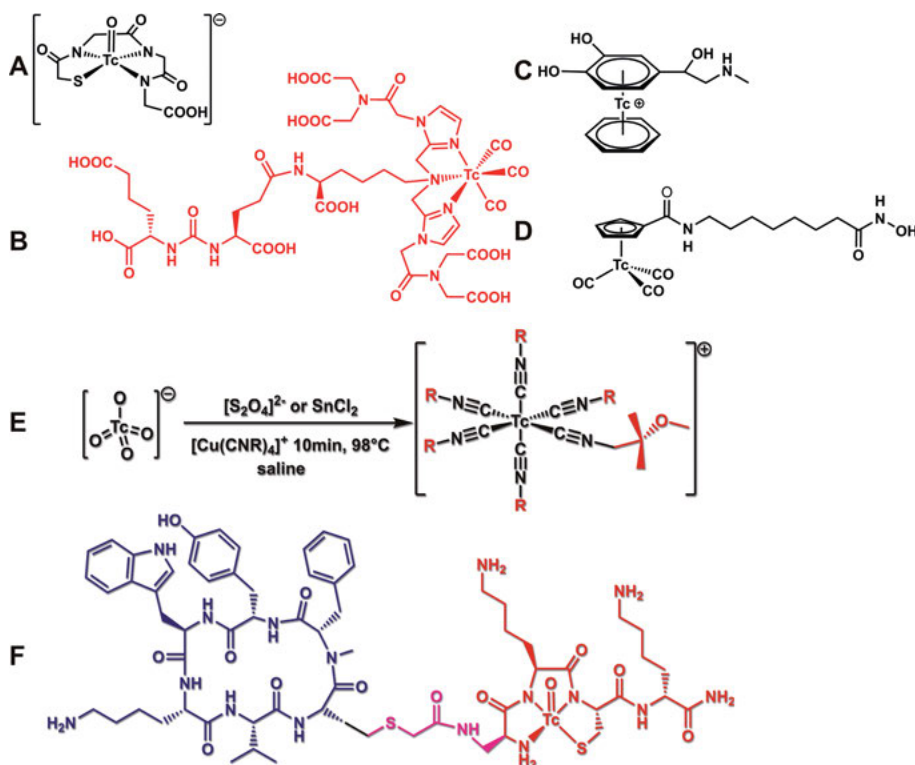
Scheme 1. Classes of radiopharmaceuticals and molecular imaging agents: A 1st generation perfusion agent for kidney function imaging (**A**, Technescan®), a 2nd generation prostate-specific membrane antigen (PSMA) targeting agent (**B**, MIP-1404), and future 3rd generation lead structure integrated inhibitors (**C** and **D**). The routine preparation of Cardiolite® as the gold standard in myocardial imaging (**E**). NeoTect® (TcO-depreotide), a peptide labelled with the $[^{99m}Tc=O]^{3+}$ core (**F**). Detailed references are given in the corresponding sections.

$[^{99m}TcO_4]^-$ alone accumulates in the thyroid, thus following essentially the biological path of iodide (I^-) to which it is similar in terms of charge and size. It is indeed a good indication for the stability of a radiopharmaceutical if no activity is found in the thyroid, i.e., the radiopharmaceutical does not decompose and its ^{99m}Tc is not oxidized to $[^{99m}TcO_4]^-$ [43, 44]. Conversion of $[^{99m}TcO_4]^-$ into a complex useful as radiopharmaceutical, *de novo* or targeting, demands reduction and complexation by a ligand which is able to stabilize the resulting oxidation state under *in vivo* conditions. Remaining in the oxidation state $+VII$ is possible. For doing so, synthetic labelling strategies require activation of the robust $[^{99m}TcO_4]^-$, while offering appropriate ligands that can bind strongly to at least three facially oriented coordinating sites. This has been successfully achieved with the *fac*-$[^{99m}TcO_3]^+$ core but is too specific for widespread application (see Section 3.4) [45–48].

Labelling strategies for all three categories of radiopharmaceuticals are conceptually similar. A reducing agent reduces $[^{99m}TcO_4]^-$ to a lower oxidation state and a ligand present in solution traps and stabilizes this state to a high extent. Alternatively, auxiliary ligands present in large excess binding weaker to the ^{99m}Tc center stabilize an intermediate and are then replaced in a second step by the final ligand, free or bound to a targeting biomolecule or pharmaceutical.

Along this line, the typical "cores" in ^{99m}Tc or ^{99}Tc chemistry are obtained, namely the $[^{99(m)}Tc^V=O]^{3+}$, the $[^{99(m)}Tc^V\equiv N]^{2+}$, and the *fac*-$[^{99(m)}Tc^I(CO)_3]^+$ cores. Numerous multidentate chelators are known, adapted to the corresponding electronic structure of the core (see Section 3), which stabilize these moieties. In view of a theranostic strategy or the preparation of complexes for radionuclide therapy with $^{186/188}Re$, there are differences in the chemical behavior of rhenium and technetium to be considered. Whereas Tc is readily reduced by, e.g., Sn^{2+}, rhenium is much less reactive since its oxidation power is lower. Thus, rhenium often demands heating while many reactions with technetium are performed at room temperature. In accordance with these differences is the observation that Re complexes are more sensitive for re-oxidation. Therefore, radiopharmaceuticals in the $+V$ oxidation state are generally different for the two elements with regard to their physiological stabilities [12].

Besides these chemical considerations, there are further aspects to be considered when aiming at preclinical trials and for ultimate use in hospitals. The preparation of ^{99m}Tc radiopharmaceuticals is performed on site, i.e., in the hospital, due to the in line availability of ^{99m}Tc. This means that the following requirements must be met for routine application:

– reactions are done directly from the generator eluate, i.e., $[^{99m}TcO_4]^-$ in saline

– the yield of the synthesis must be quantitative > 98 % reaction times must be as short as possible, generally < 60 min

– yields must be tolerant to changing conditions

– no toxic or reactive ingredients, no organic solvents apart from ethanol

– stable under physiological conditions for at least 24 h.

All current 1st generation radiopharmaceuticals fulfill these conditions. The example for the preparation of Cardiolite® is given in Scheme 1 E as an illustrative example.

For 2nd generation radiopharmaceuticals, more requirements apply since the biomolecules will bind to a receptor, present in very low concentrations.

– the biomolecule must tolerate the reaction conditions
– its concentration should be as low as possible, typically in the submicromolar range
– no receptor saturation with unlabelled targeting molecules
– receptor affinity and selectivity must be maintained.

Combining these conditions, it is obvious that the type of complexes as well as the ligands is limited. This contrasts to the typical requirements for metal complexes applied in medicinal inorganic chemistry with essentially unlimited conditions and compounds.

The strength of these conditions results in a few 99mTc-radiopharmaceuticals entering clinical routine. Already the > 98 % yield request is rarely achieved and demands high experimental skills [21] and water solubility is a concern. Scheme 1 F gives a typical example for a 99mTc-based labelled peptide, 99mTcO-depreotide (NeoTect®), which fulfilled these conditions and was market-introduced. Neo-Tect® was only the second peptide that obtained regulatory approval. NeoTect® was approved for lung tumor imaging. The peptide comprises a cyclic hexa-peptide containing a somatostatin receptor (SSTR) binding sequence and a line-ar tetra-peptide, which coordinates to the 99mTc core at the Dap-Lys-Cys se-quence (Dap = α-diaminopropionic acid). Since the bifunctional chelator comprises stereochemically active amino acids, diastereomers formed. For NeoTect®, at least two were detected by HPLC. Likely structures have been elucidated with model ligands [49].

For the labelling of a biomolecule, the targeting molecule must be derivatized with a so-called bifunctional chelator (BFC). A BFC consists of two functions, one for coordination to the metal, the other one for covalent conjugation to the targeting molecule. The two functions should be orthogonal to each other since the conjugation to the biomolecule is usually done first by activating the linking function. Labelling follows under conditions outlined above in the post-labelling approach, the normal and most convenient strategy. The request for orthogonality can be bypassed with the pre-labelling approach. Coordination to 99mTc is done in a first step and conjugation to the bioactive function follows. Pre-labelling is in practice not convenient since excess, non-labelled ligand will also bind to the target. Thereby a lot of "cold", unlabelled material is left, blocking the targeted receptor and increasing the image background. The design of BFC ligands for various radionuclides has been described in a review by Boros et al. [50].

2.3. Multi-Modality Imaging

Multi-modality imaging has gained increased attention, mainly in the field of PET and in combination with magnetic resonance imaging (MRI) or computed tomography (CT) but also in SPECT. SPECT is usually combined with optical methods such as fluorescence imaging or with ultrasound. It allows assessing molecular targets with two (or more) different modalities showing, e.g., function and anatomy. Dual imaging, the typical case, allows combining the high sensitivity of radionuclides with the high spatial resolution of, e.g., MRI. This leads to enhanced accuracy and therefore to a better prediction of progress or digress of a disease [17, 51, 52]. Whereas PET/MRI or PET/CT is routinely performed in clinics, SPECT/MRI or SPECT/CT with ^{99m}Tc in particular is still rare and only a limited number of studies are published [53]. One example for SPECT/MRI combination is a pioneering study by Blanco et al. [54]. They used iron oxide-filled micelles as ligands for the $[^{99m}Tc(CO)_3]^+$ core. In this approach, the iron oxides inside the micelles act as good ligands for this core and accumulate ^{99m}Tc in this way. Stability tests and biodistribution in mice assessed the versatility of this combination. The $[^{99m}Tc(OH_2)_3(CO)_3]^+$ complex was not released as is evident from its *in vivo* behavior but the radioactivity followed the biological path usually found for iron oxide nanoparticles. The retention of this ^{99m}Tc complex in the micelles may not only be of importance for dual-modality imaging agents but for the targeted delivery of ^{99m}Tc in general. Another publication describes the preparation of Fe_3O_4-Au core-shell dumbbell-like nanoparticles, decorated with a combination of 2,3-diaminopropionic acid as ligand and PSMA targeting molecules on the same framework [55]. The particularity of this approach is the anchor group that acts as both, as chelate for the ^{99m}Tc core and as conjugation site for the targeting molecules. Since the nanoparticle surface-bound molecule carries amino and carboxylate groups, they can serve as anchoring groups for essentially any targeting molecule (Schemes 2A and 2B).

A recent study reported about Au nanoparticles, non-covalently entrapped by polyethylenimine polymers. The polymers were previously conjugated to diethylene-triamine-pentaacetate (DTPA), wrapped around the Au nanoparticles and then labelled with ^{99m}Tc. Although the structure is not known, it is probably a ^{99m}Tc^V or ^{99m}Tc^{IV} complex chelated by DTPA. These nanoparticles are pH-responsive due to free amine groups, stable *in vivo* and may therefore be adopted as excellent dual mode contrast agent for SPECT/CT imaging of cancer cells of different types (Scheme 2C) [56].

As a more curious but probably relevant study in the context of ^{99m}Tc-labelled iron oxide NPs, their formation from strongly acidic solutions as found in nuclear waste was investigated. The incorporation of ^{99}Tc in different oxides and their leaching was studied. It seems that the iron oxide particles retain the ^{99}Tc very well. Replacing ^{99}Tc by ^{99m}Tc could thus offer an approach towards correspondingly labelled dual-modality SPECT/MRI imaging agents [57].

More typical for dual-modality imaging with ^{99m}Tc is its combination with fluorophores, acting as ligands or being pendent to them. These are not dual-modality imaging agents in the canonical sense since they do not allow non-invasive
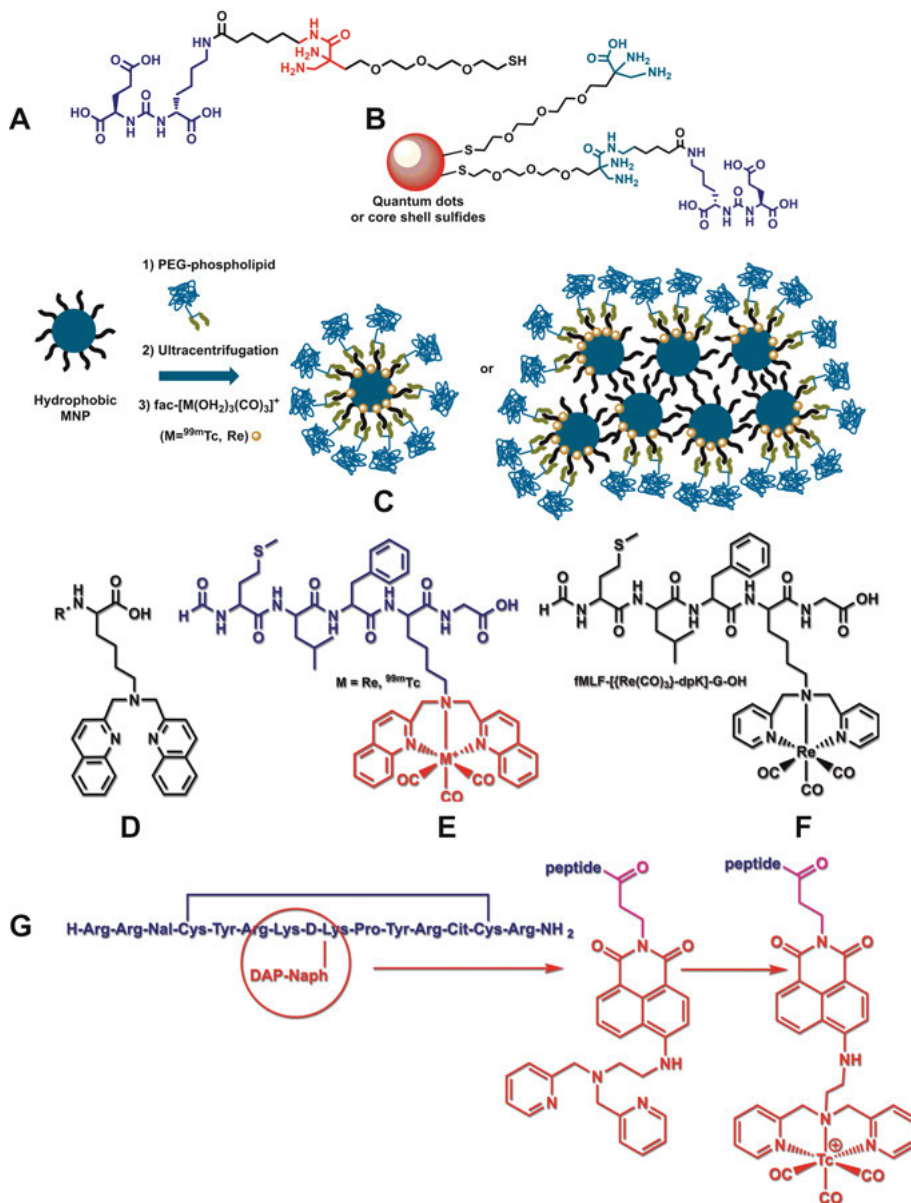
Scheme 2. A PSMA-targeting agent (blue) conjugated to a 2,3-diaminopropionic acid group (red) with a thiol anchor (**A**), decorating the basic ligand (green) and the conjugated system A to NPs (**B**). Magnetic NPs, iron-oxide filled micelles labelled selectively with [^{99m}Tc(OH$_2$)$_3$(CO)$_3$]$^+$ (**C**) [54]. Dual-modality labelling with the SAACQ (single amino acid chelate quinoline) system (**D**) [58] and incorporation with SPPS at any peptide position (**E**). The SAAC non-fluorescent unit has higher labelling efficiency (**F**) [62]. The dipicolylamine ligand with a pendent amino group, bound to a fluorescent naphtylimide group in the peptide antagonist for the CXCR4 receptor (**G**) [63].

visualization by two methodologies. They allow though visualization of subcellular structures for learning about the mode of action and localization of a particular radiopharmaceutical and the sites of accumulation. A few examples are given here and more are to be found in the sections with the corresponding ^{99m}Tc cores. A widely applied approach with respect to combined SPECT/optical imaging is the single amino acid chelate quinoline (SAACQ) ligand [58]. The complex with the $[Re(CO)_3]^+$ core shows fluorescence with emission maxima at 425 and 580 nm. The combination with targeting molecules allows a precise detection of its subcellular distribution. The homologue with ^{99m}Tc gives insights into the biodistribution of the compounds. The SAACQ system is a general tool since it can be incorporated in many types of biomolecules (Scheme 2D to 2F). Originally, it was combined with a chemotactic fMLF peptide by SPPS and coordinated to $[Re(OH_2)_3(CO)_3]^+$ or labelled with the ^{99m}Tc homologue. Affinity to leukocytes was determined and the *in vitro* and *in vivo* images were correlated [59].

For the labelling of neural stem cells, a specific peptide was subjected to the same procedure as above and labelled with Re and ^{99m}Tc, respectively. Epifluorescence and SPECT/CT showed a correlation of both imaging methods [60]. This approach is multi-valent and can be applied to any peptide library by simple SPPS procedures. It thus represents a versatile platform for the synthesis of metallopeptides for targeting any desired site [61]. Reducing the SAACQ ligand to its pyridyl analogue, the so-called SAAC bifunctional chelator, fluorescence of its $[Re(CO)_3]^+$ complex is retained albeit in another wavelength range. Therefore, even with this reduced-size ligand, optical and radioimaging is possible. One example for dual-modality imaging was performed with the 14-residue phosphatidylserine (PS)-binding peptide FNFRLKAGQKIRFG (PSBP-0). Substitution of some amino acids by others increased the affinities towards phosphatidylserine. The incorporation of the SAAC system increased its affinity even further, contrasting a trend found in many biomolecules derivatized with a bifunctional chelator/complex. Generally, affinities decrease or are often completely lost upon such structural changes. The metallo-peptide showed then very nice uptake and retention in apoptotic cells [62].

In an extended architecture, the dipicolylamine ligand as in SAAC was combined with a pendent fluorescent naphtylimide moiety. The second function of this bifunctional chelator was conjugated to the amide group and the whole construct conjugated to a cyclic T140 peptide, an antagonist for the CXCR4 receptor. This chemokine receptor is overexpressed in many tumour cell lines. It could be shown by confocal fluorescence microscopy that the $[Re(CO)_3]^+$ complex accumulates much better in cell lines that did express the CXCR4 receptor than in others that did not. This finding correlated very well with the corresponding ^{99m}Tc bioconjugate. Both methods in combination with each other allow a reliable confirmation of specific receptor binding sites, a characteristic that is not easily confirmed by one single method only (Scheme 2G) [63].

## 3. BUILDING BLOCKS AND CORE STRUCTURES FOR LABELLING

3.1. The $[^{99m}Tc^{V}=O]^{3+}$ Core

With $[^{99m}TcO_4]^-$ as the starting material, the oxidation state $+V$ and the structural fragment $[^{99m}Tc=O]^{3+}$ are easily accessible by a two-electron reduction with, e.g., Sn^{2+} but also with other reducing agents such as $[BH_4]^-$, $[SO_3]^{2-}$, $[S_2O_4]^{2-}$, Zn^0, and many others. The stability and accessibility of $[^{99m}Tc=O]^{3+}$ has been discovered early in the history of radiopharmaceutical chemistry. The fundamental chemistry as well as the synthesis of *de novo* radiopharmaceuticals was therefore dominated for decades by this fragment. The most important commercial ^{99m}Tc-based imaging agents are still with this core. The MAG3 (mercaptoacetyl-glycine-glycine-glycine) complex $[^{99m}Tc^{V}O(MAG_3)]^-$ for instance, routinely applied for the quantification of kidney functions, is a successful radiopharmaceutical. TcO-MAG3 was developed in the late Eighties and it is commercially available still nowadays [64, 65] (Scheme 1A).

The $[^{99m}Tc=O]^{3+}$ core is typically stabilized by two bidentate or one tetradentate chelator. It is between an A- and a B-type metal center and therefore ideally coordinated to N, S, O or P ligands. Numerous tetradentate ligands with all donor-atom mutations have been prepared. The principal nature of these ligands can be found in many reviews but some general coordinating features of the $[^{99(m)}Tc=O]^{3+}$ core shall be outlined [3, 5, 6, 17, 66–70], together with a few newer original studies. The core is best stabilized with tetradentate ligands that can deprotonate to compensate the $3+$ charge of the core. Amides, carboxylates, thiolates but also aliphatic amines are best suited for this purpose. The resulting complexes are generally of square-pyramidal structures with the coordination site *trans* to the oxo ligand remaining unoccupied. If the tetradentate or the two bidentate ligands remain neutral, such as, e.g., with phosphine ligands, charge is not compensated enough, and the $[^{99(m)}Tc=O]^{3+}$ core is transformed into the *trans*-dioxo core $[O=^{99(m)}Tc=O]^+$. The commercial radiopharmaceutical Myoview® for cardio imaging [71] is a prominent example of this class.

Most complexes maintain though the $[^{99(m)}Tc=O]^{3+}$ moiety with tetradentate ligands. The versatility of these ligands is not only the high thermodynamic stabilities they provide but also the resemblance of many of them to peptide sequences. Although many have been solely prepared as *de novo* radiopharmaceuticals, as, e.g., the MAG3 complex, they are sometimes designed to comprise a second function for conjugation to targeting molecules (as in MAG3). Alternatively, they can easily be extended to obtain bifunctional systems, simply by attaching another amino acid to one of the termini. This is a routine approach and convenient for obtaining strongly coordinating bifunctional ligands with sequences of choice.

A few illustrative examples of the recent past shall be given. The gastrin-releasing peptide receptor (GRPR) has emerged in nuclear oncology as an attractive molecular target due to its high-density expression in a wide spectrum of human cancers (prostate and breast cancers). Amongst the GRPR-binding
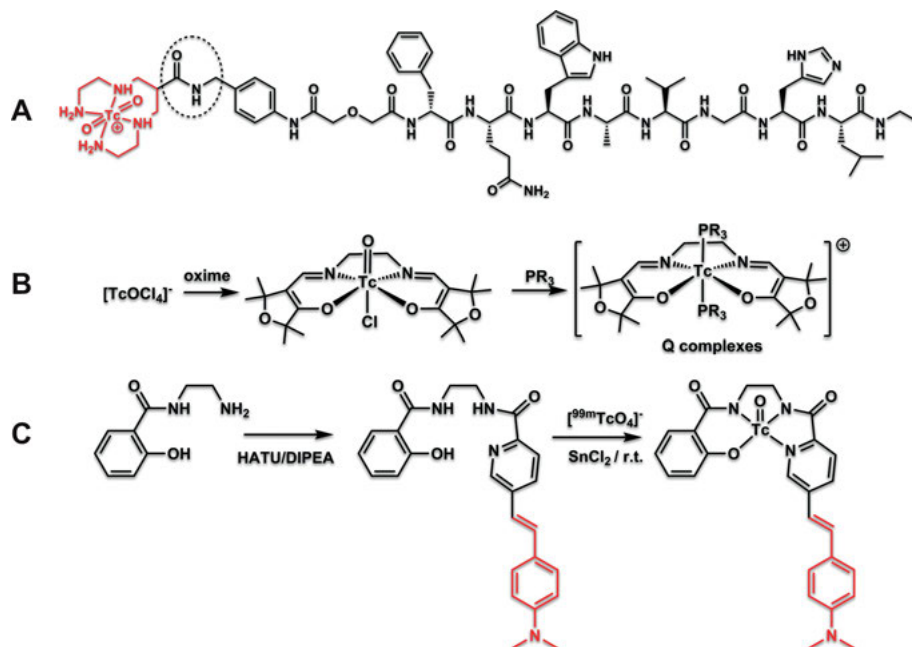
Scheme 3. Demobesin, a peptide antagonist for the gastrin-releasing peptide receptor with an aliphatic tetramine ligand. Labelling with ^{99m}Tc gives highly stable complexes comprising the $[O=^{99m}Tc^V=O]^+$ fragment (**A**) [72]. Stepwise preparation of the $^{99m}Tc^{III}$ "Q compound", a myocardial imaging agents (**B**) [73–75]. A complex design for targeting $A\beta_{1-42}$ fibrils in Alzeimer patients: The neutral complex is built from the $[^{99m}Tc=O]^{3+}$ and contains a styrylpyridyl group that binds tightly to plaques (**C**) [76].

peptides, Demobesin has been studied for a long time. For labelling, a tetraden-tate aliphatic amine ligand was conjugated to the N-terminus of Demobesin. Various constituents such as the amino acid sequence, the linker between the N-terminus and the chelator, and the C-terminus were altered to obtain insights into structure-activity relationships. All modifications gave GRPR antagonists with receptor affinities in the low nanomolar range. The labelling procedure is prototypical for generating the $[^{99m}Tc=O]^{3+}$ core and for coordination to the N_4 ligand. Since this ligand is neutral, the $[O=^{99m}Tc=O]^+$ core is ultimately formed. About 20 μM solutions of the peptide were labelled at room temperature with Sn^{2+} as reducing agent. The resulting labelled peptide showed reasonable stabili-ty in blood and good imaging of tumor xenografts in mice. The procedure for labelling with the $[^{99m}Tc=O]^{3+}$ core shows its versatility for this kind of *in vitro*/*in vivo* studies (Scheme 3A) [72].

Complexes comprising the $[^{99(m)}Tc=O]^{3+}$ core are often converted to Tc^{III} by reductive removal of the terminal oxo ligand. This reactivity was the background for the development of a series of intensely investigated $^{99m}Tc^{III}$ complexes, namely the so-called "Q compounds", designed for but never introduced in com-mercial myocardial imaging [73, 74]. In these complexes, the tetradentate ligands

are of the Schiff-base type (Scheme 3B) and thus relatively rare in radiopharmaceutical chemistry. A study by Jurisson et al. [75] outlined the reactivity differences between rhenium and technetium. For both elements, the $[M=O(Schiff-base)]^+$ (M = [99]Tc, Re) complexes are obtained from $[MOCl_4]^-$. Rhenium demands high temperatures for coordination whereas ^{99}Tc reacts at room temperature. For both elements, only heating of $[M=O(Schiff-base)]^+$ in the presence of phosphines induces reduction to the M(III) complexes under formation of the Q compound $[M(PR_3)_2(Schiff-base)]^+$. The same reaction conditions apply for ^{99m}Tc, but heating is done in the presence of the Schiff base together with the phosphine [75].

The imaging of amyloid plaques with a [99m]Tc[V] radiopharmaceutical is a last example in the discussion about complexes comprising the $[^{99m}Tc=O]^{3+}$ core. Although amyloid plaques are rather the field of the $[^{99m}Tc(CO)_3]^+$ core (see Section 3.3), this example shows that also other cores might be appropriate for diagnosing Alzheimer's disease. For interacting with aggregated amyloid-β peptides in the brain, compounds must be neutral and lipophilic, carrying typically groups that intercalate into these plaques. In this exemplary study, the styryl-pyridyl group was chosen since it is known to bind strongly to the Aβ plaques in post-mortem brain. A novel, tri-anionic ligand was coupled first to a styrylpyridyl-type biomolecule then coordinated to $[Re=O]^{3+}$ and the $[^{99m}Tc=O]^{3+}$ core via two deprotonated amide units, a phenolate group and pyridine nitrogen (Scheme 3C) [76].

The rhenium complexes showed decent affinities for $A\beta_{1-42}$ fibrils. The ^{99m}Tc homologues were prepared according to standard routes by reducing $[^{99m}TcO_4]^-$ with $SnCl_2$ in water. Yields were satisfying but could not be optimized. It was found for the rhenium and the ^{99m}Tc complex that they suffered from transmetalation to some extent, in particular to histidine, when present.

Many $[^{99m}Tc=O]^{3+}$ complexes are stable under physiological conditions, and this stability is of thermodynamic nature. Appropriate ligands may exchange, which leads to transmetalation since these radiopharmaceuticals are in general under "out-of-equilibrium" conditions.

3.2. The $[^{99m}Tc^V\equiv N]^{2+}$ Core

Amongst the different cores for radiopharmaceuticals, the $[^{99m}Tc^V\equiv N]^{2+}$ core did play a central role for new myocardial imaging agents. Research with this core for this field is still pursued but its mono-cationic complexes could not compete with Cardiolite®, the commonly used imaging agent for heart problems. The $[^{99m}Tc^V\equiv N]^{2+}$ core can be stabilized by a variety of mono- and multidentate ligands, typically belonging to the class B ligands, medium-soft to soft donors. As with the $[^{99m}Tc^V=O]^{3+}$ core, the $[^{99m}Tc^V\equiv N]^{2+}$ core can be produced in one step as outlined below. As the O^{2-} ligand, the N^{3-} ligand is a very strong π-donor and exerts a distinct trans-influence. Therefore, most complexes display a distorted square pyramidal geometry. If six-coordinate, the ligand *trans* to the nitrido group is generally only very weakly bound. The flexibility of the co-

ligands around the $[^{99m}Tc^V{\equiv}N]^{2+}$ core made it attractive for radiopharmaceutical purposes and corresponding research started already in the Nineties. The remaining coordination sites of the $[^{99m}Tc^V{\equiv}N]^{2+}$ core are flexible, a multitude of ligands can be bound, adapted to the properties of the selected target [77].

One of the more successful compounds was $[^{99m}TcN(NOEt)_2]$, a neutral myocardial imaging agent [78]. Despite many research efforts ever since, a new product was not commercialized but many interesting fundamental studies undertaken. Duatti et al. introduced a new and remarkable concept in which they developed a strategy for the preparation of asymmetric $[^{99m}Tc^V{\equiv}N]^{2+}$-based complexes with a high degree of molecular flexibility [79]. This concept, the most widely applied one in nitrido chemistry, follows a [3+2] strategy. Generally, the $[^{99m}Tc^V{\equiv}N]^{2+}$ core is formed first by reacting $[^{99m}TcO_4]^-$ with $SnCl_2$ and succinic-dihydrazide, which produces an intermediate comprising the $[^{99m}Tc^V{\equiv}N]^{2+}$ core but of unknown composition. In a second step, the two ligands, mostly a facially coordinating tridentate P_3 or P_2N ligand and a bidentate ligand, often a dithiocarbamate (dtc), are added together. This produces very good yields of asymmetric complexes, e.g., of the type $[^{99m}TcN(P_2N)(L)]^+$ (Scheme 4A). Whole series of *de novo* complexes have been prepared along this strategy, mostly for myocardial perfusion imaging but also targeting radiopharmaceuticals [80–82].

In a recent study, the influence of the groups attached to the phosphines and amines in P_3 or P_2N, respectively, for heart uptake and persistence were studied in detail by biokinetics. In contrast to earlier reports, in which the bidentate ligand was bis(N-ethoxyxyethyl)-dithiocarbamate (BDODC), this ligand was re-
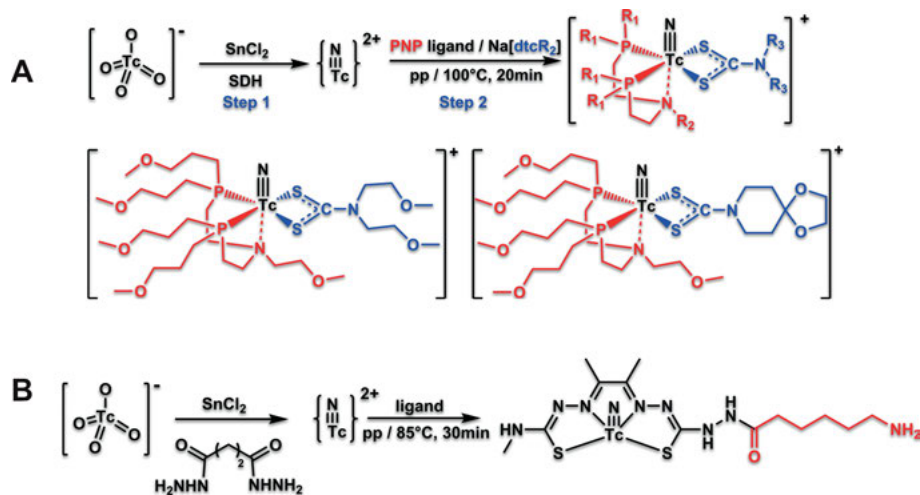
Scheme 4. Reduction with $SnCl_2$ in the presence of succinic-dihydrazide leads to an unknown complex with the $[^{99m}Tc{\equiv}N]^{3+}$ moiety (step 1), reaction with a tridentate PNP ligand and a dithiocarbamate bound to a bioactive moiety "R" gives [3+2] mixed ligand complexes (step 2, **A**) [80–82]. Complexes with the $[^{99m}Tc{\equiv}N]^{2+}$ core and a tetradentate thiosemicarbazone ligand. An aminohexadecanoic acid bound to one of the hydrazides links to biomolecules (**B**) [84].

placed by a bicyclic dithiocarbamate DASD. Pharmacokinetics was comparable to the one of commercial Cardiolite® but it did not exceed it, making further improvements necessary. However, the high flexibility and versatility of the $[^{99m}Tc^V\equiv N]^{2+}$ core is clearly demonstrated in this study. One of the drawbacks in $[^{99m}Tc\equiv N]^{3+}$ chemistry is the concomitant formation of homoleptic complexes with two dithiocarbamates coordinated to the nitrido core. The presence of this unwanted side product requests post-synthetic purification which is in general not appropriate for practical application [83].

Besides the dtc ligands, thiosemicarbazones are also versatile chelators for the $[^{99m}Tc^V\equiv N]^{2+}$ core. The basic thiosemicarbazone ligand can conveniently be bi-functionalized by conjugating an acid to one of the hydrazine subunits as done in a recent study [84] with 6-aminohexanoic acid. The long linker to the carboxylate group was chosen since it was the intention to couple it enzymatically to glutamine (Gln) residues of bioactive molecules by transglutaminase. The $[^{99m}Tc^V\equiv N]^{2+}$ core was synthesized as previously described and then subjected to the pure ligand for stability studies. Especially in serum, the complexes showed some instabilities after 24 h. In the enzymatic assay, conjugation was very slow but the desired product could be isolated and labelled in good yields. The instability of the complex impedes the application of the system but the method of benefitting from an enzymatic coupling assay to a bifunctional chelator, rarely applied in this field, is remarkable (Scheme 4B) [84].

For improving stabilities of the $[^{99m}Tc^V\equiv N]^{2+}$ core, many basic studies with ^{99m}Tc have been undertaken with tri-, tetra-, and pentadentate ligands, mainly in the group of Abram et al. A focus was put on thiourea and thiosemicarbazone ligands since these ligands are versatile for other metal centers such as copper or gallium [85–88].

3.3. The *fac*-$[^{99m}Tc(CO)_3]^+$ Core

Besides the $[^{99m}Tc^V=O]^{3+}$ and the $[^{99m}Tc^V\equiv N]^{2+}$ core, the *fac*-$[^{99m}Tc(CO)_3]^+$ fragment is most intensely studied in recent radiopharmaceutical chemistry. Introduced as a Kit formulation as early as 2001, this core is directly prepared from $[^{99m}TcO_4]^-$ in < 15 min and in quantitative yields. The preparation of $[^{99m}Tc(OH_2)_3(CO)_3]^+$ fulfils thus all requirements for routine application. Boranocarbonate $[H_3BCO_2H]^-$ serves as a reducing agent and as a CO releaser at the same time. Heating to 100 °C in a microwave oven or thermally gives > 98 % yield in 10–30 min [89]. Whereas the CO ligands in the $[^{99m}Tc(CO)_3]^+$ core are very tightly bound, the three H_2O ligands can be replaced by a huge variety of ligands, mono-, bi- or tridentate. In this complex, [99(m)]Tc is in the oxidation state +I. Therefore, it is a d^6 system resulting in robust rather than in thermodynamically stable complexes. The chemistry of $[^{99m}Tc(OH_2)_3(CO)_3]^+$ has been reviewed many times. A focus is put on newer studies to give some representative examples for the multi-purpose applications of $[^{99m}Tc(OH_2)_3(CO)_3]^+$ [70, 90]. Together with many fundamental studies with ^{99}Tc and Re, the complex has been

applied to the preparation of *de novo*, first generation radiopharmaceuticals and to the labelling of a large variety of targeting biomolecules.

One of the unique applications of $[^{99m}Tc(OH_2)_3(CO)_3]^+$ is its ability to form robust complexes with monodentate ligands, comparable to the Cardiolite® complex. Complexes with monodentate ligands are often too unstable against challenges from the numerous coordinating sites in biological systems. The *fac*-$[^{99m}Tc(CO)_3]^+$ core binds for instance very tightly to the imidazole group in the histidine side chain. This was taken as an opportunity to coordinate the *fac*-$[^{99m}Tc(CO)_3]^+$ moiety to his-tags in recombinant single-chain variable fragments (scFv) of antibodies as early as 1999 [91]. Simple mixing of $[^{99m}Tc(OH_2)_3(CO)_3]^+$ with scFv's or affibodies in buffer leads to a quantitative and mostly stable labelling without the need of bifunctional chelators. Binding is relatively slow, which sometimes requires higher scFv concentrations than that of an ideal requirement (Scheme 5A).

The affibody (HE)$_3$-ZIGF1R (HE = histidine-glutamic acid) was stably labelled with *fac*-$[^{99m}Tc(CO)_3]^+$ in quantitative yields. The affibody is very well suited for the visualization of the insulin-like growth factor-1 receptor (IGF) expression in malignant tumors [92]. The authors could nicely show that the radioconjugate $[^{99m}Tc(CO)_3]^+$-(HE)$_3$-ZIGF1R accumulated in IGF-1R-expressing organs (pancreas, stomach, lung, and salivary gland) in mice. In addition, this conjugate showed a 3.6-fold lower accumulation in untargeted organs such as liver and spleen than the ^{111}In-labelled affibody ^{111}In-DOTA-ZIGF1R. The ease of labelling, the high serum stability, and the retention of affinity to the target receptor makes this kind of labelling a very attractive option for affibodies. Since His-tags comprise typically three or more histidines, there are different options for coordination. Stabilities can be improved, if the his-tag does not only consist of histidines but also of other amino acids in the tag. The sequence of the tag may also influence the biological behavior and the coordination to the $[^{99m}Tc(CO)_3]^+$ may vary, depending on the type of additional amino acids.

To obtain a more precise insight into coordination of a tris-his-tag in which the histidines are separated by other amino acids, sequences with the attractive abbreviations HAHAHA, HEHEHE or HIHIHI and others, have been studied in great detail [93]. The recombinant proteins frequently bear a his$_6$ tag, which often leads to enhanced accumulation in the liver. Fewer histidines should reduce this accumulation while affinities and labelling stabilities should be maintained. The authors compared these characteristics with affibodies targeting the herceptin receptor 2 (HER2) a human epidermal growth factor receptor 2, which promotes the growth of cancer cells. For almost all affibodies, labelling yield was quantitative, despite the presence of only three coordinating histidines. Stabilities against large excesses of free histidine was very good as well as serum stability. The stability against histidine is very indicative for kinetic stability since one would expect in this $\Delta G° ≈ 0$ reaction a rapid transmetalation, if thermodynamic equilibria and stabilities would apply. The best biodistribution with strongly reduced liver accumulation was found for the HEHEHE tag, probably due to the negatively charged peptide sequence [94, 95]. For improving efficiency of binding to such tags, a novel mixed cysteine/hexahistidine peptide was synthesized. The superiority
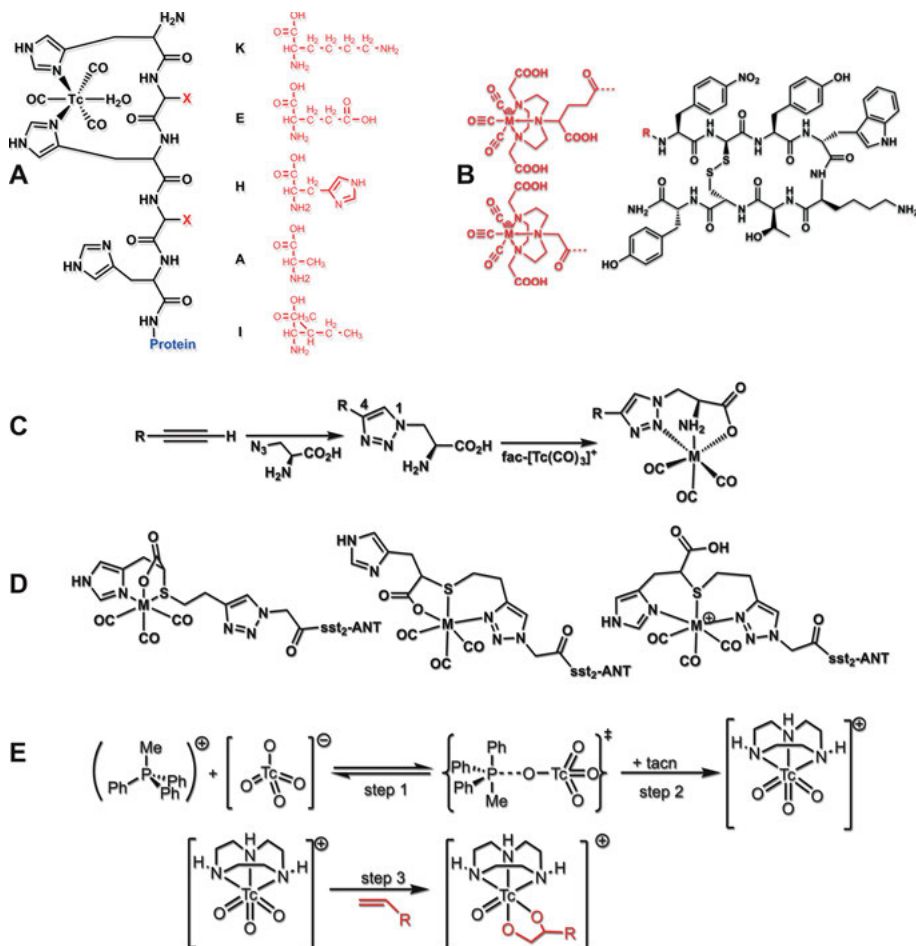
Scheme 5. The *fac*-[99mTc(CO)₃]⁺ fragment coordinating to a HXHXHX tag in recombinant proteins. The amino acids "X" may replace the H₂O bound to 99mTc. This way of labelling yields very stably 99mTc labelled proteins (**A**) [93]. Labelling of the somatostatin receptor ligand with an SSTR antagonist conjugated to different NOTA type ligands (**B**) [111]. Click-to-chelate strategy for the orthogonal conjugation of a chelator to an alkyne bound to a biomolecule (**C**) [113–115]. Competing coordination modes when an additional chelator is subjected to the click methodology (**D**) [112]. Complexes with the *fac*-[99mTcO₃]⁺ core: activation of [99mTcO₄]⁻ with phosphonium salts (step 1), coordination to triazacyclononane (step 2), and [3+2] cycloaddition for conjugating to bioactive functions "R" (step 3, **E**) [45, 46, 119].

of such a construct over non-cysteine containing peptides was shown by comparing the two peptide sequences CKLAAALEHHHHHH and LAAALEHHHHHH. Whereas the former showed 92 % binding to the *fac*-[Re(CO)₃]⁺ core (and accordingly to the [99mTc(CO)₃]⁺ core), the latter coordinated only 9 %. This finding may influence the construction of future tags in recombinant proteins [96, 97].

The direct labelling procedure through the histidine tag was applied to various recombinant proteins. Examples are trastuzamab [98], rituximab [99, 100], annexin V [101–103], and others [104, 105]. Since many conditions, different yields and methods of purifications were reported along these studies, Badar et al. [106] reported an optimized procedure for the labelling of four his-tagged proteins. They took many factors into account, in particular the Na^+ content of the labelling solution and the competition by non-his-tagged proteins. From their study, they concluded that a single procedure is not possible but that conditions have to be optimized from protein to protein. However, by optimizing respective conditions, reproducible, robust, and short preparations with high specific activities were achieved.

One of the very few macromolecular radiopharmaceuticals, which has been approved by the FDA, is [^{99m}Tc]Tilmanocept (Lymphoseek®). It is clinically used for mapping lymph nodes in cancer management and supports surgery in the cancer treatment. Tilmanocept consists of a large dextran backbone derivatized with mannose for better binding to the mannose receptors in the reticuloendothelial cells of the sentinel lymph node. Additionally, it carries DTPA groups, which form a complex with ^{99m}Tc. The radiopharmaceutical is routinely applied and relevant for the sentinel lymph node detection [107–109].

The fac-[^{99m}Tc(CO)$_3$]$^+$ core is also often applied in the labelling of peptides. In contrast to the above-mentioned his-tagged proteins, bifunctional chelators are required for this purpose. A multitude of bifunctional ligands was introduced over the years. Sometimes, the chelators are even the same as for other nuclides like the lanthanide(III) (Ln^{3+}) series. NODAGA and NOTA are prototypical for these radionuclides. Targeting SSTR-positive neuroendocrine tumors with radiopharmaceuticals is still an incentive [110]. Recently, sst2-ANT, denoting the potent SSTR2 antagonist 4-NO$_2$-Phe-c(DCys-Tyr-DTrp-Lys-Thr-Cys)-DTyr-NH$_2$ was derivatized with NODAGA or NOTA and labelled with the fac-[^{99m}Tc(CO)$_3$]$^+$ core (Scheme 5B) [111]. Whereas many peptides labelled with this organometallic moiety show high lipophilicity due to the neutral character of the final complex, this bioconjugate carries acetic acid side groups, which render the peptide hydrophilic leading to reduced liver accumulation.

The [^{99m}Tc]Tc-NOTA-sst2-ANT complex showed high tumor uptake (16.7 %) and rapid clearance in a SSTR-tumor mouse model. Interestingly, the NODAGA analogue, having a longer linker and one carboxylate group more, showed only small tumor uptake (2.7 %). Uptake in both cases was receptor-mediated. This example shows that even small changes in the linker between chelator and targeting molecule or even in the nature of the chelator have a drastic effect on the *in vivo* behavior. Based on the structures and the charges, such changes in biodistribution are very difficult to predict. The same peptide conjugate was also labelled with fac-[^{186}Re(CO)$_3$]$^+$ for radionuclide therapy. The matching behavior between the ^{99m}Tc and the ^{186}Re was demonstrated quantitatively as one of the few examples confirming the matched-pair concept. In a parallel study with the antagonist peptide sst2-ANT, click chemistry was employed for conjugating a facially coordinating N,S,O ligand chelator to this inhibitor. The resulting complex was neutral and therefore of lipophilic nature. The peptides labelled with

both Re and ^{99m}Tc displayed the same and expected nanomolar SSTR2 affinities. Whereas an identical coordination pattern is expected for the $[M(CO)_3]^+$ (M = ^{99m}Tc, Re) cores, differences in retention times on HPLC indicated conjugates for rhenium are different from those formed with ^{99m}Tc. These differences were attributed to a competing *N*-triazole donor ligand formed during click conjugation, representing one of the rare cases in which Re and Tc behave differently [112]. Whereas click chemistry for the introduction of bifunctional chelators is an excellent orthogonality-providing strategy, care has to be taken if the triazole is not assumed to participate in coordination as it is the case in the original "click to chelate" chemistry [113–115]. Otherwise, as in the described study, multiple products may result (Scheme 5C and 5D).

The examples described in this section illustrate progress in different fields of radiopharmacy. The labelling chemistry is the focus of this section and some examples may overlap with what is discussed below.

3.4. Miscellaneous Cores

Besides the "classical" cores, there is essentially only one further building block that has found some resonance, namely the high-valent *fac*-$[^{99m}Tc^{VII}O_3]^+$ core. Complexes with ^{99}Tc and this core have been synthesized in the early time of ^{99}Tc chemistry, either by oxidation of the *fac*-$[^{99}TcL^3(CO)_3]^+$ complex, in which L^3 is a tripodal, facially coordinating ligand, or under highly acidic conditions starting directly from $[^{99}TcO_4]^-$ [116, 117].

The preparation of *fac*-$[^{99m}Tc^{VII}O_3]^+$ complexes requires activation of $[^{99m}TcO_4]^-$ in water and concomitant coordination preferentially by a tripod ligand. Ligands of lower denticities do not stabilize the $^{99m}Tc^{VII}$ core against hydrolysis. Braband and Abram reported a new method towards complexes of the type *fac*-$[^{99}Tc(tacn)O_3]^+$ (tacn = 1,4,7-triazacyclononane), which did serve as a model for corresponding ^{99m}Tc chemistry [118]. They prepared the $[^{99}Tc^VOCl(tacn)]^{2+}$ precursor and oxidized it to the corresponding $^{99}Tc^{VII}$ complex. Later, Tooyama et al. synthesized a multitude of *fac*-$[^{99}Tc^{VII}(L^3)O_3]^+$ complexes by direct activation of $[^{99}TcO_4]^-$ in organic solvents [119]. The high stability of *fac*-$[^{99}Tc(tacn)O_3]^+$ was an incentive for direct preparations of this complex in water. The three nitrogens in the tacn framework can be derivatized with 2nd functions for conjugation to vectors. Braband et al. reported *fac*-$[^{99m}Tc^{VII}(L^3)O_3]^+$ complexes directly from aqueous solution by activation of $[^{99m}TcO_4]^-$ with phosphonium cations in the presence of tripod ligands (Scheme 5E) [47, 120, 121]. One of the particularly attractive properties of *fac*-$[^{99m}Tc^{VII}(tacn)O_3]^+$-type complexes is their reactivity towards alkenes and alkynes. The high-valent *fac*-$[^{99}Tc(tacn)O_3]^+$ core undergoes a convenient [3+2] cycloaddition with these functionalities to form $^{99(m)}Tc^V$ complexes with a 1,2-dihydroxylato ligand. Since alkenes can be introduced in many biomolecules, this is an excellent strategy to label targeting molecules with the *fac*-$[^{99m}TcO_3]^+$ fragment along an orthogonal concept. Some examples have been reported, but

they have not been pursued further [45, 46]. The relatively subtle reaction conditions for quantitative preparation may be one of the reasons for neglecting this core. Scheme 5E displays the synthetic steps for the preparation of $^{99m}Tc^{VII}$-type complexes and subsequent reactions with alkenes. A review by Kühn et al. provides a more comprehensive overview for complexes with the *fac*-$[^{99m}TcO_3]^+$ and *fac*-$[ReO_3]^+$ core [48].

4. SELECTED EXAMPLES OF ^{99m}Tc RADIOPHARMACEUTICALS

4.1. Myocardial Imaging Agents

Radiopharmaceuticals with ^{99m}Tc routinely applied for heart imaging represent the most relevant class of radiopharmaceuticals in routine clinical application. In fact, among the *de novo* imaging agents, they are commercially the most successful ones. The aforementioned Cardiolite® (^{99m}Tc-sestamibi) was the last of this kind that has been successfully introduced into the market. It became an important compound already in the Eighties [122, 123] and was a prototype for many subsequent studies. Cardiolite® or ^{99m}Tc-sestamibi is an organometallic, low-valent and binary $^{99m}Tc^I$ complex that fulfils all conditions as outlined in Section 2.2. In this kit, the isocyanide ligands (methoxy-isobutylisocyanide) are coordinated to a Cu(I) center for stabilization and for allowing lyophilisation of the kit. Reduction is done by $SnCl_2$ in a rapid process. The cationic complex $[^{99m}Tc(MIBI)_6]^+$ is extremely stable due to the d^6 electronic configuration. The uptake is mainly a metabolism-dependent process and the mitochondrial accumulation is due to the high negative charge across its membrane. The success of Cardiolite® inspired a lot of subsequent research going on until today but no new myocardial imaging agent could really compete with it. Since the patent expired many years ago, Cardiolite® is available from different companies.

Another important myocardial imaging agent is a complex with the $[O=^{99m}Tc^V=O]^+$ core. It has been commercialized as Myoview® nowadays by GE Healthcare [124]. The core is coordinated by two bidentate phosphine ligands and carries a mono-cationic charge. It has lower heart uptake than Cardiolite® but still does show good accumulation and retention in the heart [125]. Similar ligands as in Myoview® have also been applied for the $[^{99m}Tc\equiv N]^{2+}$ core and been subjected for targeting different diseases [74].

Newer developments in the *de novo* radiopharmaceutical field are based on the $[^{99m}Tc(CO)_3]^+$ core. In one example, a tridentate PNP ligand with a pendent crown-ether showed nice and persistent heart uptake [126]. Following this principle, Santos et al. [127, 128] focused on tris-pyrazolylmethane-type ligands in which the pyrazoles were substituted with different functionalities to yield, e.g., 3,4,5-tris(methoxymethyl)pyrazole (TMEOP). Bearing a total of nine $-CH_2OCH_3$ groups, the complex $[^{99m}Tc(TMEOP)(CO)_3]^+$ (Scheme 6A and 6B) showed an
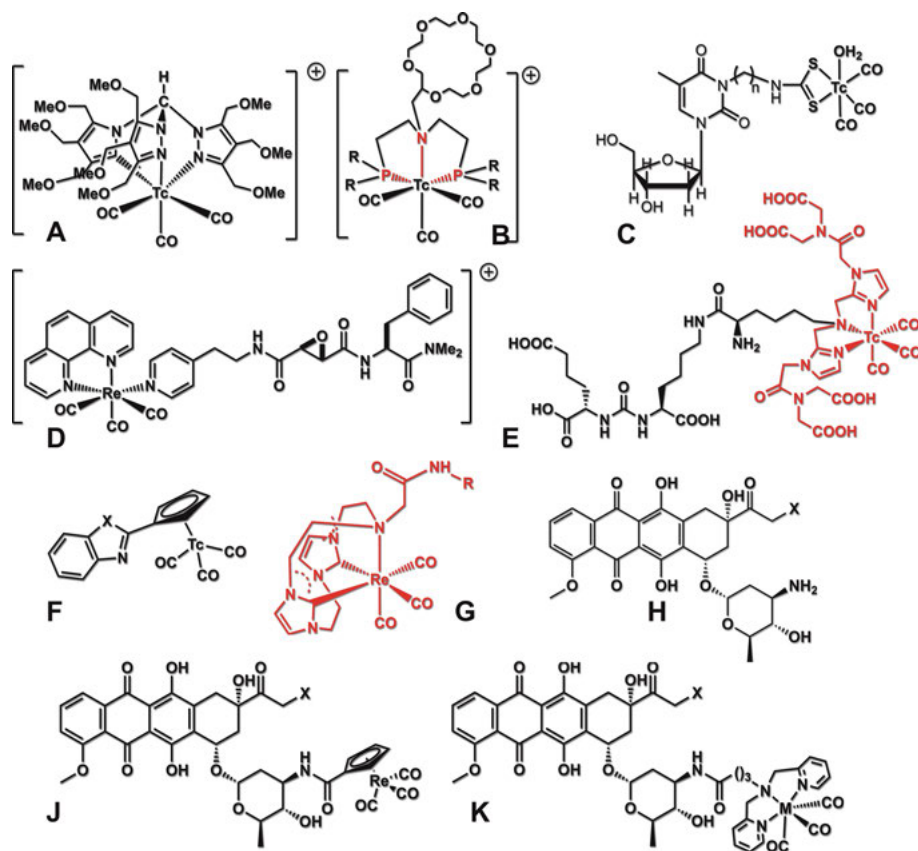
Scheme 6. A cationic tris-pyrazolyl-methane complex (**A**) and a complex with a PNP set of donors (**B**) for myocardial imaging correct [127, 128]. A nucleotide transporter targeting compound based on the dtc ligand (**C**) [130], a cysteine protease cathepsin L inhibitor (**D**) [129], and the inhibitor MIP-1405 for the prostate specific membrane antigen PSMA (**E**) [140–142] for cancer imaging. A piano-stool complex with the *fac*-$[^{99m}Tc(CO)_3]^+$ core (**F**) [154] and a macrocyclic bis-carbene ligand providing high stability to the same core (**G**) [155]. Doxorubicin (**H**) derivatized with rhenium or ^{99m}Tc complexes (**J** and **K**) [163, 164].

excellent biodistribution profile. Heart uptake was fast and stable, liver clearance better than in Cardiolite and SPECT images clean [127, 128]. Despite, this complex was not pursued, probably since it did not offer substantial advantages from a marketing point of view.

The example of $[^{99m}Tc(TMEOP)(CO)_3]^+$ shows that excellent biodistribution profiles and even superiorities to market-introduced radiopharmaceuticals are mostly not sufficient from a marketing point of view. New radiopharmaceuticals must have a marketing asset to the state-of-the-art imaging agent. Just having slightly better *in vivo* behavior is generally not enough.

4.2.   Cancer Imaging

The imaging of tumors with [99mTc] is one of the most intensely researched fields in radiopharmacy. A few examples have been discussed in Section 3 with respect to the different cores. For cancer imaging, [99mTc] complexes are conjugated to targeting biomolecules such as peptides or proteins. Newer examples have also focused on small molecules such as pharmaceuticals or metabolically relevant natural structures such as thymidine or cysteine protease cathepsin L inhibitors. The following example with cathepsin L is of particular interest for perspective [99mTc] chemistry. Together with the rhenium homologue described in parallel, the compounds are multi-modality imaging agents, combining radioactivity with luminescence. The principle of inhibition is based on epoxysuccinyl inhibitors. They block the action of these proteases by selective binding and covalent modification of sites, which favour the epoxy-ring opening reaction. The inhibitor CLIK-148 (Scheme 6D) was derivatized with a bipyridyl unit for coordination to the fac-[Re(CO)$_3$]$^+$ moiety. The ligand sphere was completed by a monodentate pyridine, which led to highly luminescent complexes [129]. Different to other papers, a careful analysis of the rate constants towards different CTS's were determined. Since the reactivity of the epoxy-ring plays a crucial role, the influence of the metal complex on these rates is decisive for application. Although not done yet with [99mTc], conjugates with cysteine protease cathepsin L inhibitors might open a new track against visualizing rapidly proliferating cells.

Dithiocarbamate mentioned above stabilize the [99mTcN]$^{2+}$ core. This soft ligand group is also versatile for the [99mTc(CO)$_3$]$^+$ core and is convenient for introducing biomolecules. Duan et al. [130, 131] introduced a –CH$_2$–NH$_2$ group to thymidine at the N3 position and subsequently combined it with CS$_2$ to obtain a dtc function. Labelling in high yields were achieved and the tracer stable against all challenges. It could be shown that the conjugate was actively transported by nucleotide transporters [130, 131]. This is particularly interesting since derivatization of small, natural molecules with complexes usually does lead to the loss of transporter recognition (Scheme 6C).

By far the most investigated cancer-targeting small molecules are inhibitors of the prostate specific membrane antigen PSMA (Scheme 6E). Due to the relevance and wide-spread occurrence of prostate cancer (PC), inhibitors to the antigen have attracted an enormous attention since about a decade. PSMA is a type II integral membrane glycoprotein that was detected on the human prostatic carcinoma cell [132]. Since almost all prostate cancers exhibit this antigen, it is an attractive target for detecting PC and metatheses derived from the primary tumor. There are several types of receptor ligands and the ones of importance in the context of [99mTc] radiopharmaceuticals are urea-based. As shown in Scheme 6E, the basic inhibitor type comprises a glutamic acid, an urea group, and a terminal lysine, the side chain of which can be used for modification with ligands. This PSMA inhibitor has mainly been labelled with [68Ga]$^{3+}$ and with [99mTc]. The corresponding radiopharmaceuticals were evaluated in many preclinical and clinical trials with great success [133–137]. For [68Ga], the complex [[68Ga](Glu-NH-CO-NH-Lys(Ahx))-HEBD-CC was found versatile for PET/CT, a modern multi-modality procedure. Since the parallel availability of the [99mTc]

compounds, MIP-1404 (Scheme 1B) and MIP-1405 allow for SPECT/CT, these imaging agents have been pursued as well [138, 139]. MIP-1404 (Scheme 1B) finished Phase III clinical trials and is currently introduced into the market by ROTOP Pharmaka GmbH. A recent SPECT/CT study described a summary of 225 patients with PC lesions. This study disclosed tracer-positive lesions detection in 77 % of all patients with metastasis in lymph nodes, bone, lung, and other locations [140]. Clearly, MIP-1404 is applicable also for SPECT/CT and is therefore interesting for hospitals with lower instrumentation and radionuclide costs [140–142].

Radio-guided surgery is a further albeit little applied strategy for radiopharmaceuticals that has recently been reported. Radio-guided surgery includes different steps: Patients are selected based on PSMA ^{68}Ga PET results and then injected with ^{99m}Tc MIP-1404. Subsequent SPECT/CT images are taken to confirm MIP-1404 uptake in some lesions of preoperative ^{68}Ga findings. In a last step, PSMA-radio-guided surgery is performed. *In vivo* and *ex vivo* γ-probe measurements allow to reliably identify metastatic prostate cancer lesions. This study could demonstrate the feasibility of intraoperative identification and surgical removal of lymph node metastases [143].

PSMA inhibitors are of the greatest value for oncology. For nuclear medicine imaging and for theranostic applications in particular, PSMA is also investigated with matched-pair radionuclides such as ^{64}Cu/^{67}Cu [144, 145]. There are other attempts for PSMA theranostics, not following the matched-pair strategy but rather with radionuclides from the "3+ family", e.g., ^{111}In, ^{177}Lu, and ^{225}Ac. Since chelators for these metal centers are often similar or equal, there is great promise for combining imaging with radionuclide that could serve also as a model for the ^{99m}Tc/^{188}Re pair [146].

4.3. Neurodegenerative Diseases

The targeting of brain receptors with ^{99m}Tc complexes is a long-standing incentive. Challenges bringing ^{99m}Tc complexes into the brain are primarily to overcome the blood-brain-barrier in a reasonable brain-blood-barrier first-pass percentage. Metal complexes are often not lipophilic enough or the molecular weights are too high for efficient extraction. For radiopharmaceuticals labelled with main group radioisotopes such as ^{11}C or ^{18}F, this is a minor problem since these labels do not change molecular weight, structure or physico-chemical properties to a significant extent. A comprehensive review described the progress made in this field in the context of amyloid plaque targeting [147]. There are essentially two ^{99m}Tc-based radiopharmaceuticals, which are or have been clinically applied. One is the neutral, oxime-based complex, oxotechnetium-hexamethylpropyleneamine oxime [^{99m}Tc^{V}O(HMPAO)] which is sold under the trade name Ceretec® [148]. The compound is used for measuring a percentage of reduced brain perfusion in patients with Alzheimer's disease (AD) when compared to healthy persons. After passing the blood-brain-barrier, the complex is trapped in the brain, supposedly by enzymatic conversion to a more hydrophilic species [149].

In the recent past, research mainly focused on the targeting of amyloid plaques with complexes comprising the *fac*-[^{99m}Tc(CO)$_3$]$^+$ moiety. Detailed reviews discussed these recent developments in the pursuit of suitable ^{99m}Tc-based amyloid imaging probes are available [150–152]. Only a few studies will be presented at this place as relevant for the development of ^{99m}Tc radiopharmaceutical chemistry. In a recent study combining cyclopentadienyl chemistry of ^{99m}Tc with the targeting of amyloid plaques, the phenyl ring in 2-phenylbenzothiazole or 2-phenylbenzimidazole, compounds well known for strongly interacting with plaques, have been replaced by the piano-stool complex [(η^5-C$_5$H$_4$-R)^{99m}Tc(CO)$_3$]. "R" represents the benzothiazole moiety of 2-arylbenzothiazole, the classical Aβ (amyloid beta, peptides of 36–43 amino acids) binding structure originally developed as the neutral analogue of thioflavin T. Thioflavin is the histological dye used in the clinic for *ex vivo* visualization of Aβ plaques in AD brain. The complex was synthesized along the double ligand transfer strategy from the corresponding ferrocene precursor (Scheme 6F) [153].

As determined by confocal microscopy, the rhenium analogues showed high affinities for Aβ42 aggregates in the low nanomolar range. The ^{99m}Tc analogues with benzothiazole showed a very high first-pass brain uptake of about 8 %. This remarkable uptake though was strongly reduced for a benzimidazole analogue. Whereas the uptake is excellent, the washout was relatively rapid too and reduced to 4 % after 15 min and to 0.2 % after 90 min, reflecting the problem of brain retention. Still, amongst the ^{99m}Tc-based radiopharmaceuticals, this is one of the most favorable examples reported so far. It shows the advantage of the integrated over the pendent approach. In the pendent approach, a chelator is attached to, e.g., the benzothiazole moiety, i.e., a new fragment is introduced which might impede brain uptake. This is obvious from a report that employed the pendent strategy with benzothiazoles. A tridentate chelator was conjugated to this moiety and quantitatively labelled with [^{99m}Tc(CO)$_3$]$^+$. Whereas stability was excellent, brain uptake was very small and not useful for imaging. The authors speculated that a brain with plaques might have a higher retention but this remains to be proven [154].

Besides neutral complexes, there is evidence that cationic complexes bind strongly to Aβ plaques. Interesting from a chemical point of view, Donnelly et al. [155] reported recently thioamide complexes of Re and ^{99m}Tc as well as a complex with a tridentate bis-carbene ligand that binds to the [Re(CO)$_3$]$^+$ and the *fac*-[^{99m}Tc(CO)$_3$]$^+$ core equally well (Scheme 6G). When the carbene ligand was acyclic, coordination isomers were found, if macrocyclic, one single complex was obtained. The ligands carried a pendent stilbene or benzothiazole group. The capacity of these compounds to bind to amyloid plaques in human AD brain tissue was evaluated and selective binding to the Aβ plaques was found. No evidence of non-specific binding demonstrates the potential of NHC ligands and cationic complexes to be incorporated into diagnostic imaging agents for Alzheimer's disease. Carbene ligands represent a group of very strong chelators, which are only little explored. There are a number of complexes with ^{99m}Tc for the [O=^{99m}Tc=O]$^+$ and the *fac*-[^{99m}Tc(CO)$_3$]$^+$ core but they have found little application for molecular imaging purposes [156, 157]. Barnard et al. [158] re-

ported a generally applicable strategy in the matched-pair approach towards complexes with the *fac*-[^{99}Tc(CO)$_3$]$^+$ core, and a bidentate mono-carbene complex. N3 in the imidazolium precursor for the carbene may carry a targeting function as described in this report [158].

Targeting and imaging of Alzheimer's disease remains persistent in molecular imaging. Whereas the majority of studies is done with copper radionuclides, ^{99m}Tc-labelled compounds play an important role in low oxidation states due to the flexibility of chelators and the option of integrating a ^{99m}Tc core into the overall structure without introducing additional chelators [159].

4.4. $^{186/188}$Re Homologues for Radionuclide Therapy

The matched-pair strategy, i.e., ^{99m}Tc complexes for imaging and $^{186/188}$Re for radionuclide therapy, is an early idea [160]. It relates to the principle that homologous compounds of the two elements have closely or even identical physiological *in vivo* behavior. The base for this idea is the requirement of stability of both complexes under *in vivo* conditions and the possibility of synthesizing the homologues along similar lines. Since technetium and rhenium complexes show different reactivities in some oxidation states, the matched-pair concept was never really shown, e.g., with complexes comprising the [M=O]$^{3+}$ core. Complexes with M=Re are more susceptible to re-oxidation and less stable, i.e., they decompose faster under *in vivo* conditions. Some complexes cannot be synthesized with one or the other element, keeping the initially mentioned conditions in mind [9]. Only with the advent of the [M(CO)$_3$]$^+$ core, the matched-pair hypothesis gained evidence. The success of the matched-pair concept in a few studies shall be discussed below. One of the problems that remains to be solved for the [M(CO)$_3$]$^+$ core is the synthesis of the ^{188}Re homologue. Whereas technetium is easy to be reduced to the +I state, rhenium is more robust, less oxidizing and demands harsher conditions. An optimized procedure has been published which allows access to [^{188}Re(OH$_2$)$_3$(CO)$_3$]$^+$ but is not as straight as the one for ^{99m}Tc [161].

One example for which both, the ^{188}Re and the ^{99m}Tc-labelled peptide substance P undecapeptide have been applied was based on the respective [M≡N]$^{2+}$ cores. A tridentate pincer-type SNS ligand was coupled via an amide to the peptide. The coordination sphere around the [M≡N]$^{2+}$ core was completed with a monodentate phosphine ligand and both complexes subjected to *in vitro* and *in vivo* experiments. Whereas the ^{99m}Tc conjugate could be prepared according to the published two-step procedure [162], the preparation of the ^{188}Re homologue was more demanding than the one for ^{99m}Tc, demonstrating the differences in rhenium and technetium chemistry in the higher oxidation states. Still, the labelled peptides showed a high *in vitro* affinity for the respective receptor and an analogues biodistribution. The findings support the validity of the matched-pair concept [162].

The matched-pair technology was also successfully verified with antibody fragments, namely with rituximab (RTX), the human IgG1-type chimeric form of the parent murine antibody ibritumomab. Rituximab was pre-reduced to gener-

ate free sulfhydryl groups and then directly labelled with the corresponding carbonyls. After 3 h of incubation, labelling was quantitative and the bioconjugate was stable in serum without release of carbonyl complexes. Both conjugates $M(CO)_3$-RTX showed comparable pharmacokinetic profiles, corroborating the matched-pair concept. It is however not clear how the binding occurs, the reduced sulfhydryl groups may be one option, exposed histidines formed upon unfolding after reduction another [99].

Small molecules are an equal option for the matched-pair strategy. Imstepf et al. [163, 164] selected the cytotoxic anthracycline compound doxorubicin (Scheme 6H) as a carrier for both, rhenium and technetium. The conjugate of $[(Cp\text{-}COOH)Re(CO)_3]^+$ to daunosamine sugar was accumulated in the mitochondria to a much larger extent than the parent doxorubicin (Scheme 6J). Topoisomerase inhibition was maintained and IC_{50} values were only slightly diminished as compared to the parent doxorubicin. With an amino-dipyridyl chelator (Scheme 6K), doxorubicin was also labelled and the uptake in the cell nucleus and the mitochondria quantified with ICP-MS and radioactivity measurements. The uptake was essentially identical, confirming once more the matched-pair approach [163, 164].

The last example does not compare $^{186/188}$Re with ^{99m}Tc but is rather a comparison to non-radioactive, cold rhenium homologous. Shifting the matched-pair concept from the ^{99m}Tc/$^{186/188}$Re couple to ^{99m}Tc/Re describes a little explored direction, leading to a different kind of theranostics. Whereas in the classical matched-pair concept therapy was radionuclide-based, chemotherapy replaces radionuclide therapy albeit the same compounds are applied. An advantage of this change in paradigm is the fact that carrier-added ^{186}Re can be employed. Therapeutically active lead structures, labelled with reactor-produced ^{186}Re, can take over both functions, as chemotherapeutics due to the presence of substantial amounts of "cold" rhenium, and radionuclide therapy due to the presence of ^{186}Re. Thus, this is a newer and rarely reported approach but a true asset to many other radionuclides subjected to radiopharmaceutical studies.

5. ^{99}Tc AND Re CHEMISTRY AS MODEL FOR ^{99m}Tc RADIOPHARMACEUTICALS

5.1. Characterization of ^{99m}Tc Radiopharmaceuticals

The structural authenticity of ^{99m}Tc-labelled compounds of all types as discussed in the previous sections needs to be determined prior to any *in vivo* studies. Only radiopharmaceuticals with known structures will find approval by the regulatory authorities. Since the absolute amounts and the concentrations of any preparation are extremely low, classical methods such as NMR, X-ray structure analysis, and other methods do hardly apply. Mass spectrometry might give hints in rare cases but one single method typically does not allow for an unambiguous characteriza-

tion. To characterize a new radiopharmaceutical, the compounds or the conjugates are if possible synthesized with cold rhenium in macroscopic amounts with the long-lived ground state ^{99}Tc. Fully characterized Re or ^{99}Tc compounds are then subjected to HPLC and the retention times are determined. Their comparisons with the ^{99m}Tc homo/analogues are a FDA-accepted method for assessing the chemical composition of the radiopharmaceutical.

Typically, a true co-injection is required, where both compounds are analyzed by HPLC in the same injection [165]. This procedure is done with most of the compounds described in the previous sections. It is typically not possible for proteins due to the numerous binding sites and since binding do not always occur reproducibly. Other criteria apply in such cases. Since Re and Tc are sometimes not fully identical (they still represent two different elements), albeit in the same group of the periodic table, retention times may not be fully identical. If required for later registration, comparison of ^{99m}Tc with the ^{99}Tc compound is the only way to identify conclusively the composition of the radiopharmaceutical. This is rarely done due to the lack of facilities for working with ^{99}Tc, but it is essential for critical cases such as the recently described formation of dinuclear ^{99m}Tc compounds [166].

5.2. Rhenium and Technetium in Molecular Theranostics

Theranostics refers to the combination of imaging and therapeutic entities combined in one carrier. The carriers are usually nanomaterials decorated with anchoring groups for, e.g., a receptor-targeting molecule, while providing sites for binding to radionuclides or MRI agents. The nanomaterials by themselves may be part of the theranostic agent by being for instance a super paramagnetic iron oxide nanoparticle or a quantum dot [167]. Many combinations of therapeutic entities with radionuclides as imaging portions have been published, but examples with ^{99m}Tc (or ^{188}Re) are comparably rare [168–170].

Nanoparticles (NPs) are in general not "atom-precise" carriers although they are often close to mono-disperse. Since this chapter focuses on molecular ^{99m}Tc imaging agents, they will not be discussed in more detail but referred to the references given above. One example though shall illustrate the principle of theranostics with ^{99m}Tc. Gold nanoparticles are excellent carriers since targeting portions and imaging compounds can easily be anchored by, e.g., sulfhydryl or thioether groups. Felber et al. [55, 171] reported about such Au NPs. The multifunctional molecule shown in Scheme 7B was developed, which served the same time as conjugation site for targeting peptides, PSMA in this case, and as chelator for the *fac*-[^{99m}Tc(CO)$_3$]$^+$ core (Scheme 7A and 7B). TEM showed that these NPs are actively internalized on LNCaP cells. The coating was stable in serum and no release of labelled ligands was found. *In vivo* though, the NPs did bind essentially to bones due to the high affinity of the coating ligands for Ca^{2+}.

The approach is still convenient since, besides PSMA, other targeting molecules of choice can be conjugated while the remaining ligands, coated to the surface

via the same molecule, are labelled in high yields and stabilities with the *fac*-[^{99m}Tc(CO)$_3$]$^+$ core [55, 171].

A concept of molecular theranostics is based on small molecules. As mentioned in the previous sections, complexes with rhenium and technetium are often true homologues as evident from the matched-pair examples given in Section 4.4. A radionuclide-based theranostic approach may now be represented by a matched-pair combination of $^{186/188}$Re (therapy) and ^{99m}Tc (imaging).

Assuming that both radiopharmaceuticals have identical pharmacokinetic properties, the combination will lead to new theranostic opportunities. Examples are rare, one with the antibody rituximab as discussed before [99]. For targeting bone calcification with phosphonato-bearing radiopharmaceuticals, Blower et al. [172] prepared ^{99m}Tc and ^{188}Re homologues with the [M≡N]$^{2+}$ core. The ligand dithiocarbamate coordinates well to this core. The dtc ligand was derivatized with a linker bearing two terminal phosphonato groups. The dithiocarbamatebisphosphonate ligand dtc-BP and its complexes of ^{99m}Tc and ^{188}Re bind well to exposed Ca^{2+} in bones. Accordingly, both neutral complexes [^{99m}Tc(dtc-BP)$_2$] and

Scheme 7. A joint organic building block for binding a biomolecule (red, **A**) or a ligand (**B**) for the *fac*-[^{99m}Tc(CO)$_3$]$^+$ core to Au nanoparticles [55, 171]. Bone imaging agents with pendent phosphonato groups (**C** and **D**), both were prepared with ^{99m}Tc and ^{188}Re for the matched-pair concept [172] and a series of cytotoxic rhenium complexes (**E** and **F** [178], **G** [184], and **H** [185]).

[^{188}Re(dtc-BP)$_2$] showed excellent bone uptake and *in vivo* stabilities (Scheme 7C and 7D). Despite these advantages over the commercialized bone-imaging agents such as, e.g., ^{99m}Tc-methyl diphosphonate, ^{99m}Tc-MDP, better stabilities and hydroxyapatite affinities will probably not lead to a new radiopharmaceutical for marketing reasons. At least the ^{188}Re compound could be used for palliation since the ^{188}Re analogue of ^{99m}Tc-MDP does not exist [172].

An extension to the purely radionuclide-based theranostic concept is the application of a "cold" cytotoxic rhenium complex with its "hot" ^{99m}Tc homologue. Such combinations are established in pharmaceutical chemistry, where many new compounds under development are fluorinated for different purposes. Exchanging the ^{19}F in the cold lead structures with ^{18}F allows for the convenient determination of pharmacokinetics and metabolites as a standard method [173]. Translating this concept to metallic elements leads to an approach in which a cold rhenium complex is cytotoxic while its ^{99m}Tc homologue must be synthetically accessible and should display the same *in vivo* properties. In complementation to radionuclide theranostics with the same compounds but labelled with a therapeutic and a diagnostic radionuclide, this concept is referred to as "molecular theranostics".

Only since recently, rhenium complexes are considered as cytotoxic and relevant for medicinal inorganic chemistry. Research with rhenium has not found the attention it deserves and focuses are generally put on the platinum group elements. To change this view, Gasser et al. and others revised this picture by presenting a variety of rhenium complexes, which showed substantial cytotoxicities [174–182]. With the exception of a photochemically active rhenium complex for photodynamic therapy, the chemical/biological mode of action is mostly not well known. A comprehensive review discusses the mode of actions of Re, Os, and Ir complexes, which have found to be cytotoxic [183]. This is an incentive for preparing the homologous ^{99m}Tc compound. Comparable pharmacokinetics will open the door to a new approach in theranostics based on well-defined molecular complexes rather than on nanoparticles [178, 184, 185]. Scheme 7E to 7H displays a number of rhenium complexes with proven cytotoxicity.

5.3. Future Concepts toward Imaging Compounds in ^{99m}Tc and ^{99}Tc Chemistry

The theranostic concept described in Section 5.2 relies on "cold" rhenium complexes and ^{99m}Tc. Most of the rhenium-based cytotoxic agents are *de novo* compounds with no conjugating targeting moieties, although they do exist in the sense of second generation cytotoxic agents or radiopharmaceuticals [186]. To extend this concept even more, a newer strategy aims at the integration of the metal complex in a given lead structure (integrated approach, third generation). This concept is new for molecular imaging, but it has been used successfully in medicinal inorganic chemistry for many years. Taking clinically applied pharmaceuticals, a phenyl ring was replaced for instance by a ferrocene. The structural changes in the lead structure were minimal and the metal complex, in this case

ferrocene, would provide some additional activities. The pioneering compound in this principle is ferrocifen (Scheme 8A), an analogue of the anti-cancer agent tamoxifen. Jaouen et al. and others pioneered this strategy and many other bioactive compounds with cold metals followed [187–194].

To enable the same strategy for radionuclides required the preparation of ^{99m}Tc cyclopentadienyl complexes according to the conditions listed in Section 2.2. In this case, a phenyl ring in the lead structure could be replaced by a cyclopentadiene and is then labelled with the *fac*-[^{99m}Tc(CO)$_3$]$^+$ core. The so-formed radiopharmaceutical complex comprises still the structure of the lead with a planar phenyl replaced by a planar cyclopentadienyl ligand and the ^{99m}Tc moiety underneath.

Katzenellenbogen et al. introduced in the Nineties the so-called double-ligand-transfer reaction for exchanging in a ferrocene complex one "Fe(Cp)" unit by the *fac*-[^{99m}Tc(CO)$_3$]$^+$ moiety [195–197]. The drawbacks of this synthetic pathway were organic solvents, chromium compounds, and high temperatures. Still, proof of principle could be given for the validity of the integrated concept. It was applied in different studies with pharmaceutical lead structures but also by simply attaching a ^{99m}Tc piano stool complex to targeting portions [153, 198–202]. Wald et al. [203] simplified the double ligand transfer concept by using cyclopentadiene (HCp) precursors, bearing an α-keto group attached to HCp. This acidified the HCp enough to be deprotonated at physiological conditions, which allowed for the formation of piano-stool complexes [(η^5-C$_5$H$_4$-R)^{99m}Tc(CO)$_3$] from water and at 100 °C [203, 204]. Whereas this method still had its limitations, Liu et al. [205] reported an approach starting from Diels-Alder dimerized HCp (Scheme 8C), carrying two carboxylic acid groups at each fragment. A one pot reaction starting from [^{99m}TcO$_4$]$^-$ in water and at 100 °C cleaved the dimer in a retro Diels-Alder reaction and led to quantitative formation of [(η^5-C$_5$H$_4$-R)^{99m}Tc(CO)$_3$]-type compounds [205]. The carboxylate groups can be conjugated to any targeting portion or be part of a bioactive lead structure. Can et al. [41] applied the retro-Diels-Alder synthesis for targeting carbonic anhydrases (CA), a receptor frequently overexpressed on rapidly proliferating cells (Scheme 8D). Two sulfonamide-bearing residues bind strongly to Zn^{2+} in CAs, which leads to visualization of such sites. They could show that the ^{99m}Tc-CAs did not only have nanomolar affinities for the receptors but also exhibited a dramatically increased selectivity towards CA subtypes, corroborating the validity of the concept [41]. This new development was subsequently transferred to benzamides for malignant melanoma targeting and model peptides [206, 207].

Most clinical pharmaceuticals carry more than one functionality on a phenyl ring. To extend the development of integrated radiopharmaceuticals, the basic HCp framework should be derivatized with two or more groups on its periphery. Such cyclopentadiene structures do not dimerize anymore but may also not be acidic enough for deprotonating under physiological conditions. Frei et al. did this extension by applying a Wittig-type ring closure reaction for the formation of cyclopentadiene constructs carrying three variable functional groups, two of them being capable of being further conjugated to targeting or cytotoxic moieties [208]. They applied the concept to HCp cores with one or two PSMA-targeting
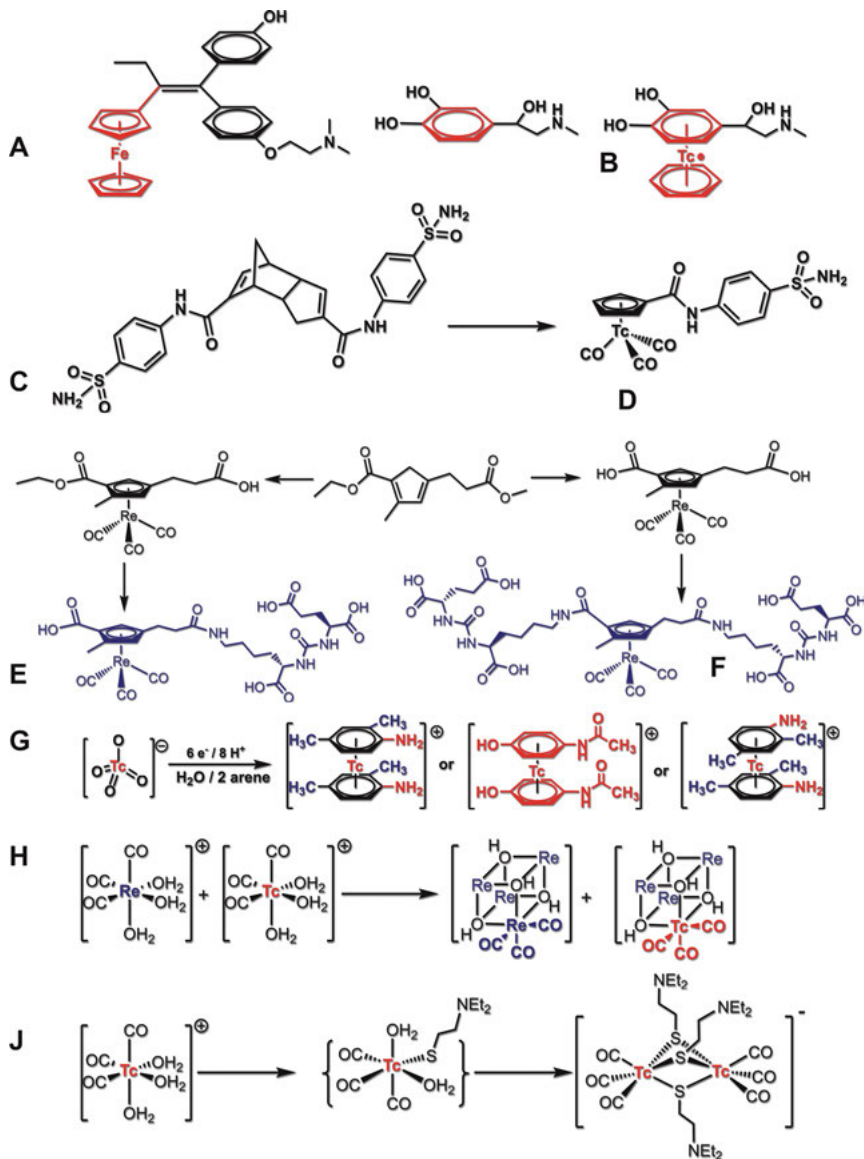
Scheme 8. Perspective concepts in imaging and therapy: bioactive molecules with integrated metals, a tamoxifen [187] and an epinephrine mimic (**A** and **B**) [211]; piano-stool type complex of ^{99m}Tc starting from the Diels-Alder dimerized dicyclopentadiene precursor (**C**) with a pendent carbonic anhydrase (CA) inhibitor (**D**) [206, 207]; multifunctional Cp-ligands, introduction of PSMA with peptide coupling gives a mono- and bis-functionalized, PSMA-targeting molecule (**E** and **F**) [208, 217, 218]; multi-functional sandwich complexes of the bis-arene types, single-step preparation with ^{99m}Tc in water (**G**) [211]; multinuclear Re/^{99m}Tc or [99m]Tc$_2$ compounds (^{99m}Tc in red): Self-assembly of $[^{99m}Tc(OH_2)_3(CO)_3]^+$ and $[Re(OH_2)_3(CO)_3]^+$ to a tetranuclear cluster (**H**) and formation of a dinuclear [99m]Tc$_2$ complex (**J**) [166, 215].

vectors. Labelled with the *fac*-$[^{99m}Tc(CO)_3]^+$ core, it could be shown that the doubly functionalized radiopharmaceutical had a much higher affinity for its antigen than the one that was classically labelled with one moiety only [208]. The basic cyclopentadiene framework from these studies represents a multi-variable core for systematically conjugating other bioactive portions. Such a construct will allow for a systematic screening of novel radiopharmaceuticals with the cyclopentadiene architecture at their centers. In these reports, labelling was possible directly in water and from $[^{99m}TcO_4]^-$ (Scheme 8E and 8F) [209–211], consistent with requirements for routine application.

A cyclopentadiene is not a phenyl and complexes based on $[^{99m}Tc(\eta^6-C_6H_6)_2]^+$ would come closer to a fully integrated approach. $[^{99m}Tc(\eta^6-C_6H_6)_2]^+$ complexes are known since the Sixties, but essentially no subsequent chemistry was done with them. To attempt a preparation of these cores or building blocks is a challenge, since the original complexes were synthesized in pure arenes as solvents in the presence of $AlCl_3$ and Al^0 or Zn^0 as reducing agents. Above, stability in aqueous systems was unknown and arene complexes of the neighboring elements are either oxidatively or hydrolytically unstable, or both [209]. A revised preparation of $[Re(\eta^6-C_6H_6)_2]^+$ and $[^{99}Tc(\eta^6-C_6H_6)_2]^+$ showed that these basic frameworks are extremely stable against oxygen at any pH and temperature [210]. These are the ideal properties but the challenge remained to select a pharmaceutical and introduce a ^{99m}Tc moiety to specific phenyls. Nadeem et al. reported then a successful preparation of bis-arene ^{99m}Tc complexes with highly functionalized arenes in one-step and from $[^{99m}TcO_4]^-$ in water [211]. This strategy for reacting $[^{99m}TcO_4]^-$ directly with underivatized phenyl-bearing molecules and yielding exclusively $[^{99m}Tc(\eta^6-arene)_2]^+$ is an important step towards ^{99m}Tc-based imaging agents. For obtaining multi-functional complexes, the arene rings were functionalized by active groups such as halides, amines, and carboxylates. These groups were easily conjugated to targeting vectors or cytotoxic entities [212–214]. Such post-functionalizations are synthetically demanding and regioselective introduction of multi-functional groups are challenging. Therefore, this is not a route to go for ^{99m}Tc, since time and conditions would not be appropriate for a routine preparation. Since reference rhenium compounds are needed, post-functionalization for this purpose is an option.

Most ^{99m}Tc radiopharmaceuticals are mononuclear compounds. It is a paradigm that di- or multinuclear complexes, i.e., cluster compounds, do not exist since kinetics of bimolecular reactions at the high dilutions outlined in Table 1 is prohibitively slow. Clusters are even rare in medicinal inorganic chemistry. They would deliver a high metal payload, are atom-precise in contrast to nanomaterials, and can be derivatized at their surfaces. With respect to radiopharmaceuticals, an incomplete cluster of cold metals could be completed by a ^{99m}Tc fragment, which will lead to a combination of a therapeutic moiety with imaging. An example has been given recently. Rhenium and technetium clusters with μ-OH bridges are known for the *fac*-$[M(CO)_3]^+$ cores. They form *in situ* and are stable moieties. Mixing the precursors $[Re(OH_2)_3(CO)_3]^+$ and $[^{99m}Tc(OH_2)_3(CO)_3]^+$ under slightly alkaline conditions leads to the quantitative, self-assembled formation of the cubane-like tetranuclear cluster $[^{99m}TcRe_3(\mu^3-OH)_4(CO)_{12}]$ (Scheme 8H).

This cluster also forms by a post-assembly process. The incomplete cubane cluster $[Re_3(\mu_2\text{-OH})_3(\mu_3\text{-OH})(CO)_9]^-$ is labelled with *fac*-$[^{99m}Tc(CO)_3]^+$ to obtain the complete cubane system [215]. Other metal fragments can be introduced with the post-assembly strategy, a strategy not yet considered for imaging or therapy.

Finally, it was shown that dinuclear $^{99m}Tc_2$ complexes do exist with appropriate ligands. Coordination of a thiolato ligand to a *fac*-$[^{99m}Tc(CO)_3]^+$ core changes the electronic properties of the metal center. Subsequent ligand substitution may become very fast and di- or even trinuclear complexes will form at high dilution. It was reported that the dinuclear complex $[^{99m}Tc_2(\mu\text{-SR})_3(CO)_6]^-$ (R = $-CH_2CH_2NEt_2$) forms quantitatively along this reaction pathway and evidence for small amounts of trinuclear clusters were found as well (Scheme 8J) [166]. This implies that side products in syntheses of ^{99m}Tc complexes may well be di- or multinuclear species. Di- or multinuclear clusters combining hot and cold elements become an option for ^{99m}Tc compounds.

One last study belongs to clusters but also to a new way of labelling. Archibald et al. [216] reported recently about the inclusion of $[^{99m}TcO_4]^-$ into a self-assembled tetranuclear cobalt cluster. The cobalt cluster takes $[^{99m}TcO_4]^-$ up into its cavity with high affinity and selectivity. $[^{99m}TcO_4]^-$ remains non-covalently bound and is not released, even in the presence of other competing anions such as chloride. *In vivo*, the filled cluster loses small amounts of $[^{99m}TcO_4]^-$ though. The concept of taking host-guest chemistry for labelling rather than covalent frameworks is a prospective development, which is elegant and will have impact on labelling strategies [216].

6. CONCLUDING REMARKS

Radiopharmaceutical chemistry with ^{99m}Tc is proceeding along many concepts and strategies as reported in this chapter. Numerous targets are under investigation with approaches comprising the different cores reasonably applicable to a future imaging agent under clinical routine conditions. Whereas ^{99m}Tc or ^{99}Tc chemistry was more a "stand-alone" research in the past, it is nowadays accompanied and complemented with rhenium chemistry. This is not only due to the indispensable structural characterization of the tiny amounts of ^{99m}Tc homologues, but even more due to the perception that rhenium complexes have by themselves cytotoxic properties that might well complement the standard, metal-containing drugs such as cisplatin. This leads to the concept of theranostics, which is valid for group 7 elements, in particular for the low oxidation states with the *fac*-$[M(CO)_3]^+$ cores. All cores have this option though, as outlined in a number of examples discussed above.

Research on pure "*de novo*" complexes has decreased and the foci are on targeting complexes. Within this concept, combinable between rhenium and technetium, progress has been made for obtaining multi-modality imaging/therapeutic agents. This includes the integrated approach with third-generation compounds mimicking structures of lead pharmaceuticals already in clinical routine.

Fluorescent rhenium complexes may thereby be visualized on the subcellular level with fluorescence microscopy, whereas the γ-emission allows for *in vivo* imaging. Examples for this concept have been reported. Taken all together, there is a plethora of new opportunities, combinations of modalities and chemical approaches available.

ACKNOWLEDGMENTS

ABBREVIATIONS

Aβ	amyloid beta
Ahx	6-aminohexanoic acid
DOTA	tetraazacyclododecane-1,4,7,10-tetraacetic acid
DTPA	diethylenetriamine pentaacetate
FDA	Food and Drug Administration
GRPR	gastrin-releasing peptide receptor
IC_{50}	inhibitory concentration (half maximal)
ICP-MS	inductively coupled plasma mass spectrometry
IGF	insulin-like growth factor
MAG3	mercaptoacetylglycine-glycine-gylcine
MDP	methyldiphosphonate
MIBI	methoxy iso butyl isonitrile
NODAGA	1,4,7-triazacyclononane-1-glutaric acid-4,7-diacetic acid
NOTA	1,4,7-triazacyclononane-1,4,7-triacetic acid
PC	prostate cancer
PS	phosphatidylserine
PSMA	prostate-specific membrane antigen
SAACQ	single amino acid chelate quinoline
scFv	single-chain variable fragment
SSTR	somatostatin receptor
tacn	1,4,7-triazacyclononane

REFERENCES

1. V. Drozdovitch, A. B. Brill, R. J. Callahan, J. A. Clanton, A. DePietro, S. J. Goldsmith, B. S. Greenspan, M. D. Gross, M. T. Hays, S. C. Moore, J. A. Ponto, W. W. Shreeve, D. R. Melo, M. S. Linet, S. L. Simon, *Health Phys.* **2015**, *108*, 520–537.
2. K. Tanaka, K. Fukase, *Org. Biomol. Chem.* **2008**, *6*, 815–828.
3. M. D. Bartholoma, A. S. Louie, J. F. Valliant, J. Zubieta, *Chem. Rev.* **2010**, *110*, 2903–2920.

4. T. J. Wadas, E. H. Wong, G. R. Weisman, C. J. Anderson, *Chem. Rev.* **2010**, *110*, 2858–2902.

5. R. Alberto, in *Comprehensive Coordination Chemistry II*, Vol. 5, Eds. J. A. Mc Cleverty, T. S. Meer, Elsevier Science, Amsterdam, **2003**, pp. 127–271.

6. R. Alberto, in *Bioorganometallics*, Ed. G. Jaouen, Wiley-VCH, Weinheim, **2006**, pp. 97–124.

7. N. Lepareur, F. Lacoeuille, C. Bouvry, F. Hindre, E. Garcion, M. Cherel, N. Noiret, E. Garin, F. F. R. Knapp, Jr., *Front. Med.* **2019**, *6*. doi: 10.3389/fmed.2019.00132.

8. R. Alberto, in *Medicinal Organometallic Chemistry*, Vol. 32 of *Topics in Organometallic Chemistry*, Eds. G. Jaouen and N. Metzler-Nolte, Springer, Heidelberg, Dordrecht, London, New York, **2010**, pp. 219–246.

9. P. Blower, *Dalton Trans.* **2006**, 1705–1711.

10. P. S. Donnelly, *Dalton Trans.* **2011**, *40*, 999–1010.

11. S. R. Banerjee, K. P. Maresca, L. Francesconi, J. Valliant, J. W. Babich, J. Zubieta, *Nucl. Med. Biol.* **2005**, *32*, 1–20.

12. S. Jurgens, W. A. Herrmann, F. E. Kuhn, *J. Organomet. Chem.* **2014**, *751*, 83–89.

13. G. R. Morais, A. Paulo, I. Santos, *Organometallics* **2012**, *31*, 5693–5714.

14. M. Morais, A. Paulo, L. Gano, I. Santos, J. D. G. Correia, *J. Organomet. Chem.* **2013**, *744*, 125–139.

15. C. Bolzati, D. Carta, N. Salvarese, F. Refosco, *Anti-Cancer Agents Med. Chem.* **2012**, *12*, 428–461.

16. R. Alberto, H. Braband, M. Benz, M. Felber, S. Imstepf, *Nucl. Med. Biol.* **2014**, *41*, 613–613.

17. A. Louie, *Chem. Rev.* **2010**, *110*, 3146–3195.

18. S. Liu, *Chem. Soc. Rev.* **2004**, *33*, 445–461.

19. S. Bhattacharyya, M. Dixit, *Dalton Trans.* **2011**, *40*, 6112–6128.

20. J. R. Dilworth, S. I. Pascu, in *The Radiopharmaceutical Chemistry of Rhenium and Technetium*, Eds. N. Long, W.-T. Wong, John Wiley & Sons, Chichester, UK, **2015**, pp. 163–174.

21. S. Liu, S. Chakraborty, *Dalton Trans.* **2011**, *40*, 6077–6086.

22. A. Boschi, L. Uccelli, P. Martini, *Appl. Sci.* **2019**, *9,* 2526.

23. M. U. Akbar, M. R. Ahmad, A. Shaheen, S. Mushtaq, *J. Radioanal. Nucl. Chem.* **2016**, *310*, 477–493.

24. F. F. Knapp, A. L. Beets, S. Guhlke, P. O. Zamora, H. Bender, H. Palmedo, H. J. Biersack, *Anticancer Res.* **1997**, *17*, 1783–1795.

25. E. Boros, A. B. Packard, *Chem. Rev.* **2019**, *119*, 870–901.

26. G. S. Thomas, J. Maddahi, *J. Nucl. Cardiol.* **2010**, *17*, 993–998.

27. M. Mahesh, M. Madsen, *J. Am. Coll. Radiol.* **2017**, *14*, 681–683.

28. X. Hou, J. Tanguay, K. Buckley, P. Schaffer, F. Benard, T. J. Ruth, A. Celler, *Phys. Med. Biol.* **2016**, *61*, 542–553.

29. T. M. Martin, T. Harahsheh, B. Munoz, Z. Hamoui, R. Clanton, J. Douglas, P. Brown, G. Akabani, *J. Radioanal. Nucl. Chem.* **2017**, *314*, 1051–1062.

30. A. Tsechanski, A. F. Bielajew, J. P. Archambault, E. Mainegra-Hing, *Nucl. Instrum. Methods Phys. Res. Sect. B* **2016**, *366*, 124–139.

31. K. Buckley, P. Martini, M. Dodd, S. McDiarmid, V. Hanemaayer, B. Hook, J. Kumlin, S. Zeisler, P. Schaffer, C. Marshall, A. Dabkowski, M. Talboys, S. Wiltshire, F. Devillet, D. Blampain, B. Nactergal, *Eur. J. Nucl. Med. Mol. Imag.* **2017**, *44*, S275–S275.

32. P. Schaffer, K. Buckley, A. Celler, J. Klug, M. Kovacs, F. Prato, J. Valliant, S. Zeisler, T. Ruth, F. Benard, Annual Meeting of the Society of Nuclear Medicine and Molecular Imaging, Baltimore, 2015, *J. Nucl. Med.* **2015**, *56,* suppl. 3, Abstract 164.

33. B. Guerin, A. Zyuzin, E. J. van Lier, R. Lecomte, J. E. van Lier, *Eur. J. Nucl. Med. Mol. Imag.* **2010**, *37*, S251–S251.

34. N. M. Uzunov, L. Melendez-Alafort, M. Bello, G. Cicoria, F. Zagni, L. De Nardo, A. Selva, L. Mou, C. Rossi-Alvarez, G. Pupillo, G. Di Domenico, L. Uccelli, A. Boschi, F. Groppi, A. Salvini, A. Taibi, A. Duatti, P. Martini, M. Pasquali, M. Loriggiola, M. Marengo, L. Strada, S. Manenti, A. Rosato, J. Esposito, *Phys. Med. Biol.* **2018**, *63*, 185021.

35. P. Martini, A. Boschi, G. Cicoria, F. Zagni, A. Corazza, L. Uccelli, M. Pasquali, G. Pupillo, M. Marengo, M. Loriggiola, H. Skliarova, L. Mou, S. Cisternino, S. Carturan, L. Melendez-Alafort, N. M. Uzunov, M. Bello, C. R. Alvarez, J. Esposito, A. Duatti, *Appl. Rad. Isotopes* **2018**, *139*, 325–331.

36. M. L. Bonardi, F. Groppi, S. Manenti, E. Sabbioni, *Nucl. Med. Biol.* **2010**, *37*, 716–716.

37. X. C. Hou, J. Tanguay, F. Benard, K. Buckley, P. Schaffer, T. Ruth, A. Celler, Annual Meeting of the Society of Nuclear Medicine and Molecular Imaging, San Diego, 2016, *J. Nucl. Med.* **2016**, *57* suppl. 2, Abstract 1873.

38. X. Hou, J. Tanguay, M. Vuckovic, K. Buckley, P. Schaffer, F. Benard, T. J. Ruth, A. Celler, *Phys. Med. Biol.* **2016**, *61*, 8199–8213.

39. M. L. Bonardi, F. Groppi, S. Manenti, E. Persico, L. Gini, *Appl. Radiat. Isotopes* **2010**, *68*, 1595–1601.

40. F. Groppi, S. Manenti, L. Gini, M. L. Bonardi, *J. Radioanal. Nucl. Chem.* **2015**, *305*, 179–182.

41. D. Can, B. Spingler, P. Schmutz, F. Mendes, P. Raposinho, C. Fernandes, F. Carta, A. Innocenti, I. Santos, C. T. Supuran, R. Alberto, *Angew. Chem. Int. Ed.* **2012**, *51*, 3354–3357.

42. V. Akurathi, L. Dubois, N. G. Lieuwes, S. K. Chitneni, B. J. Cleynhens, D. Vullo, C. T. Supuran, A. M. Verbruggen, P. Lambin, G. M. Bormans, *Nucl. Med. Biol.* **2010**, *37*, 557–564.

43. C. C. Chen, L. E. Holder, W. A. Scovill, A. M. Tehan, D. S. Gann, *J. Nucl. Med.* **1997**, *38*, 834–839.

44. H. L. Jiang, T. R. DeGrado, *Theranostics* **2018**, *8*, 3918–3931.

45. H. Braband, Y. Tooyama, T. Fox, R. Alberto, *Chem. Eur. J.* **2009**, *15*, 633–638.

46. H. Braband, Y. Tooyama, T. Fox, R. Simms, J. Forbes, J. F. Valliant, R. Alberto, *Chem. Eur. J.* **2011**, *17*, 12967–12974.

47. H. Braband, M. Benz, Y. Tooyama, R. Alberto, *Chem. Commun.* **2014**, *50*, 4126–4129.

48. E. M. Hahn, A. Casini, F. E. Kuhn, *Coord. Chem. Rev.* **2014**, *276*, 97–111.

49. M. V. Cantorias, R. C. Howell, L. Todaro, J. E. Cyr, D. Berndorff, R. D. Rogers, L. C. Francesconi, *Inorg. Chem.* **2007**, *46*, 7326–7340.

50. E. Boros, B. V. Marquez, O. F. Ikotun, S. E. Lapi, C. L. Ferreira, *Coordination Chemistry and Ligand Design in the Development of Metal Based Radiopharmaceuticals*, in *Ligand Design in Medicinal Inorganic Chemistry*, Ed. T. Storr, Blackwell Science Publ., Oxford, UK, **2014**, pp. 47–79.

51. L. E. Jennings, N. J. Long, *Chem. Commun.* **2009**, 3511–3524.

52. S. R. Cherry, *Semin. Nucl. Med.* **2009**, *39*, 348–353.

53. M. P. Coogan, F. L. Thorp-Greenwood, *Dalton Trans.* **2011**, *40*, 6129–6143.

54. N. G. Blanco, M. Jauregui-Osoro, M. Cobaleda-Siles, C. R. Maldonado, M. Henriksen-Lacey, D. Padro, S. Clark, J. C. Mareque-Rivas, *Chem. Commun.* **2012**, *48*, 4211–4213.

55. M. Felber, R. Alberto, *Nanoscale* **2015**, *7*, 6653–6660.

56. J. Zhu, L. Zhao, J. Yang, L. Chen, J. Shi, J. Zhao, X. Shi, *Langmuir* **2019**, *35*, 13405–13412.

57. W. W. Lukens, S. A. Saslow, *Dalton Trans.* **2018**, *47*, 10229–10239.

58. K. P. Maresca, S. M. Hillier, F. J. Femia, C. N. Zimmerman, M. K. Levadala, S. R. Banerjee, J. Hicks, C. Sundararajan, J. Valliant, J. Zubieta, W. C. Eckelman, J. L. Joyal, J. W. Babich, *Bioconjugate Chem.* **2009**, *20*, 1625–1633.

59. K. A. Stephenson, S. R. Banerjee, T. Besanger, O. O. Sogbein, M. K. Levadala, N. McFarlane, J. A. Lemon, D. R. Boreham, K. P. Maresca, J. D. Brennan, J. W. Babich, J. Zubieta, J. F. Valliant, *J. Am. Chem. Soc.* **2004**, *126*, 8598–8599.

60. P. Schaffer, J. A. Gleave, J. A. Lemon, L. C. Reid, L. K. K. Pacey, T. H. Farncombe, D. R. Boreham, J. Zubieta, J. W. Babich, L. C. Doering, J. F. Valliant, *Nucl. Med. Biol.* **2008**, *35*, 159–169.

61. M. P. Coogan, R. P. Doyle, J. F. Valliant, J. W. Babich, J. Zubieta, *J. Labelled. Compd. Rad.* **2014**, *57*, 255–261.

62. C. Y. Xiong, K. Brewer, S. L. Song, R. Zhang, W. Lu, X. X. Wen, C. Li, *J. Med. Chem.* **2011**, *54*, 1825–1835.

63. W. L. Turnbull, L. Yu, E. Murrell, M. Milne, C. L. Charron, L. G. Luyt, *Org. Biomol. Chem.* **2019**, *17*, 598–608.

64. D. Eshima, J. Andrew Taylor, A. R. Fritzberg, S. Kasina, L. Hansen, J. F. Sorenson, *J. Nucl. Med.* **1987**, *28*, 1180–1186.

65. D. L. Nosco, R. G. Manning, A. Fritzberg, *J. Nucl. Med.* **1986**, *27*, 939–939.

66. G. Bandoli, A. Dolmella, M. Porchia, F. Refosco, F. Tisato, *Coord. Chem. Rev.* **2001**, *214*, 43–90.

67. D. L. Nosco, J. A. Beaty-Nosco, *Coord. Chem. Rev.* **1999**, *184*, 91–123.

68. S. Liu, D. S. Edwards, *Chem. Rev.* **1999**, *99*, 2235–2268.

69. J. R. Dilworth, S. J. Parrott, *Chem. Soc. Rev.* **1998**, *27*, 43–55.

70. U. Abram, R. Alberto, *J. Brazil. Chem. Soc.* **2006**, *17*, 1486–1500.

71. E. Deutsch, K. Libson, S. Jurisson, L. F. Lindoy, *Prog. Inorg. Chem.* **1983**, *30*, 75.

72. B. A. Nock, D. Charalambidis, W. Sallegger, B. Waser, R. Mansi, G. P. Nicolas, E. Ketani, A. Nikolopoulou, M. Fani, J.-C. Reubi, T. Maina, *J. Med. Chem.* **2018**, *61*, 3138–3150.

73. C. Rossetti, G. Vanoli, G. Paganelli, M. Kwiatkowski, F. Zito, F. Colombo, C. Bonino, A. Carpinelli, R. Casati, K. Deutsch, M. Marmion, S. R. Woulfe, F. Lunghi, E. Deutsch, F. Fazio, *J. Nucl. Med.* **1994**, *35*, 1571–1580.

74. J. R. Ballinger, T. Muzzammil, M. J. Moore, *J. Nucl. Med.* **1997**, *38*, 1915–1919.

75. J. E. Baumeister, K. M. Reinig, C. L. Barnes, S. P. Kelley, S. S. Jurisson, *Inorg. Chem.* **2018**, *57*, 12920–12933.

76. D. J. Hayne, J. M. White, C. A. McLean, V. L. Villemagne, K. J. Barnham, P. S. Donnelly, *Inorg. Chem.* **2016**, *55*, 7944–7953.

77. S. Agostini, C. Bolzati, E. Didone, M. Cavazza-Ceccato, F. Refosco, L. Aloj, C. Arra, M. Aurilio, A. L. Tornesello, D. Tesauro, G. Morelli, *J. Pept. Sci.* **2007**, *13*, 211–219.

78. R. Pasqualini, A. Duatti, *J. Chem. Soc., Chem. Commun.* **1992**, 1354–1355.

79. C. Bolzati, A. Boschi, A. Duatti, S. Prakash, L. Uccelli, *J. Am. Chem. Soc.* **2000**, *122*, 4510–4511.

80. K. Hatada, L. M. Riou, M. Ruiz, Y. Yamamichi, A. Duatti, R. L. Lima, A. R. Goode, D. D. Watson, G. A. Beller, D. K. Glover, *J. Nucl. Med.* **2004**, *45*, 2095–2101.

81. C. Bolzati, A. Mahmood, E. Malago, L. Uccelli, A. Boschi, A. G. Jones, F. Refosco, A. Duatti, F. Tisato, *Bioconjugate Chem.* **2003**, *14*, 1231–1242.

82. C. Bolzati, L. Uccelli, A. Boschi, S. Prakash, E. Malago, A. Duatti, A. Piffanelli, F. Refosco, F. Tisato, *J. Nucl. Med.* **2000**, *41*, 248p–248p.

83. N. Salvarese, D. Carta, C. Marzano, G. Gerardi, L. Melendez-Alafort, C. Bolzati, *J. Med. Chem.* **2018**, *61*, 11114–11126.

84. N. Salvarese, B. Spolaore, S. Marangoni, A. Pasin, A. Galenda, S. Tamburini, G. Cicoria, F. Refosco, C. Bolzati, *J. Inorg. Biochem.* **2018**, *183*, 18–31.

85. J. D. C. Gomez, A. Hagenbach, U. I. M. Gerling-Driessen, B. Koksch, N. Beindorff, W. Brenner, U. Abram, *Dalton Trans.* **2017**, *46*, 14602–14611.

86. P. I. D. Maia, H. H. Nguyen, A. Hagenbach, S. Bergemann, R. Gust, V. M. Deflon, U. Abram, *Dalton Trans.* **2013**, *42*, 5111–5121.

87. J. Schroer, U. Abram, *Polyhedron* **2011**, *30*, 2157–2161.

88. H. H. Nguyen, T. N. Trieu, U. Abram, *Z. Anorg. Allg. Chem.* **2011**, *637*, 1330–1333.

89. R. Alberto, R. Schibli, A. P. Schubiger, U. Abram, H. J. Pietzsch, B. Johannsen, *J. Am. Chem. Soc.* **1999**, *121*, 6076–6077.

90. R. Alberto, R. Schibli, R. Waibel, U. Abram, A. P. Schubiger, *Coord. Chem. Rev.* **1999**, *192*, 901–919.

91. R. Waibel, R. Alberto, J. Willuda, R. Finnern, R. Schibli, A. Stichelberger, A. Egli, U. Abram, J. P. Mach, A. Pluckthun, P. A. Schubiger, *Nat. Biotechnol.* **1999**, *17*, 897–901.

92. A. Orlova, C. Hofstrom, J. Strand, Z. Varasteh, M. Sandstrom, K. Andersson, V. Tolmachev, T. Graslund, *Eur. J. Nucl. Med. Mol. Imag.* **2013**, *40*, 439–449.

93. C. Hofstrom, M. Altai, H. Honarvar, J. Strand, J. Malmberg, S. J. Hosseinimehr, A. Orlova, T. Graslund, V. Tolmachev, *J. Med. Chem.* **2013**, *56*, 4966–4974.

94. A. Orlova, C. Hofstrom, J. Malmberg, S. Ahlgren, T. Graslund, V. Tolmachev, *Eur. J. Nucl. Med. Mol. Imag.* **2010**, *37*, S264–S265.

95. V. Tolmachev, C. Hofstrom, J. Malmberg, S. Ahlgren, S. J. Hosseinimehr, M. Sandstrom, L. Abrahmsen, A. Orlova, T. Graslund, *Bioconjugate Chem.* **2010**, *21*, 2013–2022.

96. R. Tavare, J. Williams, K. Howland, P. J. Blower, G. E. D. Mullen, *J. Inorg. Biochem.* **2012**, *114*, 24–27.

97. R. Tavare, R. T. M. De Rosales, P. J. Blower, G. E. D. Mullen, *Bioconjugate Chem.* **2009**, *20*, 2071–2081.

98. W. J. Chen, C. L. Yen, S. T. Lo, K. T. Chen, J. M. Lo, *Appl. Radiat. Isot.* **2008**, *66*, 340–345.

99. C. R. Dias, S. Jeger, J. A. Osso, C. Mueller, C. De Pasquale, A. Hohn, R. Waibel, R. Schibli, *Nucl. Med. Biol.* **2011**, *38*, 19–28.

100. U. Pandey, M. Kameswaran, H. D. Sarma, G. Samuel, *Appl. Radiat. Isotopes* **2014**, *86*, 52–56.

101. J. F. Tait, C. Smith, D. F. Gibson, *Bioconjugate Chem.* **2002**, *13*, 1119–1123.

102. M. L. Biechlin, A. Bonmartin, F. N. Gilly, M. Fraysse, A. D. d'Hardemare, *Nucl. Med. Biol.* **2008**, *35*, 679–687.

103. M. A. Teran, E. Martinez, A. L. Reyes, A. Paolino, M. Vital, P. Esperon, J. P. Pacheco, E. Savio, *Nucl. Med. Biol.* **2011**, *38*, 279–285.

104. V. R. Solomon, C. Gonzalez, E. Alizadeh, W. Bernhard, S. V. Hartimath, K. Barreto, C. R. Geyer, H. Fonge, *Eur. J. Med. Chem.* **2018**, *157*, 437–446.

105. Y. Hu, G. Liu, H. Zhang, Y. Li, B. D. Gray, K. Y. Pak, H. S. Choi, D. Cheng, H. Shi, *Mol. Imag. Biol.* **2018**, *20*, 249–259.

106. A. Badar, J. Williams, R. T. M. de Rosales, R. Tavare, F. Kampmeier, P. J. Blower, G. E. D. Mullen, *Eur. J. Nucl. Med. Mol. Imag. Res.* **2014**, *4*, 14.

107. C. Tausch, A. Baege, C. Rageth, *Oncotargets Ther.* **2014**, *7*, 1151–1158.

108. J. Kim, M. Ross, M. Faries, S. P. Leong, C. R. Scoggins, R. Orahood, *Ann. Surg. Oncol.* **2008**, *15*, 65–65.

109. D. R. Vera, A. M. Wallace, C. K. Hoh, R. F. Mattrey, *J. Nucl. Med.* **2001**, *42*, 951–959.

110. G. Makris, L. Radford, F. Gallazzi, S. Jurisson, H. Hennkens, D. Papagiannopoulou, *J Organomet. Chem.* **2016**, *805*, 100–107.

111. G. Makris, M. Kuchuk, F. Gallazzi, S. S. Jurisson, C. J. Smith, H. M. Hennkens, *Nucl. Med. Biol.* **2019**, *71*, 39–46.

112. L. L. Radford, D. Papagiannopoulou, F. Gallazzi, A. Berendzen, L. Watkinson, T. Carmack, M. R. Lewis, S. S. Jurisson, H. M. Hennkens, *Bioorg. Med. Chem.* **2019**, *27*, 492–501.

113. T. L. Mindt, H. Struthers, L. Brans, T. Anguelov, C. Schweinsberg, V. Maes, D. Tourwe, R. Schibli, *J. Am. Chem. Soc.* **2006**, *128*, 15096–15097.

114. H. Struthers, T. L. Mindt, R. Schibli, *Dalton Trans.* **2010**, *39*, 675–696.

115. H. Struthers, B. Spingler, T. L. Mindt, R. Schibli, *Chem. Eur. J.* **2008**, *14*, 6173–6183.

116. J. A. Thomas, A. Davison, *Inorg. Chem.* **1992**, *31*, 1976–1978.

117. H. J. Banbery, W. Hussain, I. G. Evans, T. A. Hamor, C. J. Jones, J. A. Mccleverty, H. J. Schulte, B. Engles, W. Kläui, *Polyhedron* **1990**, *9*, 2549–2551.

118. H. Braband, U. Abram, *Inorg. Chem.* **2006**, *45*, 6589–6591.

119. Y. Tooyama, H. Braband, B. Spingler, U. Abram, R. Alberto, *Inorg. Chem.* **2008**, *47*, 257–264.

120. H. Braband, M. Benz, R. Alberto, *Nucl. Med. Biol.* **2014**, *41*, 613–613.

121. H. Braband, M. Benz, R. Alberto, *J. Biol. Inorg. Chem.* **2014**, *19*, S762–S762.

122. M. J. Abrams, A. Davison, A. G. Jones, C. E. Costello, H. Pang, *Inorg. Chem.* **1983**, *22*, 2798–2800.

123. A. G. Jones, M. J. Abrams, A. Davison, J. W. Brodack, A. K. Toothaker, S. J. Adelstein, A. I. Kassis, *Int. J. Nucl. Med. Biol.* **1984**, *11*, 225–234.

124. J. D. Kelly, A. M. Forster, B. Higley, C. M. Archer, F. S. Booker, L. R. Canning, K. W. Chiu, B. Edwards, H. K. Gill, M. Mcpartlin, K. R. Nagle, I. A. Latham, R. D. Pickett, A. E. Storey, P. M. Webbon, *J. Nucl. Med.* **1993**, *34*, 222–227.

125. B. F. Bernard, E. P. Krenning, W. A. P. Breeman, G. Ensing, H. Benjamins, W. H. Bakker, T. J. Visser, M. de Jong, *Nucl. Med. Biol.* **1998**, *25*, 233–240.

126. L. R. Goethals, I. Santos, V. Caveliers, A. Paulo, F. De Geeter, P. G. Lurdes, C. Fernandes, T. Lahoutte, *Contrast Media Mol. Imag.* **2011**, *6*, 178–188.

127. C. Moura, F. Mendes, L. Gano, I. Santos, A. Paulo, *J. Inorg. Biochem.* **2013**, *123*, 34–45.

128. F. Mendes, L. Gano, C. Fernandes, A. Paulo, I. Santos, *Nucl. Med. Biol.* **2012**, *39*, 207–213.

129. M. Huisman, J. P. Kodanko, K. Arora, M. Herroon, M. Alnaed, J. Endicott, I. Podgorski, J. J. Kodanko, *Inorg. Chem.* **2018**, *57*, 7881–7891.

130. X. J. Duan, Q. Ruan, Q. Q. Gan, X. Q. Song, S. Fang, X. R. Zhang, J. B. Zhang, *J Organomet. Chem.* **2018**, *868*, 154–163.

131. X. J. Duan, X. R. Zhang, Q. Q. Gan, S. A. Fang, Q. Ruan, X. Q. Song, J. B. Zhang, *MedChemComm* **2018**, *9*, 705–712.

132. R. S. Israeli, C. T. Powell, W. R. Fair, W. D. W. Heston, *Cancer Res.* **1993**, *53*, 227–230.

133. S. R. Banerjee, M. Pullambhatla, Y. Byun, S. Nimmagadda, G. Green, J. J. Fox, A. Horti, R. C. Mease, M. G. Pomper, *J. Med. Chem.* **2010**, *53*, 5333–5341.

134. M. Schafer, U. Bauder-Wust, K. Leotta, F. Zoller, W. Mier, U. Haberkorn, M. Eisenhut, M. Eder, *EJNNMI Res.* **2012**, *2*.

135. S. M. Hillier, K. P. Maresca, F. J. Femia, J. C. Marquis, C. A. Foss, N. Nguyen, C. N. Zimmerman, J. A. Barrett, W. C. Eckelman, M. G. Pomper, J. L. Joyal, J. W. Babich, *Cancer Res.* **2009**, *69*, 6932–6940.

136. S. M. Hillier, K. P. Maresca, G. L. Lu, R. D. Merkin, J. C. Marquis, C. N. Zimmerman, W. C. Eckelman, J. L. Joyal, J. W. Babich, *J. Nucl. Med.* **2013**, *54*, 1369–1376.

137. G. L. Lu, K. P. Maresca, S. M. Hillier, C. N. Zimmerman, W. C. Eckelman, J. L. Joyal, J. W. Babich, *Bioorg. Med. Chem. Lett.* **2013**, *23*, 1557–1563.

138. S. Vallabhajosula, B. Polack, Y. S. Jhanwar, A. Nikolopoulou, T. Armor, S. T. Tagawa, D. Scherr, B. Robinson, S. J. Goldsmith, J. W. Babich, *Eur. J. Nucl. Med. Mol. Imag.* **2014**, *41*, S236–S236.

139. S. Vallabhajosula, A. Nikolopoulou, J. W. Babich, J. R. Osborne, S. T. Tagawa, I. Lipai, L. Solnes, K. P. Maresca, T. Armor, J. L. Joyal, R. Crummet, J. B. Stubbs, S. J. Goldsmith, *J. Nucl. Med.* **2014**, *55*, 1791–1798.

140. C. Schmidkonz, C. Hollweg, M. Beck, J. Reinfelder, T. I. Goetz, J. C. Sanders, D. Schmidt, O. Prante, T. Bauerle, A. Cavallaro, M. Uder, B. Wullich, P. Goebell, T. Kuwert, P. Ritt, *Prostate* **2018**, *78*, 54–63.

141. J. Reinfelder, T. Kuwert, M. Beck, J. C. Sanders, P. Ritt, C. Schmidkonz, P. Hennig, O. Prante, M. Uder, B. Wullich, P. Goebell, *Clin. Nucl. Med.* **2017**, *42*, 26–33.

142. C. Schmidkonz, M. Cordes, M. Beck, T. Goetz, D. Schmidt, O. Prante, T. Bauerle, M. Uder, B. Wullich, P. Goebell, T. Kuwert, P. Ritt, *J. Nucl. Med.* **2018**, *59*.

143. T. Maurer, S. Robu, M. Schottelius, K. Schwamborn, I. Rauscher, N. S. van den Bereg, F. W. B. van Leeuwen, B. Haller, T. Horn, M. M. Heck, J. E. Gschwend, M. Schwaiger, H.-J. Wester, M. Eibere, *Eur. Urol.* **2019**, *75*, 659–666.

144. S. Ponnala, A. Amor-Coarasa, J. Kelly, N. Zia, W. Clarence, A. Nikolopoulou, P. Donnelly, J. Babich, *J. Nucl. Med.* **2019**, *60*.

145. J. C. dos Santos, B. Beijer, U. Bauder-Wust, M. Schafer, K. Leotta, M. Eder, M. Benesova, C. Kleist, F. Giesel, C. Kratochwil, K. Kopka, U. Haberkorn, W. Mier, *J. Nucl. Med.* **2020**, *61*, 70–79.

146. J. M. Kelly, A. Amor-Coarasa, A. Nikolopoulou, D. Kim, C. Williams, S. Vallabhajosula, J. W. Babich, *Nucl. Med. Biol.* **2017**, *55*, 38–46.

147. G. R. Morais, A. Paulo, I. Santos, *Eur. J. Org. Chem.* **2012**, 1279–1293.

148. S. Jurisson, E. O. Schlemper, D. E. Troutner, L. R. Canning, D. P. Nowotnik, R. D. Neirinckx, *Inorg. Chem.* **1986**, *25*, 543–549.

149. T. Sasaki, Y. Fujibayashi, M. Senda, *J. Nucl. Med.* **1998**, *39*, 2178–2183.

150. Y. P. Yang, M. C. Cui, *Eur. J. Med. Chem.* **2014**, *87*, 703–721.

151. D. J. Hayne, S. Lim, P. S. Donnelly, *Chem. Soc. Rev.* **2014**, *43*, 6701–6715.

152. J. L. Hickey, P. S. Donnelly, *Coord. Chem. Rev.* **2012**, *256*, 2367–2380.

153. M. Sagnou, B. Mavroidi, A. Shegani, M. Paravatou-Petsotas, C. Raptopoulou, V. Psycharis, I. Pirmettis, M. S. Papadopoulos, M. Pelecanou, *J. Med. Chem.* **2019**, *62*, 2638–2650.

154. M. Sagnou, S. Tzanopoulou, C. P. Raptopoulou, V. Psycharis, H. Braband, R. Alberto, I. C. Pirmettis, M. Papadopoulos, M. Pelecanou, *Eur. J. Inorg. Chem.* **2012**, 4279–4286.

155. S. P. Fletcher, A. Noor, J. L. Hickey, C. A. McLean, J. M. White, P. S. Donnelly, *J. Biol. Inorg. Chem.* **2018**, *23*, 1139–1151.

156. M. Benz, H. Braband, R. Alberto, *J. Biol. Inorg. Chem.* **2014**, *19*, S797–S797.

157. M. Benz, H. Braband, R. Alberto, *Nucl. Med. Biol.* **2014**, *41*, 615–615.

158. C. Y. Chan, P. A. Pellegrini, I. Greguric, P. J. Barnard, *Inorg. Chem.* **2014**, *53*, 10862–10873.

159. K. Oukoloff, M. Cieslikiewicz-Bouet, S. Chao, E. D. Bran-quinho, C. Bouteiller, L. Jean, P. Y. Renard, *Curr. Med. Chem.* **2015**, *22*, 3278–3304.

160. E. Deutsch, K. Libson, J. L. Vanderheyden, A. R. Ketring, H. R. Maxon, *Nucl. Med. Biol.* **1986**, *13*, 465–477.

161. S. H. Park, S. Seifert, H. J. Pietzsch, *Bioconjugate Chem.* **2006**, *17*, 223–225.

162. K. Smilkov, E. Janevik, R. Guerrini, M. Pasquali, A. Boschi, L. Uccelli, G. Di Domenico, A. Duatti, *Appl. Radiat. Isot.* **2014**, *92*, 25–31.

163. S. Imstepf, V. Pierroz, R. Rubbiani, M. Felber, T. Fox, G. Gasser, R. Alberto, *Angew. Chem. Int. Ed.* **2016**, *55*, 2792–2795.

164. S. Imstepf, V. Pierroz, P. Raposinho, M. Bauwens, M. Felber, T. Fox, A. B. Shapiro, R. Freudenberg, C. Fernandes, S. Gama, G. Gasser, F. Motthagy, I. R. Santos, R. Alberto, *Bioconjugate Chem.* **2015**, *26*, 2397–2407.

165. J. J. Darrow, J. Avorn, A. S. Kesselheim, *J. Am. Med. Assoc.* **2020**, *323*, 164–176.

166. R. Bolliger, A. Frei, H. Braband, G. Meola, B. Spingler, R. Alberto, *Chem. Eur. J.* **2019**, *25*, 7101–7104.
167. S. S. Kelkar, T. M. Reineke, *Bioconjugate Chem.* **2011**, *22*, 1879–1903.
168. M. Varani, F. Galli, S. Auletta, A. Signore, *Clin. Transl. Imaging* **2018**, *6*, 271–292.
169. N. Drude, L. Tienken, F. M. Mottaghy, *Methods* **2017**, *130*, 14–22.
170. F. M. Mottaghy, *Methods* **2017**, *130*, 1–3.
171. M. Felber, M. Bauwens, J. M. Mateos, S. Imstepf, F. M. Mottaghy, R. Alberto, *Chem. Eur. J.* **2015**, *21*, 6090–6099.
172. J. K. Bordoloi, D. Berry, I. U. Khan, K. Sunassee, R. T. M. de Rosales, C. Shanahan, P. J. Blower, *Dalton Trans.* **2015**, *44*, 4963–4975.
173. W. S. El-Deiry, C. C. Sigman, G. J. Kelloff, *J. Clin. Oncol.* **2006**, *24*, 3261–3273.
174. M. Patra, M. Wenzel, P. Prochnow, V. Pierroz, G. Gasser, J. E. Bandow, N. Metzler-Nolte, *Chem. Sci.* **2015**, *6*, 214–224.
175. A. Leonidova, G. Gasser, *ACS Chem. Biol.* **2014**, *9*, 2180–2193.
176. G. Gasser, N. Metzler-Nolte, *Curr. Opin. Chem. Biol.* **2012**, *16*, 84–91.
177. G. Gasser, I. Ott, N. Metzler-Nolte, *J. Med. Chem.* **2011**, *54*, 3–25.
178. K. M. Knopf, B. L. Murphy, S. N. MacMillan, J. M. Baskin, M. P. Barr, E. Boros, J. J. Wilson, *J. Am. Chem. Soc.* **2017**, *139*, 14302–14314.
179. B. L. Murphy, S. C. Marker, V. J. Lambert, J. J. Woods, S. N. MacMillan, J. J. Wilson, *J Organomet. Chem.* **2020**, *907*.
180. C. C. Konkankit, A. P. King, K. M. Knopf, T. L. Southard, J. J. Wilson, *ACS Med. Chem. Lett.* **2019**, *10*, 822–827.
181. A. P. King, S. C. Marker, R. V. Swanda, J. J. Woods, S. B. Qian, J. J. Wilson, *Chem. Eur. J.* **2019**, *25*, 9206–9210.
182. M. Munoz-Osses, D. Siegmund, A. Gomez, F. Godoy, A. Fierro, L. Llanos, D. Aravena, N. Metzler-Nolte, *Dalton Trans.* **2018**, *47*, 13861–13869.
183. C. C. Konkankit, S. C. Marker, K. M. Knopf, J. J. Wilson, *Dalton Trans.* **2018**, *47*, 9934–9974.
184. J. Yang, J. X. Zhao, Q. Cao, L. Hao, D. X. Zhou, Z. J. Gan, L. N. Ji, Z. W. Mao, *ACS Appl. Mater. Interfaces* **2017**, *9*, 13900–13912.
185. I. Kitanovic, S. Z. Can, H. Alborzinia, A. Kitanovic, V. Pierroz, A. Leonidova, A. Pinto, B. Spingler, S. Ferrari, R. Molteni, A. Steffen, N. Metzler-Nolte, S. Wolfl, G. Gasser, *Chem. Eur. J.* **2014**, *20*, 2496–2507.
186. L. Quental, P. Raposinho, F. Mendes, I. Santos, C. Navarro-Ranninger, A. Alvarez-Valdes, H. Y. Huang, H. Chao, R. Rubbiani, G. Gasser, A. G. Quiroga, A. Paulo, *Dalton Trans.* **2017**, *46*, 14523–14536.
187. G. Jaouen, A. Vessieres, S. Top, *Chem. Soc. Rev.* **2015**, *44*, 8802–8817.
188. E. Hillard, A. Vessieres, L. Thouin, G. Jaouen, C. Amatore, *Angew. Chem. Int. Ed.* **2006**, *45*, 285–290.
189. S. Top, B. Dauer, J. Vaissermann, G. Jaouen, *J. Organomet. Chem.* **1997**, *541*, 355–361.
190. M. Patra, G. Gasser, M. Wenzel, K. Merz, J. E. Bandow, N. Metzler-Nolte, *Organometallics* **2010**, *29*, 4312–4319.
191. M. Navarro, W. Castro, C. Biot, *Organometallics* **2012**, *31*, 5715–5727.
192. E. A. Hillard, G. Jaouen, *Organometallics* **2011**, *30*, 20–27.
193. D. R. van Staveren, N. Metzler-Nolte, *Chem. Rev.* **2004**, *104*, 5931–5985.
194. M. Patra, G. Gasser, *Nat. Rev. Chem.* **2017**, *1*, 0066.
195. F. Minutolo, J. A. Katzenellenbogen, *J. Am. Chem. Soc.* **1998**, *120*, 4514–4515.
196. T. W. Spradau, J. A. Katzenellenbogen, *Bioconjugate Chem.* **1998**, *9*, 765–772.
197. T. W. Spradau, W. B. Edwards, C. J. Anderson, M. J. Welch, J. A. Katzenellenbogen, *Nucl. Med. Biol.* **1999**, *26*, 1–7.
198. L. Mei, T. W. Chu, *Progress in Chemistry* **2011**, *23*, 1493–1500.

199. B. C. Lee, D. H. Kim, I. Lee, Y. S. Choe, D. Y. Chi, K. H. Lee, Y. Choi, B. T. Kim, *J. Med. Chem.* **2008**, *51*, 3630–3634.

200. C. L. Ferreira, C. B. Ewart, S. R. Bayly, B. O. Patrick, J. Steele, M. J. Adam, C. Orvig, *Inorg. Chem.* **2006**, *45*, 6979–6987.

201. M. Saidi, S. Seifert, M. Kretzschmar, R. Bergmann, H. J. Pietzsch, *J. Organomet. Chem.* **2004**, *689*, 4739–4744.

202. S. Top, S. Masi, G. Jaouen, *Eur. J. Inorg. Chem.* **2002**, 1848–1853.

203. J. Wald, R. Alberto, K. Ortner, L. Candreia, *Angew. Chem. Int. Ed.* **2001**, *40*, 3062–3066.

204. J. Bernard, K. Ortner, B. Spingler, H. J. Pietzsch, R. Alberto, *Inorg. Chem.* **2003**, *42*, 1014–1022.

205. Y. Liu, B. Spingler, P. Schmutz, R. Alberto, *J. Am. Chem. Soc.* **2008**, *130*, 1554–1556.

206. H. W. P. N'Dongo, P. D. Raposinho, C. Fernandes, I. Santos, D. Can, P. Schmutz, B. Spingler, R. Alberto, *Nucl. Med. Biol.* **2010**, *37*, 255–264.

207. Q. Nadeem, Y. J. Shen, M. F. Warsi, G. Nasar, M. A. Qadir, R. Alberto, *J. Labelled Compd. Rad.* **2017**, *60*, 394–400.

208. A. Frei, B. Spingler, R. Alberto, *Chem. Eur. J.* **2018**, *24*, 10156–10164.

209. G. Pampaloni, *Coord. Chem. Rev.* **2010**, *254*, 402–419.

210. M. Benz, H. Braband, P. Schmutz, J. Halter, R. Alberto, *Chem. Sci.* **2015**, *6*, 165–169.

211. Q. Nadeem, G. Meola, H. Braband, R. Bolliger, O. Blacque, D. Hernandez-Valdes, R. Alberto, *Angew. Chem. Int. Ed.* **2020**, *59*, 1197–1200.

212. D. Hernandez-Valdes, G. Meola, H. Braband, B. Spingler, R. Alberto, *Organometallics* **2018**, *37*, 2910–2916.

213. G. Meola, H. Braband, S. Jordi, T. Fox, O. Blacque, B. Spingler, R. Alberto, *Dalton Trans.* **2017**, *46*, 14631–14637.

214. G. Meola, H. Braband, P. Schmutz, M. Benz, B. Spingler, R. Alberto, *Inorg. Chem.* **2016**, *55*, 11131–11139.

215. A. Frei, P. P. Mokolokolo, R. Bolliger, H. Braband, M. S. Tsosane, A. Brink, A. Roodt, R. Alberto, *Chem. Eur. J.* **2018**, *24*, 10397–10402.

216. B. P. Burke, W. Grantham, M. J. Burke, G. S. Nichol, D. Roberts, I. Renard, R. Hargreaves, C. Cawthorne, S. J. Archibald, P. J. Lusby, *J. Am. Chem. Soc.* **2018**, *140*, 16877–16881.

217. M. Hatanaka, Y. Himeda, I. Ueda, *J. Chem. Soc., Perkin Trans. 1* **1993**, 2269–2274.

218. A. Frei, E. Fischer, B. C. Childs, J. P. Holland, R. Alberto, *Dalton Trans.* **2019**, *48*, 14600–14605.

8

Paramagnetic Metal Ion Probes for ^{19}F Magnetic Resonance Imaging

Petr Hermann,[1] *Jan Blahut,*[2] *Jan Kotek,*[1] *and Vít Herynek*[3]

[1]Department of Inorganic Chemistry, Faculty of Science, Charles University (Univerzita Karlova), Hlavova 2030, CZ-128 43 Prague 2, Czech Republic
<petr.hermann@natur.cuni.cz>

[2]NMR Laboratory, Faculty of Science, Charles University (Univerzita Karlova), Hlavova 2030, CZ-128 43 Prague 2, Czech Republic

[3]First Faculty of Medicine, Center for Advanced Preclinical Imaging, Charles University (Univerzita Karlova), Salmovská 3, CZ-120 00 Prague 2, Czech Republic

Abstract: "Classical" magnetic resonance imaging (MRI) is based on imaging of water protons and the technique is commonly used in clinical and preclinical practice. The ^{19}F nuclide has nuclear magnetic properties similar to those of ^{1}H and can be used for MRI on common commercial scanners with only minor modifications. The ^{19}F MRI is a potentially interesting tool for preclinical or even clinical imaging. As there is no abundance of ^{19}F in a living body, ^{19}F MRI requires contrast agents (CAs) containing fluorine atoms and is presented as "hot-spot" imaging. In this text, we present how the current development of ^{19}F MRI CAs is influenced by utilization of paramagnetic metal ions as relaxation agents through shortening the long ^{19}F relaxation times. The theory behind the change of relaxation times is briefly introduced. Influence of lanthanide(III) and transition metal ions on the relaxation properties of the ^{19}F nucleus in defined molecules and in nanoobjects is reviewed and differences between complexes of these two metal ion families are discussed. The ^{19}F tracers are best utilized as responsive MRI CAs and various responsive modes of the probes are reviewed and evaluated. As ^{19}F MRI requires some special consideration about acquisition techniques, the main differences between ^{1}H and ^{19}F MRI are discussed. Briefly, some outlook for the technique is suggested.

Keywords: ^{19}F MRI · cell labelling · fluorine-containing ligand · fluorine NMR · relaxation time enhancement · responsive probes

1. INTRODUCTION

Magnetic resonance imaging (MRI) is commonly used for clinical and preclinical imaging. Besides ^{1}H, other nuclei may be also used for MRI or MR spectroscopy (MRS), e.g., ^{13}C, ^{23}Na or ^{31}P [1], although their concentration and sensitivity are substantially lower compared to those of ^{1}H. Utilization of fluorine (^{19}F) for MRI/MRS is quite specific. Its concentration in living organisms is negligible and potential use of fluorine in imaging therefore requires a suitable fluorinated tracer (often termed as a contrast agent, CA) [2]. A fluorine MR image thus provides a distribution of the tracer in the space with zero background, usually presented as a "hot-spot" imaging, and requires co-localization with an anatomical ^{1}H MR image [3]. Fluorine is a naturally monoisotopic element, and ^{19}F and ^{1}H nuclei have comparable gyromagnetic ratios, $\gamma(^{19}\text{F}) = 251.8 \cdot 10^{6}$ versus $\gamma(^{1}\text{H}) = 267.5 \cdot 10^{6}$ rad s^{-1} T^{-1}, leading to very similar Larmor frequencies. Standard preclinical or clinical commercial MR scanners can thus be used for ^{19}F detection with minor hardware and software changes only, and their frequency range usually covers the frequency of ^{19}F including whole transmit and receive paths. The only special piece of hardware, which is necessary, is a dedicated ^{19}F radio frequency coil.

The main issue of ^{19}F MRI/MRS is sensitivity. Most of current applications require molecular ^{19}F probes in at least mM concentrations at the site of interest. There are two main routes towards sensitivity improvement. The first approach

is an increase of the number of equivalent fluorine atoms in the probe itself and/or enhancement of a local concentration of ^{19}F nuclei (e.g., by targeting). The second way is the reduction of long ^{19}F relaxation times to optimal values which enable faster acquisitions and accumulation of more spectra within a given time. The relaxation times are most conveniently altered by introduction of a paramagnetic metal ion in the vicinity of ^{19}F nuclei as it leads to so-called paramagnetic relaxation enhancement (PRE) [4, 5]. Ideally, both approaches should be combined to reach detection limits as low as possible.

The high number of fluorine atoms is most easily attained by utilization of soft nanoparticles (micelles) containing polyfluorous organic molecules. A paramagnetic complex can be bound on the surface of the nanoparticles or dissolved in their fluorous core (Section 3.2). Alternatively, paramagnetic metal ions can be complexed in discrete ligand molecules containing a maximized amount of ^{19}F nuclei (Section 3.1).

2. PARAMAGNETICALLY INDUCED RELAXATION OF THE ^{19}F NUCLEUS

For application in MRI, two relaxation rates R_{iK}, ($i = 1, 2$) and associated relaxation times $T_{iK} = 1/R_{iK}$ are typically distinguished for the nucleus K (in this context ^{19}F). The longitudinal relaxation time (T_1) is associated with a build-up of equilibrium magnetization aligned with an external magnetic field, while the transversal relaxation time (T_2) corresponds to the decrease of spin-coherence generated by radio frequency pulses, due to non-coherent processes. A paramagnetic center in a CA can increase the relaxation rates up to four orders of magnitude. Thus, the diamagnetic contribution can usually be neglected. In solution, the ^{19}F NMR signal linewidth (LW) is dominantly determined by the paramagnetic T_2. Therefore, the so-called T_2^* time obtained as $T_2^* = 1/(\pi \cdot \text{LW})$ is a reasonable and easily accessible estimation of T_2.

Nuclear relaxation induced by a paramagnetic center can proceed by several mechanisms. The contribution of each one is proportional to the strength of the metal ion-nucleus interaction and to the accessibility of random fluctuations at frequency ω [equal to the electron (ω_S) or nuclear (ω_K) Larmor frequencies, or their combinations]. This accessibility is characterized by a spectral density function J given by Equation (1) where τ_λ is the general correlation time of the fluctuation.

$$J(\omega, \tau_\lambda) = \frac{\tau_\lambda}{1 + \tau_\lambda^2 \omega^2} \tag{1}$$

The spectral density J reaches a maximum for $\tau_\lambda \approx 1/\omega$. Therefore, the maximal longitudinal relaxation enhancement is reached if the electron or nuclear Larmor frequency is matched with fluctuations in the system. Unfortunately, the undesired transversal relaxation is also sensitive to fluctuation at zero frequency [$\omega = 0$, therefore, $J(\omega, \tau_\lambda) = \tau_\lambda$]. Then, the R_{2K} increases even for $\tau_\lambda \gg 1/\omega$ and is

always faster than or equal to the R_{1K} relaxation rate and, therefore, the T_2/T_1 ratio may never exceed unity. The fluctuations of an interaction between the paramagnetic center and the observed nuclei may have three different sources:

Chemical exchange (exchange time, τ_M) is the fluctuation of the mutual distance between the metal ion and the measured nucleus due to chemical processes (e.g., solvent molecule exchange or isomerism). This modulation is of a large importance for "classical" Gd^{3+}-based ^1H MRI CAs (see Chapter 2) but it can be neglected for molecular ^{19}F MRI CAs without profound internal dynamics.

Molecular rotation (rotational correlation time, τ_R) is connected with a change of the mutual metal-nucleus orientation with respect to the external magnetic field caused by molecular motion/tumbling. In a simplified description (free rotation of a spherical CA molecule), τ_R can be estimated by the Stokes-Einstein equation, $\tau_R = \eta \cdot M/(\varrho \cdot N_A \cdot k_B \cdot T)$, where M is the molar mass, N_A and k_B are Avogadro and Boltzmann constants, respectively, and η and ϱ are solvent viscosity and density, respectively. In aqueous solutions, values for τ_R range from $3 \cdot 10^{-11}$ s for hexaaqua metal ion complexes to 10^{-6} s for large macromolecules ($M \approx 10^6 \, g \, mol^{-1}$).

Electron relaxation (electron correlation time, τ_e). In a magnetic field, the electron spin rapidly flips between different M_S states inducing further fluctuations in paramagnetic systems (for a detailed description see [6]). A note: Application of this description is fairly limited as more general approaches do not introduce τ_e at all [7]. The electron relaxation process is generally multi-exponential for electron spin $S > \frac{1}{2}$; however, it is usually approximated by a single correlation time, τ_e. The value of the electron relaxation time differs significantly between various metal ions and depends on the temperature, magnetic-field (in some cases), and also on coordination geometry (especially for d-elements). A list of the values can be found in [8].

The nuclear relaxation rates, R_{iK} ($i = 1, 2$), can be mediated by three different interactions. (*i*) By direct delocalization of unpaired electron density to the position of observed nuclei K (so-called *contact mechanism*) characterized by the hyperfine coupling constant A_K, or (*ii*) by through-space interaction between unpaired electron density and the nuclear dipole (*dipole-dipole mechanism*). In the following discussion, we approximate electron magnetic dipole moments as point-dipole on the position of the metal ion [6]. In a strong magnetic field, (*iii*) the third mechanism arises through dipole-dipole interaction between observed nuclei and the time-averaged electron dipole moment induced by a difference in populations of the electronic M_s levels in the magnetic field (*Curie mechanism*). The equations for longitudinal (R_1) and transversal (R_2) relaxations rates can be derived [9] as follows in Equations (2)–(7):

$$R_{1K}^{con} = \frac{2}{3} \left(\frac{A_K}{\hbar} \right)^2 S(S+1) \frac{\tau_{c,con}}{1 + \omega_S^2 \tau_{c,con}^2} \tag{2}$$

$$R_{2K}^{con} = \frac{1}{3} \left(\frac{A_K}{\hbar} \right)^2 S(S+1) \left(\tau_{c,con} + \frac{\tau_{c,con}}{1 + \omega_S^2 \tau_{c,con}^2} \right) \tag{3}$$

$$R_{1K}^{\mathrm{DD}} = \frac{2}{15} \left(\frac{\mu_0}{4\pi}\right)^2 \frac{\gamma_K^2 g_e^2 \mu_B^2 S(S+1)}{r_K^6} \left(\frac{7\tau_{\mathrm{c,DD}}}{1 + \omega_S^2 \tau_{\mathrm{c,DD}}^2} + \frac{3\tau_{\mathrm{c,DD}}}{1 + \omega_K^2 \tau_{\mathrm{c,DD}}^2}\right) \quad (4)$$

$$R_{2K}^{\mathrm{DD}} = \frac{1}{15} \left(\frac{\mu_0}{4\pi}\right)^2 \frac{\gamma_K^2 g_e^2 \mu_B^2 S(S+1)}{r_K^6} \left(4\tau_{\mathrm{c,DD}} + \frac{13\tau_{\mathrm{c,DD}}}{1 + \omega_S^2 \tau_{\mathrm{c,DD}}^2} + \frac{3\tau_{\mathrm{c,DD}}}{1 + \omega_K^2 \tau_{\mathrm{c,DD}}^2}\right)$$

$$(5)$$

$$R_{1K}^{\mathrm{Cur}} = \frac{2}{5} \left(\frac{\mu_0}{4\pi}\right)^2 \frac{\omega_K^2 g_e^4 \mu_B^4 S^2 (S+1)^2}{(3k_B T)^2 r_K^6} \left(\frac{3\tau_{\mathrm{c,Cur}}}{1 + \omega_K^2 \tau_{\mathrm{c,Cur}}^2}\right) \quad (6)$$

$$R_{2K}^{\mathrm{Cur}} = \frac{1}{5} \left(\frac{\mu_0}{4\pi}\right)^2 \frac{\omega_K^2 g_e^4 \mu_B^4 S^2 (S+1)^2}{(3k_B T)^2 r_K^6} \left(4\tau_{\mathrm{c,Cur}} + \frac{3\tau_{\mathrm{c,Cur}}}{1 + \omega_K^2 \tau_{\mathrm{c,Cur}}^2}\right) \quad (7)$$

where μ_0 is the vacuum magnetic permeability; γ_K is the gyromagnetic ratio of the observed nuclei; g_e is the free electron g-value which can be replaced by the effective g-value, g_J, for metal ions with a strong spin-orbit coupling (e.g., Ln^{3+}); μ_B is the Bohr magneton; S is the spin quantum number (replaced by the J quantum number for Ln^{3+} ions); k_B is the Boltzmann constant; T is the thermodynamic temperature; A_K is the hyperfine coupling constant and r_K is the distance between the metal ion and the observed nucleus. Different types of fluctuations affect the above mentioned relaxation mechanisms. In the contact mechanism, electron distribution on the position of the observed nuclei is not altered by molecular tumbling and, therefore, only the electron relaxation and the chemical exchange determine the contact correlation time, $\tau_{\mathrm{c,con}} = (\tau_M^{-1} + \tau_e^{-1})^{-1}$. For the dipole-dipole relaxation mechanism, all processes may play a role and the correlation time equals to $\tau_{\mathrm{c,DD}} = (\tau_R^{-1} + \tau_M^{-1} + \tau_e^{-1})^{-1}$. Typically, the electron relaxation time τ_e controls the time $\tau_{\mathrm{c,DD}}$ but, for small (rapidly tumbling) complexes of metal ions with a slow electron relaxation (Gd^{3+}, Mn^{2+}, Fe^{3+}, or sometimes Cu^{2+}), rotation tumbling (τ_R) dominates. The Curie mechanism is not affected by the electron relaxation time and, thus, $\tau_{\mathrm{c,Cur}} = (\tau_R^{-1} + \tau_M^{-1})^{-1}$. There is no chemical exchange for molecular ^{19}F MRI CAs and, therefore, τ_M can be neglected in all cases.

Instead of a comprehensive discussion of various parameter effects on relaxation rates, which can be found in many publications [6, 9], we have decided to illustrate the applications of Equations (2)–(7) on several practically important examples (Figure 1).

Lanthanide(III) ions. The Ln^{3+} ions were the first choice for the paramagnetic relaxation enhancement (PRE). The electron magnetic dipole moment μ_{eff} (associated with the J quantum number due to the significant spin-orbit coupling) varies significantly within the Ln^{3+} series and therefore, relaxation properties can be tuned by a proper choice of the metal ion. For the small molecules, both
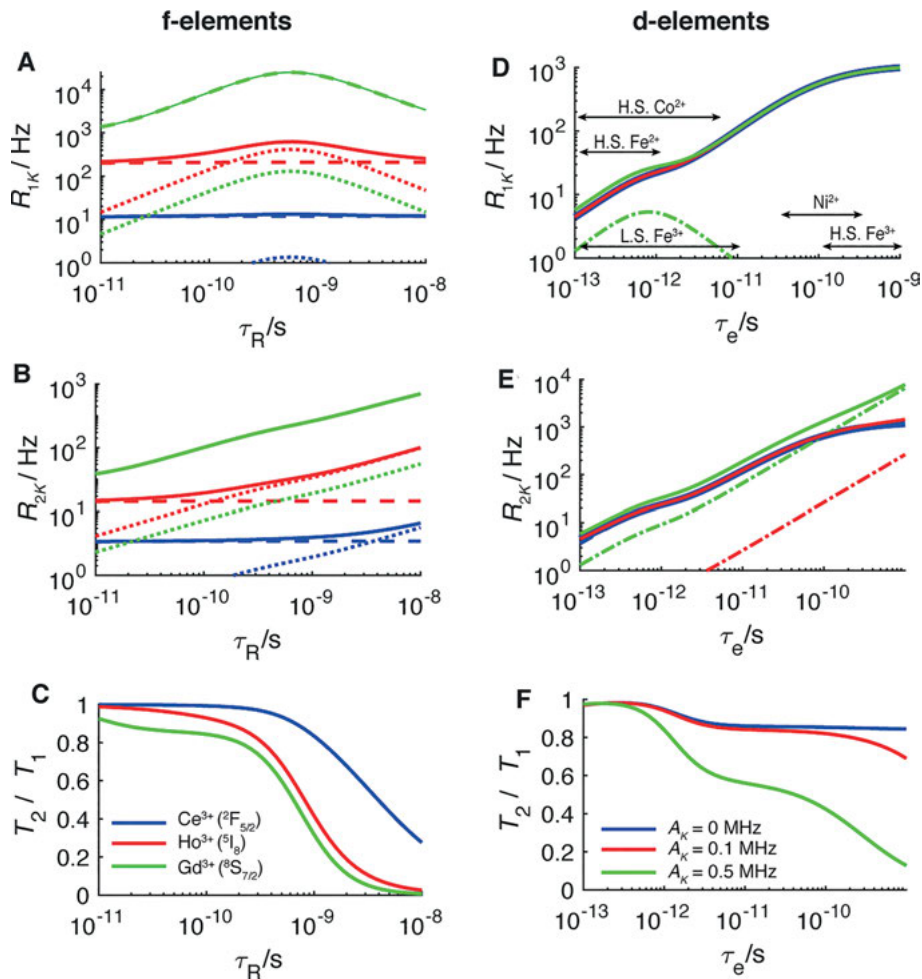
Figure 1. Simulated longitudinal (**A**, **D**) and transversal (**B**, **E**) ^{19}F nuclear relaxation rates and CA efficiency represented by the T_2/T_1 ratio (**C**, **F**) for Ln^{3+} (**A–C**) and TM ions (**D–F**). The data were simulated for a distance between the metal ion and the ^{19}F nucleus of 5 Å, an external magnetic field of 7 T, and at 298 K in dependence on the rotation correlation time τ_R for Ln^{3+} ions (**A–C**) and on the electron correlation time τ_e for transition metal ions (**D–F**). The full lines indicate overall paramagnetically induced relaxation, while the dashed, dot-dashed and dotted lines correspond to dipole-dipole, contact, and Curie relaxations, respectively. Simulation of the lanthanide-induced relaxation (**A–C**) was performed without contact interaction, using the electron relaxation time $\tau_e = 4 \cdot 10^{-13}$ for Ce^{3+} (blue, $J = 5/2$) and Ho^{3+} (red, $J = 8$), and $\tau_e = 5 \cdot 10^{-8}$ s for Gd^{3+} (green, $J = 7/2$) [6]. In simulation of the d-metal-induced relaxation ($S = 1$ was used for simulation in all cases), a medium rotation correlation time $\tau_R = 10^{-10}$ s was fixed to analyze the contribution of the contact mechanism (dot-dashed lines) for different hyperfine coupling constants $A_K = 0$, 0.1, and 0.5 MHz (blue, red and green lines, respectively). Arrows in **D** indicate usual values of τ_e for octahedral complexes of selected ions. An extensive list of the electron correlation times can be found in [8].

R_1 and R_2 are dominated by the dipole-dipole mechanism. For all Ln^{3+} (except Gd^{3+}), the electron relaxation is extremely fast ($\approx 10^{-13}$ s), much faster than the rotational tumbling ($\tau_e \ll \tau_R$) and, therefore, the relaxation induced by dipole-dipole mechanism is independent of the size of the molecule (Figure 1A and 1B). However, the Curie relaxation contributes significantly to relaxation in CAs with slower rotational tumbling (i.e., for larger molecules). The Curie relaxation is generally more important for transversal relaxation and, therefore, decreases the T_2/T_1 ratio (Figure 1C). For Ln^{3+} ions with high J (e.g., Ho^{3+} or Dy^{3+}), a significant decrease of the CA efficiency may be observed even for medium-sized molecules ($M \approx 500$ g mol^{-1}). For Gd^{3+}, the situation is complicated by its extremely slow electron relaxation ($\approx 10^{-9}$ s) which, in addition, changes with the external magnetic field making the correct theoretical description fairly complicated [7]. In the very simplified frame of Equations (2)–(7), we can state that T_1 and T_2 in ^{19}F MRI CAs based on Gd^{3+} are purely dominated by the dipole-dipole relaxation which depends on the rotation tumbling, in contrary to other Ln^{3+} ions. For medium-sized molecules, the transversal relaxation rate is already unfeasibly fast for nuclei close to Gd^{3+}. For more distant nuclei, a reasonably good signal with acceptable T_2/T_1 ratio can be obtained for molecules with $\tau_R < 1/\omega_{19F}$; but for molecules with slower rotational tumbling ($\tau_R \gg 1/\omega_{19F}$), T_2/T_1 decreases rapidly.

Transition metal (TM) ions. For d-element-based ^{19}F MRI CAs, the situation is more complicated. On the one hand, the Curie relaxation mechanism is typically negligible due to the small effective magnetic dipole moment μ_{eff} of TM ions. On the other hand, the contact contribution can be significant as the unpaired electron density occupies valence d-orbitals involved in covalent metal–ligand bonds providing the strong hyperfine coupling (e.g., $A_K = -0.3$ MHz for ^{19}F in the N–CH_2CF_3 group bound to the cyclam ring in a high-spin (HS) Co^{2+} complex) [10]. The electron relaxation is typically slower for TM ions than for Ln^{3+} (except Gd^{3+}) and varies significantly among TM ions (Figure 1D–F). The slowest electron relaxation (roughly 10^{-8}) was reported for a HS half-occupied d^5 configuration (e.g., HS-Mn^{2+} or HS-Fe^{3+}), whereas it is much faster for ions with other electron configurations. In systems with slow electron relaxation, the contact mechanism significantly increases R_2 due to the zero-frequency fluctuations (the first term in Equation (3)). T_1 is typically not affected by the contact relaxation mechanism. Significant delocalization of the unpaired electrons of the metal ion (with the slow electron relaxation) towards the observed nucleus may therefore result in a substantial drop-down of the T_2/T_1 ratio.

3. METAL COMPLEXES AS RELAXATION CONTRAST AGENTS

3.1. Fluorine-Containing Metal Complexes

Besides suitable relaxation properties introduced above, the metallic complexes considered as probes for ^{19}F MRI/MRS have to fulfill some "practical" require-

ments. They should contain as many as possible chemically and magnetically identical fluorine atoms in the ligand or the conjugate structure. It must be balanced to keep their solubility in (miscibility with) water. Thus, hydrophobicity of groups such as $-CF_3$ has to be offset by charged and/or hydrophilic groups. The complexes must be non-toxic as relatively high doses are applied, i.e., their high *in vivo* stability must be ensured by a high thermodynamic stability and, mainly, high kinetic inertness (it implies use of pre-organized macrocyclic ligands). Not all complexes studied till now have been endowed with all features listed above as they have been used in proof-of-principle studies which have helped to understand principles behind the ^{19}F MRI/MRS probes.

Throughout the following text, charges of complex species are omitted for sake of clarity.

3.1.1. *Lanthanide(III) Complexes*

The Ln^{3+} ions require coordination numbers (CN) eight or nine and the best chelators are polydentate ligands derived from macrocyclic DOTA (structures of ligands discussed throughout this chapter are shown in Figures 2 and 3) where ring amines (N_4-plane) and four pendant arm oxygen atoms (O_4-plane) are bound to the central Ln^{3+} ion. A coordinated water molecule may cap the O_4-plane and it transfers Gd^{3+}-induced relaxation to the bulk water protons in the Gd^{3+}-based MRI CAs (Chapter 2). The Ln^{3+}–ligand binding is mostly ionic as Ln^{3+} inner-shell f-electrons do not participate in metal–ligand bonding. Therefore, Ln^{3+} ions influence ^{19}F NMR parameters mainly through dipolar ("through space") interaction and bond topology could be mostly neglected. The Ln^{3+} complexes of DOTA-like ligands can occur as diastereoisomers originating from mutual arrangements of the macrocycle and pendant chelate rings (Chapter 2). These diastereoisomers (occurring as pairs of enantiomers), termed as square-antiprismatic (SA) and twisted square-antiprismatic (TSA), are in solution in a slow exchange on the NMR timescale and they are manifested by two sets of signals for NMR-active nuclei of the ligands. The number of NMR signals can be multiplied if any other "asymmetry" (e.g., another chirality center or *cis-trans* rotamers on the amide bond) is introduced. The isomerism issue is illustrated, e.g., on Tb(**L1a**) and Tb(**L2a**) complexes where the major ^{19}F peaks have 50 and 87 % of overall signal intensity, respectively [11]. For ^{19}F MRI CA, the isomerism should be suppressed as much as possible by ligand design and choice of the metal ion.

The paramagnetic Ln^{3+} ions alter both chemical shift and relaxation of the ligand NMR-active nuclei (Section 2). The changes are commonly related to properties of diamagnetic "standards" as the free ligand or complexes of diamagnetic ions, Y^{3+}, La^{3+} or Lu^{3+}. The δ_F is governed mainly by magnetic properties of Ln^{3+} and mutual Ln^{3+} and ^{19}F spatial arrangement (i.e., by the $Ln\cdots F$ distance and the direction of the Ln-F vector). Similarly, variations in the ^{19}F relaxation times are mainly given by the magnetic properties of Ln^{3+}, the $Ln\cdots F$ distance, the external magnetic field (B_0), and also by an overall tumbling of the complex (or more precisely, tumbling of the Ln-F vector; τ_R). Chemical shifts are highly
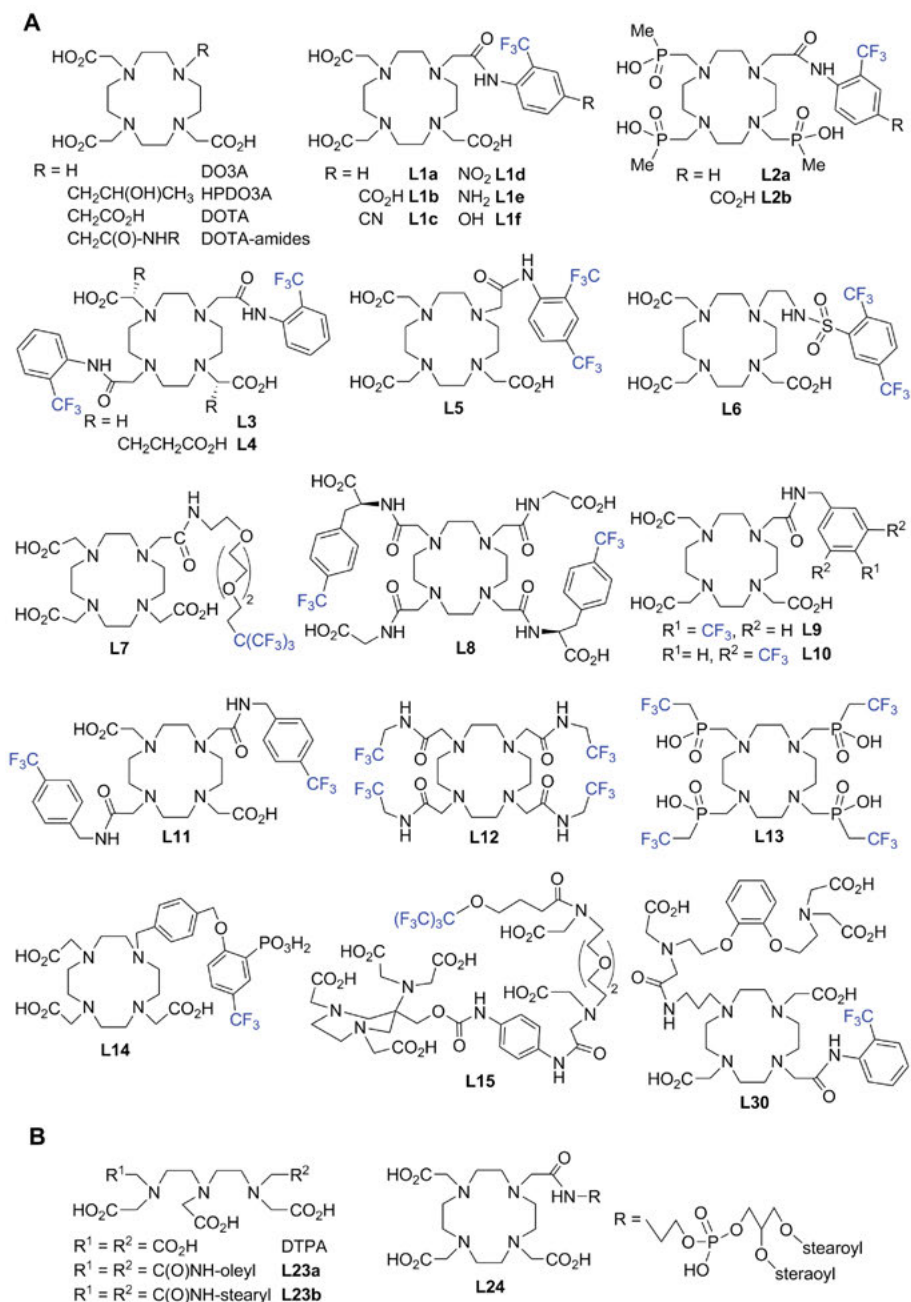
Figure 2. Structures of ligands for Ln^{3+} ions in molecular complexes (**A**) and used for non-covalent interactions (**B**). Fluorine-containing groups detected in ^{19}F MRI/MRS are in blue.

influenced by the magnetic anisotropy of the Ln^{3+} ion caused by the ligand field, and also relaxations are somewhat affected [12]. With appropriate (fast) MRI acquisition sequences (Section 4), the ^{19}F MRI sensitivity gain reachable with paramagnetics is mainly given by the values of T_1 (the pulse sequence should be optimal for the particular T_1) and T_2 (it should be as long as possible), the T_2/T_1 ratio (as close as possible to 1), and the number of magnetically equivalent ^{19}F nuclei (as high as possible). As stated above (Section 2), easily accessible T_2^* are usually used in such evaluations. The NMR-related properties of ^{19}F nuclei are altered according to the magnetic/relaxation properties of each Ln^{3+} ion and the structures of the complexes. Selected data are listed in Table 1.

The first work on Ln-based ^{19}F MRI CAs [13] clearly showed that Ln^{3+} ions can significantly decrease ^{19}F relaxation times with a reasonably good T_2^*/T_1 ratio, and that relaxation times are tunable. In these early works, Ln^{3+} complexes of ligands containing phenyl-CF_3 group(s) attached onto the DOTA skeleton through amide bond(s) (e.g., ligands **L1**–**L5**) and the related DO3A-aminoethyl-sulfonamide **L6** were investigated [4, 11, 13, 14]. These complexes can be used to explain how the structure of ligands and the metal ions change the relaxation of ^{19}F. In the research, Y^{3+} complexes used as diamagnetic standards had T_1 relaxation times comparable to those of common diamagnetic organic molecules (0.3–1.5 s).

The metal ion-to-fluorine (M···F) distance r_{MF} is a very important parameter as it influences the relaxations with a coefficient r_{MF}^{-6} (Section 2). The Ln···F influence on the relaxation times (and on δ_F) was illustrated, e.g., by a comparison of data for complexes of ligands **L5** and **L6** with *ortho*- and *para*-CF_3, or *ortho*- and *meta*-CF_3 groups, respectively [13]. Paramagnetically-induced changes of δ_F and ^{19}F T_1 were systematically larger for the o-CF_3 than for the more distant m/p-CF_3. Analogously, T_1 of ^{19}F nuclei for a given Ln^{3+} complex were reduced in the order Ln(**L1b**) > Ln(**L2a**) > Ln(**L1f**) and it corresponds to a gradually shorter Ln···F distance in the complexes [14]. Investigations of this wide family of complexes (ligands **L1**–**L5**) led to the conclusion that optimal Ln···F distances (for a given Ln^{3+} ion and B_0) should be in a range of 5.7–6.3 Å [14] and $r_{LnF} < \approx 5.5$ Å would lead to too short relaxation times (and too broad NMR signals). It should be noticed that the Ln···F distances could be calculated from relaxation data obtained at several magnetic fields (Equations (4)–(7), Section 2) and they agreed with those obtained by density functional theory (DFT) calculations [14, 15].

As T_1 and T_2 change with magnetic field strength in different ways (at higher fields, the Curie contribution is more important for T_2 than for T_1; Section 2), optimal T_2/T_1 ratio and optimal Ln···F distance are changed with B_0. It was suggested that, with a suitable Ln···F distance, $Tb^{3+}/Ho^{3+}/Dy^{3+}$ complexes and Er^{3+}/Tm^{3+} complexes should be suitable for lower ($B_0 < 4.7$ T) or higher ($B_0 > 7$ T) magnetic fields, respectively [14]. Substitution of carboxylate pendant arms in **L1a** for phosphinate ones led to ligand **L2a**. The Ln···F distances in Ln(**L2a**) are about 0.3 Å shorter than those in Ln(**L1a**) [11]. It led to a larger reduction of T_1 for Ln(**L2a**) versus Ln(**L1a**), but T_2^*/T_1 was still up to 0.74–0.84 (Table 1).

Tumbling of the Ln-F vector, another parameter important for the design of ^{19}F MRI CAs, can be approximated by tumbling of the whole complex character-

Table 1. [19]F chemical shifts (δ_F) and relaxation times (T_1 and T_2 or T_2^*, at 9.4 T) of Ln^{3+} complexes of selected fluorine-containing ligands (see Figure 2).

Ligand	Ln^{3+}	δ_F (ppm)	T_1 (ms)	T_2 or T_2^* (ms)	T_2/T_2^*-to-T_1 ratio	Refs.
L1a	Tb	−51.9	8.6	8.4	0.98	[11]
	Dy	−64.9	7.2	4.6	0.63	
	Ho	−64.2	9.2	6.6	0.72	
	Er	−64.8	15.4	6.4	0.41	
	Tm	−77.4	19.6	11.0	0.56	
L1d	Tb	−52.5	7.5	4.8	0.64	[15]
	Dy	−66.7	6.2	2.8	0.45	
	Ho	−57.9	8.1	5.2	0.65	
	Tm	−78.1	21.3	11.2	0.53	
L2a	Tb	−47.7	6.8	3.8	0.55	[11]
	Dy	−63.6	5.4	4.0	0.74	
	Ho	−61.5	8.3	7.0	0.84	
	Er	−72.6	9.2	7.3	0.79	
	Tm	−89.5	15.9	11.9	0.75	
L9	Eu	−61.6	769.2	95.2	0.12	[21, 22]
	Gd	−61.3	2.8	2.5	0.89	
	Tb	−67.1	69.0	14.5	0.21	
	Tm	−58.5	135.1	30.2	0.22	
	Yb	−60.1	476.2	28.2	0.06	
L10	Eu	−62.2	769.2	126.6	0.16	[21, 22]
	Gd	−62.5	0.9	0.7	0.82	
	Tb	−74.7	22.8	11.3	0.50	
	Tm	−53.9	44.4	21.3	0.48	
	Yb	−58.7	256	32.1	0.13	
L12[a]	Eu	−72.4	360	41	0.11	[23]
	Gd	−72.0	12	0.14	0.01	
	Tb	−54.1	6.3	1.3	0.21	
	Dy	−52.4	5.9	2.2	0.37	
	Ho	−61.8	7.6	5.4	0.71	
	Er	−76.5	14	8.8	0.63	
	Tm	−83.3	26	16	0.62	
	Yb	−75.9	130	55	0.42	
L13[b]	Ce	−56.8	287	124.4	0.43	[24]
	Dy	−45.0	6.9	3.9	0.57	
	Ho	−51.9	9.8	8.2	0.84	
	Tm	−65.0	6.5	4.9	0.75	
	Yb	−59.0	76	72.1	0.95	

[a] B_0 = 7 T.
[b] B_0 = 4.7 T.

ized by τ_R. For complexes of this ligand family, their τ_R was determined to be in a range of 200–350 ps [4, 14, 15]. To increase the number of identical fluorine atoms, the small complex units can be conjugated onto a polymer backbone; however, macromolecules usually present a slower molecular tumbling, i.e., longer τ_R. As the T_2/T_1 ratio significantly decreases at $\tau_R \gg 1/\omega_S$ (Section 2) there is a trade-off between a higher number of ^{19}F nuclei and the T_2/T_1 ratio. In addition, the $T_{1,2}$ also depend on μ_{eff} of the particular metal ion and this influence is also B_0-dependent. A result of the interplay of these parameters is that a larger number of fluorine atoms introduced through increasing the size of the whole molecule (connected with slower molecular tumbling) might not necessarily improve the sensitivity of ^{19}F MRI probes as τ_R has to be optimized as well with respect to the external B_0 and to the magnetic moment of Ln^{3+} ion. This was shown on conjugates of the **L1b/L2b** complexes with chitosan or the PAMAM dendrimer [4, 16]. Therefore, large molecules, e.g., polymers, should be considered for paramagnetic ^{19}F MRI CAs with care and this approach is more appropriate for diamagnetic organic molecules with long ^{19}F relaxation times.

With these complexes, the sensitivity of the measurements (expressed as signal-to-noise ratio, SNR) could be significantly increased (and thus overall acquisition time decreased) down to sub-millimolar probe concentrations if suitable acquisition sequences are applied (Section 4) [4, 17, 18].

Over the time, complexes of other ligands have been investigated. The sensitivity gain due to more fluorine atoms was proven with the perfluoro-*t*-butyl group (nine identical ^{19}F) bound onto the DOTA-monoamide chelator unit through a flexible tri-PEG chain, **L7** [19]. Change of the parameters (versus the diamagnetic standard) was small for the light Ln^{3+} ions. The more significant changes were observed for Gd^{3+} and heavy Ln^{3+} ion (Tb^{3+}–Er^{3+}) complexes, with T_1 and T_2^*/T_1 ratio (at 9.4 T) for, e.g., Gd^{3+} and Tb^{3+} complexes: 4.23 ms and 0.39, and 72.6 ms and 0.57, respectively. Values of ^{19}F T_1 and T_2^*/T_1 ratio (at 7 T) of the complexes of the DOTA derivative **L8** with two $-CF_3$ groups, 714 ms and 0.078 (Eu^{3+}), 5.5 ms and 0.47 (Gd^{3+}), and 31 ms and 0.68 (Tb^{3+}), were similar to the values for the other complexes presented in Table 1 [20]. However, the complexes were present in solution as a mixture of isomers and it led to a "dilution" of the equivalent ^{19}F nuclei. Data obtained for complexes of DOTA-amides with one or two (p-CF_3)-benzylamino group(s) (**L9** or **L11**, respectively) [21, 22], or one (m-CF_3)$_2$-benzylamino group (**L10**) [21, 22] conforms with the other values in Table 1. Thus, the Gd^{3+} ion accelerated the relaxation much more than all the other ions, but with the best T_2^*/T_1 ratio, and the **L9** and **L11** complexes exhibited slower relaxations than those for the **L10** complexes due to the shorter distance (DFT calculations) of the m-CF_3 group from Ln^{3+} ($Ln \cdots F$ 7.4 Å) versus p-CF_3 ($Ln \cdots F$ 9.1 Å). The ^{19}F MRI phantom studies of the **L10** complexes revealed that the Tb^{3+} complex was the best [22] with a detection limit of 5 mM (SNR $\approx$40, 7 T, 10 min). Similar results were obtained for the Gd^{3+} complexes with other pulse sequence [21].

The DOTA-tetraamide **L12** contains twelve identical ^{19}F nuclei and only one isomer was observed for its complexes (i.e., single ^{19}F NMR signal) [23]. The NMR parameters of the complexes and their trends are similar to the other

ones (Table 1). The average Ln···F distance of ≈6.26 Å for the Tm(**L12**) complex estimated from the relaxation data agreed with those from DFT calculations and X-ray diffraction. Heavy Ln^{3+} ions suitably shortened the ^{19}F relaxation times. However, the T_2*/T_1 ratio was significantly decreased in rat blood due to a more significant reduction of T_2* versus T_1 because of a longer τ_R of the complexes in blood comparing to that in pure water. The Tm(**L12**) complex in rat blood was detectable at 0.5 mM (SNR 2.3, 9.4 T).

Another chelator with twelve chemically identical ^{19}F nuclei is the ligand **L13** [24]. Its Ln^{3+} complexes formed preferentially one diastereoisomer in solution (90–95 %). The relaxation times cannot be fully compared with those in Table 1 because of a lower B_0. A detection limit was 0.625–1.25 mM (SNR 2–4, 4.7 T, ≈15 min) but a better performance could not be assessed as ultra-fast sequences were not available on the used scanner. These probes were well detectable after their injection into rat muscle and were fully stable *in vitro* (no decomposition in rat plasma, 37 °C, 10 days).

Most of the complexes of several DO3A derivatives with short linkers terminated by one –CF_3 on benzene ring displayed several ^{19}F NMR resonances due to the presence of isomers except the complexes of **L14** [25]. Relaxation data for Ln(**L14**) complexes correspond to those of other complexes in Table 1. In phantoms, the Gd^{3+} complex was detectable even at 0.1 mM (7 T, 60 min). Another moiety used for Ln^{3+} complexation is the triaza-cycloheptane-based AAZTA skeleton in ligand **L15** [26]. Its Dy^{3+} complex exhibited T_1 and T_2* relaxation times of 157 and 17 ms, respectively, clearly influenced by PRE compared to its Y^{3+} complex (T_1 and T_2 1320 and 543 ms, respectively). However, the relaxation time reductions are smaller than those for systems discussed above due to a relatively long Ln···F distance.

Except complexes of the phosphorus acid DOTA analogues (**L2** and **L13**), Gd^{3+} complexes of the above discussed ligands directly bind a water molecule and can also serve as "classical" ^{1}H MRI CAs. They can be suggested as bimodal ^{19}F/^{1}H MRI probes and, in some cases, this has been explicitly considered [20, 21, 23, 25]. In addition, the Ln^{3+}–DOTA-amide complexes can exhibit a ^{1}H paraCEST (paramagnetic chemical exchange saturation transfer, Chapter 4) effect and some of them were suggested as dual ^{19}F MRI-^{1}H paraCEST agents [20, 22].

3.1.2. Transition Metal Complexes

Unlike Ln^{3+} complexes, investigations of TM ion complexes as MRI CAs have started only recently [27, 28]. The complexes offer wider structural variability than complexes of Ln^{3+} ions although the most expected coordination sphere is an octahedron. The TM ion d-electrons participate in covalent interactions more than inner f-electrons of Ln^{3+} ions. The electronic structure of the TM ions is significantly influenced by the ligand field. The ^{19}F relaxation times are influenced by TM ions similarly as by Ln^{3+} ions – they depend on the TM···^{19}F distance and on the ^{19}F nuclei spatial location, on the magnetic properties of the TM ion, on the external magnetic field, and on the rotational correlation time

τ_R of the TM-F vector. However, there are some important specific differences. The dipolar ("through space") relaxation contribution is significant, similarly to Ln^{3+} ions. Yet, for TM ions, the contact ("through bonds") relaxation contribution becomes also highly important due to the more covalent character of TM ion–ligand bonds (if compared with the Ln^{3+}–ligand bond character) and, thus, the TM ion spin density is more delocalized over the ligand atoms. The contact contribution must be considered at least up to a "distance" of 4–5 bonds between the TM ion and the ligand nucleus. In TM ion complexes, d-orbital energies and electronic structure are more dependent on the exact structure of the species (i.e., on the symmetry and strength of the ligand field determined by the ligand structure) than for Ln^{3+} complexes (Section 2). Till now, only the first-row TM ions have been considered as NMR relaxation agents and, therefore, spin multiplicity (i.e., high-spin (HS-) and low-spin (LS-) electron arrangements) has to be taken into account. The significant differences between Ln^{3+} and TM ions make applications of the TM ions as shift/relaxation agents in NMR/MRI more challenging and variable. The TM ions considered as ^{19}F MRI CAs have included HS-Fe^{2+}, HS-Co^{2+} and Ni^{2+} as well as HS-Mn^{2+} and HS-Fe^{3+}, the symmetric HS-d^5 arrangement and relaxation properties of which are similar to the f^7 state of Gd^{3+}. Complexes of LS-Fe^{2+}, LS-Co^{3+} or Zn^{2+} are commonly used as diamagnetic standards. Unlike with complexes of Ln^{3+} ions, the problem with isomers of the complexes mutually interconverting on the NMR timescale has not been observed for TM ions. A redox switch between diamagnetic/less paramagnetic and (highly) paramagnetic states of TM ion pairs as Cu^{2+}/Cu^{+}, Co^{3+}/Co^{2+}, Fe^{3+}/Fe^{2+} or Mn^{3+}/Mn^{2+} induced by external stimuli has been employed in responsive probes (Section 3.3.5). Similarly, spin cross-over from "highly paramagnetic" to "less paramagnetic" (or even diamagnetic) state was also employed in responsive probes (Section 3.3). Structures of additional ligands in TM ion complexes suggested as ^{19}F MRI CAs are shown in Figure 3 and selected relaxation data are outlined in Table 2.

Cyclam derivatives **L16** form stable complexes with Ni^{2+} ion octahedrally co-ordinated by all ligand donor atoms [29, 30]. Although complexes of cyclam derivatives can exist in several isomeric forms, only one centrosymmetric isomer with *trans* coordination of the pendant arms was found for all Ni(**L16**) complexes giving a single ^{19}F NMR resonance. The relaxation enhancement was substantial for all complexes leading to somewhat suboptimal values of the relaxation times (Table 2) but still accessible by ultra-fast imaging sequences. Average Ni···F distances 5.2–5.3 Å were estimated from X-ray diffraction. With an appropriate acquisition procedure, the detection limit for Ni(**L16a**) was 0.93 mM (SNR 2, 11.8 T, 10 min) [30]. The complexes were highly kinetically inert and suitable for *in vivo* applications [29, 30]. The Ni^{2+} complexes of the cross-bridged cyclam derivatives **L17a,b** with one (p-CF_3)- or bis(m-CF_3)-benzylamide group(s) exhibited optimal relaxation times for most fields and very good T_2^*/T_1 ratios (Table 2) [31]. Slower relaxation is partially caused by a long Ni···F distance 8.7 and 7.3 Å for Ni(**L17a**) and Ni(**L17b**), respectively, calculated from relaxation data at several magnetic fields and agreeing with those estimated from X-ray data.

The DOTA-tetraamide chelating unit is combined with two perfluoro-*t*-butyl fragments and a glucose molecule (to increase water solubility) in **L18** [32]. Its
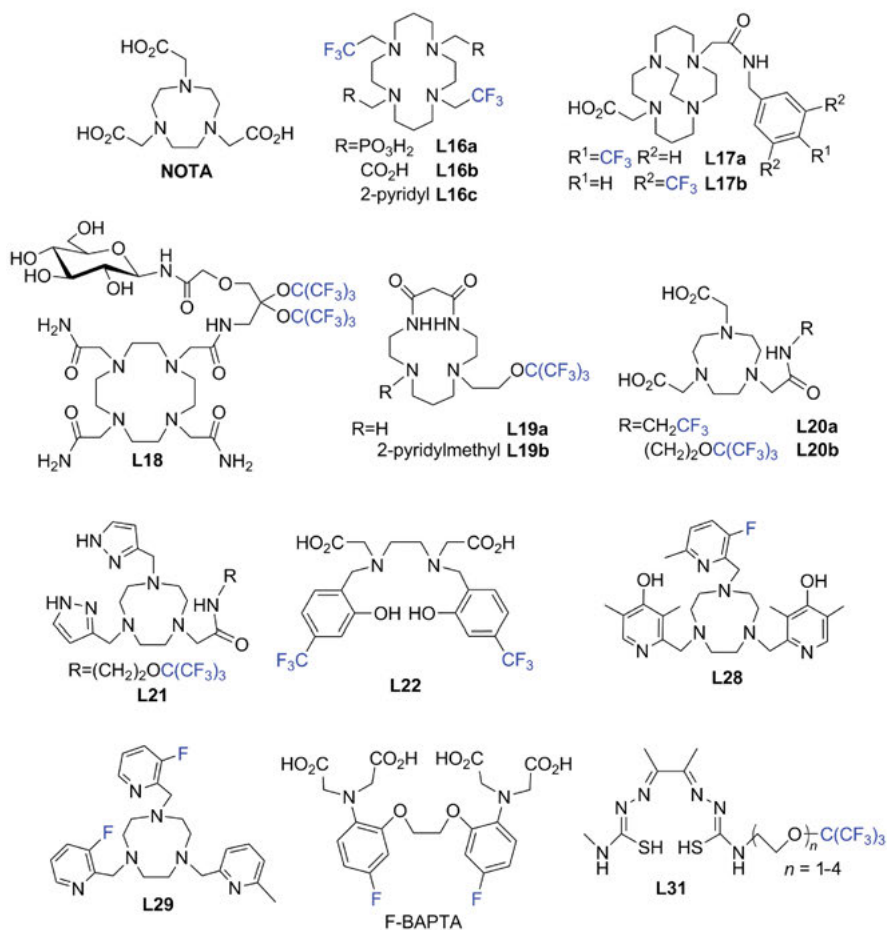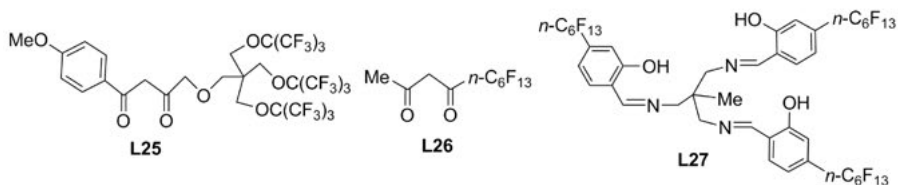
Figure 3. Structures of additional ligands for TM ions in molecular complexes (**A**) and used for non-covalent interactions (**B**). Fluorine-containing groups detected in ¹⁹F MRI/MRS are in blue.

Table 2. ^{19}F chemical shifts (δ_F) and relaxation times (T_1 and T_2 or T_2^*, at 9.4 T) of TM ion complexes of selected fluorine-containing ligands (see Figures 2 and 3).

Ligand	Metal ion	δ_F (ppm)	T_1 (ms)	T_2 or T_2^* (ms)	T_2/T_2^*-to-T_1 ratio	Ref.
L12	HS-Fe^{2+}	−70.1	5.7	5.6	0.98	[23, 36]
L16a[a]	Ni^{2+}	−26.0	2.8	0.90	0.32	[29, 30]
	HS-Co^{2+}	−25.4	12.3	9.6	0.78	
	LS-Co^{3+}	−59.2 (dia)	600	360	0.60	
L16b[a]	Ni^{2+}	−21.9	2.0	1.03	0.52	[30]
	HS-Co^{2+}	−23.0	16.1	11.0	0.68	
	LS-Co^{3+}	−59.4 (dia)	660	540	0.82	
L16c[a]	Ni^{2+}	−19.6	1.8	0.76	0.42	[30]
L17a[a]	Ni^{2+}	−59.7	29.3	24.5	0.84	[31]
L17b[a]	Ni^{2+}	−59.7	10.1	8.0	0.80	[31]
L18	ligand	−70.6 (dia)	631	532	0.56	[32]
	Ni^{2+}	−70.5	14.5	12.2	0.84	
	HS-Co^{2+}	−70.8	41.6	29.6	0.71	
	HS-Fe^{2+}	−69.8	38.4	18.0	0.47	
L19a	Ni^{2+}	−70.3 (dia)	970	800	0.82	[33]
L19b	Ni^{2+}	−67.4	18	12	0.67	[33]
L20a	HS-Co^{2+}	−75.6	18.0	6.6	0.37	[34]
	LS-Co^{3+}	−72.0	1080	800	0.74	
L20b	HS-Co^{2+}	−80.4	43	39	0.91	[34]
L21	HS-Co^{2+}	−79.6	48	42	0.88	[35]
	LS-Co^{3+}	−70.5	1050	640	0.61	
L22	HS-Mn^{2+}	−65.8	1.6	0.6	0.38	[37]
	HS-Mn^{3+}	−75.9	6.4	4.0	0.63	

[a] B_0 = 7 T.

Ni^{2+}, HS-Co^{2+}, and HS-Fe^{2+} complexes exhibited only a small paramagnetic change of δ_F probably given by a small pseudo-contact contribution due to a long M···F distance. The ^{19}F PRE was very good for all metal ions with the best T_2^*/T_1 ratios for the Ni^{2+} complex (Table 2). A very low limit of detection 0.04, 0.06, and 0.05 mM (SNR 3.5, 7 T, 12 min) was achieved for the Ni(**L18**), Co(**L18**), and Fe(**L18**) complexes, respectively. These encouraging results were attributed to the high number of ^{19}F nuclei as well as to the optimal relaxation times for the used experimental setup.

Octahedrally coordinated Ni^{2+} is paramagnetic but it is diamagnetic in square-planar complexes. The change can be potentially used in responsive probes and complexes of two dioxo-cyclam derivatives **L19** were studied to test this concept (Section 3.3.1) [33]. The Ni(**L19a**) complex is square-planar with all macrocycle

nitrogen atoms equatorially coordinated and both ring amides deprotonated. The Ni(**L19b**) complex is octahedral with the same equatorial donor set, and with the pendant pyridine and a solvent molecule bound in the axial positions. The different Ni^{2+} spin states are clearly seen from values of the relaxation times (Table 2). The detection limit is lower for the paramagnetic complex (SNR 3.5, 7 T, 10 min): 0.60 and 0.093 mM for the Ni(**L19a**) and Ni(**L19b**) complexes, respectively.

The Co^{3+}/Co^{2+} complexes of ligands **L20** and **L21** were used as ^{19}F MRS/MRI sensors for H$_2$O$_2$ (Section 3.3.5) [34, 35]. In the octahedral complexes, the pendant amide oxygen atom is bound to Co^{2+} and the deprotonated pendant amide nitrogen atom binds Co^{3+} [35]. The relaxation enhancement is clearly discernible with high T_2*/T_1 ratios for Co^{2+} complexes (Table 2). The PRE values were related to the Co⋯F distances of ≈ 6.0 Å for Co^{II}(**L20a**) (DFT calculations) or 7–8 Å for Co^{II}(**L20b**) and Co^{II}(**L21**) complexes (X-ray data). In bovine serum albumin, T_1 was almost unchanged but T_2* decreased to 15 and 7 ms for Co(**L20b**) and Co(**L21**), respectively [35]. With appropriate pulse sequences, limits of detection were 0.17, 0.16, and 0.53 mM for the Co^{II}(**L20b**), Co^{II}(**L21**), and Co^{III}(**L21**) complexes (SNR 4, 7 T, 12.5 min), respectively, being lower for the paramagnetic ones [35]. Recently, a study of Co^{3+}/Co^{2+} *trans*-octahedral complexes of **L16a,b** with axial carboxylate/phosphonate groups showed slightly diminishing ^{19}F PRE but with better T_2*/T_1 ratios for Co^{2+} complexes (when compared to Ni^{2+} complexes) (Table 2) [10]. The Co⋯F distance was ≈5.2 Å (X-ray data and DFT calculations). Detailed spin density calculations revealed a significant unpaired spin delocalization even over four-bond "distant" ^{19}F nuclei proving the importance of the contact contribution to PRE in TM ion complexes.

Spin cross-over of Fe^{2+}and/or its oxidation have been employed in responsive probes (Section 3.3). Explicit ^{19}F relaxation data were published for the Fe^{II}(**L12**) complex [23, 36]. The DOTA-tetraamide is octacoordinated in the TSA arrangement. Crystal structures show that Fe⋯F distances are in the range of 5.22–6.84 Å. Relaxation of the^{19}F nuclei is rather fast (Table 2) but with a surprisingly high T_2*/T_1 ratio leading to a detection limit of 2.0 mM (SNR 3, 7 T).

Ligand **L22** forms HS-Mn^{2+} and -Mn^{3+} complexes and the redox potential of the pair is suitable for detection of thiols (Section 3.3.5) [37]. Complexes of both ions accelerate relaxation of the ligand ^{19}F nuclei and, as expected, Mn^{2+} PRE is significantly higher than that of Mn^{3+}.

In general, the chemistry of TM ion complexes related to ^{19}F MRI is much less understood than that of Ln^{3+} complexes. However, TM ion complexes offer a lot of possibilities. Their magnetic properties seem to be tunable in a wide range with mostly better T_2*/T_1 ratios, when compared to Ln^{3+} complexes. Variability of spin states (different redox states, spin cross-over) of several TM ions proposes another advantage over Ln^{3+} ions (Section 3.3). However, it is necessary to accumulate more well-interpreted experimental data to place the tracer design on the more rational basis.

3.2.   Non-covalent Interactions of Metal Ion Complexes and Fluorine-Containing Compounds

Perfluorinated organic molecules are very hydrophobic, and they easily form soft self-assembled nano- or microparticles in water which can be stabilized by suitable surfactants to form micelles with the fluorine-containing core and with a hydrophilic shell. Emulsions of some compounds (e.g., perfluoro-decaline, per-fluoro-tributylamine) dissolve O_2 and show very low chemical toxicity and, therefore, they were introduced as potential blood substitutes [38]. Although the fluorine-containing compounds discussed below are not always formally pure perfluoro-hydrocarbons but contain also other elements (Cl, Br, O or N), a simple term "perfluorocarbon" (PFC) will be used for the particle cores. Ligands discussed below are shown in Figures 2 and 3.

The PFC nanoparticles were decorated by amphiphilic Gd^{3+} complexes of DTPA-bis(monoalkyl-amides) where the alkyl is oleyl or stearyl (**L23a** or **L23b**, respectively) or with DTPA- or DOTA-monoamides (e.g., **L24**) with di(fatty acyl)-glycero-phosphoethanolamine (acyl = palmitoyl or stearoyl, respectively) [39–41]. Perfluoro-15-crown-5 (a conveniently symmetric compound with a single ^{19}F NMR/MRI resonance; 20 equivalent ^{19}F) formed micelles (170–230 nm) decorated by Gd(**L23a**) with loading $3–5 \cdot 10^4$ Gd^{3+} per micelle, the T_1 of which was shortened several times [42]. Such a relatively small change of relaxation time is in agreement with a model taking into account the diffusion of the PFC molecules inside the large (100–300 nm) hydrophobic core [43]. In the micelles, T_1 cannot be further shortened due to a long mean distance between the core PFC molecules and Gd^{3+} bound on the outer side of the shell. However, even such a relatively small decrease of T_1 led to a signal enhancement by 125 % [42]. Internalization of the decorated micelles into cells was followed by ^{19}F MRI as the Gd^{3+} chelates are quickly separated from the covering layer during endocytosis, leading to an ON/OFF ^{19}F relaxation switch [43]. Other studies of perfluoro-15-crown-5 micelles (90–100 nm) confirmed a small (but statistically significant) shortening of ^{19}F T_1 [44] and the effect significantly depended on the hydrophobic anchor. The Gd(**L23b**) complex with two separated chains was bound more tightly compared to more flexible derivatives having one bis(stearoyl) anchor, e.g., Gd(**L24**). These amphiphilic complexes bound in the lipid shell influences the PFC core T_1 relaxation only at low magnetic fields (1.5–3 T, currently used in the clinics) but they had no effect on ^{19}F T_1 and significantly reduced ^{19}F T_2 at $B_0 > 6$ T [44, 45].

A significantly shorter ^{19}F T_1 can be achieved if a paramagnetic ion is introduced directly into the PFC core. Thus, highly fluorinated tris(β-diketonato) metal complexes were "dissolved" directly in the PFC and ^{19}F T_1 of the PFC was shortened by more than one order of magnitude [46]. The best results were obtained for the Fe^{3+} complex, whereas the Mn^{2+} and Gd^{3+} complexes suffered from too fast transversal relaxation (very short T_2) leading to a significant ^{19}F NMR signal broadening while the diamagnetic Ga^{3+} complex had only negligible effect on ^{19}F relaxation [46]. A further study employing 1,1,1-tris(perfluoro-*t*-butoxymethyl)ethane as the PFC core and an analogous perfluoro-fragment in

the β-diketone **L25** confirmed the best relaxation properties of the Fe^{3+} complex over Mn^{2+} and selected Ln^{3+} complexes [47]. The Fe(**L26**)$_3$ complex kept a reasonably high T_2^*/T_1 ratio at high magnetic fields for a range of PFC materials [48]. Among several TM ion complexes, only complexes of Mn^{4+}, Fe^{3+}, Co^{3+}, and Ga^{3+} with fluorinated tripodal Schiff-bases (e.g., **L27**) were reasonably stable and the Fe^{3+} complex was showed to have the best relaxation properties among them [49].

Nanoobjects with a hydrophilic core and a bilayer lipid membrane (liposomes) were also employed [50]. Liposomes encapsulating a mixture of NH_4PF_6 and the Tm(HPDO3A) complex showed a ^{1}H paraCEST effect due to exchange of water from the inner aqueous pool with the outer bulk water but the ^{19}F NMR signal of the PF_6^- anion quenched due to a short average distance of the fluorine atoms from the paramagnetic Tm^{3+}. Upon heating above the liposome's melting temperature (when its lipid bilayer collapsed), the inner aqueous solution was spilled into the bulk water and the CEST effect disappeared. Simultaneously, the ^{19}F NMR signal was sharpened due to the increased distance of the PF_6^- anion from Tm^{3+} as a consequence of the dilution [50].

3.3.   Applications of ^{19}F Magnetic Resonance Imaging Contrast Agents and Probes

No natural background in ^{19}F MRI predestines fluorinated CAs for "hot-spot" imaging. They can be typically used as responsive ("smart") CAs, the signals of which are modulated by external stimuli or for a long-time cell tracking. The response can be reached by several principally different mechanisms shown in Figure 4. (*i*) A spacer between a ^{19}F reporter and a paramagnetic metal ion can be selectively cleaved off changing the reporter ^{19}F NMR/MRI signal (Figure 4A). (*ii*) A flexible spacer can interact with the analyte thereby changing the spatial separation of the ^{19}F reporter and the paramagnetic metal ion (Figure 4B). (*iii*) A change of δ_F and ^{19}F relaxation upon (paramagnetic) metal ion binding to a fluorine-containing ligand (Figure 4C). (*iv*) The ^{19}F shift/relaxation change upon change of the number of unpaired electrons of the metal ion (change of oxidation state or HS/LS cross-over) in the complex of the fluorine-containing ligand (Figure 4D). Structures of the ligands discussed here are depicted in Figures 2 and 3.

The ^{19}F NMR/MRI signal is often poorly detectable, if the paramagnetic ion is present in a too close vicinity of ^{19}F nuclei, and the signal becomes visible after an elongation of the M···F distance. For this purpose, metal ions with half-filled orbitals showing the long electron relaxation (f^7: Gd^{3+} or d^5: Mn^{2+}/Fe^{3+}) are mostly used as they produce significant T_2 shortening (the signal diminishing is caused by PRE broadening and a low T_2^*/T_1 ratio). However, some metal ions offer modulation of δ_F and/or T_1 with a high T_2^*/T_1 ratio (Section 3.1), leading to overall faster imaging experiments and a better SNR compared to diamagnetic standards.
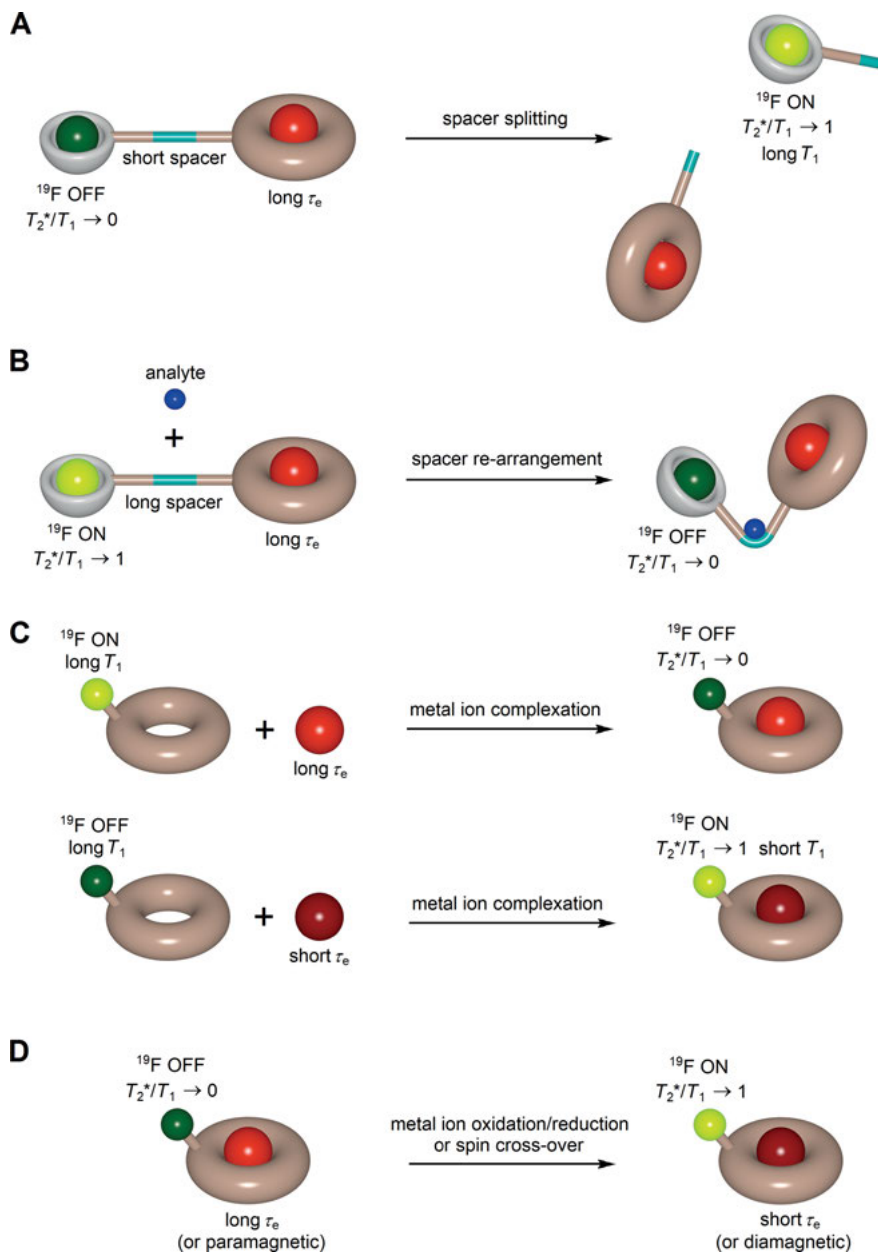
Figure 4. Main mechanisms employed in the design of responsive ^{19}F MRI agents. The ON/OFF switch is realized by the choice of an appropriate pulse sequence. (**A**) Spacer splitting leads to separation of the paramagnetic complex and the ^{19}F reporter (molecule, nanoparticle). (**B**) Spacer re-arrangement caused by interaction with the analyte changes the mutual position of the paramagnetic complex and the ^{19}F reporter. (**C**) Paramagnetic metal complexation alters the ^{19}F relaxation times of the ligand. (**D**) Change of the electronic structure of the metal ion alters the ^{19}F relaxation times of the complex.

3.3.1. pH-Responsive Contrast Agents

Many Gd^{3+}-based ^{1}H MRI CAs, the relaxation properties of which depend on their protonation state, have been designed; however, quantification of the ^{1}H relaxation change with pH requires an accurate knowledge of the Gd^{3+} probe concentration. It can be overcome by ratiometric methods using a pH-independent resonance signal. In this respect, a proof-of-concept study employed the ^{1}H/^{19}F MRI ratiometric probe where a paramagnetic Gd^{3+} complex was used as a pH reporter and a simple fluorinated probe as the pH-independent standard (Gd^{3+} had no effect on the ^{19}F MRI signal) [51]. The potential of paramagnetic Ln^{3+} complexes with DOTA-mono- and -diamides bearing the (CF_3)-benzyl-amide moiety(-ies) **L9**, **L10**, and **L11** for a ratiometric pH determination through combination of ^{1}H paraCEST effect (originating from the exchange of amide protons with bulk water) with ^{19}F MRI signal intensity was investigated [22]. The TM ion (Fe^{2+}, Co^{2+}, Ni^{2+}) complexes of the DOTA-tetraamide derivative **L18** were suggested for the ratiometric pH determination using ^{1}H paraCEST as the reporter method and ^{19}F MRI to define a probe concentration [32]. The Fe^{II}(**L12**) complex was used analogously [36]. The Ln^{3+} complexes of the DO3A-sulfamides (e.g., **L6**) were found to alter their δ_F and ^{19}F relaxations with pH due to protonation and deprotonation (and simultaneous coordination) of the amide group which alter the spatial position of the $–CF_3$ groups [13]. A slow exchange (in respect to the NMR timescale) between protonated and deprotonated species of Eu(**L6**) enabled ratiometric pH determination [13]. The pH dependence of δ_F was also observed for a related mono-[2-(CF_3)-phenyl] derivative [15]. Deprotonation of the amide group in Ln^{3+} complexes of DOTA-[(o-CF_3)-phenyl]-monoamide derivatives (e.g., **L1**, **L5**) led to a δ_F change. The pK_a values were modulated by the other substituents on the phenyl ring leading to probes suitable for a biologically relevant pH range [14].

A change between diamagnetic square-planar and paramagnetic octahedral Ni^{2+} complexes of 5,7-dioxocyclams **L19** with the protonable/coordinate methylpyridine pendant arm and the reporting perfluoro-t-butoxymethyl moiety was also suggested as potential pH probe [33]. The LS-to-HS spin cross-over in the octahedral Fe^{2+} complex of a 1,4,7-triazacyclononane (tacn)-based ligand **L28** was induced by a ligand field decrease caused by deprotonation of the hydroxy groups of **L28** and it resulted in a significant magnetic susceptibility and δ_F change (> 30 ppm) [52].

3.3.2. Temperature-Responsive Contrast Agents

Irreversible thermo-responsive liposomes the inner pool of which consisted of an aqueous solution of the paramagnetic Tm(HPDO3A) complex and NH_4PF_6 were already mentioned above (Section 3.2) [50]. The Fe^{2+} complexes of tacn-based ligands (e.g., **L29**) changing their magnetic susceptibility with temperature due to the HS/LS spin cross-over were suggested as thermo-responsive agents [53].

3.3.3.   *Enzyme-Responsive Contrast Agents*

Incorporation of an enzyme-cleavable spacer between the ^{19}F reporter and the paramagnetic ion is an obvious choice for (irreversible) detection of enzymatic activity. The PFC nanoparticles covered by a solid silica shell were decorated with a caspase-sensitive oligopeptide terminated with the Gd^{3+} complex of a DOTA-monoamide derivative. The ^{19}F MRI signal of the PFC was quenched although the complex was located far away from the nanoparticle core and appeared upon cleavage of the spacer by caspase [54, 55]. The caspase activity was also studied on a simple conjugate of a Gd^{3+}-DOTA-monoamide complex with a caspase-cleavable oligopeptide terminated with 4-(CF_3O)-benzylamine [56]. Similarly, the perfluoro-*t*-butyl group (the solubility of which was increased by an oligo-PEG fragment) [57] or 3,5-bis(CF_3)-benzylamine [58] were bound to a Gd^{3+}-DOTA-monoamide through an oligopeptide as ^{19}F reporters whose NMR signals were activated after cleavage of the spacer by a metalloproteinase. A bimodal ^{19}F MRI-fluorescence agent employing 7-amino-4-(CF_3)-coumarin was developed to detect caspase activity. Its binding to Gd^{3+}-DOTA-monoamide through the oligopeptide spacer produced a non-fluorescent and ^{19}F MRI-silent conjugate. Upon caspase action, free coumarin and the complex were released, and both luminescence and ^{19}F MRI signals appeared [59].

Another cleavage mechanism includes enzymatic action followed by self-immolative decomposition of a (*p*-hydroxy)-benzyl carbamate ester conjugated to a Gd^{3+} complex. Once the original enzymatically cleavable (*p*-alkoxy)-benzyl group is transformed to the (*p*-hydroxy)-benzyl group, the benzyl-carbamate ester decomposes to CO_2 and the free Gd^{3+}-containing fragment. With fluorine on the benzyl group, it leads to a rise of the ^{19}F MRI signal. With the galactosyl residue used as the *p*-alkoxy substituent, the conjugate with the Gd^{3+} complex served as a probe for galactosidase activity and gene expression [60]. Based on a similar galactosidase-induced self-immolative process, the agent bearing the *p*-(CF_3)-benzyl group as the ^{19}F MRI reporter bound to the carbamate nitrogen atom was suggested as a dual ^1H-^{19}F MRI agent [61]. Self-immolation of a carbamate *p*-hydroxy/amino-benzyl ester derivative of a DOTA-monoamide or **L2b** complexed to Dy^{3+}, Ho^{3+} or Tm^{3+} was used to detect esterase/peptidase activity [62]. Analogously, lactamase activity was detected if cephalosporin as the enzyme-sensitive fragment was incorporated into a linker between the Gd^{3+}-DTPA-monoamide complex and the terminal *p*-(CF_3)-benzoyl reporting group [63].

A less common paramagnetic TM ion complex formation was used to detect galactosidase activity through splitting of the galactoside-to-"phenol" bond leading to a formation of free phenolic derivatives (e.g., 3-fluororesorcinol or fluorinated 2-hydroxybenzaldehyde-benzoylhydrazone) which are capable to bind Fe^{3+} [64]. The formation of the complexes led to a change of the ligand ^{19}F relaxation time (giving an ON/OFF ^{19}F MRI switch) and δ_F (for ^{19}F MRS).

3.3.4. Metal Ion-Responsive Contrast Agents

Some time ago, it was observed that the fluorinated ligand F-BAPTA shows a δ_F change by more than 20 ppm in the presence of Fe^{2+} and even several ppm upon complexation of diamagnetic Ca^{2+} or Zn^{2+} ions. Therefore, F-BAPTA was suggested as a Ca^{2+}-responsive probe [65]. An analogous EGTA-like fragment with an *o*-dioxo-phenylene group was used as a Ca^{2+}-binding unit in a conjugate with DO3A-[*o*-(CF_3)-phenyl]-monoamide **L30** [62]. It was found that Dy^{3+} and Tm^{3+} complexes of the conjugate show a change of δ_F by ≈ 4 ppm with Ca^{2+} concentration. The perfluoro-*t*-butyl reporting group in the AAZTA derivative **L15** is separated from Dy^{3+} by the EGTA unit effectively binding Ca^{2+} ions [26]. Upon Ca^{2+} complexation, an average distance between the paramagnetic center and the ^{19}F nuclei is changed, influencing ^{19}F T_1 only slightly but significantly affecting ^{19}F T_2. When the diamagnetic Y^{3+} analogue is used, only negligible changes of δ_F, T_1, and T_2 were observed. Thus, a cocktail of Y^{3+}/Dy^{3+} complexes can be employed for ratiometric Ca^{2+} sensing with the Y^{3+} probe as an internal standard.

If the value of the exchange rate constant between the free and complexed ligand is smaller than the frequency separation of their ^{19}F NMR peaks and the signals relax slowly, measurement of ^{19}F chemical exchange saturation transfer (^{19}F-CEST) between the complexed and free ligand is possible. This approach was used for detection of diamagnetic Mg^{2+}, Ca^{2+} and Zn^{2+}, and paramagnetic Fe^{2+} ions with F-BAPTA and its difluoro analogue [66, 67]. Sub-millimolar concentrations of diamagnetic metal ions like Mg^{2+}, Ca^{2+} and Zn^{2+} ions were detected by ^{19}F-CEST utilizing DTPA-diamides of *ortho*-fluorinated anilines as ligands [68].

3.3.5. Redox-Responsive Contrast Agents

A redox-cleavable spacer between a ^{19}F reporter and a paramagnetic ion can be used to study the redox status of the sample. The silica-coated nanoparticles with a PFC core decorated on the SiO_2 surface by Gd^{3+} complexes of DTPA or DO3A derivatives through a disulfide bridge were used for ^{19}F MRI detection of reductants [69]. A disulfide bridge was also used to connect the 3,5-bis(CF_3)-benzamide fragment and the Gd^{3+}-DOTA-monoamide complex conjugated to aminoluciferin and the conjugate formed nanoparticles with a hydrophobic core. It showed no ^{19}F MRI signal due to large PRE, no luminescence due to quenching of aminoluciferin by the amide bond, and a high ^{1}H longitudinal relaxivity due to a macromolecular character of the aggregate. Upon splitting of the disulfide bond by glutathione, ^{1}H relaxivity dropped but fluorescence and ^{19}F MRI signals rose [70].

The Gd^{3+} complex of DOTA conjugated through the *N,N'*-hydrazide group to the 3,5-bis(CF_3)-benzoic acid is ^{19}F NMR silent. The hydrazide group was selectively oxidized to N_2 by HClO, the Gd^{3+}-DOTA complex and the 3,5-bis(CF_3)-benzoic acid were disconnected. It resulted in the appearance of a ^{19}F NMR/MRI signal [71].

The different coordination ability of the Cu^{2+}/Cu^+ pair was employed to detect reductive conditions. Several cyclam derivatives bearing one or two fluorine-containing pendant arms formed Cu^{2+} complexes which were silent in ^{19}F MRI. After reduction of paramagnetic Cu^{2+} to diamagnetic Cu^+ by cysteine, the complexes dissociated and the signal of the free ligand became visible [72]. A similar approach was used employing the ATSM ligand family with fluorinated tags, perfluoro-*t*-butoxy-PEG groups (e.g., **L31**) [73]. Its Cu^{2+} complex was ^{19}F MRI-silent due to PRE but, after reduction to diamagnetic Cu^+, the ^{19}F MRI signal rose as a result of complex dissociation. A bimodal Cu^{2+} complex of an ATSM derivative with the $–CH_2CF_3$ group and the fluorescein moiety was developed [74]. Its Cu^{2+} complex was ^{19}F MRI- and fluorescence-silent but reduction to Cu^+ led to the development of both ^{19}F MRI and luminescence signals.

The paramagnetic HS-Co^{2+} complex of **L20a** can be oxidized to the diamagnetic LS-Co^{3+} complex by various reactive oxygen species (ROS). The change is reflected by a sharper and increased ^{19}F NMR signal due to a significant change of relaxation times [34]. The Co^{2+} complex of **L20b** bearing the perfluoro-*t*-butyloxy group was used to detect H_2O_2 and peroxidase activity [35].

A pair of Mn^{3+}/Mn^{2+} complexes of **L22** was suggested as a redox-responsive probe [37]. Whereas the Mn^{2+} complex showed high ^{1}H longitudinal relaxivity and a very broad ^{19}F NMR signal due its HS-d^5 state, the ^{19}F NMR signal of the Mn^{3+} complex is shifted by ≈ 10 ppm and is much sharper and easy to detect. A suitable value of the Mn^{3+}/Mn^{2+} redox potential enables detection of various ROS.

3.3.6. *Contrast Agents Responsive to Other Stimuli*

Phosphates and phosphate ester anions of AMP, ADP or ATP were bound to a dinuclear Zn^{2+} complex of 2,6-bis[(dipicolyl)aminomethyl]-4-fluorophenol and the complex served as ^{19}F NMR receptor for the anions [75]. The structurally similar phosphate-binding motif of a Zn^{2+} complex of 1,3-bis[(dipicolyl)amino-methyl]benzene was coupled to Gd^{3+}-DOTA-monoamide. When such a receptor was added to a solution of the *p*-(CF_3)-phenyl-phosphate monoester serving as a probe, its ^{19}F NMR signal was gradually broadened and disappeared due to phosphate binding to Zn^{2+} ions located close to the Gd^{3+}-DOTA unit. In addition of diphosphate which binds to the receptor more strongly than *p*-(CF_3)-phenyl-phosphate, the ^{19}F NMR signal of the probe was restored [76]. Complexes of DO3A derivatives with Ln^{3+} ions are able to coordinate two inner-sphere water molecules which can be easily replaced by bidentate anions. The Ho^{3+} and Tm^{3+} complexes of DO3A-monoamide with a (CF_3)-phenyl group were suggested as anion-responsive probes for citrate, lactate, phosphate or bicarbonate. Replacement of the water molecules with these anions resulted in a change of δ_F and the ^{19}F signal linewidth [62].

3.3.7. *Long-Term Cell Labelling*

Long-term cell labelling to track cells after transplantation is a very attractive utilization of ^{19}F MRI probes [77]. Surprisingly, paramagnetic ^{19}F MRI tracers

have been used relatively rarely for cell labelling/tracking. Micelles incorporating the paramagnetic complex Gd(**L24**) on their surface were used for cell tracking and reduction of [19]F T_2 (but no alteration of T_1) was observed after the cell internalization [45]. The quickly relaxing and non-toxic Ni(**16a**) complex was used for *in vitro* labelling of mesenchymal stem cells [30].

4. [19]F MAGNETIC RESONANCE IMAGING MEASUREMENTS

Although MR scanner manufacturers usually do not provide their own ^{1}H/^{19}F radio frequency coils, several commercial companies offer dedicated coils, both surface and volume ones.

An obvious requirement is to use one coil for both ^{1}H and [1]F MRI to acquire a ^{19}F image and the anatomical ^{1}H background during one session without repositioning of the measured object. The simplest way to solve this problem is a single-loop coil with capacitors tunable in a broad range of frequencies covering both proton and fluorine ranges, as it was used in [78, 79]. This solution might not be very convenient due to an inhomogeneous B_1 profile, a sensitivity strongly dependent on the distance of the object from the coil, a longer time needed for tuning, and a necessity of mechanically resilient capacitors. Therefore, other concepts of dual frequency coils were examined [80], which include a design with two separated perpendicularly oriented coil sets, one tuned to ^{1}H and the other one for ^{19}F, e.g., resonator volume coils [81]. This concept enables construction of volume coils with higher sensitivity and more homogeneous excitation across a larger volume. To avoid mechanical switching between the ^{1}H and ^{19}F circuits, pin-diode switches were introduced in the coils [82, 83]. A high SNR can be reached with a fluorine cryoprobe [84] providing spatially highly resolved ^{19}F images. Multichannel ^{1}H/^{19}F coils for human studies have been designed and constructed [85].

Both MRI and MRS can be used for ^{19}F detection [86, 87]. While MRI provides information about spatial distribution of the ^{19}F probe, it may suffer from a low signal (due to small image voxels) if the probe contains magnetically non-equivalent ^{19}F nuclei. If we surrender spatial resolution, MRS may provide substantially higher signals. Spectral resolution of MRS also enables discrimination of probes containing ^{19}F nuclei with different δ_F [88], which is strongly affected by bound paramagnetic metal ions.

One of the major issues is the concentration of a fluorinated tracer. While the concentration of water in the human body is approx. 45 M, body concentrations of externally added ^{1}H MRI CAs are in the sub-millimolar range. Similarly, mM concentrations of fluorinated tracers are commonly taken as a detection threshold in ^{19}F MRI [86, 89] with diamagnetic ^{19}F probes, within a reasonable scanning time (5–10 min), depending on magnetic field strength and experimental setting including image voxel size. The detection limit is estimated to be $\approx 4 \cdot 10^{16}$ of (diamagnetic) ^{19}F nuclei per image voxel with SNR 3 at 7 T [87, 89, 90].

To increase the signal intensity, several approaches besides already discussed probe design should be considered. The simplest approach is an increase of the image voxel which of course leads to worsened spatial resolution. It might not be a too serious problem if the probe is also detectable by ^{1}H MRI due to the presence of a paramagnetic ion. The ^{1}H MRI then provides exact localization of the probe (albeit non-specific) linked with the specific ^{19}F MRI having lower resolution [24, 29, 37]. Another obvious solution is an increase of the number of acquisitions, as the SNR increases with the square root of the acquisition number. However, lengthening of the scanning time is strictly limited in *in vivo* studies. Introduction of paramagnetic ions into the probes substantially shortens repetition time and, thus, enables to shorten scanning time and/or increase a number of repetitions. For instance, an estimated 80-times reduction of T_1 in the case of PFC nanoemulsions containing chelated Fe^{3+} may lower the detection limit more than 8-times [46].

Sequence choice and sequence optimization are crucial parameters, and they should be carefully tailored to the used ^{19}F probe. Basic principles are the same for both ^{1}H and ^{19}F MRI, mainly the sequence timing should correspond to the nucleus relaxation times. The fluorine "hot-spot" MR imaging implicates that the timing is usually targeted to gain the maximum signal, not contrast. Diamagnetic fluorine probes have long relaxation times and, therefore, standard turbospin echo sequences may be used for a faster filling of the k-space. Long T_1 (up to several seconds) requires a long repetition time. Longer T_2 (tens to hundreds of milliseconds) enables acquisition of more echoes before the signal vanishes. Each echo can be utilized for calculation of one row of the image k-space. Therefore, during one scan, several rows can be acquired accelerating the image acquisition. Optimization of the echo train length means setting echo time (echo spacing), turbofactor (i.e., a number of echoes per scan), and repetition time to fully employ long T_1 and T_2 with respect to the bandwidth and image geometry.

Paramagnetic metal ions induce substantial reduction of relaxation times down to several milliseconds for T_1 and a sub-millisecond range for T_2. The MR signal should be acquired before the signal vanishes due to short T_2 and, therefore, the used sequence requires faster timing. While spin echo-based sequences have echo spacing of several milliseconds, shorter echo times may be reached using gradient echo sequences with echoes in the sub-millisecond range, or *via* ultra-short echo time (UTE) or zero-echo time (ZTE) sequences with radial k-space filling [18]. Although one echo at a time can be obtained for a gradient echo sequence, the substantial reduction of T_1 enables repetition time shortening up to two orders of magnitude and accelerated image acquisition. More acquisitions can be obtained within the same scanning time and it leads to a better SNR and a lower detection limit [13]. As the static magnetic field strength of the scanner has a substantial impact on relaxation times, especially in the presence of paramagnetic metal ions (as discussed above, Sections 2 and 3), it should also be considered while optimizing the sequence parameters [4]. In a simplified way, standard turbospin echo sequences are better for diamagnetic compounds, while paramagnetic probes benefit from gradient echo, UTE or ZTE sequences.

5. CONCLUSIONS AND OUTLOOK

^{19}F MRI has been proven to be a viable alternative to "classical" ^{1}H MRI in utilizations where "hot-spot" imaging is advantageous. The sensitivity issues can be overcome by using fluorous soft nanoparticles. The detectability of such ^{19}F MRI CAs was pushed closer to that of Gd^{3+}-based ^{1}H MRI CAs due to a very high number of (semi)equivalent fluorine atoms. These supramolecular assemblies have some limitations due to their (particle) size regarding the stability in body/cellular fluids, problematic tissue *in vivo* targeting, body elimination, etc. Another sensitivity improvement relies on the shortening of long relaxation times of the ^{19}F nucleus. The best approach seems to be a combination of a high number of fluorine atoms in the nanoparticles or in defined molecules, with the short relaxation times induced by paramagnetic metal ions. Traditional trivalent lanthanides used in NMR and MRI for a long time have been recently supplemented with transition metal ions which bring interesting possibilities for tuning of various physico-chemical properties. However, it is essential to keep in mind two main differences in the effect of paramagnetic metal ions in ^{1}H and ^{19}F MRI. (*i*) Paramagnetic relaxation of bulk water is mediated mainly by chemical exchange of the coordinated water molecule in Gd^{3+}-based ^{1}H MRI CAs. However, paramagnetic ions are mostly directly bound to the ^{19}F MRI probes and their influence on ^{19}F relaxation times is usually much stronger, mainly due to the short distance between the metal ion and fluorine atom. It is the most crucial parameter in the design of the ^{19}F MRI CA and must be carefully optimized. (*ii*) Water ^{1}H relaxation times strongly depend on the probe concentration (there is a linear correlation between relaxation rate and concentration). The ^{19}F relaxation has no direct concentration dependence as the interaction between the ^{19}F nuclei in the molecule/nanoobject and the directly bound paramagnetic metal ions is usually much stronger than their interaction with other paramagnetics in the solution.

It should be stressed again that the ^{19}F MRI "hot-spot" imaging should be ideally complemented with "classical" ^{1}H MRI. The tracers can also be localized in a particular tissue by targeting and concentrated up to a level which can be detected. Metal-based ^{19}F probes offer a "colorful" imaging due to differences in the probe δ_F as well as various responsive mechanisms which are more diverse than those available for "classical" ^{1}H MRI. Combination of ^{1}H and ^{19}F MRI tracers is very suitable for the design of ratiometric responsive probes. Generally, the paramagnetic tracers are expected to substantially boost sensitivity and may open a way to new applications. Mainly in recent years, the chemistry of the ^{19}F MRI CAs and MR methodology behind the imaging have been significantly improved and ^{19}F MRI/MRS has found its way into experimental preclinical (now mainly for the study of the physiological status of tissues by responsive agents, cell labeling, and cell transplant tracking) and even clinical practice.

ACKNOWLEDGMENTS

ABBREVIATIONS

AAZTA	1,4-bis(carboxymethyl)-6-[bis(carboxymethyl)]amino-6-methylperhydro-1,4-diazepine; 6-amino-6-methylperhydro-1,4-diazepine-N,N',N'',N'''-tetraacetic acid
ADP	adenosine 5′-diphosphate
AMP	adenosine 5′-monophosphate
ATP	adenosine 5′-triphosphate
ATSM	diacetyl-2,3-bis(N^4-methyl-3-thiosemicarbazone)
BAPTA	1,2-bis(o-aminophenoxy)ethane-N,N,N',N'-tetraacetic acid, see Figure 3
CA	contrast agent
CEST	chemical exchange saturation transfer
CN	coordination number
DFT	density functional theory
DO3A	1,4,7,10-tetraazacyclododecane-1,4,7-triacetic acid, see Figure 2
DOTA	1,4,7,10-tetraazacyclododecane-1,4,7,10-tetraacetic acid, see Figure 2
DTPA	diethylenetriamine-N,N,N',N'',N''-pentaacetic acid, see Figure 2
EGTA	ethyleneglycol-bis(2-aminoethyl ether)-N,N,N',N'-tetraacetic acid
HPDO3A	10-(2-hydroxypropyl)-1,4,7,10-tetraazacyclododecane-1,4,7-triacetic acid, see Figure 2
HS	high-spin
LS	low-spin
LW	linewidth
MR	magnetic resonance
MRI	magnetic resonance imaging
MRS	magnetic resonance spectroscopy
NMR	nuclear magnetic resonance
PAMAM	polyamidoamine (dendrimer)
paraCEST	paramagnetic chemical exchange saturation transfer
PEG	polyethyleneglycol
PFC	perfluorocarbon
PRE	paramagnetic relaxation enhancement
ROS	reactive oxygen species
SA	square-antiprismatic / square-antiprism
SNR	signal-to-noise ratio
tacn	1,4,7-triazacyclononane
TM	transition metal (d-element)

TSA	twisted square-antiprismatic / twisted square-antiprism
UTE	ultrashort echo time
ZTE	zero-echo time

REFERENCES

1. S. Konstandin, L. R. Schad, *Magn. Reson. Mater. Phys. Biol. Med.* **2014**, *27*, 1–4.

2. I. Tirotta, V. Dichiarante, C. Pigliacelli, G. Cavallo, G. Terraneo, F. B. Bombelli, P. Metrangolo, G. Resnati, *Chem. Rev.* **2015**, *115*, 1106–1129.

3. J. Ruiz-Cabello, B. P. Barnetta, P. A. Bottomley, J. W. M. Bulte, *NMR Biomed.* **2011**, *24*, 114–129.

4. P. Harvey, I. Kuprov, D. Parker, *Eur. J. Inorg. Chem.* **2012**, 2015–2022.

5. K. L. Peterson, K. Srivastava, V. C. Pierre, *Front. Chem.* **2018**, *6*, 160.

6. I. Bertini, C. Luchinat, G. Parigi, E. Ravera, *NMR of Paramagnetic Molecules*, 2nd ed., Elsevier, Amsterdam, **2017**, pp. 77–126.

7. D. Kruk, J. Kowalewski, *J. Chem. Phys.* **2009**, *130*, 174104.

8. I. Bertini, C. Luchinat, G. Martini, in *Handbook of Electron Spin Resonance*, Eds. C. P. Poole, H. A. Farach, AIP Press, New York, **1994**, pp. 80–302.

9. A. J. Pell, G. Pintacuda, C. P. Grey, *Prog. Nucl. Magn. Reson. Spectrosc.* **2019**, *111*, 1–271.

10. J. Blahut, L. Benda, J. Kotek, G. Pintacuda, P. Hermann, *Inorg. Chem.* **2020**, *59*, 10071–10082.

11. K. H. Chalmers, M. Botta, D. Parker, *Dalton Trans.* **2011**, 904–913.

12. E. A. Suturina, K. Mason, C. F. G. C. Geraldes, N. F. Chilton, D. Parker, I. Kuprov, *Phys. Chem. Chem. Phys.* **2018**, *20*, 17676–17686.

13. P. K. Senanayake, A. M. Kenwright, D. Parker, S. K. van der Hoorn, *Chem. Commun.* **2007**, 2923–2925.

14. K. H. Chalmers, E. De Luca, N. H. M. Hogg, A. M. Kenwright, I. Kuprov, D. Parker, M. Botta, J. I. Wilson, A. M. Blamire, *Chem. Eur. J.* **2010**, *16*, 134–148.

15. A. M. Kenwright, I. Kuprov, E. De Luca, D. Parker, S. U. Pandya, P. K. Senanayake, D. G. Smith, *Chem. Commun.* **2008**, 2514–2516.

16. E. De Luca, P. Harvey, K. H. Chalmers, A. Mishra, P. K. Senanayake, J. I. Wilson, M. Botta, M. Fekete, A. M. Blamire, D. Parker, *J. Biol. Inorg. Chem.* **2014**, *19*, 215–227.

17. K. H. Chalmers, A. M. Kenwright, D. Parker, A. M. Blamire, *Magn. Reson. Med.* **2011**, *66*, 931–936.

18. F. Schmid, C. Holtke, D. Parker, C. Faber, *Magn. Reson. Med.* **2013**, *69*, 1056–1062.

19. Z.-X. Jiang, Y. Feng, Y. B. Yu, *Chem. Commun.* **2011**, *47*, 7233–7235.

20. N. Cakić, T. Savić, J. Stricker-Shaver, V. Truffault, C. Platas-Iglesias, C. Mirkes, R. Pohmann, K. Scheffler, G. Angelovski, *Chem. Commun.* **2016**, *52*, 9224–9227.

21. R. Pujales-Paradela, T. Savić, D. Esteban-Gómez, G. Angelovski, F. Carniato, M. Botta, C. Platas-Iglesias, *Chem. Eur. J.* **2019**, *25*, 4782–4792.

22. R. Pujales-Paradela, T. Savić, P. Pérez-Lourido, D. Esteban-Gómez, G. Angelovski, M. Botta, C. Platas-Iglesias, *Inorg. Chem.* **2019**, *58*, 7571–7583.

23. K. Srivastava, E. A. Weitz, K. L. Peterson, M. Marjańska, V. C. Pierre, *Inorg. Chem.* **2017**, *56*, 1546–1557.

24. V. Herynek, M. Martiniskóvá, Y. Bobrova, A. Gálisová, J. Kotek, P. Hermann, F. Koucký, D. Jirák, M. Hájek, *Magn. Reson. Mater. Phys. Biol. Med.* **2019**, *32*, 115–124.

25. M. P. Placidi, M. Botta, F. K. Kálmán, G. E. Hagberg, Z. Baranyai, A. Krenzer, A. K. Rogerson, I. Tóth, N. K. Logothetis, G. Angelowski, *Chem. Eur. J.* **2013**, *19*, 11644–11660.

26. G. Gambino, T. Gambino, R. Pohmann, G. Angelowski, *Chem. Commun.* **2020**, *56*, 3492–3495.

27. A. Gupta, P. Caravan, W. S. Price, C. Platas-Iglesias, E. M. Gale, *Inorg. Chem.* **2020**, *59*, 6648−6678.

28. D. Xie, M. Yu, R. T. Kadakia, E. L. Que, *Acc. Chem. Res.* **2020**, *53*, 2−10.

29. J. Blahut, P. Hermann, A. Gálisová, V. Herynek, I. Císařová, Z. Tošner, J. Kotek, *Dalton Trans.* **2016**, *45*, 474–478.

30. J. Blahut, K. Bernášek, A. Gálisová, V. Herynek, I. Císařová, J. Kotek, J. Lang, S. Matějková, P. Hermann, *Inorg. Chem.* **2017**, *56*, 13337–13348.

31. R. Pujales-Paradela, T. Savić, I. Brandariz, P. Pérez-Lourido, G. Angelovski, D. Esteban-Gómez, C. Platas-Iglesias, *Chem. Commun.* **2019**, *55*, 4115–4118.

32. M. Yu, B. S. Bouley, D. Xie, E. L. Que, *Dalton Trans.* **2019**, *48*, 9337–9341.

33. D. Xie, L. E. Ohman, E. L. Que, *Magn. Reson. Mater. Phys. Biol. Med.* **2019**, *32*, 89–96.

34. M. Yu, D. Xie, K. P. Phan, J. S. Enriquez, J. J. Luci, E. L. Que, *Chem. Commun.* **2016**, *52*, 13885–13888.

35. M. Yu, B. S. Bouley, D. Xie, J. S. Enriquez, E. L. Que, *J. Am. Chem. Soc.* **2018**, *140*, 10546–10552.

36. K. Srivastava, G. Ferrauto, V. G. Young, Jr., S. Aime, V. C. Pierre, *Inorg. Chem.* **2017**, *56*, 12206–12213.

37. H. Chen, X. Tang, X. Gong, D. Chen, A. Li, C. Sun, H. Lin, J. Gao, *Chem. Commun.* **2020**, *56*, 4106–4109.

38. K. C. Lowe, *Blood Rev.* **1999**, *13*, 171–184.

39. G. M. Lanza, X. Yu, P. M. Winter, D. R. Abendschein, K. K. Karukstis, M. J. Scott, L. K. Chinen, R. W. Fuhrhop, D. E. Scherrer, S. A. Wickline, *Circulation* **2002**, *106*, 2842–2847.

40. A. M. Morawski, P. M. Winter, X. Yu, R. W. Fuhrhop, M. J. Scott, F. Hockett, J. D. Robertson, P. J. Gaffney, G. M. Lanza, S. A. Wickline, *Magn. Reson. Med.* **2004**, *52*, 1255–1262.

41. S. D. Caruthers, A. M. Neubauer, F. D. Hockett, R. Lamerichs, P. M. Winter, M. J. Scott, P. J. Gaffney, S. A. Wickline, G. M. Lanza, *Invest. Radiol.* **2006**, *41*, 305–312.

42. A. M. Neubauer, J. Myerson, D. Caruthers, F. D. Hockett, P. M. Winter, J. Chen, P. J. Gaffney, J. D. Robertson, G. M. Lanza, S. A. Wickline, *Magn. Reson. Med.* **2008**, *60*, 1066–1072.

43. L. Hu, L. Zhang, J. Chen, G. M. Lanza, S. A. Wickline, *J. Magn. Reson. Imaging* **2011**, *34*, 653–661.

44. A. de Vries, R. Moonen, M. Yildirim, S. Langereis, R. Lamerichs, J. A. Pikkemaat, S. Baroni, E. Terreno, K. Nicolay, G. J. Strijkers, H. Grüll, *Contrast Media Mol. Imaging* **2014**, *9*, 83–91.

45. M. B. Kok, A. de Vries, D. Abdurrachim, J. J. Prompers, H. Grüll, K. Nicolay, G. J. Strijkers, *Contrast Media Mol. Imaging* **2011**, *6*, 19–27.

46. A. A. Kislukhin, H. Xu, S. R. Adams, K. H. Narsinh, R. Y. Tsien, E. T. Ahrens, *Nature Mater.* **2016**, *15*, 662–669.

47. Q. Peng, Y. Li, S. Bo, Y. Yuan, Z. Yang, S. Chen, X. Zhou, Z.-X. Jiang, *Chem. Commun.* **2018**, *54*, 6000–6003.

48. C. Wang, S. R. Adams, H. Xu, W. Zhu, E. T. Ahrens, *ACS Appl. Biomater.* **2019**, *2*, 3836−3842.

49. A. H. Jahromi, C. Wang, S. R. Adams, W. Zhu, K. Narsinh, H. Xu, D. L. Gray, R. Y. Tsien, E. T. Ahrens, *ACS Nano* **2019**, *13*, 143−151.

50. S. Langereis, J. Keupp, J. L. J. van Velthoven, I. H. C. de Roos, D. Burdinski, J. A. Pikkemaat, H. Grüll, *J. Am. Chem. Soc.* **2009**, *131*, 1380–1381.
51. E. Gianolio, R. Napolitano, F. Fedeli, F. Arena, S. Aime, *Chem. Commun.* **2009**, 6044–6046.
52. A. I. Gaudette, A. E. Thorarinsdottir, T. D. Harris, *Chem. Commun.* **2017**, *53*, 12962–12965.
53. A. E. Thorarinsdottir, A. I. Gaudette, T. D. Harris, *Chem. Sci.* **2017**, *8*, 2448–2456.
54. K. Akazawa, F. Sugihara, M. Minoshima, S. Mizukami, K. Kikuchi, *Chem. Commun.* **2018**, *54*, 11785–11788.
55. K. Akazawa, F. Sugihara, T. Nakamura, S. Mizukami, K. Kikuchi, *Bioconjugate Chem.* **2018**, *29*, 1720−1728.
56. S. Mizukami, R. Takikawa, F. Sugihara, Y. Hori, H. Tochio, M. Wälchli, M. Shirakawa, K. Kikuchi, *J. Am. Chem. Soc.* **2008**, *130*, 794–795.
57. X. Yue, Z. Wang, L. Zhu, Y. Wang, C. Qian, Y. Ma, D. O. Kiesewetter, G. Niu, X. Chen, *Mol. Pharmaceutics* **2014**, *11*, 4208−4217.
58. H. M. Faas, J. L. Krupa, A. J. Taylor, F. Zamberlan, C. J. Philp, H. E. L. Williams, S. R. Johnson, G. E. Pavlovskaya, N. R. Thomas, T. Meersmann, *Contrast Media Mol. Imaging* **2019**, 4826520.
59. S. Mizukami, R. Takikawa, F. Sugihara, M. Shirakawa, K. Kikuchi, *Angew. Chem. Int. Ed.* **2009**, *48*, 3641–3643.
60. S. Mizukami, H. Matsushita, R. Takikawa, F. Sugihara, M. Shirakawa, K. Kikuchi, *Chem. Sci.* **2011**, *2*, 1151–1155.
61. A. Keliris, I. Mamedov, G. E. Hagberg, N. K. Logothetis, K. Scheffler, J. Engelmann, *Contrast Media Mol. Imaging* **2012**, 7, 478–483.
62. P. Harvey, K. H. Chalmers, E. De Luca, A. Mishra, D. Parker, *Chem. Eur. J.* **2012**, *18*, 8748–8757.
63. H. Matsushita, S. Mizukami, Y. Mori, F. Sugihara, M. Shirakawa, Y. Yoshioka, K. Kikuchi, *ChemBioChem* **2012**, *13*, 1579–1583.
64. J.-X. Yu, V. D. Kodibagkar, L. Liu, Z. Zhang, L. Liu, J. Magnusson, Y. Liu, *Chem. Sci.* **2013**, *4*, 2132–2142.
65. G. A. Smith, R. T. Hesketh, J. C. Metcalfe, J. Feeney, P. G. Morris, *Proc. Nat. Acad. Sci.* **1983**, *80*, 7178–7182.
66. A. Bar-Shir, A. A. Gilad, K. W. Y. Chan, G. Liu, J. W. M. Bulte, M. T. McMahon, *J. Am. Chem. Soc.* **2013**, *135*, 12164–12167.
67. A. Bar-Shir, N. N. Yadav, A. A. Gilad, P. C. M. van Zijl, M. T. McMahon, J. W. M. Bulte, *J. Am. Chem. Soc.* **2015**, *137*, 78−81.
68. Q. Peng, Y. Yuan, H. Zhang, S. Bo, Y. Li, S. Chen, Z. Yang, X. Zhou, Z.-X. Jian, *Org. Biomol. Chem.* **2017**, *15*, 6441–6446.
69. T. Nakamura, H. Matsushita, F. Sugihara, Y. Yoshioka, S. Mizukami, K. Kikuchi, *Angew. Chem. Int. Ed.* **2015**, *54*, 1007–1010.
70. M. Zheng, Y. Wang, H. Shi, Y. Hu, L. Feng, Z. Luo, M. Zhou, J. He, Z. Zhou, Y. Zhang, D. Ye, *ACS Nano* **2016**, *10*, 10075–10085.
71. A. Li, X. Tang, X. Gong, H. Chen, H. Lin, J. Gao, *Chem. Commun.* **2019**, *55*, 12455–12458.
72. J. S. Enriquez, M. Yu, B. S. Bouley, D. Xie, E. L. Que, *Dalton Trans.* **2018**, *47*, 15024–15030.
73. D. Xie, S. Kim, V. Kohli, A. Banerjee, M. Yu, J. S. Enriquez, J. J. Luci, E. L. Que, *Inorg. Chem.* **2017**, *56*, 6429−6437.
74. R. T. Kadakia, D. Xie, D. Martinez Jr, M. Yu, E. L. Que, *Chem. Commun.* **2019**, *55*, 8860–8863.
75. H. Gan, A. G. Oliver, B. D. Smith, *Chem. Commun.* **2013**, *49*, 5070–5072.
76. A. J. Plaunt, K. J. Clear, B. D. Smith, *Chem. Commun.* **2014**, *50*, 10499–10501.

77. M. Srinivas, A. Heerschap, E. T. Ahrens, C. G. Figdor, J. M. de Vries, *Trends Biotechnol.* **2010**, *28*, 363–370.

78. A. Gálisová, V. Herynek, E. Swider, E. Sticová, A. Patiková, L. Kosinová, J. Kříž, M. Hájek, M. Srinivas, D. Jirák, *Mol. Imaging Biol.* **2019**, *21*, 454–464.

79. V. Herynek, A. Gálisová, M. Srinivas, E. A. W. van Dinther, L. Kosinová, J. Růžička, M. Jiratová, J. Kříž, D. Jirák, *Biol. Procedures Online* **2017**, 19.

80. F. D. Hockett, K. D. Wallace, A. H. Schmieder, S. D. Caruthers, C. T. Pham, S. A. Wickline, G. M. Lanza, *IEEE Trans. Med. Imaging* **2011**, *30*, 22–27.

81. L. Hu, F. D. Hockett, J. Chen, L. Zhang, S. D. Caruthers, G. M. Lanza, S. A. Wickline, *J. Magn. Reson. Imaging* **2011**, *34*, 245–252.

82. C. H. Choi, S. M. Hong, Y. Ha, N. J. Shah, *J. Magn. Reson.* **2017**, *279*, 11–15.

83. P. Villa-Valverde, I. Rodriguez, D. Padro, M. Benito, C. E. Garrido-Salmon, J. Ruiz-Cabello, *Magn. Reson. Mater. Phys. Biol. Med.* **2019**, *32*, 79–87.

84. S. Waiczies, J. M. Millward, L. Starke, P. R. Delgado, T. Huelnhagen, C. Prinz, D. Marek, D. Wecker, R. Wissmann, S. P. Koch, P. Boehm-Sturm, H. Waiczies, T. Niendorf, A. Pohlmann, *Sci. Rep.* **2017**, *7*, 9808.

85. Y. Ji, H. Waiczies, L. Winter, P. Neumanova, D. Hofmann, J. Rieger, R. Mekle, S. Waiczies, T. Niendorf, *NMR Biomed.* **2015**, *28*, 726–737.

86. M. Wolters, S. G. Mohades, T. M. Hackeng, M. J. Post, M. E. Kooi, W. H. Backes, *Invest. Radiol.* **2013**, *48*, 341–350.

87. K. C. Partlow, J. J. Chen, J. A. Brant, A. M. Neubauer, T. E. Meyerrose, M. H. Creer, J. A. Nolta, S. D. Caruthers, G. M. Lanza, S. A. Wickline, *FASEB J.* **2007**, *21*, 1647–1654.

88. M. Srinivas, F. Bonetto, J. Tel, G. Schreibelt, J. Cruz, A. Heerschap, C. Figdor, J. de Vries, *Proceed. Int. Soc. Magn. Reson. Med.* (20th ISMRM Meeting, Melbourne, Australia, 2012), No. 4370.

89. H. Amiri, M. Srinivas, A. Veltien, M. J. van Uden, I. J. de Vries, A. Heerschap, *Eur. Radiol.* **2015**, *25*, 726–735.

90. F. Bonetto, M. Srinivas, A. Heerschap, R. Mailliard, E. T. Ahrens, C. G. Figdor, I. J. de Vries, *Int. J. Cancer* **2011**, *129*, 365–373.

9

Iron Oxide Nanoparticles for Bio-Imaging

Carlos F. G. C. Geraldes [1] *and Marie Hélène Delville* [2]

[1]Department of Life Sciences, Coimbra Chemistry Center and CIBIT/ICNAS,
University of Coimbra, PT-3000–456 Coimbra, Portugal
<geraldes@uc.pt>

[2]CNRS, Univ. Bordeaux, Bordeaux INP, ICMCB, UMR 5026,
87 avenue du Dr. A. Schweitzer, Pessac, F-33608, France
<marie-helene.delville@icmcb.cnrs.fr>

Abstract: Iron oxide nanoparticles (IONPs) have been studied extensively and used as platforms for bio-imaging applications. This is the result of their strong Magnetic Resonance Imaging (MRI) contrast enhancement effects which brought them to clinical use, their recent development as Magnetic Particle Imaging (MPI) probes and their versatility for multimodality imaging applications. In this chapter we first describe their main synthetic methodologies, their characterization techniques and the physico-chemical properties, *in vivo* biodistribution, excretion, toxicity and degradation processes that are at the basis of their imaging applications. The contrast mechanisms used by IONPs in MRI and MPI are described, and are illustrated by typical examples of their use for *in vivo* pre-clinical single modality and multimodality molecular imaging applications. Perspectives on their use in theranostic and potential clinical developments are also discussed.

Keywords: bio-imaging · iron oxide nanoparticles · magnetic particle imaging · magnetic resonance imaging · multimodal imaging

1. INTRODUCTION

Over the past decades, the progress made in science and technology has led to the development of novel non-invasive biomedical imaging modalities, such as X-ray computed tomography (CT), magnetic resonance imaging (MRI), optical fluorescence imaging (OI), positron emission tomography (PET), single-photon emission-computed tomography (SPECT), ultrasound (US) and photoacoustic imaging (PAI). The high sensitivity and resolution of these techniques facilitated high quality preclinical and clinical research in the domain of molecular imaging and led to enormous progress in the understanding of biological processes as well as the detection of diseases [1, 2]. Imaging agents have been introduced to overcome instrumental limitations in the different imaging techniques, amongst which are iron oxide magnetic nanoparticles (IONPs) [3]. Besides many applications in technology, such as magnetic storage media and applications in bio-sensing, medicine, such as cell separation, targeted drug delivery, and hyperthermia, IONPs have been prominently used as platforms for contrast agents (CAs) in MRI and magnetic particle imaging (MPI) [4–10]. This is due to the possibility of controlling their size, composition, surface coating and biological functionalization to direct them to specific biological targets *in vivo*. Furthermore, their magnetic parameters, such as saturation magnetization (M_s) and magnetic anisotropic constant (K_A) that affect their MRI contrast and MPI signal effects can be optimized. They can also be used as flexible platforms for multi-modal imaging applications, such as MRI-MPI, MRI-OI, and MRI-PET/SPECT, combining the advantages of each of the imaging modalities to optimize the accuracy of the

generated images. For *in vivo* applications, the IONPs should have high M_S values, a narrow particle size distribution with an average size smaller than 100 nm, with a non-toxic and biocompatible surface coating [4].

In this chapter we start by describing: (a) the principles for the design of IONPs for bio-imaging applications; (b) the chemical routes for their synthesis; (c) the physical techniques used for their basic characterization; (d) the physico-chemical properties required to optimize their efficacy in the various imaging modalities; and (e) their basic *in vivo* biodistribution, excretion, toxicity, and degradation issues. Thereafter, we discuss the physical basis for the contrast effects of IONPs on MRI and MPI imaging modalities, their advantages and disadvantages, and describe some *in vivo* preclinical applications in the area of cell targeting, molecular imaging, as well as clinical applications. Finally, we describe some examples of such applications using IONPs-based platforms for multimodal imaging, particularly with MRI-PET/SPECT combinations.

2. DESIGN AND CHARACTERIZATION OF IRON OXIDE NANOPARTICLES

2.1. Design of Iron Oxide Nanoparticles

In the frame of bio-medical imaging applications, the most widespread nanoparticles (NPs) are the ferrous ferrite magnetite (Fe_3O_4) and its oxidized equivalent the maghemite (γ-Fe_2O_3). They have been the object of much attention for more than 50 years [11] and even more since the advent of the nanoworld. Not only their size control but also their shape and surface design are required to obtain the best from NPs, such as MRI contrast and MPI signal. This is why many syntheses have been designed and developed to exercise as much control as possible on these NPs (mean size and size distribution, crystallinity, purity, which have a strong influence on not only their biocompatibility but also the performance of the intrinsic magnetic properties).

2.2. Synthetic Methods

The many methods found in the literature to generate IONPs can be sorted in two classes, those performed in aqueous media and those performed in organic solvents. The most investigated synthetic routes, when bio-applications are concerned, remain those taking place in aqueous media due to the high availability of the lab setup and the low cost of the reagents, the overall straightforwardness of the process scale-up, and the associated low toxicity of these routes. Conventionally, the aqueous process consists in the alkaline precipitation of an adequate solution of Fe(II) and Fe(III) under inert atmosphere, the so-called co-precipitation route, which will generate magnetite NPs according to Equation (1).

$$2\,Fe^{3+} + Fe^{2+} + 8\,OH^- \rightarrow Fe_3O_4 + 4\,H_2O \tag{1}$$
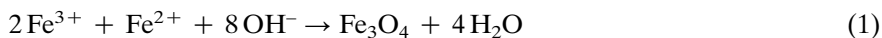
The size, the shape, and the chemical composition of the NPs strongly depend on many parameters: the iron concentration, the Fe^{2+}/Fe^{3+} ratio, the nature of salt precursors (e.g., chlorides, sulfates, nitrates), the reaction temperature, the pH, ionic strength of the media [12–17], and the aging time [18]. Following this precipitation process, an ageing step is taking place and caution should be developed to avoid irretrievable aggregation of the IONPs. To do so, two choices are possible: (i) heat the colloidal dispersion in the presence of surfactant which will provide the required stabilization of the ferrofluid in a nonpolar solvent [19] or (ii) treat the same suspension with either a very concentrated acid or base solution to provide an electrostatic stabilization in water [20, 21].

This approach by co-precipitation requires however, improvements in terms of control of both the size of the particles and their size distribution [12]. The IONPs prepared in this way tend to be somewhat polydisperse, signifying that nucleation and crystal growth are more or less concomitant all along the reaction process. From the time when the model developed by La Mer and Dinegar was published [22], based on the separation of the nucleation period and the crystal growth one, it is admitted that a swift nucleation burst followed by a subsequent slow and controlled growth is decisive to provide monodisperse particles. This can be performed by dilution of the reagents or by addition of organic species to modulate the reactivity of water. The effect of organic ions for example on the formation of metal oxides can be rationalized considering two competing mechanisms: (i) an early chelation of the metal ions which prevents the nucleation and leads to large particles because the number of nuclei formed in solution is low and the overall system is controlled by the particle growth, (ii) or a post-adsorption of additives/surfactants on the nuclei and the growing crystals to inhibit their growth and favor the formation of small particles. For example, size-controlled maghemite NPs were prepared starting with the formation of magnetite in the presence of trisodium citrate, in an alkaline medium, and the subsequent oxidation by $Fe(NO_3)_3$ at 90 °C for 30 min [21]. The particle size increased from 2 to 8 nm by varying the molar ratio in citrate and metal ions (Fe^{2+} and Fe^{3+}). The role of more than a few organic anions, such as carboxylate and hydroxy carboxylate ions, on the formation of iron oxides or oxyhydroxides was extensively studied [23–25].

Recent advances in the co-precipitation method led to a scale-up of the process with continuous monitoring of the magnetization [26]. An interesting alternative to these conventional routes to prepare these hydrophilic magnetite NPs in one step in aqueous media relies on the hydrothermal process. Recently, this rapid and easily scalable hydrothermal synthesis of NPs has been reported and exploited [27–29].

The thermal decomposition of organometallic compounds generally yields NPs which are more crystalline as well as more monodisperse and in the diameter range of 5–30 nm. This method has been widely used to produce Fe or Fe-alloy NPs since the sixties. From now on, it is also applied to iron oxides [30] and various approaches and improvements have since been developed. Iron carbonyl, acetate, acetylacetonate, carboxylate, cupferronate, and chloride are some of the most commonly used precursors as long as the thermal decomposition in

high-boiling organic solvents is used (e.g., *o*-dichlorobenzene, oleylamine, octyl ether) [31–34]. Long chain organic acids or amines play a role of stabilizing agent, providing hydrophobic NPs which require an additional step to make them hydrophilic. Still, NPs when produced in 2-pyrrolidone, which acts as both stabilizing agent and liquid medium for the thermal decomposition of $Fe(acac)_3$, are directly water-dispersible [35, 36]. If the oxidation number of iron in the precursor is zero, as for $Fe(CO)_5$, the thermal decomposition essentially leads to amorphous iron NPs [12, 37]. These NPs formed in such a way are very sensitive and readily oxidized in air [38] or by other oxidation reagents. γ-Fe_2O_3 NPs can also be directly obtained in such a reaction medium by introducing a mild oxidizing agent (e.g., trimethylamine oxide) into the reaction solution [39]. When the iron in the other precursors is "pre-oxidized", the iron oxide NPs are then obtained right away [30]. Their size and morphology are influenced by the nature and relative amounts of iron precursors, solvents, and stabilizing agents, as well as the reaction conditions, i.e., the temperature and the reaction time. This thermal decomposition process also gives rise to a variety of ferrite NPs by playing with the organometallic precursors of metals other than Fe leading to the development of FeM (finite element method) alloy NPs. The later may be oxidized simultaneously or successively [32]. Other strategies such as the polyol synthesis were also developed and provide particles with very different structures and morphologies in the nanometer size range [4, 40]. Over the past two decades, the microwave-assisted synthesis was also applied to generate NPs reducing the synthesis time from hours to minutes, and increasing both the product yield and material properties as well as the experiments' reproducibility as compared to a conventional heating [41, 42]. The preparation routes for transition-metal oxide NPs, and especially iron oxide NPs, rely on non-hydrolytic pathways, in non-aqueous solvents [43]. These syntheses give a good control on the structure, size, and morphology of the formed NPs.

However, besides the required rigorous and strong control of the synthetic conditions, including oxygen-free atmosphere, long reaction time, and high reaction temperatures, there are potential issues from a bio-application point of view with this thermal process: the use of detrimental stabilizing agents that may decrease the efficiency of the NPs subsequent surface modifications and the use of toxic solvents which may be detrimental for the biocompatibility of the NPs. Moreover, these stabilizing agents, which are most of the time surfactants that bind to the NP surface, make them hydrophobic, so that additional steps are needed to transfer and stabilize these particles in an aqueous medium for a subsequent use in biomedical applications. This transfer to water may suffer from irreversible aggregation of the particles even if methods to avoid this outcome have been developed [44].

2.3. Physical Characterization Techniques

There are many physical techniques used to characterize the physicochemical properties of NPs. X-ray diffraction (XRD) with conventional and synchrotron

radiation sources is one of them. The XRD pattern of a crystalline phase gives rise to the reflections (peaks) of different intensities which give a fingerprint of the crystalline structure of the NP. XRD also provides information about the crystal size and perfection, and its structural parameters (unit cell edge lengths). The average crystal size can be calculated from the XRD line broadening based on the Scherrer formula (Equation (2a)) which describes the corrected width of an XRD line at an angle θ as a function of the average size of the coherently scattering domain *D* perpendicular to the *hkl* plane:

$$D = \frac{K\lambda}{\beta \, cos \, \theta} \tag{2a}$$

where β is defined in Equation (2b)

$$\beta = \sqrt{B^2 + b^2} \tag{2b}$$

β is the true width of the X-ray peak at its half height and *K* is a shape factor (0.89 for a sphere). The true width can be corrected from the instrumental width with Equation (2b) where *B* and *b* are the widths at half height of the most intense peak of the sample and of a well-crystallized sample reference. Magnetic NPs used in biomedical applications are generally monocrystalline and the size of the scattering domain *D* usually corresponds in a first approximation to the NPs size. However, the Scherrer formula does not necessarily take into account passivation layers or surface structural defects or surface strains due to the synthesis method used or to the post-synthesis oxidation processes. All these surface defects also participate in the enlargement of the peaks and the true crystal size is then underestimated when this parameter is neglected. The size of the magnetic NPs and their size distribution are then estimated using other techniques such as Mössbauer spectroscopy [45–48], extended X-ray absorption fine structure, infrared spectroscopy, transmission electron microscopy (TEM), photon correlation spectroscopy (PCS) or also alternate current and direct current magnetometry.

   These techniques may reveal features not visible by XRD which are usually attributed to the defects and the formation of a less ordered layer on the particle surface. In some cases, the stabilizing agent is also reported influencing the structure of the particles surface and the magnetization values [49]. Because of their limited number of cubic cell units, NPs can be considered as less-ordered systems which are neither completely crystalline nor completely amorphous, explaining why an exact determination of their size often requires the combination of different analytical techniques. Additionally, in certain cases, XRD on its own is not able to distinguish ferrites such as magnetite and maghemite, which both have the same inverse spinel structure, so that neutron diffraction is used to proceed to the differentiation. Infrared [50] and Raman [51] spectroscopies, electron diffraction, and high resolution electron microscopy (HR-TEM) also provide additional useful information. Eventually, X-ray spectroscopy (XPS) can also be used to provide information on the oxidation state of iron in small particles because

both the ferrous and ferric ions can be detected and quantified on the spectra [52].

The overall size of the particle core is determined by TEM (crystalline and amorphous parts) which also provides details on the size distribution and the shape of the particles as well as a weighted mean value, when performed on a statistically significant number of NPs provided the sample preparation does not affect the results by inducing inadequate NPs aggregation on the grid. HR-TEM gives access to the atomic arrangement in the crystals. It is then used to study lattice fringe, lattice vacancies and defects, the disorder and thickness of the surface layer [53]. Small-angle neutron scattering is also used to determine the size, polydispersity, shape (shape ratio), and structure of NPs [54]. Infrared spectra and diffuse reflectance IR spectroscopies can be used not only to provide additional structural characterizations on maghemite by analysis of different vibrational modes [50] but also on the coating at the periphery of the NP (shell, corona, ligands, etc.). Raman spectroscopy is a complementary technique useful to get insights into the chemical composition and structure of magnetic fluids based on ferrites [51], as well as to give suitable information regarding the structure and bonding of the molecules adsorbed at the surface [55].

As far as the characterization of NPs in solution is required, PCS and zeta potential (ζ-potential) measurements are very useful. PCS, also termed dynamic light scattering (DLS) or quasi-elastic light scattering (QLS), is a classical technique which determines the average size of NPs dispersed in a liquid phase, their diffusion coefficient in solution and then the hydrodynamic radius of a corresponding sphere, and the corresponding size distribution [56]. A colloidal fluid stability characterized by its ζ-potential, (the electrical potential at the shear plane or slipping plane), depends on the surface charge density, the shear plane location, and the surface structure and it is a very important parameter with respect to many features of the dispersed materials [57, 58].

The comparison of the variation of the ζ-potential with the pH of surface-modified NPs with that of pristine NPs is useful to check their isoelectric point (IEP) and to investigate the stability of these dispersions. The comparison of IEPs can help in understanding the nature of the surface site groups and on the effectiveness and quality of the surface modification [59, 60].

2.4.   Physical Properties Relevant for Bio-imaging

In the specific case of IONPs, *the* physical property which prevails for bio-imaging is their magnetism. Maghemite as an example is ferrimagnetic at ambient temperature, unstable at high temperatures, and it drops its magnetic susceptibility with time [61]. For sizes smaller than 10 nm, the NPs become superparamagnetic at ambient temperature, with the spins associated to the iron ions present in a single magnetic domain corresponding to the size of the NP. Then, their thermal energy is comparable to the energy needed for the spins to flip their direction in an applied magnetic field, with a rapid randomization of the magnetic dipoles. Such NPs are called superparamagnetic because their magnetization

appears to be zero on average with no external field but becomes magnetized in its presence, similarly to a paramagnet. This means that it is possible to make an analogy between the behavior of the small magnetic moment of a single paramagnetic atom and that of the much larger magnetic moment of a nanosized magnetic particle which is the result of the coupling of many atomic spins and forms monodomains [62]. Surface effects and defects as well as chemical surface modifications have a strong influence on the magnetic properties of the IONPs; they induce a net magnetization decrease with increasing temperature [63] and coercivity of the oxide nanoparticles [64].

2.5. *In Vivo* Distribution, Toxicity, and Degradation

Iron oxide NPs have been comprehensively used over the past two decades, not only as operative bio-imaging contrast agents but also as nanocarriers of various types of bio-molecules such as drugs, nucleic acids, and peptides for a controlled delivery to specific organs, tumors and tissues. Their most relevant and important criteria to be tuned to control their *in vivo* pharmacokinetics and biodistribution are their size and their size distribution, their charge, their surface coating (molecules or polymers), and their plasma protein adsorption. All these parameters have been reviewed in excellent reviews which also take into account the short- and long-term side effects of the IONPs in light of both the biological barriers in the body and the NP design [4, 65]. Liver uptake of IONPs is the most effective elimination pathway of these nanoparticles, even when the IONPs are tuned for specific targeting of tissues or organs. It is in this organ that mechanisms involved in intracellular degradation of IONPs similar to those related to ferritin are assumed to take place. In the case of ferritin, the protein shell first is dissolved by lysosomal proteases; the internal IONPs are then released and rapidly dissolved in the acidic environment of the lysosomes [66]. After their degradation, the excess of iron in the organs needs to be regulated through the innate clearance mechanisms of the body [67] or it would otherwise induce acute inflammation and toxicity through reactive oxygen species generation [68–71].

Many groups worldwide have been working to contribute to the IONPs safety so that nowadays they can be used widely in bio-medical applications since several years even if in limited domains, thanks to the increased efficiency of the new strategies of functionalization and coating developed to increase their biocompatibility, colloidal stability, and to avoid phagocytosis by the reticuloendothelial system. IONPs and superparamagnetic IONPs have been and are still involved in numerous clinical studies; some of them approved by the U. S. Food and Drug Administration in iron replacement therapies, as MRI contrast agents in imaging and for cancer treatment by magnetic hyperthermia, to treat anemia due to chronic kidney disease and so on [68, 72–76].

3.   IRON OXIDE NANOPARTICLES FOR MAGNETIC RESONANCE IMAGING

3.1.   Effect of Iron Oxide Nanoparticles on Magnetic Resonance Imaging Contrast Enhancement

MRI is one of the most powerful clinical imaging tools available, due to its unique properties. Despite its relatively low sensitivity, it is non-invasive, free of ionizing radiation, and provides tomographic images with large penetration depth, outstanding spatial resolution (maximum 10 μm in preclinical systems and 50 μm in clinical scanners) and high soft tissue image contrast. This contrast results mainly from differences in NMR intensities of abundant tissue water protons, which derive mostly from their longitudinal ($R_1 = 1/T_1$) and transverse ($R_2 = 1/T_2$) nuclear spin relaxation rates [77]. The image contrast between normal and diseased tissues can be enhanced by applying contrast agents (CAs) that can selectively increase these parameters [77–79]. The efficacy of CAs is given by their relaxivity, the longitudinal or transverse relaxation rate enhancement for a solution containing 1 mM of magnetic metal ions (r_1 and r_2, respectively, in $mM^{-1}\ s^{-1}$).

Presently, the clinically used CAs are based on highly stable paramagnetic Gd^{3+}-containing chelates. Because they have $r_1 > r_2$, they lead to bright areas in T_1-weighted (T_{1w}) images, and are called positive or T_1 CAs. T_2 or negative CAs have $r_2/r_1 > 2$, giving rise to dark areas in T_{2w} or T_{2w}^* images, and consist of superparamagnetic IONPs of size 1–150 mm [77–79]. The most common ones are ultrasmall superparamagnetic iron oxides (USPIO, 5–40 nm, with only one nanocrystal in the core), and superparamagnetic iron oxides (SPIO, 60–150 nm, with several nanocrystals in the core). These NPs have been thoroughly investigated as MRI contrast agents and some were approved for clinical use in Europe [4].

The r_1 and r_2 values of superparamagnetic NPs have inner-sphere (IS) and outer-sphere (OS) contributions. The IS contribution arises from the exchange of the protons of water molecules directly coordinated to the paramagnetic $Fe^{2+/3+}$ ions on the surface of the NPs with bulk water. The r_{1IS} and r_{2IS} are often negligible for small NPs, with low surface-to-volume ratios [4]. The OS mechanism has usually much larger relaxivity contributions, as it results from the diffusion of the water molecules in the magnetic field inhomogeneities generated by the magnetized NPs in their vicinity. It is governed by the volume fraction of the superparamagnetic particles (v), the diffusion correlation time ($\tau_D = d^2/4D$, where d is the diameter of the particle and D is the diffusion coefficient), and the magnetization of the NP ($M = M$s) at the B_0 value of the clinical MRI scanner (Figure 1).

In a colloidal dispersion of superparamagnetic NPs in the presence of a magnetic field, the return of the magnetization to equilibrium by T_1 and T_2 relaxation is determined by two different mechanisms, known as the Néel and Brownian relaxation processes, with relaxation times τ_N and τ_B, respectively (see Figure 2 below) [4]. The magnetic energy of a NP single domain varies with the orientation of its magnetization vector (relative to the crystallographic directions). The directions
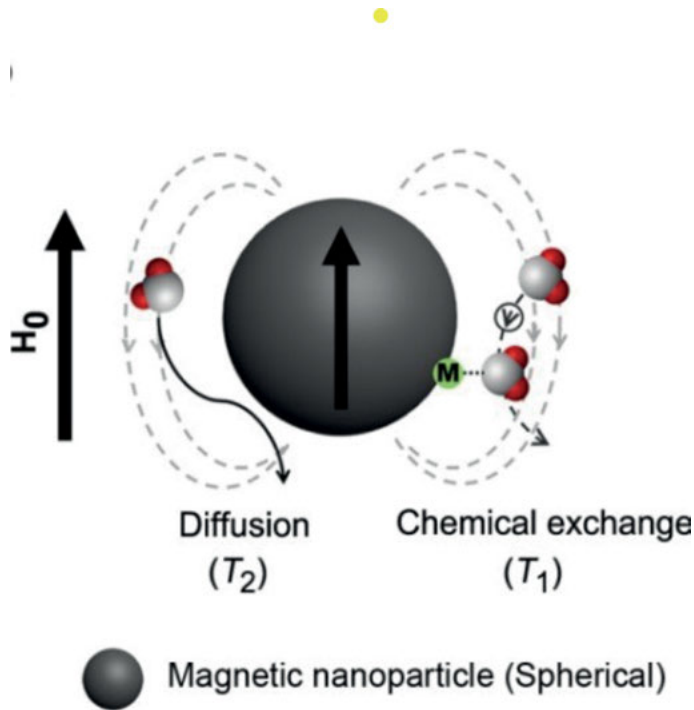
Figure 1. Illustration of the inner sphere and outer sphere contributions to the T_2 relaxation of water protons induced by a magnetic nanoparticle.

that minimize this energy are known as anisotropy directions or easy axis and thus, the energy increases with the tilt angle θ between the magnetization vector and the easy directions. The total amplitude of this variation is the anisotropic energy (E_A) and it is proportional to the crystal volume V (Equation 3):

$$E_A = K_A V \tag{3}$$

where K_A is the anisotropy constant. At high anisotropy, the magnetization is locked in the easy axes, according to Boltzman's law which favors the direction of the lower E_A. The Néel relaxation describes the return to equilibrium of the magnetization of each of the NPs after a perturbation that tilts it away from the direction of its easy axis, and thus it defines the fluctuations that arise from the jumps of the magnetization between different easy directions (Figure 2). The Néel relaxation time is a function of E_A according to the Arrhenius law (Equation 4),

$$\tau_N = \tau_0 \exp(E_A/k_B T) = \tau_0 \exp(K_A V/k_B T) \tag{4}$$

where k_B is the Boltzman constant and T is the absolute temperature. The pre-exponential factor (τ_0) depends on E_A. For USPIO at room temperature, with a
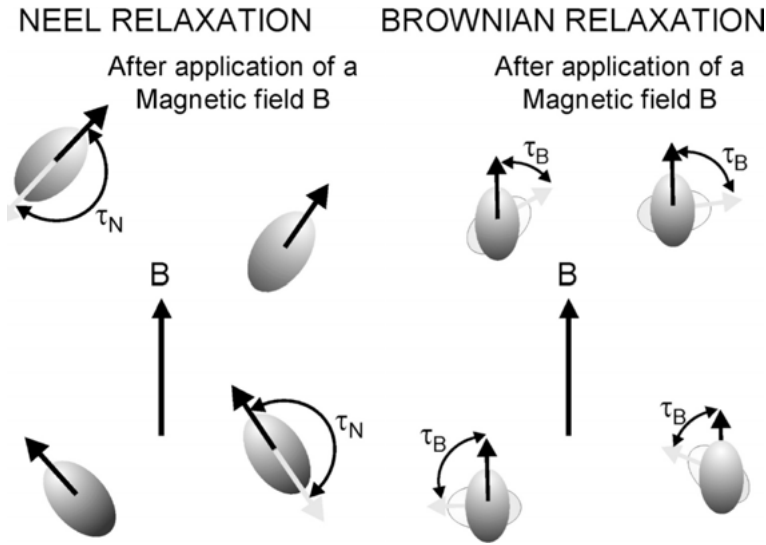
Figure 2. Illustration of the two components of the magnetic relaxation of a magnetic fluid. Reproduced from ref. [4], with permission from the American Chemical Society, copyright 2008.

radius lower than 4 nm, the low anisotropy condition applies. Thus, for small E_A and high T, $E_A \ll kT$, and $\tau_N \approx \tau_0$ decreases as E_A increases. However, large NPs, such as SPIO, with many crystal domains, may have very high anisotropy energy. With $E_A \gg kT$, $\tau_N \approx \exp(E_A/kT)$ increases very fast with increasing E_A.

The second process is the Brownian relaxation, defined by the relaxation time τ_B (Figure 2), which characterizes the viscous rotation of the particle (Equation 5),

$$\tau_B = 3 V_H \eta / k_B T \tag{5}$$

where η is the viscosity of the aqueous dispersion and V_H is the hydrodynamic volume.

The global magnetic relaxation rate of the colloid is the sum of the Néel and Brownian relaxation rates, $\tau^{-1} = \tau_N^{-1} + \tau_B^{-1}$, where τ is the global magnetic relaxation time. For large particles, $\tau_B \ll \tau_N$, because τ_B is proportional to V and τ_N increases exponentially with V. This fast rotation process becomes dominant and the corresponding fast magnetic relaxation allows the solution of the NPs to be always at thermodynamic equilibrium. This is characteristic of a superparamagnetic material, where the magnetization variation with the external magnetic field (H) is proportional to a Langevin function and leads to a characteristic magnetization curve $M(H)$ which saturates at high H, defining the saturation magnetization M_S [80].

In these systems, r_1 and r_2 can be described by Freed's model for paramagnetic systems using the diffusion correlation time (τ_D) and considering the electron

spin longitudinal relaxation time τ_{S1} equal to the Néel relaxation time τ_N. When $\tau_D \ll \tau_N$, Freed's equations reduce to the earlier equations of Ayant. The corresponding theory and equations have been described in the literature [4].

The magnetization of the superparamagnetic IONPs reaches its saturation value M_S at $B_0 \leq 0.5\ T$, which is at the lower limit for the clinical MRI scanners commonly used. Therefore, their R_2 is usually independent of B_0. For small spherical NPs, where $\tau_D \ll 1/\Delta\omega$ (with $1/\Delta\omega = 3/(\gamma\mu_0 M_S)$) the motional narrowing regime (MAR) applies, and R_2 and R_2^* are linearly dependent on τ_D^2, M_S^2, d^2 and V, (e.g., Equation 6),

$$R_2 = 16\pi\gamma^2\mu_0^2 V\ M_S^2\tau_D^2 d^2/[405\ (1+L/d)] \tag{6}$$

where M_S is the saturation magnetization of the NP with diameter d and volume V, γ is the gyromagnetic factor of the proton, $\mu_0 = 4\pi\ 10^{-7}$ (in T.m.A^{-1}) is the magnetic susceptibility of vacuum and L is the thickness of the impermeable layer around the superparamagnetic core [4, 7, 80]. For clusters of NPs and hybrids, M_S and V refer to the whole NP, and an intra-aggregate volume fraction, Φ_{intra}, is defined in order to obtain a corrected relaxivity $r_2' = r_2 \cdot \Phi_{intra}$. A linear correlation between r_2'/M_S^2 and d^2 has been observed, according to Equation (6) for a series of nanomaterials obeying the MAR regime [80]. The proportionality of R_2 to M_S^2 predicts that smaller NPs, with higher surface to volume ratios, will have a reduced M_S value due to a large contribution of paramagnetic canted magnetic spin states on their surface, reducing the obtained relaxivity [5]. For large NPs, R_2^* and R_2 reach a very large maximum, but while R_2^* remains constant as a function of τ_D, R_2 decreases from that maximum [80].

Besides the size increase and aggregation, the relaxivities of IONPs can be enhanced by increasing M_S through the introduction of transition metal dopants in ferrites (MFe_2O_4, M = Ni, Co, Mn) and by changing their shape, such as octopods or nanoplates [8, 9].

3.2.   Preclinical and Clinical Applications

Dextran-stabilized USPIO NPs have been clinically approved, such a Ferumoxtran-10 (Combidex, Sinerem) [4, 78]. USPIOs are clinically used in lymph node imaging, due to the capacity of these very small NPs to extravasate from the blood vessels into interstitial spaces and to be transported to normal lymph nodes through the lymphatic vessels, while these same nodes that have been invaded by malignant cells cannot take up the NPs by phagocytosis of their macrophages, and thus do not become dark in T_{2w} images [81]. USPIOs are also used in bone marrow imaging, perfusion imaging, and MR angiography [9, 82, 83].

Several dextran-stabilized SPIO NP formulations have been clinically approved, including Ferucarbotran (Resovist or Supravist) and Ferumoxides (Feridex or Endorem) [4, 78, 84], but many of them are no more on the market due to low use in clinics. They are the most commonly used T_2 CAs due to their very high r_2 and (r_2/r_1) $\approx$ 4–23 (at 0.47 T). Their most common clinical applications

are in liver diseases, such as primary liver tumors or liver metastasis because SPIO are selectively taken up by the Kupffer cells in the normal liver tissue, which are absent in these pathological tissues. A strong negative contrast is observed between normal and abnormal tissues in T_{2w} images, showing the pathology as a bright region in the image. However, their fast liver uptake leads to a limited blood lifetime, which limits their use for imaging molecular and biological functions in *in vivo* MRI [9, 82–84]. Their large r_2 values can also hamper the interpretation of T_{2w} images due to the difficulty in distinguishing the CA-induced darkening from partial-volume artifacts, motion ones, and tissue inhomogeneities.

3.3. Multifunctional T_1/T_2 Magnetic Resonance Imaging Contrast Agents

The conventional single-mode use of IONPs described above either as T_1 or T_2 CAs still sometimes generates artifacts and interpretation ambiguities in MR images. To overcome these problems, T_1-T_2 dual mode CAs have been developed and used to obtain complementary T_{1w} and T_{2w} MRI images [8, 9]. These can be designed by using NPs with a single type of contrast material, or with combined T_1 and T_2 materials in the same NPs. The first type includes superparamagnetic USPIOs with appropriate size and magnetization to have low $(r_2/r_1) \approx$ 1.6–2.5 (at 0.47 T), providing T_1 and T_2 contrast, although the second is relatively weak [85].

Superparamagnetic magnetite nanoplates have also been reported with strong T_1 and T_2 contrast effects [86]. In the second type, superparamagnetic IONPs (used as T_2 materials) are tailored by incorporating a paramagnetic T_1 material (Gd^{3+} or Mn^{2+}). This material can be located (a) outside the T_2 contrasting IONPs using a core-shell approach (e.g., $Fe_3O_4@Gd_2O_3$ [87] or $Fe_3O_4@SiO_2$ with adsorbed Gd^{3+} complexes [88]) or conjugating the superparamagnetic core with a paramagnetic Gd^{3+} or Mn^{2+} complex at its surface [89]; or (b) inside it by doping the IONPs with Gd_2O_3 (GdIONPs) [90]. However, the magnetic fields generated by each contrast material disturb the relaxation process of the other, especially the strong magnetic fields generated by the IONPs T_2 materials on T_1 relaxation, resulting in signal attenuation. This effect is proportional to the inverse sixth power of the distance (d^{-6}) between the two types of materials and depends on their relative positions within the NP (Figure 3) [91]. For systems with a superparamagnetic T_2 core within a paramagnetic T_1 shell (case (a) above), the respective induced magnetic fields oppose each other strongly quenching the r_1 value, as verified experimentally by increasing the core-shell separation with a silica layer of increasing thickness [87], or by increasing the distance between the core and the pendant shell paramagnetic complexes through longer spacer groups [91]. In contrast, when the paramagnetic material resides inside the superparamagnetic iron oxide, the magnetic fields of both materials reinforce each other, strongly enhancing the r_1 value and causing a synergistic T_1-T_2 enhancement effect [90].

T_2 contrast materials T_1 contrast materials

a) T_1 images

Pre-injection   1 h

b) T_2 images

Pre-injection   1 h

c) T_1 images

Pre-injection   1 h

d) T_2 images

Pre-injection   1 h
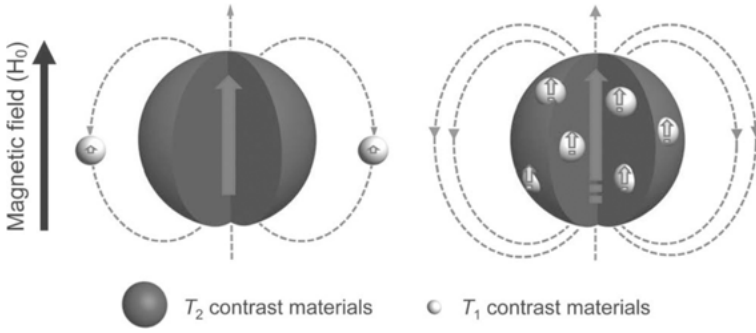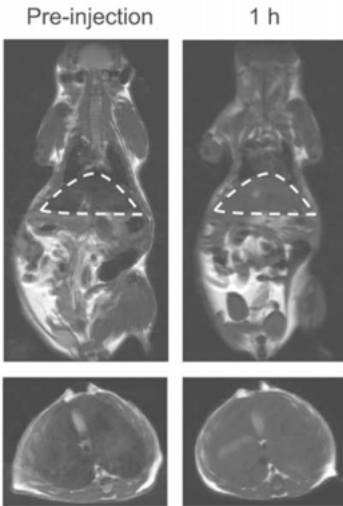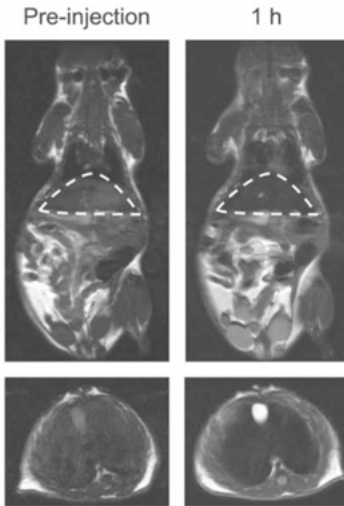
Figure 3. **Top left**: Mechanism of the reduction of the local magnetic field intensity of the T_1 contrast material when located outside the T_2 contrast material. **Top right**: Mechanism of simultaneous enhancement of the local magnetic field strengths of the T_1 and T_2 contrast materials when the first is located inside the second. (**a**) T_{1w} and (**b**) T_{2w} *in vivo* MR images of BALB/c mice (top: coronal plane, bottom: transverse plane) before and after intravenous injection of GdIONPs with a dose of 2.0 mg Fe/kg. The regions of the liver in the coronal planes were circled by white dashed lines. (**c**) T_{1w} and (**d**) T_{2w} *in vivo* MR images of nude mice orthotopically inoculated with HepG2 liver cancer cells (sagittal plane) before and after intravenous injection of Gd-IONPs with the same dose. Light grey arrows: gallbladder; dark grey arrows: liver; white dotted circles and white arrows: liver tumor. Reproduced with permission from [90]; copyright 2012, John Wiley & Sons.

These T_1-T_2 dual mode CAs improve the accuracy of the interpretation of MRI images because they show bright MRI signals ("ON" responses) in the positive T_1 mode and dark signals ("ON" responses) in the negative T_2 mode, as opposed to, e.g., Gd(DTPA) and Feridex, which do not show "ON" responses in the T_2 mode and T_1 mode, respectively. Therefore, only the dual mode CAs are able to remove T_1 and T_2 image artifacts by an "AND logic" used in MRI of small biological targets, such as in stem cell tracking, lymph nodes, small tumors, and cardiovascular plaques [8, 9, 92].

4. IRON OXIDE NANOPARTICLES FOR MAGNETIC PARTICLE IMAGING

4.1. Physical Basis of Magnetic Particle Imaging

Besides their use as MRI contrast agents described above, IONPs have recently been applied in new imaging techniques, such as magnetic particle imaging (MPI), magneto-motive ultrasound imaging (MMUS), and magneto-photoacoustic imaging (MPA). Combined with traditional imaging modalities (MPI with MRI, MMUS, and MPA with US imaging) which provide anatomical information, they can be used to map the distribution of IONPs in biological systems, as all these techniques use the same IONPs as tracers. Here we concentrate on the description of the MPI technique, which was initially developed by Gleich and Weizenecker at Philips Research in Hamburg [93]. Since then, MPI has found many preclinical and clinical imaging applications in fields like angiography, blood pool, perfusion and cancer imaging, and stem cell tracking.

The physics governing MPI is totally different from MRI and an overview of the physics, hardware and reconstruction theory of MPI can be found in the literature [93–96]. When the IONPs used in MPI (mostly SPIO NPs) are under an external magnetic field (H) their magnetic moments become aligned parallel to H, resulting in a steady-state magnetization (M). MPI relies on the non-linearity of the increase of M with H as described by the Langevin equation, until it reaches a saturation value (M_S). In response to an oscillating external magnetic field (modulation field) generated by a transmitter coil, with a drive frequency

$1f_1$, the IONPs generate a time-dependent magnetization $M(t)$ which, besides $1f_1$, includes a series of harmonic frequencies ($2f_1$, $3f_1$, etc.). It generates electromagnetic signals (S) which are detected by a receiver coil and are converted into MPI images (Figure 4a). However, when the IONPs are exposed to a strong external field, they are magnetically saturated and do not respond to the applied modulation field, with the suppression of $M(t)$ and its harmonic frequencies S (Figure 4b). Thus, the MPI signal can be acquired in a spatially selective way by applying an additional strong static gradient magnetic field (selection field) that
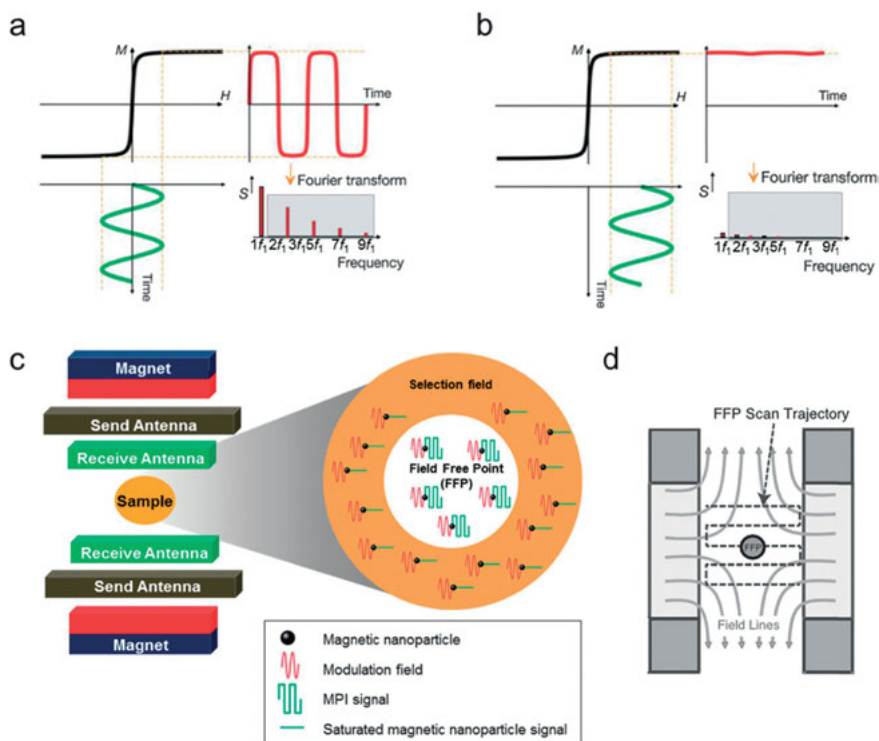
Figure 4.   Basics of magnetic particle imaging (MPI). (**a**) and (**b**) Response of the IONPs to an external magnetic field. (**a**) When the modulation field (H, green curve) with a frequency f_1 is applied, time-dependent magnetization ($M(t)$, red curve) and harmonics frequencies (S, red bars) are induced. The harmonics indicated by the grey box are used for MPI image generation. (**b**) When an additional time-independent external magnetic field (selection field) is added, the NPs are magnetically saturated and the magnetization of the nanoparticles is not changed by the modulation field, resulting in neither $M(t)$ nor S. (**c**) Schematic of the MPI instrument and the MPI signal generation. The magnet generates a selection field (orange region) that has a field-free point (FFP, white region) in the center. In addition, the sending antenna creates a modulation field to magnetize the NPs. The MPI signal produced by the IONPs located in the FFP is detected by the receiving antenna. (**d**) Illustration of FFP raster scanning. Reproduced with permission from [8]; copyright 2015, Royal Society of Chemistry.

saturates the non-linear magnetization of the IONPs in all regions except at a region in its center where it is zero, called the field-free point (FFP) (Figure 4c). Thus, the only IONPs to generate harmonics that make the MPI signal are those located in the FFP. The FFP is rapidly scanned along the whole field-of-view to create the entire MPI image by time-varying drive fields with a 25 kHz frequency (Figure 4d). As the received MPI signal occurs at the same time as the much stronger drive field, its frequency is filtered off in order not to interfere with the signal detection at the receiver coil, also filtering off the fundamental frequency of the IONPs ($1f_1$). Thus, the MPI image is obtained only from the signal harmonics.

The direct visualization of the SPIO tracers by their induced signal in MPI is the source of the many advantages of this imaging technique. Its signal is exactly proportional to the SPIOs concentration in the imaging volume, has no background tissue signal and no depth signal attenuation, similar to PET/SPECT techniques and unlike OI, US, CT, and PAI. MPI enables hotspot imaging, as opposed to the negative contrast in T_2^*-MRI using the same SPIOs. MPI has an excellent sensitivity (~ 200 nM Fe), which is similar to PET/SPECT and about 10^7 times higher than the water proton sensitivity of 7T MRI. It also does not use ionizing radiation.

Among the drawbacks of MPI are a relatively low spatial resolution and the absence of anatomical background information, which forces it to be used together with MRI, CT or US imaging. The spatial resolution of MPI (currently ~ 1 mm for each dimension in a mouse) depends only on the saturation properties of the SPIO NPs and the strength of the magnetic field gradient. While it is comparable to PET/SPECT, it is lower than CT or MRI. Besides increasing the field gradient, the resolution can be improved by optimizing the magnetization response of the NPs to the modulating field by reducing the width at half-height of the field derivative of the M(H) function of the NPs (Figure 4a). This can be done by controlling the physical properties of the NPs through chemistry, using diameters in the 20–25 nm range, low polydispersity, high magnetization, and optimized magnetic Néel/Brownian relaxation. 2D and 3D MPI techniques have also been developed [93–96].

4.2. Preclinical and Clinical Applications

Preclinical MPI scanners are available and some SPIO formulations have been approved as CAs for human studies. Many IONP-based MRI tracers have been developed, such as the commercial formulations Resovist and Sinerem, and many preclinical *in vivo* applications have been reported (Figure 5) [8, 10, 95]. The high sensitivity and quantitative nature of MPI allows the *in vivo* rodent real-time tracking of SPIO-labeled transplanted stem cells as they localize to target sites with a much higher precision than using MRI, which is very useful in the evaluation of cell therapy [97, 98]. Advanced 3D image reconstruction techniques and the use of SPIOs tailored for long circulation (and sometimes targeted) allowed the development of MPI blood pool imaging in animal models, not only for angiography applications, but also for general blood volume imaging
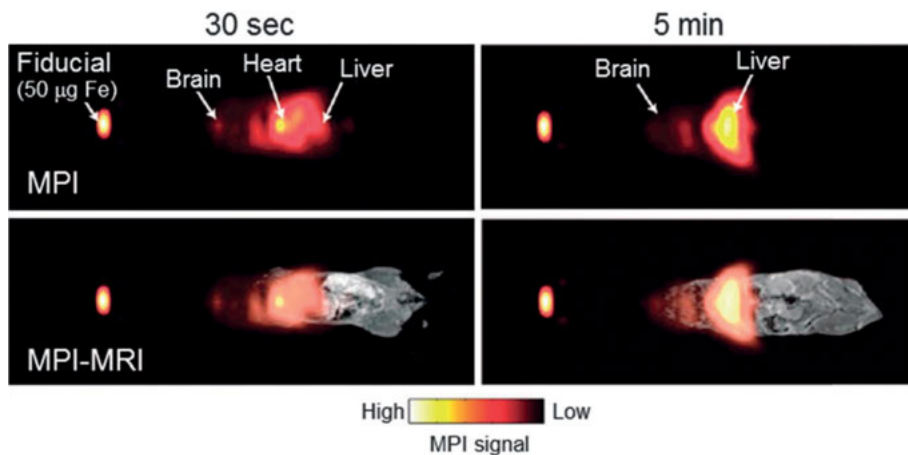
Figure 5. Full-body MPI-MRI dual-modal imaging using Resovist for an *in vivo* mouse biodistribution study. Resovist is observed in the brain, heart, and liver 30 sec after injection, followed by significant accumulation in the liver after 5 min. Reproduced with permission from [8]; copyright 2015, Royal Society of Chemistry.

studies, such as blood perfusion imaging, with applications in the diagnosis and staging of stroke and cancer [99–102].

5. IRON OXIDE NANOPARTICLES IN MULTIMODAL IMAGING

5.1. Multimodal Imaging Nanoprobes

The basic biomedical imaging modalities are applied clinically to achieve precise and sensitive detection of diseases and disorders. However, it is sometimes difficult to achieve this goal because each modality has its own advantages but also its intrinsic limitations [5–10]. A current widespread approach to overcome their specific limitations consists in combining two or more CAs into a single NP unit which can then be analyzed by these multiple techniques. This can be done either consecutively or simultaneously; it only depends on the degree of development of the hospital techniques satisfying the clinical needs and the patient comfort [6, 9, 103–127].

5.2. Examples of Iron Oxide Nanoparticles for Multimodal Imaging Involving Magnetic Resonance Imaging

Multimodal imaging nanoplatforms based on IONPs usually combine the high spatial resolution and unlimited tissue penetration with imaging modalities endowed with high sensitivity (e.g., PET, SPECT), with sensitive techniques limited

Table 1. List of the different multimodal nanoparticles and the type of techniques they are used for.

Modalities	Nanoobjects	Type	Ref.
2	Fe_3O_4@Au nanocomposite particles	MRI/CT	[138]
	Au-Fe_3O_4 Janus NPs		[139]
	QDs / SPIO and Gd^{3+} NPs	MRI/Fluorescence	[140]
	Fe_3O_4@Au	MRI/NIRF[a]	[141]
	SPIO and Cy5.5 dye		[142]
	SPIO and carbon dots and Gd^{3+}	MRI/MRI (T_1/T_2)	[143]
	See the reviews	MRI/PAT[b]	[120, 144]
	SPIO and various other agents	MRI/PET	[136, 145–148]
	SPIOs	MRI/ THMI	[149, 151]
	Magnetite and PLA microbubbles	MRI/US	[150]
	SPIO and ^{124}I	MRI/PET	[108]
	SPIO and ^{64}Cu		[152–154]
3	SPIO and ^{64}Cu and Cy5.5	MRI/NIRF[a]/PET	[122] [128]
	^{68}Ga-[MNP-SiO_2(NIR797)]	MRI/NIRF[a]/PET	[109, 155]
	Fe_3O_4@$NaLuF_4$:Yb,Er/Tm Core-shell NPs	MRI/CT/NIRF[a]	[156]
	SWNTs@PEG and iron metal NPs and protamine	MRI/PAT[b]/Raman	[157]
	γ-Fe_2O_3@silica NPs, Gd^{3+} Eu^{3+}complexes	MRI/MRI(T_1/ T_2)/ Fluorescence	[88]
≥ 4	Graphene oxide and SPIO and dye	MRI/PAT[b]/ Fluorescence	[125]
	Cobalt-ferrite MNP@SiO_2(RITC)-PEG/NH_2 and luciferase protein and ^{68}Ga	MRI/PET/BRET[d]/ Fluorescence	[158]
	SPION and RGD peptide and Nile red	MRI/MM-OCT[e]/US/ fluorescence	[159]
	MNPs and QDs	MRI/OI	[160]
	^{64}Cu and SPIO and NIR dye	PET-CT/MRI/NIRF[a]	[161]

[a]NIRF: near infra-red fluorescence; [b]PAT: photoacoustic tomography; [c] THMI: terahertz molecular imaging; [d]BRET: bioluminescence resonance energy transfer; [e]MM-OCT: magnetomotive optical coherence tomography; SPIO: superparamagnetic iron oxide; QDs: quantum dots; MNP: magnetic nanoparticle; SWNTs: single-walled nanotubes; PEG: polyethileneglycol; RITC: rhodamine B isothiocyanate; RGD: arginylglycyl-aspartic acid; PLA: polylactic acid (these are defined in the list of abbreviations)

by low tissue penetration (e.g., OI, PAI, US) or with techniques providing low contrast between adjacent soft tissues (CT). An example is combining the anatomical resolution of MRI with the sensitivity of OI, obtaining a powerful technique to find and quantify tumor size, especially for tumors or metastases that are too small for MRI detection on its own. The relevant MR/OI agents have been applied to monitor enzymes activity, in brain tumor imaging, and to detect and monitor apoptosis and atherosclerosis [128].

Other kinds of multimodal contrast agents [7, 115–118, 120, 123–125, 129–133] such as probes with three imaging modes are considered, for example MRI/NIRF/PET [128], and even four [128, 134–136] which are gathered in Table 1.

As an example, difficulty in delineating brain tumor margins has been identified as a major obstacle for further efficient treatment. The up-to-date imaging methods are often limited by inadequate sensitivity, lack of specificity and spatial resolution. To overcome this issue, Kircher et al. [137] recently showed that a unique triple-modality MRI-photoacoustic-Raman (MRI/PAT Raman imaging) nanoparticle (MPRNPs) could accurately help delineate the margins of brain tumors in living mice both in preoperative and intraoperative ways. The probes were detected by the three modalities with a sensitivity at the picomolar level both *in vitro* and in the living mice. Intravenous injection of the MPRNPs into the mice bearing glioblastoma led to the accumulation and retention of the MPRNP only in the tumors. This behavior allowed a non-invasive tumor delineation by the three modalities and through the intact skull. Raman imaging helped guiding the intraoperative tumor resection thanks to its accurate delineation of the tumor margins.

Besides combining complementary techniques, which do not interfere with each other in order to obtain a maximum overall synergistic effect, the design of the multimodal imaging probes should not lead to complex synthetic procedures. It should be taken into account that the use of appropriate relative concentrations of the active probes compensates for the different sensitivities of the techniques used, and limits the NPs size to values well below 100 nm in order to optimize their *in vivo* biodistribution. This approach would involve the administration of a single dose of NPs containing multiple agents with a potential reduction of side effects to patients.

6.   GENERAL CONCLUSIONS

Due to their unique magnetic properties, stability and biocompatibility, IONPs play already a very important role in preclinical bioimaging applications using MRI and MPI and as nanoplatforms for multimodality imaging. While the MRI technique is well established, there is a need for a better understanding of the toxicity mechanisms of IONPs, which could greatly enhance their clinical applications. Improvements in the scanner hardware and image reconstruction techniques could make MPI join MRI, CT and nuclear imaging in clinical translation. Improved modulation of IONPs size, composition, shape and surface modification

will allow them to further progress in other fields, such as multimodality imaging and theranostic, e.g., drug delivery or hyperthermia cancer treatment [162].

ABBREVIATIONS AND DEFINITIONS

acac	acetylacetonate
CA	contrast agent
CT	X-ray computed tomography
E_A	anisotropy energy
FFP	field-free point
HR-TEM	high resolution electron microscopy
IEP	isoelectric point
IONP	iron oxide nanoparticle
IS	inner-sphere
K_A	magnetic anisotropic constant
MAR	motional narrowing regime
MMUS	magneto-motive ultrasound imaging
MPA	magneto-photoacoustic imaging
MPI	magnetic particle imaging
MPRNP	MRI/PAT/Raman imaging nanoparticle
MRI	magnetic resonance imaging
M_s	saturation magnetization
NIRF	near-infrared fluorescence
NP	nanoparticle
OI	optical fluorescence imaging
OS	outer-sphere
PAI	photoacoustic imaging
PAT	photoacoustic tomography
PCS	photon correlation spectroscopy
PET	positron emission tomography
SANS	small-angle neutron scattering
SPECT	single-photon emission-computed tomography
SPIO	superparamagnetic iron oxide
TEM	transmission electron microscopy
US	ultrasound imaging
USPIO	ultrasmall superparamagnetic iron oxide
XPS	X-ray spectroscopy
XRD	X-ray diffraction

REFERENCES

1. R. Weissleder, B. D. Ross, A. Rehemtulla, S. S. Gambhir, *Molecular Imaging: Principles and Practice*, People's Medical Publishing House, Shelton, Connecticut, **2010**.

2. *The Chemistry of Molecular Imaging*, Ed. N. Long, W.-T. Wong, John Wiley & Sons, Inc., Hoboken, NJ, USA, **2015**.

3. *Design and Applications of Nanoparticles in Biomedical Imaging*, Ed. J. W. M. Bulte, M. M. J. Modo, Springer International Publishing, Cham, Switzerland, **2016**.

4. S. Laurent, D. Forge, M. Port, A. Roch, C. Robic, L. Vander Elst, R. N. Muller, *Chem. Rev.* **2008**, *108*, 2064–2110.

5. J. Cheon, J.-H. Lee, *Acc. Chem. Res.* **2008**, *41*, 1630–1640.

6. A. Louie, *Chem. Rev.* **2010**, *110*, 3146–3195.

7. D.-E. Lee, H. Koo, I.-C. Sun, J. H. Ryu, K. Y. Kim, I. C. Kwon, *Chem. Soc. Rev.* **2012**, *41*, 2656–72.

8. T.-H. Shin, Y. Choi, S. Kim, J. Cheon, *Chem. Soc. Rev.* **2015**, *44*, 4501–4516.

9. N. Lee, D. Yoo, D. Ling, M. H. Cho, T. Hyeon, J. Cheon, *Chem. Rev.* **2015**, *115*, 10637–10689.

10. B. R. Smith, S. S. Gambhir, *Chem. Rev.* **2017**, *117*, 901–986.

11. U. Schwertmann, R. M. Cornell, *Iron Oxides in the Laboratory: Preparation and Characterization*, Wiley-VCH, Weinheim, Germany, **2000**.

12. A. H. Lu, E. L. Salabas, F. Schueth, *Angew. Chem., Int. Ed.* **2007**, *46*, 1222–1244.

13. R. Massart, V. Cabuil, *J. Chim. Phys. Phys.-Chim. Biol.* **1987**, *84*, 967–973.

14. T. Sugimoto, E. Matijevic, *J. Colloid Interface Sci.* **1980**, *74*, 227–243.

15. N. M. Gribanov, E. E. Bibik, O. V. Buzunov, V. N. Naumov, *J. Magnetism Magnetic Materials* **1990**, *85*, 7–10.

16. X.-P. Qiu, *Chin. J. Chem.* **2000**, *18*, 834–837.

17. T. Iwasaki, N. Mizutani, S. Watano, T. Yanagida, T. Kawai, *J. Exp. Nanosci.* **2010**, *5*, 251–262.

18. I. Martinez-Mera, M. E. Espinosa-Pesqueira, R. Perez-Hernandez, J. Arenas-Alatorre, *Mater. Lett.* **2007**, *61*, 4447–4451.

19. M. T. Lopez-Lopez, J. D. G. Duran, A. V. Delgado, F. Gonzalez-Caballero, *J. Colloid Interface Sci.* **2005**, *291*, 144–151.

20. R. Massart, *IEEE Trans. Magn.* **1981**, *MAG-17*, 1247–1248.

21. A. Bee, R. Massart, S. Neveu, *J. Magnetism Magnetic Materials* **1995**, *149*, 6–9.

22. V. K. LaMer, R. H. Dinegar, *J. Am. Chem. Soc.* **1950**, *72*, 4847–4854.

23. T. Ishikawa, S. Kataoka, K. Kandori, *J. Mater. Sci.* **1993**, *28*, 2693–2698.

24. T. Ishikawa, T. Takeda, K. Kandori, *J. Mater. Sci.* **1992**, *27*, 4531–4535.

25. K. Kandori, Y. Kawashima, T. Ishikawa, *J. Colloid Interface Sci.* **1992**, *152*, 284–288.

26. I. Milosevic, F. Warmont, Y. Lalatonne, L. Motte, *RSC Adv.* **2014**, *4*, 49086–49089.

27. L. Maurizi, F. Bouyer, J. Paris, F. Demoisson, L. Saviot, N. Millot, *Chem. Comm.* **2011**, *47*, 11706–11708.

28. G. Thomas, F. Demoisson, R. Chassagnon, E. Popova, N. Millot, *Nanotechnology* **2016**, *27*, 135604.

29. G. Thomas, F. Demoisson, J. Boudon, N. Millot, *Dalton Trans.* **2016**, *45*, 10821–10829.

30. J. Rockenberger, E. C. Scher, A. P. Alivisatos, *J. Am. Chem. Soc.* **1999**, *121*, 11595–11596.

31. L. Zhou, B. He, J. Huang, *ACS Applied Materials & Interfaces* **2013**, *5*, 8678–8685.

32. U. Jeong, X. Teng, Y. Wang, H. Yang, Y. Xia, *Adv. Materials* **2007**, *19*, 33–60.

33. W. Baaziz, B. P. Pichon, S. Fleutot, Y. Liu, C. Lefevre, J.-M. Greneche, M. Toumi, T. Mhiri, S. Begin-Colin, *J. Phys. Chem. C* **2014**, *118*, 3795–3810.

34. M. Pauly, B. P. Pichon, P. Panissod, S. Fleutot, P. Rodriguez, M. Drillon, S. Begin-Colin, *J. Mater. Chem.* **2012**, *22*, 6343–6350.

35. Z. Li, H. Chen, H. Bao, M. Gao, *Chem.Mater.* **2004**, *16*, 1391–1393.

36. Z. Li, L. Wei, M. Y. Gao, H. Lei, *Adv. Materials* **2005**, *17*, 1001–1005.

37. K. Butter, A. P. Philipse, G. J. Vroege, *J. Magnetism Magnetic Materials* **2002**, *252*, 1–3.

38. Y. Sun, X. Zuo, S. K. R. S. Sankaranarayanan, S. Peng, B. Narayanan, G. Kamath, *Science* **2017**, *356*, 303–307.

39. C. H. Griffiths, M. P. O'Horo, T. W. Smith, *J. Appl. Physics* **1979**, *50*, 7108–7115.

40. R. A. Frimpong, J. Z. Hilt, *Nanomedicine* **2010**, *5*, 1401–1414.

41. M. Baghbanzadeh, L. Carbone, P. D. Cozzoli, C. O. Kappe, *Angew. Chem. Int. Ed.* **2011**, *50*, 11312–11359.

42. S. Horikoshi, N. Serpone, in *Microwave Chemistry*, Eds. G. Cravotto, D. Carnaroglio, Walter de Gruyter, Berlin, Germany, **2017**, pp. 248–269.

43. E. Carenza, V. Barceló, A. Morancho, J. Montaner, A. Rosell, A. Roig, *Acta Biomaterialia* **2014**, *10*, 3775–3785.

44. M. Branca, M. Ibrahim, D. Ciuculescu, K. Philippot, C. Amiens, in *Handbook of Nanoparticles*, Ed. M. Aliofkhazraei, Springer International Publishing, Cham, Switzerland, **2016**, pp. 1279–1311.

45. E. Tronc, *Nuovo Cimento Soc. Ital. Fis., D* **1996**, *18D*, 163–180.

46. J. Tucek, R. Zboril, *Czech. J. Phys.* **2005**, *55*, 893–911.

47. J. Tucek, R. Zboril, D. Petridis, *J. Nanosci. Nanotechnol.* **2006**, *6*, 926–947.

48. C. J. Serna, F. Bødker, S. Mørup, M. P. Morales, F. Sandiumenge, S. Veintemillas–Verdaguer, *Solid State Comm.* **2001**, *118*, 437–440.

49. P. Tartaj, M. D. P. Morales, S. Veintemillas-Verdaguer, T. Gonzalez-Carreño, C. Serna, in *Handbook of Magnetic Materials*, Ed. K. H. J. Buschow, Elsevier Science, Amsterdam, **2006**, *16*, 403–482.

50. M. P. Morales, S. Veintemillas-Verdaguer, M. I. Montero, C. J. Serna, A. Roig, L. Casas, B. Martínez, F. Sandiumenge, *Chem. Mater.* **1999**, *11*, 3058–3064.

51. D. L. A. de Faria, S. Venâncio Silva, M. T. de Oliveira, *J. Raman Spect.* **1997**, *28*, 873–878.

52. J. Rubio-Zuazo, A. Chainani, M. Taguchi, D. Malterre, A. Serrano, G. R. Castro, *Phys. Rev. B* **2018**, *97*, 235148.

53. S. Brice-Profeta, M. A. Arrio, E. Tronc, N. Menguy, I. Letard, C. Cartier dit Moulin, M. Noguès, C. Chanéac, J. P. Jolivet, P. Sainctavit, *J. Magnetism Magnetic Materials* **2005**, *288*, 354–365.

54. P. Lindner, T. Zmeb, *Neutrons, X-Rays and Light: Scattering Methods Applied to Soft Condensed Matter*, Elsevier Science B.V., Amsterdam, **2002**.

55. M. Sousa, F. Tourinho, J. Rubim, *J. Raman Spect.* **2000**, *31*, 185–191.

56. N. De Jaeger, H. Demeyere, R. Finsy, R. Sneyers, J. Vanderdeelen, P. van der Meeren, M. van Laethem, *Particle & Particle Systems Characterization* **1991**, *8*, 179–186.

57. R. J. Hunter, *Foundations of Colloid Science*, 2nd Ed., Oxford University Press, Oxford, UK, **2001**.

58. H. Ohshima, *Adv. Colloid Interface Sci.* **1995**, *62*, 189–235.

59. M. Di Marco, I. Guilbert, M. Port, C. Robic, P. Couvreur, C. Dubernet, *Int. J. Pharmaceutics* **2007**, *331*, 197–203.

60. M. Di Marco, C. Sadun, M. Port, I. Guilbert, P. Couvreur, C. Dubernet, *Int J Nanomedicine* **2007**, *2*, 609–622.

61. R. Dronskowski, *Adv. Functional Materials* **2001**, *11*, 27–29.

62. T. Neuberger, B. Schöpf, H. Hofmann, M. Hofmann, B. von Rechenberg, *J.Magnetism Magnetic Materials* **2005**, *293*, 483–496.

63. E. Tronc, A. Ezzir, R. Cherkaoui, C. Chanéac, M. Noguès, H. Kachkachi, D. Fiorani, A. M. Testa, J. M. Grenèche, J. P. Jolivet, *J. Magnetism Magnetic Materials* **2000**, *221*, 63–79.

64. F. E. Spada, F. T. Parker, C. Y. Nakakura, A. E. Berkowitz, *J. Magnetism Magnetic Materials* **1993**, *120*, 129–135.

65. J. P. M. Almeida, A. L. Chen, A. Foster, R. Drezek, *Nanomedicine* **2011**, *6*, 815–835.

66. T. Skotland, T.-G. Iversen, K. Sandvig, *Nanomedicine: Nanotechnology, Biology and Medicine* **2010**, *6*, 730–737.

67. E. Alphandéry, S. Faure, O. Seksek, F. Guyot, I. Chebbi, *ACS Nano* **2011**, *5*, 6279–6296.

68. N. M. Dissanayake, K. M. Current, S. O. Obare, *Int. J. Mol. Sci.* **2015**, *16*, 23482–23516.

69. Z. Yarjanli, K. Ghaedi, A. Esmaeili, S. Rahgozar, A. Zarrabi, *BMC Neuroscience* **2017**, *18*, 51.

70. U. S. Patil, S. Adireddy, A. Jaiswal, S. Mandava, B. R. Lee, D. B. Chrisey, *Int. J. Mol. Sci.* **2015**, *16*, 24417–24450.

71. Q. Feng, Y. Liu, J. Huang, K. Chen, J. Huang, K. Xiao, *Scientific Reports* **2018**, *8*, 2082.

72. N. V. S. Vallabani, S. Singh, A. Karakoti, *Curr. Drug Metab.* **2018**, *20*.

73. L. H. Reddy, J. L. Arias, J. Nicolas, P. Couvreur, *Chem. Rev.* **2012**, *112*, 5818–5878.

74. N. V. Srikanth Vallabani, S. Singh, A. S. Karakoti, *Curr. Drug Metab.* **2019**, *20*, 457–472.

75. K. Ulbrich, K. Holá, V. Šubr, A. Bakandritsos, J. Tuček, R. Zbořil, *Chem. Rev.* **2016**, *116*, 5338–5431.

76. T. Vangijzegem, D. Stanicki, S. Laurent, *Expert Opin. Drug Delivery* **2019**, *16*, 69–78.

77. *The Chemistry of Contrast Agents in Medical Magnetic Resonance Imaging*, 2nd. Ed., John Wiley & Sons, Ltd, Hoboken, New Jersey, **2013**.

78. C. F. G. C. Geraldes, S. Laurent, *Contrast Media & Molecular Imaging* **2009**, *4*, 1–23.

79. J. Wahsner, E. M. Gale, A. Rodríguez-Rodríguez, P. Caravan, *Chem. Rev.* **2019**, *119*, 957–1057.

80. Q. L. Vuong, J.-F. Berret, J. Fresnais, Y. Gossuin, O. Sandre, *Adv. Healthcare Mater.* **2012**, *1*, 502–512.

81. M. G. Harisinghani, J. Barentsz, P. F. Hahn, W. M. Deserno, S. Tabatabaei, C. H. van de Kaa, J. de la Rosette, R. Weissleder, *New England J. Medicine* **2003**, *348*, 2491–2499.

82. H. B. Na, I. C. Song, T. Hyeon, *Adv. Mater.* **2009**, *21*, 2133–2148.

83. Y. X. Wang, S. M. Hussain, G. P. Krestin, *Eur. Radiol.* **2001**, *11*, 2319–2331.

84. R. Weissleder, A. Bogdanov, E. A. Neuwelt, M. Papisov, *Adv. Drug Del. Rev.* **1995**, *16*, 321–334.

85. Z. Li, P. W. Yi, Q. Sun, H. Lei, H. Li Zhao, Z. H. Zhu, S. C. Smith, M. B. Lan, G. Q. Lu, *Adv. Funct. Materials* **2012**, *22*, 2387–2393.

86. Z. Zhou, Z. Zhao, H. Zhang, Z. Wang, X. Chen, R. Wang, Z. Chen, J. Gao, *ACS Nano* **2014**, *8*, 7976–7985.

87. J.-S. Choi, J.-H. Lee, T.-H. Shin, H.-T. Song, E. Y. Kim, J. Cheon, *J. Am. Chem. Soc.* **2010**, *132*, 11015–11017.

88. S. L. C. Pinho, J. Sereno, A. J. Abrunhosa, M.-H. Delville, J. Rocha, L. D. Carlos, C. F. G. C. Geraldes, *Inorg. Chem.* **2019**, *58*, 16618–16628.

89. K. H. Bae, Y. B. Kim, Y. Lee, J. Hwang, H. Park, T. G. Park, *Bioconjugate Chemistry* **2010**, *21*, 505–512.

90. Z. Zhou, D. Huang, J. Bao, Q. Chen, G. Liu, Z. Chen, X. Chen, J. Gao, *Adv. Mater.* **2012**, *24*, 6223–6228.

91. J.-S. Choi, S. Kim, D. Yoo, T.-H. Shin, H. Kim, M. D. Gomes, S. H. Kim, A. Pines, J. Cheon, *Nature Materials* **2017**, *16*, 537–542.

92. T.-H. Shin, J.-S. Choi, S. Yun, I.-S. Kim, H.-T. Song, Y. Kim, K. I. Park, J. Cheon, *ACS Nano* **2014**, *8*, 3393–3401.

93. B. Gleich, J. Weizenecker, *Nature* **2005**, *435*, 1214–1217.

94. *Magnetic Particle Imaging: A Novel SPIO Nanoparticle Imaging Technique,* Eds. T. M. Buzug, J. Borgert, Vol. 140 of *Springer Proceedings in Physics,* Springer, Heidelberg, New York, Dordrecht, London, **2012**.

95. M. H. Pablico-Lansigan, S. F. Situ, A. C. S. Samia, *Nanoscale* **2013**, *5*, 4040–4055.

96. P. W. Goodwill, J. J. Konkle, B. Zheng, E. U. Saritas, S. M. Conolly, *IEEE Transactions on Medical Imaging* **2012**, *31*, 1076–1085.

97. J. W. M. Bulte, P. Walczak, M. Janowski, K. M. Krishnan, H. Arami, A. Halkola, B. Gleich, J. Rahmer, *Tomography* **2015**, *1*, 91–97.

98. B. Zheng, M. P. von See, E. Yu, B. Gunel, K. Lu, T. Vazin, D. V. Schaffer, P. W. Goodwill, S. M. Conolly, *Theranostics* **2016**, *6*, 291–301.

99. A. P. Khandhar, R. M. Ferguson, H. Arami, K. M. Krishnan, *Biomaterials* **2013**, *34*, 3837–3845.

100. P. W. Goodwill, E. U. Saritas, L. R. Croft, T. N. Kim, K. M. Krishnan, D. V. Schaffer, S. M. Conolly, *Adv. Mater.* **2012**, *24*, 3870–3877.

101. P. Ludewig, N. Gdaniec, J. Sedlacik, N. D. Forkert, P. Szwargulski, M. Graeser, G. Adam, M. G. Kaul, K. M. Krishnan, R. M. Ferguson, A. P. Khandhar, P. Walczak, J. Fiehler, G. Thomalla, C. Gerloff, T. Knopp, T. Magnus, *ACS Nano* **2017**, *11*, 10480–10488.

102. E. Y. Yu, M. Bishop, B. Zheng, R. M. Ferguson, A. P. Khandhar, S. J. Kemp, K. M. Krishnan, P. W. Goodwill, S. M. Conolly, *Nano Letters* **2017**, *17*, 1648–1654.

103. Y. Hu, S. Mignani, J.-P. Majoral, M. Shen, X. Shi, *Chem. Soc. Rev.* **2018**, *47*, 1874–1900.

104. R. Thomas, I.-K. Park, Y. Y. Jeong, *Int. J. Mol. Sci.* **2013**, *14*, 15910–15930, 15921 pp.

105. R. Southworth, R. T. Martin de Rosales, L. K. Meszaros, M. T. Ma, G. E. D. Mullen, G. Fruhwirth, J. D. Young, C. Imberti, J. Bagunya-Torres, E. Andreozzi, P. J. Blower, *Adv. Inorg. Chem.* **2016**, *68*, 1–41.

106. D. Shi, M. E. Sadat, A. W. Dunn, D. B. Mast, *Nanoscale* **2015**, *7*, 8209–8232.

107. Q. Le Trequesser, H. Seznec, M.-H. Delville, *Nanotechnol. Rev.* **2013**, *2*, 125–169.

108. E. B. Ehlerding, P. Grodzinski, W. Cai, C. H. Liu, *ACS Nano* **2018**, *12*, 2106–2121.

109. N. Lee, T. Hyeon, *Chem. Soc. Rev.* **2012**, *41*, 2575–2589.

110. R. Thomas, I.-K. Park, Y. Y. Jeong, *Int. J. Mol. Sci.* **2013**, *14*, 15910–15930.

111. M. Abe, *MTA Dialog* **2009**, *10*, 994–997.

112. W.-Y. Huang, J. J. Davis, *Dalton Trans.* **2011**, *40*, 6087–6103.

113. T. B. Huff, Y. Shi, Y. Fu, H. Wang, J.-X. Cheng, *IEEE J. Sel. Top. Quantum Electron.* **2008**, *14*, 4–9.

114. J. Y. Hwang, J. Park, B. J. Kang, D. J. Lubow, D. Chu, D. L. Farkas, K. K. Shung, L. K. Medina-Kauwe, *PLoS One* **2012**, *7*, e34463.

115. P. A. Jarzyna, A. Gianella, T. Skajaa, G. Knudsen, L. H. Deddens, D. P. Cormode, Z. A. Fayad, W. J. M. Mulder, *Wiley Interdiscip. Rev.: Nanomed. Nanobiotechnol.* **2010**, *2*, 138–150.

116. J. Kim, Y. Piao, T. Hyeon, *Chem. Soc. Rev.* **2009**, *38*, 372–390.

117. A. Masotti, *Recent Pat. Nanotechnol.* **2010**, *4*, 53–62.

118. A. Masotti, *Recent Pat. Nanotechnol.* **2011**, *5*, 163–177.

119. J. R. McCarthy, R. Weissleder, *Multimodal Imaging and Therapy with Magnetofluorescent Nanoparticles*, John Wiley & Sons, Inc., Hoboken, New Jersey, **2011**, pp. 593–613.

120. P. Sharma, A. Singh, S. Brown, N. Bengtsson, G. Walter, S. Grobmyer, N. Iwakuma, S. Santra, E. Scott, B. Moudgil, in *Cancer Nanotechnology*, Vol. 624, Eds. S. R. Grobmyer, B. M. Moudgil, Humana Press, Totowa, New Jersey, **2010**, pp. 67–81.

121. L. Wang, M. B. O'Donoghue, W. Tan, *Nanomedicine (London, U. K.)* **2006**, *1*, 413–426.

122. J. Xie, K. Chen, J. Huang, S. Lee, J. Wang, J. Gao, X. Li, X. Chen, *Biomaterials* **2010**, *31*, 3016–3022.

123. H. Xing, W. Bu, S. Zhang, X. Zheng, M. Li, F. Chen, Q. He, L. Zhou, W. Peng, Y. Hua, J. Shi, *Biomaterials* **2012**, *33*, 1079–1089.

124. R. X. Xu, *Contrast Media Mol. Imaging* **2011**, *6*, 401–411.

125. K. Yang, L. Hu, X. Ma, S. Ye, L. Cheng, X. Shi, C. Li, Y. Li, Z. Liu, *Adv. Mater.* **2012**, *24*, 1868–1872.

126. K.-T. Yong, I. Roy, M. T. Swihart, P. N. Prasad, *J. Mater. Chem.* **2009**, *19*, 4655–4672.

127. P. Zrazhevskiy, M. Sena, X. Gao, *Chem. Soc. Rev.* **2010**, *39*, 4326–4354.

128. L. E. Jennings, N. J. Long, *Chem. Comm.* **2009**, 3511–3524.

129. J. Gao, H. Gu, B. Xu, *Acc. Chem. Res.* **2009**, *42*, 1097–1107.

130. P.-J. Chen, S.-H. Hu, C.-S. Hsiao, Y.-Y. Chen, D.-M. Liu, S.-Y. Chen, *J. Mater. Chem.* **2011**, *21*, 2535–2543.

131. J. E. Lee, N. Lee, T. Kim, J. Kim, T. Hyeon, *Acc. Chem. Res.* **2011**, *44*, 893–902.

132. M. E. Gindy, R. K. Prud'homme, *Expert Opin. Drug Del.* **2009**, *6*, 865–878.

133. R. Sharma, A. Sharma, C. J. Chen, *Open Nanomed. J.* **2010**, *3*, 10–23.

134. S. R. Cherry, *J. Clin. Pharmacol.* **2001**, *41*, 482–491.

135. S. R. Cherry, *J. Nucl. Med.* **2006**, *47*, 1735–1745.

136. S. R. Cherry, A. Y. Louie, R. E. Jacobs, *Proc. IEEE* **2008**, *96*, 416–438.

137. M. F. Kircher, A. de la Zerda, J. V. Jokerst, C. L. Zavaleta, P. J. Kempen, E. Mittra, K. Pitter, R. Huang, C. Campos, F. Habte, R. Sinclair, C. W. Brennan, I. K. Mellinghoff, E. C. Holland, S. S. Gambhir, *Nat. Med.* **2012**, *18*, 829–834.

138. H. Cai, K. Li, M. Shen, S. Wen, Y. Luo, C. Peng, G. Zhang, X. Shi, *J. Mater. Chem.* **2012**, *22*, 15110–15120.

139. D. Kim, M. K. Yu, T. S. Lee, J. J. Park, Y. Y. Jeong, S. Jon, *Nanotechnology* **2011**, *22*, 155101.

140. D. Janczewski, Y. Zhang, G. K. Das, D. K. Yi, P. Padmanabhan, K. K. Bhakoo, T. T. Y. Tan, S. T. Selvan, *Microsc. Res. Tech.* **2011**, *74*, 563–576.

141. Y. T. Lim, M. Y. Cho, J. K. Kim, S. Hwangbo, B. H. Chung, *ChemBioChem* **2007**, *8*, 2204–2209.

142. Z. Medarova, M. Kumar, S.-W. Ng, A. Moore, *Methods Mol. Biol.* **2009**, *555*, 1–13.

143. S. Wu, L. Zhang, J. Zhong, Z. Zhang, *Cytotherapy* **2010**, *12*, 859–869.

144. L.-S. Bouchard, M. S. Anwar, G. L. Liu, B. Hann, Z. H. Xie, J. W. Gray, X. Wang, A. Pines, F. F. Chen, *Proc. Natl. Acad. Sci. USA* **2009**, *106*, 4085–4089.

145. C. Catana, Y. Wu, M. S. Judenhofer, J. Qi, B. J. Pichler, S. R. Cherry, *J. Nucl. Med.* **2006**, *47*, 1968–1976.

146. B. J. Pichler, H. F. Wehrl, A. Kolb, M. S. Judenhofer, *Seminars in Nuclear Medicine* **2008**, *38*, 199–208.

147. M. K. Werner, H. Schmidt, N. F. Schwenzer, *Am. J. Roentgenology* **2012**, *199*, 272–277.

148. H. Zaidi, A. Del Guerra, *Medical Physics* **2011**, *38*, 5667–5689.

149. J. Y. Park, H. J. Choi, G.-E. Nam, K.-S. Cho, J.-H. Son, *IEEE Trans. Terahertz Sci. Technol.* **2012**, *2*, 93–98.

150. B. Xu, R. Lu, H. Dou, K. Tao, K. Sun, Y. Qiu, J. Ding, D. Zhang, J. Li, W. Shi, K. Sun, *Colloid Polym. Sci.* **2012**, *290*, 1617–1626.

151. J.-C. Park, M.-K. Yu, G.-I. An, S.-I. Park, J.-M. Oh, H.-J. Kim, J.-H. Kim, E.-K. Wang, I.-H. Hong, Y.-S. Ha, T.-H. Choi, K.-S. Jeong, Y.-M. Chang, M. J. Welch, S.-Y. Jon, J.-S. Yoo, *Small* **2010**, *6*, 2863–2868.

152. H.-Y. Lee, Z. Li, K. Chen, A. R. Hsu, C. Xu, J. Xie, S. Sun, X. Chen, *J. Nucl. Med.* **2008**, *49*, 1371–1379.

153. X. Yang, H. Hong, J. J. Grailer, I. J. Rowland, A. Javadi, S. A. Hurley, Y. Xiao, Y. Yang, Y. Zhang, R. J. Nickles, W. Cai, D. A. Steeber, S. Gong, *Biomaterials* **2011**, *32*, 4151–4160.

154. R. T. M. de Rosales, R. Tavare, R. L. Paul, M. Jauregui-Osoro, A. Protti, A. Glaria, G. Varma, I. Szanda, P. J. Blower, *Angew. Chem., Int. Ed.* **2011**, *50*, 5509–5513.

155. J. S. Kim, Y.-H. Kim, J. H. Kim, K. W. Kang, E. L. Tae, H. Youn, D. Kim, S.-K. Kim, J.-T. Kwon, M.-H. Cho, Y.-S. Lee, J. M. Jeong, J.-K. Chung, D. S. Lee, *Nanomedicine* **2012**, 7, 219–229.

156. X. Zhu, J. Zhou, M. Chen, M. Shi, W. Feng, F. Li, *Biomaterials* **2012**, *33*, 4618–4627.

157. N. K. Devaraj, E. J. Keliher, G. M. Thurber, M. Nahrendorf, R. Weissleder, *Bioconjugate Chem.* **2009**, *20*, 397–401.

158. D. W. Hwang, H. Y. Ko, S.-K. Kim, D. Kim, D. S. Lee, S. Kim, *Chem. Eur. J.* **2009**, *15*, 9387–9393.

159. R. John, F. T. Nguyen, K. J. Kolbeck, E. J. Chaney, M. Marjanovic, K. S. Suslick, S. A. Boppart, *Mol. Imaging Biol.* **2012**, *14*, 17–24.

160. R. Koole, W. J. M. Mulder, S. M. M. van, G. J. Strijkers, A. Meijerink, K. Nicolay, *Wiley Interdiscip. Rev.: Nanomed. Nanobiotechnol.* **2009**, *1*, 475–491.

161. M. Nahrendorf, H. Zhang, S. Hembrador, P. Panizzi, D. E. Sosnovik, E. Aikawa, P. Libby, F. K. Swirski, R. Weissleder, *Circulation* **2008**, *117*, 379–387.

162. Y. Hu, S. Mignani, J.-P. Majoral, M. Shen, X. Shi, *Chem. Soc. Rev.* **2018**, *47*, 1874–1900.

10

Magnetic Resonance Contrast Enhancement and Therapeutic Properties of Corrole Nanoparticles

James Teh and Lali Medina Kauwe

Department of Biomedical Sciences, Cedars-Sinai Medical Center,
Los Angeles, CA 90048, USA
<james.teh@cshs.org>
<medinal@cshs.org>

Abstract: Magnetic resonance imaging provides a valuable means of detecting diseased tissue in the clinic but the contribution of conventional clinically-used contrast agents is generally limited to their effect on augmenting tissue visibility. Sulfonated metallated corroles have the potential to offer image contrast in addition to therapeutic and diagnostic activities. Their delivery by targeted particles enables such corroles to be transported to specific sites in the body for multifunctional activities including detection, diagnosis, and therapy, thus acting as targeted "theranostics". This chapter summarizes the body of work accumulated thus far on tumor-targeted biological particles delivering sulfonated metallated corroles. In particular, we highlight the unique features of bioparticles containing manganese-metallated corroles and their theranostic impact that includes magnetic resonance imaging. Importantly, the bioparticles described in this chapter are nano-sized, biologically-based particles in contrast to synthetic formulations comprising the majority of the nanomedicine field. Accordingly, the particular biological activities of these particles are discussed at length as they impart features allowing for tissue-activated contrast enhancement that provides tumor-specific detection as well as intervention.

Keywords: bioparticles · HerPBK10 · HPK · magnetic resonance imaging · nanobiologics · sulfonated corroles · theranostics · tumor targeting

1.   INTRODUCTION

1.1.   Magnetic Resonance Imaging

Among the medical imaging modalities available in hospitals and clinics, magnetic resonance imaging (MRI) is frequently utilized by physicians for diagnostic and treatment applications. Unlike other ionizing radiation imaging modalities involving radioisotopes, MRI is a non-invasive and radiation-free imaging technique, which can perform in real-time to provide high anatomic three-dimensional resolution of the body. The sensitivity of MRI to distinguish between different soft tissues in the body makes it attractive for imaging major organs and diseased tissues such as tumors.

Hydrogen is abundant in the human body due to its high content in water and fat. The hydrogen nucleus contains a single proton and functions as a magnetic pole that can spin randomly in the body [1]. MRI is based on the alignment of hydrogen protons when placed in a strong magnetic field. Furthermore, as radio wave frequencies are added, different tissues will resonate differently depending on the strength of the magnetic field and the frequency. When the radio frequency pulse is off, the proton "relaxes" and emits a radio wave signal, which helps generate an image that can be used for diagnostic purposes as different tissues relax at different rates [1].

The "relaxation" of protons is measured as T1 or T2. T1 is the "longitudinal" relaxation or the time it takes for the protons to go back to their original state, while T2 is the "transverse" relaxation or the decay in the longitudinal plane.

Tissues and fluids with short T1 relaxation are bright, while short T2 relaxation are dark. Structures containing fat are bright in T1 and structures containing water are bright in T2. Typically, in diseased tissue, such as infections or tumors, there is an increase in water in the tissue. However, the contrast is sometimes not enough to distinguish between normal and diseased tissues [2]. Thus, to improve detailed delineation with high spatial and temporal resolutions in the body, magnetic resonance (MR) contrast agents play a critical role [2, 3].

Contrast agents used in MRI function by decreasing the relaxation time and thus improve visibility to distinguish diseased from normal tissues. Paramagnetic metal ions such as gadolinium (Gd) or manganese (Mn) improve T1 relaxation time and yield a bright contrast [4]. Superparamagnetic iron oxide nanoparticles work best to improve the effectiveness of T2 relaxation times, which provides a dark contrast. Metal ions with a high spin number or unpaired electrons, such as Mn^{2+} which has 5 unpaired electrons, make good contrast agents [5, 6]. Porphyrin-chelated Mn^{2+} ions have been used to enhance contrast in tumors. The chelated version of manganese is safer than the free manganese which is known to have neurotoxic effects [6].

1.2.   Corroles in Cancer

Corroles are macrocyclic aromatic compounds, which share structural similarity to cobalamin (vitamin B_{12}) [7]. Corrole shares the structural characteristic of four pyrrole rings located in the inner core with tetrapyrrolic macrocycles such as porphyrin and corrin. However, corrole differs by one less methine bridge (=CH–) and an inner core with three NH groups [8]. This structural characteristic helps corroles to stabilize metal ions in high oxidation states (+3). Metal ions are stabilized with corroles to produce 'metallated corrole' complexes that are resistant to hydrolysis [8], attribute by the strong metal-nitrogen covalent bonds [9, 10]. In addition, corroles stabilized with different metal ions have been shown to produce intense light absorptions in the visible region with luminescence quantum yields reaching over 50 % [11].

The corrole has undergone multiple changes to its macrocyclic structure in order to adapt to various applications. A modification to the corrole involves functionalizing two adjacent pyrroles with two sulfonic acid head groups, producing the bis-sulfonated corrole, S2FB (Figure 1A) [12]. By introducing two ionizable moieties, the physical property of the corrole changes from lipophilic to amphiphilic, which is beneficial for biomedical applications. Even with the insertion of metals to S2FB, solubility in aqueous and physiological conditions remains unchanged. Likewise, metal ions are not released from the corroles, when the metallated corroles are subjected to physiological conditions [13, 14]. Through the structural modification and stability under physiological environment without the loss of metal ions, metallated corroles are excellent candidates for their use as cancer therapeutic agents.

Metallated corroles show potential utility as cancer therapeutic agents with high cytotoxicity in various types of cancer cells. An *in vitro* cytotoxicity study of metallated corroles was conducted using sulfonated gallium(III) corroles (**S2Ga**;
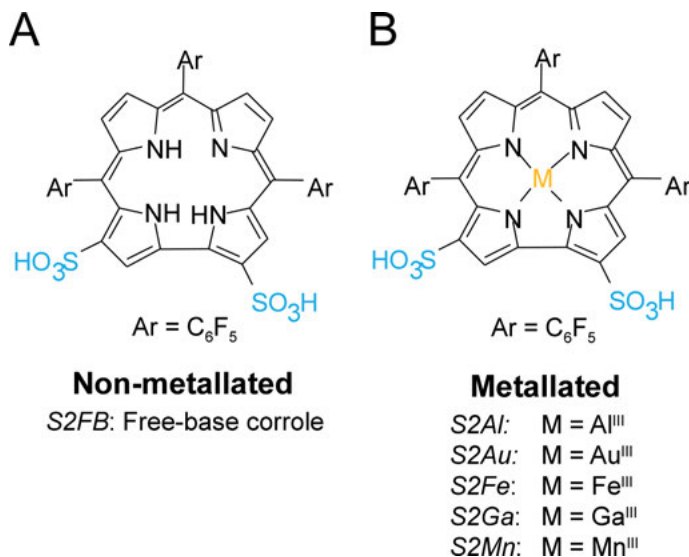
Figure 1. Chemical structures of non-metallated and metallated bis-sulfonated corroles, with sulfonates highlighted in blue.

Figure 1B) on MDA-MB-435, HeLa, and 293 cells, which led to a reduction in cell viability at high concentration (30 µM) after several days [15]. Another cytotoxicity study was performed in MDA-MB-231 and OVCAR-3 cells treated with sulfonated aluminum(III) corrole (S2Al) and S2Ga. S2Al-treated MDA-MB-231 and OVCAR-3 cells showed a significant reduction in cell viability as compared to S2Ga-treated cells at equal dose (30 µM) [16]. A comprehensive panel of various metallated corroles (Au, Sb, Mn, Al, Fe, and Ga) was tested for their cytotoxic efficacy on DU145, MDA-MB-231, OVCAR-3, and SK-MEL-28 cancer cells. Of the six metallated corroles tested with the cancer cell lines, S2Au was an effective cytotoxic agent with reported IC_{50} values 5–10 times more potent than the least effective metallated corrole, S2Ga [17].

Apart from the potential direct therapeutic application against cancer, metallated corroles have been studied for fluorescence imaging to visualize cancer cells. S2Ga emits an intense red fluorescence signal and has been investigated for detecting and tracking cellular uptake and non-invasive *in vivo* imaging [18, 19]. In addition, metallated corroles are thermally and photochemically stable, and can function as photosensitizers, by generating singlet oxygen with high quantum efficacy and imparting utility as a potential cancer therapeutic [15, 20].

2. PROTEIN-CORROLE PARTICLES

2.1. Corroles as Theranostic Cargo

Corroles bearing sulfonate groups acquire a negatively charged amphipolar nature that enables strong binding to proteins such as transferrin or human serum albu-

min (HSA), with reported K_d values of ≤ 1 nM and 10 nM, respectively [21, 22]. Recombinant cell-invading proteins derived from the adenovirus capsid penton base (PB) have been used to assist the uptake of anionic molecules including bis-sulfonated corroles into cancer cells [23, 24]. These observations paved the way for using corroles as physiologically compatible cargo that could be delivered by protein-based vehicles and impart a therapeutic, imaging, diagnostic, or combinatorial function depending on the type of corrole being delivered.

Depending on the metal ion, corroles can assume fluorescent, paramagnetic, cytotoxic, and/or cytoprotective activity or a combination of such activities [25–30]. Both, a sulfonated gallium(III) corrole (S2Ga) and a non-metallated or free base corrole (S2FB) emit bright red fluorescence when excited within the UV range, and exhibit toxicity to cultured human tumor cell lines representing breast cancer, ovarian cancer, melanoma, and cervical carcinoma [28, 29]. The pH of the surrounding environment alters the fluorescence lifetime of S2Ga [20]. This property has enabled its use as a diagnostic probe for broadcasting microenvironmental conditions during intracellular trafficking [20] or distinguishing tumor from non-tumor tissue in mouse tumor models, both *in vivo* and *ex vivo* [31]. Photoexcitation of S2Ga at its maximum fluorescence wavelength (λmax) generated singlet oxygen that induced rapid damage to cells that had taken up therapeutic particles containing S2Ga [32, 33]. Excitation at a secondary absorbance peak (~620 nm) yielded nearly as effective cell damage [32], thus enabling the use of longer wavelengths for irradiation that would support penetration into deeper tissue.

The sulfonated manganese(III) (S2Mn), and iron(III) (S2Fe) corroles bear paramagnetic properties that can be used for MR detection [25]. Despite their cytotoxic property at high concentrations, both S2Mn and S2Fe exhibit antioxidant properties at low pharmacologic concentrations [26, 27, 34].

2.1.1. *Carrier Protein Properties*

The anionic sulfonate groups located on one side of the corrole macrocycle – thus imparting an amphipolar nature – prevent non-specific cell entry due to repulsion by the negatively charged cell membrane [35]. This feature has the potential to direct corrole delivery into target cells *via* a membrane-penetrating protein. Engineered recombinant proteins derived from the membrane-lytic capsid of adenovirus have been used as cell-penetrating carriers for sulfonated corroles [20, 28, 29].

The recombinant chimeric protein **HPK** – also known as HerPBK10 [36] – uses the cell surface receptor HER3 to target and enter tumors [37]. HPK contains the receptor-binding region of the HER3 ligand, neuregulin-1α1 (amino acids 35–239, comprising the Ig-like and EGF-like domains) [38], fused to a membrane-penetrating moiety derived from the adenovirus capsid penton base protein modified with a polylysine tail (Figure 2) [36, 39]. HPK can self-assemble with a variety of anionic therapeutic molecules (including nucleic acids, chemotherapy agents, and sulfonated corroles), resulting in serum-stable cargo-encapsulated protein particles or bioparticles (~20–40 nm diameter, depending on the payload) with tumor-
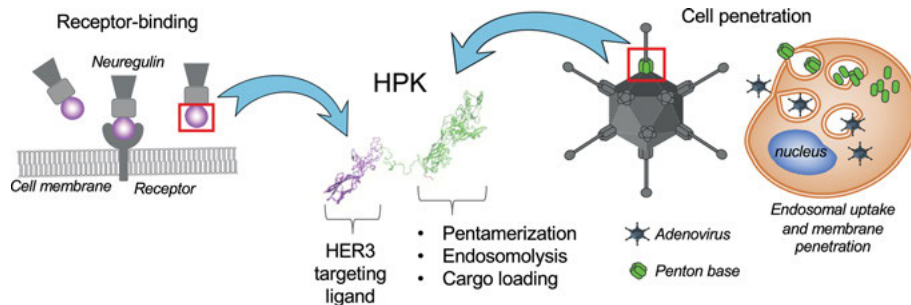
Figure 2. Schematic of HPK functional domains. HPK is shown as a ribbon structure with each domain highlighted by a different color.

homing capability [28, 29, 36, 40, 41]. Systemic delivery of particles loaded with tumoricidal drugs in mice bearing subcutaneous HER3-expressing tumors has resulted in tumor-preferential accumulation and tumor growth ablation at > 10 times lower dose compared to the corresponding untargeted drug, while sparing heart and liver tissue, and with no detectable immunogenicity [25, 28, 37, 41]. The protein alone shows no effect on tumor growth, while exhibiting a reduction in growth signaling normally elicited by wild-type neuregulin [37].

2.1.2. Particle Assembly and in vitro Characterization

Structural modeling and molecular dynamics simulations combined with a large body of functional assays using dynamic light scattering (DLS), transmission electron microscopy (TEM), native gel electrophoresis, and isothermal titration calorimetry have shed light on the assembly and delivery mechanism of HPK, and offer new insight on the adenovirus capsid penton base protein [37, 40]. These studies together suggest that the penton base moiety of HPK drives its self-assembly into stable pentamers resembling viral penton base capsomeres (which normally occupy each vertex of the viral icosahedral shell) [42]. A ring-like structure can be observed under TEM resembling such capsomeres, [43] and co-precipitation assays confirm that HPK interaction occurs through the penton base domain (Figure 3A) [40].

Pentamerization places the polylysine domain of each protein monomer at a single face on the pentamer, forming a highly charged surface that interacts strongly with negatively charged molecules [36, 37, 39–41]. DLS and TEM of HPK supported the structural models which together suggested that the polylysine moiety on HPK causes charge repellance between pentamers while assembly with anionic cargo such as sulfonated corroles neutralizes those charges and allows HPK pentamers to converge (Figure 3B) [40].

Structural complementarity and interaction of hydrophobic residues enables penton base pentamers from certain adenovirus serotypes to form pseudocapsids known as dodecahedrons, consisting of twelve pentamers [44–47]. The introduction of sulfonated corroles as cargo may influence the complementary interaction
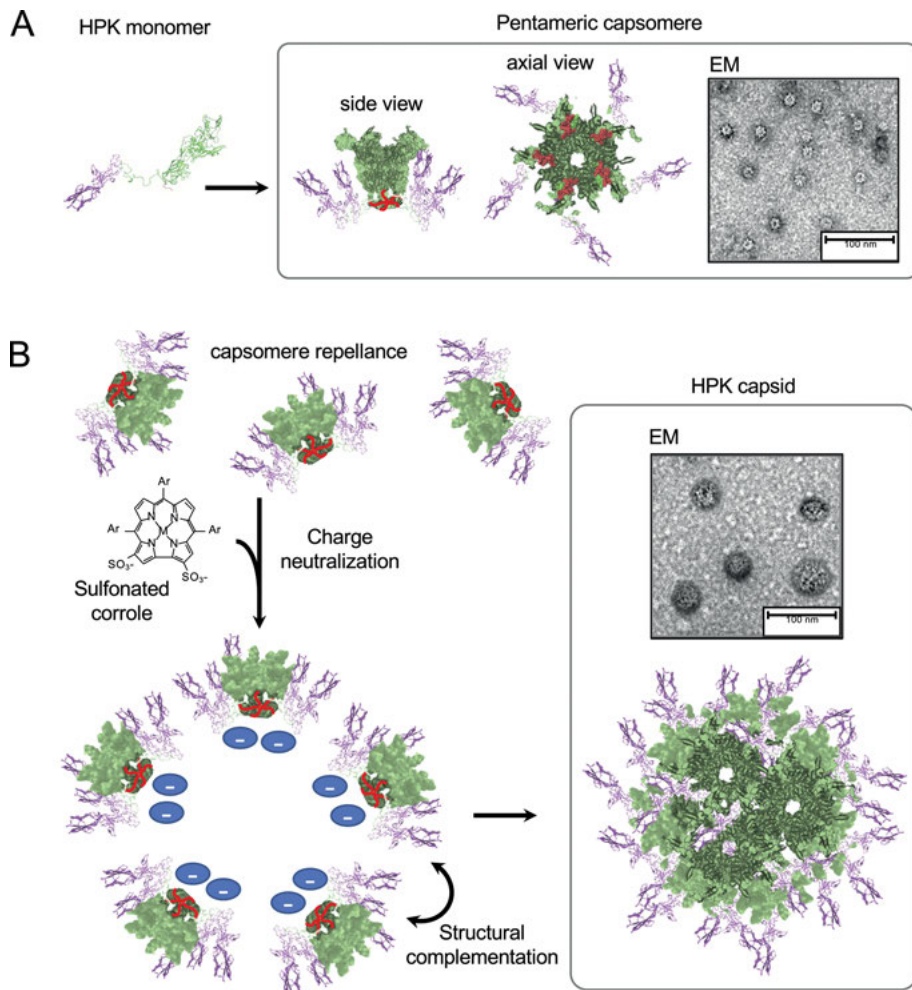
Figure 3. Schematic of HerMn assembly. (**A**) Self-assembled HPK capsomeres. Inset, TEM of capsomeres. (**B**) Assembly into HerMn particles. Graphic illustrates convergence of HPK capsomeres upon exposure to S2Mn (represented by blue ovals labeled with minus sign), followed by structural complementation to form a capsid. **Inset**: TEM of assembled particles.

between HPK pentamers and yield higher order capsids containing well over twelve pentamers to accommodate the payload, which may account for the spherical structures seen under TEM that appear larger than dodecahedrons (Figure 3B) [40].

Particles formed from the combination of HPK with either S2Ga or S2Mn have been designated **HerGa** and **HerMn**, respectively. Both particles resist corrole transfer to serum proteins and exhibit high stability in storage at different temperatures [25, 28, 29].

2.2. *In cellulo* Activity

2.2.1. *Cell Entry*

The HPK particle recognizes the same receptor binding site as wild-type neuregulin, but the multivalency of the particle can outcompete circulating neuregulins, while inducing a high degree of HER3 clustering on tumor cells [37, 40]. Receptor binding is followed by rapid uptake via receptor-mediated endocytosis and transient passage through early endosomes, while avoiding lysosomes and exhibiting penetration into the cytoplasm. These properties supported HPK-mediated delivery of RNA interference – which requires entry of small interfering RNAs into the cytoplasm – and are necessary for sulfonated corrole delivery as well. Mechanistic studies performed using HerGa show that the corrole elicits elevated intracellular levels of superoxide after cytoplasmic entry [20]. Use of HPK truncation mutants demonstrated that the penton base domain mediates this endosomolytic effect [20, 40].

The mechanism of endosomal membrane penetration has been elucidated using structural modeling and supported by functional assays. Together, these approaches have suggested that by pentamerization a solvent-accessible pore lined with charged amino acids is formed that can undergo protonation in an acidic environment [40]. This in turn causes a strong positive charge-mediated repellence of the protein monomers, thus exposing buried hydrophobic domains for interaction with membrane lipids, causing potential membrane destabilization. The acidifying environment of the maturing endosome during particle uptake and intracellular trafficking would provide the trigger for this activity, which is necessary for depositing corroles and other anionic cargo into the cytoplasm.

2.2.2. *Intracellular Trafficking and Intracellular Corrole Targets*

The intracellular trafficking pattern of HPK after receptor binding and internalization in tumor cell lines echoes that of wild-type penton base [48, 49] and the whole virus [50–52]. Post-endosomal virus and soluble penton base transport relies on an intact cytoskeleton for dynein-directed movement along microtubules toward the nucleus [48, 50–52]. Similarly, HPK rapidly transits toward the nuclear periphery after internalization and substantially distributes to the cytoskeletal fraction in subcellular fractionation studies [40]. HPK exhibits transient passage through early endosomes and avoidance of lysosomes where degradation of particles would otherwise take place [40]. These findings are supported by the fluorescence lifetime pattern of HerGa during tumor cell uptake, which indicates entry into a slightly acidifying environment early after internalization followed by return to a relatively neutral pH environment while still inside the cell [20].

Once in the cytoplasm, both HerGa and HerMn collapse the cytoskeleton and mitochondrial membrane potential through corrole-mediated superoxide elevation and oxidative damage to these structures [20]. Studies using truncation mutants of HPK to deliver S2Ga into cultured tumor cells demonstrated that the

penton base portion of HPK was necessary for this activity [20]. Moreover, S2Ga alone, which did not show detectable entry into the cytoplasm, lacked the ability to increase intracellular superoxide levels and cause cytoskeletal and mitochondrial damage [20]. Together these findings indicate that both Ga and Mn corroles must be exposed within the cytoplasm to access subcellular compartments, which requires lysis of endosomes after endocytotic uptake.

2.3. *In vivo* Activity

2.3.1. *Tumor Targeting*

Both HerGa and HerMn exhibit tumor-preferential targeting in mice bearing xenografts of human MDA-MB-435 tumors after systemic delivery – bypassing most normal tissue including the heart – and reduce tumor growth at low pharmacologic dose [25, 28, 37]. In these models, harvested heart and liver tissue showed negligible damage or apoptosis, and appeared in similar health as from mice receiving vehicle (saline) alone. Corresponding dosages of each corrole alone (S2Ga and S2Mn) had little to no effect on tumor cell survival *in vitro* and *in vivo* [25, 28, 37]. In mice bearing two different tumors characterized by high and low expression of HER3, systemic delivery of HPK particles exhibited preferential entry into the high HER3-expressing tumors [40, 41].

Human HER2+ breast tumors with acquired resistance to clinical growth factor inhibitors – including Herceptin® (trastuzumab) and Tykerb® (lapatinib) – exhibit augmented cell surface HER3 levels compared to their drug-sensitive counterparts [37, 53–60], and show correspondingly augmented targeting by HerGa accompanied by augmented sensitivity to HerGa [37]. Metastatic lesions arising from these tumors show even higher HER3 levels and correspondingly higher homing by systemic HPK particles [37]. HerGa exhibited prolonged tumor retention which, by virtue of its fluorescence, could be detectable in tumors up to 30 days after intratumoral injection but was cleared from non-tumor tissue sooner when injected subcutaneously [33].

2.3.2. *In vivo Dynamics*

Studies using HerGa show that the particles are deficient in immunostimulatory potency compared to whole adenovirus serotype 5 (Ad5), when used in a prime-boost regimen to elicit neutralizing antibody response in mice [28]. Antibody binding assays support molecular dynamics simulations suggesting that the HPK ligands are placed in a solvent-exposed position that partially masks the penton base domain from immune recognition [40].

3. CELL-TARGETED IMAGING

3.1. Corroles and Magnetic Resonance

Another biomedical application for metallated corroles is as MR contrast agents to distinguish cancerous from normal tissue. A panel of metallated corroles (S2Mn, S2Ga, and S2Fe) were analyzed in a 3T MRI system to identify suitable MR contrast agents. S2Mn provided the most efficient T1 relaxation shortening and contrast enhancement over S2Ga or S2Fe [25]. Furthermore, increased concentration of S2Mn led to a further decrease in T1 relaxation time and a brighter contrast signal.

Direct injection of S2Mn into tumor tissue at titrating concentrations enabled the determination of detection threshold by MRI, and demonstrated that a bright contrast enhancement could be detectable at or above 33 nmoles of S2Mn, including up to two weeks after injection [25]. HerMn was able to enhance contrast in tumor tissue in comparison to S2Mn alone. In mice with subcutaneous HER3+ MDA-MB-435 tumors, systemically delivered HerMn exhibited tumor-preferential accumulation and enhanced contrast significantly better than S2Mn, HPK alone or saline treated [25]. Interestingly, Gd exhibits considerably greater T1 shortening compared to equivalent concentrations of S2Mn *in vitro*; however, when tested *in vivo*, HerMn showed greater tumor contrast compared to Gd. This could be accounted for by the tumor targeting of HerMn [25] in comparison to the potentially broader tissue distribution of Gd which is not targeted. Additionally, the prolonged retention of corroles in tumor tissue [33] suggests that HerMn may serve as a longer lasting contrast agent compared to the rapid clearance of Gd. Hence, HerMn may have some advantages in comparison to conventional [61] contrast agents used in the clinic and thus could be developed as a valuable tool for MRI to detect tumor tissue for clinical surgical applications.

3.2. Cell-Triggered Release and Contrast Enhancement

Assembly of S2Mn with HPK results in slower T1 relaxation, suggesting that encapsulation reduces S2Mn access to water molecules.[25] The capsid formation occurring when HPK is exposed to anionic cargo such as S2Mn facilitates the convergence of HPK capsomeres into a stable capsid shell enclosing trapped S2Mn cargo, as demonstrated by structural modeling [40]. The slowed T1 relaxation time upon assembly with HPK supports this model [25] and provides evidence that S2Mn is mainly enclosed within the capsid rather than bound to the outside.

This observation was reversed upon uptake of HerMn into cultured tumor cells, which resulted in a faster T1 relaxation time post- versus pre-uptake [25]. These findings suggest that after cell entry, the particle releases S2Mn enabling re-exposure to water molecules. The endocytotic entry of the HPK capsid into maturing endosomes and its pH-mediated dismantling as determined through the functional assays and structural modeling described earlier [40] suggests that

HerMn can undergo pH-mediated dispersion of HPK capsid units and release of S2Mn cargo. In agreement, shifting HerMn particles in solution to an acidic pH resulted in an enhanced T1 time shortening, whereas S2Mn alone were unaffected by low pH [25].

4. THERAPEUTIC PROPERTIES

4.1. Tumor Detection

The cell-triggered enhancement of T1 shortening by HerMn adds an advantage for tumor detection, as this feature can provide tumor-activated contrast and hence tumor-specific detection after systemic delivery. This is based on the properties of the HPK protein shell, which minimizes S2Mn interaction with water molecules during capsid-mediated transport to the target tissue. However, when internalized into tumor cells and dismantled through acid-mediated dispersion, S2Mn is released into the water-rich intracellular milieu (Figure 4). The serum-stability of the HPK capsid has been well-established to support this model, as HPK assembly with corroles results in negligible exchange with serum proteins [28, 29]. A similar assembly with nucleic acids shows that the resulting particle protects and prevents nucleic acid degradation by serum nucleases [36, 39–41]. S2Mn alone is unable to target and penetrate tumor cells *in vitro* and *in vivo* without the HPK carrier, and hence shows no detectable contrast in tumors after systemic delivery [25]. Accordingly, tumor cell entry is critical to induce an effect.

4.2. Tumor-Targeted Therapy

The preferential accumulation of HerMn in tumor tissues over non-tumor tissues after systemic delivery implies that a potential therapeutic effect could be targeted as well. Mice bearing subcutaneous xenografts of HER3+ human MDA-MB-435 tumors received HerMn systemically following a regimen mirroring chemotherapeutic treatment in the clinic, which entailed a short sequential period of continuous delivery, followed by intermittent delivery at spaced-out time intervals [25]. This treatment resulted in reduction of tumor growth and partial regression in contrast to control treatments that included mock (saline) treatments, S2Mn alone, and empty particles [25]. On cultured MDA-MB-435 tumor cells, HerMn exhibited improved therapeutic efficacy over clinically used targeted therapies, including trastuzumab and trastuzumab-pertuzumab combination treatments, which target the ErbB receptor family members HER2 and HER3 [25]. The potential adverse effect of trastuzumab on heart tissue of treated patients highlights the need for vigilance in testing developmental and experimental therapeutics for both efficacy and safety [62]. Human cardiosphere-derived cells (CDCs), which represent the adult major cardiac cell types [63], were used to test potential cardiotoxicity despite the avoidance of HerMn accumulation in
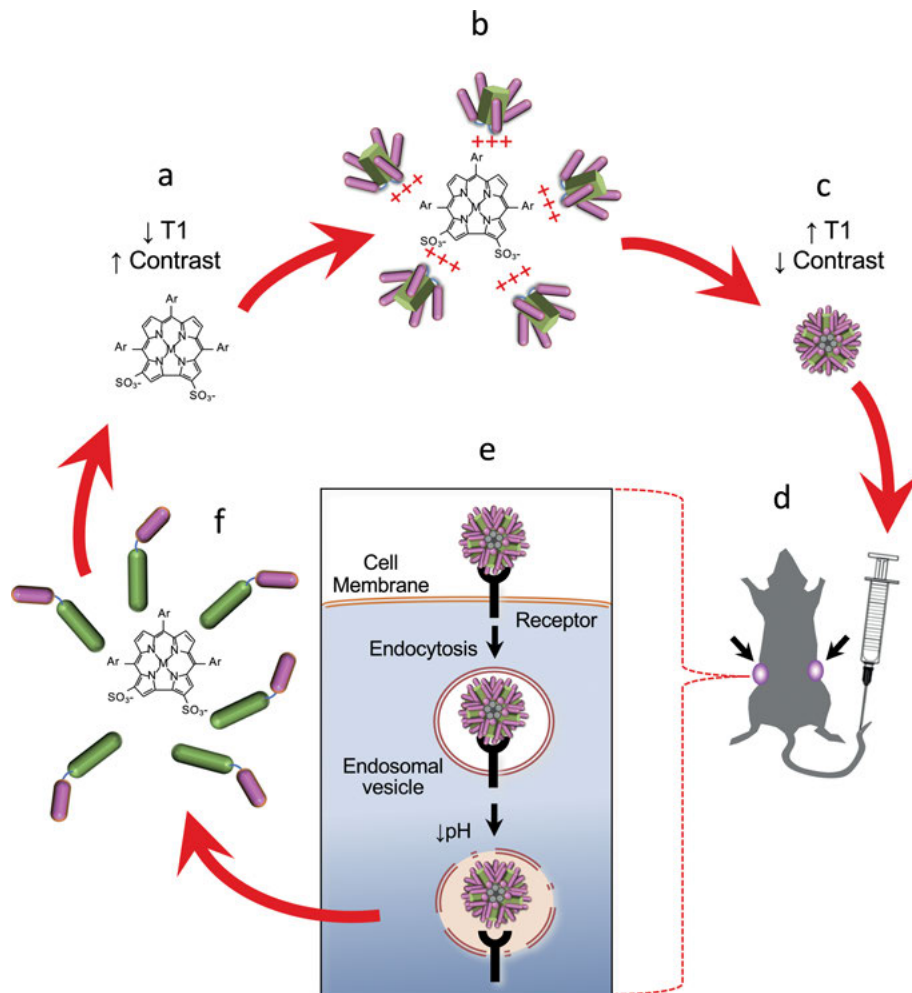
Figure 4. Schematic of tissue-triggered contrast enhancement by HerMn broken down into steps. Step **a**: free S2Mn in solution bearing T1 shortening (↓T1) and MRI contrast enhancing properties. Step **b**: electrostatic attraction between HPK and S2Mn, promoting HPK convergence into particles. Step **c**: assembled particle with reduced capacity for T1 shortening (↑T1) and MRI contrast enhancement. Step **d**: systemic delivery into tumor-bearing mice (tumors indicated by arrows), showing enlargement of (step **e**) receptor-mediated tumor uptake and entry into acidifying endosomes. Step **f**: exposure to low acid environment causing HPK dispersion, endosomolysis, and release of S2Mn, restoring T1 shortening and contrast enhancing capabilities.

the hearts of treated mice. Importantly, whereas trastuzumab cannot recognize mouse HER2 and thus rodent models would be inappropriate for testing heart safety and toxicity, HPK cross-reacts with both mouse and human HER3 [40], and thus a potentially greater body of information may be gleaned from studies

on both mouse and human tissues. HerMn exhibited no detectable toxicity to human CDCs, even at pharmacologically high molar concentrations, in contrast to doxorubicin, which has well-established cardiotoxic effects [40].

5. CONCLUDING REMARKS AND FUTURE DIRECTIONS

The corrole-containing bioparticle, HerMn, bears several advantages over conventional contrast agents used in the clinic, including the ability to target tumors after systemic delivery, tumor-specific detection owing to its tumor-triggered contrast enhancement, therapeutic efficacy due to the tumoricidal activity of S2Mn, and safety to non-tumor tissue such as the heart. While S2Mn offers the tumor toxicity and MR enhancement properties, the HPK carrier protein comprising the particle shell provides the active targeting and cellular interactions that allow cell-triggered release of S2Mn, and thus tumor-activated T1 shortening and contrast enhancement. Together these features have the potential to provide clinically-relevant tumor detection and intervention in a single particle.

A shortcoming of S2Mn as an MR contrast agent is its considerably reduced T1 shortening capacity compared to Gd. However, *in vivo* studies in mouse tumor models show that tumor contrast is greater in HerMn-treated mice in comparison to those receiving Gd, which in part may be due to the prolonged tumor retention afforded by HPK. If so, future developments could include synthesis and testing of new corrole species that may provide greater contrast enhancement, while retaining the other theranostic advantages of S2Mn and other sulfonated corroles.

ACKNOWLEDGMENTS

ABBREVIATIONS

Ad5	adenovirus serotype 5
CDC	cardiosphere-derived cells
DLS	dynamic light scattering

EGF	epidermal growth factor
HER2	human epidermal growth factor receptor 2
HER3	human epidermal growth factor receptor 3
HerGa	HPK preincubated with S2Ga
HerMn	HPK preincubated with S2Mn
HPK	HerPBK10
HSA	human serum albumin
IC_{50}	half maximal inhibitory concentration
Ig	immunoglobulin
MR	magnetic resonance
MRI	magnetic resonance imaging
S2FB	bis-sulfonated free-base corrole
S2Fe	bis-sulfonated iron(III) corrole
S2Ga	bis-sulfonated gallium(III) corrole
S2Mn	bis-sulfonated manganese(III) corrole
TEM	transmission electron microscopy

REFERENCES

1. A. Berger, *BMJ* **2002**, *324*, 35.
2. A. Datta, K. N. Raymond, *Acc. Chem. Res.* **2009**, *42*, 938–947.
3. H. Cabral, N. Nishiyama, K. Kataoka, *Acc. Chem. Res.* **2011**, *44*, 999–1008.
4. Z. Zhou, R. Bai, J. Munasinghe, Z. Shen, L. Nie, X. Chen, *ACS Nano* **2017**, *11*, 5227–5232.
5. D. Pan, S. D. Caruthers, A. Senpan, A. H. Schmieder, S. A. Wickline, G. M. Lanza, *Wiley Interdiscip. Rev. Nanomed. Nanobiotechnol.* **2011**, *3*, 162–173.
6. Z. Zhen, J. Xie, *Theranostics* **2012**, *2*, 45–54.
7. C. Rovira, K. Kunc, J. Hutter, M. Parrinello, *Inorg. Chem.* **2001**, *40*, 11–17.
8. Z. Gross, H. B. Gray, *Comments Inorg. Chem.* **2006**, *27*, 61–72.
9. A. E. Meier-Callahan, A. J. Di Bilio, L. Simkhovich, A. Mahammed, I. Goldberg, H. B. Gray, Z. Gross, *Inorg. Chem.* **2001**, *40*, 6788–6793.
10. R. K. Hocking, S. DeBeer George, Z. Gross, F. A. Walker, K. O. Hodgson, B. Hedman, E. I. Solomon, *Inorg. Chem.* **2009**, *48*, 1678–1688.
11. B. Ventura, A. Degli Esposti, B. Koszarna, D. T. Gryko, L. Flamigni, *New J. Chem.* **2005**, *29*, 1559–1566.
12. Z. Gross, N. Galili, I. Saltsman, *Angew. Chem. Int. Ed.* **1999**, *38*, 1427–1429.
13. R. D. Teo, H. B. Gray, P. Lim, J. Termini, E. Domeshek, Z. Gross, *Chem.Commun.* **2014**, *50*, 13789–13792.
14. L. Yun, H. Vazquez-Lima, H. Fang, Z. Yao, G. Geisberger, C. Dietl, A. Ghosh, P. J. Brothers, X. Fu, *Inorg. Chem.* **2014**, *53*, 7047–7054.
15. H. Agadjanian, J. J. Weaver, A. Mahammed, A. Rentsendorj, S. Bass, J. Kim, I. J. Dmochowski, R. Margalit, H. B. Gray, Z. Gross, L. K. Medina-Kauwe, *Pharm. Res.* **2006**, *23*, 367–377.
16. P. Lim, A. Mahammed, Z. Okun, I. Saltsman, Z. Gross, H. B. Gray, J. Termini, *Chem. Res. Toxicol.* **2012**, *25*, 400–409.
17. M. Soll, T. K. Goswami, Q. C. Chen, I. Saltsman, R. D. Teo, M. Shahgholi, P. Lim, A. J. Di Bilio, S. Cohen, J. Termini, H. B. Gray, Z. Gross, *Sci. Rep.* **2019**, *9*, 2294.

18. H. Agadjanian, J. Ma, A. Rentsendorj, V. Valluripalli, J. Y. Hwang, A. Mahammed, D. L. Farkas, H. B. Gray, Z. Gross, L. K. Medina-Kauwe, *Proc. Natl. Acad. Sci. USA* **2009**, *106*, 6105–6110.

19. M. Pribisko, J. Palmer, R. H. Grubbs, H. B. Gray, J. Termini, P. Lim, *Proc. Natl. Acad. Sci. USA* **2016**, *113*, E2258–E2266.

20. J. Y. Hwang, J. Lubow, D. Chu, J. Ma, H. Agadjanian, J. Sims, H. B. Gray, Z. Gross, D. L. Farkas, L. K. Medina-Kauwe, *Mol. Pharm.* **2011**, *8*, 2233–2243.

21. A. Mahammed, H. B. Gray, J. J. Weaver, K. Sorasaenee, Z. Gross, *Bioconjug. Chem.* **2004**, *15*, 738–746.

22. A. Haber, H. Agadjanian, L. K. Medina-Kauwe, Z. Gross, *J. Inorg. Biochem.* **2008**, *102*, 446–457.

23. H. Agadjanian, D. Chu, J. Y. Hwang, S. Wachsmann-Hogiu, A. Rentsendorj, L. Song, V. Valluripalli, J. Lubow, J. Ma, B. Sharifi, D. L. Farkas, L. K. Medina-Kauwe, *Nanomedicine* **2012**, *7*, 335–352.

24. L. K. Medina-Kauwe, *Ther. Deliv.* **2013**, *4*, 267–277.

25. J. D. Sims, J. Y. Hwang, S. Wagner, F. Alonso-Valenteen, C. Hanson, J. M. Taguiam, R. Polo, I. Harutyunyan, G. Karapetyan, K. Sorasaenee, A. Ibrahim, E. Marban, R. Moats, H. B. Gray, Z. Gross, L. K. Medina-Kauwe, *J. Control Release* **2015**, *217*, 92–101.

26. L. Kupershmidt, Z. Okun, T. Amit, S. Mandel, I. Saltsman, A. Mahammed, O. Bar-Am, Z. Gross, M. B. Youdim, *J. Neurochem.* **2010**, *113*, 363–373.

27. A. Kanamori, M. M. Catrinescu, A. Mahammed, Z. Gross, L. A. Levin, *J. Neurochem.* **2010**, *114*, 488–498.

28. H. Agadjanian, J. Ma, A. Rentsendorj, V. Valluripalli, J. Y. Hwang, A. Mahammed, D. L. Farkas, H. B. Gray, Z. Gross, L. K. Medina-Kauwe, *Proc. Natl. Acad. Sci. USA* **2009**, *106*, 6105–6110.

29. H. Agadjanian, J. J. Weaver, A. Mahammed, A. Rentsendorj, S. Bass, J. Kim, I. J. Dmochowski, R. Margalit, H. B. Gray, Z. Gross, L. K. Medina-Kauwe, *Pharm. Res.* **2006**, *23*, 367–737.

30. J. Bendix, I. J. Dmochowski, H. B. Gray, A. Mahammed, L. Simkhovich, Z. Gross, *Angew. Chem., Int. Ed.* **2000**, *39*, 4048–4051.

31. J. Y. Hwang, S. Wachsmann-Hogiu, V. K. Ramanujan, J. Ljubimova, Z. Gross, H. B. Gray, L. K. Medina-Kauwe, D. L. Farkas, *Mol. Imaging Biol.* **2012**, *14*, 431–442.

32. J. Y. Hwang, J. Lubow, J. D. Sims, H. B. Gray, A. Mahammed, Z. Gross, L. K. Medina-Kauwe, D. L. Farkas, *J. Biomed. Optics* **2012**, *17*, 015003.

33. J. Y. Hwang, J. Lubow, D. Chu, J. Sims, F. Alonso-Valenteen, H. B. Gray, Z. Gross, D. L. Farkas, L. K. Medina-Kauwe, *J. Controlled Release* **2012**, *163*, 368–373.

34. A. Haber, M. Aviram, Z. Gross, *Chem. Sci.* **2011**, *2*, 295–302.

35. D. L. Daleke, *J. Lipid Res.* **2003**, *44*, 233–242.

36. L. K. Medina-Kauwe, M. Maguire, N. Kasahara, L. Kedes, *Gene Therapy* **2001**, *8*, 1753–1761.

37. J. D. Sims, J. M. Taguiam, F. Alonso-Valenteen, J. Markman, H. Agadjanian, D. Chu, J. Lubow, R. Abrol, D. Srinivas, A. Jain, B. Han, Y. Qu, P. Mirzadehgan, J.-Y. Hwang, A. Rentsendorj, A. Chung, J. Lester, B. Y. Karlan, H. B. Gray, Z. Gross, A. Giuliano, X. Cui, L. K. Medina-Kauwe, *J. Controlled Release* **2018**, *271*, 127–138.

38. X. Han, N. Kasahara, Y. W. Kan, *Proc. Natl. Acad. Sci. USA* **1995**, *92*, 9747–9751.

39. L. K. Medina-Kauwe, N. Kasahara, L. Kedes, *Gene Therapy* **2001**, *8*, 795–803.

40. F. Alonso-Valenteen, S. Pacheco, D. Srinivas, A. Rentsendorj, D. Chu, J. Lubow, J. Sims, T. Miao, S. Mikhael, J. Y. Hwang, R. Abrol, L. K. Medina Kauwe, *Nucl. Acids Res.* **2019**, *47*, 11020–11043.

41. H. Agadjanian, D. Chu, J. Y. Hwang, S. Wachsmann-Hogiu, A. Rentsendorj, L. Song, V. Valluripalli, J. Lubow, J. Ma, B. Sharifi, D. L. Farkas, L. K. Medina-Kauwe, *Nanomedicine* **2012**, *7*, 335–352.

42. C. Zubieta, G. Schoehn, J. Chroboczek, S. Cusack, *Mol. Cell.* **2005**, *17*, 121–135.

43. W. C. Russell, *J. Gen. Virol.* **2009**, *90*, 1–20.

44. P. Fender, *Methods Mol. Biol.* **2014**, *1089*, 61–70.

45. E. Szolajska, W. P. Burmeister, M. Zochowska, B. Nerlo, I. Andreev, G. Schoehn, J. P. Andrieu, P. Fender, A. Naskalska, C. Zubieta, S. Cusack, J. Chroboczek, *PLoS One* **2012**, *7*, e46075.

46. A. Villegas-Mendez, M. I. Garin, E. Pineda-Molina, E. Veratti, J. A. Bueren, P. Fender, J.-L. Lenormand, *Mol. Ther.* **2010**, *18*, 1046–1053.

47. M. Zochowska, A. Paca, G. Schoehn, J. P. Andrieu, J. Chroboczek, B. Dublet, E. Szolajska, *PLoS One* **2009**, *4*, e5569.

48. A. Rentsendorj, J. Xie, M. MacVeigh, H. Agadjanian, S. Bass, D. H. Kim, J. Rossi, S. F. Hamm-Alvarez, L. K. Medina-Kauwe, *Gene Ther.* **2006**, *13*, 821–836.

49. S. S. Hong, B. Gay, L. Karayan, M. C. Dabauvalle, P. Boulanger, *Virology.* **1999**, *262*, 163–177.

50. P. L. Leopold, R. G. Crystal, *Adv. Drug Deliv. Rev.* **2007**, *59*, 810–821.

51. S. Kelkar, B. P. De, G. Gao, J. M. Wilson, R. G. Crystal, P. L. Leopold, *J. Virol.* **2006**, *80*, 7781–7785.

52. P. L. Leopold, G. Kreitzer, N. Miyazawa, S. Rempel, K. K. Pfister, E. Rodriguez-Boulan, R. G. Crystal, *Human Gene Therapy* **2000**, *11*, 151–165.

53. M. Narayan, J. A. Wilken, L. N. Harris, A. T. Baron, K. D. Kimbler, N. J. Maihle, *Cancer Res.* **2009**, *69*, 2191–2194.

54. J. T. Garrett, M. G. Olivares, C. Rinehart, N. D. Granja-Ingram, V. Sanchez, A. Chakrabarty, B. Dave, R. S. Cook, W. Pao, E. McKinely, H. C. Manning, J. Chang, C. L. Arteaga, *Proc. Natl. Acad.Sci. USA* **2011**, *108*, 5021–5026.

55. J. T. Garrett, C. R. Sutton, M. G. Kuba, R. S. Cook, C. L. Arteaga, *Clin. Cancer Res.* **2013**, *19*, 610–619.

56. I. Hutcheson, D. Barrow, M. Hasmann, R. Nicholson, *Molecular Cancer Therapeutics* **2007**, *6*, A118.

57. G. D. L. Phillips, C. T. Fields, G. Li, D. Dowbenko, G. Schaefer, K. Miller, F. Andre, H. A. Burris, K. S. Albain, N. Harbeck, V. Dieras, D. Crivellari, L. Fang, E. Guardino, S. R. Olsen, L. M. Crocker, M. X. Sliwkowski, *Clin. Cancer Res.* **2014**, *20*, 456–468.

58. N. V. Sergina, M. Rausch, D. Wang, J. Blair, B. Hann, K. M. Shokat, M. M. Moasser, *Nature* **2007**, *445*, 437–441.

59. A. Chakrabarty, V. Sanchez, M. G. Kuba, C. Rinehart, C. L. Arteaga, *Proc. Natl. Acad. Sci. USA* **2012**, *109*, 2718–2723.

60. J. A. Engelman, K. Zejnullahu, T. Mitsudomi, Y. Song, C. Hyland, J. O. Park, N. Lindeman, C. M. Gale, X. Zhao, J. Christensen, T. Kosaka, A. J. Holmes, A. M. Rogers, F. Cappuzzo, T. Mok, C. Lee, B. E. Johnson, L. C. Cantley, P. A. Janne, *Science* **2007**, *316*, 1039–1043.

61. S. Aime, P. Caravan, *J. Magn. Res. Imag.* **2009**, *30*, 1259–1267.

62. D. J. Slamon, B. Leyland-Jones, S. Shak, H. Fuchs, V. Paton, A. Bajamonde, T. Fleming, W. Eiermann, J. Wolter, M. Pegram, J. Baselga, L. Norton, *New Engl. J. Med.* **2001**, *344*, 783–792.

63. L. Barile, M. Gherghiceanu, L. Popescu, T. Moccetti, G. Vassalli, *Stem Cells Int.* **2013**, *2013*, 916837.

11

Positron Emission Tomography (PET) Driven Theranostics

Suresh Pandey,[1] *Giovanni Battista Giovenzana,*[2]
Dezsö Szikra,[3] *and Zsolt Baranyai*[1]

[1]Bracco Imaging Spa, Bracco Research Center, Via Ribes 5, I-10010 Colleretto Giacosa, Italy
<zsolt.baranyai@bracco.com>,

[2]Dipartimento di Scienze del Farmaco, Università del Piemonte Orientale,
Largo Donegani 2/3, I-28100 Novara, Italy and

[3]Scanomed Ltd., Nagyerdei Krt. 98, H-4032 Debrecen, Hungary

Abstract: "Theranostics" or "theragnostics" is a concept combining therapy and diagnostics, particularly *in vivo* to maximize efficient delivery of targeted therapeutic agents to the tumors. It enables "personalized medicine", meaning that the therapy is tailored to the needs of a given patient. Diagnostic imaging has also a great role in the monitoring of therapy, because continuation or change of treatment plan can be decided based on the information about the tracer accumulation in the tumors. In this chapter we briefly describe positron emission tomography-based theranostics in cancer treatment and diagnosis, with a focus on metal-based agents. The chapter will cover the thermodynamics, formation and dissociation kinetics of metal ion-based radiopharmaceuticals for the selection of optimal chelates for the complexation of radiometals and the development of novel and more effective cancer specific theranostic agents.

Keywords: diagnostic isotopes · chelating agents · kinetic · peptide receptor radionuclide therapy · positron emission tomography · targeting agents · theranostics · therapeutic isotopes · thermodynamic

1. THERANOSTICS IN THE CONTEXT OF CANCER TREATMENT

"Theranostics", coined by combining a few letters from the words <u>thera</u>peutics and diag<u>nostics,</u> is a relatively new concept in the field of nuclear medicine with the goal of delivering personalized cancer treatment [1]. Theranostics may involve two different radionuclide elements (theranostic isotope pair with different elements, e.g., Netspot™, ^{68}Ga(DOTATATE) for positron emission tomography (PET) imaging and Lutathera®, ^{177}Lu(DOTATATE) for β therapy), or the same element with different radionuclide properties (theranostic isotope pair with the same element, e.g., AdreView™, ^{123}I-MIBG for single photon emission computed tomography (SPECT) imaging and Azedra®, ^{131}I-MIBG for β therapy). There are many advantages for using the radionuclide pair of the same element or radioiso-

topes for theranostic applications where possible (for example, ^{64}Cu for PET and ^{67}Cu for β therapy) [2].

The majority of therapeutic radioisotopes are metallic and need to be complexed by a chelating agent (CA, e.g. DOTA, DTPA, etc.) for safe *in vivo* delivery (e.g., Quadramet®, ^{153}Sm(EDTMP)), with a few exceptions (e.g., Xofigo®, ^{223}RaCl$_2$). Furthermore, CAs are typically conjugated to a targeting moiety with (or without) a linker at a site away from the molecular recognition/binding site to precisely deliver the radioactivity to diseased tissues with minimal exposure to normal tissues. They can be called molecular radiopharmaceuticals. Recently, significant attention has been devoted towards the linker, which can play a crucial role in modulating the *in vivo* properties of the whole radiopharmaceutical (e.g., ^{177}Lu(PSMA-617)) [3]. Since a lot of theranostic radionuclide combinations are possible, numerous criteria should be considered in the selection of the theranostic pairs in addition to their chemical and physical properties.

2.   LIMITATION OF FDG/PET ONCOLOGY

2.1. ^{18}F-2-Fluoro-2-deoxy-D-glucose (FDG): Promise and Pitfalls

^{18}F-2-Fluoro-2-deoxy-D-glucose (FDG) is a PET radiotracer targeting one of the key metabolic pathways in the cell: carbohydrates. In fact, FDG is so successful (widely available and used) that it often synonyms with PET and is considered a gold standard in PET oncology. FDG has been the undisputed market leader in the PET field since its approval by the U. S. Food and Drug Administration (FDA) in 1994 and currently it accounts for ~90 % of the total sales volume. FDG PET combined with computed tomography (CT) or magnetic resonance imaging (MRI) has good diagnostic accuracy in lung cancer, head and neck cancer, the majority (if not all) of breast cancers, lymphoma, and melanoma [4].

Although quite successful in the above oncology cases, there is enough clinical evidence documenting FDG to be of limited value in the case of prostate, bladder, renal, and gastric cancer, brain cancer/metastasis, and inflammation as well as follow-up until 12 weeks post chemotherapy. Due to the suboptimal specificity and sensitivity of FDG, new radiotracers with improved diagnostic sensitivity, specificity, and accuracy represent an area of intense research. These include molecules targeting metabolic pathways other than carbohydrate, such as amino acids, fatty acids, nucleotides, steroids, and hypoxia. Some of these radiotracers have been under development for decades and have not yet established the same success as FDG.

2.2.   Beyond FDG: Biomarkers

In recent years, due to advancement in technologies, our understanding of complex cancer biology (omics) has led to the identification of numerous biomarkers,

a few of them clinically validated. The latter better represent the evolution and progression of certain types of cancer. Many cancer types are slowly progressing due to their lower metabolic rate and are often missed by FDG scans. For example, FDG has a limited role in neuroendocrine tumors (NETs) and its use is generally not advised. Rather, somatostatin receptor (SSTR) is a proven NET biomarker [5].

Similarly, FDG is not useful in prostate cancer and has limited value. This led towards development of tracers targeting different pathways/biomarkers in prostate cancer such as lipid biosynthesis, fatty acid metabolism, amino acid metabolism, prostate specific membrane antigen (PSMA), and gastrin-releasing peptide receptor [6]. Axumin, [18F]-fluciclovine, which targets amino acid metabolism is the most widely used PET tracer for the diagnosis of prostate cancer at present. Current research however, seems to be pointing to PSMA as the most promising biomarker for castration-resistant prostate cancer (CRPC) at low PSMA values and is a focal point for the research and the development of theranostics.

FDG is the most common tracer used in breast cancer (except for lobular breast cancer), primarily for staging and follow-up [7]. For sentinel lymph node assessment 99mTc-lymphoseek, which targets the mannose receptor, is primarily used and bone scans are performed with 99mTc-MDP (methylenediphosphate) or Na[18F], targeting calcium in the bone. 18F-FLT (fluorothymidine) is also used in a subset of cases to predict/monitor treatment response. Some investigations are carried out with 99mTc-sestamibi and 18F-fluciclovine in cases of lobular breast cancer. Similarly, FDG is used in cases of brain cancer (high grade glioma) but the signals are often very difficult to interpret due to background signal from normal FDG uptake. Based on preliminary clinical studies, 18F-fluciclovine seems to provide a superior diagnostic assessment for brain metastases and primary brain cancer.

Epidermal growth factor receptor (EGFR), human epidermal growth factor receptor-2 (HER2), carbonic anhydrase-IX (CAIX), poly(ADP-ribose) polymerase 1 (PARP1), and urokinase-type plasminogen activator receptor (uPAR) are among the approved clinical biomarkers, and PET radiotracers for each of these biomarkers are in early to mid-stages of clinical development. Nevertheless, as treatment options are becoming more personalized due to an advanced knowledge of cancer biology, it is also opening niche spaces for personalized imaging.

2.3. Positron Emission Tomography Agents Based Upon Biomarkers

There were only a few FDA approved PET radiopharmaceuticals (Table 1) before the modernization act of the FDA by the US congress in 1997 (creating industry guidelines and regulations, 21 CFR 212). Since then, there has been much interest in bringing new radiopharmaceuticals into the market. Many theranostic agents are at advanced stages (phase 3) of clinical development targeting biomarkers such as SSTR and PSMA.

Table 1. FDA-approved PET radiopharmaceuticals.

Trade Name/Name	Year	Indication	Target(Biomarker)	Manufacturer
Cardiogen-82®; ^{82}RbCl	1989	cardiology	blood flow agent	Bracco; Draximage
^{18}F-FDG	1994	oncology, neurology	carbohydrate metabolism	various
^{13}NH$_3$	2007	cardiology	blood flow agent	various
Na^{18}F	2011	oncology, cardiology	seeks bone calcium	various
^{11}C-Choline	2012	oncology (PCa)	lipid pathway	Mayo Clinic and few others
Amyvid™; ^{18}F-Florbetapir	2012	neurology (AD)	β-amyloid plaque	Eli-Lilly
Vizamyl™; ^{18}F- Flutemetamol	2013	neurology (AD)	β-amyloid plaque	GE Healthcare
Neuraceq™; ^{18}F-Florbetaben	2014	neurology (AD)	β-amyloid plaque	Alliance Medical
Netspot™; ^{68}Ga(DOTATATE)	2016	oncology (NET)	SSTR2	Novartis (AAA)
Axumin®; ^{18}F-Fluciclovine	2016	oncology (PCa)	AA transporter	Bracco (BED)
^{68}Ga(DOTATOC)	2019	oncology (NET)	SSTR2	University of Iowa; AAA; ITM
^{18}F-FDOPA	2019	neurology (PD)	dopaminergic nerve terminals	Feinstein Inst. for Medical Research

PCa: prostate cancer; AD: Alzheimer's disease; NET: neuroendocrine tumor; PD: Parkinson's disease; AAA: Advanced Accelerator Applications; BED: Blue Earth Diagnostics; ITM: Isotopen Technologien München AG

3. ISOTOPES OF THERANOSTIC APPLICATIONS

3.1. Suitable Isotopes for Radiodiagnosis and Radiotherapy

The medical application of radioisotopes for diagnosis and therapy has gone through a long journey of development. The availability of these techniques made possible "personalized medicine", tailoring the therapy to the needs of an individual patient, based on the precise information obtained with these methods. With an increasing number of patients receiving isotope therapy, high inter-patient differences were found, highlighting the importance of precise dosimetry with an appropriately chosen positron-emitting pair of the therapeutic isotope.

3.1.1. *Diagnostic Isotopes*

^{18}F: The first widely applied and still the most important isotope for PET. The easy- and high-yield production with affordable price cyclotrons made ^{18}F so successful. It can be quite efficiently introduced into organic molecules by fluorination, although requiring automated synthesis systems and good manufacturing practices production. Its optimal half-life (109.77 min) enables transportation of the labelled tracer but gives a tolerable radiation dose to the patient. The short positron range yields good image resolution. The formation of ternary complexes of Al^{3+}-$^{18}F^{-}$-CAs relies on the use of aqueous fluoride, simplifying labelling and allowing one to obtain multi-curie activities [8].

^{68}Ga: The availability of commercial ^{68}Ge/^{68}Ga generators (Obninsk 1996) enabled the use of ^{68}Ga-labelled tracers for NET and later prostate cancer. The high positron energy of ^{68}Ga (E_{max}= 1900 keV) decreases the image quality by causing lower resolution and higher noise. ^{68}Ga is helping the introduction of new tracers for PET centers without cyclotrons, but the limited activity that a generator can provide is not sufficient to handle a high number of patients. The increasing demand for ^{68}Ga can be seen in the high interest in the introduction of liquid targets for the production with cyclotrons, yielding only limited activity, and being rather risky to operate. A simple and affordable solid target system for ^{68}Ga production is needed. The ~1 h half-life and the 2 % limit for $^{66/67}$Ga contaminants do not allow a long range transportation of the produced isotope because the radionuclidic purity quickly falls under the acceptable limit.

^{44}Sc: ^{44}Sc is an emerging PET isotope, a competitor of ^{68}Ga in some aspects. It is available from a generator (^{44}Ti/^{44}Sc) and it can be produced in medical cyclotrons [9]. The main advantage of ^{44}Sc over ^{68}Ga is the longer half-life (3.97 h), enabling production by medical cyclotrons before production of ^{18}F and transportation together with FDG. Sc^{3+}-complexes are similar to Lu^{3+}-complexes, resulting in similar biodistribution [10]. ^{44}Sc forms a theranostic pair with ^{47}Sc, but the availability of ^{47}Sc is hardly comparable to ^{177}Lu. ^{43}Sc, with almost the same half-life (3.89 h) and lacking the high energy γ-emission (1157 keV, 99.9 %) characteristic of ^{44}Sc, would be more beneficial for human use but it is much less available due to the production with research cyclotrons (^{40}Ca(α,p)^{43}Sc) [11]. The more convenient logistics associated with the longer half-life of ^{44}Sc might be enough to replace ^{68}Ga in current applications.

^{64}Cu: The use of ^{64}Cu has a long history with several successful examples [12], but lacks a fast development. Constantly present in preclinical and clinical experiments, no ground-breaking application led to a broad use. It can be produced with low-energy medical cyclotrons, but the investment costs of solid targetry and of the target material (enriched ^{64}Ni) are a strong limit.

^{89}Zr: The half-life of ^{89}Zr (78.4 h) favorably matches the pharmacokinetics of antibodies. It can be produced from natural Y foil [13]. Deferoxamine (DFO) is the most widely used chelator for ^{89}Zr. While ^{89}Zr(DFO) was not stable enough in animal experiments [14], it has performed well in humans. Gasser et al. modified the DFO chelator, increasing *in vivo* stability [15]. 1,2-HOPO was also found to form an inert complex with Zr [16].

^{52}Mn: ^{52}Mn has a good chance to replace ^{89}Zr, as it has better coordination and imaging properties (mean positron range: 0.63 mm, approximately half of that of ^{89}Zr). A Mn^{2+} complex with DOTA is more stable than Zr(DFO) [17]. It can be easily produced by irradiation of natural Cr. The accompanying high energy γ-radiation is a disadvantage, significantly increasing patient dose, but this is also true for other isotopes, like ^{64}Cu.

3.1.2.   Therapeutic Isotopes

The choice of a therapeutic radionuclide is often made by the availability of the isotope rather than matching the decay characteristics (half-life, α- or β-energy, etc.) for a specific disease.

^{67}Cu: ^{67}Cu is a low-energy β-emitter, with a γ-line, suitable for SPECT imaging. It can only be produced (^{68}Zn(p,2p)^{67}Cu) in high energy cyclotrons, limiting its broader application.

^{47}Sc: ^{47}Sc (3.35d, 100 % β 142.6 keV, 68.4 %, 203.9 keV, 31.6 %, γ 159.4 keV 68.3 %) can be produced with a cyclotron or linac from V, Ti or Cr target materials. Reactor production from ^{47}Ti is possible, but the production of ^{47}Ca decaying to ^{47}Sc with $t_{1/2}$ = 4.5 d is the most efficient.

^{90}Y: ^{90}Y(DOTATOC) showed unexpected success in the treatment of NET. Two decades before, ^{90}Y was the most frequently used therapeutic isotope, but the clinical application and the scientific interest gradually shifted from ^{90}Y to ^{177}Lu, due to the lower kidney toxicity and the better therapeutic efficiency for small tumors [18]. The difference is caused by the shorter mean path of β-particles emitted by ^{177}Lu.

^{177}Lu: ^{177}Lu has become the standard therapeutic isotope for peptide receptor radionuclide therapy (PRRT), with treatment of NET and prostate cancer. With a maximum β-range of 2 mm, it is optimal for the treatment of small metastases. Its γ-lines (112.9 and 208.4 keV) allow SPECT imaging for patient dosimetry.

^{161}Tb: ^{161}Tb can be produced in a high flux reactor by the neutron irradiation of enriched ^{160}Gd (^{160}Gd(n,γ)^{161}Gd → ^{161}Tb). It has similar decay characteristics to ^{177}Lu (6.89 and 6.65 day half-life, 522 and 497 keV maximum β-energy, respectively), but ^{161}Tb has more low-energy Auger and conversion electrons, leading to a higher dose per decay in the case of small tumors. This advantage becomes important in the 10–15 μm range. The higher efficacy of ^{161}Tb was shown by Müller et al. on prostate cancer cell lines as well as in *in vivo* preclinical experiments [19]. The use of ^{161}Tb, instead of ^{177}Lu yields an approximately 1.4 times higher adsorbed tumor dose [20].

^{225}Ac: ^{225}Ac decays with 4 α-emissions and was used in several preclinical and clinical studies. Currently, it is available as a daughter of ^{229}Th, and via the irradiation of long half-life radioactive target materials (^{232}Th(p,2p6n)^{225}Ac, ^{226}Ra(p,2n)^{225}Ac and ^{226}Ra(γ,n)^{225}Ra → ^{225}Ac). The α-decay of ^{225}Ac to ^{213}Bi has a recoil effect, leading to the release of the daughter nuclide from the complex, resulting in a high unwanted dose to healthy tissues (e.g., kidneys). Several ^{225}Ac-labelled antibodies were successfully used in preclinical and clinical studies [21]. The driving force of the further development of α-therapy is the success of

^{225}Ac(DOTA-PSMA). It was used in a recent clinical trial on patients with prostate cancer without prior chemotherapy [22].

^{213}Bi: ^{213}Bi is available from an ^{225}Ac/^{213}Bi generator. ^{213}Bi-labelled substance P was used successfully in patients with local administration to gliomas [23]. The injected activity remained in the tumors, and no nephrotoxicity was observed. ^{213}Bi(DOTATOC) was also successful in the treatment of tumors not responding to β-therapy [24].

^{223}Ra: Despite much effort to find an appropriate chelator to form a stable complex with ^{223}Ra [25], no candidates met the stability and inertness requirements for *in vivo* use. An interesting approach, to bind Ra to the surface of solid nanoparticles by adsorption, seems to solve the problems associated with the recoil of the isotope during α decay. It was found that daughter isotopes can be resorbed on the solid surface. However, the high liver uptake of nanoparticles inhibits the use of these carriers in α-therapy.

^{149}Tb: ^{149}Tb emits a single low energy α-particle besides positron emission and γ-radiation. It was produced by Beyer et al. [26] in the $Nd(^{12}C,5n)^{149}Dy \rightarrow {}^{149}Tb$ reaction and proton-induced spallation of Tb target, followed by online isotope separation [27]. Its potential was shown by Müller et al. [28], but broader application requires an affordable production route.

^{212}Pb: ^{212}Pb decays to the α-emitter ^{212}Bi with β-emission and is produced from ^{228}Th, available from spent nuclear fuel [29]. It forms a theranostic pair with ^{203}Pb, produced from ^{nat}Tl (^{203}Tl(p,n)^{203}Pb). ^{212}Pb(DOTA-trastuzumab) was used in preclinical experiments with prostate cancer models [30] and ^{212}PbTCMC-trastuzumab in clinical trials for HER-positive tumors [31].

3.2. "Matched Pairs" of Isotopes for Tandem Application

"Real" theranostics with diagnostic and therapeutic functions are characterized by identical biodistribution. This is most often done by labelling the same molecule with a diagnostic or a therapeutic isotope of the same element. Examples of "real" theranostic pairs are: $^{44/43/47}$Sc, $^{64/67}$Cu, $^{206/213}$Bi, $^{86/90}$Y, $^{152/161}$Tb. These are rarely used in clinical practice, mainly because of the poor availability of one of the isotope pair. Imperfect, but practically useful pairs are ^{68}Ga(DOTATOC) and ^{177}Lu(DOTATATE) or ^{68}Ga/^{177}Lu(PSMA-617). ^{68}Ga- and ^{177}Lu-labelled peptides have a different biodistribution, but they are still good enough to determine the receptor positivity of the tumor lesions of the patient, and to monitor their response to isotope therapy [32].

Although Tb-isotopes offer a unique possibility to perform PET/SPECT imaging and α/β/Auger electron therapy, the lack of cost-efficient decentralized production methods of Tb isotopes does not allow its broader application. An interesting approach is the development of "radiohybrids" by dual isotope labelling with the currently available isotopes (^{18}F, ^{68}Ga, ^{177}Lu) [33]. This is a family of compounds, containing both a metal chelator and a silicon-fluoride acceptor in a single molecule. These compounds can be simultaneously labelled with metal ions and fluoride. The intended application determines the labelling agent, which

should be a radioactive or non-radioactive isotope. The same biodistribution can be achieved with an ^{18}F-^{175}Lu-labelled diagnostic and a ^{19}F-^{177}Lu-labelled therapeutic tracer.

3.3. Practical Requirements for Diagnostic and Therapeutic Radiopharmaceuticals

Four key properties stand out for the selection of a diagnostic radionuclide: (i) low β^+ energy resulting in higher resolution with appropriate half-life (hours), (ii) wide availability, (iii) low cost of commercial production, and (iv) easy and fast radiolabelling (kit type method) at low or room temperature. Probably one radioisotope cannot fulfill all requirements, leaving room for more than one diagnostic radioisotope. Though there are numerous diagnostic radioisotopes in preclinical and early clinical phase, the two most successful ones in commercial and clinical use are ^{18}F and ^{68}Ga, with ^{18}F as the main workhorse of PET imaging.

In the case of a therapeutic/theranostic radioisotope, an important requirement is the availability in chemically pure and preferably no carrier-added form so that high specific activity radiopharmaceuticals can be produced for the maximum delivery of radiation to the targeted lesions. In addition, if the radionuclide has an imaging component (γ-rays) then it could be exploited for dosimetry. High stability is crucial because the residence time of radiotherapeutics must be rather longer (a few hours/days) within lesions to exert a meaningful biological effect.

Therapeutic isotopes cause radiation-induced cell death, based on irreparable DNA damage through direct or indirect interaction with double-stranded DNA. β-particles produce infrequent ionizations along their path, causing more reparable DNA damage. The ionization density of α-particles and Auger electron emitters is much higher. An amount of 1–4 α-particles, flying through the cell nucleus is enough to kill a mammalian cell, but several thousands of β-particles are needed to reach the same effect.

Radionuclides with higher β-energy have a higher penetration range in soft tissue, causing a "crossfire effect" beneficial for large tumors but not optimal for small ones. With more precise targeting becoming available, the focus is shifted from isotopes with longer penetration range (^{90}Y) to those with shorter (^{177}Lu) and lately to α-emitters (^{225}Ac) for an even more localized effect [34]. Shifting from late stage treatment to first line therapy changes the requirements of therapy: besides efficient tumor cell killing, side effect reduction becomes more important [35].

Auger electron emitters offer a very selectively targeted therapeutic option with fewer side effects because the decaying atom has to be within nanometer range from the DNA. The importance of close proximity to the cell nucleus was proven by Constantini et al. [36], who modified an ^{111}In-labelled monoclonal antibody with a nuclear localization peptide sequence, which caused a 6-fold increase in the radiotoxicity to breast cancer cells.

4.   METAL COMPLEXES AND THEIR IMPORTANCE

The use of radiometal ions for diagnostic and therapeutic applications relies on their coordination with chelating agents (CAs) [37]. Besides high thermodynamic stability, the kinetic of the formation and dissociation of the radiometal complex must be considered for the limited timescale offered by fast decaying radioisotopes and to reduce potential *in vivo* dissociation. Moreover, the CA must be provided with an additional, reactive functional group to be employed to link with the targeting molecular vector (biomolecules or small molecules), hence, they are called bifunctional chelating agents (BFCAs) [38, 39]. The basic principles and experimental methods for the characterization of the equilibrium and kinetic properties of "cold" metal complexes are summarized in Chapter 2 of this book. Chapter 3 gives a comprehensive overview of Mn^{2+} complexes, not discussed here in detail. In this chapter the equilibrium and kinetic properties of the metal complexes are discussed by considering some example CAs proposed for the complexation of the most important radiometal ions.

4.1.   Acyclic, Semicyclic, and Cyclic Chelators

The number of CAs for nuclear medicine is steadily growing due to the constant research in this field. CAs can be classified according to their molecular structure and in detail according to their structural backbone, i.e., acyclic, mesocyclic, and macrocyclic CAs.

Acyclic CAs (Figure 1) include linear chain polyaminopolycarboxylic acids and are exemplified by the archetypal hexadentate EDTA, forming quite stable complexes with Ga^{3+} [40]. The phosphonic analog of EDTA (EDTMP) forms a stable complex with $^{153}Sm^{3+}$, used in the palliative treatment of bone metastases [41]. The homolog DTPA shows a higher denticity and is more suited for the coordination of metal ions with higher coordination requirements such as $^{111}In^{3+}$ and radiolanthanides [37, 42]. HBED shares with EDTA the denticity with a different mixed phenolic-carboxylic functionalization. Once more, the oxygenated donor groups impart a marked affinity for Ga^{3+}. Aromatic heterocycles play an active role in coordination through ring heteroatoms and suitably placed functional groups. DEDPA is a hexadentate CA with a central ethylenediamine symmetrically supporting two picolinic acid residues, resulting in a significant affinity for Ga^{3+} [37]. Closely related is HOX, where two 8-hydroxyquinoline ("oxine") moieties are located on an ethylenediamine unit, once more leading to an highly effective CA for Ga^{3+} [43]. Hydroxypyridones (HOPOs) are versatile and efficient bidentate heterocycles, widely used to build a variety of CAs. 3,4,3-HOPO is an example where four coordinating hydroxypyridone units are located on a linear tetramine, yielding an overall octadentate CA with a strong affinity for Zr^{4+} [44]. A longer linear backbone is shown by deferoxamine, a natural siderophore isolated from *Streptomyces sp.* and featuring four hydroxamic acid residues and a terminal amino group. The latter is especially useful to link the CA
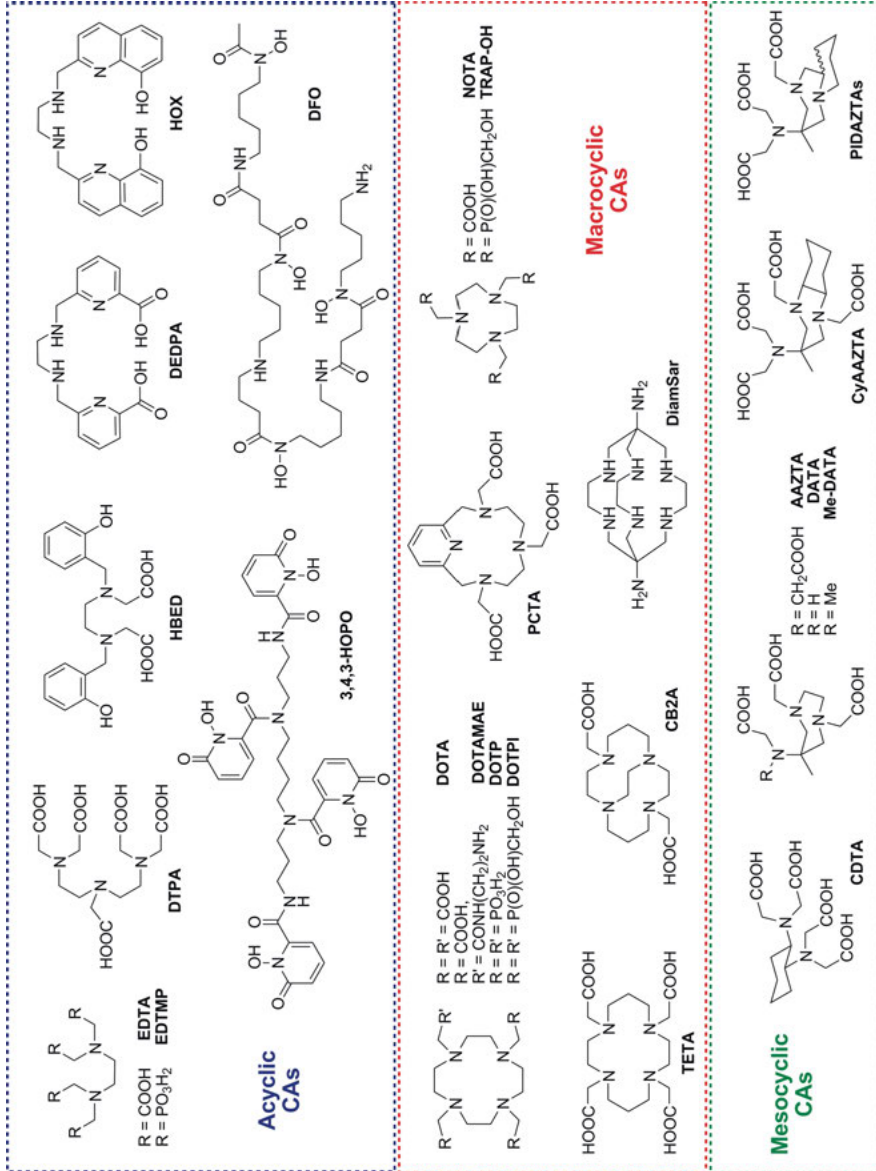
Figure 1. Chelating agents.

to targeting vectors, while the four hydroxamate groups efficiently coordinate "hard" metal ions such as Ga^{3+} and Zr^{4+} [37, 44].

Macrocyclic CAs (Figure 1) share a molecular skeleton with at least one large ring (> 8 atoms), hosting donor atoms and eventually bearing functionalized pendant arms. Macrocyclic CAs are typified by DOTA (1,4,7,10-tetraazacyclododecane, "cyclen"), a 12-membered cyclic tetraamine with 4 carboxymethyl pendant arms. The preorganization to chelation of the macrocyclic ring and the octadenticity lead to the formation of highly inert complexes with most metal ions. DOTA represents a universal workhorse in terms of thermodynamic stability of the corresponding complexes, the latter being used in almost all diagnostic techniques (Gd^{3+}, $^{111}In^{3+}$, $^{177}Lu^{3+}$, $^{44}Sc^{3+}$, $^{68}Ga^{3+}$, $^{213}Bi^{3+}$, and even $^{225}Ac^{3+}$) [37, 42, 44, 45]. The inertness of metal complexes associated with the macrocyclic backbone of DOTA is the base for the preparation of several derivatives. Among them, it is worth noting that the substitution of the carboxylic groups of DOTA with phosphonate/phosphinate groups yields interesting CAs such as DOTP and DOTPI, respectively. The highly charged phosphonate and the modular phosphinate allow the preparation of markedly stable complexes of $^{213}Bi^{3+}$, $^{64}Cu^{2+}$, and $^{177}Lu^{3+}$ [37, 44].

Formal fusion of the "cyclen" ring with a coordinating pyridine leads to the still more stiff PCTA. Its lower denticity reduces the thermodynamic stability of the corresponding complexes with respect to DOTA, but the increased rigidity of the pyridine-containing macrocycle ("pyclen") compensates on the side of the kinetic inertness, comparable to that of DOTA chelates and making PCTA suitable for labelling with radioisotopes of In^{3+}, Y^{3+}, and Lu^{3+} [37]. Smaller rings are represented by derivatives of the 9-membered 1,4,7-triazacyclononane, such as NOTA and the phosphinic counterparts such as the TRAP family [37, 42, 44]. These hexadentate macrocyclic CAs form stable complexes of Ga^{3+} with favorable labeling kinetics. Larger rings mostly include at least one 14-membered ring such as TETA, that may be considered an expanded version of DOTA. The expanded ring is more flexible and efficiently accommodates Cu^{2+} [44]. Moreover, its flexibility has been modulated in the macrobicyclic derivative CB-TE2A, further raising the stability of the corresponding Cu^{2+}-complex [44]. A unique combination of fast formation and high inertness of the metal complex is shown by the macrobicyclic CA known as sarcophagine (the bifunctional derivative DiamSar is shown in Figure 1), forming an extremely stable Cu^{2+}-sepulchrate [44].

Mesocyclic CAs have a backbone based on medium-membered rings (5–8 atoms) (Figure 1). This class includes the six-membered CDTA, formally an EDTA rigidified through the formal fusion with a cyclohexane ring. CDTA forms stable complexes with Mn^{2+} and bifunctional derivatives were studied as potential PET agents [46]. AAZTA shows a favourable size match of with most metal ions leading to the efficient chelation of several d- and f-metal ions of diagnostic and therapeutic interest, among them Gd^{3+}, $^{44}Sc^{3+}$, $^{64}Cu^{2+}$, $^{68}Ga^{3+}$, $^{111}In^{3+}$, and $^{177}Lu^{3+}$ [47–49]. In addition, the relative flexibility of the diazepane ring allows a very fast complexation reaction. The role of the side arms of AAZTA has been studied for Ga^{3+}, with the hexadentate derivative DATA showing comparable

complexation efficiency [37]. The effect of the rigidification of the seven-membered ring on the thermodynamic and kinetic stability of Ga^{3+} complexes was also investigated in the bicyclic derivatives CyAAZTA [50] and PIDAZTAs [51].

4.2. Thermodynamic and Kinetic Properties of Metal Complexes for Radiopharmaceutical Applications

4.2.1. Thermodynamics

Acyclic, mesocyclic, and macrocyclic CAs and their derivatives form highly stable complexes with $M^{2+/3+}$ ions by the coordination of all the donor atoms of the hexa-, hepta- or octadentate ligands. The stability constants (log K_{ML}) of the M^{2+} and M^{3+} complexes formed with acyclic, mesocyclic, and macrocyclic CAs are listed in Table 2.

The Cu^{2+} ion ($3d^9$, 57–73 pm, CN = 4–6) has a borderline hardness with high affinity to O and N donor atoms. Beside acyclic chelates, several meso- and macrocyclic N_3 and N_4 CAs have been developed to obtain N_2O_4, N_3O_3, N_3S_3, and N_4O_2 coordination of the Cu^{2+} ion.[44] The presence of more basic donor atoms in the pendant arms and in the ligand backbone leads to an increase in the log K_{CuL} value of the Cu^{2+} complexes. Interestingly, the stability constants of Cu(EHPG) and Cu(HBED), sharing the same functional groups, differ by ~2 log K units, showing that the overall molecular connectivity plays an important role. The log K_{CuL} of Cu(cyclam) is higher than that of Cu(cyclen) (log $K_{Cu(cyclen)}$ = 24.8; log $K_{Cu(cyclam)}$ = 27.2) [53], due to a better size match of the Cu^{2+} ion and the 14-membered macrocycle. Nevertheless, the log K_{CuL} value of Cu(DOTA) and Cu(TETA) are similar, indicating that the size of the functionalized macrocycle has practically no influence on the log K_{ML} of the Cu^{2+}-complexes due to the formation of similar distorted octahedral coordination geometries. The log K_{ML} of Cu^{2+} complexes formed with cyclam and cross-bridged bicyclic CB2A are very similar (log $K_{Cu(cyclam)}$ = 27.2, log $K_{Cu(CB2A)}$ = 27.1) [54]. However, functionalization of the cross-bridged CA with picolinate pendant arms significantly improves the stability of the corresponding Cu^{2+} complex [44].

The Ga^{3+} ion is a classic hard cation with small size (CN = 6: 62 pm) and the +3 charge. Ga^{3+} ion forms stable complexes with O, N, and S donor atoms [37]. Ga^{3+} complexes of CAs are generally characterized by N_2O_4, N_3O_3, N_3S_3, N_4O_2, and O_6 coordination in distorted octahedral geometries [37, 42]. The similarity of Fe^{3+} and Ga^{3+} ions results in the strong affinity of Ga^{3+} for transferrin (log K_{GaTf} = 18.88, log K_{Ga2Tf} = 17.65) and hydroxamate-based siderophores (e.g., DFO) [37]. Heterocyclic oxygenated pendant arms such as picolinate (DEDPA) and 8-hydroxyquinoline (HOX) are particularly beneficial in the coordination of Ga^{3+} resulting in an increase of 7 and 12 units in the log K_{GaL} value with respect to EDTA [43, 55]. Moreover, the efficient formation of Ga^{3+} complexes with tris(hydroxypyridinone) ligands has also been demonstrated [37]. The speciation of the Ga^{3+}-AAZTA-like systems at pH> 5 shows the dominance of Ga(L)OH ternary species [49, 51], formed even in the Ga^{3+}-EDTA, Ga^{3+}-CDTA, and

Table 2. Stability constants of Cu^{2+}, Ga^{3+}, Sc^{3+}, Ln^{3+}, In^{3+}, and Bi^{3+} complexes formed with acyclic, mesocyclic, and macrocyclic CAs at 25 °C [37, 42, 44, 45, 52].

Ligands	I	$\log K_{CuL}$	$\log K_{GaL}$	$\log K_{ScL}$	$\log K_{LnL}$	$\log K_{InL}$	$\log K_{BiL}$
EDTA	0.1 M KNO$_3$	19.19	21.7	23.1	17.6 (Y) 19.9 (Lu)	25.09	28.2
CDTA	0.1 M KNO$_3$	21.92	24.38	26.0	19.1 (Y) 21.5 (Lu)	29.37	31.2
EDTMP	0.1 M KNO$_3$	23.21	31.83	–	21.8 (Gd)	–	–
HBED	0.1 M KCl	22.95	38.51	–	18.9 (Gd) 20.4 (Lu)	27.9	–
EHPG	0.1 M KCl	25.27	33.89	–	–	26.68	–
DEDPA	0.15 M NaCl	19.2	28.22	–	–	26.60	–
AAZTA	0.1 M KCl	22.27	21.15	27.69	20.2 (Gd) 21.9 (Lu)	29.86	–
CyAAZTA	0.1 M KCl	20.11	21.92	–	18.3 (Gd) 17.7 (Lu)	–	–
Me-DATA	0.15 M NaCl	18.36	21.54	–	–	–	–
PIDAZTA	0.15 M NaCl	19.14	21.70	–	14.5 (Gd) 16.4 (Lu)	–	–
DTPA	0.1 M KNO$_3$	23.40	25.11	27.43	22.1 (Y) 22.4 (Lu)	29.48	35.6
NOTA	0.1 M Me$_4$NCl	21.99	29.63	16.5	13.7 (Gd) 15.9 (Lu)	26.2	–
DOTA	0.1 M NaCl	22.00	26.05	30.79	24.9 (Y) 25.4 (Lu)	24.53	30.3

PCTA	0.1 M Me$_4$NNO$_3$	18.79	19.39	–	20.3 (Y) 20.6 (Lu)	21.42	–
TETA	0.1 M KNO$_3$	21.60	19.74	–	14.8 (Y) 15.3 (Lu)	21.89	–

Some other logK_{ML} values: Ga(HOX): 34.4, Y(HOX): 23.78, Lu(HOX): 24.66, In(HOX): 31.38 (0.16 M NaCl, 25 °C); Y(CHX-A''-DTPA): 24.2 (0.1 M NaClO$_4$; 25 °C); Ga(TACN-HP): 45.6, In(TACN-HP): 28.2 (0.1 M KCl, 25 °C); Ga(TACN-TM): 34.2, In(TACN-TM): 36.1 (0.1 M KCl, 25 °C), Cu(DO3A): 22.87, Y(DO3A): 21.5, Lu(DO3A): 23.4 (0.1 M Me$_4$NCl, 25 °C); Bi(CHX-A''-DTPA): 34.9 (0.1 M NaClO$_4$, 25 °C); Bi(p-NO$_2$-Bn-neunpa): 28.76 (0.16 M NaCl, 25 °C); Bi(DO3A): 26.85 (1.0 M NaCl, 25 °C); Bi(DO3A-Bu): 26.8 (1.0 M NaBr, 25 °C); Bi(DO2PA): 32.0, Bi(Me-DO2PA): 34.2 (0.5 M KCl, 25 °C); Ga(DO3AM^{Bu}): 24.66 (0.1 M Me$_4$NCl, 25 °C), Ga(DFO): 28.65, In(DFO): 21.39 (0.1 M KCl, 25 °C)

Ga^{3+}-DTPA systems [56, 57]. The better size match of the Ga^{3+} ion and the cavity of the NOTA ligand is clearly visible in the log K_{GaL} value of Ga(NOTA), 5 log K units higher than that of Ga(DOTA).

Sc^{3+}, Y^{3+}, and Ln^{3+} ions belong to the class of rare earth (RE) metals, classic hard cations as a result of the small size (80–116 pm, CN = 8–9) and the +3 charge. The stability constant of the Ln(DTPA) complexes increases from La^{3+} to Dy^{3+}, then remains practically constant for the heavier Ln^{3+} ions with a slight decrease at the end of the series. Remarkable improvements in the thermodynamic stability of Y^{3+} complexes were achieved by rigidifying the backbone of DTPA by fusion with a cyclohexane ring ("CHX" ligands) [37]. AAZTA encapsulates Sc^{3+}, Y^{3+}, and Ln^{3+} ions by virtue of the relatively flexible meso-cyclic coordination cage [47–49]. The macrocyclic DOTA is the dominant chelator for these metal ions. The log K_{LnL} values of Ln(DOTA) complexes increase from La^{3+} to Gd^{3+}, then it remains practically constant for the smaller Ln^{3+}. The relationship between the basicity of amines and the log K_{LnL} of Ln^{3+} complexes with macrocyclic ligands has been extensively studied [58, 59].

The In^{3+} ion is also a classical hard cation, with +3 charge and relatively small size (62–92 pm, CN = 7–8). The In^{3+} ion has a high affinity for O and N donor atoms and to the "softer" thiolate groups. The complexation of the In^{3+} ion is generally tackled with N_2O_4, N_3O_3, N_3S_3, N_3O_4, N_3O_5, N_4O_2, and O_6 coordination in distorted octahedral, pentagonal bipyramidal, and square antiprismatic geometries [37, 42, 52]. The log K_{InL} of In^{3+} complexes formed with EDTA, DEDPA, and HOX ligands shows that picolinate and 8-hydroxyquinoline pendants lead to an increase of 1.5 and 6.5 orders of magnitude in the log K_{InL} value. The log K_{InL} of In^{3+} complexes with macrocyclic CAs follows the trend: TETA<DOTA<NOTA, explained by the excessively large cavity of DOTA and TETA for the small In^{3+} ion. Interestingly, the log K_{InL} of In(DFO) is about 7 orders of magnitude smaller than that of Ga(DFO) [37, 42].

The intense charge density and the small radius (59–89 pm) of Zr^{4+} result in the acidity of the coordinated aqua ligands and the tendency to form oxides/hydroxides [60]. The Zr^{4+} complexes (CN = 8) of hexa- and octadentate CAs are generally characterized by dodecahedral geometry [44]. Despite the high log K_{ZrL} values of Zr(EDTA) and Zr(DTPA), hydrolysis of the Zr^{4+} ion may occur with the release of the metal ion at pH > 5 in both cases [61]. According to theoretical calculations, DFO is coordinated to the Zr^{4+} ion by three hydroxamate groups, whereas the remaining two coordination sites are occupied by two water molecules [62].

Bi^{3+} is a soft metal ion and forms stable complexes with CAs containing O, N, and S donor atoms [63]. The Bi^{3+} ion in complexes has an ionic radius of $0.96-1.17$ Å and CN = 8. The higher stability constant of Bi(CDTA) complex with respect to Bi(EDTA) (~3 log K units) reflects the higher basicity of CDTA. However, the higher basicity of the *trans*-1,2-diaminocyclohexyl moiety of the CHX-A″-DTPA ligand does not improve the log K_{BiL} of the Bi(CHX-A″-DTPA) complex [37]. Tetraazamacrocyclic CAs have also been proposed for the complexation of the Bi^{3+} ion [37]. Based on the size of the Bi^{3+} ion, the stability constant of the Bi(DOTA) complex is higher than expected due to the covalent

character of the interaction between Bi^{3+} and N atoms. Replacing one COO^- with OH (Bi(DO3A-Bu)) or its removal (Bi(DO3A)) depresses log K_{BiL} by 3.5 units. Interestingly, the log K_{BiL} of the Bi^{3+} complex formed with the DOTA derivatives possessing two picolinate (DO2PA), two picolinates and two methyl groups (Me-DO2PA) are higher by 2 and 4 log K units than that of the Bi(DOTA) complex [37].

4.2.2. Formation Kinetics

The formation reactions of complexes with $M^{2+/3+}$ ions are usually rapid with flexible multidentate CAs, and often slow with rigid ones [64]. In complex formation the metal ion penetrates the coordination cage formed by the donor atoms of the CAs. The formation of the Cu^{2+}-complexes with tri- and tetraazamacrocyclic CAs is usually slow in acidic condition, where the CAs are present in the form of protonated species. Formation of the Cu^{2+} complex occurs upon direct encounter of the Cu^{2+} ions and the protonated unsubstituted macrocycle (e.g., cyclen). However, the macrocyclic CAs with coordinating pendants interact with the Cu^{2+} ions in a two-steps mechanism: (i) the rapid formation of the out-of-cage complex $^\#[Cu(H_xL)]$ by the coordination of the pendant arms to the metal ion, (ii) the rate-determining deprotonation of the ring amine(s) of the out-of-cage complex $^\#[Cu(H_xL)]$ with the penetration of the metal ion in the cage [65]. Interestingly, cross-bridged cyclam derivatives with coordinating side arms [66, 67] show fast complexation of the Cu^{2+} ion under mild reaction conditions.

The M^{3+} complexes of NOTA, DOTA, and their derivatives are formed slowly because the metal ion must enter into the pre-organized coordination cage formed by the donor atoms (M^{3+} = Ga^{3+} and Ln^{3+} ions) [45, 68]. The formation reactions of the M^{3+} complexes with NOTA and its derivatives takes place by the rapid formation of a monoprotonated $^*[M(HNOTA)]^+$ intermediate (M^{3+} coordinated by the COO^- groups, proton likely located on a ring N atom), then deprotonating and rearranging to the product in a slow, OH^- catalyzed rate-determining process [68, 69]. The complexation of the M^{3+} ion with DOTA and its derivatives occurs through the diprotonated $^*[M(H_2DOTA)]^+$ intermediate in which the metal ion is coordinated by the deprotonated COO^- of the pendants [45]. The rate determining step is the H_2O- (k_{H2O}) and OH^--assisted (k_{OH}) deprotonation of the monoprotonated $^*[M(HDOTA)]$ intermediate followed by the rearrangement of the deprotonated intermediate to the final complex (Figure 2) [45]. Although the formation mechanism of [Ln(PCTA)] complexes is similar, the formation of [Ln(DOTA)]$^-$ complexes is about 10 times slower than that of the corresponding [Ln(PCTA)] complexes, due to the preorganization of PCTA [45]. Several DOTA derivatives with α-substituted pendants (e.g., DOTMA) and with symmetrically arranged alkyl substituents on the tetrazamacrocycle have been developed to enhance the preorganization of the CA [45]. However, the formation rate of the [Eu(DOTMA)]$^-$ complex is ~10^3 times smaller than that of [Eu(DOTA)]$^-$ confirming that the substituted pendants slow the formation of the Ln^{3+} chelates [45].
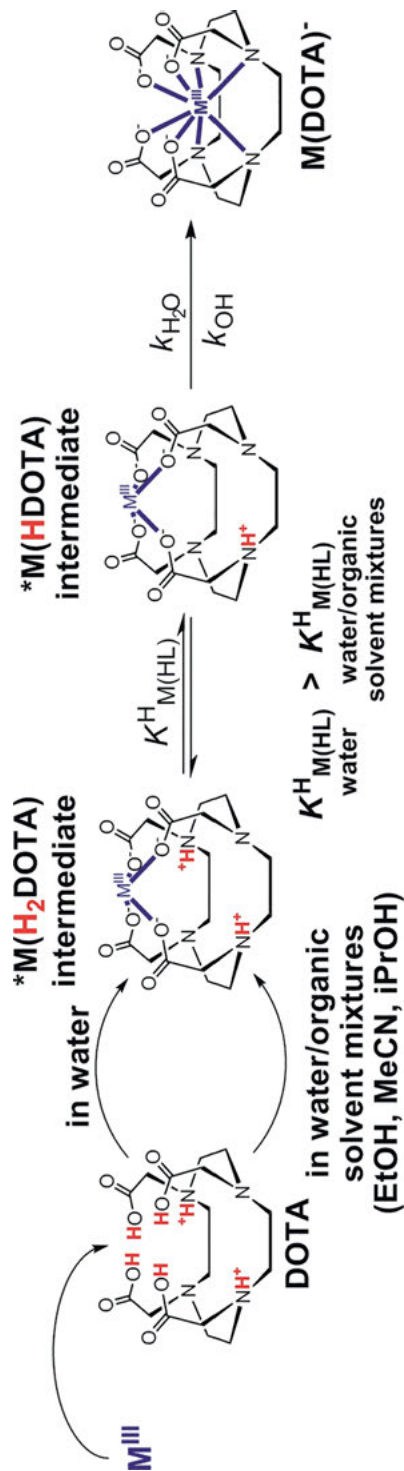
Figure 2. Formation of M(DOTA) complexes. Adapted with permission from [70]; copyright (2018) American Chemical Society.

Kinetic studies reveal that the formation mechanism of M(DOTA)$^-$ complexes is similar in water and water/EtOH mixtures ($\leq 70\%_{v/v}$ EtOH) [70]. However, EtOH indirectly accelerates the formation of [M(DOTA)]$^-$ complexes by decreasing the protonation constant ($K_{M(HL)}^H$, Figure 2) of the kinetically active *[M(HDOTA)], resulting in the faster formation of the final complex.

4.2.3.   Kinetic Inertness

One of the key parameters for safe *in vivo* application is the kinetic inertness (kinetic stability) of metal complexes, required to avoid the release of the metal ion and of the free CA, and the delivery of the radioisotope in the form of an intact complex to the target [37, 42, 44, 45]. Despite the high log K_{ML} value, the extremely low concentration of the radiopharmaceuticals and the high excess of competitors (trans-metallation and trans-chelation reactions) may establish the thermodynamic force for the *in vivo* dissociation of the metal complexes. The dissociation of metal complexes formed with acyclic, mesocyclic, and triaza- and tetraazamacrocyclic CAs and their derivatives may take place by the same mechanism (Chapter 2 of this book, Figure 4). However, the contribution of the different pathways to the overall dissociation rate differs considerably depending on the nature of the metal ion and of the CA. Dissociation of Ln^{3+} complexes formed with acyclic ligands may occur by the assistance of metal ions (k_M) via the formation of heterodinuclear complexes (K_M). Recent studies indicate that the metal ion-assisted dissociation of Gd(DTPA) derivatives can be neglected in the presence of bioligands (e.g., citrate) due to the chelation of exchangeable Cu^{2+}, Zn^{2+}, Ca^{2+}, and Fe^{3+} ions. The dissociation of the Gd(DTPA) derivatives mainly occurs by endogenous ligands (carbonate, phosphate, citrate, etc.) assisted paths (k_L) via the formation of ternary complexes (K_L) in physiological conditions [71]. For Sc^{3+}, Y^{3+}, and Ln^{3+} complexes formed with mesocyclic and 9- to 13-membered triaza- and tetraazamacrocyclic CAs the acid-catalyzed decomplexation is the most important path (k_H, k_H^H) by the formation of protonated intermediates (K_H), whereas the direct attack of the endogenous metal ions (k_M, K_M) has a negligible role in the dissociation of the metal complexes. On the other hand, the strong hydrolytic properties of Ga^{3+} and Bi^{3+} strongly influence the dissociation of the corresponding complexes formed with mesocyclic and polyazamacrocyclic CAs, taking place with the assistance of the OH$^-$ ion (k_{OH}) via the formation of ternary hydroxo complexes (K_{OH}) [72].

The kinetics of metal and ligand exchange reactions of Cu^{2+}, Ga^{3+}, Ln^{3+}, Y^{3+}, and Sc^{3+} complexes have been extensively investigated [45, 64, 73]. The transmetallation of Ln(EDTA) complexes takes place by the proton-assisted path (Ce(EDTA): $k_1 = 2.9 \times 10^3$ M^{-1}s^{-1}, $k_1 = k_H \times K_H$). Ln^{3+} complexes of rigidified EDTAs show a significantly slower acid-catalyzed dissociation (Ce(CDTA): $k_1 = 60$ M^{-1}s^{-1}) [73]. A similar approach has been used to improve the kinetic inertness of Ga^{3+} and In^{3+} complexes of EDTA analogs with rigid pendants (DEDPA [55], HOX [43]). The introduction of a cyclohexane ring into the DTPA backbone yields the more rigid CHX-A"-DTPA, forming Y^{3+} complexes with a slower acid-catalyzed dissociation than that of the parent Y(DTPA) [74].

In metal complexes of mesocyclic, and 9- to 13-membered azamacrocyclic ligands, the $M^{2+/3+}$ ion is placed in the coordination cage formed by N and O donor atoms, generally hindering the interactions with bioligands due to the lack of a free coordination site at the $M^{2+/3+}$ ion. However, the protons can compete with the $M^{2+/3+}$ ions by the formation of protonated $M(H_xL)$ complexes which is the first step in the dissociation reaction. The dissociation of the protonated $M(H_xL)$ complex is more likely to occur by proton transfer from the pendant to the nitrogen of the ligand backbone causing the release of the $M^{2+/3+}$ ion. The proton-assisted dissociation of the Cu^{2+} complexes formed by unfunctionalized CAs reveals that the kinetic inertness of the Cu(cyclam) complex is about 20 times higher than that of Cu(cyclen) due to the better size match between the Cu^{2+} ion and the cavity of the cyclam ligand [75]. The presence of coordinating pendants markedly influences the dissociation rate of the Cu^{2+} complexes with macrocyclic CAs. The kinetic inertness of Cu(NOTA) is significantly lower than that of Cu(DOTA) due to the lability of the [Cu(HNOTA)] complex [65]. According to the dissociation half-lives measured in 5 M HCl, the Cu^{2+} complexes of cross-bridged cyclam derivatives [66, 67] show a high kinetic inertness due to the constrained structure of the macrocycle.

Rates of the acid-catalyzed dissociation of Ln^{3+} complexes formed with meso- and macrocyclic CAs are strongly influenced by the size of the Ln^{3+} ion as well as by the structure of the CAs. The k_1 values of Ln(AAZTA) [47], Ln(NOTA) [69], and Ln(DOTA) [45] decrease in parallel with the size of the Ln^{3+} ion due to a better size match between the smaller Ln^{3+} ions and the coordinating cage. However, the k_1 values of Ln(NOTA) complexes are significantly higher than those of the Ln(DOTA) complexes due to the lower denticity and the smaller cavity of NOTA. The k_1 values of Ln^{3+} complexes formed with the octadentate DOTA derivatives are lower than those of the corresponding heptadentate PCTA complexes, due to the more favorable protonation of the PCTA ligand [45]. The acid-catalyzed dissociation of Ln(DOTA) complexes is faster than with rigid DOTA derivatives as a result of the increased preorganization due to the presence of α-substituted pendants (e.g., DOTMA) or of alkyl groups on the macrocycle [45].

The dissociation reactions of the Ga^{3+} complexes formed with mesocyclic ligands occur by the OH⁻-assisted pathway (k_{OH}, Chapter 2 of this book, Figure 4) via the formation of monohydroxo [Ga(L)OH] complexes (Ga(AAZTA): $k_{OH} = 3.0 \times 10^{-6}$ s⁻¹; Ga(CyAAZTA): $k_{OH} = 1.7 \times 10^{-5}$ s⁻¹; Ga(Me-DATA): $k_{OH} = 8.0 \times 10^{-6}$ s⁻¹; Ga(PIDAZTA-S): $k_{OH} = 1.4 \times 10^{-4}$ s⁻¹, Ga(PIDAZTA-R): $k_{OH} = 4.3 \times 10^{-7}$ s⁻¹) [49–51, 76]. The comparison of the k_{OH} and k_1 rate constants of Ga^{3+} complexes formed with mesocyclic and macrocyclic CAs indicates that the OH⁻-assisted dissociation is faster than that of the proton-assisted decomplexation, confirming the key role of the OH⁻-assisted dissociation at pH ≥ 7 [45, 49].

5. METALLIC AND NON-METALLIC THERANOSTIC AGENTS

5.1 Non-Hodgkin's Lymphoma

Diagnosis of lymphomas is accurately assessed by FDG PET imaging [77]. Zeva-lin® (^{90}Y(DTPA-Ibritumomab) Tiuxetan) and Bexxar® (^{131}I-Tositumomab) are the two FDA-approved radioimmunotherapy agents for the treatment of non-Hodgkin's lymphoma. Both monoclonal antibodies (mAb) bind to the CD20 antigen presented on B-cells. Since ^{90}Y is a pure beta emitter without any imag-
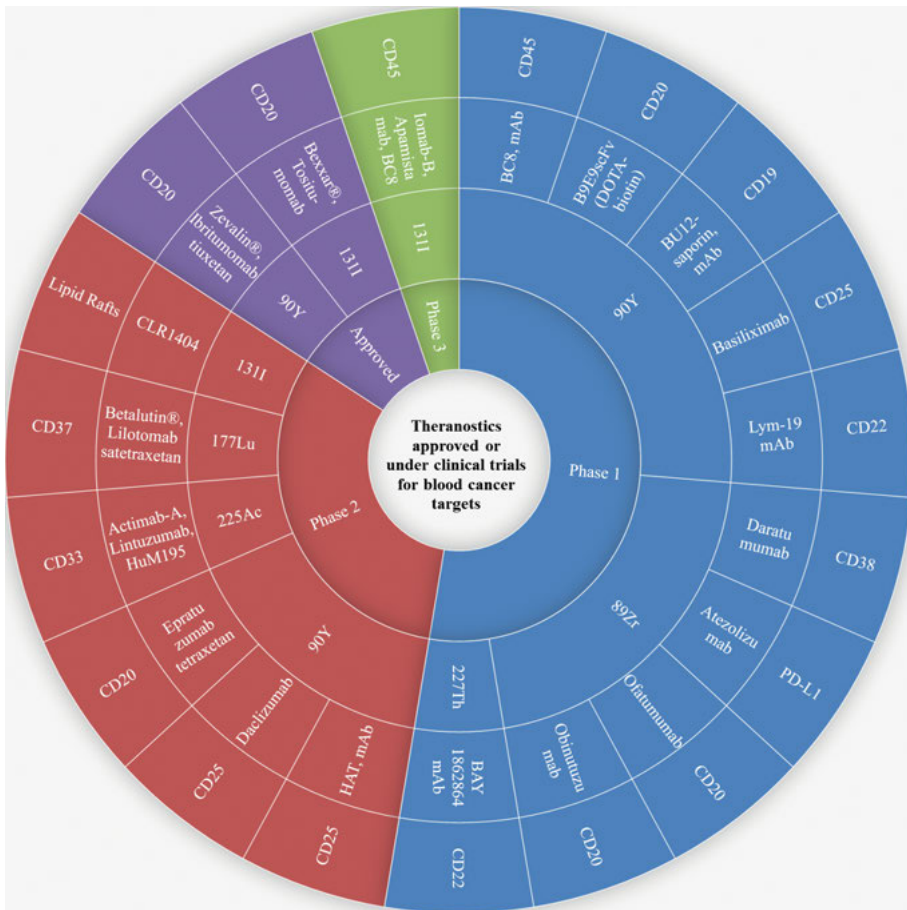
Figure 3. Theranostic agents approved or under clinical trials against blood cancer targets. CD: cluster of differentiation; mAb: monoclonal antibody; outermost circle denotes the biological target; 2nd to outermost circle denotes the name of therapeutic agent; 2nd to innermost circle denotes the radioisotope which is attached to the therapeutic agent while the innermost circle denotes the development stage of the agent.

ing radiation, the surrogate radionuclide ^{111}In is used for guiding the dosimetry, target engagement and biodistribution before initiation of Zevalin®. Developments in the area of radioimmunotherapy has been recently reviewed [78, 79] and theranostic agents targeting different targets against blood cancers (e.g., lymphoma's and leukemia's) are represented in Figure 3.

5.2. Neuroendocrine Tumors: Somatostatin Receptor 2, Meta-iodo-benzyl-guanidine

The neuroendocrine tumor (NET) is a rare cancer type that originates in neuroendocrine cells which possess traits like nerve cells and hormone-producing cells. NET can occur anywhere in the body but is most commonly found in the lungs, pancreas, and intestine. NETs grow at different rates; some grow slowly and some grow very quickly and metastasize to other body parts. PRRT is a molecularly targeted theranostic which can be used to treat NET provided they express certain receptors or neurotransmitters such as SSTR or norepinephrine/noradrenaline.

5.2.1. *Somatostatin Receptor Agonist Probe*

Somatostatin receptors (SSTR's) are overexpressed by NET cells found on the neuroendocrine glands. There are 5 main subtypes of SSTR (SSTR1-to-5) among which SSTR2 is the most commonly overexpressed in NET. TATE, TOC, and NOC are the 3 main somatostatin agonist derivatives (8-membered cyclic peptides) with minor deviations in one or two peptide units leading to different binding affinities for the SSTR's [80]. These peptides (molecular vectors) are conjugated with a macrocyclic chelate (e.g., DOTA, NODAGA, SAR) for radio-labeling with the PET radioisotopes ^{64}Cu/^{68}Ga for diagnostic imaging and with β^- (^{177}Lu, ^{90}Y, [67]Cu) and/or α- ([212]Pb, [213]Bi, [225]Ac) radioisotopes for radiotherapy. Many of these combinations are being developed as theranostic agents for the treatment of NET. Netspot® ([68]Ga(DOTATATE)) and Lutathera® ([177]Lu(DOTATATE)) represent classical molecular theranostic agents for the management of NET overexpressing SSTR2 receptors.

Similarly, [68]Ga(DOTATOC) and ^{177}Lu/[90]Y(DOTATOC) represent another theranostic pair for the treatment of SSTR2 overexpressing NET. [64]Cu(DOTATATE) has recently finished its phase 3 clinical trial and an NDA was filed with the FDA in 2020. The reason for the development of [64]Cu(DOTATATE) was the cited unavailability of [68]Ge/^{68}Ga generators and identification of more lesions at late time point (next day) PET imaging. A few more PET and theranostic agents, such as [68]Ga(DOTANOC), [64]Cu(SARTATE), and AlphaMedix™ or [212]Pb(DOTAMTATE), and [67]Cu(SARTATE), respectively, are in clinical trials. Numerous attempts to make an ^{18}F derivate of SSTR have been documented but only a few have been evaluated in man [80].

5.2.2. *Somatostatin Receptor Antagonist Probe*

Results from the past decade have confirmed that antagonists are preferable over agonists in the case of SSTR [81]. Antagonists have many more binding sites on tumor cells compared to agonists and show much higher tumor uptake. SSTR antagonists ^{177}Lu(DOTA)-JR11 or ^{177}Lu(OPS201), and ^{68}Ga(NODAGA)-JR11 or ^{68}Ga-OPS202, are currently under phase 2 development. In a comparative phase 2 study ^{68}Ga-OPS202 was able to pick up additional liver metastases compared to the agonist ^{68}Ga(DOTATOC) demonstrating its higher sensitivity and specificity [82].

5.2.3. *Meta-iodo-benzyl-guanine Analog*

Meta-iodo-benzyl-guanine (MIBG), a structural analog of guanethidine, resembles noradrenaline/ norepinephrine, a neurotransmitter which is taken up by certain NET. AdreView™, ^{123}I- Iobenguane/MIBG is an FDA-approved SPECT tracer for diagnosis of NET in the brain. Its fluorinated derivative, ^{18}F-MFBG is currently in phase 2 clinical trials. Recently, Azedra®, which is the high-specific activity form of ^{131}I-Iobenguane/MIBG, has been approved by the FDA for theranostic treatment of NET [83].

5.3.   Prostate Cancer: Prostate Specific Membrane Antigen

^{11}C-choline, targeting lipid biosynthesis/metabolism, was the first PET agent approved by the FDA in 2012 for the diagnosis of prostate cancer. The short half-life of the ^{11}C radioisotope and the need for an onsite cyclotron are the major barriers to the clinical adoption of ^{11}C-choline. Axumin®, ^{18}F-fluciclovine, is the most recent PET radiotracer approved by the FDA for the diagnosis of prostate cancer. Currently, it has the highest reported sensitivity, specificity and accuracy for diagnosis at PSA values of ~2 ng/mL or higher [84]. It can be manufactured at large scale and the long half-life of ^{18}F ensures its reliable delivery from centralized PET radiopharmacies, similar to FDG. As the sensitivity and specificity of both approved agents vary significantly and are still quite mediocre at low PSA values (< 1 ng/mL), there is an unmet need to find more sensitive and specific agents for the accurate diagnosis of prostate cancer.

5.3.1. *Prostate Specific Membrane Antigen Inhibitors*

Some of the most exciting research and development in the field of prostate cancer is currently focused upon small peptide inhibitors (based upon the Glu-urea-Lys/ Glu motif) for PSMA which bind to its extracellular domain. There are numerous small molecule PSMA-targeted theranostic agents under various stages of clinical development [85]. ^{68}Ga(PSMA-11) and ^{18}F-DCFPyL are the front-runner PET imaging agents, having completed phase 3 clinical trials (NDA under process)

while ^{18}F-rhPSMA-7.3 is just entering a phase 3 clinical trial. Similarly, ^{18}F-DCFC, ^{68}Ga(PSMA-R2), ^{68}Ga(CTT1057), and ^{68}Ga(P16–093) all have finished phase 1 trials. Besides small molecules, macromolecules such as minibody ^{89}Zr(Df-IAB2M) and mAb ^{89}Zr(DFO)-huJ591 have also finished early clinical trials (phase 1, 2) [78]. Interestingly, a number of small molecules such as ^{18}F-PSMA-1007, Al[^{18}F](F-PSMA-11), ^{68}Ga(PSMA-617), and ^{68}Ga(THP-PSMA) are also in advanced clinical trials outside the USA but none of these trials are FDA-approved [86].

^{177}Lu(PSMA-617) is the leading small molecule theranostic (β) radiopharmaceutical under development for treating metastatic castration-resistant prostate cancer (mCRPC) [85, 87]. It is currently under a pivotal clinical trial (phase 3) in addition to a number of early phase trials in combination with approved and new targeted agents including checkpoint inhibitors for prostate cancer. ^{131}I-MIP-1095 is another small molecule β therapeutic which currently is under phase 2 clinical trial while ^{177}Lu(PSMA-R2) is in a phase 1,2 and ^{177}Lu(CTT1403) is in a phase 1 trial. ^{177}Lu(DOTA)-J591 mAb is also under a phase 2 clinical trial for treatment of mCRPC patients.

There are also a number of α therapeutics, small molecule and mAb, labelled with ^{225}Ac and ^{227}Th in early (phase 1) clinical trials. Furthermore, from clinical trials it has been reported that mCRPC patients which are resistant to β therapy often respond well to α therapeutics. This phenomenon has also been observed in the case of SSTR2-targeted agents.

5.4. Breast Cancer: Human Epidermal Growth Factor Receptor 2

^{18}F-FDG is the most common tracer used in breast cancer for staging and follow-up [7].

HER2 is a 185 kDa transmembrane phosphoglycoprotein belonging to the EGFR family of tyrosine kinases [88]. HER2 overexpression in cancers is correlated with tumor aggressiveness and worse survival. Overexpression and amplification of HER2 can be detected in about 15 % of all primary breast cancers, and this group of patients benefits significantly from anti-HER2 therapies. Various HER2-targeted molecular vectors, such as monoclonal antibodies [78], antibody-based fragments, diabodies, nanobodies, non-immunoglobulin scaffolds, affibodies [89], peptides, and designed ankyrin-repeat proteins, have been explored in the clinic for HER2-positive breast cancer diagnosis and therapy over the past decade.

Antibody trastuzumab- or pertuzumab-based imaging probes have been developed by several groups for *in vivo* imaging of HER2 [78]. A first in-human study with ^{89}Zr-pertuzumab against HER2 in breast cancer has been performed at the Memorial Sloan Kettering Cancer Center [90]. ^{89}Zr-labelled trastuzumab and ^{111}In-labelled trastuzumab were developed to detect HER2-positive lesions in patients with metastatic breast cancer [78]. The radionuclides usually used for HER2 PET imaging are ^{18}F, ^{64}Cu, ^{68}Ga, ^{89}Zr, and ^{124}I while for theranostic

applications ^{131}I, [212]Pb, and ^{177}Lu have been used. Probes which are under clinical trials for HER-2 associated breast cancer are described below. ^{18}F-GE226 (or ^{18}F-FBA-$Z_{HER2:2891}$) is a molecularly targeted PET probe to image HER2 status *in vivo*. $Z_{HER2:2891}$ (a 61 amino acid peptide) is an affibody labelled with ^{18}F using the prosthetic approach [91]. It binds to the HER2 receptor with high affinity at a different epitope than trastuzumab. However, the prosthetic approach using FBA relies on time-consuming multistep manipulations and the Al[^{18}F] labeling method has been attempted with the NOTA and NODAGA chelate.

^{68}Ga-ABY-025 is an affibody-based molecular vector which is the most advanced PET probe under development. Anti-HER2 affibody imaging 4 h after injection with high peptide content discriminated HER2-positive metastases. PET standard uptake value correlated with biopsy HER2 scores (r = 0.91, p < 0.001). Uptake was five times higher in HER2-positive than in HER2-negative lesions with no overlap (p = 0.005). ^{68}Ga-ABY-025 PET correctly identified conversion and mixed expression of HER2 and targeted treatment was changed in 3 of the 16 patients. This agent accurately quantifies whole-body HER2 receptor status in metastatic breast cancer [92].

5.5.   Colon Cancer: Tumor-Associated Glycoprotein 72

A literature review points to insufficient evidence for routine use of FDG PET/CT in primary colorectal cancer (CRC) and only a small amount of evidence supports its use in the pre-operative staging of recurrent and metastatic CRC [93]. Among many biomarkers for colorectal cancer, the tumor-associated glycoprotein 72 (TAG-72) has been under evaluation for quite some time. It is overexpressed by a wide variety of adenocarcinomas including colorectal, gastric, esophageal, pancreatic, endometrial, ovarian, lung, prostate, and breast [94]. CC49 mAb (IDEC159) is one of the most studied mAbs against TAG-72. It has been labelled with various metallic theranostic radioisotopes such as ^{177}Lu, ^{111}In, ^{90}Y, [213]Bi (DOTA as the CA) as well as with ^{131}I, [124]I, ^{123}I and evaluated in the clinic, but has not advanced beyond phase 2 clinical trials [95]. Later, engineered and non-engineered single-chain variable fragments (scFv) of CC49, such as diabodies, AVP04–07, AVP-0458, etc. were labelled with diagnostic radioisotopes ^{123}I, [124]I, ^{131}I, ^{64}Cu, etc. and evaluated in preclinical and clinical settings showing promising results [96]. 3E8 is a newer humanized mAb with superior properties compared to humanized mAb CC49 against TAG-72. An engineered scFv fragment of 3E8 is currently under preclinical development for diagnostic [123/124]I, theranostic ^{131}I, and surgical ^{125}I guidance [97].

5.6.   Renal Cancer: Carbonic Anhydrase IX

The renal cell carcinoma (RCC) classic triad of flank pain, hematuria, and flank mass is uncommon (10 %) and is indicative of advanced disease. 70 % of RCC

is due to clear-cell renal cancer carcinoma (ccRCC) and in 95 % of ccRCC, carbonic anhydrase IX (CAIX) has been found to be overexpressed [98]. The role of CAIX in cancer biology makes it a relevant target for molecular imaging and therapy. Imaging of CAIX would enable one to distinguish between primary renal cell carcinoma and benign tumors of kidneys. A high level of CAIX expression is essential for finding patients who would most likely respond to CAIX-targeting therapy. The most advanced molecule is a mAb-based probe (^{177}Lu/[89]Zr-Girentuximab, Rencarex) in phase 2/3 [78]. Girentuximab labelled with the radioisotopes [89]Zr, ^{177}Lu, [124/131]I, ^{90}Y, and ^{111}In has been evaluated in clinical trials. A comparative study on four affibody variants against CAIX was recently published [89]. Investigators from the Johns Hopkins University have published promising preclinical studies on a CAIX high affinity dual-motif inhibitor (XY-IMSR) that has been extensively studied using ^{111}In and ^{64}Cu radioisotopes with potential towards development as a theranostic agent [99].

6.　CONCLUDING REMARKS AND FUTURE DIRECTIONS

PET has unsurpassed sensitivity among diagnostic modalities, being the workhorse for detection of oncologic and neurologic diseases. Limitations of the archetypal PET agent FDG in certain cases such as neuroendocrine tumors and prostate cancer prompted development of new tracers, the fruits of which have started to show in recent approval of new metal-based and non-metal-based PET agents. Decades of highly planned research from esteemed centers around the world identified two undisputed biomarkers, SSTR2 (neuroendocrine tumor) and PSMA (prostate cancer) among a few others for theranostic development.

The growing importance of conjugated metallic tracers in theranostic applications will prompt continuous efforts in research and development of novel and efficient chelating agents. Future efforts will be devoted to the development of CAs combining a fast and efficient complexation reaction with a substantial inertness of the corresponding chelate, especially for metal ions of interest for nuclear medicine applications. Due to the spectacular performance of radiopharmaceuticals, a renaissance of nuclear medicine, chiefly focused towards personalized medicine (both diagnostics and theranostics) in the field of oncology is happening of which the clear beneficiary is the whole society.

ABBREVIATIONS AND DEFINITIONS

1,2-HOPO	1,2-hydroxypyridinone
^{18}F-DCFPyL	2-(3-(1-carboxy-5-[(6-[^{18}F]fluoropyridine-3-carbonyl)-amino]-pentyl)-ureido)-pentanedioic acid
AAZTA	6-amino-6-methylperhydro-1,4-diazepinetetraacetic acid
BFCA	bifunctional chelating agent
CA	chelating agent

CAIX	carbonic anhydrase IX
CB2A	cross-bridged-cyclam diacetic acid
ccRCC	clear-cell renal cancer carcinoma
CDTA	*trans*-1,2-cyclohexanediamine-*N,N,N′,N′*-tetraacetic acid
CHX-A″-DTPA	2-aminoethyl-*trans*-(*S,S*)-cyclohexane-1,2-diaminepentaacetic acid
CRC	colorectal cancer
CRPC	castration-resistant prostate cancer
CT	computed tomography
CyAAZTA	3-amino-3-methyldecahydro-1*H*-1,5-benzodiazepine-*N,N′,N″,N″* tetraacetic acid
DATA	1,4-di(acetate)-6-(amino(methyl)-acetate)-perhydro-1,4-diazepane
DEDPA	ethylenediamine-*N,N′*-dipicolinic acid
DFO	desferroxamine
DO2PA	1,4,7,10-tetraazacyclododecane-1,7-dipicolinic acid
DO3A	1,4,7,10-tetraazacyclododecane-1,4,7-triacetic acid
DO3A-Bu	10-[1,3,4-trihydroxybut-2-yl]-1,4,7,10-tetraazacyclododecane-1,4,7-triacetic acid
DOTA	1,4,7,10-tetraazacyclododecane-1,4,7,10-tetraacetic acid
DOTAM-TATE	1,4,7,10-tetraazacyclododecane-1,4,7-triacetamide-Tyr^3-octreotate
DOTANOC	[DOTA,1-Nal^3]octreotide
DOTATATE	DOTA-(Tyr^3)-octreotate
DOTATOC	DOTA-D-Phe^1-Try^3-octreotide
DOTMA	α,α′,α″,α‴-tetramethyl-1,4,7,10-tetraazacyclododecane-1,4,7,10-tetraacetic acid
DOTP	1,4,7,10-tetraazacyclododecane-1,4,7,10-tetrakis(methylenephosphonic) acid
DOTPI	1,4,7,10-tetraazacyclododecane-1,4,7,10-tetrakis[methylene(2-carboxyethylphosphinic acid)]
DTPA	diethylenetriaminepentaacetic acid
EDTA	ethylenediaminetetraacetic acid
EDTMP	ethylenediamine-tetrakis(methylenephosphonic) acid
EGFR	epidermal growth factor receptor
FDA	Food and Drug Administration
FDG	2-[^{18}F]fluoro-2-deoxy-D-glucose
HBED	*N,N′*-bis(2-hydroxybenzyl)ethylenediamine-*N,N′*-diacetic acid
HER-2	human epidermal growth factor receptor 2
HOX	ethylenebis(iminomethylene)-bis(8-quinolinol)
MDP	methylenediphosphonate
MIBG	meta-iodo-benzyl-guanidine
MRI	magnetic resonance imaging
NET	neuroendocrine tumor
neunpa	diethylenetriamine-N,N'-diacetic-N,N'-bis(picolinic) acid

NODAGA	1,4,7,10-tetraazacyclododececane,1-(glutaric acid)-4,7,10-triacetic acid
NOTA	1,4,7-tetraazacyclononane-1,4,7-triacetic acid
PARP1	poly(ADP-ribose) polymerase 1
PCTA	3,6,9,15-tetraazabicyclo[9.3.1]pentadeca-1(15),11,13-triene-3,6,9-triacetic acid
PET	positron emission tomography
PIDAZTA	4-amino-4-methylperhydropyrido[1,2-a][1,4]diazepin-N,N',N'-triacetic acid
PRRT	peptide receptor radionuclide therapy
PSMA	prostate specific membrane antigen
SARTATE	1,8-diaminosarcofagine- Tyr^3-octreotate
SPECT	single-photon emission computed tomography
SSTR	somatostatin receptor
TACN-HP	1,4,7-triazacyclononane-1,4,7-tris(3-hydroxy-6-pyridin-2-ylmethyl)
TACN-TM	1,4,7-Tris(2-mercaptoethyl)-1,4,7-triazacyclononane
TAG-72	tumor-associated glycoprotein 72
TCMC	1,4,7,10-tetraaza-1,4,7,10-tetra-(2-carbamoylmethyl)cyclododecane
TETA	1,4,8,11-tetraazacyclotetradecane-1,4,8,11-tetraacetic acid
TRAP	1,4,7-tetraazacyclononane-1,4,7-tris(methylenephosphinic) acid
uPAR	urokinase-type plasminogen activator receptor

REFERENCES

1. H. Jadvar, X. Chen, W. Cai, U. Mahmood, *Radiology* **2018**, *286*, 388–400.
2. S. M. Qaim, B. Scholten, B. Neumaier, *J. Radioanal. Nucl. Chem.* **2018**, *318*, 1493–1509.
3. M. Benešová, U. Bauder-Wüst, M. Schäfer, K. D. Klika, W. Mier, U. Haberkorn, K. Kopka, M. Eder, *J. Med. Chem.* **2016**, *59*, 1761–1775.
4. A. Almuhaideb, N. Papathanasiou, J. Bomanji, *Ann. Saudi Med.* **2011**, *31*, 3–13.
5. E. Panagiotidis, A. Alshammari, S. Michopoulou, E. Skoura, K. Naik, E. Maragkoudakis, M. Mohmaduvesh, M. Al-Harbi, M. Belda, M. E. Caplin, C. Toumpanakis, J. Bomanji, *J. Nucl. Med.* **2017**, *58*, 91–96.
6. K. L. Wallitt, S. R. Khan, S. Dubash, H. H. Tam, S. Khan, T. D. Barwick, *RadioGraphics* **2017**, *37*, 1512–1536.
7. G. A. Ulaner, *Am. J. Roentgenol.* **2019**, *213*, 254–265.
8. K. Kersemans, K. De Man, J. Courtyn, T. Van Royen, S. Piron, L. Moerman, B. Brans, F. De Vos, *Appl. Radiat. Isot.* **2018**, *135*, 19–27.
9. N. P. van der Meulen, M. Bunka, K. A. Domnanich, C. Müller, S. Haller, C. Vermeulen, A. Türler, R. Schibli, *Nucl. Med. Biol.* **2015**, *42*, 745–751.
10. C. A. Umbricht, M. Benešová, R. M. Schmid, A. Türler, R. Schibli, N. P. van der Meulen, C. Müller, *EJNMMI Res.* **2017**, *7*, 9.
11. R. Walczak, S. Krajewski, K. Szkliniarz, M. Sitarz, K. Abbas, J. Choiński, A. Jakubowski, J. Jastrzębski, A. Majkowska, F. Simonelli, A. Stolarz, A. Trzcińska, W. Zipper, A. Bilewicz, *EJNMMI Phys.* **2015**, *2*, 33.

12. D. Ma, F. Lu, T. Overstreet, D. E. Milenic, M. W. Brechbiel, *Nucl. Med. Biol.* **2002**, *29*, 91–105.

13. A. M. Dabkowski, S. J. Paisey, M. Talboys, C. Marshall, *Acta Phys. Pol. A* **2015**, *127*, 1479–1482.

14. W. E. Meijs, J. D. M. Herscheid, H. J. Haisma, H. M. Pinedo, *Int. J. Rad. Appl. Instrum. A.* **1992**, *43*, 1443–1447.

15. M. Patra, A. Bauman, C. Mari, C. A. Fischer, O. Blacque, D. Häussinger, G. Gasser, T. L. Mindt, *Chem. Commun.* **2014**, *50*, 11523–11525.

16. F. Guérard, M. Beyler, Y.-S. Lee, R. Tripier, J.-F. Gestin, M. W. Brechbiel, *Dalton Trans.* **2017**, *46*, 4749–4758.

17. S. A. Graves, R. Hernandez, J. Fonslet, C. G. England, H. F. Valdovinos, P. A. Ellison, T. E. Barnhart, D. R. Elema, C. P. Theuer, W. Cai, R. J. Nickles, G. W. Severin, *Bioconjug. Chem.* **2015**, *26*, 2118–2124.

18. L. Bodei, M. Cremonesi, M. Ferrari, M. Pacifici, C. M. Grana, M. Bartolomei, S. M. Baio, M. Sansovini, G. Paganelli, *Eur. J. Nucl. Med. Mol. Imaging* **2008**, *35*, 1847–1856.

19. C. Müller, C. A. Umbricht, N. Gracheva, V. J. Tschan, G. Pellegrini, P. Bernhardt, J. R. Zeevaart, U. Köster, R. Schibli, N. P. van der Meulen, *Eur. J. Nucl. Med. Mol. Imaging* **2019**, *46*, 1919–1930.

20. C. Müller, J. Reber, S. Haller, H. Dorrer, P. Bernhardt, K. Zhernosekov, A. Türler, R. Schibli, *Eur. J. Nucl. Med. Mol. Imaging* **2014**, *41*, 476–485.

21. M. R. McDevitt, D. Ma, L. T. Lai, J. Simon, P. Borchardt, R. K. Frank, K. Wu, V. Pellegrini, M. J. Curcio, M. Miederer, N. H. Bander, D. A. Scheinberg, *Science* **2001**, *294*, 1537–1540.

22. M. Sathekge, F. Bruchertseifer, O. Knoesen, F. Reyneke, I. Lawal, T. Lengana, C. Davis, J. Mahapane, C. Corbett, M. Vorster, A. Morgenstern, *Eur. J. Nucl. Med. Mol. Imaging* **2019**, *46*, 129–138.

23. D. Cordier, F. Forrer, F. Bruchertseifer, A. Morgenstern, C. Apostolidis, S. Good, J. Müller-Brand, H. Mäcke, J. C. Reubi, A. Merlo, *Eur. J. Nucl. Med. Mol. Imaging* **2010**, *37*, 1335–1344.

24. C. Kratochwil, F. L. Giesel, F. Bruchertseifer, W. Mier, C. Apostolidis, R. Boll, K. Murphy, U. Haberkorn, A. Morgenstern, *Eur. J. Nucl. Med. Mol. Imaging* **2014**, *41*, 2106–2119.

25. G. Henriksen, P. Hoff, R. H. Larsen, *Appl. Radiat. Isot.* **2002**, *56*, 667–671.

26. G. J. Beyer, J. J. Čomor, M. Daković, D. Soloviev, C. Tamburella, E. Hagebø, B. Allan, S. N. Dmitriev, N. G. Zaitseva, *Radiochim. Acta* **2002**, *90*, 247–252.

27. G.-J. Beyer, M. Miederer, S. Vranješ-Đurić, J. J. Čomor, G. Künzi, O. Hartley, R. Senekowitsch-Schmidtke, D. Soloviev, F. Buchegger, and the ISOLDE Collaboration, *Eur. J. Nucl. Med. Mol. Imaging* **2004**, *31*, 547–554.

28. C. Müller, J. Reber, S. Haller, H. Dorrer, U. Köster, K. Johnston, K. Zhernosekov, A. Türler, R. Schibli, *Pharmaceuticals* **2014**, *7*, 353–365.

29. R. W. Atcher, A. M. Friedman, J. J. Hines, *Int. J. Rad. Appl. Instrum. A.* **1988**, *39*, 283–286.

30. K. Yong, M. Brechbiel, *AIMS Med. Sci.* **2015**, *2*, 228–245.

31. R. F. Meredith, J. Torgue, M. T. Azure, S. Shen, S. Saddekni, E. Banaga, R. Carlise, P. Bunch, D. Yoder, R. Alvarez, *Cancer Biother. Radiopharm.* **2013**, *29*, 12–17.

32. R. P. Baum, H. R. Kulkarni, *Theranostics* **2012**, *2*, 437–447.

33. A. Wurzer, D. DiCarlo, A. Schmidt, R. Beck, M. Eiber, M. Schwaiger, H.-J. Wester, *J. Nucl. Med.* **2020**, *61*, 735–742.

34. A. I. Kassis, *Semin. Nucl. Med.* **2008**, *38*, 358–366.

35. E. A. M. Ruigrok, W. M. van Weerden, J. Nonnekens, M. de Jong, *Pharmaceutics* **2019**, *11*, 560.

36. D. L. Costantini, C. Chan, Z. Cai, K. A. Vallis, R. M. Reilly, *J. Nucl. Med.* **2007**, *48*, 1357–1368.

37. T. I. Kostelnik, C. Orvig, *Chem. Rev.* **2019**, *119*, 902–956.

38. L. Lattuada, A. Barge, G. Cravotto, G. B. Giovenzana, L. Tei, *Chem. Soc. Rev.* **2011**, *40*, 3019–3049.

39. G. B. Giovenzana, L. Lattuada, R. Negri, *Isr. J. Chem.* **2017**, *57*, 825–83.

40. M. Hofman, D. Binns, V. Johnston, S. Siva, M. Thompson, P. Eu, M. Collins, R. J. Hicks, *J. Nucl. Med.* **2015**, *56*, 405–409.

41. Y. Yang, M. J. Pushie, D. M. L. Cooper, M. R. Doschak, *Mol. Pharm.* **2015**, *12*, 4108–4114.

42. T. J. Wadas, E. H. Wong, G. R. Weisman, C. J. Anderson, *Chem. Rev.* **2010**, *110*, 2858–2902.

43. X. Wang, M. de G. Jaraquemada-Peláez, Y. Cao, J. Pan, K.-S. Lin, B. O. Patrick, C. Orvig, *Inorg. Chem.* **2019**, *58*, 2275–2285.

44. E. Boros, A. B. Packard, *Chem. Rev.* **2019**, *119*, 870–901.

45. Z. Baranyai, G. Tircsó, F. Rösch, *Eur. J. Inorg. Chem.* **2020**, *2020*, 36–56.

46. C. Vanasschen, E. Molnár, G. Tircsó, F. K. Kálmán, É. Tóth, M. Brandt, H. H. Coenen, B. Neumaier, *Inorg. Chem.* **2017**, *56*, 7746–7760.

47. Z. Baranyai, F. Uggeri, G. B. Giovenzana, A. Bényei, E. Brücher, S. Aime, *Chem. Eur. J.* **2009**, *15*, 1696–1705.

48. G. Nagy, D. Szikra, G. Trencsényi, A. Fekete, I. Garai, A. M. Giani, R. Negri, N. Masciocchi, A. Maiocchi, F. Uggeri, I. Tóth, S. Aime, G. B. Giovenzana, Z. Baranyai, *Angew. Chem. Int. Ed.* **2017**, *56*, 2118–2122.

49. Z. Baranyai, F. Uggeri, A. Maiocchi, G. B. Giovenzana, C. Cavallotti, A. Takács, I. Tóth, I. Bányai, A. Bényei, E. Brücher, S. Aime, *Eur. J. Inorg. Chem.* **2013**, 147–162.

50. A. Vágner, C. D'Alessandria, G. Gambino, M. Schwaiger, S. Aime, A. Maiocchi, I. Tóth, Z. Baranyai, L. Tei, *ChemistrySelect* **2016**, *1*, 163–171.

51. E. Farkas, A. Vágner, R. Negri, L. Lattuada, I. Tóth, V. Colombo, D. Esteban-Gómez, C. Platas-Iglesias, J. Notni, Z. Baranyai, G. B. Giovenzana, *Chem. Eur. J.* **2019**, *25*, 10698–10709.

52. E. W. Price, C. Orvig, *Chem. Soc. Rev.* **2013**, *43*, 260–290.

53. T. Chen, X. Wang, Y. He, C. Zhang, Z. Wu, K. Liao, J. Wang, Z. Guo, *Inorg. Chem.* **2009**, *48*, 5801–9.

54. X. Sun, M. Wuest, G. R. Weisman, E. H. Wong, D. P. Reed, C. A. Boswell, R. Motekaitis, A. E. Martell, M. J. Welch, C. J. Anderson, *J. Med. Chem.* **2002**, *45*, 469–477.

55. E. Boros, C. L. Ferreira, J. F. Cawthray, E. W. Price, B. O. Patrick, D. W. Wester, M. J. Adam, C. Orvig, *J. Am. Chem. Soc.* **2010**, *132*, 15726–15733.

56. W. R. Harris, A. E. Martell, *Inorg. Chem.* **1976**, *15*, 713–720.

57. R. Delgado, M. do Carmo Figueira, S. Quintino, *Talanta* **1997**, *45*, 451–462.

58. J. Huskens, D. A. Torres, Z. Kovacs, J. P. André, C. F. G. C. Geraldes, A. D. Sherry, *Inorg. Chem.* **1997**, *36*, 1495–1503.

59. K. Kumar, M. F. Tweedle, M. F. Malley, J. Z. Gougoutas, *Inorg. Chem.* **1995**, *34*, 6472–6480.

60. C. Ekberg, G. Källvenius, Y. Albinsson, P. L. Brown, *J. Solut. Chem.* **2004**, *33*, 47–79.

61. G. Anderegg, E. Bottari, *Helv. Chim. Acta* **1967**, *50*, 2341–2349.

62. J. P. Holland, V. Divilov, N. H. Bander, P. M. Smith-Jones, S. M. Larson, J. S. Lewis, *J. Nucl. Med.* **2010**, *51*, 1293–1300.

63. *Chemistry of Arsenic, Antimony and Bismuth*, Ed. N. C. Norman, Springer Netherlands, **1998**.

64. D. W. Margerum, G. R. Cayley, D. C. Weatherburn, G. K. Pagenkopf, in *Coordination Chemistry*, Ed. A. E. Martell, Am. Chem. Soc., Washington, DC, **1978**, pp. 1–220.

65. V. Kubicek, Z. Bohmova, R. Sevcikova, J. Vanek, P. Lubal, Z. Polakova, R. Michalicova, J. Kotek, P. Hermann, *Inorg. Chem.* **2018**, *57*, 3061–3072.

66. L. M. P. Lima, Z. Halime, R. Marion, N. Camus, R. Delgado, C. Platas-Iglesias, R. Tripier, *Inorg. Chem.* **2014**, *53*, 5269–5279.

67. D. J. Stigers, R. Ferdani, G. R. Weisman, E. H. Wong, C. J. Anderson, J. A. Golen, C. Moore, A. L. Rheingold, *Dalton Trans.* **2010**, *39*, 1699–1701.

68. J.-F. Morfin, É. Tóth, *Inorg. Chem.* **2011**, *50*, 10371–10378.

69. E. Brucher, A. D. Sherry, *Inorg. Chem.* **1990**, *29*, 1555–1559.

70. M. Perez-Malo, G. Szabo, E. Eppard, A. Vagner, E. Brücher, I. Tóth, A. Maiocchi, E. H. Suh, Z. Kovács, Z. Baranyai, F. Rösch, *Inorg. Chem.* **2018**, *57*, 6107–6117.

71. Z. Baranyai, Z. Pálinkás, F. Uggeri, A. Maiocchi, S. Aime, E. Brücher, *Chem. Eur. J.* **2012**, *18*, 16426–16435.

72. C. F. Baes, R. E. Mesmer, *The Hydrolysis of Cations*, John Wiley & Son, New York, London, Sydney, Toronto, **1976**.

73. E. Brücher, G. Tircsó, Z. Baranyai, Z. Kovács, A. D. Sherry, in *The Chemistry of Contrast Agents in Medical Magnetic Resonance Imaging*, Eds. A. E. Merbach, L. Helm, E. Tóth, John Wiley & Sons Ltd., **2013**, pp. 157–208.

74. M. W. Brechbiel, O. A. Gansow, C. G. Pippin, R. D. Rogers, R. P. Planalp, *Inorg. Chem.* **1996**, *35*, 6343–6348.

75. L. H. Chen, C. S. Chung, *Inorg. Chem.* **1988**, *27*, 1880–1883.

76. E. Farkas, J. Nagel, B. P. Waldron, D. Parker, I. Tóth, E. Brücher, F. Rösch, Z. Baranyai, *Chem. Eur. J.* **2017**, *23*, 10358–10371.

77. T. C. El-Galaly, D. Villa, L. C. Gormsen, J. Baech, A. Lo, C. Y. Cheah, *J. Intern. Med.* **2018**, *284*, 358–376.

78. K. L. Moek, D. Giesen, I. C. Kok, D. J. A. de Groot, M. Jalving, R. S. N. Fehrmann, M. N. Lub-de Hooge, A. H. Brouwers, E. G. E. de Vries, *J. Nucl. Med. Off. Publ. Soc. Nucl. Med.* **2017**, *58*, 83S-90S.

79. S. M. Larson, J. A. Carrasquillo, N.-K. V. Cheung, O. W. Press, *Nat. Rev. Cancer* **2015**, *15*, 347–360.

80. E. Pauwels, F. Cleeren, G. Bormans, C. M. Deroose, *Am. J. Nucl. Med. Mol. Imaging* **2018**, *8*, 311–331.

81. M. Fani, G. P. Nicolas, D. Wild, *J. Nucl. Med.* **2017**, *58*, 61S-66S.

82. G. P. Nicolas, S. Beykan, H. Bouterfa, J. Kaufmann, A. Bauman, M. Lassmann, J. C. Reubi, J. E. F. Rivier, H. R. Maecke, M. Fani, D. Wild, *J. Nucl. Med.* **2018**, *59*, 909–914.

83. D. A. Pryma, B. B. Chin, R. B. Noto, J. S. Dillon, S. Perkins, L. Solnes, L. Kostakoglu, A. N. Serafini, M. H. Pampaloni, J. Jensen, T. Armor, T. Lin, T. White, N. Stambler, S. Apfel, V. A. DiPippo, S. Mahmood, V. Wong, C. Jimenez, *J. Nucl. Med.* **2019**, *60*, 623–630.

84. J. D. Evans, K. R. Jethwa, P. Ost, S. Williams, E. D. Kwon, V. J. Lowe, B. J. Davis, *Pract. Radiat. Oncol.* **2018**, *8*, 28–39.

85. K. Kopka, M. Benešová, C. Bařinka, U. Haberkorn, J. Babich, *J. Nucl. Med.* **2017**, *58*, 17S-26S.

86. S. Boschi, J. T. Lee, S. Beykan, R. Slavik, L. Wei, C. Spick, U. Eberlein, A. K. Buck, F. Lodi, G. Cicoria, J. Czernin, M. Lassmann, S. Fanti, K. Herrmann, *Eur. J. Nucl. Med. Mol. Imaging* **2016**, *43*, 2122–2130.

87. M. Eiber, W. P. Fendler, S. P. Rowe, J. Calais, M. S. Hofman, T. Maurer, S. M. Schwarzenboeck, C. Kratowchil, K. Herrmann, F. L. Giesel, *J. Nucl. Med.* **2017**, *58*, 67S-76S.

88. H. Gong, L. Sampath, J. L. Kovar, D. M. Olive, in *Molecular Imaging*, Ed. B. Schaller, InTech, Rijeka, **2012**, pp. 351–374.

89. S. Ståhl, T. Gräslund, A. E. Karlström, F. Y. Frejd, P.-Å. Nygren, J. Löfblom, *Trends Biotechnol.* **2017**, *35*, 691–712.

90. G. A. Ulaner, S. K. Lyashchenko, C. Riedl, S. Ruan, P. B. Zanzonico, D. Lake, K. Jhaveri, B. Zeglis, J. S. Lewis, J. A. O'Donoghue, *J. Nucl. Med.* **2018**, 59, 900–906.

91. S. Trousil, S. Hoppmann, Q.-D. Nguyen, M. Kaliszczak, G. Tomasi, P. Iveson, D. Hiscock, E. O. Aboagye, *Clin. Cancer Res.* **2014**, *20*, 1632–1643.

92. J. Sörensen, I. Velikyan, D. Sandberg, A. Wennborg, J. Feldwisch, V. Tolmachev, A. Orlova, M. Sandström, M. Lubberink, H. Olofsson, J. Carlsson, H. Lindman, *Theranostics* **2016**, *6*, 262–271.

93. J. Brush, K. Boyd, F. Chappell, F. Crawford, M. Dozier, E. Fenwick, J. Glanville, H. McIntosh, A. Renehan, D. Weller, M. Dunlop, *Health Technol. Assess. Winch. Engl.* **2011**, *15*, 1–192, iii–iv.

94. S. P. Povoski, I. S. Hatzaras, C. M. Mojzisik, E. W. Martin, *Expert Rev. Mol. Diagn.* **2011**, *11*, 667–670.

95. R. F. Meredith, D. J. Buchsbaum, R. D. Alvarez, A. F. LoBuglio, *Clin. Cancer Res.* **2007**, *13*, 5643s–5645s.

96. L. Li, F. Turatti, D. Crow, J. R. Bading, A.-L. Anderson, E. Poku, P. J. Yazaki, L. E. Williams, D. Tamvakis, P. Sanders, D. Leong, A. Raubitschek, P. J. Hudson, D. Colcher, J. E. Shively, *J. Nucl. Med.* **2010**, *51*, 1139–1146.

97. N. E. Long, B. J. Sullivan, H. Ding, S. Doll, M. A. Ryan, C. L. Hitchcock, E. W. Martin, K. Kumar, M. F. Tweedle, T. J. Magliery, *J. Biol. Chem.* **2018**, *293*, 9030–9040.

98. N. K. Tafreshi, M. C. Lloyd, M. M. Bui, R. J. Gillies, D. L. Morse, *Subcell. Biochem.* **2014**, *75*, 221–254.

99. I. Minn, S. M. Koo, H. S. Lee, M. Brummet, S. P. Rowe, M. A. Gorin, P. Sysa-Shah, W. D. Lewis, H.-H. Ahn, Y. Wang, S. R. Banerjee, R. C. Mease, S. Nimmagadda, M. E. Allaf, M. G. Pomper, X. Yang, *Oncotarget* **2016**, *7*, 56471–56479.

12

Magnetic Resonance Theranostics: An Overview of Gadolinium(III)-Based Strategies and Magnetic Particle Imaging

Shaunna M. McLeod and Thomas J. Meade

Departments of Chemistry, Molecular Biosciences, Neurobiology, and Radiology,
Northwestern University, 2145 Sheridan Road, Evanston, IL 60208, USA
<tmeade@northwestern.edu>

Abstract: Theranostics, or the combination of therapy and diagnostic imaging in a single platform, are a booming field of research in the 21st century. Theranostics have been widely investigated across biomedical imaging modalities as they show great promise for image-guided

drug delivery, non-invasive treatment monitoring and personalized medicine. Examples of magnetic resonance imaging (MRI) theranostics are extensive in the literature, owing to the technique's tunable soft-tissue contrast, limitless depth penetration, high resolution, and lack of ionizing radiation. This chapter will provide an overview of gadolinium(III)-based MRI theranostics, and evaluate both small molecule and nanomaterial strategies. A discussion of nanomaterial platforms will be divided into subcategories: metal-based nanomaterials encompassing metal oxides, metal sulfides, gold nanostructures, and lanthanide upconversion nanoparticles; carbon nanomaterials; mesoporous silica nanoparticles; dendrimers and polymers; and biomolecular nanomaterials. While therapeutic and targeting strategies will predominantly focus on cancer, examples featuring other disease states will be highlighted. An overview of magnetic particle imaging (MPI) theranostics will also be included, as this emerging area holds significant biomedical promise.

1.   INTRODUCTION

The term "theranostic" was coined in the early 2000s to define materials that combine therapy and diagnostic imaging in a single platform [1]. Since then, this interdisciplinary research area has grown rapidly, prompting the launch of a dedicated journal in 2011 [2]. The primary advantage of theranostic strategies is the power to image diseased tissue and deliver therapeutic cargo in the same dose at the same time, overcoming differences in biodistribution, pharmacokinetics and delivery that plague decoupled approaches. Additional benefits include the ability to non-invasively evaluate therapeutic delivery kinetics and efficacy, allowing for the visualization of drug distribution, accumulation, and release over the course of a single treatment [1]. With these capabilities, theranostic platforms provide a path forward for personalized medicine applications, optimizing patient care for their individual needs [3].

Theranostic agents employ several imaging modalities, including magnetic resonance (MR), ultrasound, nuclear (CT, SPECT, PET, see Chapter 11), and optical imaging techniques. The scope of this theranostics review will focus on MR imaging (MRI) which benefits from excellent soft tissue contrast, high resolution, and the lack of harmful ionizing radiation [4]. Specifically, we will provide an overview on gadolinium(III)-based contrast agent strategies, as these agents are a staple of clinical diagnostic imaging and provide T_1-weighted positive contrast in MRI (see Chapter 2). Beyond Gd(III)-based contrast agents, magnetic resonance spectroscopy (MRS) is a notable complement to MRI theranostics, providing crucial biomarker and tumor metabolism information over the course of treatment [5]. Readers interested in MRI theranostic applications using iron oxide nanoparticles [6–9], manganese(II) contrast agents [10–15], or fluorine-19 probes [16, 17] should consult the associated references.

This chapter will cover both small molecule [18, 19] and nanomaterial [20–22] Gd(III)-based MRI theranostics. The primary focus will be cancer therapy and targeting, however, examples highlighting other disease states will also be dis-

cussed. In addition, an overview of magnetic particle imaging (MPI) is included. MPI is an emerging imaging method related to MRI that displays significant promise in theranostic applications [23].

2. GADOLINIUM(III) SMALL MOLECULE CONJUGATES
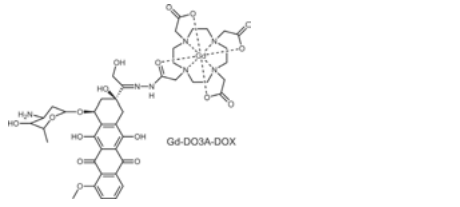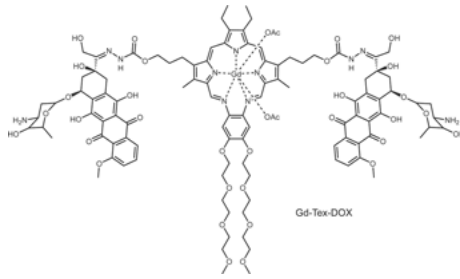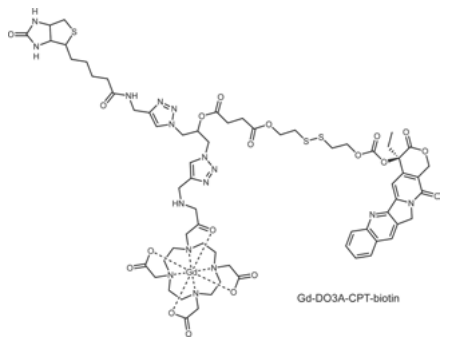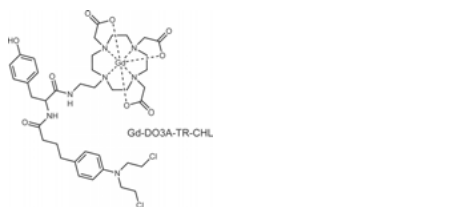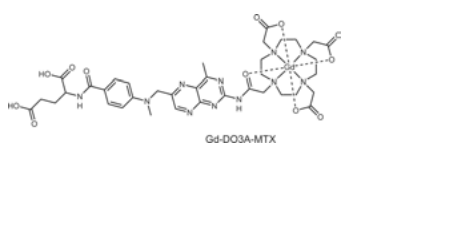
While nanomaterial theranostics are more prevalent, small molecule Gd(III) complex approaches are still a thriving research area [17, 18]. The diagnostic imaging handle on these small molecule conjugates are derived from the clinically approved Gd(III) MRI contrast agent structures, i.e., they feature Gd(III) chelated by 1,4,7,10-tetraazacyclododecane-1,4,7,10-tetracetic acid (DOTA), 1,4,7,10-tetraazacyclododecane-1,4,7-trisacetic acid (DO3A), diethylenetriamine-pentaacidic acid (DTPA), or diethylenetriaminetetraacetic acid (DTTA) ligands [24]. These complexes are then conjugated to the therapeutic moiety of choice: organic chemotherapeutics (Section 2.1), platinum anticancer drugs (Section 2.2), or porphyrin derivatives for photodynamic therapy (Section 2.3). An advantage of this approach is a potentially easier path forward towards clinical translation. With well-established and clinically approved diagnostic and therapeutic components making up the theranostic platform, small molecule conjugates can overcome some uncertainty and barriers associated with nanomedicine translation.
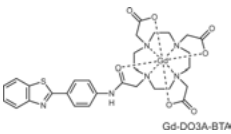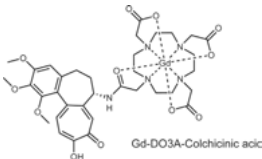
2.1. Organic Chemotherapeutic Drug Conjugates

A straightforward approach for medicinal chemists in the theranostic field is to combine well-known organic chemotherapeutics with the diagnostic success of Gd(III) MRI contrast agents. One challenge is ensuring that the therapeutic and imaging capacities are maintained along with designing synergistic effects. Targeting groups and prodrug strategies, where the agent is metabolized to the active drug post-administration, are often employed for improved selectivity and delivery to tumors. The drug conjugates covered in this section are summarized in Table 1.

In an early study, doxorubicin (Dox), a widely administered chemotherapeutic, was conjugated to Gd(III)-DO3A [25]. Dox is a DNA intercalator, interfering with DNA replication by inhibiting the progression of topoisomerase II, leading to apoptosis [26]. Dox-based chemotherapy is notorious for its off-target side effects, making a prodrug strategy attractive. In this approach Dox was covalently attached to the Gd(III) complex via an acid-labile hydrazone linker. The proposed prodrug-procontrast complex would cleave at this linker upon cellular uptake (i.e., lower pH). The active drug would then release and produce a concurrent change in relaxivity of the contrast agent, allowing for visualization of intracellular drug release. The experiments were limited to solution studies, but analysis showed that 90 % of Dox was released within 16 hours at pH 4.5. There

Table 1. Theranostic Gd(III)-organic chemotherapeutic drug conjugates.

Structure	Notes	Ref.
Gd-DO3A-DOX	*MR Contrast*: Gd-DO3A *Chemotherapeutic*: Doxorubicin (Dox) *Mechanism*: DNA intercalator, interferes with DNA replication and induces cell death	[25]
Gd-Tex-DOX	*MR Contrast*: Gd-texaphyrin *Chemotherapeutic*: Doxorubicin (Dox) *Mechanism*: DNA intercalator, interferes with DNA replication and induces cell death	[27]
Gd-DO3A-CPT-biotin	*MR Contrast*: Gd-DO3A *Chemotherapeutic*: Camptothecin (CPT) *Mechanism*: Topoisomerase I inhibitor, causes DNA damage and subsequent apoptosis. Complex also features biotin group for tumor targeting	[31]
Gd-DO3A-TR-CHL	*MR Contrast*: Gd-DO3A *Chemotherapeutic*: Chlorambucil (CHL) *Mechanism*: DNA alkylating agent, interferes with DNA replication and induces apoptosis	[33]
Gd-DO3A-MTX	*MR Contrast*: Gd-DO3A *Chemotherapeutic*: Methotrexate (MTX) *Mechanism*: Folate analog, inhibits dihydrofolate reductase, downstream effects of inhibiting DNA, RNA, and protein synthesis	[34]

Structure	Notes	Ref.
 Gd-DO3A-BTA	*MR Contrast*: Gd-DO3A *Chemotherapeutic*: Benzothiazole aniline (BTA) *Mechanism*: Many proposed anticancer mechanisms (see references)	[35, 36]
 Gd-DO3A-Colchicinic acic	*MR Contrast*: Gd-DO3A *Chemotherapeutic*: Colchicine *Mechanism*: Tubulin binding and vascular disrupting agent, leads to tumor necrosis and cell death	[37]

was a change in relaxivity upon activation, albeit producing negative contrast. While optimization of the activatable MR contrast handle is necessary, the hydrazone linker is a viable potential delivery strategy [25].

In fact, a Gd(III)-texaphyrin theranostic was reported that exploited the same acid-labile hydrazone linkage in a prodrug platform [27]. Texaphyrins are expanded pentaaza porphyrins that form stable metal complexes suitable for a variety of biomedical applications, including theranostics [28]. The first theranostic Gd(III)-texaphyrin was developed to monitor radiation therapy in cancer treatment by MRI [29]. In the hydrazone linkage study, the Gd(III)-texaphyrin was conjugated to two Dox molecules. Upon entering acidic tumor environments, the active drug releases with a simultaneous turn-on fluorescence signal from the free Dox molecule. The dual fluorescence-MRI imaging capabilities were studied extensively *in vitro* and enabled the image-guided evaluation of cellular uptake and localization. Anticancer efficacy was also characterized and showed a cancer-cell selective release of the active payload [27]. A similar Gd(III)-texaphyrin-Dox theranostic was developed with a disulfide prodrug linkage and studied in metastatic liver cancer models. The complex was incorporated into a targeted liposomal carrier (see Section 3.5) to improve solubility and tumor uptake [30].

Exploiting a similar anticancer mechanism, the drug camptothecin (CPT) was incorporated into a theranostic with Gd(III)-DO3A and biotin for tumor-targeting [31]. CPT is a topoisomerase I inhibitor, preventing DNA religation and results in DNA damage and apoptosis [26]. Coupling CPT with hydrophilic Gd(III)-DO3A improves water solubility of the drug, which promotes biotin receptor-mediated endocytosis [32]. A prodrug self-immolative disulfide linker was also incorporated to release CPT in the reducing intracellular environment, with the active drug producing a turn-on fluorescent signal upon release. Control compounds without the targeting biotin or disulfide linker for CPT release were synthesized to compare in cellular and *in vivo* studies. By utilizing fluorescence microscopy, the highest fluorescence was observed for the prodrug compound in biotin receptor overexpressed cancer cell lines, supporting both the proposed

uptake and release mechanisms. *In vitro* cell uptake was also visualized by MRI. The prodrug compound had improved cytotoxicity and selectivity compared to free CPT and the two control compounds in the same biotin receptor overexpression cell lines. The study culminated in an *in vivo* tumor model in mice. The biotin-targeting compound showed a much brighter signal in the tumor than the untargeted control, and mice treated with the prodrug compound had significantly smaller tumors than those treated with free CPT [31]. These results are very promising and adaptable for other molecular MR theranostics, demonstrating the power of targeted and prodrug strategies.

Other examples of organic chemotherapeutic conjugates for Gd(III)-DO3A based MR theranostics include chlorambucil (CHL), methotrexate (MTX), benzothiazole aniline (BTA), and colchicine (Table 1). CHL is a DNA alkylating agent, featuring two chloroethyl groups that react to form adducts with DNA. This reaction interferes with DNA replication and induces apoptosis. CHL was conjugated to Gd(III)-DO3A through a tyrosine linkage and produced favorable *in vitro* relaxation and cytotoxic properties [33]. MTX is a folate analog that inhibits dihydrofolate reductase, with the downstream effects of inhibiting DNA, RNA, and protein synthesis. Interestingly, MTX is not only an effective drug for cancer, but also a widely used treatment for autoimmune diseases such as rheumatoid arthritis. The Gd(III)-DO3A-MTX theranostic construct was evaluated *in vitro* and *in vivo* in glioma cancer models, and it displayed especially encouraging imaging performance [34]. There are many proposed anticancer mechanisms for BTA derivatives, with the inhibition of carbonic anhydrase being the best studied [35]. The theranostic conjugate DO3A-BTA with and without Gd(III) showed antiproliferative activity *in vivo*, and the Gd(III) complex showed uptake in the cytosol and nucleus by MRI of cell fractions [36]. Finally, colchicine is a tubulin-binding and vascular-disrupting agent, leading to tumor necrosis and inhibition of cell division. The Gd(III)-DO3A-colchicine theranostic was evaluated in ovarian cancer models *in vitro* and *in vivo*. Contrast enhancement and evidence of necrosis was observed by MRI in the tumor and confirmed by *ex vivo* histology [37]. These six examples demonstrate success across a diverse range of anticancer mechanisms for small molecule Gd(III)-organic chemotherapeutic theranostics. Incorporation of targeting and prodrug handles in the molecular structure are especially impactful in terms of tumor delivery and selectivity.

2.2. Platinum Anticancer Drug Conjugates

Two of the biggest successes in medicinal inorganic chemistry are Gd(III) MRI contrast agents and Pt(II) anticancer drugs. Naturally, combining these platforms into multinuclear heterometallic complexes is a compelling theranostic strategy. Pt-based drugs are ubiquitous in chemotherapy regimens. Three are clinically approved by the FDA, including cisplatin and carboplatin (Figure 1a). These square planar complexes bind and crosslink DNA, leading to apoptosis. While extremely effective at treating solid tumors, Pt-based therapies encounter signifi-

cant off-target effects and chemoresistance, making targeted and prodrug strategies appealing [38]. Theranostic approaches can have a synergistic effect in this regard. They can alter cell uptake or incorporate selective targeting and release mechanisms, all with the ability to monitor treatment non-invasively. Recent progress in this area has yielded a number of viable theranostics. Structures of the Gd(III)-Pt anticancer complexes examined in this section are shown in Figure 1.

In 2014, Zhu et al. reported a Gd(III)-Pt(II) complex featuring Gd(III) chelated by a modified DTPA ligand (Figure 1b) [39]. Two pyridine groups on the Gd(III)-complex substitute for a Cl$^-$ ligand on two cisplatin molecules, producing the final complex with two Pt(II) moieties. DNA binding was characterized by circular dichroism, and differences were observed in the cellular uptake between the Gd(III)-Pt(II) construct and the Gd(III)-only control. The Pt(II) units promoted cellular uptake, with the theranostic accumulating in the cytoplasm at a higher level than the control. Uptake was also observed in the nucleus, though inspection of molar ratios suggested partial dissociation of the Pt(II) complex. With cytotoxicity comparable to cisplatin and good *in vivo* MRI performance, this theranostic was an encouraging early example [39]. Another Gd(III)-Pt(II) approach utilized a luminescent cyclometalated Pt(II) complex to provide a bioimaging handle in addition to MRI (Figure 1c). This Gd(III)-Pt(II) construct also used a pyridine substituent to coordinate Pt(II), this time from a modified Gd(III)-DO3A chelate. Experiments primarily focused on physical characterization of the complex with some preliminary cellular microscopy. Still, the favorable luminescence and relaxivity properties could provide a method to track the intracellular fate of the Pt(II) therapeutic and to monitor off-target effects [40].

Pt(IV) prodrug strategies are an emerging tactic to combat chemoresistance and off-target effects. Pt(IV) complexes are octahedral and inert in the extracellular environment. Upon reduction to Pt(II) intracellularly, the axial ligands dissociate releasing the active Pt(II) drug [41]. The first examples of theranostic Gd(III)-Pt(IV) prodrug complexes were reported using Gd(III)-DO3A modified with a carboxylic acid tail to act as an axial ligand for cisplatin and carboplatin (Figure 1d). The cisplatin analogue showed better cellular uptake and toxicity and more favorable MR contrast enhancement *in vitro* across multiple cancer cell lines compared to the carboplatin platform [42]. Compellingly, the complex can be further modified to couple targeting or multimodal imaging functionality in the second axial position of Pt(IV).

A unique small molecule Gd(III)-Pt(II) theranostic construct benefits from both Pt(II) anticancer therapy and photodynamic therapy (PDT) (Figure 1e). Porphyrins are widely studied as photosensitizers for PDT (see Section 2.3). In this example Gd(III) is coordinated in the tetra(4-pyridyl) porphyrin ring for MRI contrast. The pyridine groups once again substitute for a Cl$^-$ ligand on cisplatin, yielding a final complex with four Pt(II) groups. The two modes of treatment provided synergistic antitumor effects *in vivo* along with positive MRI results for image-guided cancer therapy [43]. Ultimately, the combination of these two longstanding metals in medicine strategies has yielded multiple complexes for theranostic applications.
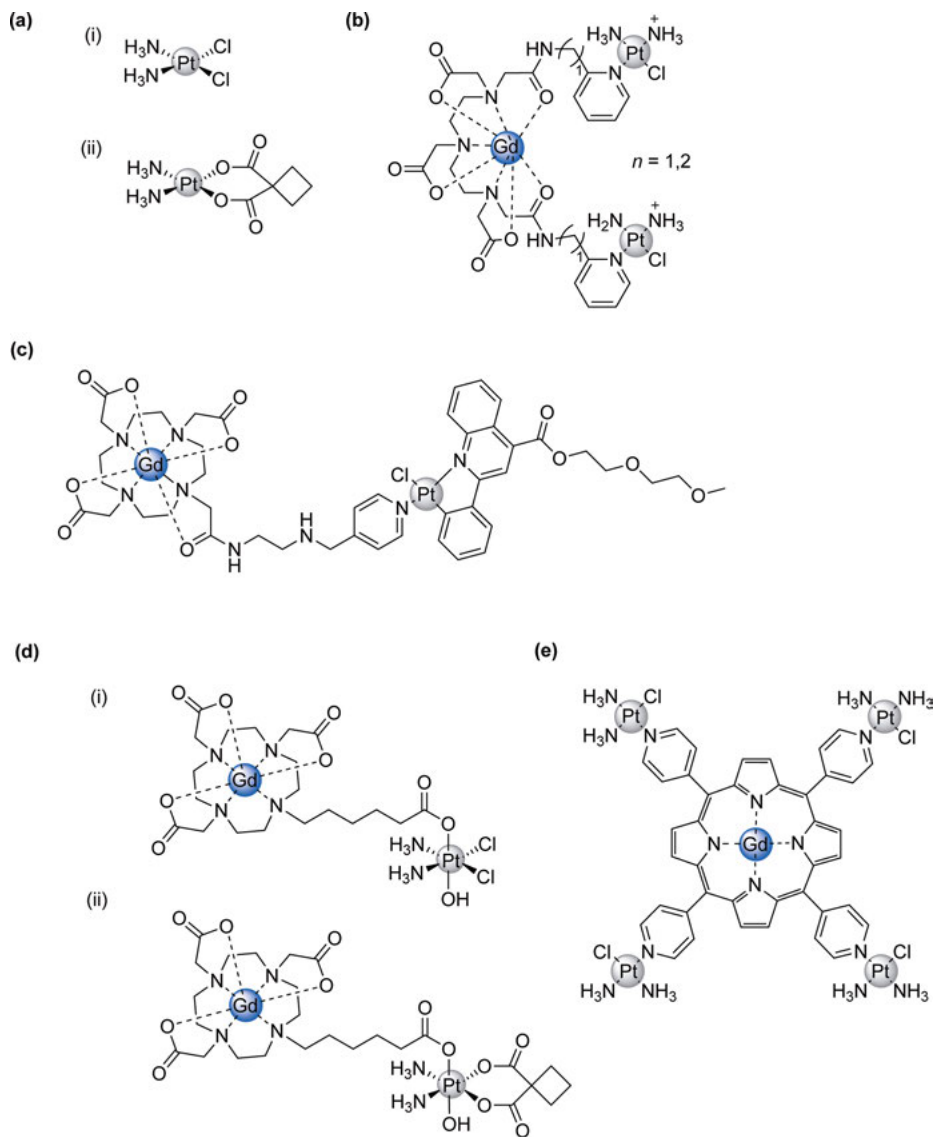
Figure 1. Gd(III)-Pt anticancer complexes reported to have theranostic applications. **(a)** Two of the FDA-approved Pt(II) anticancer drugs (i) cisplatin and (ii) carboplatin. **(b)** A Gd(III)-Pt(II) complex featuring Gd(III) chelated by a modified DTPA ligand. The pyridine group on the Gd(III) complex substitutes for a Cl⁻ ligand on cisplatin producing the final complex with two Pt(II) moieties. The Pt(II) units promoted cellular uptake of the Gd(III) complex and cytotoxicity was found to be comparable to cisplatin [39]. **(c)** A Gd(III)-Pt(II) compound containing a cyclometalated Pt(II) complex that possesses luminescent properties. The modified Gd(III)-DO3A complex uses the pyridine substituent to substitute for DMSO on the Pt(II) precursor molecule. The favorable luminescence and relaxivity properties provide a method to track the intracellular fate of the therapeutic and monitor off-target effects [40]. **(d)** Two Gd(III)-Pt(IV) prodrug strategies where Gd(III)-DO3A modified with a carboxylic acid tail is used as an axial ligand for (i) cisplatin and (ii) carboplatin. The agent remains intact in the extracellular environment but upon reduction to Pt(II) intracellularly, the axial ligands dissociate releasing the active Pt(II) drug [42]. **(e)** A Gd(III)-Pt(II) theranostic platform functionalized with both Pt(II) anticancer therapy and photodynamic therapy (PDT) from the porphyrin ligand. The Gd(III) is coordinated in the tetra(4-pyridyl) porphyrin ring and the pyridine groups substitute for a Cl⁻ ligand on cisplatin, yielding a complex with four Pt(II) groups. The two modes of treatment provided synergistic antitumor effects *in vivo* along with promising MRI results for image-guided cancer therapy [43].

2.3. Combined Magnetic Resonance Imaging and Photodynamic Therapy

Light-activated therapies are increasingly popular due to their selective and minimally invasive nature. In photodynamic therapy, absorption of light excites a photosensitizer molecule to a singlet state which undergoes intersystem crossing (ISC) to a long-lived triplet excited state. This triplet state is quenched by reaction with biomolecules or molecular oxygen to produce cytotoxic reactive oxygen species (ROS) that prove effective for cancer therapy [44]. The primary limitation of PDT is tissue depth penetration. PDT that uses two-photon excitation in the near infrared region (NIR) is a developing direction. Careful design of the photosensitizer is crucial to achieve excitation at the desired wavelength, as well as provide appropriate solubility and stability for biological applications. Tetrapyrrolic derivatives are the most widely studied constructs, although ruthenium(II) polypyridyl complexes have also recently reached clinical trials for PDT applications [45, 46]. Current research focuses on tumor targeting and tuning the photophysical properties.

Theranostic approaches are attractive in order to monitor delivery of the photosensitizer before light activation, providing high spatial control for treatment. MRI-PDT constructs benefit from several cooperative effects: porphyrin derivatives have a high affinity for tumor tissues and can act as an efficient delivery vehicle for MR contrast; conjugation of a Gd(III) complex to a large porphyrin moiety can slow down rotational dynamics, significantly enhancing relaxivity; and through the heavy atom effect Gd(III) can promote ISC in the photosensitizer [47]. A representative example of this MRI-PDT theranostic strategy is shown in Figure 2. This complex features one Gd(III)-DOTA complex conjugated to a zinc
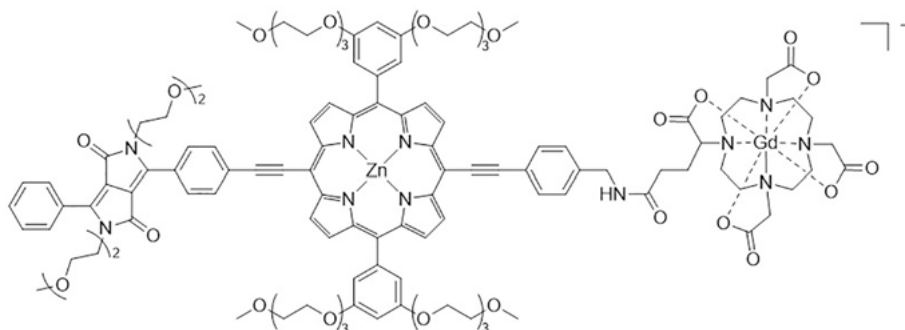
Figure 2. A representative example of a combined MRI-PDT theranostic [47]. The PDT comes from the porphyrin photosensitizer and MR contrast from the appended Gd(III) complex. This complex has only one conjugated Gd(III)-DOTA complex, but up to four complexes per molecule have been reported with DO3A, DTPA, DTTA being alternative Gd(III) chelation handles. The porphyrin ring typically features functionalization to improve water solubility and increase the excitation wavelength into the near infrared region. Specific strategies include metal coordination, extended conjugation, and the incorporation of hydrophilic groups.

porphyrin derivative functionalized with hydrophilic substituents to improve solubility. Proton relaxivity at 20 MHz was found to be 20 mM^{-1}s^{-1}, significantly higher than that of Gd(III)-DOTA alone (4–5 mM^{-1}s^{-1}). The conjugate displayed good two-photon absorption in the 910–940 nm range, corresponding well with the therapeutic window. The complex was also able to generate singlet oxygen with quantum yields ranging from 0.42 to 0.68 depending on solution composition. Preliminary cellular studies show low toxicity before light activation and significant phototoxicity with one- and two-photon light [47]. Following up on this study, the same group developed a Zn(II) porphyrin dimer with two Gd(III)-DOTA complexes attached to enhance photophysical properties and cell uptake [48].

Other examples of MRI-PDT theranostics feature modified tetraphenylporphyrin molecules with Gd(III) complexes conjugated off each phenyl ring, for a total of four Gd(III) moieties per molecule [49, 50]. Both of these examples leave the porphyrin unmetallated and utilize linear Gd(III)-DTTA chelation handles. Zn(II)-porphyrazine-Gd(III) conjugates were also developed bearing one, two, four, or eight Gd(III)-DO3A complexes per molecule. Tumor targeting, MRI, and NIR imaging abilities were all assessed with favorable *in vivo* results, but PDT applications were not fully explored [51, 52]. With continued advances in photosensitizer design and synthesis, MRI-PDT theranostics show great potential for clinical translation.

3. GADOLINIUM(III)-BASED NANOMATERIAL STRATEGIES

While small molecule strategies have a slight edge when it comes to clinical translation, nanomaterial theranostics offer a number of advantages. The size of nanomaterial constructs prevents them from being rapidly cleared through the kidneys,

promoting longer circulation and accumulation in tumors through the enhanced permeability and retention effect [53]. The high surface area of these materials provides high loading capacities for not only imaging and therapeutic functionality but also targeting ligands and cloaking agents [1]. A goal of theranostic development is the modular synthesis of multifunctional materials. Nanomaterial strategies present an easier path forward, in this regard, compared to the significant organic synthesis expertise required for small molecule approaches. This section explores the development and evaluation of Gd(III)-based MR theranostics across the following platforms: metal-based nanoparticles (NPs), including gadolinium oxide, gold, and lanthanide upconversion NPs (Section 3.1); carbon nanomaterials (Section 3.2); mesoporous silica NPs (Section 3.3); dendrimers and polymers (Section 3.4); and biomolecular nanomaterials (Section 3.5).

3.1.   Metal-Based Nanomaterials

Gadolinium oxide (Gd_2O_3) NPs are a growing class of T_1 MRI contrast agents, and an alternative to the well-studied Gd(III) coordination complexes. Through tuning the synthesis, different morphologies, sizes, coatings, and relaxation properties can be obtained for the Gd_2O_3 NPs. They range from sub-10 nm nanospheres to hollow and porous NPs over 100 nm in diameter [54]. Biocompatible coatings and functionalization of these NPs provide opportunities for multimodal imaging, therapy, and targeting. Ultrasmall Gd_2O_3 NPs (1.0–2.5 nm) have found success as theranostics, exploiting the high neutron capture cross section of ^{157}Gd for the combination of neutron capture therapy and MRI [55, 56]. Platforms with cyclic arginine-glycine-aspartic acid peptides (cRGDs) for tumor targeting [57], pH-sensitive fluorescence imaging [58], and blood-brain barrier permeability [59] have been explored *in vitro* and *in vivo*. A unique ZnO-core Gd_2O_3-shell NP system was functionalized with folic acid (FA) and Dox for targeted anticancer activity [60]. Another study doped Gd_2O_3 NPs with Mn to improve T_1 contrast enhancement and to provide Fenton-like activity for ROS-based cancer treatment [61]. Other Gd(III)-based nanomaterials use self-assembly strategies to coordinate Gd^{3+} ions with the chemotherapeutic gemcitabine [62] or PDT photosensitizer hypericin [63], forming supramolecular structures.

Beyond primarily Gd(III) compositions, gold nanostructures are a popular inorganic material for biomedical applications. These materials possess the unique optical phenomenon of localized surface plasmon resonance. The wavelength of the plasmonic resonance is dependent on particle size and shape. By tuning particle morphology, optical absorption in the NIR region can be achieved. NIR absorption is ideal for phototherapy applications due to high tissue depth penetration, and photothermal therapy (PTT) is a common application for gold materials. PTT is similar to PDT but does not require oxygen. In PTT, the photosensitizer material is excited and generates heat, thermally ablating surrounding cells [64]. Targeting agents to tumor cells is essential for high therapeutic efficacy and the minimization of off-target toxicity. Several Gd(III)-gold nanorod constructs have been proposed as MRI-PTT theranostics, allowing for image-guided delivery and activation [65–67]. Gold nanospheres designed for MRI-PTT and X-ray

computed tomography (CT) functionality have also been explored for multimodal imaging applications [68]. A gold nanostar platform was developed as a quintuple-modality theranostic probe. It featured surface-enhanced Raman scattering and two-photon luminescence in addition to MRI, PTT, and CT [69]. Other examples of MRI-PTT theranostics beyond gold nanomaterials include Prussian blue nanoparticles [70] and molybdenum disulfide nanosheets [71].

The combination of MRI and CT contrast in the same construct is attractive for improving the accuracy and comprehensiveness of diagnosis. CT contrast agents need to be strong X-ray absorbers, a property that scales exponentially with atomic number [72]. Lead sulfide and bismuth sulfide nanoparticles act as both suitable CT contrast agents and photothermal agents. Thus, conjugation of these materials with Gd(III) complexes yield theranostics for MRI/CT image-guided PTT [73, 74]. Lanthanide upconversion NPs are also an attractive platform for multimodal imaging, combining MRI contrast from Gd(III) with luminescent properties. Upconversion is a process where material converts low energy photons (typically NIR) to higher energy photons, minimizing photodamage and maximizing tissue depth penetration [75]. In one study, upconversion NPs benefitted from trimodal imaging capabilities with luminescence, MRI, and CT; chemotherapy from Dox and CPT; and tumor targeting from folic acid [76]. Other theranostic upconversion NP platforms use their photoactive properties for PDT coupled with Gd(III)-enhanced MRI [77, 78]. The primary challenge for these metal-based nanomaterial theranostics is biocompatibility. Stability and toxicity are a key consideration looking towards clinical translation, and much work must be devoted to studying compatible and functional surface coatings.

3.2.   Carbon Nanomaterials

Carbon nanomaterials benefit from high biocompatibility and low toxicity. Strong absorption in the infrared (IR) and NIR regions also make carbon materials well-suited for PTT applications. In addition, the sp^2 carbon structure provides a means of loading drugs or nucleic acid cargo via hydrophobic and π-π stacking interactions [79, 80]. Further functionalization with imaging and targeting groups yield theranostic capabilities. Graphene oxide (GO) is a single sheet carbon material with excellent properties for biomedical applications. In one study, GO was functionalized with polyethylene glycol (PEG) to improve physiological stability and as a handle to conjugate Gd(III)-DTPA. The nanocarrier was then loaded with Dox via adsorption, with the Dox acting as an anticancer agent as well as a fluorescent handle to monitor cellular uptake. This construct exhibited MR relaxation enhancement and high drug loading, demonstrating that GO is a promising theranostic nanocarrier strategy [81]. Gd(III)-GO theranostic strategies using PTT [82] and non-Dox chemotherapeutics [83, 84] have also been explored. Outside of GO, carbon quantum dots functionalized with Gd(III)-DTPA were developed for MRI-guided radiotherapy of tumors [85]. Continued research and development is needed to capitalize on the favorable properties and potential clinical translation for carbon nanomaterials.

3.3. Mesoporous Silica Nanoparticles

Like carbon nanomaterials, silica NPS are chemically inert and highly biocompatible. While they do not possess any distinct properties on the nanoscale, silica NPs have precise and tunable structures and surface chemistry. Mesoporous silica NPs (MSNs) are a class of silica materials that feature tunable pore sizes and volumes. These pores can encapsulate cargo for biomedical purposes. They offer two areas for MSN functionalization: the interior pores or exterior surface [86]. Studies examining how MSN characteristics and conjugation methods can affect relaxation properties in Gd(III)-MSNs are prevalent in the literature. For Gd(III)-MSNs, high MRI efficacy is not dependent on high payload of Gd(III) chelates, but on the water exchange rates and rotational flexibility of the metal centers in the particles [87].

Gd(III)-complex surface conjugation is the most common functionalization method for theranostics, with chemotherapeutics loaded in the nanopores. Two targeted Gd(III)-MSN platforms were developed for the pH-controlled [88] or redox-responsive [89] release of Dox upon delivery to tumors. Surface-conjugated Gd(III)-MSNs have been further functionalized for bimodal imaging applications. Examples combining proton and fluorine-19 MRI [90], Ru(II)-based luminescence and PDT [91], and ultrasound-stimulated cargo release [92] were all recently reported.

Doping Gd_2O_3 NPs into MSN pores is another way to produce MRI functionality. Further europium doping creates luminescent and MRI-active materials for theranostics [93–95]. In one study, MSN pores co-loaded with Gd_2O_3 and Dox were functionalized with a pH-responsive coating for controlled Dox release [96]. A trimodal imaging theranostic agent was also developed with this doping method. Once again, Gd_2O_3 and Dox were loaded into the MSN pores, followed by encapsulation in a thermosensitive liposome. The liposome was loaded with indocyanine green (ICG), which contributes to both PDT and PTT along with fluorescence and photoacoustic imaging. Upon NIR irradiation, ICG generates heat to breakdown the liposome, thus releasing Dox after image-guided delivery. The proposed theranostic was studied *in vitro* and *in vivo* with promising results [97].

3.4. Dendrimers and Polymers

Polymer nanoparticles offer controllable size, biocompatibility, and precise design of functionality within polymer subunits [98]. Dendrimers are symmetric, hyperbranched polymers that form near-spherical particles. The core of the dendrimer can carry cargo through covalent or non-covalent attachment, while the surface allows for conjugation of targeting, imaging, or therapy molecules. The high density of dendrimers compared to linear structures is advantageous and provides many points for incorporation of functional groups [98, 99]. While most examples of dendrimer MR theranostics use iron oxide particles for T_2 contrast, a few Gd(III)-based constructs have been developed. Multiple studies encapsulated Gd(III) complexes and Dox in dendrimer particles for theranostic treatment of cancer

[100–102]. Another dendrimer approach combined Gd(III) MR contrast with fluorescence and prostate tumor targeting for image-guided surgery [103]. A gene therapy MR theranostic for pancreatic cancer was also developed and evaluated *in vivo*, which highlighted the benefits of targeted image-guided delivery [104]. Other *in vivo* studies of Gd(III)-dendrimer theranostics demonstrate the potential of these structures for clinical applications in skin cancer [105].

Copolymer nanoparticle platforms benefit from amphiphilic self-assembly and release strategies for theranostic applications. Typically, a hydrophilic block on the outside like PEG is used to provide water solubility and biocompatibility, while a hydrophobic interior block of the polymer is used to load anticancer drugs and other cargo [99]. One specific approach utilized polycaprolactone as the hydrophobic block with two different lengths of hydrophilic polyglutamic acid blocks on either end. The ends of the polymer are functionalized with FA for targeting and Gd(III)-DTPA for MR contrast. The polymers self-assemble into a vesicle with the FA terminal group on the outside and Gd(III)-DTPA on the interior. Electrostatic interactions with the polyglutamic acid chains allow for the loading of Dox to complete the theranostic particle. These particles were studied *in vitro* and *in vivo*, demonstrating high contrast enhancement and slow release of Dox at neutral conditions with faster release at acidic tumor conditions [106]. Other examples of block copolymer particles loaded with Dox and functionalized with Gd(III) saw analogous sustained release of the chemotherapeutic and contrast enhancement [107–109], with some incorporating release strategies responsive to light [110, 111] or pH and temperature [112, 113]. Similar polymeric Gd(III)-theranostic particles adopted alternative therapeutic approaches including gemcitabine [114], CPT [115, 116], and Pt anticancer drugs [117] along with MoS_2 based PTT [118]. The responsive nature of these block copolymer materials is a distinct advantage over other nanoplatforms, allowing for programmable release of cargo upon irradiation or changes in cellular environment.

Multiple imaging modalities can also be incorporated into these polymeric materials. Gd-doped upconversion particles were functionalized with a layered copolymer coating to track gene therapy delivery by luminescence and MRI [119]. An MR-photoacoustic imaging (PAI) theranostic was also developed with PTT for tumor treatment. PAI activity was from a perylene derivative incorporated into the polymer [120]. PAI uses optical absorption to enable ultrasound detection, making it a strategy well-suited to be coupled with phototherapy and NIR imaging applications. To that end, a semiconducting polymer was developed for PAI, PTT, and NIR fluorescence emission applications and then further functionalized with Gd(III) to provide tri-modal image-guided PTT [121].

Outside of cancer treatment applications, theranostics are also being developed for neurodegenerative disease [122]. A study using Gd(III)-based MRI targeted cerebral amyloid angiopathy (CAA), a condition found in Alzheimer's disease characterized by the deposition of amyloid beta protein in blood vessels. A polymeric theranostic particle was constructed with chitosan, a polysaccharide, conjugated with Gd(III)-DTPA and loaded with cyclophosphamide, an immunosuppressant drug for CAA. An antibody-targeting group was conjugated to the surface of the nanocarrier to improve localization of the amyloid protein. The

goal of the study was to target amyloid protein, provide early detection for CAA, and treat the resulting inflammation. *In vitro* and *in vivo* studies were promising, showing sustained drug release and contrast enhancement in the disease model [123].

3.5. Biomolecular Nanomaterials

Minimizing the toxicity of the nanocarrier is a high priority in theranostic design. Therefore, an assembly of biomolecules seems like an ideal nanomaterial for *in vivo* studies and clinical translation. Common biomaterials explored for these applications include lipids, proteins, and DNA.

The amphiphilic nature of lipids makes them well-suited to form supramolecular structures. Lipid micelles in aqueous conditions form by assembly of the hydrophilic heads into a spherical particle with the hydrophobic tails oriented towards the interior. This kind of structure makes it possible to load hydrophobic cargo in the interior and conjugate hydrophilic groups on the exterior for multifunctional applications [124]. One micellular theranostic used the interior core to encapsulate a water insoluble NIR dye, IR825, for NIR fluorescent imaging and PTT. In combination with a porphyrin-derivative photosensitizer for PDT and Gd(III) chelation, this theranostic micelle assembly combined MR, NIR, and PA imaging capabilities with PTT and PDT for synergistic antitumor effects *in vitro* and *in vivo* [125]. Another micelle construct combined Gd(III)-DO3A with Pt(II) anticancer therapy. This assembly provided enhanced contrast and tumor growth inhibition along with fewer side effects *in vivo* [126].

Liposomes are spherical assemblies formed by a lipid bilayer, with a hydrophilic encapsulated core and hydrophobic membrane for loading cargo. As with micelle nanocarriers, liposomes have also been studied as MR theranostics, with examples of multimodal imaging and therapy applications [30, 127, 128]. Liposomes designed for MR-guided phototherapies are also prevalent [129, 130]. Comparable to polymeric theranostics, liposomal carriers can also capitalize on responsive and sustained drug release strategies. Thermosensitive liposomes were developed for the release of cargo upon magnetic heating. The liposome was loaded with two forms of MR contrast, Gd(III)-DTPA and iron oxide NPs. The Gd(III)-DTPA is released along with the drug upon heating while the iron oxide NPs remain in the liposomes. This dual contrast allows for the monitoring of liposome position and condition by the T_2-weighted MR contrast and correlate drug release with changes in T_1 MR contrast [131]. Another study investigated the liposomal delivery of curcumol for ovarian cancer treatment with Gd(III)-DTPA enhanced MRI. Curcumol has low bioavailability due to poor water solubility, thus loading in the lipid bilayer improved delivery and antitumor effects [132]. Finally, unique lipid-latex particles were developed for macrophage targeting with a fluorescent core, Gd(III)-DTPA, and hydrophobic drugs for the treatment and monitoring of inflammatory disease [133].

Other common biomolecules used for theranostic strategies are protein nanocarriers. Bovine serum albumin (BSA) is the most popular due to its commercial

availability. BSA effectively coordinates metal ions, such as Gd(III), and is frequently used in biocompatible NP syntheses [134]. Most examples of Gd(III)-BSA theranostics couple the MR contrast with PTT, using organic dyes [135, 136], metal sulfides [137, 138], or Ru nanodots [139] as the phototherapy handle. The same studies also benefit from multimodal imaging functionality, namely PAI or NIR imaging, due to the photoactive molecules present. Beyond proteins, tobacco mosaic virus particles [140] and thermosensitive DNA complexes [141] were also studied as biomolecule theranostic nanocarriers for MRI-PTT applications.

4. MAGNETIC PARTICLE IMAGING THERANOSTICS

Magnetic particle imaging is a developing tracer-based biomedical imaging modality. The use of tomographic imaging to determine the spatial distribution of tracer particles makes MPI analogous to techniques like PET and SPECT, where a signal is only observed when the tracer is present. However, MPI also has strong ties to MRI. Like MRI, MPI has an excellent safety profile using applied magnetic fields to generate the signal. The most common MPI tracers are superparamagnetic iron oxide NPs (SPIONs) which are widely used T_2-weighted MRI contrast agents. MPI has several distinct advantages over MRI, namely a faster image acquisition, positive contrast enhancement with SPIONs, and no background signal allowing for direct quantitative analysis. Moreover, MPI has millimeter resolution and zero signal attenuation at any tissue depth [23, 142]. With these favorable capabilities, MPI is being pursued for many biomedical applications, including theranostics. Tracer development for these purposes is an active MPI research area, with much work devoted to NP fabrication and the understanding of magnetization on the nanoscale. Size, uniformity, stability, surface coating, blood circulation time, and targeting efficiency are all important design considerations [143, 144].

A deeper discussion of MPI physics and image generation can be found elsewhere [23, 142]. Briefly, MPI depends on the electronic magnetization of SPIONs. Changes in magnetization are visualized in the same way as MRI by using gradient fields and receiver coils. However, MRI examines the change in nuclear magnetization not electronic magnetization, a distinction that makes MPI a much more sensitive technique. SPIONs are locked in place and oriented by the MPI gradient field except for a small area called the field free region (FFR). When an excitation field is applied, only the SPIONs in the FFR reorient, producing a signal. By moving the FFR throughout the field of view, a comprehensive image is created [145].

Magnetic hyperthermia is the most common therapeutic technique to be coupled with MPI. Magnetic hyperthermia works by heating NPs with alternating magnetic fields. This causes the particles to generate and release heat that can be used to thermally ablate tissue or raise the temperature of the surrounding tissue by a few degrees to enhance the effects of chemotherapy. The specific excitation of particles in the FFR through MPI offers precise control of hyperthermia and avoids healthy tissue with high tracer accumulation. Studies have

explored particle development [146], hardware engineering [147], and *in vivo* applications of this theranostic strategy. Compellingly, the *in vivo* work showed exact control of magnetic hyperthermia and impressive reduction of tumor volume [148]. The SPIONs still accumulate in many off-target organs such as the spleen and liver. Therefore, strategies for selective delivery and targeting are being investigated. One study found improved magnetic hyperthermia treatment using breast cancer targeted particles, which is promising for the development of more effective MPI-magnetic hyperthermia theranostics [149].

An alternative therapeutic method is loading SPIONs in nanocarriers for multi-modal applications with MPI. Hypoxia-targeted exosomes were loaded with SPIONs, lipophilic fluorescent dye, and the anticancer drug Olaparib for image-guided tracking of delivery and treatment in a breast cancer model [150]. A block copolymer construct that loaded a prodrug analogue of Dox and SPIONs in the nanocarrier for quantitative imaging of drug delivery was also investigated [151].

Another polymeric MPI-theranostic platform was developed for drug release monitoring. SPIONs form the core of the nanocarrier, with the shell composed of a biocompatible polymer loaded with Dox. In acidic conditions, the nanocarrier degrades allowing for sustained Dox release and changes in SPION distribution. This results in a linear and quantitative MPI signal change that correlates with drug release [152].

The outlook for MPI theranostics is encouraging. SPION-labeled aerosols have been used for MPI monitoring of lung therapies, a notoriously difficult organ to image [153, 154]. Applications in stem cell tracking [155, 156] and brain imaging [157] are also being explored. While MPI is a relatively new technique, its efficacy in a broad range of biomedical areas is quickly making it an indispensable molecular imaging modality.

5. CONCLUSIONS

This chapter provides an overview of the current progress in Gd(III)-based MRI theranostics. While clinical trials of MR theranostics have been limited, this field is extremely promising for advances in personalized medicine and image-guided therapies. Small molecule strategies have a potentially easier path forward towards clinical translation by combining already approved diagnostic and therapeutic components into a single theranostic platform. However, nanomaterials offer several advantages. Their large size promotes passive tumor targeting via the enhanced permeability and retention effect and provides high surface areas for the conjugation of various functionalities.

For MRI applications, nanomaterials provide a boost in contrast enhancement not only from a high payload of Gd(III), but also from changes in rotational dynamics and water exchange. Nanomaterial platforms can provide multimodal imaging handles, synergistic therapeutic cargos, and tumor targeting all in one construct without complex organic synthesis. Responsive and sustained drug release strategies have also been particularly effective in amphiphilic polymer and

lipid materials. Toxicity, stability, and reproducibility remain as challenges for nanocarrier theranostics. Thus, more rigorous *in vivo* testing is required to translate their advantageous properties to the clinic. While still an emerging technique, MPI theranostics benefit from exceptional precision and selectivity of treatment. These MPI platforms perhaps hold the most promise for biomedical applications, as they are only limited by the development and access of MPI scanners. Both MRI and MPI are excellent, noninvasive, radiation-free imaging handles with strong potential in theranostic applications.

ACKNOWLEDGMENTS

ABBREVIATIONS AND DEFINITIONS

BSA	bovine serum albumin
BTA	benzothiazole aniline
CAA	cerebral amyloid angiopathy
CHL	chlorambucil
CPT	camptothecin
CT	computed tomography
DMSO	dimethyl sulfoxide
DO3A	1,4,7,10-tetraazacyclododecane-1,4,7-trisacetic acid
DOTA	1,4,7,10-tetraazacyclododecane-1,4,7,10-tetraacetic acid
Dox	doxorubicin
DTPA	diethylenetriaminepentaacidic acid
DTTA	diethylenetriaminetetraacetic acid
FA	folic acid
FDA	Food and Drug Administration
FFR	field free region
GO	graphene oxide
ICG	indocyanine green
IR	infrared
ISC	intersystem crossing
MPI	magnetic particle imaging
MR	magnetic resonance
MRI	magnetic resonance imaging
MRS	magnetic resonance spectroscopy
MSN	mesoporous silica nanoparticle
MTX	methotrexate

NIR   near infrared region
NP   nanoparticle
PAI   photoacoustic imaging
PDT   photodynamic therapy
PEG   polyethylene glycol
PET   positron emission tomography
PTT   photothermal therapy
ROS   reactive oxygen species
SPECT   single-photon emission computed tomography
SPION   superparamagnetic iron oxide nanoparticle

REFERENCES

1. S. S. Kelkar, T. M. Reineke, *Bioconjugate Chem.* **2011**, *22*, 1879–1903.
2. X. Chen, *Theranostics* **2011**, *1*, 1–2.
3. V. Ozdemir, B. Williams-Jones, S. J. Glatt, M. T. Tsuang, J. B. Lohr, C. Reist, *Nat. Biotechnol.* **2006**, *24*, 942–946.
4. Y. Jeong, H. S. Hwang, K. Na, *Biomater. Res.* **2018**, *22*, 20/21–20/13.
5. M.-F. Penet, J. Jin, Z. Chen, Z. M. Bhujwalla, *Top. Magn. Reson. Imaging* **2016**, *25*, 215–221.
6. W. Xie, Z. Guo, F. Gao, Q. Gao, D. Wang, B.-s. Liaw, Q. Cai, X. Sun, X. Wang, L. Zhao, *Theranostics* **2018**, *8*, 3284–3307.
7. A. A. Abd Elrahman, F. R. Mansour, *J. Drug Delivery Sci. Technol.* **2019**, *52*, 702–712.
8. N. V. Srikanth Vallabani, S. Singh, A. S. Karakoti, *Curr. Drug Metab.* **2019**, *20*, 457–472.
9. Z. Shen, T. Chen, X. Ma, W. Ren, Z. Zhou, G. Zhu, A. Zhang, Y. Liu, J. Song, Z. Li, H. Ruan, W. Fan, L. Lin, J. Munasinghe, X. Chen, A. Wu, *ACS Nano* **2017**, *11*, 10992–11004.
10. D. Pan, S. D. Caruthers, G. Hu, A. Senpan, M. J. Scott, P. J. Gaffney, S. A. Wickline, G. M. Lanza, *J. Am. Chem. Soc.* **2008**, *130*, 9186–9187.
11. H. Zuo, W. Chen, B. Li, K. Xu, H. Cooper, Z. Gu, Z. P. Xu, *Chem. Eur. J.* **2017**, *23*, 14299–14306.
12. M. Shi, S. Wang, S. Zheng, P. Hou, L. Dong, M. He, C. Wu, X. Zhang, F. Zuo, K. Xu, J. Li, *Colloids Surf. B* **2020**, 185, 110625.
13. Y. Shi, F. Guenneau, X. Wang, C. Hélary, T. Coradin, *Nanotheranostics* **2018**, *2*, 403–416.
14. Y. Wu, L. Xu, J. Qian, L. Shi, Y. Su, Y. Wang, D. Li, X. Zhu, *Biomater. Sci.* **2020**, *8*, 712–719.
15. J. T. Brewster, G. D. Thiabaud, P. Harvey, H. Zafar, J. F. Reuther, S. Dell'Acqua, R. M. Johnson, H. D. Root, P. Metola, A. Jasanoff, L. Casella, J. L. Sessler, *Chem.* **2020**, *6*, 703–724.
16. M. H. Cho, S. H. Shin, S. H. Park, D. K. Kadayakkara, D. Kim, Y. Choi, *Bioconjugate Chem.* **2019**, *30*, 2502–2518.
17. J. Zhu, H. Zhang, K. Chen, Y. Li, Z. Yang, S. Chen, X. Zheng, X. Zhou, Z.-X. Jiang, *Adv. Healthcare Mater.* **2020**, *9*, 1901331.
18. R. Kumar, W. S. Shin, K. Sunwoo, W. Y. Kim, S. Koo, S. Bhuniya, J. S. Kim, *Chem. Soc. Rev.* **2015**, *44*, 6670–6683.
19. S. Lacerda, E. Tóth, *ChemMedChem* **2017**, *12*, 883–894.

20. Y. Liu, N. Zhang, *Biomaterials* **2012**, *33*, 5363–5375.

21. V. Nandwana, M. De, S. Chu, M. Jaiswal, M. Rotz, T. J. Meade, V. P. Dravid, *Cancer Treat. Res.* **2015**, *166*, 51–83.

22. S. Gan, Y. Lin, Y. Feng, L. Shui, H. Li, G. Zhou, *Int. J. Nanomed.* **2018**, *13*, 4263–4281.

23. M. H. Pablico-Lansigan, S. F. Situ, A. C. S. Samia, *Nanoscale* **2013**, *5*, 4040–4055.

24. L. Frullano, P. Caravan, *Curr. Org. Synth.* **2011**, *8*, 535–565.

25. L. Frullano, B. Tejerina, T. J. Meade, *Inorg. Chem.* **2006**, *45*, 8489–8491.

26. Y. Pommier, E. Leo, H. Zhang, C. Marchand, *Chem. Biol.* **2010**, *17*, 421–433.

27. M. H. Lee, E.-J. Kim, H. Lee, S. Y. Park, K. S. Hong, J. S. Kim, J. L. Sessler, *Chem. Commun.* **2016**, *52*, 10551–10554.

28. C. Preihs, J. F. Arambula, D. Magda, H. Jeong, D. Yoo, J. Cheon, Z. H. Siddik, J. L. Sessler, *Inorg. Chem.* **2013**, *52*, 12184–12192.

29. S. W. Young, F. Qing, A. Harriman, J. L. Sessler, W. C. Dow, T. D. Mody, G. W. Hemmi, Y. Hao, R. A. Miller, *Proc. Natl. Acad. Sci. USA* **1996**, *93*, 6610–6615.

30. M. H. Lee, E.-J. Kim, H. Lee, H. M. Kim, M. J. Chang, S. Y. Park, K. S. Hong, J. S. Kim, J. L. Sessler, *J. Am. Chem. Soc.* **2016**, *138*, 16380–16387.

31. Z. Yang, H. Lin, J. Huang, A. Li, C. Sun, J. Richmond, J. Gao, *Chem. Commun.* **2019**, *55*, 4546–4549.

32. S. Chen, X. Zhao, J. Chen, J. Chen, L. Kuznetsova, S. S. Wong, I. Ojima, *Bioconjugate Chem.* **2010**, *21*, 979–987.

33. J. Kaur, Y. Tsvetkova, K. Arroub, S. Sahnoun, F. Kiessling, S. Mathur, *Chem. Biol. Drug Des.* **2017**, *89*, 269–276.

34. D. Xu, Y. He, S.-T. Lu, Y.-S. Li, A. Baidya, H. Mei, B. Wu, *Drug Des., Dev. Ther.* **2018**, *12*, 3301–3309.

35. A. Irfan, F. Batool, S. A. Zahra Naqvi, A. Islam, S. M. Osman, A. Nocentini, S. A. Alissa, C. T. Supuran, *J. Enzyme Inhib. Med. Chem.* **2020**, *35*, 265–279.

36. H.-K. Kim, M.-K. Kang, K.-H. Jung, S.-H. Kang, Y.-H. Kim, J.-C. Jung, G. H. Lee, Y. Chang, T.-J. Kim, *J. Med. Chem.* **2013**, *56*, 8104–8111.

37. T. L. Kalber, N. Kamaly, S. A. Higham, J. A. Pugh, J. Bunch, C. W. McLeod, A. D. Miller, J. D. Bell, *Bioconjugate Chem.* **2011**, *22*, 879–886.

38. S. Dasari, P. Bernard Tchounwou, *Eur. J. Pharmacol.* **2014**, *740*, 364–378.

39. Z. Zhu, X. Wang, T. Li, S. Aime, P. J. Sadler, Z. Guo, *Angew. Chem., Int. Ed.* **2014**, *53*, 13225–13228.

40. O. J. Stacey, A. J. Amoroso, J. A. Platts, P. N. Horton, S. J. Coles, D. Lloyd, C. F. Williams, A. J. Hayes, J. J. Dunsford, S. J. A. Pope, *Chem. Commun.* **2015**, *51*, 12305–12308.

41. T. C. Johnstone, K. Suntharalingam, S. J. Lippard, *Chem. Rev.* **2016**, *116*, 3436–3486.

42. C. J. Adams, T. J. Meade, *Chem. Sci.* **2020**, *11*, 2524–2530.

43. B. Wu, X.-Q. Li, T. Huang, S.-T. Lu, B. Wan, R.-F. Liao, Y.-S. Li, A. Baidya, Q.-Y. Long, H.-B. Xu, *Biomater. Sci.* **2017**, *5*, 1746–1750.

44. D. van Straten, V. Mashayekhi, H. S. de Bruijn, S. Oliveira, D. J. Robinson, *Cancers* **2017**, *9*.

45. S. Monro, K. L. Colón, H. Yin, J. Roque, P. Konda, S. Gujar, R. P. Thummel, L. Lilge, C. G. Cameron, S. A. McFarland, *Chem. Rev.* **2019**, *119*, 797–828.

46. C. Imberti, P. Zhang, H. Huang, P. J. Sadler, *Angew. Chem., Int. Ed.* **2020**, *59*, 61–73.

47. J. Schmitt, V. Heitz, A. Sour, F. Bolze, P. Kessler, L. Flamigni, B. Ventura, C. S. Bonnet, E. Tóth, *Chem. Eur. J.* **2016**, *22*, 2775–2786.

48. J. Schmitt, S. Jenni, A. Sour, V. Heitz, F. Bolze, A. Pallier, C. S. Bonnet, E. Tóth, B. Ventura, *Bioconjugate Chem.* **2018**, *29*, 3726–3738.

49. J. Luo, L.-F. Chen, P. Hu, Z.-N. Chen, *Inorg. Chem.* **2014**, *53*, 4184–4191.

50. A. Sour, S. Jenni, A. Orti-Suarez, J. Schmitt, V. Heitz, F. Bolze, P. Loureiro de Sousa, C. Po, C. S. Bonnet, A. Pallier, E. Tóth, B. Ventura, *Inorg. Chem.* **2016**, *55*, 4545–4554.

51. Y. Song, H. Zong, E. R. Trivedi, B. J. Vesper, E. A. Waters, A. G. M. Barrett, J. A. Radosevich, B. M. Hoffman, T. J. Meade, *Bioconjugate Chem.* **2010**, *21*, 2267–2275.

52. E. R. Trivedi, Z. Ma, E. A. Waters, K. W. Macrenaris, R. Subramanian, A. G. M. Barrett, T. J. Meade, B. M. Hoffman, *Contrast Media Mol. Imaging* **2014**, *9*, 313–322.

53. A. K. Iyer, G. Khaled, J. Fang, H. Maeda, *Drug Discovery Today* **2006**, *11*, 812–818.

54. G. Thirumalraj, M. S. Nachiappan, K. R. Arun, *J. Bionanosci.* **2015**, *9*, 409–423.

55. J. T. Masiakowski, J. L. Horton, L. J. Peters, *Med. Phys.* **1992**, *19*, 1277–1284.

56. G. Leinweber, D. P. Barry, M. J. Trbovich, J. A. Burke, N. J. Drindak, H. D. Knox, R. V. Ballad, R. C. Block, Y. Danon, L. I. Severnyak, *Nucl. Sci. Eng.* **2006**, *154*, 261–279.

57. M. Y. Ahmad, M. W. Ahmad, H. Cha, I.-T. Oh, T. Tegafaw, X. Miao, S. L. Ho, S. Marasini, A. Ghazanfari, H. Yue, H.-K. Ryeom, J. Lee, K. S. Chae, Y. Chang, G. H. Lee, *Eur. J. Inorg. Chem.* **2018**, 3070–3079.

58. S. L. Ho, H. Cha, I. T. Oh, K.-H. Jung, M. H. Kim, Y. J. Lee, X. Miao, T. Tegafaw, M. Y. Ahmad, K. S. Chae, Y. Chang, G. H. Lee, *RSC Adv.* **2018**, *8*, 12653–12665.

59. Z. Shen, T. Liu, Z. Yang, Z. Zhou, W. Tang, W. Fan, Y. Liu, J. Mu, L. Li, V. I. Bregadze, S. K. Mandal, A. A. Druzina, Z. Wei, X. Qiu, A. Wu, X. Chen, *Biomaterials* **2020**, *235*, 119783.

60. A. Wozniak, N. Babayevska, T. Zalewski, M. Wozniak-Budych, S. Jurga, B. F. Grzeskowiak, M. Drobna, M. Wiweger, R. Slomski, *Mater. Sci. Eng., C* **2017**, *80*, 603–615.

61. Z. Zhao, K. Xu, C. Fu, H. Liu, M. Lei, J. Bao, A. Fu, Y. Yu, W. Zhang, *Biomaterials* **2019**, *219*, 119379.

62. L. Li, R. Tong, M. Li, D. S. Kohane, *Acta Biomater.* **2016**, *33*, 34–39.

63. E. Chen, X. Chen, X. Yuan, S. Wei, L. Zhou, J. Zhou, J. Shen, *Dalton Trans.* **2017**, *46*, 5151–5158.

64. L. Cheng, C. Wang, L. Feng, K. Yang, Z. Liu, *Chem. Rev.* **2014**, *114*, 10869–10939.

65. T. Guo, Y. Lin, Z. Li, S. Chen, G. Huang, H. Lin, J. Wang, G. Liu, H.-H. Yang, *Nanoscale* **2017**, *9*, 56–61.

66. A. Pitchaimani, T. D. T. Nguyen, L. Maurmann, J. Key, S. H. Bossmann, S. Aryal, *J. Biomed. Nanotechnol.* **2017**, *13*, 417–426.

67. A. K. Parchur, G. Sharma, J. M. Jagtap, V. R. Gogineni, P. S. LaViolette, M. J. Flister, S. B. White, A. Joshi, *ACS Nano* **2018**, *12*, 6597–6611.

68. Y. Zeng, D. Zhang, M. Wu, Y. Liu, X. Zhang, L. Li, Z. Li, X. Han, X. Wei, X. Liu, *ACS Appl. Mater. Interfaces* **2014**, *6*, 14266–14277.

69. Y. Liu, Z. Chang, H. Yuan, A. M. Fales, T. Vo-Dinh, *Nanoscale* **2013**, *5*, 12126–12131.

70. S. S. Kale, R. A. Burga, E. E. Sweeney, Z. Zun, R. W. Sze, A. Tuesca, J. A. Subramony, R. Fernandes, *Int. J. Nanomed.* **2017**, *12*, 6413–6424.

71. J. Liu, J. Zheng, H. Nie, D. Zhang, D. Cao, Z. Xing, B. Li, L. Jia, *J. Colloid Interface Sci.* **2019**, *548*, 131–144.

72. H. Lusic, M. W. Grinstaff, *Chem. Rev.* **2013**, *113*, 1641–1666.

73. Y. Zou, H. Jin, F. Sun, X. Dai, Z. Xu, S. Yang, G. Liao, *ACS Appl. Nano Mater.* **2018**, *1*, 2294–2305.

74. H. Guo, X. Zhao, H. Sun, H. Zhu, H. Sun, *Nanotechnology* **2019**, *30*, 75101.

75. F. Wang, X. Liu, *Chem. Soc. Rev.* **2009**, *38*, 976–989.

76. G. Tian, W. Yin, J. Jin, X. Zhang, G. Xing, S. Li, Z. Gu, Y. Zhao, *J. Mater. Chem. B* **2014**, *2*, 1379–1389.

77. Y. Zhang, G. K. Das, V. Vijayaragavan, Q. C. Xu, P. Padmanabhan, K. K. Bhakoo, S. Tamil Selvan, T. T. Y. Tan, *Nanoscale* **2014**, *6*, 12609–12617.

78. L. Zeng, Y. Pan, R. Zou, J. Zhang, Y. Tian, Z. Teng, S. Wang, W. Ren, X. Xiao, J. Zhang, L. Zhang, A. Li, G. Lu, A. Wu, *Biomaterials* **2016**, *103*, 116–127.

79. D. Chen, C. A. Dougherty, K. Zhu, H. Hong, *J. Controlled Release* **2015**, *210*, 230–245.

80. Y. Gao, *J. Funct. Biomater.* **2018**, *9*, 16/11–16/15.

81. M. Zhang, Y. Cao, Y. Chong, Y. Ma, H. Zhang, Z. Deng, C. Hu, Z. Zhang, *ACS Appl. Mater. Interfaces* **2013**, *5*, 13325–13332.

82. Z. Li, H. Ke, J. Wang, Z. Miao, X. Yue, *J. Nanosci. Nanotechnol.* **2016**, *16*, 2201–2209.

83. M. S. Usman, M. Z. Hussein, S. Fakurazi, M. Masarudin, F. F. A. Saad, *PLoS One* **2018**, doi: 101371/journal.pone.0201228.

84. M. S. Usman, M. Z. Hussein, A. U. Kura, S. Fakurazi, M. J. Masarudin, F. F. A. Saad, *Molecules* **2018**, *23*, 500.

85. F. Du, L. Zhang, L. Zhang, M. Zhang, A. Gong, Y. Tan, J. Miao, Y. Gong, M. Sun, H. Ju, C. Wu, S. Zou, *Biomaterials* **2017**, *121*, 109–120.

86. J. L. Vivero-Escoto, R. C. Huxford-Phillips, W. Lin, *Chem. Soc. Rev.* **2012**, *41*, 2673–2685.

87. F. Carniato, L. Tei, M. Botta, *Eur. J. Inorg. Chem.* **2018**, 4936–4954.

88. G. Zhang, J. Gao, J. Qian, L. Zhang, K. Zheng, K. Zhong, D. Cai, X. Zhang, Z. Wu, *ACS Appl. Mater. Interfaces* **2015**, *7*, 14192–14200.

89. Chen, X. Zhou, W. Nie, Q. Zhang, W. Wang, Y. Zhang, C. He, *ACS Appl. Mater. Interfaces* **2016**, *8*, 33829–33841.

90. M. Bouchoucha, R. B. van Heeswijk, Y. Gossuin, F. Kleitz, M.-A. Fortin, *Langmuir* **2017**, *33*, 10531–10542.

91. S. Lechevallier, R. Mauricot, H. Gros-Dagnac, S. Chevreux, G. Lemercier, E. Phonesouk, M. Golzio, M. Verelst, *ChemPlusChem* **2017**, *82*, 770–777.

92. C.-A. Cheng, W. Chen, L. Zhang, H. H. Wu, J. I. Zink, *J. Am. Chem. Soc.* **2019**, *141*, 17670–17684.

93. S. Gandhi, K. Thandavan, B.-J. Kwon, H.-J. Woo, S. S. Yi, H. S. Lee, J. H. Jeong, K. Jang, D. S. Shin, *RSC Adv.* **2014**, *4*, 5953–5962.

94. D. A. Eurov, D. A. Kurdyukov, D. A. Kirilenko, J. A. Kukushkina, A. V. Nashchekin, A. N. Smirnov, V. G. Golubev, *J. Nanopart. Res.* **2015**, *17*, 1–10.

95. S.-M. Hsiao, B.-Y. Peng, Y. S. Tseng, H.-T. Liu, C.-H. Chen, H.-M. Lin, *Microporous Mesoporous Mater.* **2017**, *250*, 210–220.

96. K. He, J. Li, Y. Shen, Y. Yu, *J. Mater. Chem. B* **2019**, *7*, 6840–6854.

97. Q. Sun, Q. You, J. Wang, L. Liu, Y. Wang, Y. Song, Y. Cheng, S. Wang, F. Tan, N. Li, *ACS Appl. Mater. Interfaces* **2018**, *10*, 1963–1975.

98. S. Mignani, J. Rodrigues, H. Tomas, A.-M. Caminade, R. Laurent, X. Shi, J.-P. Majoral, *Sci. China Mater.* **2018**, *61*, 1367–1386.

99. S. Ray, Z. Li, C.-H. Hsu, L.-P. Hwang, Y.-C. Lin, P.-T. Chou, Y.-Y. Lin, *Theranostics* **2018**, *8*, 6322–6349.

100. J. H. Lee, K. J. Chen, S. H. Noh, M. A. Garcia, H. Wang, W. Y. Lin, H. Jeong, B. J. Kong, D. B. Stout, J. Cheon, H. R. Tseng, *Angew. Chem. Int. Ed.* **2013**, *52*, 4384–4388.

101. J. Zhu, Z. Xiong, M. Shen, X. Shi, *RSC Adv.* **2015**, *5*, 30286–30296.

102. X. Dong, M. A. Tahir, L. Zhang, C. G. Schafer, *New J. Chem.* **2019**, *43*, 5987–5995.

103. M. Tan, Z. Ye, D. Lindner, S. M. Brady-Kalnay, Z.-R. Lu, *Pharm. Res.* **2014**, *31*, 1469–1476.

104. Q. Wang, J. Li, S. An, Y. Chen, C. Jiang, X. Wang, *Int. J. Nanomed.* **2015**, *10*, 4479–4490.

105. M. Filippi, V. Catanzaro, D. Patrucco, M. Botta, L. Tei, E. Terreno, *J. Controlled Release* **2017**, *248*, 45–52.

106. Q. Liu, S. Chen, J. Chen, J. Du, *Macromolecules* **2015**, *48*, 739–749.

107. Q. Liu, H. Zhu, J. Qin, H. Dong, J. Du, *Biomacromolecules* **2014**, *15*, 1586–1592.

108. J. Ma, H. Dong, H. Zhu, C.-w. Li, Y. Li, D. Shi, *J. Mater. Chem. B* **2016**, *4*, 6094–6102.

109. X. Xie, Y. Chen, Z. Chen, Y. Feng, J. Wang, T. Li, S. Li, X. Qin, C. Wu, C. Zheng, J. Zhu, F. You, Y. Liu, H. Yang, *ACS Appl. Mater. Interfaces* **2019**, *11*, 43865–43878.

110. Y. Li, Y. Qian, T. Liu, G. Zhang, S. Liu, *Biomacromolecules* **2012**, *13*, 3877–3886.

111. L. Zhang, Z. Yang, W. Zhu, Z. Ye, Y. Yu, Z. Xu, J. Ren, P. Li, *ACS Biomater. Sci. Eng.* **2017**, *3*, 1690–1701.

112. R. Liu, S. Liang, C. Jiang, X. Wang, Y. Gong, P. Li, Z. Xu, H. Xu, P. K. Chu, *RSC Adv.* **2015**, *5*, 87512–87520.

113. R. Liu, S. Liang, C. Jiang, L. Zhang, T. Yuan, P. Li, Z. Xu, H. Xu, P. K. Chu, *J. Mater. Chem. B* **2016**, *4*, 1100–1107.

114. S.-M. Lee, Y. Song, B. J. Hong, K. W. MacRenaris, D. J. Mastarone, T. V. O'Halloran, T. J. Meade, S. T. Nguyen, *Angew. Chem. Int. Ed.* **2010**, *49*, 9960–9964.

115. X. Hu, G. Liu, Y. Li, X. Wang, S. Liu, *J. Am. Chem. Soc.* **2015**, *137*, 362–368.

116. S. Tian, G. Liu, X. Wang, G. Zhang, J. Hu, *Polymers* **2016**, *8*, 226/221–226/217.

117. Z. Yang, Y. Dai, L. Shan, Z. Shen, Z. Wang, B. C. Yung, O. Jacobson, Y. Liu, W. Tang, S. Wang, L. Lin, G. Niu, P. Huang, X. Chen, *Nanoscale Horiz.* **2019**, *4*, 426–433.

118. Y. Yu, B. Chi, L. Lin, Z. Yang, Q. He, Z. Xu, C. Yi, J. Wang, *J. Mater. Chem. B* **2018**, *6*, 6391–6398.

119. L. He, L. Feng, L. Cheng, Y. Liu, Z. Li, R. Peng, Y. Li, L. Guo, Z. Liu, *ACS Appl. Mater. Interfaces* **2013**, *5*, 10381–10388.

120. X. Hu, F. Lu, L. Chen, Y. Tang, W. Hu, X. Lu, Y. Ji, Z. Yang, W. Zhang, C. Yin, W. Huang, Q. Fan, *ACS Appl. Mater. Interfaces* **2017**, *9*, 30458–30469.

121. X. Hu, Y. Tang, Y. Hu, F. Lu, X. Lu, Y. Wang, J. Li, Y. Li, Y. Ji, W. Wang, D. Ye, Q. Fan, W. Huang, *Theranostics* **2019**, *9*, 4168–4181.

122. S. Ramanathan, G. Archunan, M. Sivakumar, S. Tamil Selvan, A. L. Fred, S. Kumar, B. Gulyas, P. Padmanabhan, *Int. J. Nanomed.* **2018**, *13*, 5561–5576.

123. E. K. Agyare, K. M. Jaruszewski, G. L. Curran, J. F. Poduslo, J. T. Rosenberg, S. C. Grant, A. K. Paravastu, V. J. Lowe, S. Ramakrishnan, K. K. Kandimalla, *J. Controlled Release* **2014**, *185*, 121–129.

124. A. Puri, K. Loomis, B. Smith, J. H. Lee, A. Yavlovich, E. Heldman, R. Blumenthal, *Crit. Rev. Ther. Drug Carrier Syst.* **2009**, *26*, 523–580.

125. H. Gong, Z. Dong, Y. Liu, S. Yin, L. Cheng, W. Xi, J. Xiang, K. Liu, Y. Li, Z. Liu, *Adv. Funct. Mater.* **2014**, *24*, 6492–6502.

126. J. Feng, Q. Luo, Y. Chen, B. Li, K. Luo, J. Lan, Y. Yu, S. Zhang, *Bioconjugate Chem.* **2018**, *29*, 3402–3410.

127. S. Li, B. Goins, L. Zhang, A. Bao, *Bioconjugate Chem.* **2012**, *23*, 1322–1332.

128. L. Ren, S. Chen, H. Li, Z. Zhang, C. Ye, M. Liu, X. Zhou, *Nanoscale* **2015**, *7*, 12843–12850.

129. P. Skupin-Mrugalska, L. Sobotta, A. Warowicka, B. Wereszczynska, T. Zalewski, P. Gierlich, M. Jarek, G. Nowaczyk, M. Kempka, J. Gapinski, S. Jurga, J. Mielcarek, *J. Inorg. Biochem.* **2018**, *180*, 1–14.

130. C. Zhang, D. Wu, L. Lu, X. Duan, J. Liu, X. Xie, X. Shuai, J. Shen, Z. Cao, *ACS Biomater. Sci. Eng.* **2018**, *4*, 2597–2605.

131. S. Ray, W. Chen, Z. Li, J. I. Zink, Y.-Y. Lin, C.-A. Cheng, *Nanotheranostics* **2019**, *3*, 166–178.

132. J. Wang, Y. Song, M. Zhang, Z. Wu, Y.-J. Xu, J. Lin, D. Ling, Y. Sheng, Y. Lu, Q. Wu, *J. Mater. Chem. B* **2019**, *7*, 2938–2947.

133. V. Bagalkot, M. A. Badgeley, T. Kampfrath, J. A. Deiuliis, S. Rajagopalan, A. Maiseyeu, *J. Controlled Release* **2015**, *217*, 243–255.
134. Q. Chen, Z. Liu, *Adv. Mater.* **2016**, *28*, 10557–10566.
135. Y. Wang, T. Yang, H. Ke, A. Zhu, Y. Wang, J. Wang, J. Shen, G. Liu, C. Chen, Y. Zhao, H. Chen, *Adv. Mater.* **2015**, *27*, 3874–3882.
136. Z. Yang, W. He, H. Zheng, J. Wei, P. Liu, W. Zhu, L. Lin, L. Zhang, C. Yi, Z. Xu, J. Ren, *Biomaterials* **2018**, *161*, 1–10.
137. W. Yang, W. Guo, W. Le, G. Lv, F. Zhang, L. Shi, X. Wang, J. Wang, S. Wang, J. Chang, B. Zhang, *ACS Nano* **2016**, *10*, 10245–10257.
138. L. Chen, X. Zhou, W. Nie, W. Feng, Q. Zhang, W. Wang, Y. Zhang, Z. Chen, P. Huang, C. He, *ACS Appl. Mater. Interfaces* **2017**, *9*, 17786–17798.
139. P. Xu, H. Wu, D. Wang, G. Zhao, F. Li, B. Qiu, Z. Guo, Q. Chen, *Adv. Healthcare Mater.* **2018**, *7*, 1800322.
140. H. Hu, Q. Yang, S. Baroni, H. Yang, S. Aime, N. F. Steinmetz, *Nanoscale* **2019**, *11*, 9760–9768.
141. Q. Zhan, X. Shi, J. Zhou, L. Zhou, S. Wei, *Small* **2019**, *15*, e1803926.
142. T. Knopp, N. Gdaniec, M. Moeddel, *Phys. Med. Biol.* **2017**, *62*, R124–R178.
143. L. M. Bauer, S. F. Situ, M. A. Griswold, A. C. S. Samia, *J. Phys. Chem. Lett.* **2015**, *6*, 2509–2517.
144. H. Arami, E. Teeman, A. Troksa, H. Bradshaw, K. Saatchi, A. Tomitaka, S. S. Gambhir, U. O. Hafeli, D. Liggitt, K. M. Krishnan, *Nanoscale* **2017**, *9*, 18723–18730.
145. X. Y. Zhou, Z. W. Tay, P. Chandrasekharan, E. Y. Yu, D. W. Hensley, R. Orendorff, K. E. Jeffris, D. Mai, B. Zheng, P. W. Goodwill, S. M. Conolly, *Curr. Opin. Chem. Biol.* **2018**, *45*, 131–138.
146. L. M. Bauer, S. F. Situ, M. A. Griswold, A. C. S. Samia, *Nanoscale* **2016**, *8*, 12162–12169.
147. D. Hensley, Z. W. Tay, R. Dhavalikar, B. Zheng, P. Goodwill, C. Rinaldi, S. Conolly, *Phys. Med. Biol.* **2017**, *62*, 3483–3500.
148. W. Tay, P. Chandrasekharan, A. Chiu-Lam, D. W. Hensley, R. Dhavalikar, X. Y. Zhou, E. Y. Yu, P. W. Goodwill, B. Zheng, C. Rinaldi, S. M. Conolly, *ACS Nano* **2018**, *12*, 3699–3713.
149. Y. Du, X. Liu, Q. Liang, X.-J. Liang, J. Tian, *Nano Lett.* **2019**, *19*, 3618–3626.
150. K. O. Jung, H. Jo, J. H. Yu, S. S. Gambhir, G. Pratx, *Biomaterials* **2018**, *177*, 139–148.
151. E. G. Fuller, G. M. Scheutz, A. Jimenez, P. Lewis, S. Savliwala, S. Liu, B. S. Sumerlin, C. Rinaldi, *Int. J. Pharm.* **2019**, *572*, 118796.
152. X. Zhu, J. Li, P. Peng, N. Hosseini Nassab, B. R. Smith, *Nano Lett.* **2019**, *19*, 6725–6733.
153. Z. W. Tay, P. Chandrasekharan, X. Y. Zhou, E. Yu, B. Zheng, S. Conolly, *Theranostics* **2018**, *8*, 3676–3687.
154. F. Wegner, T. M. Buzug, J. Barkhausen, *Theranostics* **2018**, *8*, 3691–3692.
155. B. Zheng, M. P. von See, E. Yu, B. Gunel, K. Lu, T. Vazin, D. V. Schaffer, P. W. Goodwill, S. M. Conolly, *Theranostics* **2016**, *6*, 291–301.
156. Q. Wang, X. Ma, H. Liao, Z. Liang, F. Li, J. Tian, D. Ling, *ACS Nano* **2020**, *14*, 2053–2062.
157. L. L. Israel, A. Galstyan, E. Holler, J. Y. Ljubimova, *J. Controlled Release* **2020**, *320*, 45–62.

13

Luminescence Imaging of Cancer Cells

Jorge H. S. K. Monteiro,[1] *Josiane A. Sobrinho,*[2]
and Ana de Bettencourt-Dias[2]

[1]Department of Chemistry, Humboldt State University, Arcata, CA 95521, USA
<jorge.monteiro@humboldt.edu>

[2]Department of Chemistry, University of Nevada, Reno,
Reno, NV 89557, USA
<abd@unr.edu>

Abstract: Bioimaging *in vivo* and *in vitro* of cells and animals enables the scientific community to study physiological processes, toxicity of compounds, and mechanisms of cell death. All the insights gained from these studies enable the development of better therapeutics. Bioimaging agents range from emissive organic molecules, to polymers, to systems containing metals. In

---

this chapter, we will highlight recent advancements in the development and use of metal-containing systems, molecular, polymeric and nanostructures, for bioimaging of cancer cells and tumors in animals.

Keywords: cancer cell imaging · cytotoxicity · lanthanide-based luminophores · luminescent sensors · nanoparticles · transition metal-based luminophores · tumor imaging · theranostics

1. LUMINESCENCE IMAGING

In vivo luminescence cell and animal imaging enables gathering of real-time on physiological processes, increasing our understanding of cell growth and cell metabolism, and cell death and the underlying mechanisms [1]. Many dyes and fluorescent proteins are regularly used for bioimaging [2, 3]. Each dye has its own chemical and photophysical properties, which affect their efficiency to target and image different cell areas, or to sense specific products of cellular metabolism. The use of common dyes is limited in an anaerobic environment, which limits their usefulness to image frequently hypoxic tumor environments, as fluorescent proteins require oxygen to generate the fluorescent chromophore [4, 5]. Other fluorophores cannot be used for deep tissue imaging, due to emission and absorption at wavelength ranges where biological tissue is not transparent to exciting and emitting photons [6], as highlighted in Figure 1.

The use of metal-based luminophores has several advantages. They can be easily functionalized to tailor chemical and photophysical properties, they usually display high emission quantum yields and long luminescence lifetimes, which
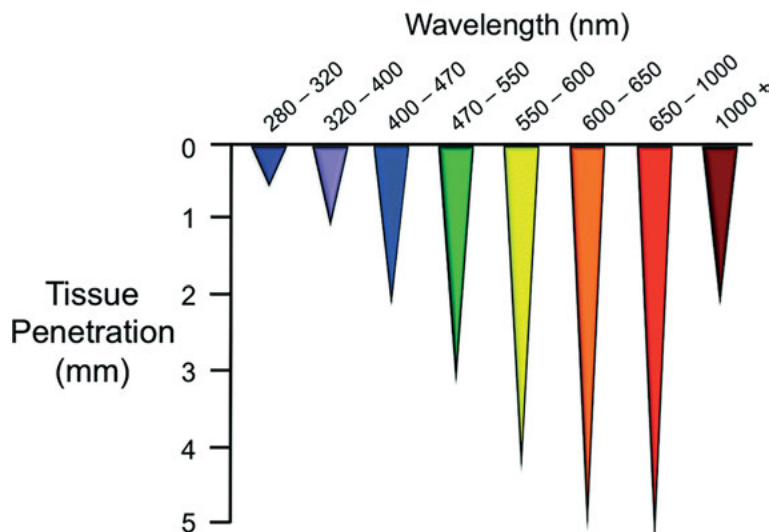
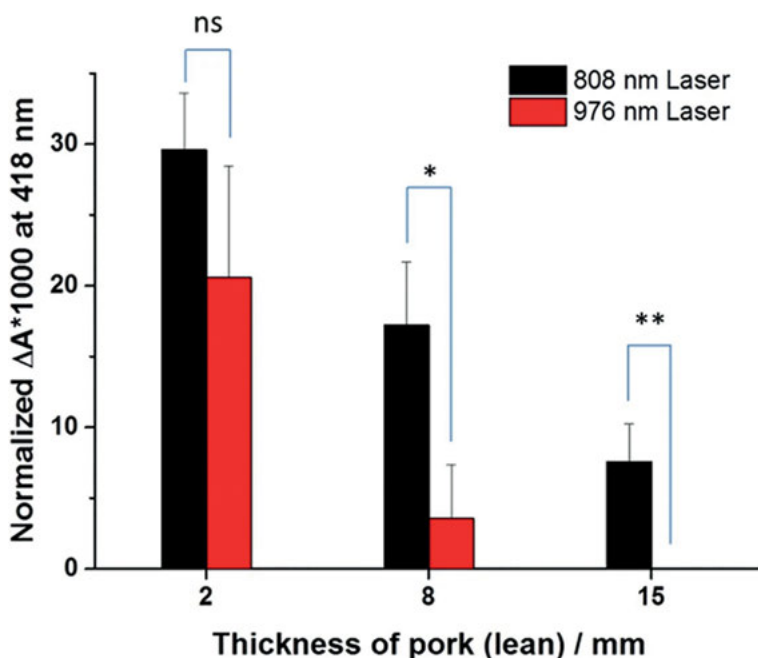**Figure 1.** Tissue penetration as a function of the excitation wavelength. Reproduced with permission from [205], copyright 2016, The Royal Society of Chemistry.

enable time-delayed detection and thus a higher signal-to-noise ratio once background auto-fluorescence decays, and large Stokes shifts, which enable effective discrimination between excitation and emission wavelengths and reduce self-quenching. They are also bio-, photo-, and thermally stable and are, as small molecules, unlikely to disrupt cellular processes. In addition, ligands bound to the metal can be functionalized for specific applications, such as targeting biomolecules. Since different metal complexes emit in different regions of the electromagnetic spectrum, they can be used for multiplex imaging [7].

Several of the systems known target specific small molecules, and are thus used as specific sensors for biologically relevant chemical species such as NO or CO [8]. As will be reviewed in this chapter, luminophores are frequently deployed as therapeutic agents as well [9]. Recent developments in this area have given rise to the new designation of theranostics, a field which combines **ther**apy, for example through the cytotoxicity of the dye, and diag**nostics**, which is accomplished through bioimaging [10, 11]. Several of the newly isolated metal-based systems for theranostics have the added advantage of better cancer-specific cytotoxicity over currently used platinum cancer drugs, and could help sidestep known cancer resistance to cisplatin [12, 13].

The extraordinary importance of this topic has resulted in several recent reviews [7, 9, 14–16]. To complement those efforts, in this chapter we highlight selected recent examples of metal-based luminescent systems that have been assessed for application in imaging, therapy or sensing.

2. CELLULAR IMAGING WITH NANOSTRUCTURES

2.1. Gold-Based Nanoparticles and Nanoclusters

Gold-based nanostructures are promising for biomedical applications due to their high biocompatibility and chemical inertness. Additionally, the ease tuning of their electronic and optical features through modulation of size, shape, surface chemistry, composition, and aggregation state, has led to a plethora of systems with distinctive photophysical and chemical properties, thus making these systems powerful and versatile platforms for imaging.

In gold nanoparticles (AuNPs), light-matter interaction results in a collective coherent oscillation of free electrons in the conduction band, creating an enhanced electric field localized on the NP surface, called localized surface plasmon resonance (LSPR). This phenomenon, which can be modulated by particle size, shape, and composition is responsible for the large absorption and scattering cross-sections [17, 18]. LSPR has driven the development of AuNP-based theranostic materials with fluorescence imaging capability, either in conjugate systems due to the plasmon-enhanced fluorescence effect that allows the incorporation of weak quantum emitters [19], or by exploring the fluorescent and therapeutic properties of AuNPs themselves, which are largely known for their photothermal effect and application in photothermal therapy (PTT) [20].

In AuNPs, the conventional one-photon excitation is an inefficient process mostly due to the large density of electronic states [21]. On the other hand, AuNPs show outstanding two-photon absorption (TPA) and two-photon excited luminescence (TPEL) properties [17]. TPA and TPEL use low energy excitation wavelengths that lead to reduced photodamage and deeper tissue penetration (Figure 1). Along with the non-linearity of the process, this enables three-dimensional (3D) imaging [22]. Excitation energies resonant with LSPR strongly enhance both incident and emitted light, and thus two-photon absorption cross-sections (σ_{TPA}) significantly higher than other luminophores [23], without the blinking or photobleaching seen in the latter [17].

Owing to their easily tunable LSPR, gold nanorods (AuNRs) are the most studied for TPEL imaging. AuNRs coated with conformation-constrained peptides to obtain a more rigid structure showed improved target ability for TPEL imaging and PTT in A549 cells [24]. TPEL-guided photothermal chemotherapy of osteosarcoma cells and 3D tumor models was achieved through the coating of AuNRs with a folate-targeted polysaccharide; the system worked as a carrier for the anticancer drug nutlin-3, showing near-infrared (NIR)-triggered and pH-sensitive drug release in addition to efficient photothermal action [25]. Hierarchical nanoplatforms, composed of mesoporous silica-coated AuNRs, indocyanine green, and 5-fluorouracil (5-FU) were synthesized for *in vivo* multimodal imaging, as well as trimodal synergistic therapy such as PTT, photodynamic therapy (PDT), and chemotherapy in A375 cancer cells and tumor-bearing mice. Gold nanobipyramids [26] and nanostars [27] displayed enhanced photothermal ablation of cancers *in vivo* and *in vitro*. Hollow gold nanospheres coated with a heterobifunctional polymer showed a larger σ_{TPA} than AuNRs (1.02×10^6 GM at 820 nm) and efficient photothermal conversion for TPEL-guided photothermal therapy in HeLa cells [28].

Despite all the advantages, the large size and non-biodegradable nature of AuNRs constitute significant drawbacks for *in vivo* applications. Their high surface energy favors serum protein adsorption, which prevents control over organ distribution, excretion pathways, and biocompatibility. Smaller NPs with *in vivo* hydrodynamic diameters below the threshold of kidney filtration (< 5.5 nm) to allow for efficient renal clearance, such as Au nanoclusters (AuNCs) are thus preferred [29]. AuNCs, considered a link between discrete metal-ligand complexes and metallic NPs, are composed of ligand-stabilized gold cores containing a few to hundreds of atoms and have optical properties considerably different from the conventional plasmonic NPs [30]. Due to the smaller size, usually < 3 nm, a strong quantum confinement effect takes place, breaking the continuous band structure of AuNPs into discrete energy states. This shuts down the plasmonic properties, and gives the NCs molecule-like optical properties, with single HOMO-LUMO electronic transitions [31, 32]. Although their emission efficiency is higher than what is observed for AuNPs, they are still not competitive when compared to organic dyes and quantum dots (QDs) [33]. The high susceptibility of their intrinsic fluorescence to other substances [34] is another drawback, especially if applied to the imaging of chemically complex environments like living cells and tissues. Their optical properties are highly dependent

on structure, thus requiring stable ligand-protected NCs to ensure structural integrity [35].

Several synthetic strategies have been developed to improve structural stability and optical properties of AuNCs through selection of appropriate ligands [36]. The encapsulation of thiolate monolayer-coated AuNCs [37–42], or the one-pot synthesis of AuNC-coated using several molecules and macromolecules as template [43–46] have yielded AuNCs with superior capability for the imaging of cancer cells. Plant protein-stabilized AuNCs coated with red blood cell membranes yielded NPs for imaging of MCF-7 cells and tumor bearing-mice with excellent biocompatibility, tumor enrichment ability and prolonged blood circulating life [47]. The controlled biological assembly of AuNCs conjugated with streptavidin and biotin-specific binding motifs yielded materials with good biocompatibility, amplified emission signals, and long emission lifetimes. Large σ_{TPA} ($\sim 2.27 \times 10^5$ GM at ~770 nm) were obtained, allowing for imaging of MCF-7 breast cancer cells through one- and two-photon excitation and fluorescence lifetime imaging [48]. Liu and collaborators synthesized a water-soluble and photostable atomic-precision AuNC with 25 gold atoms and 18 peptide ligands in a cage-like structure as an efficient NIR-II fluorophore under 808 nm excitation. After intravenous injection in mice, *in vivo* high-resolution images of tumor metastasis and neovascularization of damaged brain tissue after a stroke were obtained [49].

Accurate targeted cancer imaging may be achieved through the *in situ* biosynthesis of ligand-protected AuNCs [50]. Wang and collaborators synthesized luminescent AuNC-DNA complexes through the treatment of cells or tumors with an Au^{III} precursor and DNA from a tumor suppressor. They imaged the cancer cells in real-time, and the inhibition of A549 and HeLa cell proliferation and tumor growth in mice were observed without significant side effects in healthy organs and tissues [51].

Sensing of species of biological interest is of particular relevance in the initial assessment of pathological conditions and may be accomplished by monitoring analyte-induced changes in the AuNC emission. Intracellular sensing of several analytes has been reported [38, 39, 43, 44, 52–57]. Real-time monitoring of viscosity changes inside A549 cancer cells was also demonstrated [58].

Ligand-coated AuNCs have been used as nanocarriers for the targeted delivery of chemotherapy drugs [45] or photosensitizers (PSs) [59]. Their ability to generate singlet oxygen ($^1O_2$) [35, 60] and other highly reactive oxygen species (hROS) [61, 62] showed promise for theranostic materials. Coupling of an antimicrobial peptide (AMP) to conjugated polymer (CP)-coated AuNCs yielded an image-guided multitherapeutic platform. The CP displayed high photothermal conversion efficiency upon NIR-light irradiation for PTT, while the AMP provided a complementary antimicrobial treatment [63].

The advances in the AuNC chemistry have paved the way for the development of other metal nanoclusters for bioimaging, such as Cu [64], Mo [65], Ru [66], Rh [67], Pd [68], Ag [69], Ir [70], and Pt [71].

2.2.   Transition Metal-Based Nanoparticles

Quantum dots, one of the most versatile classes of semiconductor-based lumino-phores, are classified as quasi-zero-dimensional semiconducting nanocrystals generally composed of groups II–VI, III–V, and IV–VI of the periodic table [72, 73]. They display broad excitation and narrow emission bands with large Stokes shifts, which are essential for efficient multiplexing imaging [74]. They possess superior optical properties when compared to their organic counterparts, such as high brightness, significant resistance to photobleaching, and long fluorescence lifetime. In addition, they are easily conjugated to different biomarkers while retaining or increasing emission efficiency [75]. Their luminescence arises from the recombination of electron-hole pairs, or excitons, generated upon excitation of electrons from the valence to the conduction bands. Their size, typically 2–10 nm, results in a strong quantum confinement effect, that leads to tunable emission wavelength depending on core size, composition and surface chemistry [76].

Due to their reduced size, the large surface-to-volume ratios and irregular surfaces result in a large number of defects that lead to luminescence quenching, which can be reduced by passivating the QD surface [77–79] with organic layers or inorganic core@shell architectures [80, 81]. Coating strategies can reduce leaching of heavy atoms in Cd-based QDs that, although toxic both *in vitro* and *in vivo*, still represent the vast majority of publications [82, 83]. Further environmental concerns arise in the synthesis of Cd-based QDs, as hazardous organometallic routes at high temperatures are generally involved [84]. Thus, ligand-assisted aqueous routes with reduced toxicity have been described [85–88]. A biosynthetic approach for the synthesis of Cd-based QDs in *E. coli* was reported by Tian and coworkers. The resulting biocompatible QDs were success-fully used to image MDA-MB-231 cells and 4T1 tumor-bearing nude mice [89].

Sarkar and coworkers [90] demonstrated that the emission range could be tuned from the visible up to the NIR-II (950–2000 nm) with varying x in $Hg_xCd_{1-x}Se$ alloy QDs while maintaining a small and equal size, allowing direct comparison of molecular labeling performance across a broad range of wavelengths. Coating with click-functional multidentate polymers yielded QDs with high quantum yield (QY) in the NIR-II (14−33 %), and long-term stability in aqueous media during continuous excitation, without inducing significant toxicity in living cells even at high concentrations. Four different compositions conjugated to growth factors, nucleic acids, and antibodies, were used to image human growth factor in the breast cancer cell MDA-MB-231, RNA in HeLa cells and to label proteins in mouse adipose tissues [90].

PbS QDs are among the most explored NIR emitters, due to QYs that can reach 60 % [91–93]. Qiu and coworkers [94] reported the synthesis of polyethyl-ene glycol (PEG)-coated PbS/CdS/ZnS QDs showing upconversion (UC) lumi-nescence through a phonon-assisted single-photon process, even when excited by a 980 nm laser at low power. The QDs exhibited high NIR emission QYs of 4.6 %, and improved water solubility and biocompatibility, enabling the bioimag-ing of sarcoma 180-bearing nude mice with few heat effects [94].

Due to the Cd^{2+} toxicity and its leaching even in the presence of passivating layers [83], other materials with lower toxicity, such as zinc [84, 95] and Mn^{2+}-doped zinc [96–98] chalcogenides have been pursued for fluorescence imaging of cancer cells, while Ag chalcogenide QDs were demonstrated as a low toxicity alternative to PbS NIR-emitting QDs [99, 100]. Zhang and coworkers [101] developed Ag_2Te QDs coated with poly(lactic-*co*-glycolic acid) and encapsulated within 4T1 cancer cell membranes as efficient NIR-II fluorophores. The cell membrane-camouflaged Ag_2Te QDs showed stable bright fluorescence at 1300 nm, prolonged blood circulation time, good biocompatibility, and homotypic targeting ability for enhanced *in vivo* tumor imaging [101].

In recent years, ternary I–III–VII-based semiconductor QDs like $CuInS_2$ or $AgInS_2$ and their I–II–III–VII alloys with ZnS have gained high interest as alternatives to binary QDs for cancer bioimaging [102–106]. In addition to low toxicity, their optical properties can be easily tuned from the visible to the NIR by varying size, composition, and surface coating [107]. ZnAgInSe/ZnS QDs coated with α-cyclodextrin-doxorubicin (DOX), and folic acid were applied to the multi-color fluorescent imaging of H22 cells. The nanoprobe showed prolonged circulation time in blood, effective accumulation at the tumor site, enhanced internalization by tumor cells, and efficient pH and H_2O_2 dual-sensitive DOX-release at malignancy sites *in vivo* [108].

Two-dimensional (2D) layered nanomaterials have emerged as a new generation of photoluminescent materials for bioimaging [109, 110]. Transition metal dichalcogenides (TMDs) are an important class of 2D materials with the general formula MX_2[111]. The exfoliation of TMD into few layers leads to an indirect-to-direct bandgap transition that results in strong luminescence [112], which can be improved by reducing the lateral dimensions to < 100 nm, when strong quantum confinement and edge effects take place [113]. These 2D-QDs have been explored for bioimaging [114] and biosensing of molecules and macromolecules of biological interest [115, 116] in cancer cells, and as drug nanocarriers [117] and photothermal agents [118] for theranostics.

Sweet and coworkers [119] reported the synthesis of MoS_2 QDs modified with lipoic acid-terminated PEG and conjugated with antibodies for the TPEL imaging of targeted prostate cancer LnCaP cells. The QDs showed high σ_{TPA} (58,960 GM) and high brightness (47,000 GM) upon 1064 nm excitation, good photostability, and biocompatibility [119]. Chen and coworkers [120] developed a platform for cellular imaging, *in vivo* imaging, biosensing, and drug delivery based on monolayer-MoS_2 nanodots with the ability of surface adsorbing thiolated molecules. A turn-on luminescent probe was designed by using 6-mercaptopurine (6-MP) as an efficient quencher of the MoS_2 emission; in the presence of glutathione (GSH), 6-MP is efficiently released, thereby switching on MoS_2 fluorescence and allowing for the sensitive and selective detection of GSH in erythrocytes and live HeLa cells. Similarly, thiolated doxorubicin (DOX-SH)-loaded M-MoS_2 nanodots (NDs) worked as GSH-responsive nanocarriers for DOX-SH delivery in HeLa cells and mice with improved cytotoxicity [120].

MXenes, another promising class of 2D-based materials, consist of transition metal carbides, nitrides, and carbonitriles with the general formula $M_{n+1}Xn$

(n = 1–3), where (n + 1) layers of an early transition metal M are connected by n layers of X, carbon or nitrogen, in an $[MX]_nM$ manner [121]. Since the initial discovery of Ti_3C_2 in 2011, MXenes have received growing attention in the biomedical area [122, 123]. They display a large active and hydrophilic surface that eases functionalization, excellent biocompatibility, strong light absorption in the NIR region that can be used for TPA and PTT, and ferromagnetism suitable for magnetic resonance imaging. Nano-sized MXenes display luminescence, mainly assigned to quantum confinement and vacancy defects, that is explored for bioimaging [124].

Their use in cell luminescence imaging was first reported in 2017 when Xue and coworkers synthesized monolayered Ti_3C_2 MXene quantum dots (MQDs) exhibiting excitation-dependent photoluminescence with QY ~10 % for the imaging of RAW264.7 cells [125]. Since then, Ti_3C_2 MQDs have been reported as sensors to quantitatively monitor the intracellular pH in MCF-7 cells [126], and for the detection of intracellular GSH in HeLa cells [127]. Yang and coworkers [128] synthesized biodegradable, biocompatible, and photostable Nb_2C MQDs for fluorescence imaging of NIH 3T3 cells. To further demonstrate Nb_2C MQDs as fluorescent probes, poly(vinyl alcohol)/Nb_2C MQDs composite hydrogels in different shapes were subcutaneously implanted on the backs of shaved mice, and the fluorescence imaging displayed their exact location with intact shapes and clear boundaries between the hydrogels and surrounding tissues [128].

Although the semiconductor-based luminescent nanoparticles, as discussed above, represent the largest segment of TM-based nanomaterials for bioimaging, metal-centered emitting materials, with particular focus on the TM-doped oxides, have been receiving growing attention. Persistent luminescent nanoparticles (PLNPs), also-called long-lasting afterglow NPs, luminesce for several minutes to even days after ceasing excitation, and can be reactivated under appropriate excitation light [129–131]. This enables the long-term, real-time assessment of their *in vivo* biodistribution [132–138]. Bioimaging, biosensing, and cell tracking
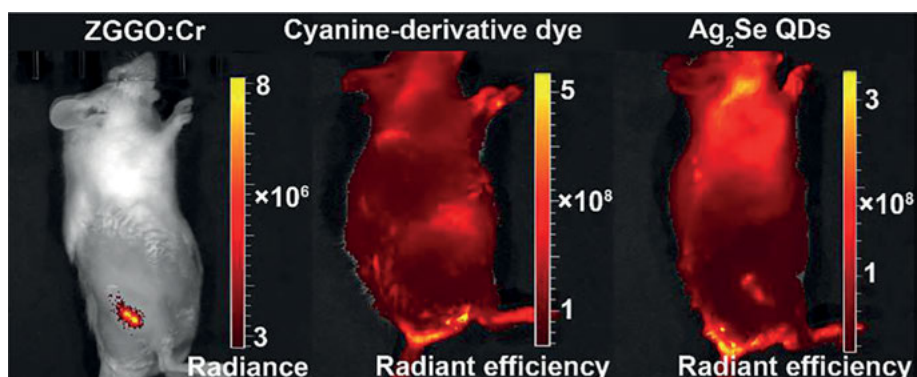
Figure 2. Comparison of optical *in vivo* imaging using PLNPs, ZGGO:Cr (**left**) or conventional fluorescent probes, cyanine or QDs (**middle** and **right**). Reproduced with permission from [136], copyright 2017, American Chemical Society.

thus happen without interference of the short-lived autofluorescence and light scattering (Figure 2), improving signal-to-noise ratio and sensitivity, with deep tissue penetration, and low photodamage [139].

In general, two main elements are involved in persistent luminescence, namely the emitters, which usually consist of transition metal (TM) ions or lanthanide (Ln) ions doped in a host material, and traps, which are responsible for the energy storage. After ceasing excitation, the energy stored in the traps gradually returns to the emitting ion and is then released through photonic emission.

Most work has focused on chromium-doped zinc gallates ($ZnGa_2O_4:Cr^{3+}$, ZGO) or gallogermanates ($Zn_{1+x}Ga_{2-2x}Ge_xO_4:Cr^{3+}$). Other host lattices such as $Gd_3Ga_5O_{12}$ [140], $LaAlO_3$ [132], $GdAlO_3$ [141], $LiGa_5O_8$ [135], and emitting ions such as Mn^{2+} [142] have been reported. They have been used for the luminescence-guided resection of tumors [143], *in vivo* targeted imaging of cancers [144], biosensing of chemical species *in vitro* and *in vivo* [145], and as nanocarriers for chemotherapeutics [146] and photosensitizers [147]. $ZGO:Cr^{3+}$ PLNPs and IR780 PS were encapsulated by a temperature-responsive "wax seal" shell and used for the photothermal-triggered persistent PDT in tumor-bearing mice. Upon 808 nm laser irradiation, the embedded IR780 generates heat that provides tumor hyperthermia treatment, and melts the shell, turning on the photodynamic effect. PLNPs pre-excited with a white light-emitting diode continually generated $^1O_2$ for 25 min after excitation ceased through the persistent energy transfer from the NPs to the IR780, thus providing localized and outstanding persistent therapeutic effects [148].

Co-doping of NP with metallic ions provides additional energy states for trapping electrons, allowing the tuning of the afterglow lifetime and intensity [130, 131, 149–152]. Co-doped PLNPs with improved properties were applied to the real-time tracking of cancer cells [153], cell-mimicking [154] and bacterial biofilm-coated [155] chemotherapeutic nanocarriers, and X-ray excited nanocarriers for PSs [156]. Mesoporous silica-coated $ZGO:Cr^{3+},Sn^{4+}$ was used as a nanocarrier for the anticancer drug afatinib. The NIR PLNPs showed persistent luminescence lifetime lengthened by several hours after Sn^{4+} doping. Further, coating with the aptamer MAGE-A3 increased the accumulation in CL1–5 lung cancer metastatic tumor cells via active transport. The NIR persistent luminescence signal was repeatedly observed throughout the intratracheal and intravenous treatment of tumors in mice after reactivation with a UV flashlight for 120 s [157].

3. TRANSITION METAL COMPLEXES AS IMAGING AND THERAPY AGENTS

Imaging agents based on TMs have several advantages, namely the ability of tuning properties through targeted functionalization. Single molecule imaging agents are more easily isolated than NPs, which frequently suffer from crystallinity and aggregation problems. Earth-abundant TMs provide safer and less expensive alternatives to NPs based on Cd or Au. Heavier TMs are investigated as luminophores as well, as long lifetimes of the emissive metal-to-ligand charge-
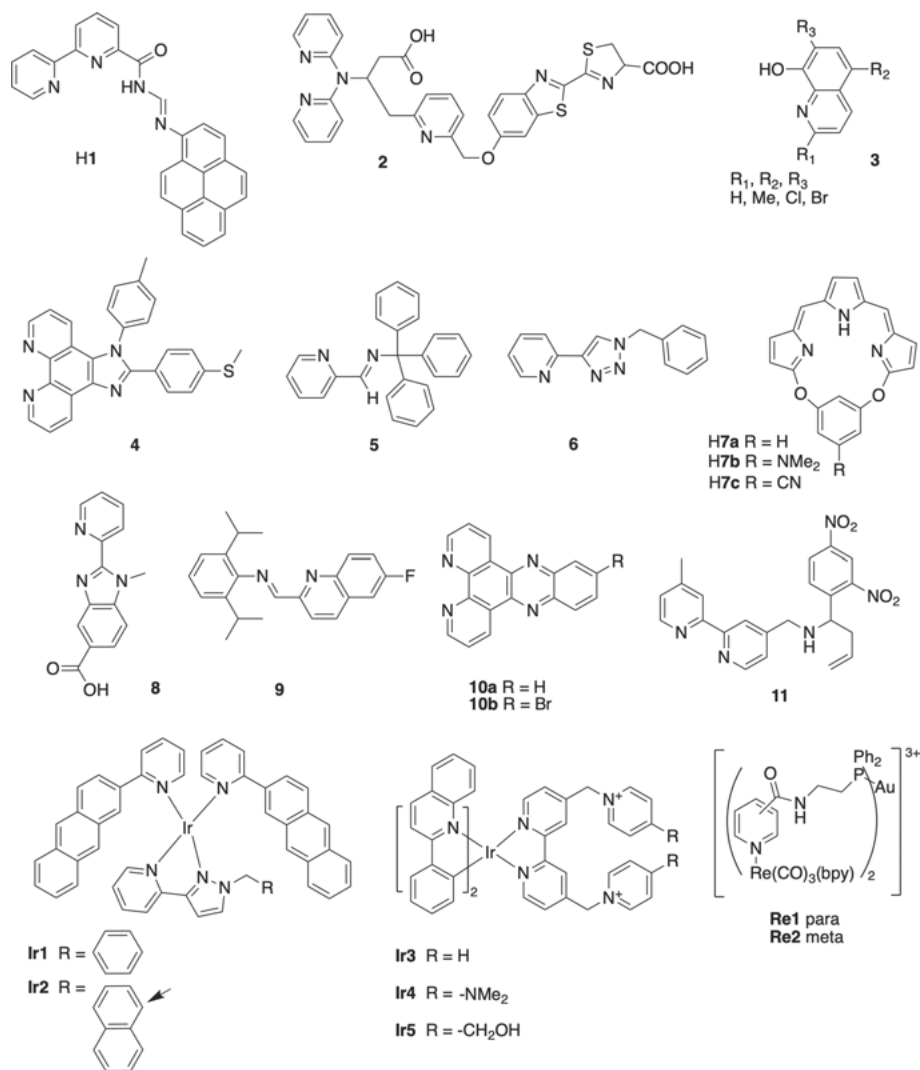
Figure 3. Compounds mentioned in Section 3. Arrow indicates atom at which substitution occurs.

transfer (MLCT) or ligand-to-metal charge transfer (LMCT) excited states enable time-gated detection, with increased signal-to-noise ratio.

Hossain and coworkers [158] described a pyrene-appended bipyridine hydrazone H1 (Figure 3) that showed ability to penetrate the membrane of Vero cells with negligible cytotoxicity. Upon exposure to Cu^{2+} in the cellular environment, the resulting complex shows turn-on green luminescence. *In vitro*, the ligand showed selectivity towards Cu^{2+} in the presence of competing metal ions. A bioluminescent probe based on the luciferin-luciferase system to sense Fe^{2+} was

described by Feng and coworkers [159]. These authors postulate that, in the presence of Fe^{2+}, compound **2** (Figure 3) generates an oxidized species that luminesces in the presence of luciferase. The turn-on luminescence was observed in ES-2-Fluc cells and in mice, with intensities proportional to the amount of exogenous Fe^{2+}.

Hetero-trimetallic complexes **Re1** and **Re2** (Figure 3) with red emissive Re^I-based MLCT states were described by Luengo and coworkers [160]. Confocal microscopy showed accumulation of the complexes at the edge of the inner cell membrane and in areas within the nucleus of A549 cells. The displayed cytotoxicity is attributed to targeting of DNA by the bioactive Au^I-containing fragment with values of half maximal inhibitory concentration (IC_{50}) of 42.44 and 36.09 μM for **Re1** and **Re2**, respectively.

Meng and coworkers [161] isolated 14 Ir^{III} complexes with an 8-oxychinolin-base ligand **3** (Figure 3), where R_1, R_2, and R_3 have different permutations of the substituents H, Me, Cl or Br. These red-emitters were used to image HeLa, SK-OV-3/DDP and HL-7702 cells. Confocal microscopy showed that they localize in the mitochondrial inner membrane inducing mitochondrial disfunction, which results in cell apoptosis with selected efficiencies higher than cisplatin.

Mitochondrial imaging in living cells was pursued as well by Liu and coworkers [162], who focused on the complexes **Ir1** and **Ir2** (Figure 3) with phenyl-benzo[g]quinoline ligands as NIR emitters. Confocal phosphorescence microscopy showed that both complexes successfully transfect the mitochondrial membrane of HeLa cells. Both emit at ~700 nm with efficiencies of 0.62 and 0.85, respectively, are photostable and show low phototoxicity at the concentrations needed for living cell imaging.

To allow for fluorescence sensing of periodate in the cellular environment, Wang and coworkers [163] synthesized and isolated a bis-bipyridine Ir^{III} complex, with the phenanthroline-based ligand **4** (Figure 3). The complex, which displayed very low cytotoxicity with an IC_{50} higher than the dosage used for imaging, displayed turn-off emission, that enabled detecting different concentrations of periodate in HeLa cells down to 0.077 μM.

Huang and coworkers [164] isolated complexes **Ir3** and **Ir4** (Figure 3), which, upon exposure to glutathione, generate the emissive **Ir5**. The latter is also an efficient $^1O_2$ generator. Incubation of **Ir3** with HeLa, A549 and HepG3 cancer and 3T3-L1 and HL-7702 healthy cells led to increased complex luminescence within the cancer cells and increased cytotoxicity towards these as well, which the authors attributed to the GSH-rich environment within these cells.

The blue MLCT emission of the half-sandwich cyclopentadienyl complex of Ir^{III} with the iminopyridine-based ligand **5** (Figure 3) was detected through confocal microscopy within A549 lung cancer cells [165]. Li and coworkers demonstrated that the complex, which accumulates in the nucleus, causes nuclear morphological changes which result in cell death, with an IC_{50} of 5.1 μM, lower than the value of 21.3 μM observed for cisplatin.

Another example of a red luminescent cyclopentadienyl Ir^{III} complex has ligand **9** (Figure 3) bound to the metal ion [166]. The complex showed cytotoxicity towards HeLa and A549 cancer cells, with IC_{50} of 1.5 and 1.2 μM, respectively,

and accumulation in the lysosomes. The authors observed lysosomal damage with release of cathepsin B.

Li and coworkers [165] isolated the half-sandwich cyclopentadienyl Ir[III] complex with ligand **8** (Figure 3), as described above. They further demonstrated that a related blue-emitting benzenyl Ru[II] complex accumulates within A549 lung cancer cells in the lysosome and, in higher quantities, in the mitochondria and determined an IC_{50} of 29.2 μM.

To increase the biocompatibility of imaging agents, Zhao and coworkers [167] embedded a $[Ru(bpy)_2\mathbf{8}]^{2+}$ complex (bpy = bipyridine, **8** Figure 3) with bovine serum albumin in a hydrogel, yielding a water-soluble red and green emitting material that could be followed *in vitro* by confocal microscopy. The hydrogel-based system was readily uptaken by normal liver LO2 cells and Hep-G2 liver cancer cells and displayed an IC_{50} of 15.6 μg/mL towards the latter, and an about 8-fold lower cytotoxicity (IC_{50} = 106.2 mg/mL) towards the former. The same authors isolated the analogous Os[II] complex with ligand **8** (Figure 3) [168]. The complex emits at 700 to 850 nm, and was readily uptaken into A549 cells, where it accumulates in the lysosomes and displays photocytotoxicity with an IC_{50} of 31.7 μM, while the Ru[II] complex shows low photocytotoxicity with IC_{50} = 442 μM upon irradiation with 633 nm light.

Omar and coworkers [169] isolated a red-emitting (QY ~40 %) homoleptic Ru[II] complex with ligand **6** (Figure 3). Confocal microscopy showed that it accumulates in the lysosome and endosome of HeLa and EJ bladder carcinoma cells, with low dark and light toxicity.

Yu and coworkers isolated $[Ru(phen)_2\mathbf{10}]^{2+}$ (phen = phenanthroline, **10** = **10a**, **10b** Figure 3), which were encapsulated into oligonucleotides [170]. The resulting polymeric materials had improved emission with respect to the free complexes and easily penetrated the cell membrane of MDA-MB-231 tumor cells xenografted in zebrafish. Their luminescence was observed *in vivo*, highlighting the location of the xenografts (Figure 4A).

Liu and coworkers [171] isolated the weakly luminescent complex $[Ru(bpy)_2\mathbf{11}]^{2+}$ (**11** Figure 3) which, in the presence of formaldehyde in acidic environment, undergoes rearrangement; hydrolysis of **11** generates a luminescent complex, which is a turn-on sensor for formaldehyde. The compound penetrated the membrane of HeLa cells, and its emission intensity was proportional to the concentration of cell lysosomal formaldehyde and to tumor-derived endogenous formaldehyde in naked mice (Figure 4B).

Yao and coworkers [172] incorporated the new Pd[II] complexes with ligands **7** (Figure 3) into silica NPs, to prevent oxidation in the cellular environment and incubated them with HeLa cells. NIR emission showed their localization in the lysosomes. The silica-supported complex with **7b** displayed pH-dependent emission in HeLa cells, making them potential intracellular pH sensors. Injection of the silica-supported complexes with **7a** and **7c** into 4T1 tumor-bearing mice showed accumulation at the tumor site, enabling distinction between diseased and healthy tissue.

Lin and coworkers [173] isolated a new Schiff-base complex **Pt1** (Figure 3), which displays aggregation-induced phosphorescence. Upon co-polymerization
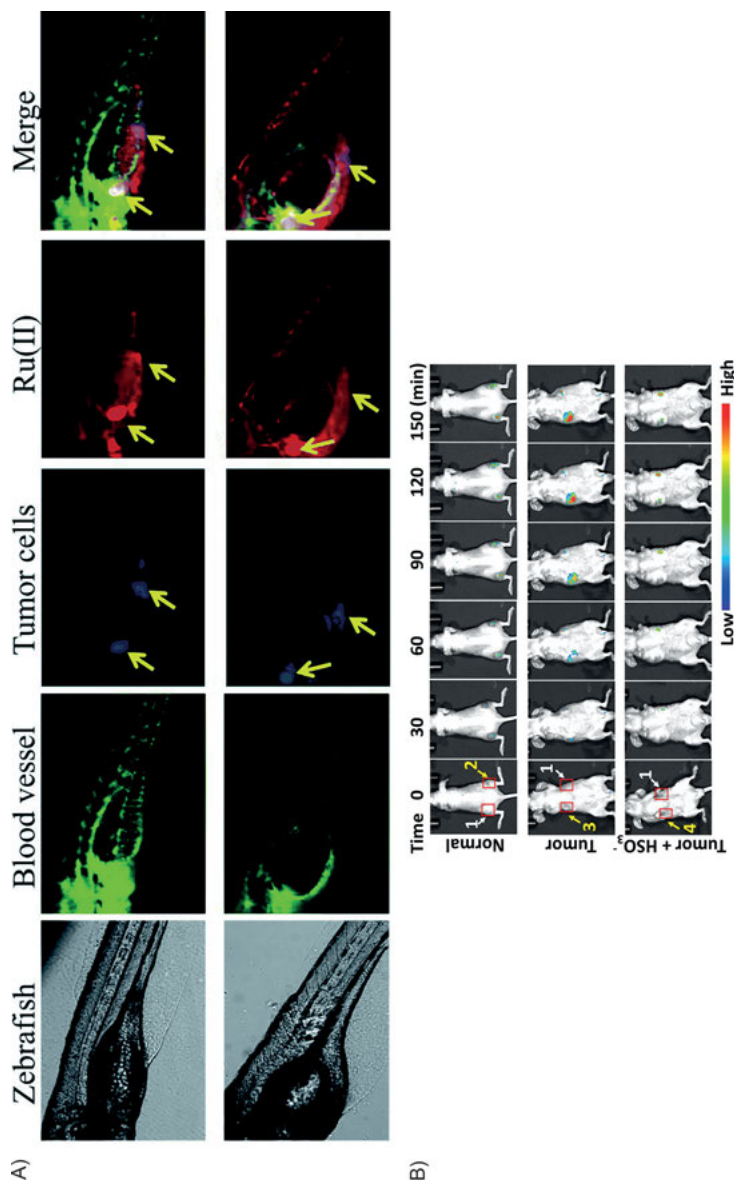
Figure 4. (**A**) Imaging of MDA-MB-231 tumors in zebrafish highlighted by [Ru(phen)$_2$**10a**]$^{2+}$ (top row) and [Ru(phen)$_2$**10b**]$^{2+}$ (bottom row). Reproduced with permission from [170]; copyright 2018, The Royal Society of Chemistry. (**B**) Time-dependent imaging of tumor-derived endogenous formaldehyde in naked live mice. Highlighted area 1 corresponds to a saline injection followed by injection of [Ru(bpy)$_2$**11**]$^{2+}$. Area 2 corresponds to an injection of formaldehyde scavenging NaHSO$_3$ followed by injection of the complex. Area 3 shows the tumor into which the complex was directly injected. Area 4 shows a tumor pre-treated with NaHSO$_3$ and then injected with the complex. Reproduced with permission from [171]; copyright 2019, American Chemical Society.
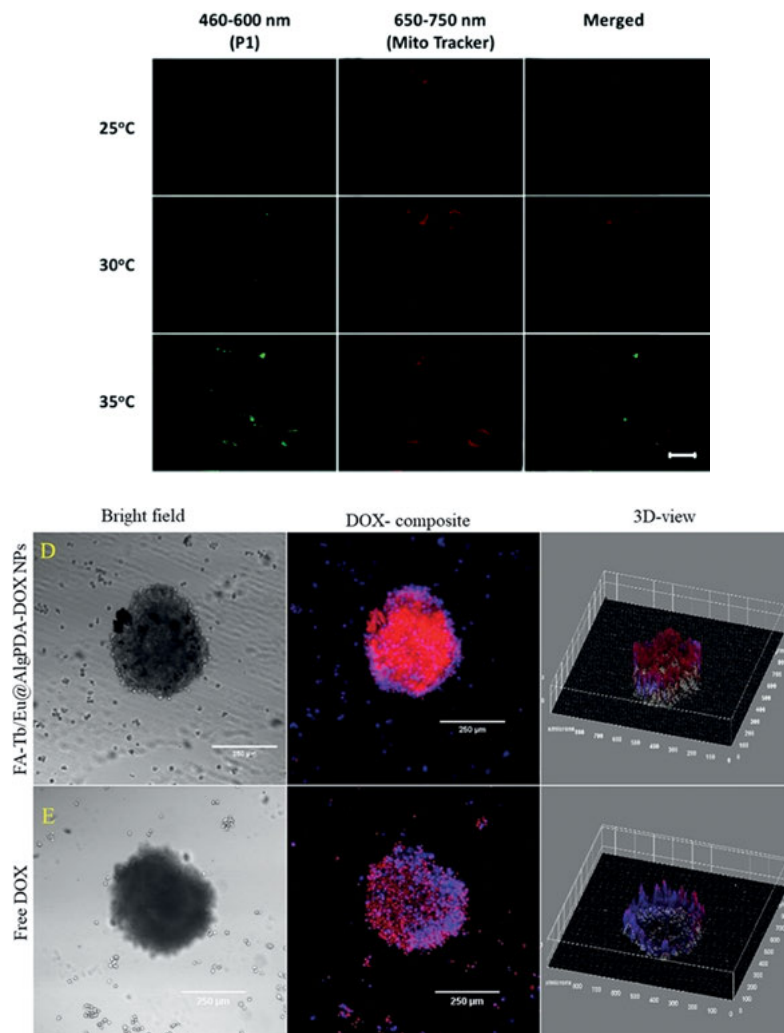
Figure 5. (**A**) Confocal laser scanning microscopy images of HepG2 cells labeled with **Pt1** (left column) and Mito Tracker Deep Red (middle column) at 25 °C, 30 °C and 35 °C. Scale bar is 15 μm. Reproduced with permission from [173]; copyright 2019, The Royal Society of Chemistry. (**B**) Luminescence imaging of LnNPs functionalized with folic acid/AlgPDA/DOX (first row), and free DOX (second row) in HeLa cells. First, second, and third columns correspond to bright field channel, luminescence channel, and 3D reconstruction, respectively. Reproduced with permission from [187]; copyright 2019, American Chemical Society.

with the thermosensitive hydrophilic *N*-isopropylacrylamide hydrogel, a thermosensitive probe was obtained. Incubation with HepG2 cells showed that **Pt1** localizes in the mitochondria and that the observed emission intensity depends on the temperature of the medium (Figure 5A).

4. LANTHANIDES IN CELLULAR LUMINESCENCE IMAGING

4.1. Lanthanide-Containing Nanoparticles

In addition to the advantageous properties displayed by NPs, lanthanide-doped NPs (LnNPs) display emission lifetimes in the range of micro- to milliseconds, and narrow emission bands that allow time-gated imaging and spectral resolution, respectively [174–176]. $4f$-$4f$ transitions, which are responsible for the Ln-centered luminescence properties, are parity forbidden with low molar extinction coefficients that lead to low emission intensity. Thus, luminescence imaging requires high excitation power and long acquisition times that damage tissues, and thus alternative sensitization strategies have been pursued [177–179].

Ln that emit in the NIR are particularly interesting for imaging, due to the NIR-tissue transparency (Figure 1) [179–183]. Nd^{III}-based NPs are excited and emit at ~808 nm ($^4F_{9/2} \leftarrow {}^4I_{9/2}$) and ~1055 nm ($^4F_{9/2} \rightarrow {}^4I_{11/2}$), respectively [180, 183] and are particularly interesting due to the reduced heating effect that accompanies excitation at ~808 nm [182]. The use of sensitizer-activator pairs Yb^{III}/Er^{III} or Nd^{III}/Ho^{III} enables NIR-to-NIR luminescence imaging [179, 181]. X-ray light, which has unlimited penetrability, is an alternative to the NIR excitation for deep tissue and *in vivo* luminescence imaging [184–186]. X-ray luminescence imaging of MDA-MB-31 and MCF-7 cells was successfully obtained using the NPs NaLuF$_4$:Gd^{III}, Eu^{III}@NaLuF$_4$:Gd^{III}@NaLuF$_4$:Gd^{III}, Tb^{III}[185]. The low X-ray dosage needed for sensitization did not significantly affect cell viability.

LnNPs functionalized with DOX are frequently used drug delivery systems [187–188]. Electrostatic interactions between surface-coated alginate-poly(dopamine) (AlgPDA) NPs and DOX enabled delivery of the drug to cancer cells [187]. The higher cytotoxicity observed for the NP system, compared with free DOX, is a result of higher penetration of the NPs in the cells (Figure 5B) [187]. Controlled release of DOX as a function of pH and temperature was achieved using LnNPs functionalized with thermo-responsive poly(*N*-isopropylacrylamide-co-methacrylic acid) [188].

Radiodynamic therapy was accomplished using NaLuF$_4$:Gd^{III}, Eu^{III}@NaLuF$_4$:Gd@NaLuF$_4$:-Gd^{III}, Tb^{III} functionalized with Rose Bengal, a $^1O_2$ generator, while luminescence was achieved using X-ray excitation. The Rose Bengal is excited by the Tb^{III} emission, and the Tb^{III} and Eu^{III} emissions are used to image MDA-MB-31 and MCF-7 cells [185]. Absorption of secondary electrons, generated by X-ray radiation, by Ce^{III} in the scintillating NP NaCeF$_4$:Gd,Tb, which photodecomposes water and oxygen into hROS, and Tb^{III} ions decreased the viability of A549 cells and *in vivo* tumor size [186].

4.2. Up-converting Nanoparticles

Low-energy excitation of Ln compounds is achieved through TPA [189, 190] or UC [191, 192]. The latter is achieved through excited-state absorption or energy

transfer up-conversion [193–199]. UCNPs have large potential for luminescence imaging; however, the synthesis of the correct crystalline phase, low σ_{TPA}, low cell-penetrability, undesirable accumulation in the body, and limited tissue penetrability of the 980 nm radiation are limiting factors for their use. Several strategies have been described to isolate the useful hexagonal $NaYF_4$ host [200, 201].

In Mn[II]-doped UCNPs, increase of the Er[III]-based red emission intensity ($^4F_{9/2} \rightarrow {}^4I_{15/2}$) was attributed to the energy transfer Er[III]($^4S_{3/2}$) $\rightarrow$ Mn[II]($^4T_1$) followed by back transfer Mn[II]($^4T_1$) $\rightarrow$ Er[III]($^4F_{9/2}$) [202, 203]. Use of lithography to synthesize sandwich structures of the type Au/UCNP/Au allowed control of the distance Au-UCNP and of the homogeneity, resulting in a 1,000-fold enhancement of the UC emission [204].

The most common UCNPs contain the Yb[III]/Er[III] activator/sensitizer pair, and the UC emission is excited at 980 nm, where there is lower tissue scattering (Figure 1) [205]. However, the penetration depth is not high enough for *in vivo* applications that require imaging of deeper parts of the body. Co-doping the matrix with Nd[III] allows excitation at 808 nm ($^4F_{5/2} \leftarrow {}^4I_{9/2}$ transition), the region in which scattering by the tissues and cells is lower, allowing deeper imaging (Figure 6) [206, 207].

The large sizes of UCNPs result in accumulation in the body and low cell penetrability, which can be improved with surface coating strategies [208–211]. Lyposome-coated $NaYF_4$:7 % Nd[III]@$NaYF_4$ UCNPs have half-lives in the blood,

Figure 6. Tissue penetration as a function of excitation wavelength. Reproduced with permission from [207]; copyright 2015, Springer Nature.

liver, and spleen of 17.96 min, 23 h, and 17.9 h, respectively, and non-coated ones of 20.56 min, 52 h, and 175 h, respectively [212].

Dye-modified UCNPs have been demonstrated as sensors for a variety of analytes [198, 199, 213–220]. To avoid leaching of the dye and compromising the sensing properties, the dye is chemically bonded to the surface of the UCNP. $NaYF_4$: 20 % Yb, 0.5 % Tm, chemically functionalized with the Ru-DNPH complex, allows specific detection of HOCl in MDA-MB-31 cells, and *in vivo* in the range 0–20 mM [215]. To modulate the energy transfer UCNP–dye, the 3-(N-morpholino)propanesulfonic dye was chemically bonded to $NaYF_4@NaYF_4$:Yb, Tm@$NaYF_4$:Yb, and Er@$NaYF_4$. The proximity of the emitting ions to the surface improves the quenching efficiency of the UC emission; in the presence of hydroxyl radicals, the azide bond is broken, and the dye is released, resulting in the increase of the UC emission intensity [214]. Improvement of the quenching efficiency was achieved by using complementary DNA labeled with two quenchers adsorbed to the $NaYF_4@NaYF_4$:Yb, Er UCNP surface for sensing of micro-RNA-21 in MCF-7 cells with values comparable to those of established real-time polymerase chain reaction methods [216].

Sensing of GSH in the range 0 – 3.5 nM in HeLa cells and *in vivo* was possible with formation of a chromophore capable of sensitizing UC emission, resulting in a 30-fold boost in the emission intensity [213]. The use of DNA fragments highly selective towards Zn^{II} [218] and formation of S–S bonds to improve energy transfer and local accumulation in inflamed areas [199] were some strategies used to improve Zn^{II} sensing *in vitro* and *in vivo*. Multiplex detection of intracellular Ca^{II} and pH in HeLa cells was possible with $NaYF_4@NaYF_4$:Yb, Tm/Ho@$NaYF_4$ UCNPs functionalized with Fluo-4 and SNARF-4F [221].

UCNPs functionalized with DOX are useful drug delivery systems [222, 223], and an increasing number of systems is available to deliver DNA or RNA fragments for use in gene therapy [224]. Attachment of DOX to UCNP surfaces via imine bonds is a strategy for specific delivery to target cells; the acidic pH characteristic of cancer cells breaks the imine bonds, releasing the DOX in the target cells. This kind of drug delivery system is highly selective towards cancer cells, allowing efficient treatment using lower concentrations. Functionalization with DOX and 5-FU enables drug release at low pH, and the system is thus selective for cancer cells [222, 223].

UCNPs functionalized with PSs or inorganic materials capable of generating hROS lead to theranostic compounds for PDT [225–229]. The use of quenchers such as diarylethene, that only in its open form allows energy transfer from $NaGdF_4@NaGdF_4$:Yb, Er@$NaGdF_4$ to the PS, avoids producing $^1O_2$ outside the target cells. The closed and opened forms are achieved by exciting the sample at 365 and 808 nm, respectively, with full reversibility even after ten cycles [225].

A MnO_2 honeycomb structure loaded with $NaGdF_4$:Yb, Er@$NaGdF_4$:Yb@$NaNdF_4$:Yb and chlorin-e6 was used to decompose the H_2O_2 produced inside hypoxic cancer cells, which resulted in improved photocytotoxicity when compared with the system without MnO_2 [228]. In $NaGdF_4$:Yb, Tm@$NaGdF_4$ coated with CeO_x, the latter decomposes H_2O_2 into hROS [229]. Emission in a broad range of wavelengths was observed for the UCNP $NaYF_4$:Y, Yb, Er coated with

Zn-phthalocyanine (Pc), a green, and Rose Bengal, a red absorber, with higher photocytotoxicity than the systems containing only ZnPc or only Rose Bengal [227].

4.3. Molecular Luminescence Agents

4.3.1. *One-Photon Excitation*

The color pure emission due to the line-like spectra of Ln ion complexes is sensitized through an appended ligand chromophore [230, 231]. This antenna effect leads to a large Stokes shift of sensitized emission. As ligands are easily derivatized, the chemical and spectroscopic properties of the Ln complexes can be tuned [232–237]. The isolation of several Ln coordination complexes containing fluorobenzoate ligands with varying degrees of fluorination allowed concluding that fluorination of the *orto* position relative to the carboxylate group yields the best compound for luminescence imaging of HeLa cells [237]. Amino ($-NH_2$) or tiol (-SH) groups from a protein or antibody react with isothiocyanato, chlorosulphonyl, 2,4-dichloro-1,3,5-triazinyl, or *N*-hydroxysuccinimide from Ln complexes to form bioconjugates [238–241]. This method yields luminescent compounds with target cells [242–244]. [Eu(BHHTEGST)] (Figure 7A) conjugated with the G2O3 antibody enabled time-gated luminescence imaging of *Giardia cyst* cells [244].

Multi-dentate ligands reduce vibrational quenching and prevent coordination of solvent molecules that contribute to quenching through, for example, O-H oscillators. Diethylenetriaminepentaacetate or 1,4,7,10-tetraazacyclododecane-1,4,7,10-tetraacetic acid (dota)-based ligands (Figure 7B) with Nd^{III} yield NIR-emitting complexes that were used for whole-body NIR luminescence imaging, albeit with high excitation power and long acquisition lifetimes, as direct metal-centered excitation was used [245, 246]. More benign excitation was achieved through heterometallic Zn^{II}/Yb^{III}, Zn^{II}/Nd^{III} metallocrowns [247, 248], and Yb^{III} complexes containing porphyrin-based ligands [249–251], resulting in complexes with high emission QY in the NIR. In the complexes $[Yb(L_P)(L_K)]$ (L_P = porphyrin, L_K = Kläui ligand; Figure 7A) the Yb^{III} is well shielded from vibrational quenching through the solvent molecules, and absorption in the green-red region is used to sensitize the Yb^{III}-NIR emission. $[Yb(L_{COOH})(L_K)]$ (Figure 7A) was used in NIR luminescence imaging of HeLa cells and *in vivo*, with -COOH-enabled sensing of pH between pH 1 and 5, and PET quenching between pH 5 and 9 in solution and *in vivo* [251].

Luminescent Ln complexes are known as sensors for a variety of analytes [252–259]. [Eu(bhhct-bped)(bpt)] (Figure 7A) selectively senses Cu^{2+} in the range 0.25–2.5 μM in HepG2 cells [260]. Functionalization of a terpyridine with an anthracene moiety yielded $[Eu(dhh)_3(atpy)]$ (Figure 7A) that selectively senses $^1O_2$ in the concentration range 2.5–100 μM in HepG2 cells [261].

Substitution of ligands with triphenylphosphonium, morpholine or methyl phenyl sulfonamide yielded accumulation of Ln luminescent complexes in the mito-
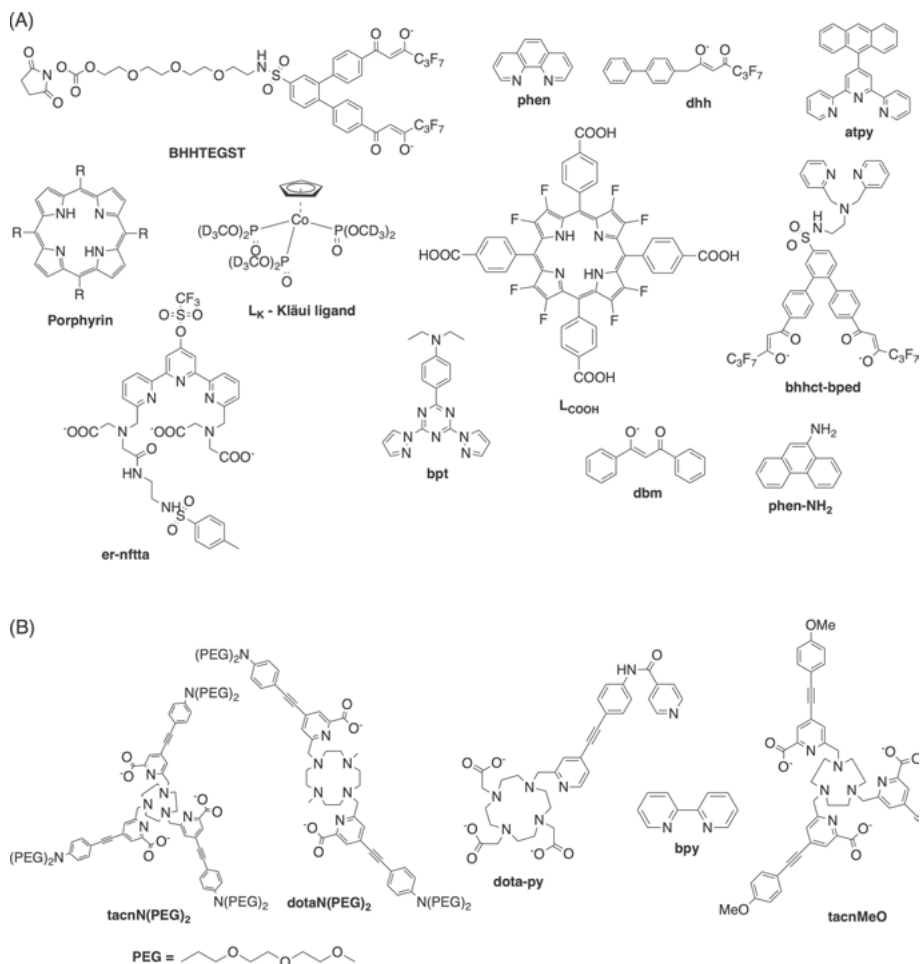
Figure 7. Compounds discussed in Section 4.

chondria, lysosomes, and endoplasmic reticulum, respectively [252, 259, 262]. Functionalization of a terpyridine-based ligand with methyl phenyl sulfonamide and trifluoromethanesulfonyl-moieties yielded [Ln(er-nftta)] (Ln = Eu^{III} or Tb^{III}) (Figure 7A) that selectively sensed superoxide in the concentration range 0 – 50 μM in HepG2, HK-2 cells, kidney tissue, and *in vivo* [259]. In the presence of superoxide, the trifluoromethanesulfonyl moiety was released, which caused an increase and decrease in the Tb^{III} and Eu^{III} emission intensities, respectively, allowing for ratiometric sensing.

The sensing of chemical species using specific reactions with ligands is useful, but the process is not reversible. Zinc fingers modified with 7-nitro-2,1,3-benzoxadiazole (nbd) and [Nd(dota)] yielded a system that selectively sensed Zn^{II} using the Nd^{III}-centered NIR emission. The presence or absence of Zn^{II} causes

configuration changes in the zinc finger that are reflected in changes of the Nd^{III} emission intensity due to modulation of the nbd $\rightarrow Nd^{III}$ energy transfer [263].

4.3.2.   Two-Photon Excitation

TPA has been used to excite Ln complexes in the biological window [264–269]. High two-photon brightness, one of the critical factors for obtaining good quality luminescence imaging, is achieved by the presence of charge transfer states [190, 233, 270], high complex rigidity [271], or use of plasmonic bands [272]. TPEL (λ_{exc} = 975 nm) of $[Eu(dbm)_3(phen-NH_2)]$ (Figure 7A) deposited onto a glass substrate is only observed in the presence of a layer of triangular Ag nanoprisms [272].

NIR-to-NIR luminescence imaging allows higher signal-to-noise ratio and luminescence imaging of deep tissues. Conventional confocal microscopes do not allow measurement of emission in the 950–1050 nm range due to optical filtering schemes, and photomultiplier tube detectors that are optimized for the visible range. By modifying the optical filtering schemes and connecting an adequate NIR detector, Andraud and coworkers successfully obtained images using a combination of TPEL and NIR-to-NIR luminescence imaging [273]. Determination of the 3D blood capillary network in mouse brain using the NIR-emitting $[Yb(dpaN(PEG)_2)]^{3-}$ (Figure 7B) validated the setup, and shortly after that, the first example of NIR-to-NIR luminescence imaging using $[Yb(tacnN(PEG)_2)]^+$ (Figure 7B) was reported [274]. Due to the possibility of both visible and NIR emission, Sm^{III} complexes have been explored. TPEL imaging of T24 cells in the visible and NIR was possible using $[Sm(tacnMeO)]$ with an image quality similar to the analogous Yb^{III} complex [275].

Photoactivated DNA damage and TPEL imaging were possible using the heterobimetallic $[Eu(dota-py)(H_2O)RuCl(bpy)_3]^+$ (Figure 7B). Upon illumination at 488 nm, $[RuCl(bpy)_3]^+$ is released, which increased the Eu^{III} emission intensity, leading to DNA damage [276].

5.   CONCLUDING REMARKS

The development of improved metal-containing imaging agents has been an active and fruitful area of research, as shown by the work highlighted here. The versatility provided by the ability to functionalize ligands, decorate NP surfaces, or tune photophysical properties by controlling NP size, makes metal-containing systems especially attractive for bioimaging. They can be tailored to target specific types of cells, or display specific subcellular localization. Frequently the metal-containing systems are cytotoxic, or they can be engineered as drug delivery agents, making them prime candidates for use in the field of theranostics. Considering the unique photophysical properties of the systems mentioned here, one can only expect a continued growth of the families of metal-containing compounds for use as luminophores in bioimaging.

ACKNOWLEDGMENTS

ABBREVIATIONS

$^1O_2$	singlet oxygen
2D	two-dimensional
2D-QD	two-dimensional quantum dots
3D	tridimensional
5-FU	5-fluorouracil
6-MP	6-mercaptopurine
AlgPDA	alginate-poly(dopamine)
AMP	antimicrobial peptide
AuNCs	gold nanoclusters
AuNPs	gold nanoparticles
AuNRs	gold nanorods
bpy	bipyridine
CP	conjugated polymer
DAPI	4,6-diamidino-2-phenylindole
DNPH	dinitrophenylhydrazine
dota	1,4,7,10-tetraazacyclododecane-1,4,7,10-tetraacetic acid
DOX	doxorubicin
GM	Goeppert Mayer
HepG2	hepatocyte carcinoma
hROS	highly reactive oxygen species
IC_{50}	half maximal inhibitory concentration
LMCT	ligand-to-metal charge transfer
LnNPs	lanthanide-doped nanoparticles
LSPR	localized surface plasmon resonance
MLCT	metal-to-ligand charge-transfer
MP	mercaptopurine
MQDs	MXene quantum dots
nbd	7-nitro-2,1,3-benzoxadiazole
NCs	nanoclusters
NDs	nanodots
NIR	near-infrared
NPs	nanoparticles
Pc	phthalocyanine
PDT	photodynamic therapy
PEG	polyethylene glycol
phen	phenanthroline
PLNPs	persistent luminescent nanoparticles
PS	photosensitizer

PTT	photothermal therapy
QDs	quantum dots
QY	quantum yield
σ_{TPA}	two-photon absorption cross-section
TM	transition metal
TMDs	transition metal dichalcogenides
TPA	two-photon absorption
TPEL	two-photon excited luminescence
UC	up-conversion
UCNPs	up-converting nanoparticles
ZGGO	zinc gallogermanate
ZGO	zinc gallate

REFERENCES

1. F. W. B. van Leeuwen, J. C. H. Hardwick, A. R. van Erkel, *Radiology* **2015**, *276*, 12–29.
2. M. G. Romei, S. G. Boxer, *Annu. Rev. Biophys.* **2019**, *48*, 19–44.
3. T. Stearns, *Curr. Biol.* **1995**, *5*, 262–264.
4. H. E. Chia, E. N. G. Marsh, J. S. Biteen, *Curr. Opin. Chem. Biol.* **2019**, *51*, 98–104.
5. H. F. Ozbakir, N. T. Anderson, K.-C. Fan, A. Mukherjee, *Bioconjugate Chem.* **2020**, *31*, 293–302.
6. D. Barolet, *Semin. Cutan. Med. Surg.* **2008**, *27*, 227–238.
7. K. Y. Zhang, Q. Yu, H. Wei, S. Liu, Q. Zhao, W. Huang, *Chem. Rev.* **2018**, *118*, 1770–1839.
8. Y. Chen, R. Guan, C. Zhang, J. Huang, L. Ji, H. Chao, *Coord. Chem. Rev.* **2016**, *310*, 16–40.
9. K. Qiu, Y. Chen, W. Rees, L. Ji, H. Chao, *Coord. Chem. Rev.* **2019**, *378*, 66–86.
10. S. Jeelani, R. C. J. Reddy, T. Maheswaran, G. S. Asokan, A. Dany, B. Anand, *J. Pharm. Bioallied. Sci.* **2014**, *6*, S6–S8.
11. U. Wiesing, *Medicine, Health Care and Philosophy* **2019**, *22*, 593–597.
12. S. A. Aldossary, *Biomed. Pharmacol. J.* **2019**, *12*, 7–15.
13. D. M. Cheff, M. D. Hall, *J. Med. Chem.* **2017**, *60*, 4517–4532.
14. R. Guan, L. Xie, T. W. Rees, L. Ji, H. Chao, *J. Inorg. Biochem.* **2020**, *204,* 110985.
15. C.-N. Ko, G. Li, C.-H. Leung, D.-L. Ma, *Coord. Chem. Rev.* **2019**, *381*, 79–103.
16. E. Babu, J. Bhuvaneswari, P. M. Mareeswaran, P. Thanasekaran, H.-M. Lee, S. Rajagopal, *Coord. Chem. Rev.* **2019**, *380*, 519–549.
17. N. Gao, Y. Chen, L. Li, Z. Guan, T. Zhao, N. Zhou, P. Yuan, S. Q. Yao, Q.-H. Xu, *J. Phys. Chem. C* **2014**, *118*, 13904–13911.
18. A. Kumar, S. Kim, J.-M. Nam, *J. Am. Chem. Soc.* **2016**, *138*, 14509–14525.
19. J.-F. Li, C.-Y. Li, R. F. Aroca, *Chem. Soc. Rev.* **2017**, *46*, 3962–3979.
20. M. Kim, J.-H. Lee, J.-M. Nam, *Adv. Sci.* **2019**, *6*, 1900471.
21. J.-E. Park, J. Kim, J.-M. Nam, *Chem. Sci.* **2017**, *8*, 4696–4704.
22. Y. Shen, A. J. Shuhendler, D. Ye, J. J. Xu, H. Y. Chen, *Chem. Soc. Rev.* **2016**, *45*, 6725–6741.
23. J. Olesiak-Banska, M. Waszkielewicz, P. Obstarczyk, M. Samoc, *Chem. Soc. Rev.* **2019**, *48*, 4087–4117.
24. L. Xie, X. Zhi, N. Xiao, C.-J. Fang, C.-H. Yan, *RSC Adv.* **2018**, *8*, 26517–26522.

25. A. Li Volsi, C. Scialabba, V. Vetri, G. Cavallaro, M. Licciardi, G. Giammona, *ACS Appl. Mater. Interfaces* **2017**, *9*, 14453–14469.

26. S. K. Maji, S. Yu, K. Chung, M. Sekkarapatti Ramasamy, J. W. Lim, J. Wang, H. Lee, D. H. Kim, *ACS Appl. Mater. Interfaces* **2018**, *10*, 42068–42076.

27. X. Han, Y. Xu, Y. Li, X. Zhao, Y. Zhang, H. Min, Y. Qi, G. J. Anderson, L. You, Y. Zhao, G. Nie, *ACS Nano* **2019**, *13*, 4379–4391.

28. E. T. Vickers, M. Garai, S. Bonabi Naghadeh, S. Lindley, J. Hibbs, Q.-H. Xu, J. Z. Zhang, *J. Phys. Chem. C* **2018**, *122*, 13304–13313.

29. M. Yu, J. Xu, J. Zheng, *Angew. Chem. Int. Ed.* **2019**, *58*, 4112–4128.

30. I. Chakraborty, T. Pradeep, *Chem. Rev.* **2017**, *117*, 8208–8271.

31. J. Yang, F. Wang, H. Yuan, L. Zhang, Y. Jiang, X. Zhang, C. Liu, L. Chai, H. Li, M. Stenzel, *Nanoscale* **2019**, *11*, 17967–17980.

32. E. Porret, X. Le Guével, J.-L. Coll, *J. Mater. Chem. B* **2020**, *8*, 2216–2232.

33. D. Li, Z. Chen, X. Mei, *Adv. Colloid Interface Sci.* **2017**, *250*, 25–39.

34. X. Ran, Z. Wang, F. Pu, Z. Liu, J. Ren, X. Qu, *Chem. Commun.* **2019**, *55*, 15097–15100.

35. J. Xia, X. Wang, S. Zhu, L. Liu, L. Li, *ACS Appl. Mater. Interfaces* **2019**, *11*, 7369–7378.

36. N. El-Sayed, V. Trouillet, A. Clasen, G. Jung, K. Hollemeyer, M. Schneider, *Adv. Healthcare Mater.* **2019**, *8*, 1900993.

37. A. M. Alkilany, S. Alsotari, M. Y. Alkawareek, S. R. Abulateefeh, *Sci. Rep.* **2019**, *9*, 11098.

38. X. Cao, S. Cheng, Y. You, S. Zhang, Y. Xian, *Anal. Chim. Acta* **2019**, *1092*, 108–116.

39. Y. Wang, X. Wang, X. Ma, Q. Chen, H. He, W. M. Nau, F. Huang, *Part. Part. Syst. Charact.* **2019**, *36*, 1900281.

40. J. Zhu, K. He, Z. Dai, L. Gong, T. Zhou, H. Liang, J. Liu, *Anal. Chem.* **2019**, *91*, 8237–8243.

41. X. Kang, H. Chong, M. Zhu, *Nanoscale* **2018**, *10*, 10758–10834.

42. N. Goswami, R. Bright, R. M. Visalakshan, B. Biswas, P. Zilm, K. Vasilev, *Nanoscale Adv.* **2019**, 1, 2356–2364.

43. Y. Wei, W. Luan, F. Gao, X. Hou, *Part. Part. Syst. Charact.* **2019**, *36*, 1900314.

44. L. Yang, H. Wang, D. Li, L. Li, X. Lou, H. Liu, *Chem. Mater.* **2018**, *30*, 5507–5515.

45. B. Chatterjee, A. Ghoshal, A. Chattopadhyay, S. S. Ghosh, *ACS Biomater. Sci. Eng.* **2018**, *4*, 1005–1012.

46. Y. Wang, S. Ma, Z. Dai, Z. Rong, J. Liu, *Nanoscale* **2019**, *11*, 16336–16341.

47. Z. Li, H. Peng, J. Liu, Y. Tian, W. Yang, J. Yao, Z. Shao, X. Chen, *ACS Appl. Mater. Interfaces* **2018**, *10*, 83–90.

48. X. Jiang, X. Wang, C. Yao, S. Zhu, L. Liu, R. Liu, L. Li, *J. Phys. Chem. Lett.* **2019**, *10*, 5237–5243.

49. H. Liu, G. Hong, Z. Luo, J. Chen, J. Chang, M. Gong, H. He, J. Yang, X. Yuan, L. Li, X. Mu, J. Wang, W. Mi, J. Luo, J. Xie, X. D. Zhang, *Adv. Mater.* **2019**, *31*, 1901015.

50. F. U. Rehman, T. Du, S. Shaikh, X. Jiang, Y. Chen, X. Li, H. Yi, J. Hui, B. Chen, M. Selke, X. Wang, *Nanomedicine* **2018**, *14*, 2619–2631.

51. M. Wang, Y. Chen, W. Cai, H. Feng, T. Du, W. Liu, H. Jiang, A. Pasquarelli, Y. Weizmann, X. Wang, *Proc. Nat. Acad. Sci. USA* **2020**, *117*, 308–316.

52. D. Dutta, S. K. Sailapu, A. Chattopadhyay, S. S. Ghosh, *ACS Appl. Mater. Interfaces* **2018**, *10*, 3210–3218.

53. F. Ru, P. Du, X. Lu, *Anal. Chim. Acta* **2020**, *1105*, 139–146.

54. Y. Xie, Y. Xianyu, N. Wang, Z. Yan, Y. Liu, K. Zhu, N. S. Hatzakis, X. Jiang, *Adv. Funct. Mater.* **2018**, *28*, 1702026.

55. M. Jia, W. Mi, S. Guo, Q.-Z. Yang, Y. Jin, N. Shao, *Talanta* **2020**, *216*, 120926.

56. P. Gao, S. Wu, X. Chang, F. Liu, T. Zhang, B. Wang, K.-Q. Zhang, *Bioconjug. Chem.* **2018**, *29*, 4140–4148.

57. Y. Li, M. Yuan, A. J. Khan, L. Wang, F. Zhang, *Colloids Surf. A Physicochem. Eng. Asp.* **2019**, *579*, 123666.

58. S. Pan, J. Zhou, W. Liu, Y. Ye, G. Chen, J. Xu, Z. Qian, J. Chen, H. Feng, *Analyst* **2019**, *144*, 4483–4487.

59. D. Dutta, S. K. Sailapu, A. T. Simon, S. S. Ghosh, A. Chattopadhyay, *Langmuir* **2019**, *35*, 10475–10483.

60. C. R. Lillo, M. N. Calienni, B. R. Aiello, M. J. Prieto, D. R. Sartori, J. Tuninetti, P. Toledo, S. del Valle Alonso, S. Moya, M. C. Gonzalez, J. Montanari, G. J. A. A. Soler-Illia, *Mater. Sci. Eng. C* **2020**, 110891.

61. B. A. Lakshmi, S. Kim, *Colloids Surf. B* **2019**, *178*, 230–237.

62. V. Poderys, G. Jarockyte, S. Bagdonas, V. Karabanovas, R. Rotomskis, *J. Photochem. Photobiol. B,* **2020**, *204*, 111802.

63. S. Zhu, X. Wang, S. Li, L. Liu, L. Li, *ACS Appl. Mater. Interfaces* **2020**, *12*, 11063–11071.

64. H. Ao, H. Feng, S. Pan, Z. Bao, Z. Li, J. Chen, Z. Qian, *ACS Appl. Nano Mater.* **2018**, *1*, 5673–5681.

65. A. K. Sharma, S. Pandey, N. Sharma, H. F. Wu, *Mater. Sci. Eng. C* **2019**, *99*, 1–11.

66. Z. Lu, F. Y. Huang, R. Cao, L. Zhang, G. H. Tan, N. He, J. Huang, G. Wang, Z. Zhang, *Sci. Rep.* **2017**, *7*, 41571.

67. M. P. Maman, S. Gratious, A. R. K, S. Mandal, *Dalton Trans.* **2019**, *48*, 6522–6526.

68. Y. Xin, X. Huang, Z. Li, W. Zhao, C. Wang, S. Wang, X. Yue, H. Mo, H. Li, *Biochem. Biophys. Res. Commun.* **2019**, *512*, 218–223.

69. J. Xu, X. Zhu, X. Zhou, F. Y. Khusbu, C. Ma, *Trends. Analyt. Chem.* **2020**, *124*.

70. S. Shaikh, F. U. Rehman, T. Du, H. Jiang, L. Yin, X. Wang, R. Chai, *ACS Appl. Mater. Interfaces* **2018**, *10*, 26056–26063.

71. F. Molaabasi, M. Sarparast, M. Shamsipur, L. Irannejad, A. A. Moosavi-Movahedi, A. Ravandi, B. Hajipour Verdom, R. Ghazfar, *Sci. Rep.* **2018**, *8*, 14507.

72. S. Bhandari, D. Mondal, S. K. Nataraj, R. G. Balakrishna, *Nanoscale Adv.* **2019**, *1*, 913–936.

73. M. Díaz-González, A. de la Escosura-Muñiz, M. T. Fernandez-Argüelles, F. J. García Alonso, J. M. Costa-Fernandez, *Top. Curr. Chem.* **2020**, *378*, 35.

74. S. Pandey, D. Bodas, *Adv. Colloid Interface Sci.* **2020**, *278*, 102137.

75. A. M. Wagner, J. M. Knipe, G. Orive, N. A. Peppas, *Acta Biomater.* **2019**, *94*, 44–63.

76. S. Silvi, A. Credi, *Chem Soc Rev* **2015**, *44*, 4275–4289.

77. A. Rowley, T. Parks, K. Parks, K. Medley, A. Cordner, M. Yu, *Anal. Biochem.* **2018**, *555*, 73–80.

78. P. Reiss, M. Protière, L. Li, *Small* **2009**, *5*, 154–168.

79. C. Giansante, I. Infante, *J. Phys. Chem. Lett.* **2017**, *8*, 5209–5215.

80. E. Drijvers, J. Liu, A. Harizaj, U. Wiesner, K. Braeckmans, Z. Hens, T. Aubert, *ACS Appl. Mater. Interfaces* **2019**, *11*, 38475–38482.

81. J. Sun, F. Liu, W. Yu, Q. Jiang, J. Hu, Y. Liu, F. Wang, X. Liu, *Nanoscale* **2019**, *11*, 5014–5020.

82. D. Mo, L. Hu, G. Zeng, G. Chen, J. Wan, Z. Yu, Z. Huang, K. He, C. Zhang, M. Cheng, *Appl. Microbiol. Biotechnol.* **2017**, *101*, 2713–2733.

83. Z. Ranjbar-Navazi, Y. Omidi, M. Eskandani, S. Davaran, *Trends. Anal. Chem.* **2019**, *118*, 386–400.

84. A. A. P. Mansur, H. S. Mansur, S. M. Carvalho, Z. I. P. Lobato, M. d. F. Leite, L. L. Mansur, *ACS Omega* **2018**, *3*, 15679–15691.

85. R. Harish, K. D. Nisha, S. Prabakaran, B. Sridevi, S. Harish, M. Navaneethan, S. Ponnusamy, Y. Hayakawa, C. Vinniee, M. R. Ganesh, *Appl. Surf. Sci.* **2020**, *499*, 143817.

86. A. A. P. Mansur, F. G. de Carvalho, R. L. Mansur, S. M. Carvalho, L. C. de Oliveira, H. S. Mansur, *Int. J. Biol. Macromol.* **2017**, *96*, 675–686.

87. D. G. Zayed, S. M. Ebrahim, M. W. Helmy, S. N. Khattab, M. Bahey-El-Din, J.-Y. Fang, K. A. Elkhodairy, A. O. Elzoghby, *J. Nanobiotechnology* **2019**, *17*, 7.

88. K. Shivaji, S. Mani, P. Ponmurugan, C. S. De Castro, M. Lloyd Davies, M. G. Balasubramanian, S. Pitchaimuthu, *ACS Appl. Nano Mater.* **2018**, *1*, 1683–1693.

89. L.-J. Tian, Y. Min, W.-W. Li, J.-J. Chen, N.-Q. Zhou, T.-T. Zhu, D.-B. Li, J.-Y. Ma, P.-F. An, L.-R. Zheng, H. Huang, Y.-Z. Liu, H.-Q. Yu, *ACS Nano* **2019**, *13*, 5841–5851.

90. S. Sarkar, P. Le, J. Geng, Y. Liu, Z. Han, M. U. Zahid, D. Nall, Y. Youn, P. R. Selvin, A. M. Smith, *J. Am. Chem. Soc.* **2020**, *142*, 3449–3462.

91. A. Zebibula, N. Alifu, L. Xia, C. Sun, X. Yu, D. Xue, L. Liu, G. Li, J. Qian, *Adv. Funct. Mater.* **2018**, *28*, 1703451.

92. F. Zamberlan, L. Turyanska, A. Patanè, Z. Liu, H. E. L. Williams, M. W. Fay, P. A. Clarke, Y. Imamura, T. Jin, T. D. Bradshaw, N. R. Thomas, A. M. Grabowska, *J. Mater. Chem. B* **2018**, *6*, 550–555.

93. R. Tian, H. Ma, S. Zhu, J. Lau, R. Ma, Y. Liu, L. Lin, S. Chandra, S. Wang, X. Zhu, H. Deng, G. Niu, M. Zhang, A. L. Antaris, K. S. Hettie, B. Yang, Y. Liang, X. Chen, *Adv. Mater.* **2020**, *32*, 1907365.

94. X. Qiu, X. Zhu, X. Su, M. Xu, W. Yuan, Q. Liu, M. Xue, Y. Liu, W. Feng, F. Li, *Adv. Sci.* **2019**, *6*, 1801834.

95. A. A. P. Mansur, A. J. Caires, S. M. Carvalho, N. S. V. Capanema, I. C. Carvalho, H. S. Mansur, *Colloids Surf. B* **2019**, *184*, 110507.

96. S. Bhandari, S. Pramanik, N. K. Biswas, S. Roy, U. N. Pan, *ACS Appl. Nano Mater.* **2019**, *2*, 2358–2366.

97. J. Selvaraj, A. Mahesh, V. Asokan, V. Baskaralingam, A. Dhayalan, T. Paramasivam, *ACS Appl. Nano Mater.* **2018**, *1*, 371–383.

98. R. Zhou, S. Sun, C. Li, L. Wu, X. Hou, P. Wu, *ACS Appl. Mater. Interfaces* **2018**, *10*, 34060–34067.

99. M. Cai, C. Ding, F. Wang, M. Ye, C. Zhang, Y. Xian, *Biosens. Bioelectron.* **2019**, *137*, 148–153.

100. P. Awasthi, X. An, J. Xiang, N. Kalva, Y. Shen, C. Li, *Nanoscale* **2020**, *12*, 5678–5684.

101. J.-J. Zhang, Y. Lin, H. Zhou, H. He, J.-J. Ma, M.-Y. Luo, Z.-L. Zhang, D.-W. Pang, *Adv. Healthcare Mater.* **2019**, *8*, 1900341.

102. J. Liu, X. Zhao, H. Xu, Z. Wang, Z. Dai, *Anal. Chem.* **2019**, *91*, 8987–8993.

103. M. Jiao, Y. Li, Y. Jia, C. Li, H. Bian, L. Gao, P. Cai, X. Luo, *J. Colloid Interface Sci.* **2020**, *565*, 35–42.

104. E. Soheyli, B. Ghaemi, R. Sahraei, Z. Sabzevari, S. Kharrazi, A. Amani, *Mater. Sci. Eng. C* **2020**, *111*, 110807.

105. T. Kameyama, H. Yamauchi, T. Yamamoto, T. Mizumaki, H. Yukawa, M. Yamamoto, S. Ikeda, T. Uematsu, Y. Baba, S. Kuwabata, T. Torimoto, *ACS Appl. Nano Mater.* **2020**, *3*, 3275–3287.

106. Z. Zang, X. Zeng, M. Wang, W. Hu, C. Liu, X. Tang, *Sens. Actuators B Chem.* **2017**, *252*, 1179–1186.

107. S. Jain, S. Bharti, G. K. Bhullar, S. K. Tripathi, *J. Lumin.* **2020**, *219*, 116912.

108. T. Deng, J. Wang, Y. Li, Z. Han, Y. Peng, J. Zhang, Z. Gao, Y. Gu, D. Deng, *ACS Appl. Mater. Interfaces* **2018**, *10*, 27657–27668.

109. Y. Xu, X. Wang, W. L. Zhang, F. Lv, S. Guo, *Chem. Soc. Rev.* **2018**, *47*, 586–625.

110. L. Cheng, X. Wang, F. Gong, T. Liu, Z. Liu, *Adv. Mater.* **2020**, *32*, 1902333.

111. Y. Wang, M. Qiu, M. Won, E. Jung, T. Fan, N. Xie, S.-G. Chi, H. Zhang, J. S. Kim, *Coord. Chem. Rev.* **2019**, *400*, 213041.
112. L. Su, X. Fan, T. Yin, H. Wang, Y. Li, F. Liu, J. Li, H. Zhang, H. Xie, *Adv. Optical Mater.* **2020**, *8*, 1900978.
113. B. L. Li, M. I. Setyawati, H. L. Zou, J. X. Dong, H. Q. Luo, N. B. Li, D. T. Leong, *Small* **2017**, *13*.
114. A. Vadivelmurugan, R. Anbazhagan, H.-C. Tsai, *Mater. Lett.* **2018**, *218*, 285–289.
115. Y. Zhong, F. Xue, P. Wei, R. Li, C. Cao, T. Yi, *Nanoscale* **2018**, *10*, 21298–21306.
116. X. Tang, X. Zeng, H. Liu, Y. Yang, H. Zhou, H. Cai, *Microchim. Acta* **2019**, *186*, 572.
117. L. Liu, H. Jiang, J. Dong, W. Zhang, G. Dang, M. Yang, Y. Li, H. Chen, H. Ji, L. Dong, *Colloids Surf. B* **2020**, *185*, 110590.
118. M.-H. Shin, E.-Y. Park, S. Han, H. S. Jung, D. H. Keum, G.-H. Lee, T. Kim, C. Kim, K. S. Kim, S. H. Yun, S. K. Hahn, *Adv. Healthcare Mater.* **2019**, *8*, 1801036.
119. C. Sweet, A. Pramanik, S. Jones, P. C. Ray, *ACS Omega* **2017**, *2*, 1826–1835.
120. S.-C. Chen, C.-Y. Lin, T.-L. Cheng, W.-L. Tseng, *Adv. Funct. Mater.* **2017**, *27*, 1702452.
121. H. Huang, R. Jiang, Y. Feng, H. Ouyang, N. Zhou, X. Zhang, Y. Wei, *Nanoscale* **2020**, *12*, 1325–1338.
122. K. Huang, Z. Li, J. Lin, G. Han, P. Huang, *Chem. Soc. Rev.* **2018**, *47*, 5109–5124.
123. A. Sinha, Dhanjai, H. Zhao, Y. Huang, X. Lu, J. Chen, R. Jain, *Trends. Anal. Chem.* **2018**, *105*, 424–435.
124. B. Shao, Z. Liu, G. Zeng, H. Wang, Q. Liang, Q. He, M. Cheng, C. Zhou, L. Jiang, B. Song, *J. Mater. Chem. A* **2020**, *8*, 7508–7535.
125. Q. Xue, H. Zhang, M. Zhu, Z. Pei, H. Li, Z. Wang, Y. Huang, Y. Huang, Q. Deng, J. Zhou, S. Du, Q. Huang, C. Zhi, *Adv. Mater.* **2017**, *29*, 1604847.
126. X. Chen, X. Sun, W. Xu, G. Pan, D. Zhou, J. Zhu, H. Wang, X. Bai, B. Dong, H. Song, *Nanoscale* **2018**, *10*, 1111–1118.
127. X. Xu, H. Zhang, Q. Diao, Y. Zhu, G. Yang, B. Ma, *J. Mater. Sci. Mater. Electron.* **2020**, *31*, 175–181.
128. G. Yang, J. Zhao, S. Yi, X. Wan, J. Tang, *Sens. Actuators B Chem.* **2020**, *309*, 127735.
129. S.-K. Sun, H.-F. Wang, X.-P. Yan, *Acc. Chem. Res.* **2018**, *51*, 1131–1143.
130. J. Liu, T. Lécuyer, J. Seguin, N. Mignet, D. Scherman, B. Viana, C. Richard, *Adv. Drug Deliv. Rev.* **2019**, *138*, 193–210.
131. Q. Lin, Z. Li, C. Ji, Q. Yuan, *Nanoscale Adv.* **2020**, *2*, 1380–1394.
132. M. Pellerin, E. Glais, T. Lecuyer, J. Xu, J. Seguin, S. Tanabe, C. Chanéac, B. Viana, C. Richard, *J. Lumin.* **2018**, *202*, 83–88.
133. Y. Xia, H. Bao, J. Huang, X. Li, C. Yu, Z. Zhang, H. Wang, *Biomater. Sci.* **2020**, 8, 3095–3105.
134. L.-X. Yan, L.-J. Chen, X. Zhao, X.-P. Yan, *Adv. Funct. Mater.* **2020**, *30*, 1909042.
135. A. Harizaj, O. Q. D. Clercq, B. Descamps, C. Vanhove, S. C. D. Smedt, D. Poelman, I. Lentacker, K. Braeckmans, *Part. Part. Syst. Charact.* **2019**, *36*, 1900371.
136. J. Wang, Q. Ma, X.-X. Hu, H. Liu, W. Zheng, X. Chen, Q. Yuan, W. Tan, *ACS Nano* **2017**, *11*, 8010–8017.
137. X.-H. Lin, L. Song, S. Chen, X.-F. Chen, J.-J. Wei, J. Li, G. Huang, H.-H. Yang, *ACS Appl. Mater. Interfaces* **2017**, *9*, 41181–41187.
138. L. Fu, J. Wang, N. Chen, Q. Ma, D. Lu, Q. Yuan, *Chem. Commun.* **2020**, *56*, 6660–6663.
139. X. Zhao, L.-J. Chen, K.-C. Zhao, Y.-S. Liu, J.-l. Liu, X.-P. Yan, *Trends. Anal. Chem.* **2019**, *118*, 65–72.
140. J. Shi, X. Sun, S. Zheng, J. Li, X. Fu, H. Zhang, *Biomaterials* **2018**, *152*, 15–23.
141. J. Li, C. Wang, J. Shi, P. Li, Z. Yu, H. Zhang, *J. Lumin.* **2018**, *199*, 363–371.
142. Y. Feng, D. Deng, L. Zhang, R. Liu, Y. Lv, *Sens. Actuators B Chem.* **2019**, *279*, 189–196.

143. T. Ai, W. Shang, H. Yan, C. Zeng, K. Wang, Y. Gao, T. Guan, C. Fang, J. Tian, *Biomaterials* **2018**, *167*, 216–225.
144. H. Liu, F. Ren, H. Zhang, Y. Han, H. Qin, J. Zeng, Y. Wang, Q. Sun, Z. Li, M. Gao, *J. Mater. Chem. B* **2018**, *6*, 1508–1518.
145. Y. Feng, L. Zhang, R. Liu, Y. Lv, *Biosens. Bioelectron.* **2019**, *144*, 111671.
146. Y. Lv, D. Ding, Y. Zhuang, Y. Feng, J. Shi, H. Zhang, T.-L. Zhou, H. Chen, R.-J. Xie, *ACS Appl. Mater. Interfaces* **2019**, *11*, 1907–1916.
147. J. Wang, J. Li, J. Yu, H. Zhang, B. Zhang, *ACS Nano* **2018**, *12*, 4246–4258.
148. G. Liu, S. Zhang, Y. Shi, X. Huang, Y. Tang, P. Chen, W. Si, W. Huang, X. Dong, *Adv. Funct. Mater.* **2018**, *28*, 1804317.
149. H. Zhao, C. Liu, Z. Gu, L. Dong, F. Li, C. Yao, D. Yang, *Nano Lett.* **2020**, *20*, 252–260.
150. F.-X. Su, X. Zhao, C. Dai, Y.-J. Li, C.-X. Yang, X.-P. Yan, *Chem. Commun.* **2019**, *55*, 5283–5286.
151. H.-J. Zhang, X. Zhao, L.-J. Chen, C.-X. Yang, X.-P. Yan, *Anal. Chem.* **2020**, *92*, 1179–1188.
152. S.-K. Sun, J.-C. Wu, H. Wang, L. Zhou, C. Zhang, R. Cheng, D. Kan, X. Zhang, C. Yu, *Biomaterials* **2019**, *218*, 119328.
153. H. Liu, F. Ren, X. Zhou, C. Ma, T. Wang, H. Zhang, Q. Sun, Z. Li, *Anal. Chem.* **2019**, *91*, 15064–15072.
154. J.-M. Liu, D.-D. Zhang, G.-Z. Fang, S. Wang, *Biomaterials* **2018**, *165*, 39–47.
155. Z.-H. Wang, J.-M. Liu, C.-Y. Li, D. Wang, H. Lv, S.-W. Lv, N. Zhao, H. Ma, S. Wang, *ACS Appl. Mater. Interfaces* **2019**, *11*, 36409–36419.
156. L. Song, P.-P. Li, W. Yang, X.-H. Lin, H. Liang, X.-F. Chen, G. Liu, J. Li, H.-H. Yang, *Adv. Funct. Mater.* **2018**, *28*, 1707496.
157. M.-H. Chan, W.-T. Huang, J. Wang, R.-S. Liu, M. Hsiao, *Adv. Sci.* **2020**, *7*, 1903741.
158. S. M. Hossain, V. Prakash, P. Mamidi, S. Chattopadhyay, A. K. Singh, *RSC Adv.* **2020**, *10*, 3646–3658.
159. P. Feng, L. Ma, F. Xu, X. Gou, L. Du, B. Ke, M. Li, *Talanta* **2019**, *203*, 29–33.
160. A. Luengo, V. Fernández-Moreira, I. Marzo, M. C. Gimeno, *Inorg. Chem.* **2017**, *56*, 15159–15170.
161. T. Meng, Q.-P. Qin, Z.-L. Chen, H.-H. Zou, K. Wang, F.-P. Liang, *Eur. J. Med. Chem.* **2020**, *192*, 112192.
162. Y. Liu, P. Zhang, X. Fang, G. Wu, S. Chen, Z. Zhang, H. Chao, W. Tan, L. Xu, *Dalton Trans.* **2017**, *46*, 4777–4785.
163. W. Wang, L. Lu, K.-J. Wu, J. Liu, C.-H. Leung, C.-Y. Wong, D.-L. Ma, *Sens. & Actuators B: Chem.* **2019**, *288*, 392–398.
164. T. Huang, Q. Yu, S. Liu, K. Y. Zhang, W. Huang, Q. Zhao, *ChemBioChem* **2019**, *20*, 576–586.
165. J. Li, L. Guo, Z. Tian, S. Zhang, Z. Xu, Y. Han, R. Li, Y. Li, Z. Liu, *Inorg. Chem.* **2018**, *57*, 13552–13563.
166. J. Li, Z. Tian, X. Ge, Z. Xu, Y. Feng, Z. Liu, *Eur. J. Med. Chem.* **2019**, *163*, 830–839.
167. Z. Zhao, R. Hu, H. Shi, Y. Wang, L. Ji, P. Zhang, Q. Zhang, *J. Inorg. Biochem.* **2019**, *194*, 19–25.
168. P. Zhang, Y. Yang, K. Qiu, Z. Zhao, R. Hu, C. He, Q. Zhang, H. Chao, *Chem. Commun.* **2017**, *53*, 12341–12344.
169. S. A. E. Omar, P. A. Scattergood, L. K. McKenzie, C. Jones, N. J. Patmore, A. J. H. M. Meijer, J. A. Weinstein, C. R. Rice, H. E. Bryant, P. I. P. Elliott, *Inorg. Chem.* **2018**, *57*, 13201–13212.
170. G.-N. Yu, J.-C. Huang, L. Li, R.-T. Liu, J.-Q. Cao, Q. Wu, S.-Y. Zhang, C.-X. Wang, W.-J. Mei, W.-J. Zheng, *RSC Adv.* **2018**, *8*, 30573–30581.

171. C. Liu, R. Zhang, W. Zhang, J. Liu, Y.-L. Wang, Z. Du, B. Song, Z. P. Xu, J. Yuan, *J. Am. Chem. Soc.* **2019**, *141*, 8462–8472.

172. Y. Yao, C.-L. Hou, Z.-S. Yang, G. Ran, L. Kang, C. Li, W. Zhang, J. Zhang, J.-L. Zhang, *Chem. Sci.* **2019**, *10*, 10170–10178.

173. S. Lin, H. Pan, L. Li, R. Liao, S. Yu, Q. Zhao, H. Sun, W. Huang, *J. Mater. Chem. C* **2019**, 7, 7893–7899.

174. N.-N. Dong, M. Pedroni, F. Piccinelli, G. Conti, A. Sbarbati, J. E. Ramirez-Hernandez, L. M. Maestro, M. C. Iglesias-de la Cruz, F. Sanz-Rodriguez, A. Juarranz, F. Chen, F. Vetrone, J. A. Capobianco, J. G. Sole, M. Bettinelli, D. Jaque, A. Speghini, *ACS Nano* **2011**, *5*, 8665–8671.

175. Y. Liu, D. Tu, H. Zhu, X. Chen, *Chem. Soc. Rev.* **2013**, *42*, 6924–6958.

176. H. Dong, S.-R. Du, X.-Y. Zheng, G.-M. Lyu, L.-D. Sun, L.-D. Li, P.-Z. Zhang, C. Zhang, C.-H. Yan, *Chem. Rev.* **2015**, *115*, 10725–10815.

177. G. Zhu, L. Chen, F. Zeng, L. Gu, X. Yu, X. Li, J. Jiang, G. Guo, J. Cao, K. Tang, H. Zhu, H. E. Daldrup-Link, M. Wu, *ACS Omega* **2019**, *4*, 15806–15814.

178. L. Wang, M. Liu, Y. Chen, *J. Biomed. Techn.* **2018**, *14*, 1898–1905.

179. Y. Feng, Q. Xiao, Y. Zhang, F. Li, Y. Li, C. Li, Q. Wang, L. Shi, H. Lin, *J. Mater. Chem. B* **2017**, *5*, 504–510.

180. Y. Li, F. Li, Y. Huang, H. Wu, J. Wang, J. Yang, Q. Xiao, H. Lin, *RSC Adv.* **2019**, *9*, 18070–18075.

181. X. Song, S. Li, H. Guo, W. You, X. Shang, R. Li, D. Tu, W. Zheng, Z. Chen, H. Yang, X. Chen, *Angew. Chem. Int. Ed.* **2019**, *58*, 18981–18986.

182. C. Cao, Q. Liu, M. Shi, W. Feng, F. Li, *Inorg. Chem.* **2019**, *58*, 9351–9357.

183. X. Wang, J. Shi, P. Li, S. Zheng, X. Sun, H. Zhang, *J. Lumin.* **2019**, *209*, 420–426.

184. D. González Mancebo, A. I. Becerro, A. Corral, M. Moros, M. Balcerzyk, J. M. d. l. Fuente, M. Ocaña, *ACS Omega* **2019**, *4*, 765–774.

185. C.-C. Hsu, S.-L. Lin, C. A. Chang, *ACS Appl. Mater. Interfaces* **2018**, *10*, 7859–7870.

186. X. Zhong, X. Wang, G. Zhan, Y. a. Tang, Y. Yao, Z. Dong, L. Hou, H. Zhao, S. Zeng, J. Hu, L. Cheng, X. Yang, *Nano Lett.* **2019**, *19*, 8234–8244.

187. K. D. Addisu, W.-H. Hsu, B. Z. Hailemeskel, A. T. Andrgie, H.-Y. Chou, C.-H. Yuh, J.-Y. Lai, H.-C. Tsai, *ACS Biomater. Sci. Eng.* **2019**, *5*, 5453–5469.

188. J. Wang, N. Huang, Q. Peng, X. Cheng, W. Li, *Mater. Chem. Phys.* **2020**, *239*, 121994.

189. A. Picot, A. D'Aleo, P. L. Baldeck, A. Grichine, A. Duperray, C. Andraud, O. Maury, *J. Am. Chem. Soc.* **2008**, *130*, 1532–1533.

190. A. D'Aleo, A. Picot, P. L. Baldeck, C. Andraud, O. Maury, *Inorg. Chem.* **2008**, *47*, 10269–10279.

191. F. Auzel, *J. Lumin.* **1990**, *45*, 341–345.

192. Z. Li, S. Lv, Y. Wang, S. Chen, Z. Liu, *J. Am. Chem. Soc.* **2015**, *137*, 3421–3427.

193. C. Chen, F. Wang, S. Wen, Q. P. Su, M. C. L. Wu, Y. Liu, B. Wang, D. Li, X. Shan, M. Kianinia, I. Aharonovich, M. Toth, S. P. Jackson, P. Xi, D. Jin, *Nature Comm.* **2018**, *9*, 3290.

194. J. Zhou, Q. Liu, W. Feng, Y. Sun, F. Li, *Chem. Rev.* **2015**, *115*, 395–465.

195. E. K. Lim, T. Kim, S. Paik, S. Haam, Y. M. Huh, K. Lee, *Chem. Rev.* **2015**, *115*, 327–394.

196. G. Y. Chen, H. L. Qju, P. N. Prasad, X. Y. Chen, *Chem. Rev.* **2014**, *114*, 5161–5214.

197. O. S. Wolfbeis, *Chem. Soc. Rev.* **2015**, *44*, 4743–4768.

198. C. Hao, X. Wu, M. Sun, H. Zhang, A. Yuan, L. Xu, C. Xu, H. Kuang, *J. Am. Chem. Soc.* **2019**, *141*, 19373–19378.

199. M. Zhao, R. Wang, B. Li, Y. Fan, Y. Wu, X. Zhu, F. Zhang, *Angew. Chem. Int. Ed.* **2019**, *58*, 2050–2054.

200. Y. Li, R. Wang, W. Zheng, Y. Li, *Inorg. Chem.* **2018**, *57*, 12166–12173.

201. Y. Li, R. Wang, W. Zheng, Y. Li, *Inorg. Chem.* **2019**, *58*, 8230–8236.

202. H. Deng, S. Huang, C. Xu, *Talanta* **2018**, *184*, 461–467.

203. M. Yuan, R. Wang, C. Zhang, Z. Yang, X. Yang, K. Han, J. Ye, H. Wang, X. Xu, *Nanoscale Res. Lett.* **2019**, *14*, 103–103.

204. A. Das, C. Mao, S. Cho, K. Kim, W. Park, *Nature Comm.* **2018**, *9*, 4828.

205. E. Ruggiero, S. Alonso-de Castro, A. Habtemariam, L. Salassa, *Dalton Trans.* **2016**, *45*, 13012–13020.

206. S. Hao, G. Chen, C. Yang, W. Shao, W. Wei, Y. Liu, P. N. Prasad, *Nanoscale* **2017**, *9*, 10633–10638.

207. F. Ai, Q. Ju, X. Zhang, X. Chen, F. Wang, G. Zhu, *Sci. Rep.* **2015**, *5*, 10785.

208. H. V. Duong, T. T. L. Chau, N. T. T. Dang, F. Vanterpool, M. Salmeron-Sanchez, E. Lizundia, H. T. Tran, L. V. Nguyen, T.-D. Nguyen, *ACS Omega* **2018**, *3*, 86–95.

209. D. Chávez-García, K. Juárez-Moreno, C. H. Campos, J. B. Alderete, G. A. Hirata, *J. Mater. Res.* **2017**, *33*, 191–200.

210. R. Tian, S. Zhao, G. Liu, H. Chen, L. Ma, H. You, C. Liu, Z. Wang, *Biomaterials* **2019**, *212*, 64–72.

211. M. Wang, T. Zhang, Y. Hu, Y. Qin, W. Wei, *ChemPhotoChem* **2019**, *3*, 145–150.

212. D. Li, S. He, Y. Wu, J. Liu, Q. Liu, B. Chang, Q. Zhang, Z. Xiang, Y. Yuan, C. Jian, A. Yu, Z. Cheng, *Adv. Sci.* **2019**, *6*, 1902042.

213. T. Liang, Z. Li, P. Wang, F. Zhao, J. Liu, Z. Liu, *J. Am. Chem. Soc.* **2018**, *140*, 14696–14703.

214. X. Song, J. Zhang, Z. Yue, Z. Wang, Z. Liu, S. Zhang, *Anal. Chem.* **2017**, *89*, 11021–11026.

215. R. Zhang, L. Liang, Q. Meng, J. Zhao, H. T. Ta, L. Li, Z. Zhang, Y. Sultanbawa, Z. P. Xu, *Small* **2019**, *15*, e1803712.

216. L. Yang, K. Zhang, S. Bi, J.-J. Zhu, *ACS Appl. Mater. Interfaces* **2019**, *11*, 38459–38466.

217. Y. Shi, Q. Liu, W. Yuan, M. Xue, W. Feng, F. Li, *ACS Appl. Mater. Interfaces* **2019**, *11*, 430–436.

218. Z. Yang, K. Y. Loh, Y.-T. Chu, R. Feng, N. S. R. Satyavolu, M. Xiong, S. M. N. Huynh, K. Hwang, L. Li, H. Xing, X. Zhang, Y. R. Chelma, M. Gruebele, Y. Lu, *J. Am. Chem. Soc.* **2018**, *140*, 17656–17665.

219. X. Li, H. Zhao, Y. Ji, C. Yin, J. Li, Z. Yang, Y. Tang, Q. Zhang, Q. Fan, W. Huang, *ACS Appl. Mater. Interfaces* **2018**, *10*, 39544–39556.

220. N. Wang, X. Yu, K. Zhang, C. A. Mirkin, J. Li, *J. Am. Chem. Soc.* **2017**, *139*, 12354–12357.

221. X. Song, Z. Yue, J. Zhang, Y. Jiang, Z. Wang, S. Zhang, *Chem. Eur. J.* **2018**, *24*, 6458–6463.

222. G. Li, B. Yang, C. Gu, *J. Mater. Sci.* **2020**, *55*, 738–747.

223. D. Ling, H. Li, W. Xi, Z. Wang, A. Bednarkiewicz, S. T. Dibaba, L. Shi, L. Sun, *J. Mater. Chem. B* **2020**, *8*, 1316–1325.

224. C. Song, S. Zhang, Q. Zhou, L. Shi, L. Du, D. Zhi, Y. Zhao, Y. Zhen, D. Zhao, *RSC Adv.* **2017**, *7*, 26633–26639.

225. Y. Mi, H.-B. Cheng, H. Chu, J. Zhao, M. Yu, Z. Gu, Y. Zhao, L. Li, *Chem. Sci.* **2019**, *10*, 10231–10239.

226. D. Song, S. Chi, X. Li, C. Wang, Z. Li, Z. Liu, *ACS Appl. Mater. Interfaces* **2019**, *11*, 41100–41108.

227. B. Kumar, V. S. S. Rathnam, S. Kundu, N. Saxena, I. Banerjee, S. Giri, *ChemNanoMat* **2018**, *4*, 583–595.

228. Q. Sun, F. He, C. Sun, X. Wang, C. Li, J. Xu, D. Yang, H. Bi, S. Gai, P. Yang, *ACS Appl. Mater. Interfaces* **2018**, *10*, 33901–33912.

229. T. Jia, J. Xu, S. Dong, F. He, C. Zhong, G. Yang, H. Bi, M. Xu, Y. Hu, D. Yang, P. Yang, J. Lin, *Chem. Sci.* **2019**, *10*, 8618–8633.

230. J.-C. G. Bünzli, *Coord. Chem. Rev.* **2015**, *293–294*, 19–47.

231. A. de Bettencourt-Dias, in *Luminescence of Lanthanide Ions in Coordination Compounds and Nanomaterials*, Ed. A. de Bettencourt-Dias, John Wiley & Sons Ltd, Chichester, **2014**, pp. 1–48.

232. A. de Bettencourt-Dias, P. S. Barber, S. Bauer, *J. Am. Chem. Soc.* **2012**, *134*, 6987–6994.

233. J. H. S. K. Monteiro, N. R. Fetto, M. J. Tucker, A. de Bettencourt-Dias, *Inorg. Chem.* **2020**, *59*, 3193–3199.

234. J. Monteiro, D. Machado, L. M. de Hollanda, M. Lancellotti, F. A. Sigoli, A. de Bettencourt-Dias, *Chem. Commun.* **2017**, *53*, 11818–11821.

235. R. Arppe-Tabbara, M. R. Carro-Temboury, C. Hempel, T. Vosch, T. J. Sorensen, *Chemistry* **2018**, *24*, 11885–11889.

236. K. Singh, A. Goenka, S. Ganesh, A. K. Patra, *Eur. J. Inorg. Chem.* **2018**, *2018*, 3942–3951.

237. A. S. Kalyakina, V. V. Utochnikova, I. S. Bushmarinov, I. M. Le-Deygen, D. Volz, P. Weis, U. Schepers, N. P. Kuzmina, S. Brase, *Chemistry* **2017**, *23*, 14944–14953.

238. J.-C. G. Bünzli, *Chem. Rev.* **2010**, *110*, 2729–2755.

239. C. P. Montgomery, B. S. Murray, E. J. New, R. Pal, D. Parker, *Acc. Chem. Res.* **2009**, *42*, 925–937.

240. D. Xu, M. Liu, Q. Huang, J. Chen, H. Huang, F. Deng, Y. Wen, J. Tian, X. Zhang, Y. Wei, *Talanta* **2018**, *188*, 1–6.

241. E. P. Diamandis, *Clinical Biochem.* **1988**, *21*, 139–150.

242. T. Boltersdorf, J. Ansari, E. Y. Senchenkova, L. Jiang, A. J. P. White, M. Coogan, F. N. E. Gavins, N. J. Long, *Dalton Trans.* **2019**, *48*, 16764–16775.

243. Z. Du, J. Sun, C. A. Bader, D. A. Brooks, M. Li, X. Li, S. E. Plush, *J. Inorg. Biochem.* **2018**, *178*, 32–42.

244. N. Sayyadi, R. E. Connally, A. Try, *Chem. Commun.* **2016**, *52*, 1154–1157.

245. Y. Li, X. Li, Z. Xue, M. Jiang, S. Zeng, J. Hao, *Biomaterials* **2018**, *169*, 35–44.

246. Y. Yang, P. Wang, L. Lu, Y. Fan, C. Sun, L. Fan, C. Xu, A. M. El-Toni, M. Alhoshan, F. Zhang, *Anal. Chem.* **2018**, *90*, 7946–7952.

247. I. Martinić, S. V. Eliseeva, T. N. Nguyen, F. Foucher, D. Gosset, F. Westfall, V. L. Pecoraro, S. Petoud, *Chem. Sci.* **2017**, *8*, 6042–6050.

248. I. Martinic, S. V. Eliseeva, T. N. Nguyen, V. L. Pecoraro, S. Petoud, *J. Am. Chem. Soc.* **2017**, *139*, 8388–8391.

249. Y. Ning, S. Chen, H. Chen, J.-X. Wang, S. He, Y.-W. Liu, Z. Cheng, J.-L. Zhang, *Inorg. Chem. Front.* **2019**, *6*, 1962–1967.

250. Y. Ning, J. Tang, Y.-W. Liu, J. Jing, Y. Sun, J.-L. Zhang, *Chem. Sci.* **2018**, *9*, 3742–3753.

251. Y. Ning, S. Cheng, J.-X. Wang, Y.-W. Liu, W. Feng, F. Li, J.-L. Zhang, *Chem. Sci.* **2019**, *10*, 4227–4235.

252. Z. Tang, B. Song, H. Ma, T. Luo, L. Guo, J. Yuan, *Anal. Chem.* **2019**, *91*, 2939–2946.

253. X. Liu, B. Song, H. Ma, Z. Tang, J. Yuan, *J. Mater. Chem. B* **2018**, *6*, 1844–1851.

254. J. Sun, B. Song, Z. Ye, J. Yuan, *Inorg. Chem.* **2015**, *54*, 11660–11668.

255. H. Ma, X. Wang, B. Song, L. Wang, Z. Tang, T. Luo, J. Yuan, *Dalton Trans.* **2018**, *47*, 12852–12857.

256. X. Liu, L. Guo, B. Song, Z. Tang, J. Yuan, *Meth. Appl. Fluor.* **2017**, *5*, 014009.

257. L. Tian, H. Ma, B. Song, Z. Dai, X. Zheng, R. Zhang, K. Chen, J. Yuan, *Talanta* **2020**, *212*, 120760.

258. H. Ma, B. Song, Y. Wang, D. Cong, Y. Jiang, J. Yuan, *Chem. Sci.* **2017**, *8*, 150–159.

259. Z. Tang, B. Song, W. Zhang, L. Guo, J. Yuan, *Anal. Chem.* **2019**, *91*, 14019–14028.

260. Y. Wang, H. Wang, M. Yang, J. Yuan, J. Wu, *Opt. Mater.* **2018**, *75*, 243–251.

261. J. Wu, Y. Xing, H. Wang, H. Liu, M. Yang, J. Yuan, *New J. Chem.* **2017**, *41*, 15187–15194.
262. H. Ma, B. Song, Y. Wang, C. Liu, X. Wang, J. Yuan, *Dyes Pigm.* **2017**, *140*, 407–416.
263. M. Isaac, L. Raibaut, C. Cepeda, A. Roux, D. Boturyn, S. V. Eliseeva, S. Petoud, O. Seneque, *Chemistry* **2017**, *23*, 10992–10996.
264. T. Ren, W. Xu, Q. Zhang, X. Zhang, S. Wen, H. Yi, L. Yuan, X. Zhang, *Angew. Chem. Int. Ed.* **2018**, *57*, 7473–7477.
265. B. K. Agrawalla, H. W. Lee, W. H. Phue, A. Raju, J. J. Kim, H. M. Kim, N. Y. Kang, Y. T. Chang, *J. Am. Chem. Soc.* **2017**, *139*, 3480–3487.
266. W. Denk, J. H. Strickler, W. W. Webb, *Science* **1990**, *248*, 73–76.
267. F. Helmchen, W. Denk, *Nature Meth.* **2005**, *2*, 932–940.
268. T. N. Nguyen, F. M. Ebrahim, K. C. Stylianou, *Coord. Chem. Rev.* **2018**, *377*, 259–306.
269. C. Andraud, O. Maury, *Eur. J. Inorg. Chem.* **2009**, 4357–4371.
270. A. D'Aleo, A. Picot, A. Beeby, J. A. G. Williams, B. Le Guennic, C. Andraud, O. Maury, *Inorg. Chem.* **2008**, *47*, 10258–10268.
271. L. Dai, W.-S. Lo, Y. Gu, Q. Xiong, K.-L. Wong, W.-M. Kwok, W.-T. Wong, G.-L. Law, *Chem. Sci.* **2019**, *10*, 4550–4559.
272. J. B. Rabor, K. Kawamura, J. Kurawaki, Y. Niidome, *The Analyst* **2019**, *144*, 4045–4050.
273. A. D'Aleo, A. Bourdolle, S. Brustlein, T. Fauquier, A. Grichine, A. Duperray, P. L. Baldeck, C. Andraud, S. Brasselet, O. Maury, *Angew. Chem. Int. Ed.* **2012**, *51*, 6622–6625.
274. A. T. Bui, M. Beyler, A. Grichine, A. Duperray, J.-C. Mulatier, Y. Guyot, C. Andraud, R. Tripier, S. Brasselet, O. Maury, *Chem. Commun.* **2017**, *53*, 6005–6008.
275. A. T. Bui, A. Grichine, S. Brasselet, A. Duperray, C. Andraud, O. Maury, *Chem. Eur. J.* **2015**, *21*, 17757–17761.
276. H. Li, C. Xie, R. Lan, S. Zha, C.-F. Chan, W.-Y. Wong, K.-L. Ho, B. D. Chan, Y. Luo, J.-X. Zhang, G.-L. Law, W. C. S. Tai, J.-C. G. Bunzli, K.-L. Wong, *J. Med. Chem.* **2017**, *60*, 8923–8932.

14

Iridium(III) Complexes in Bio-Imaging Including Mitochondria

Cai-Ping Tan, Jie Wang, Liang-Nian Ji, and Zong-Wan Mao [*]

MOE Key Laboratory of Bioinorganic and Synthetic Chemistry, School of Chemistry,
Sun Yat-sen University, Guangzhou 510275, P. R. China
<cesmzw@mail.sysu.edu.cn>

Abstract: Fluorescence microscopic cell imaging is a very powerful tool in medicinal research and life sciences. Fluorescence microscopy can not only image different subcellular organelles such as nuclei, mitochondria and lysosomes, but also monitor the contents of metabolic species and cellular microenvironments. Many organic fluorescent probes for optical imaging have been commercialized in the past few decades. However, organic fluorescent probes have some disadvantages, such as relatively small Stokes shifts, low signal-to-noise ratio, obvious self-quenching, and intolerance of photobleaching, which make them unsuitable for long-term tracking of biological events. Compared with organic fluorescence probes, emissive transition metal iridium(III) complexes with low-spin d^6 electronic structure have been widely used as biosensors and imaging agents in recent years. They show good chemical and photo-physical properties including large Stokes shifts, high quantum yields, long fluorescence lifetimes, and high photo-stability. In this chapter, we will focus on the applications of iridium(III) complexes in biological imaging, especially in imaging of subcellular organelles including mitochondria, lysosomes, endoplasmic reticulum, and nuclei. In order to provide readers with a comprehensive understanding of the applications of iridium complexes in life sciences, we also give a brief introduction to the progress of iridium complexes as anticancer agents in recent years, especially the anticancer agents or photosensitizers targeting mitochondria.

Keywords: anticancer · iridium · mitochondrion · phosphorescent imaging · subcellular organelles

1. INTRODUCTION

Cell imaging techniques at subcellular resolution are very powerful tools in life sciences [1]. Fluorescence microscopy can not only image different subcellular organelles, such as the nuclei, mitochondria, and lysosomes, but also monitor metabolic species and cellular microenvironments [2]. Generally, fluorescence microscopy requires the use of cell imaging agents. Organic fluorophores for cell imaging have been developed rapidly over the past few decades, and many probes for optical imaging have been commercialized for various applications. It is worth noting that organic fluorescent probes have disadvantages [3]. First, the Stokes shift of organic molecules is relatively small. There are significant overlaps between their absorption and emission spectra, which results in a low signal-to-noise ratio and severe self-quenching during imaging. Due to concentration quenching, the brightness of the probes can be reduced when they aggregate in specific subcellular organelles. Second, due to the presence of endogenous fluorescent species, such as the indole group, nicotinamide, and tryptophan, it is difficult to distinguish the signals of the probes from those of the endogenous fluorescent substances [4]. Finally, organic molecules are intolerant to photobleaching, and some organic fluorescent probes display photobleaching effects in less than one minute, which makes them unsuitable for long-term observations [5].

Compared with organic fluorescent probes, emissive transition metal complexes with low-spin d^6 electronic structures, such as ruthenium(II) and iridium(III), have been widely used in biological sensing and imaging in recent years [6].

They show good chemo-physical properties and are ideal complementary probes alternative to organic molecules for cell imaging. In this chapter, we will focus on the applications of iridium(III) complexes in biological imaging, especially in the imaging of subcellular organelles including mitochondria.

2. STRUCTURES AND PHOSPHORESCENT PROPERTIES OF IRIDIUM COMPLEXES IN BIO-IMAGING

The ground state of iridium(III) complexes has singlet spin multiplicity, and they are triplet emitters. The strong spin-orbit coupling of the metal center stabilizes the energy from the singlet state to the triplet excited state, so the Stokes shifts of Ir(III) complexes are much larger than those of organic fluorescent molecules [7]. The large Stokes shifts ensure a lack of overlap between the absorption and emission profiles and greatly reduce the degree of concentration quenching. Since the spin selection rule prohibits the change in spin multiplicity, the radiative decay of Ir(III) complexes from the triplet excited state into a singlet ground state is forbidden. The characteristic excited-state lifetimes of Ir(III) complexes are usually longer than those of organic fluorophores [8]. Iridium(III) complexes decay in the time range of hundreds of nanoseconds, while the lifetimes of the spin-allowed fluorescence of organic molecules usually fall within ten nanoseconds, which is comparable to the lifetimes of endogenous fluorescent species in cells [9]. Lifetime imaging techniques can selectively capture the signals with long lifetimes, thereby significantly reducing the unwanted background fluorescence. Time-gated imaging of signals with several hundreds of nanoseconds can completely eliminate the cellular background fluorescence, and the method can ensure that the luminescence signal collected belongs to the Ir(III) complexes completely [10]. Lifetime imaging technology is particularly useful when the excitation and emission profiles of the probe overlap with those of the endogenous fluorescent substances.

Iridium(III) complexes are kinetically inert, which can reduce the photobleaching effects [11]. They are suitable for long-term observation of living cells without causing significant loss in photoluminescence. In addition, due to the resistance to ligand exchange, the cytotoxicity of Ir(III) complexes is relatively low, making them highly biocompatible [12]. However, on the other hand, the superior photophysical properties of Ir(III) complexes endow them with the capability to sensitize O_2 to produce reactive oxygen species (ROS) including singlet oxygen ($^1O_2$). Therefore, although Ir(III) complexes are non-toxic in the dark, a large amount of $^1O_2$ can be generated in living cells upon illumination, resulting in high photocytotoxicity. In fact, many studies have shown that Ir(III) complexes have high phototoxicity, which leads to their applications in photodynamic therapy (PDT) [13].

Among various iridium complexes, the applications of cyclometalated Ir(III) in the life sciences are currently the most widely investigated, especially as cellular probes and anticancer therapeutic agents. The basic structure of this kind of complexes includes an Ir(III) center coordinated to two cyclometalated ligands

(such as phenylpyridine) and a bidentate ligand (such as diimine). By changing the ligands, qualities such as molecular charge, lipophilicity, solubility, and photophysical properties can be adjusted. At present, through structural optimization, an iridium complex can achieve emission in the entire visible spectrum, with some of them emitting light in the near-infrared (NIR) region [14].

In order to achieve a specific biological behavior, researchers usually use two strategies to design the structures of metal complexes. The first method is to introduce a targeting vector on the complexes. For example, the triphenylphosphine group or mitochondrial targeting polypeptides are often used to design complexes localized in mitochondria [15, 16]. In order to image a specific intracellular biological species, selective recognition groups need to be coupled into the structures of the complexes to achieve switch-on or ratiometric responses in the fluorescence signals [17]. Of course, rational design is not always feasible because the intracellular environments are complex. For another strategy, complexes may not have structural selectivity, but their biological behaviors can be clarified by studying the structure-activity relationship (SAR). Charge, lipophilicity, and solubility are key factors usually involved in SAR studies of Ir(III) complexes [18]. The elucidation of the SAR will help to design complexes for future applications. The disadvantage of this method is that the SAR may only be suitable for small sub-libraries of complexes with similar chemical properties. It should also be noted that the specific cell lines, drug concentrations, incubation times, and imaging protocols used by different laboratories can vary. We will focus on describing the special chemical properties of cyclometalated Ir(III) complexes, and also clarify the use of these complexes in imaging of subcellular organelles, including mitochondria, lysosomes, endoplasmic reticulum (ER), and nucleus.

3.   IRIDIUM COMPLEXES AS MITOCHONDRIAL IMAGING AGENTS

3.1.   Static Imaging and Dynamic Tracking of Mitochondrial Morphology

Mitochondria are the energy factories of a cell and play key roles in material metabolism and cell death regulation [19]. Recent studies have shown that mitochondria are highly dynamic organelles. Under metabolic and environmental stress, mitochondria change their number, size, shape, and distribution within the cytoplasm [20]. The dynamic properties of mitochondria are closely related to various diseases, such as Parkinson's disease, Alzheimer's disease, neurodegeneration, and cancer.

Fluorescent proteins and organic dyes are widely used to image mitochondria [14]. As mentioned earlier, they possess poor photostability and are not suitable for long-term tracking of dynamic mitochondria. Iridium complexes have been widely used in static imaging and dynamic tracking of mitochondria in recent
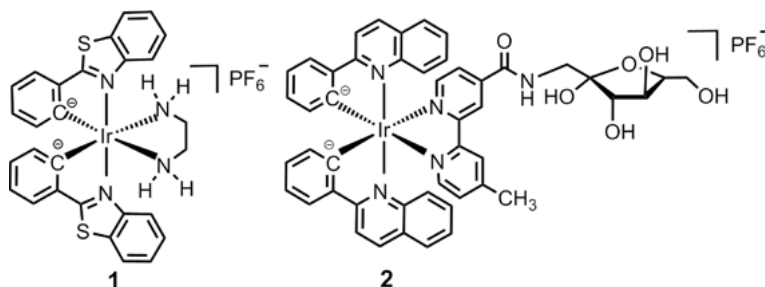
Structures 1 and 2.

years [15]. Interestingly, some Ir(III) complexes have intrinsic characteristics improving their reliability as mitochondrial targeting agents. For example, Lo et al. [21] reported the first usage of iridium complexes ($[Ir(bt)_2(en)]^+$ (**1**, en = ethylenediamine, bt = 2-phenylbenzothiazole) for mitochondrial imaging in 2012. The signals of the five iridium complexes they reported can well overlap with the signals of commercial mitochondrial dyes. These complexes do not contain targeting groups and are localized to mitochondria by their inherent characteristics. Subsequently, Lo's group designed a series of Ir(III) complexes containing fructose groups in order to increase their specific uptake by cancer cells. Complex **2** containing a fructose moiety can be transported into breast cancer MCF-7 cells by the GLUT5-mediated pathway [22].

Low cytotoxicity and high photostability are required for the long-term observation of dynamic mitochondria. Chao et al. [23] reported four phosphorescent Ir(III) complexes (**3–6**) with tunable emission colors that can specifically image mitochondria and track the dynamics of the mitochondrial morphology over long periods of time. Notably, **3–6** display some advantage over commercially available mitochondria-specific dyes, as they can stain mitochondria in both live and
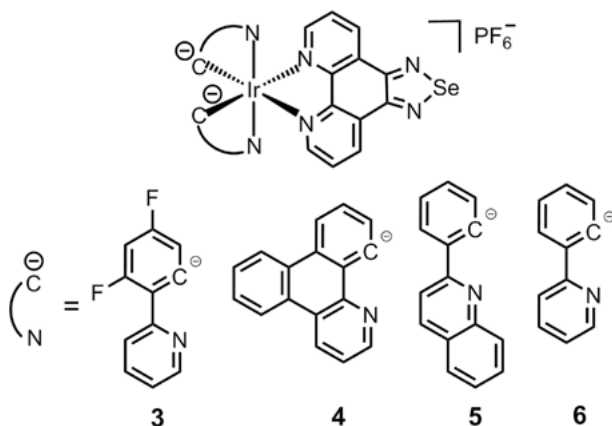
Structures 3–6.
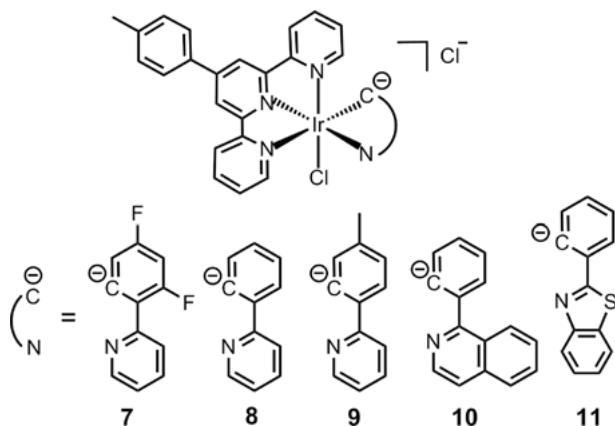
Structures 7–11.

fixed cells without prior membrane permeabilization or the replacement of the culture medium. Moreover, **3**–**6** possess superior photostability and are not sensitive to the loss of mitochondrial membrane potential (MMP) and the environmental change.

In addition to Ir complexes containing three bidentate ligands, other coordination structures have also been investigated as mitochondrial imaging agents. Chao et al. [24] reported five cyclometalated Ir(III) complexes (**7**–**11**) as mitochondria-targeted one- and two-photon phosphorescent probes for real-time imaging and tracking of mitochondrial fission and fusion. These complexes contain a tripyridine derivative and a cyclometalated ligand. **8** can track the processes of mitochondrial fission and fusion in a real-time manner with significantly simplified staining procedures as compared with commercial dyes.

As a key tool for biological imaging, NIR (emission or excitation wavelength greater than 650 nm) probes can improve tissue permeability and minimize self-fluorescence [25]. Chao et al. [14] selected 3-methyl-2-phenylquinoline as the main ligand to construct a series of two-photon excited, NIR-emitting multimodal phosphorescent imaging agents for mitochondria. Complexes **12**–**17** are able to accumulate in mitochondria and exhibit long phosphorescent lifetimes that can be applied for two-photon excited phosphorescence lifetime imaging microscopy (TPPLIM).

According to the "diffraction limit theory", the resolution limit of optical imaging is about half of the detection wavelength [26]. The wavelength range of visible light is 400–700 nm, so the resolution limit is about 200–300 nm. The theoretical and physical limit was "broken" by a series of ultra-high resolution microscopy technologies including stimulated emission microscopy, structured illumination microscopy (SIM) and stochastic optical reconstruction microscopy [27]. Chao et al. [28] discovered that an Ir(III) complex **18** can be used to track mitochondrial dynamics under SIM. The dye provides a mitochondrial image with ≈ 80 nm resolution. The structure of mitochondrial cristae can be clearly
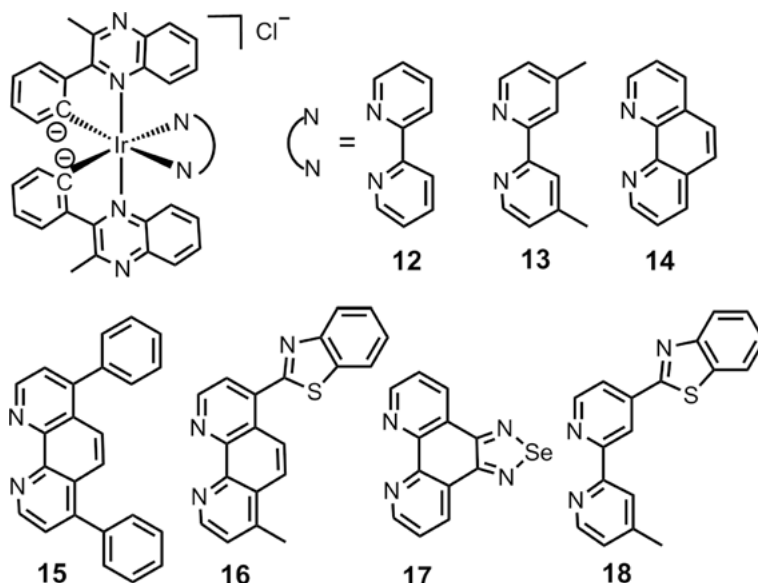
Structures 12–18.

observed and the dynamic fission and fusion of mitochondria can be recorded. Moreover, **18** can also be used to quantitatively study the functional crosstalk between mitochondria and lysosomes.

3.2. Imaging of Metal Ions and Small Signaling Molecules on Mitochondria

The structures of phosphorescent Ir(III) complexes can be easily modified by introducing specific recognition groups for metal ions and small signaling molecules. Similar to fluorescence lifetime imaging, phosphorescence lifetime imaging microscopy (PLIM) can directly measure the changes in the lifetime of the sensors in the presence of the analysts [9]. In this section, we will briefly introduce the application of iridium complexes for imaging small signaling molecules and cellular microenvironments.

He et al. [29] designed a phosphorescent cyclometalated Ir(III) complex (**19**) that displays a specific Zn^{2+}-induced enhancement of the phosphorescence quantum yield and lifetime. Furthermore, Zn^{2+}-induced phosphorescence lifetime enhancement is not affected by the lipophilicity, viscosity, and polarity of the medium. Considering the O_2-independent Zn^{2+}-induced enhancement in lifetime, **19** shows specific advantage in tracking Zn^{2+} in mitochondria. Moreover, the endogenous labile Zn^{2+} fluctuation in mitochondria triggered by S-nitrosocysteine stimulation can be visualized by **19** via PLIM.
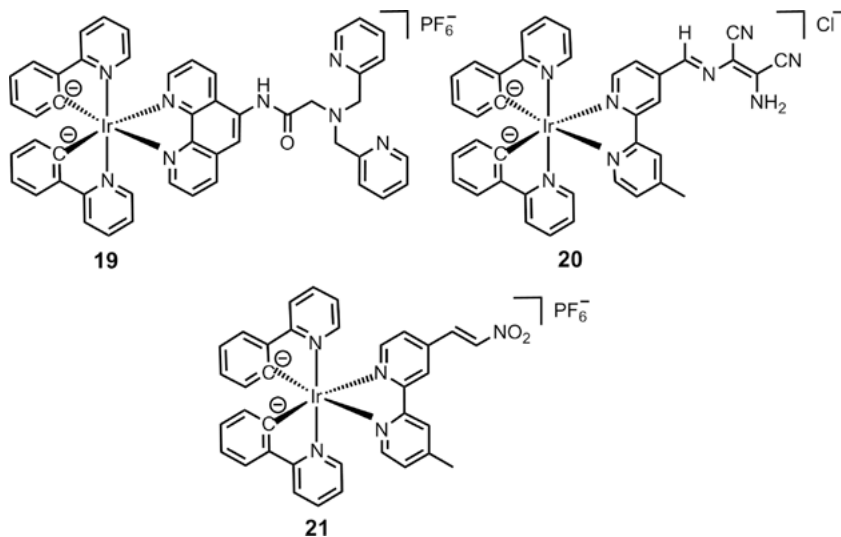
Structures 19–21.

Chao et al. [30] reported an Ir(III) complex-based two-photon phosphorescent mitochondrial hypochlorite ion probe, **20**. The complex reacts with ClO$^-$ to form an oxidized carboxylate product, which is highly selective for ClO$^-$ over other ions and ROS. **20** selectively localizes to mitochondria, and a significant enhancement in phosphorescence intensity indicates the presence of ClO$^-$ in mitochondria.

Yuan et al. [31] reported an Ir(III) complex **21** for phosphorescence/time-gated luminescence detection of cysteine (Cys) *in vitro* and *in vivo*. The complex shows high sensitivity and selectivity for Cys over other amino acids. Moreover, it accumulates in mitochondria after cellular internalization, and thus, one can monitor the mitochondrial Cys levels and Cys-mediated redox activities of live cells. **21** can image Cys levels in *D. magna*, zebrafish, and live mice.

3.3. Imaging of Mitochondrial Hypoxia

The abnormal proliferation of cancer cells will produce a local hypoxic microenvironment. It is very important to develop specific and sensitive hypoxic molecular probes for tumor diagnosis [32]. Phosphorescent metal complexes (such as platinum, iridium, and ruthenium complexes) can be used as hypoxia probes in a non-destructive, reversible, and real-time way [33].

Chao et al. [34] reported four iridium(III) complexes, **22–25**, for mitochondria imaging in hypoxic tumor cells. Under hypoxia, the phosphorescence of **22–25** was restored. When the probes are reduced by reductase to hydroquinone derivative products under hypoxia, the intensity of the emissions increases dramatical-
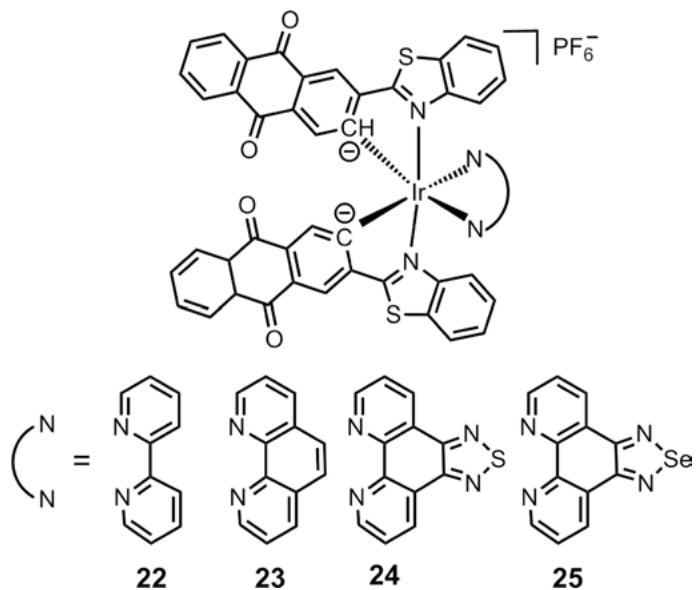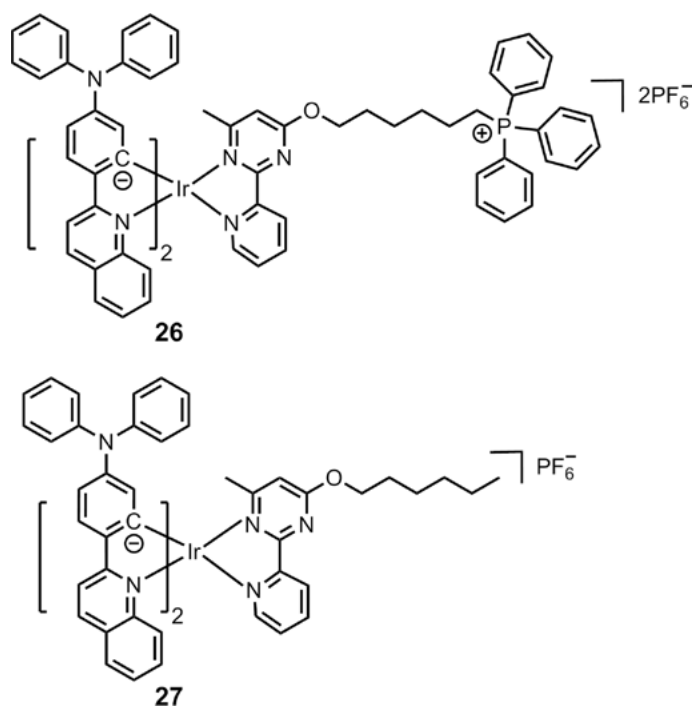
Structures 22–25.

Structures 26 and 27.

ly. More importantly, these probes can track mitochondrial morphological changes under a hypoxic environment over a long period of time.

Hypoxia can not only affect the optical properties of the complexes, but also their therapeutic effects. Huang et al. [35] reported the two Ir(III) complexes **26** and **27** that could specifically target mitochondria and lysosomes, respectively. Interestingly, they found that the mitochondria-targeted complex **26** was a more potent photosensitizer (PS) than the lysosome-targeted complex **27**, particularly under hypoxic conditions. The reason is that the mitochondria-targeted PS inhibits mitochondrial respiration, resulting in a higher intra-mitochondrial oxygen content, especially under hypoxia conditions.

4. IRIDIUM COMPLEXES AS MITOCHONDRIA-TARGETED ANTICANCER AGENTS

4.1. Cytotoxic Agents in the Dark

Iridium complexes have also attracted great interests as anticancer agents [36]. Compared with clinically used platinum complexes with square-planar structure, octahedral iridium complexes have the characteristics of easy modification, which makes them rich in molecular structure diversity and biological activities [37]. One of the obvious advantages of phosphorescent iridium complexes as anticancer drugs is that they can be developed into multifunctional anticancer agents with both anticancer and imaging functions.

In early studies, phosphorescent Ir complexes were mainly reported as biological sensing or imaging probes [38]. However, it was found that the structures of iridium complexes could be tuned to highly cytotoxic substances, which inspired researchers to study their anticancer properties [37]. Mao and Tan et al. [39] reported three cyclometalated Ir(III) complexes (**28–30**) bearing bis N-heterocyclic carbene ligands as theranostic and photodynamic anticancer agents targeting mitochondria. Complexes **28–30** display much higher antiproliferative activities than cisplatin in various cancer cells including cisplatin-resistant human lung cancer A549 cells due to their ability of initiating a cascade of events related to mitochon-
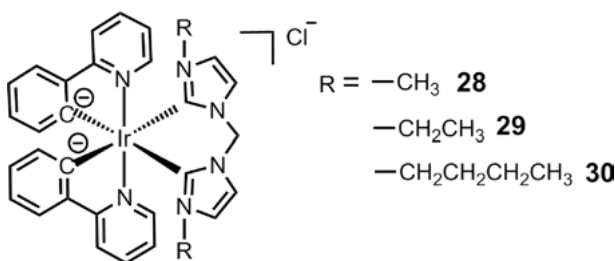
Structures 28–30.
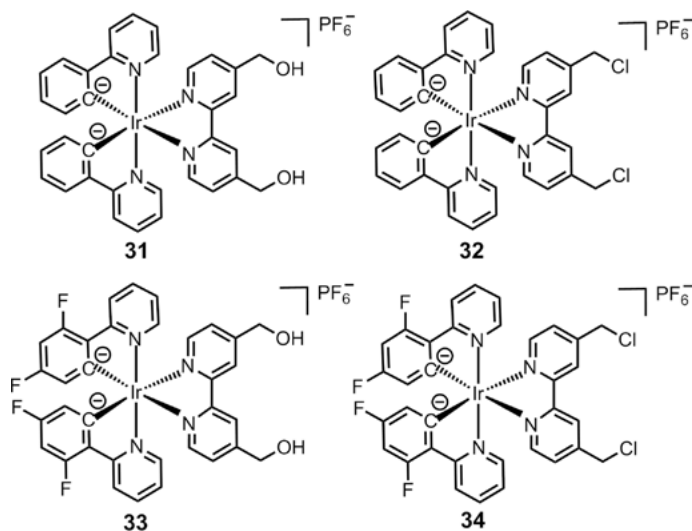
Structures 31–34.

drial dysfunction. Particularly, **30** can be used as a novel theranostic agent by inducing and real-time tracking the changes in mitochondrial morphology.

In recent years, many researchers have shown that targeting mitochondrial metabolism is an effective strategy to combat cancer. With these considerations in mind, Mao and Tan et al. [40] reported two mitochondria-immobilized phosphorescent cyclometalated Ir(III) complexes. Complexes **32** and **34**, containing reactive chloromethyl groups, can be fixed on mitochondria through nucleophilic substitution with reactive thiols at mitochondrial proteins. The strategy can improve the accumulation and retention of **32** and **34** on mitochondria, as compared with their counterparts (**31** and **33**) containing the hydroxymethyl groups. Mechanistic studies show that **32** and **34** mainly induce caspase- and ROS-mediated apoptotic cell death by attenuating the mitochondrial bioenergetic functions.

Multifunctional anticancer drugs that can kill cancer cells and visualize the physiological processes of cells simultaneously, attract the attention of many researchers [41]. Mitochondrial autophagy, termed mitophagy, is a typical example of the latter, which can selectively degrade damaged mitochondria. Mao and Tan et al. [42] reported two phosphorescent Ir(III) complexes (**35** and **36**) that can label mitochondria and induce mitophagy simultaneously. These complexes can specifically induce and track the morphological alterations in mitochondria during mitophagy, including the fusion process of mitochondria with autophagasomes as well as the engulfment of autophagasomes by lysosomes.

Many researchers have tried to combine mitochondria-targeted anticancer molecules with other drugs in order to achieve a synergistic effect. 4-hydroxy/amino-2,2,6,6-tetramethylpiperidine-N-oxyl (TEMPO) that is often used as a spin label can induce apoptosis by over-activating a variety of caspases [43]. Sadler et al. [44] designed octahedral cyclometalated Ir(III) complexes contain-
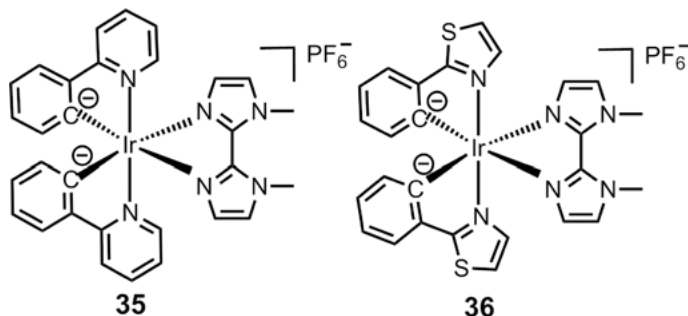
Structures 35 and 36.
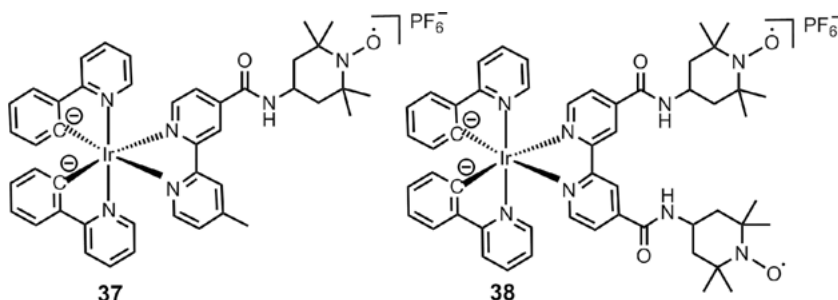
Structures 37 and 38.
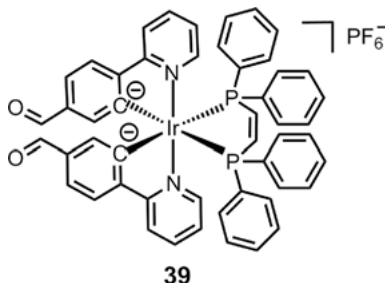
Structure 39.

ing one or two TEMPO substituents. Both **37** and **38** showed bright luminescence with long lifetimes (ca. 35–160 ns). There is spin–spin interaction between the TEMPO units in **38**. **37** and **38** located in mitochondria of PC3 prostate cancer cells. The anticancer activity of the bis-nitroxide complex **38** is much higher than that of **37** and it shows excellent selectivity for cancer cells over normal cells.

It is a great challenge to accurately and quantitatively measure the changes of microenvironmental parameters, such as viscosity, at the subcellular level. TPPLIM can quantitatively reflect the change in the microenvironment around

the fluorophores. Mao and Tan et al. [63] developed a series of Ir(III) complexes with rotating groups as quantitative probes for mitochondrial viscosity. Among them, **39** has a good two-photon absorption performance and viscosity-dependent long emission lifetime (up to 1 μs). Using the TPPLIM technology, **39** can induce mitochondrial dysfunction and quantitatively monitor the change in mitochondrial viscosity in a real-time manner.

4.2.   Photodynamic Therapeutic Anticancer Agents

Photodynamic therapy (PDT) is a promising alternative treatment to traditional chemotherapy for a variety of superficial tumors. PDT consists of two basic components: light and a photosensitizer (PS). With the participation of O_2, PS can transfer energy from light to molecular O_2, and produce cytotoxic ROS that can eventually cause cancer cell death. Rerouting PSs to subcellular organelles including mitochondria can improve the efficiency of PDT [45]. Many studies have shown that iridium complexes are very effective PSs, and they can target mitochondria to obtain high phototoxicity through novel action mechanisms [37].

   Lo et al. [46] reported a class of phosphorescent cyclometalated Ir(III) polypyridine poly(ethyleneglycol) (PEG) complexes (**40–44**) targeting mitochondria with tunable photodynamic activity. The $^1O_2$ production efficiency was highly related to the emission lifetimes of the complexes, which can be systematically controlled by changing the cyclometalating ligands. These complexes are not cytotoxic in the dark, yet they possess a high photo-induced cytotoxicity. They can facilitate efficient oxidative mitochondrial damage resulting in necrotic cell death upon photo-excitation.
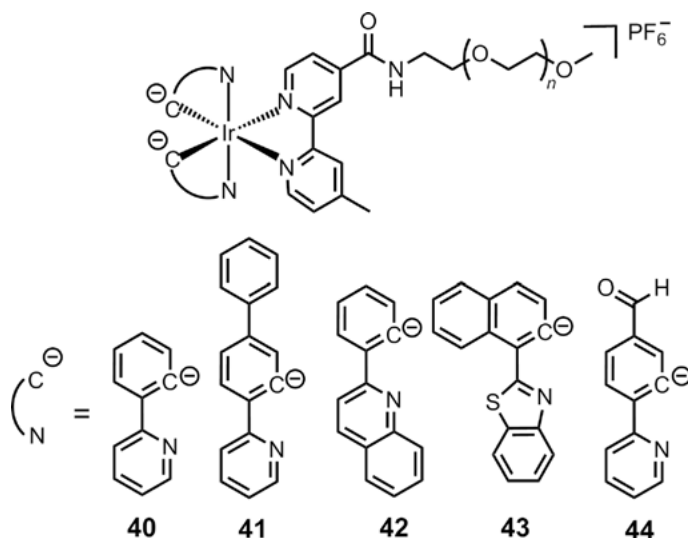
Structures 40–44.
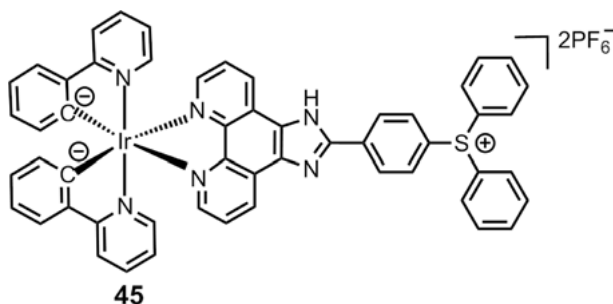
Structure 45.

In addition to photosensitization of ROS, there are other photolethal methods, and the combination of these methods may achieve better results. Mao et al. [47] designed a mitochondria-targeted dual-mode PDT agent, **45**. Light irradiation induces **45** to generate a photoacid. Photoacid and $^1O_2$ function together impair mitochondria and kill cancer cells effectively even under hypoxic conditions. **45** can make full use of the oxygen present in the tumor to induce $^1O_2$-related cancer cell death.

5. IRIDIUM COMPLEXES AS IMAGING AGENTS TARGETING OTHER SUBCELLULAR ORGANELLES

5.1. Lysosome

The lysosome was once considered to be a static organelle dedicated to the treatment and recovery of cellular waste. Recently, lysosome is found to be a highly dynamic structure, which mediates the adaptation of cell metabolism to environmental cues [48]. Lysosome-mediated signaling pathways and transcription processes can control the transition between anabolism and catabolism by sensing the state of cell metabolism [49]. Lysosomes also communicate with other subcellular organelles through the exchange of content and information and the establishment of membrane contact sites. More and more evidences show that lysosomal dysfunction plays an important role in human diseases, including neurodegenerative and metabolic diseases and cancer [50]. In summary, these findings highlight lysosomes as attractive potential therapeutic targets for a variety of diseases.

Mao and Tan et al. [51] developed the two Ir(III) complexes **46** and **47** as theranostic anticancer agents to monitor autophagic lysosomes. **47** can effectively implement two functions, namely autophagy induction and lysosomal tracking, to visualize the process of autophagosomal–lysosomal fusion. More importantly, **46** and **47** display marked two-photon absorption and emission properties, which can greatly enhance their sensitivity and expand their compatibility with other staining methods by minimizing the interference with the background noises and
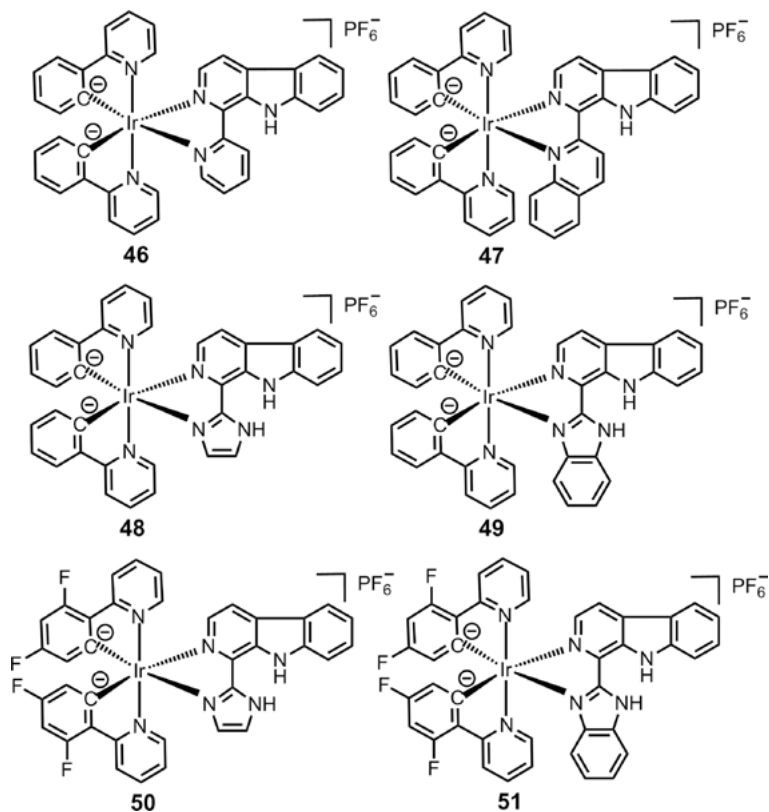
Structures 46–51.

other labeling agents. On the basis of this work, they tried to find lysosomal targeting PSs that are non-toxic under dark conditions [13]. They developed four cyclometalated Ir(III) complexes (**48–51**) with β-carboline ligands as lysosome-targeted and acidic pH-activatable cell imaging agents and PSs. Notably, complex **49** shows remarkable phototoxicity against cancer cells and high selectivity for cancer cells over normal cells. Mechanistic studies show that **49**-mediated PDT mainly induces caspase- and ROS-dependent apoptotic cell death through lysosomal damage. **49** can monitor the lysosomal integrity upon PDT, which provides a reliable and convenient method for *in situ* monitoring of the therapeutic effect and real-time assessment of treatment outcome.

Metastasis of malignant tumors is the main reason for the failure of tumor treatment [52]. PDT can eliminate solid tumors, but it cannot inhibit tumor metastasis. Mao et al. [53] developed four phosphorescent cyclometalated Ir(III) complexes, **52–55**, that can effectively inhibit several cancerous processes, including cell migration, invasion, colony formation, and angiogenesis. These complexes show a much higher $^1O_2$ quantum yield in an acidic solution than in a neutral solution, and they exhibit a high phototoxicity index, the highest being > 476.
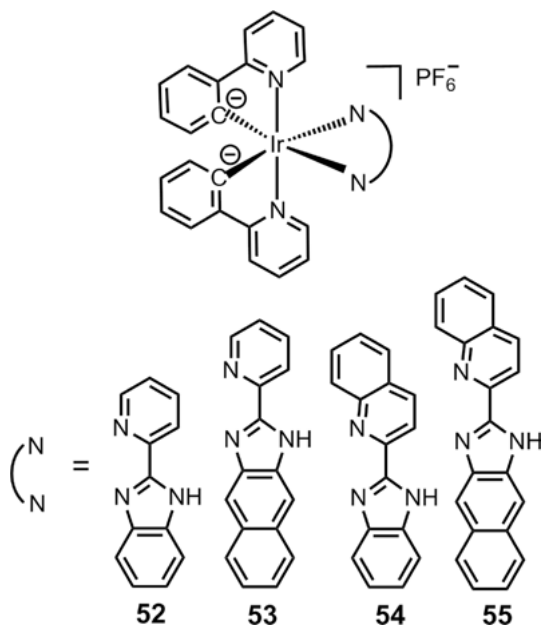
Structures 52–55.

5.2. Endoplasmic Reticulum

Hypoxia in tumor microenvironment can cause numerous unfolded or misfolded proteins to gather in the endoplasmic reticulum (ER), resulting in ER stress [54]. ER stress is an important self-defense mechanism of cells, which is closely related
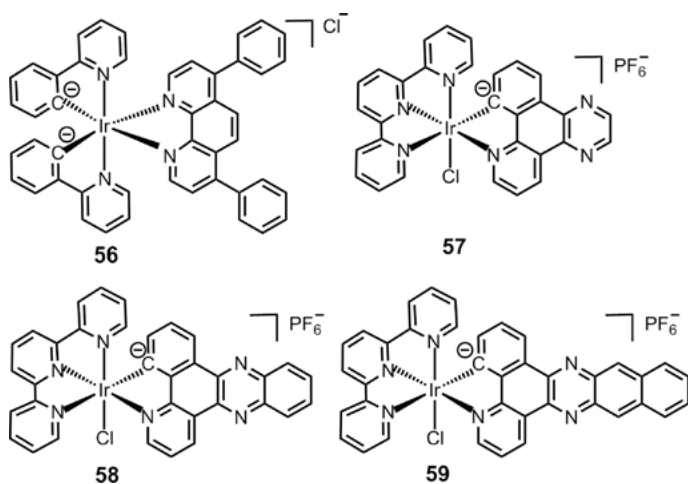
Structures 56–59.

to the occurrence and development of tumors [55]. Fei et al. [56] rationally designed a novel luminescent cationic Ir(III) complex **56** which prefers to accumulate in the ER and to cause ER stress in cells. This appears to be a main factor for triggering the rapid downstream events of mitochondria-mediated apoptosis in human cancer cells.

Chao et al. [57] rationally presented the three ER-targeted Ir(III) complexes **57–59** as PSs with a gradually extended conjugation area in the main ligand. Both their $^1O_2$ quantum yields and cytotoxicity increase along with the extent of conjugation area. Among them, **58** shows the highest photo-cytotoxicity index value. It can cause the up-regulation of the C/EBP homologous binding protein in a short period of time after PDT, which highlights its potential as an ER-localized PDT PS candidate.

5.3. Nucleus

The nucleus is the main site of genetic information storage in eukaryotic cells, where gene replication, transcription, and the processing of transcription products are carried out. The nucleus controls the genetic and metabolic activities of cells. Li et al. [58] reported a non-emissive cyclometalated Ir(III) solvent complex **60** as a non-nucleic acid-bonding fluorescence-enhanced nuclear stain. The complex specifically assembles in the nuclei of living cells and reacts with histidine/histidine-containing proteins to form a luminescent emissive product in the nuclei. **60** permeates the outer and nuclear membranes of living cells through an energy-dependent entry pathway in a very short time, accumulates in the nuclei and is converted into an intensely emissive adduct.
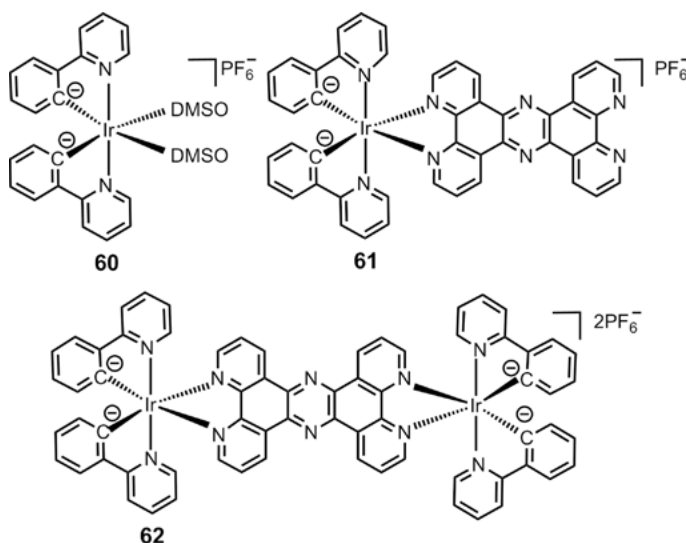
Structure 60–62.

Huang et al. [59] reported the two multifunctional phosphorescent Ir(III) complexes **61** and **62** with a long emission lifetime for specific nucleus staining and hypoxia monitoring. Taking advantage of the long emission lifetime of **61**, the influence of the auto-fluorescence of cells can be eliminated easily. The oxygen concentration is related to the emission intensity and lifetime of **63**, so that it can be applied to monitor O_2 levels in cancer cells.

6.   GENERAL CONCLUSIONS

In the last decade, researchers have made great progress on iridium complexes as bio-probes and cell-imaging agents, especially as mitochondrial imaging agents. Because of their inherent properties (e.g., positively charged and highly lipophilic), Ir(III) complexes tend to localize to mitochondria. Attributed to their outstanding photophysical properties, such as high emission quantum yields, long phosphorescence lifetimes, large Stokes shift, and high photo-stability, they are widely used as probes for the dynamic monitoring of mitochondrial behaviors, as well as imaging probes of small signaling species and microenvironmental parameters on mitochondria. At the same time, they can also be applied for PLIM. Many studies have also shown that iridium complexes are potential anticancer drugs, which can act through mechanisms different from those of platinum-based drugs. By structural modifications, Ir(III) complexes can also target other subcellular organelles including lysosomes, ER, and nuclei.

However, we should also note that many improvements are needed before Ir(III) complexes are ready for applications in the clinic: (1) Their mechanisms of action in cells, including transport and metabolism, is unknown. Their metabolic behavior *in vivo* is rarely studied, which provides obstacles for their further application in medical diagnosis and treatment. (2) Their molecular targets in cells are not clear. Because most of these complexes are not designed by targeting a specific biomolecule, the binding targets of them are unknown, which also leads to the randomness of results of their cellular behaviors. (3) At present, the structures of iridium complexes investigated for biomedical applications are very similar, and most of them are cyclometalated Ir(III) complexes. It is also of interest for researchers to explore the potential applications of iridium complexes with more diverse coordination structures.

ACKNOWLEDGMENTS

ABBREVIATIONS AND DEFINITIONS

Cys	cysteine
ER	endoplasmic reticulum
GLUT	glucose transporter
MMP	mitochondrial membrane potential
NIR	near-infrared
$^1O_2$	singlet oxygen
PDT	photodynamic therapy
PEG	poly(ethylene glycol)
PLIM	phosphorescence lifetime imaging microscopy
PS	photosensitizer
ROS	reactive oxygen species
SAR	structure-activity relationship
SIM	structured illumination microscopy
TEMPO	4-hydroxy/amino-2,2,6,6-tetramethylpiperidine-N-oxyl
TPPLIM	two-photon excited phosphorescence lifetime imaging microscopy

REFERENCES

1. T. L. Liu, S. Upadhyayula, D. E. Milkie, V. Singh, K. Wang, I. A. Swinburne, K. R. Mosaliganti, Z. M. Collins, T. W. Hiscock, J. Shea, A. Q. Kohrman, T. N. Medwig, D. Dambournet, R. Forster, B. Cunniff, Y. Ruan, H. Yashiro, S. Scholpp, E. M. Meyerowitz, D. Hockemeyer, D. G. Drubin, B. L. Martin, D. Q. Matus, M. Koyama, S. G. Megason, T. Kirchhausen, E. Betzig, *Science* **2018**, *360*, eaaq1392.

2. H. Zhu, J. L. Fan, J. J. Du, X. J. Peng, *Acc. Chem. Res.* **2016**, *49*, 2115–2126.

3. T. Terai, T. Nagano, *Curr. Opin. Chem. Biol.* **2008**, *12*, 515–521.

4. W. Becker, *J. Microsc.* **2012**, *247*, 119–136.

5. Q. S. Zheng, M. F. Juette, S. Jockusch, M. R. Wasserman, Z. Zhou, R. B. Altman, S. C. Blanchard, *Chem. Soc. Rev.* **2014**, *43*, 1044–1056.

6. A. M. H. Yip, K. K. W. Lo, *Coord. Chem. Rev.* **2018**, *361*, 138–163.

7. Q. Zhao, M. X. Yu, L. X. Shi, S. J. Liu, C. Y. Li, M. Shi, Z. G. Zhou, C. H. Huang, F. Y. Li, *Organometallics* **2010**, *29*, 1085–1091.

8. W. H. Wang, Z. F. Mao, M. D. Wang, L. J. Liu, D. W. J. Kwong, C. H. Leung, D. L. Ma, *Chem. Commun.* **2016**, *52*, 3611–3614.

9. W. Lv, T. S. Yang, Q. Yu, Q. Zhao, K. Y. Zhang, H. Liang, S. J. Liu, F. Y. Li, W. Huang, *Adv. Sci.* **2015**, *2*, 1500107.

10. L. Murphy, A. Congreve, L. O. Palsson, J. A. G. Williams, *Chem. Commun.* **2010**, *46*, 8743–8745.

11. C. H. Leung, H. J. Zhong, D. S. H. Chan, D. L. Ma, *Coord. Chem. Rev.* **2013**, *257*, 1764–1776.

12. K. K. W. Lo, *Acc. Chem. Res.* **2015**, *48*, 2985–2995.

13. L. He, Y. Li, C. P. Tan, R. R. Ye, M. H. Chen, J. J. Cao, L. N. Ji, Z. W. Mao, *Chem. Sci.* **2015**, *6*, 5409–5418.

14. C. Z. Jin, R. L. Guan, J. H. Wu, B. Yuan, L. L. Wang, J. J. Huang, H. Wang, L. N. Ji, H. Chao, *Chem. Commun.* **2017**, *53*, 10374–10377.

15. Y. Chen, T. W. Rees, L. N. Ji, H. Chao, *Curr. Opin. Chem. Biol.* **2018**, *43*, 51–57.

16. C. S. Burke, A. Byrne, T. E. Keyes, *Angew. Chem. Int. Ed.* **2018**, *57*, 12420–12424.

17. Q. Zhao, C. H. Huang, F. Y. Li, *Chem. Soc. Rev.* **2011**, *40*, 2508–2524.

18. K. K. W. Lo, K. Y. Zhang, *RSC Adv.* **2012**, *2*, 12069–12083.

19. H. Vakifahmetoglu-Norberg, A. T. Ouchida, E. Norberg, *Biochem. Biophys. Res. Commun.* **2017**, *482*, 426–431.

20. R. J. Youle, A. M. van der Bliek, *Science* **2012**, *337*, 1062–1065.

21. S. P. Y. Li, T. S. M. Tang, K. S. M. Yiu, K. K. W. Lo, *Chem. Eur. J.* **2012**, *18*, 13342–13354.

22. K. K. W. Lo, W. H. T. Law, J. C. Y. Chan, H. W. Liu, K. Y. Zhang, *Metallomics* **2013**, *5*, 808–812.

23. Y. Chen, L. P. Qiao, L. N. A. Ji, H. Chao, *Biomaterials* **2014**, *35*, 2–13.

24. H. Y. Huang, L. Yang, P. Y. Zhang, K. Q. Qiu, J. J. Huang, Y. Chen, J. J. Diao, J. K. Liu, L. N. Ji, J. G. Long, H. Chao, *Biomaterials* **2016**, *83*, 321–331.

25. S. Luo, E. Zhang, Y. Su, T. Cheng, C. Shi, *Biomaterials* **2011**, *32*, 7127–7138.

26. L. Schermelleh, A. Ferrand, T. Huser, C. Eggeling, M. Sauer, O. Biehlmaier, G. P. C. Drummen, *Nat. Cell Biol.* **2019**, *21*, 72–84.

27. E. F. Fornasiero, F. Opazo, *Bioessays* **2015**, *37*, 436–451.

28. Q. Chen, C. Jin, X. Shao, R. Guan, Z. Tian, C. Wang, F. Liu, P. Ling, J. L. Guan, L. Ji, F. Wang, H. Chao, J. Diao, *Small* **2018**, *14*, e1802166.

29. C. Zhang, M. Liu, S. Liu, H. Yang, Q. Zhao, Z. Liu, W. He, *Inorg. Chem.* **2018**, *57*, 10625–10632.

30. G. Li, Q. Lin, L. Sun, C. Feng, P. Zhang, B. Yu, Y. Chen, Y. Wen, H. Wang, L. Ji, H. Chao, *Biomaterials* **2015**, *53*, 285–295.

31. Z. Du, R. Zhang, B. Song, W. Zhang, Y. L. Wang, J. Liu, C. Liu, Z. P. Xu, J. Yuan, *Chem. Eur. J.* **2019**, *25*, 1498–1506.

32. A. L. Harris, *Nat. Rev. Cancer* **2002**, *2*, 38–47.

33. Z. Lv, L. Zou, H. J. Wei, S. J. Liu, W. Huang, Q. Zhao, *ACS Appl. Mater. Interfaces* **2018**, *10*, 19523–19533.

34. L. L. Sun, Y. Chen, S. Kuang, G. Y. Li, R. L. Guan, J. P. Liu, L. N. Ji, H. Chao, *Chem. Eur. J.* **2016**, *22*, 8955–8965.

35. W. Lv, Z. Zhang, K. Y. Zhang, H. Yang, S. Liu, A. Xu, S. Guo, Q. Zhao, W. Huang, *Angew. Chem. Int. Ed.* **2016**, *55*, 9947–9951.

36. Z. Liu, P. J. Sadler, *Acc. Chem. Res.* **2014**, *47*, 1174–1185.

37. A. Zamora, G. Vigueras, V. Rodriguez, M. D. Santana, J. Ruiz, *Coord. Chem. Rev.* **2018**, *360*, 34–76.

38. Y. H. Song, Y. C. Chiu, Y. Chi, Y. M. Cheng, C. H. Lai, P. T. Chou, K. T. Wong, M. H. Tsai, C. C. Wu, *Chem. Eur. J.* **2008**, *14*, 5423–5434.

39. Y. Li, C. P. Tan, W. Zhang, L. He, L. N. Ji, Z. W. Mao, *Biomaterials* **2015**, *39*, 95–104.

40. J. J. Cao, C. P. Tan, M. H. Chen, N. Wu, D. Y. Yao, X. G. Liu, L. N. Ji, Z. W. Mao, *Chem. Sci.* **2017**, *8*, 631–640.

41. R. Kumar, W. S. Shin, K. Sunwoo, W. Y. Kim, S. Koo, S. Bhuniya, J. S. Kim, *Chem. Soc. Rev.* **2015**, *44*, 6670–6683.

42. M. H. Chen, F. X. Wang, J. J. Cao, C. P. Tan, L. N. Ji, Z. W. Mao, *ACS Appl. Mater. Interfaces* **2017**, *9*, 13304–13314.

43. V. B. Arion, A. Dobrov, S. Goschl, M. A. Jakupec, B. K. Keppler, P. Rapta, *Chem. Commun.* **2012**, *48*, 8559–8561.

44. V. Venkatesh, R. Berrocal-Martin, C. J. Wedge, I. Romero-Canelon, C. Sanchez-Cano, J. I. Song, J. P. C. Coverdale, P. Zhang, G. J. Clarkson, A. Habtemariam, S. W. Magennis, R. J. Deeth, P. J. Sadler, *Chem. Sci.* **2017**, *8*, 8271–8278.

45. D. E. J. G. J. Dolmans, D. Fukumura, R. K. Jain, *Nat. Rev. Cancer* **2003**, *3*, 380–387.

46. S. P. Li, C. T. Lau, M. W. Louie, Y. W. Lam, S. H. Cheng, K. K. Lo, *Biomaterials* **2013**, *34*, 7519–7532.

47. L. He, M. F. Zhang, Z. Y. Pan, K. N. Wang, Z. J. Zhao, Y. Li, Z. W. Mao, *Chem. Commun.* **2019**, *55*, 10472–10475.
48. A. Ballabio, J. S. Bonifacino, *Nat. Rev. Mol. Cell Biol.* **2020**, *21*, 101–118.
49. R. E. Lawrence, R. Zoncu, *Nat. Cell Biol.* **2019**, *21*, 133–142.
50. D. J. Colacurcio, A. Pensalfini, Y. Jiang, R. A. Nixon, *Free Radic. Biol. Med.* **2018**, *114*, 40–51.
51. L. He, C. P. Tan, R. R. Ye, Y. Z. Zhao, Y. H. Liu, Q. Zhao, L. N. Ji, Z. W. Mao, *Angew. Chem. Int. Ed.* **2014**, *53*, 12137–12141.
52. N. Riggi, M. Aguet, I. Stamenkovic, *Annu. Rev. Pathol-Mech.* **2018**, *13*, 117–140.
53. F. X. Wang, M. H. Chen, Y. N. Lin, H. Zhang, C. P. Tan, L. N. Ji, Z. W. Mao, *ACS Appl. Mater. Interfaces* **2017**, *9*, 42471–42481.
54. J. R. Cubillos-Ruiz, S. E. Bettigole, L. H. Glimcher, *Cell* **2017**, *168*, 692–706.
55. M. Wang, R. J. Kaufman, *Nature* **2016**, *529*, 326–335.
56. R. Cao, J. L. Jia, X. C. Ma, M. Zhou, H. Fei, *J. Med. Chem.* **2013**, *56*, 3636–3644.
57. B. Yuan, J. P. Liu, R. T. Guan, C. Z. Jin, L. N. Ji, H. Chao, *Dalton Trans.* **2019**, *48*, 6408–6415.
58. C. Y. Li, M. X. Yu, Y. Sun, Y. Q. Wu, C. H. Huang, F. Y. Li, *J. Am. Chem. Soc.* **2011**, *133*, 11231–11239.
59. S. Liu, H. Liang, K. Y. Zhang, Q. Zhao, X. Zhou, W. Xu, W. Huang, *Chem. Commun.* **2015**, *51*, 7943–7946.

15

Imaging Bacteria with Contrast-Enhanced Magnetic Resonance

Casey J. Adams and Thomas J. Meade

Departments of Chemistry, Molecular Biosciences, Neurobiology, and Radiology,
Northwestern University, 2145 Sheridan Road, Evanston, IL 60208, USA
<tmeade@northwestern.edu>

Abstract: Bacteria play a two part role in contrast-enhanced magnetic resonance imaging (MRI). Pathogenic bacteria are an increasingly important biomedical imaging target as cases of antibiotic-resistant bacteria and hospital infection increase. However, certain bacteria have characteristics that make them ideal for use as diagnostic and theranostic MRI contrast agents. This chapter will review the roles bacteria play in contrast-enhanced MRI. First, targeted imaging strategies of bacteria are discussed (molecular and nanomaterial) followed by the ways in which bacteria and bacterial components have been used as contrast and theranostic

agents. We would like to point out that this area of MRI probes is rather embryonic and the number of reports in the literature limited.

1. INTRODUCTION

The ability to effectively detect and image bacteria continues to attract interest as a result of the number of increased cases of antibiotic-resistant bacteria and bacterial infection [1–3]. From a therapeutic standpoint, it is necessary to identify bacterial infections early and decisively in order to effectively treat patients. A *substantial* amount of research has focused on developing fluorescence and nuclear-based imaging probes (PET and SPECT) for imaging bacteria [4–6]. Recently, magnetic resonance imaging (MRI) has been exploited to image bacteria in whole animals.

MRI is the modality of choice for evaluating a number of diseases and is a staple of clinical diagnostic radiology due to its tunable soft-tissue contrast, high spatial and temporal resolution, and lack of ionizing radiation [7]. It is capable of true 3D imaging of biological structures at near-cellular resolution (~10 um) [8]. Detailed structural information in 3D can be obtained in minutes, and single slices in seconds [9–11]. Although MRI has a number of advantages, it cannot differentiate between bacterial infection and sterile inflammation [12, 13]. To overcome this limitation, contrast agents have been developed for contrast enhanced MRI of bacteria.

There are two distinct roles bacteria play in contrast-enhanced MRI. The bacteria can either be the target of a contrast agent, or they can be used *as* contrast agents. In the first case, bacteria-targeted MRI contrast agents are typically used as diagnostic or theranostic tools to identify and treat pathogenic bacteria. In the second case, whole bacteria, or parts of bacteria are used as contrast agents for a variety of applications from tumor targeting to cell tracking. This short review will highlight the various ways in which bacteria have been used in contrast-enhanced MRI, both as targets for labeling and contrast agents.

2. BACTERIA-TARGETED MAGNETIC RESONANCE IMAGING PROBES

To our knowledge, there are only a few reports of MRI contrast agents that target or label bacteria. These agents are designed to diagnose and treat bacterial infections while others are used to label bacteria for cell tracking applications. Generally speaking, bacteria-targeted MRI contrast agents can be divided into two types: molecular and nanomaterial agents.

2.1.   Molecular Approaches

There are very few examples of small molecule MRI contrast agents that target bacteria. A primary challenge is targeting bacteria with high specificity while simultaneously delivering enough of the agent to significantly enhance contrast. Meade and coworkers developed the first Gd(III) contrast agents coupled to Zn-dipicolylamine (Zn-dpa) complexes (Figure 1) [14]. The Zn-dpa moieties are cationic while the Gd(III) complex is neutral, therefore the agents take advantage of the negatively charged plasma membranes of bacteria compared to the near-neutral membranes of healthy mammalian cells.

More recently, Hu and coworkers developed a Gd(III) contrast agent coupled to neomycin, an aminoglycoside antibiotic that is toxic in both gram-positive and gram-negative bacteria (Figure 2) [15]. This theranostic agent increased the T_1 relaxation rate (R_1) of *Staphylococcus aureus* 11-fold *in vitro* and demonstrated pre-labeled cells could be detected *in vivo* without increasing contrast in macrophages. Compared with Gd-DOTA-prestained bacteria, the signal intensities
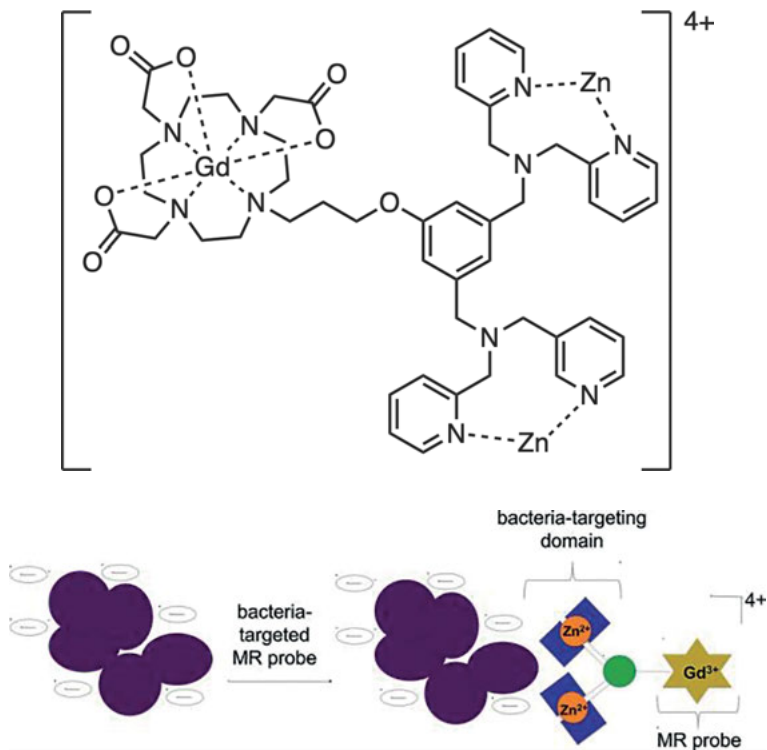
Figure 1.   Gd(III) MR contrast agent developed by Meade and coworkers using cationic Zn-dpa moieties to target the negatively charged plasma membrane of *S. aureus*. This agent shortened the T_1 of *S. aureus* by 21 % at 7 T and 44 % at 1.41 T, resulting in significant T_1-weighted contrast enhancement. Reproduced with permission from [14]; copyright 2012 John Wiley and Sons.
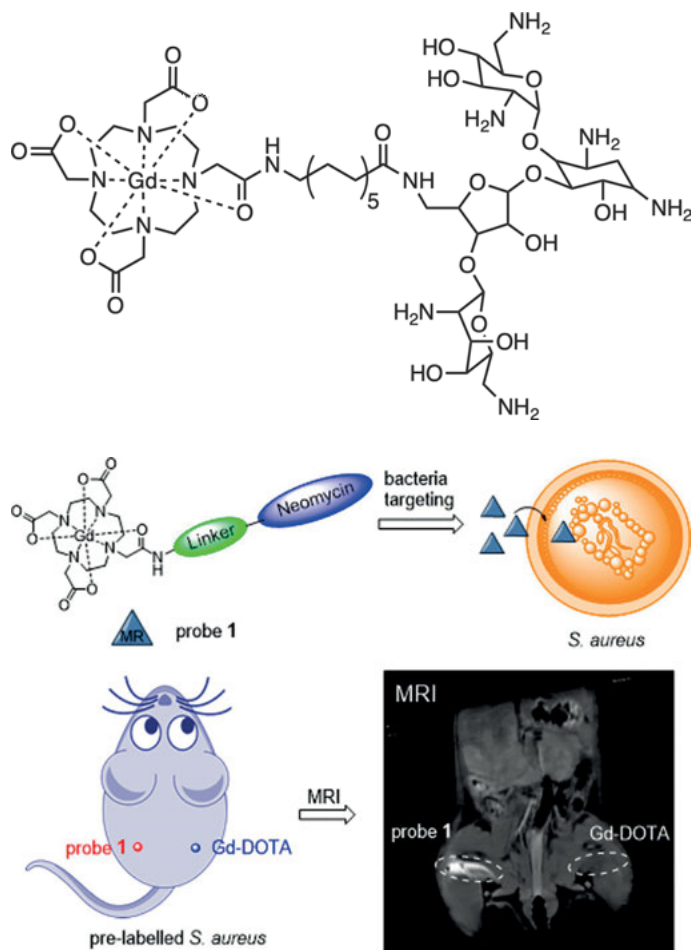
Figure 2. Gd(III)-neomycin conjugate developed by Hu and coworkers. Neomycin shows specificity for both Gram-positive and -negative bacteria over macrophage-like cells, allowing for T_1-weighted contrast enhancement in a number of cell types. Reproduced with permission from [15]; copyright 2018 American Chemical Society.

(SIs) increased by 53 % immediately after injection and 23 % 30 min after-administration of probe1-prestained bacteria. The signal was cleared within 4 h. This specificity for bacterial cells makes it a promising theranostic agent though further work is necessary to demonstrate its ability to diagnose bacterial infections *in vivo*.

2.2. Nanomaterial Approaches

Nanomaterial contrast agents have been more extensively used for contrast-enhanced MRI than molecular agents. Compared to molecular agents, nanomateri-

als allow for more versatile functionalization and deliver a much larger payload. Not surprisingly, whether molecular or nano, the targeting and labeling strategies of MR probes is largely the same.

Liu and coworkers developed amphiphilic star copolymers containing hydrophilic Gd(III) complexes and aggregation-induced emission (AIE) fluorophores (Figure 3) [16]. The positively charged portions of the material bind to the negatively charged bacterial membrane causing aggregation of the polymers. This aggregation results in a "turn-on" fluorescence signal from the AIE fluorophores while also inhibiting bacterial growth and replication. This multimodal theranostic nanomaterial was tested in both Gram-negative and Gram-positive bacteria (*Escherichia coli*, *Pseudomonas aeruginosa*, and *S. aureus*). In *E. coli*, the lead agent had a minimum inhibitory concentration (MIC) of 5.5 μg/mL and was capable of detecting ~5000 CFU/mL by MR *in vitro*, a remarkably low limit of detection.

Tan and coworkers developed magnetic graphitic nanocapsules (MGNs) that are capable of targeting *Heliobacter pylori*, a bacterium that can colonize and cause disease in the gastrointestinal (GI) tract [17]. Traditional contrast agents, such as Gd(III) complexes and superparamagnetic iron-oxide nanoparticles (SPIONs), are not compatible with the low pH found in the gastrointestinal tract. However, MGNs are stable under these conditions because the layers of graphite protect the magnetic FeCo core. When functionalized with PEG and boronic acid, these MGNs were able to target *H. pylori* by binding to peptidoglycan and enhance the observed T_2-weighted contrast *in vivo*. The MGNs had a low detection limit of ~2,000 CFU/mL of *H. pylori* and contrast enhancement was observed even after 7 days in mice.
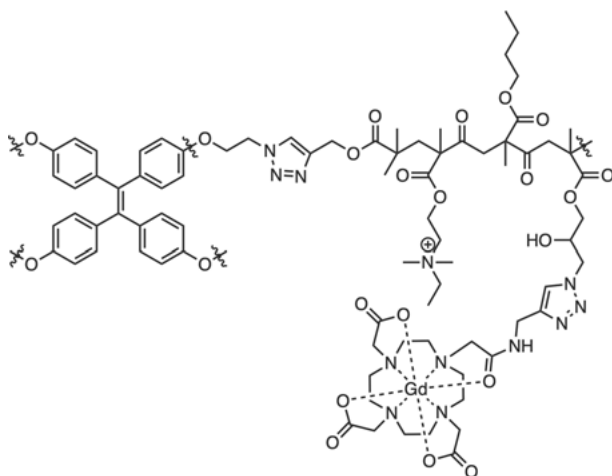
Figure 3. Amphiphilic star copolymers developed by Liu and coworkers [16]. The agent consists of an AIE moiety for "turn-on" fluorescence imaging and Gd(III) complexes for MR imaging and demonstrates antibacterial activity.

In addition to bacteria-targeted nanomaterials, there are examples of labeling bacteria with nanomaterials for cell tracking *and* theranostic applications. Faber and coworkers labeled *S. aureus* with iron-oxide nanoparticles through electrostatic interaction and were able to track infection *in vivo* [18]. Larson and coworkers also used iron-oxide nanoparticles to label *Clostridium novyi*-NT spores; however, the labeled spores were used as theranostics for bacteriolytic therapy of liver tumors [19]. By labeling with iron-oxide nanoclusters, they were able to monitor the distribution of spores, which are anaerobic and capable of colonizing the hypoxic tumor microenvironment. In this way, they could confirm colonization and monitor therapy for over a week by T_2-weighted MRI.

3.   EMPLOYING BACTERIA AS CONTRAST AGENTS

It is possible to use whole bacteria and bacterial components as MR contrast agents. Notably, magnetotactic bacteria, which produce magnetite (Fe_3O_4) in subcellular compartments called magnetosomes, have been used for T_2-weighted contrast enhancement [20, 21]. The use of magnetotactic bacteria and magnetosomes as MR contrast agents offers an alternative to using typical iron-oxide nanoparticles.

3.1.   Imaging Tumors with Magnetotactic Bacteria and Magnetosomes

There are several examples of magnetotactic bacteria and magnetosomes used as diagnostic and theranostic MRI contrast agents. Matin and coworkers showed that whole magnetotactic bacteria, *Magnetospirillum magneticum* AMB-1, were able to colonize tumors in mice and produce T_2-weighted contrast enhancement [22]. More commonly, magnetosomes are extracted from magnetotactic bacteria before being used as tumor-targeted contrast agents. These magnetosomes are commonly functionalized to display tumor-targeting groups. For instance, researchers have used EGFR and HER2 targeting peptides, pH low insertion peptide (pHLIP), and RGD/iRGD to target various different cancer types including breast cancer, melanoma, colon cancer, and glioblastoma [23–26]. Additionally, Sbarbati and coworkers used magnetosomes for magnetic fluid hyperthermia (MFH), which uses an alternating magnetic field to produce heat [27]. They were able to inhibit the growth of glioblastoma tumors using MFH while monitoring the effect of treatment by MRI. Though a promising theranostic platform, the inhomogeneous distribution of the magnetosomes in the tumors limited the efficacy.

The ability to functionalize magnetotactic bacteria and magnetosomes with a variety of groups makes them promising tools for contrast-enhanced MRI of tumors. Furthermore, there is significant potential to further develop these agents for theranostic applications (Figure 4) [25].
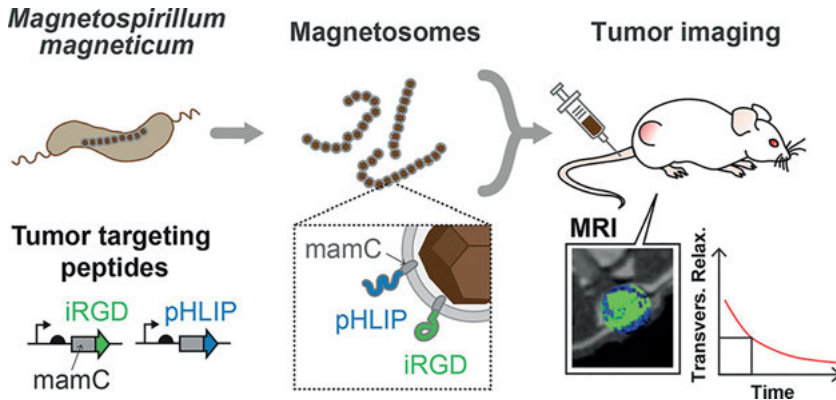
Figure 4. Schematic demonstrating the functionalization of magnetosomes with tumor-targeting peptides for T_2-weighted contrast-enhanced MRI of tumors. Whole magnetotactic bacteria or membranes surrounding magnetosomes can be functionalized. Reproduced with permission from [25]; copyright 2020 American Chemical Society.

3.2.   Cell Labeling with Magnetotactic Bacteria and Magnetosomes

Another common application for magnetotactic bacteria and magnetosomes is cell labeling and tracking of mammalian cells. Several groups have used whole magnetotactic bacteria, termed magneto-endosymbionts (MEs), to label and track a variety of cell types from cardiomyocytes to human breast cancer metastases [28–30]. These MEs were formed by internalization of *M. magneticum* AMB-1 and enhanced the T_2-weighted contrast of the labeled cells comparably to traditional iron-oxide nanoparticles. This strong T_2-weighted contrast enhancement enabled Rutt and coworkers to detect a minimum of 100 231-BR breast cancer cells *in vivo* in mice [28]. Surface modification of MEs allows them to remain and live in mammalian cells, making them promising tools for extended cell tracking. Furthermore, Yang and coworkers demonstrated that upon death of labeled cardiomyocytes in mice, MEs were cleared within one week while SPIONs remained for over two weeks [30] (Figure 5 [29]).

In addition to whole magnetotactic bacteria, researchers have also labeled mammalian cells with magnetosomes. This approach is analogous to using MEs, except that only the magnetosomes are used. This approach has been used to label and track macrophages to image inflammatory response to peritonitis in mice in a pilot *ex vivo* MRI study [31]. Additionally, magnetosomes have been coupled to near infrared fluorescent (NIRF) dyes to enable multimodal imaging of macrophages *in vitro* at a concentration of 600 cells/μL [32]. Though further work is necessary to demonstrate their *in vivo* utility, magnetosome-labeled macrophages can provide significant T_2-weighted contrast enhancement, making them promising probes for cell tracking applications.

Finally, in addition to directly labeling mammalian cells with magnetotactic bacteria and magnetosomes, several groups have used bacterial genes associated
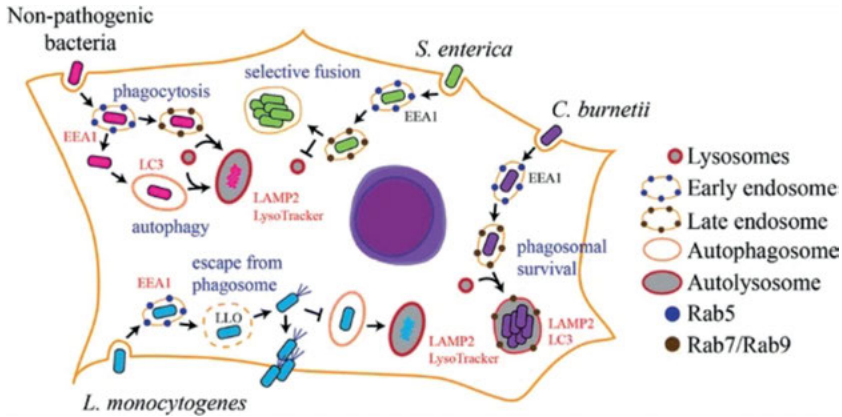
Figure 5. Schematic demonstrating interactions between bacterial cells and mammalian host cells. Magneto-endosymbionts (MEs) survive in host mammalian cells and enable long-term cell tracking by MRI. Reproduced with permission from [29]; copyright 2017 Springer Nature.

with magnetosome formation as reporter genes [33, 34]. MagA, a bacterial gene associated with iron transport, has been shown to enhance T_2-weighted contrast in transfected eukaryotic cells without loss of cell viability. The ability to detect the presence of MagA by MRI makes it a promising candidate as a reporter gene, as well as a tool for long-term cell tracking [21].

3.3.   Bacteria as Chemical Exchange Saturation Transfer Contrast Agents

An intriguing use of bacteria in contrast-enhanced MRI is with chemical exchange saturation transfer (CEST) MRI. Some bacteria inherently cause CEST contrast which researchers have termed bacCEST. Van Zijl and coworkers showed that the bacCEST from *C. novyi*-NT can be used to monitor germination of spores during bacteriolytic therapy of tumors [35]. While the spores do not behave as CEST contrast agents, they do upon germination, which provides a unique way of monitoring when *C. novyi*-NT colonizes the hypoxic tumor microenvironment. Similarly, Liu and coworkers showed bacCEST from *S. aureus* could be used to monitor the progress of antibiotic treatment [36]. They found that *S. aureus* displays similar CEST characteristics as *C. novyi*-NT and that the CEST MRI signal is dependent on the number of viable cells. Therefore, they were able to monitor the effect of antibiotic treatment *in vivo* in rat brain abscess models.

Though spores do not exhibit bacCEST contrast, Dmochowski and coworkers demonstrated that hyperpolarized ^{129}Xe can be used to detect *Bacillus anthracis* and *B. subtilis* spores through CEST NMR [37]. Specifically, ^{129}Xe diffused readily within different spore layers and the spore interior, allowing them to study

distinct spore structures at sensitivities (10^5 CFU/mL) ~7 orders of magnitude lower than in previous NMR studies [37].

4.   CONCLUSIONS

Bacteria have a nuanced role in contrast-enhanced MR imaging. Initially, molecular agents were developed to target, detect, and treat bacteria. Following these approaches, bacteria were employed as *the* MR contrast agents. While researchers have produced a wide variety of MR agent bacteria in contrast-enhanced MRI, there is significant untapped potential in this subfield. To date there are very few bacteria-targeted MR contrast agents, especially of the molecular kind.

It is not too hard to imagine that a larger library of bacteria-targeted agents with appropriate targeting groups and high specificity and loading properties inside bacteria can be developed. The successful use of magnetotactic bacteria, magnetosomes, and bacterial genes for cell labeling and tracking is very promising. With the proper modifications, contrast-enhancement created by the bacteria themselves could enable longer-term cell tracking when compared to traditional iron-oxide nanoparticles. While research on this approach is embryonic, there is enormous potential for new MRI agents and bacteria as contrast enhanced platforms.

ACKNOWLEDGMENTS

ABBREVIATIONS AND DEFINITIONS

AIE	aggregation-induced emission
CEST	chemical exchange saturation transfer
CFU	colony forming unit
DOTA	tetraazacyclododecane-1,4,7,10-tetraacetic acid
EGFR	epidermal growth factor receptor
HER2	human epidermal growth factor receptor 2
ME	magneto-endosymbiont
MGN	magnetic graphitic nanocapsule
MIC	minimum inhibitory concentration
MFH	magnetic fluid hyperthermia
MRI	magnetic resonance imaging
NIRF	near infrared fluorescence
NMR	nuclear magnetic resonance

PEG   polyethylene glycol
PET   positron emission tomography
pHLIP   pH low insertion peptide
RGD   arginylglycylaspartic acid
SI   signal intensity
SPECT   single-photon emission computed tomography
SPION   superparamagnetic iron-oxide nanoparticle
Zn-dpa   zinc-dipicolylamine

REFERENCES

1. A. Singh, R. V. Goering, S. Simjee, S. L. Foley, M. J. Zervos, *Clin. Microbiol. Rev.* **2006**, *19*, 512–530.

2. E. Hirsch, V. Tam, *Expert Review of Pharmacoeconomics & Outcomes Research* **2010**, *10*, 441–451.

3. K. E. Thorpe, P. Joski, K. J. Johnston, *Health Affairs* **2018**, *37*, 662–669.

4. A. Pandey, C. Savino, S. H. Ahn, Z. Yang, S. G. Van Lanen, E. Boros, *J. Med. Chem.* **2019**, *62*, 9947–9960.

5. S. Auletta, M. Varani, R. Horvat, F. Galli, A. Signore, S. Hess, *J. Clin. Med.* **2019**, *8*, E197.

6. M. M. Welling, A. W. Hensbergen, A. Bunschoten, A. H. Velders, H. Scheper, W. K. Smits, M. Roestenberg, F. W. B. van Leeuwen, *Clin. Translat. Imaging* **2019**, *7*, 125–138.

7. (a) A. E. Merbach, E. Tóth, *The Chemistry of Contrast Agents in Medical Magnetic Resonance Imaging*, 2nd ed., John Wiley & Sons, Ltd., New York, 2001; (b) V. Hartwig, G. Giovannetti, N. Vanello, M. Lombardi, L. Landini, S. Simi, *Int. J. Env. Res. Pub. Health* **2009**, *6*, 1778–1798.

8. (a) E. M. Shapiro, S. Skrtic, K. Sharer, J. M. Hill, C. E. Dunbar, A. P. Koretsky, *Proc. Nat. Ac. Sci. USA* **2004**, *101*, 10901–10906; (b) E. M. Shapiro, S. Skrtic, A. P. Koretsky, *Magnet. Reson. Med.* **2005** 53, 329–338; (c) P. Foster-Gareau, C. Heyn, A. Alejski, B. K. Rutt, *Magnet. Reson. Med.* **2003** 49, 968–971.

9. J. Wahsner, E. M. Gale, A. Rodríguez-Rodríguez, P. Caravan, *Chem. Rev.* **2019**, *119*, 957–1057.

10. H. Li, T. J. Meade, *J. Am. Chem. Soc.* **2019**, *141*, 17025–17041.

11. M. C. Heffern, L. M. Matosziuk, T. J. Meade, *Chem. Rev.* **2014**, *114*, 4496–4539.

12. V. Hoerr, C. Faber, *J. Pharma. Biomed. Anal.* **2014**, *93*, 136–146.

13. E. Terreno, D. D. Castelli, A. Viale, S. Aime, *Chem. Rev.* **2010**, *110*, 3019–3042.

14. L. M. Matosziuk, A. S. Harney, K. W. MacRenaris, T. J. Meade, *Eur. J. Inorg. Chem.* **2012**, *2012*, 2099–2107.

15. L. Zhang, Y. Liu, Q. Zhang, T. Li, M. Yang, Q. Yao, X. Xie, H.-Y. Hu, *Anal. Chem.* **2018**, *90*, 1934–1940.

16. Y. Li, H. Yu, Y. Qian, J. Hu, S. Liu, *Adv. Mater.* **2014**, *26*, 6734–6741.

17. Y. Li, X. Hu, D. Ding, Y. Zou, Y. Xu, X. Wang, Y. Zhang, L. Chen, Z. Chen, W. Tan, *Nature Commun.* **2017**, *8*, 15653.

18. V. Hoerr, L. Tuchscherr, J. Hüve, N. Nippe, K. Loser, N. Glyvuk, Y. Tsytsyura, M. Holtkamp, C. Sunderkötter, U. Karst, J. Klingauf, G. Peters, B. Löffler, C. Faber, *BMC Biology* **2013**, *11*, 63.

19. J. Ji, W. R. Park, S. Cho, Y. Yang, W. Li, K. Harris, X. Huang, S. Gu, D.-H. Kim, Z. Zhang, A. C. Larson, *J. Vasc. Intervent. Radiol.* **2019**, *30*, 1106–1115.e1101.

20. L. L. Hu, F. Zhang, Z. Wang, X. F. You, L. Nie, H. X. Wang, T. Song, W. H. Yang, *IEEE Transactions on Applied Superconductivity* **2010**, *20*, 822–825.

21. D. E. Goldhawk, R. Rohani, A. Sengupta, N. Gelman, F. S. Prato, *WIREs Nanomed. Nanobiotechnol.* **2012**, *4*, 378–388.

22. M. R. Benoit, D. Mayer, Y. Barak, I. Y. Chen, W. Hu, Z. Cheng, S. X. Wang, D. M. Spielman, S. S. Gambhir, A. Matin, *Clin. Cancer Res.* **2009**, *15*, 5170–5177.

23. Z. Xiang, X. Yang, J. Xu, W. Lai, Z. Wang, Z. Hu, J. Tian, L. Geng, Q. Fang, *Biomaterials* **2017**, *115*, 53–64.

24. Y. Zhang, Q. Ni, C. Xu, B. Wan, Y. Geng, G. Zheng, Z. Yang, J. Tao, Y. Zhao, J. Wen, J. Zhang, S. Wang, Y. Tang, Y. Li, Q. Zhang, L. Liu, Z. Teng, G. Lu, *ACS Applied Materials & Interfaces* **2019**, *11*, 3654–3665.

25. S. Schuerle, M. Furubayashi, A. P. Soleimany, T. Gwisai, W. Huang, C. Voigt, S. N. Bhatia, *ACS Synthetic Biology* **2020**, *9*, 392–401.

26. M. Boucher, F. Geffroy, S. Prévéral, L. Bellanger, E. Selingue, G. Adryanczyk-Perrier, M. Péan, C. T. Lefèvre, D. Pignol, N. Ginet, S. Mériaux, *Biomaterials* **2017**, *121*, 167–178.

27. S. Mannucci, S. Tambalo, G. Conti, L. Ghin, A. Milanese, A. Carboncino, E. Nicolato, M. R. Marinozzi, D. Benati, R. Bassi, P. Marzola, A. Sbarbati, *Contrast Media Mol. Imaging* **2018**, 1–12.

28. K. D. Brewer, R. Spitler, K. R. Lee, A. C. Chan, J. C. Barrozo, A. Wakeel, C. S. Foote, S. Machtaler, J. Rioux, J. K. Willmann, P. Chakraborty, B. W. Rice, C. H. Contag, C. B. Bell, B. K. Rutt, *Mol. Imaging Biology* **2018**, *20*, 65–73.

29. K. R. Lee, A. Wakeel, P. Chakraborty, C. S. Foote, L. Kajiura, J. C. Barrozo, A. C. Chan, A. V. Bazarov, R. Spitler, P. M. Kutny, J. M. Denegre, R. A. Taft, J. Seemann, B. W. Rice, C. H. Contag, B. K. Rutt, C. B. Bell, *Mol. Imaging Biology* **2018**, *20*, 55–64.

30. M. Mahmoudi, A. Tachibana, A. B. Goldstone, Y. J. Woo, P. Chakraborty, K. R. Lee, C. S. Foote, S. Piecewicz, J. C. Barrozo, A. Wakeel, B. W. Rice, C. B. Bell Iii, P. C. Yang, *Sci. Rep.* **2016**, *6*, 26960.

31. A. Hartung, M. R. Lisy, K.-H. Herrmann, I. Hilger, D. Schüler, C. Lang, M. E. Bellemann, W. A. Kaiser, J. R. Reichenbach, *J. Magn. Magn. Mater.* **2007**, *311*, 454–459.

32. M.-R. Lisy, A. Hartung, C. Lang, D. Schüler, W. Richter, J. R. Reichenbach, W. A. Kaiser, I. Hilger, *Investig. Radiology* **2007**, *42*, 235–241.

33. O. Zurkiya, A. W. S. Chan, X. Hu, *Magn. Res. Med.* **2008**, *59*, 1225–1231.

34. D. E. Goldhawk, C. Lemaire, C. R. McCreary, R. McGirr, S. Dhanvantari, R. T. Thompson, R. Figueredo, J. Koropatnick, P. Foster, F. S. Prato, *Mol. Imaging* **2009**, *8*, 7290.2009.00006.

35. G. Liu, C. Bettegowda, Y. Qiao, V. Staedtke, K. W. Y. Chan, R. Bai, Y. Li, G. J. Riggins, K. W. Kinzler, J. W. M. Bulte, M. T. McMahon, A. A. Gilad, B. Vogelstein, S. Zhou, P. C. M. van Zijl, *Magn. Res. Med.* **2013**, *70*, 1690–1698.

36. J. Liu, R. Bai, Y. Li, V. Staedtke, S. Zhang, P. C. M. van Zijl, G. Liu, *Magn. Res. Med.* **2018**, *80*, 662–671.

37. Y. Bai, Y. Wang, M. Goulian, A. Driks, I. J. Dmochowski, *Chem. Sci.* **2014**, *5*, 3197–3203.

16

Transition Metals and Imaging Probes in Neurobiology and Neurodegenerative Diseases

Ho Yu Au-Yeung and Ka Yan Tong

Department of Chemistry, The University of Hong Kong,
Pokfulam Road, Hong Kong, P. R. China
<hoyuay@hku.hk>

Abstract: Transition metals are not only important targets in the study of neurobiology and neurodegeneration, but also are useful agents for the detection and sensing of molecules involved in the pathology and diagnosis of neurodegenerative diseases. In this chapter, selected examples of fluorescent probes for imaging iron, copper, and zinc ions, small molecule neurotransmitters and aggregated proteins will be discussed to highlight the diverse roles and applications of metal ions in neurobiology and neurodegenerative diseases.

Keywords: copper · iron · neurotransmitters · protein aggregates · zinc

1.   INTRODUCTION

The human brain is the most important organ with a complex signaling network for the proper coordination of other organs and functioning of the body. The brain requires more energy than other organs and consumes about 20 % of the total body oxygen [1]. The high oxygen demand in the brain underlies the critical importance of transition metals and the associate dioxygen chemistry in the organ, and a homeostatic imbalance of transition metals is associated with aging and neurodegenerative diseases such as Alzheimer's disease (AD) and Parkinson's disease (PD) [2]. For example, a high concentration of iron, copper, and zinc, up to milli- and submillimolar level, has been found in amyloid-β (Aβ) plaques which are characteristic to AD [3–5]. Emergence of transition metals in signaling events has also led to a growing interest in understanding their neurophysiological and neuropathological significance [6].

Traditional views on transition metal bioinorganic chemistry are largely focused on metalloproteins with the transition metal deeply embedded in the protein active site [7, 8]. Many metalloproteins are tightly associated with neurobiology and neurodegenerative diseases [9, 10]. From a chemistry perspective, coordination of transition metals to protein active sites is thermodynamically highly stable and the metals are kinetically inert to exchange with external ligands, and studies of metals in neurobiology are primarily centered on related metalloproteins [11]. Recent studies, however, have revealed that exchangeable forms of transition metals could be present in significant amount and are playing critical roles in signaling and neural activity [11, 12]. Fluorescent imaging using metal-specific probes has therefore emerged as an important bioanalytical tool for the studies of these labile forms of transition metals due to its non-invasive nature, metal and oxidation state specificity, high spatiotemporal resolution, and applicability in live biological specimen.

In this chapter, fluorescent probes for imaging metals in neurobiology and small molecule neurotransmitters will be discussed. General strategies for the selective fluorescent detection of zinc, copper, and iron will be introduced and selected examples of probes for these metals will be described. In addition to

metal sensing, the use of metal chemical reactivity for the fluorescent detection of small molecule neurotransmitters will be highlighted.

2. TRANSITION METAL SENSING IN NEUROBIOLOGY

2.1. Fluorescent Probes for Zinc Sensing

Zinc exists mainly in its divalent form in biological systems. The d^{10} Zn^{2+} ion has a closed shell configuration and is diamagnetic. As a borderline Lewis acid, Zn^{2+} is known to form stable complexes with nitrogen-based ligands, and the preferential coordination to Zn^{2+} by a suitably designed ligand is a common strategy in the design of Zn^{2+}-selective fluorescent probes. In addition to achieving selectivity to Zn^{2+} against other competing metals, methods of inducing a fluorescent response upon Zn^{2+} binding and optimization of the dynamic range of the zinc probe to match the relevant variation in zinc concentrations in a particular biological event are other important considerations in the design of an effective zinc probe [13–16]. In the following, selected small molecule Zn^{2+} probes for the fluorescent imaging of the metal in neurobiological studies are discussed.

Zinpyr (ZP) is a representative class of Zn^{2+}-selective probes for fluorescent zinc imaging. The tridentate di-2-picolylamine (DPA) ligand was employed for selective Zn^{2+} coordination to ZP, in which the lone pair electrons on the sp^3 nitrogen also acts as an on-off switch for the photoinduced electron transfer (PET) to a fluorescein-based fluorophore for generating a fluorescent response. **ZP1** is an early example in the ZP family that has a good affinity to Zn^{2+} (K_d = 0.7 nM) [17, 18] (Figure 1). The probe also has a high selectivity to Zn^{2+} over other cellular abundant metal ions such as Mg^{2+} and Ca^{2+}, and is applicable in intracellular Zn^{2+} imaging in live cells such as COS-7 cells. **ZP1** and its derivatives have also been demonstrated in resolving individual synaptic boutons in acute brain slices and imaging of vesicular Zn^{2+} in dorsal cochlear nucleus in

ZP1: R = Cl
λ_{ex} = 515 nm
λ_{em} = 531 nm
Φ (free, Zn^{2+}-bound) = 0.38 (0.87)

ZP3: R = F
λ_{ex} = 502 nm
λ_{em} = 521 nm
Φ (free, Zn^{2+}-bound) = 0.15 (0.92)

ZnAF-2F
λ_{ex} = 490 nm
λ_{em} = 514 nm
Φ (free, Zn^{2+}-bound) = 0.006, 0.24

NG-DCF
λ_{ex} = 492 nm
λ_{em} = 521 nm

NG-PDX
λ_{ex} = 491 nm
λ_{em} = 520 nm
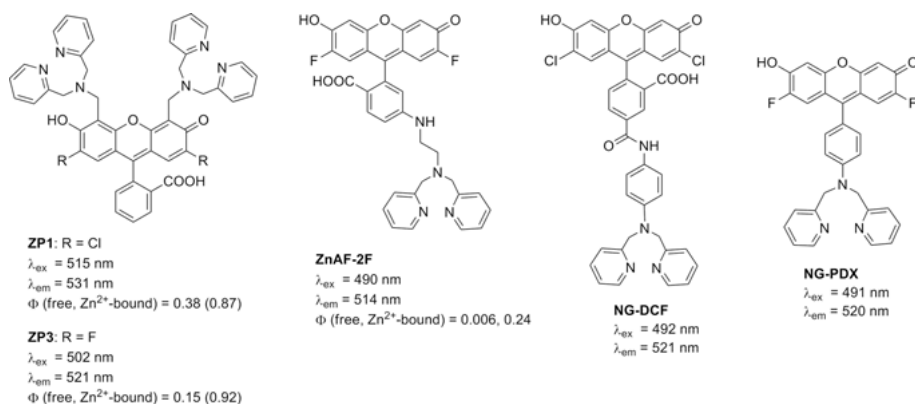
Figure 1. Examples of fluorescent Zn^{2+} probes.

brain slices [19, 20]. **ZP3** is a derivative that contains electron-withdrawing fluorine groups with a lower overall pK_a of 6.8 and a weaker background fluorescence ($\Phi = 0.15$), and has been applied in the fluorescent imaging of Zn^{2+} in hippocampal neurons and slices [21]. In particular, **ZP3** is able to visualize endogenous neuronal Zn^{2+} in acute hippocampal slices from adult rats, and a strong fluorescence was found in the hilus of dentate gyrus and the stratum lucidum of the CA3 region.

Zinc sensors based on the aminofluorescein entity (ZnAFs) are another class of Zn^{2+} probes that operate with a PET mechanism. Similar to ZP, the DPA moiety is employed in ZnAF as a Zn^{2+}-selective ligand. Compared with ZP, ZnAF shows a wider dynamic range, weaker background fluorescent and a stronger fluorescence enhancement upon Zn^{2+} binding [22–24]. The cell impermeable **ZnAF-2F** (Figure 1) has been applied in the monitoring of the stimulated release of neuronal Zn^{2+} to the extracellular space [24]. By attaching a DPA directly on an aryl group that decreases the Lewis basicity of the Zn^{2+} chelator, the Zn^{2+} binding strength and thus the dynamic range of the Zn^{2+} probe is modulated. For example, **NG-DCF** ($K_d = 1$ μM) [25] and **NG-PDX** ($K_d = 40$ μM) [26] have been designed for the imaging of Zn^{2+} translocation and the synaptic release of the metal (Figure 1). Substituting the pyridine donors in DPA with electron-donating or -withdrawing groups, replacing the pyridine donors in DPA with other donors such as pyrrole or thiophene, or changing the steric hindrance and/or denticity of the Zn^{2+} chelator are other reported strategies for tuning the Zn^{2+} affinity and dynamic range of the Zn^{2+} probes [27–30]. Many of these Zn^{2+} probes have been successfully demonstrated in imaging neuronal zinc.

By incorporating the DPA chelator onto other fluorescent platforms, Zn^{2+} probes with other properties such as low pH sensitivity, high photostability, and cell permeability for specific experiments can be easily obtained. Other Zn^{2+} probes based on other fluorophores such as tricarbocyanine, rhodamine, coumarin, seminaphthofluorescein, and 4-aminonaphthalimide have also been reported [31–39]. These probes exhibit favorable photophysical properties such as ratiometric response or near infrared (NIR) emission [33, 34].

2.2.   Fluorescent Probes for Copper Sensing

Copper can exist as the d^{10} diamagnetic Cu^+ or the d^9 paramagnetic Cu^{2+} in biological systems. For the reducing intracellular environment, a majority of fluorescent probes for copper imaging is designed for Cu^+ [40]. The redox activity of copper and its reaction with dioxygen and reactive oxygen species are also implicated in cellular oxidative stress and neurodegenerative diseases such as Alzheimer's disease and Parkinson's disease [41].

2.2.1.   *Probes for Cu$^+$ Imaging*

Cu^+ is a diamagnetic, soft Lewis acid. The use of sulfur-containing soft ligands with a coordination pocket optimal for Cu^+ is one prevalent strategy for the

CTAP-1
λ_{ex} = 365 nm
λ_{em} = 485 nm
Φ (free, Cu$^+$-bound) = 0.03, 0.14

CTAP-2
λ_{ex} = 396 nm
λ_{em} = 508 nm
Φ (free, Cu$^+$-bound) = 0.0015, 0.083

CS3
λ_{ex} = 550 nm
λ_{em} = 560 nm
Φ (free, Cu$^+$-bound) = 0.007, 0.40

CF3
λ_{ex} = 534 nm
λ_{em} = 557 nm
Φ (free, Cu$^+$-bound) = 0.026, 0.219
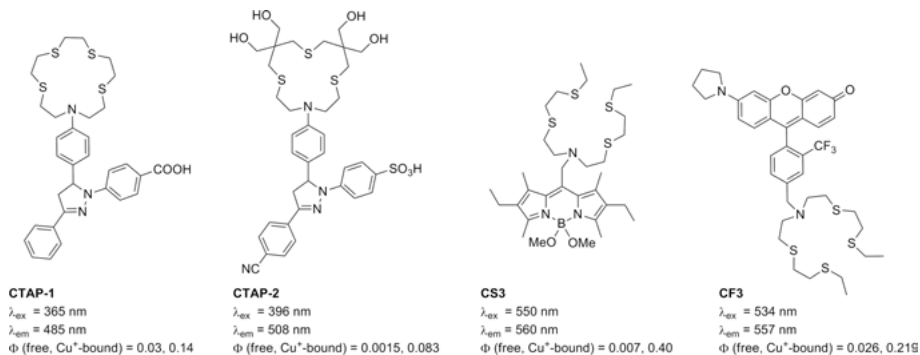
Figure 2. Examples of binding-based Cu$^+$ probes.

design of Cu$^+$ fluorescent probes [13, 14, 42, 43]. CTAP (copper-responsive tri-arylpyrazoline) and CS (copper sensor) are two major families of Cu$^+$ probes, and both feature the use of thioether-based amine ligands that control the on-off of the PET to a fluorophore for a Cu$^+$-dependent fluorescent response [44–47] (Figure 2). These probes have been employed in the studies of intracellular copper in various cell types including neurons. For examples, the BODIPY-based **CS3** has been applied in the imaging of copper redistribution in neuronal cells upon K$^+$-induced depolarization [47]. By the use of the rhodol-based **CF3**, it is found that an acute copper chelation in cultured hippocampal neurons increases the excitability of the neuronal network, suggesting a role of Cu$^+$ in the modula-tion of neural circuit activity [48]. With a Cu$^+$-selective chelator attached on other fluorophores, a collection of copper probes with various photophysical, organelle-targeting, and other properties is available [49–54]. Applications of these copper probes in the detailed understanding of the roles of copper in neu-robiology and neurodegenerative diseases are to be further explored.

Another strategy for developing selective Cu$^+$ fluorescent probes is by the use of a tris(2-pyridylmethyl)amine ligand as a Cu$^+$-selective trigger to release a caged fluorophore [55–58] (Figure 3). The copper selectivity of this bond cleav-age reaction comes from the complementarity of the chemical reactivity between the tris(2-pyridylmethyl)amine-coordinated Cu$^+$ and dioxygen (the oxidant). Other transition metal ions are found to be inactive in inducing the bond cleav-

caged, non-emissive probe

$\xrightarrow{Cu^+, O_2}$

emissive fluorophore
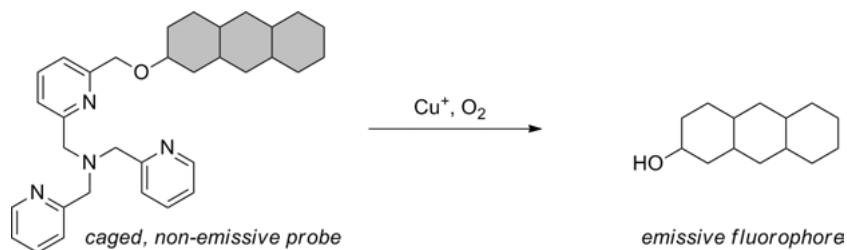
Figure 3. A Cu$^+$-induced ether bond cleavage for the release of a caged fluorophore.

age. These probes have been applied in the studies of copper in different biological systems but their use in neuronal systems and neurodegenerative diseases will have to be demonstrated [55–58].

2.2.2. *Probes for Cu^{2+} Imaging*

One concern in the development of a Cu^{2+} probe is the fluorescence quenching by the paramagnetic d^9 Cu^{2+}. Yet, there have been a few reports on Cu^{2+} that feature a Cu^{2+}-selective ligand as the metal binding motif [59–62]. For example, Tang and coworkers have reported a cyanine-based NIR probe that contains a bis(hydroxyamide)amine ligand as the Cu^{2+} chelator for copper imaging in rat hippocampal slices [62]. Another major strategy in developing fluorescent probes for Cu^{2+} is the hydrolysis of hydrazide, ester, lactone or lactam mediated by Cu^{2+} [63–70]. A few of these probes have been demonstrated in intracellular imaging of Cu^{2+} in different cells lines and in tissue samples. Oxidation mediated by Cu^{2+} is another strategy for developing Cu^{2+}-responsive fluorescent probes [71–73].

2.3. Fluorescent Probes for Iron Sensing

Iron is the most abundant transition metal in the human body with a diverse range of biological functions such as transporting dioxygen, being a cofactor for electron transfer and acting as an enzyme active site for substrate chemical transformations [74]. The redox-labile metal exists mainly as Fe^{2+} and Fe^{3+} under biologically relevant conditions. At physiological pH, free Fe^{3+} has a low aqueous solubility and trivalent iron is usually found as tightly bound form in proteins. On the other hand, divalent iron is more soluble and kinetically labile, and is thought to be more relevant to the intracellular labile iron pool (LIP) [75, 76]. Yet, the nature of LIP remains poorly understood and is to be further characterized by appropriate bioanalytical tools. Fluorescent iron probes are highly suitable for studying changes in the LIP and their characterization [13, 14, 77, 78].

Designing fluorescent turn-on probes for Fe^{2+} and Fe^{3+} is highly challenging, partly due to the paramagnetic nature of the open shell d^6 (Fe^{2+}) and d^5 (Fe^{3+}) electronic configurations and also the weaker binding to a particular ligand compared to other first row transition metals in the Irving-Williams series. Calcein [79] and Phen Green SK [80] are two commercial probes that have been applied for a long time for iron imaging. However, these two probes lack specificity towards iron oxidation states and are also not selective against other metals such as Cu^{2+} and Co^{2+}. Fluorescent iron probes of better metal selectivity and oxidation state specificity are therefore highly desirable. In the following, general strategies for iron probe development will be discussed.

2.3.1. *Probes for Fe^{2+} Imaging*

An early example of a Fe^{2+} probe features a BODIPY fluorophore linked to a terpyridine-attached cyanine. Upon Fe^{2+} coordination to the terpyridine, emis-
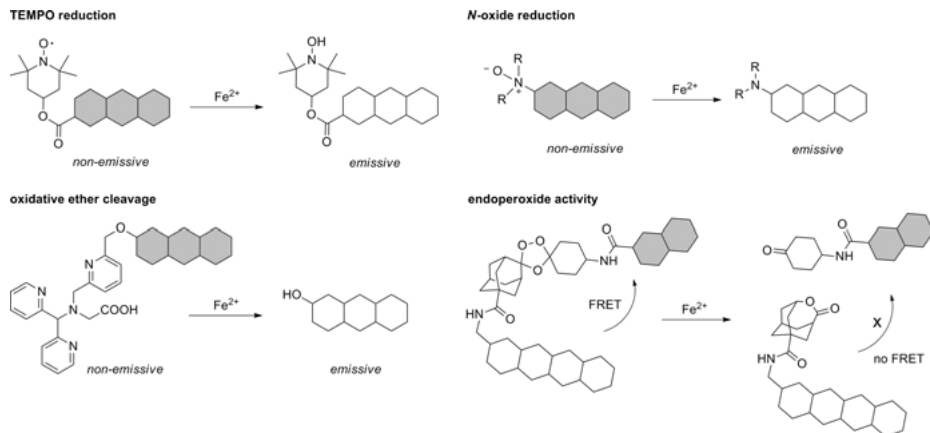
Figure 4. Strategies of Fe^{2+} probe development from Fe^{2+} reactivity.

sion from the cyanine is quenched and that from BODIPY remains unaffected to result in a change in the ratio of emissions from the two fluorophores [81].

In addition to Fe^{2+} binding by a coordination ligand, fluorescent iron probes that exploit chemical reactivity of Fe^{2+} have been reported. Based on the reduction of the stable (2,2,6,6-tetramethylpiperidin-1-yl)oxy (TEMPO) radical by Fe^{2+}, **pyrene-TEMPO** and **Rh-T** have been reported and the latter has been employed in the imaging of endogenous Fe^{2+} in live human fibroblast ws1 cells [82, 83]. More recently, Hirayama and coworkers have described a series of Fe^{2+}-selective fluorescent probes featuring an Fe^{2+}-mediated *N*-oxide reduction [84–90]. Upon reduction by Fe^{2+}, the fluorescence quenching effect from the *N*-oxide is removed and a fluorescence enhancement results. This family of Fe^{2+} probes shows different emission wavelength, sensitivity, solubility, and organelle-targeting ability, and they have been demonstrated as useful probes for imaging LIP in various cell types. In particular, a membrane-targeting derivative in the series has been applied in imaging the uptake of endosomal Fe^{2+} in primary cultured neurons [90] (Figure 4).

Inspired by the redox activity of iron in metalloproteins, Chang and coworkers have developed **IP1** which is a fluorescein derivative caged by a pentadentate ligand with three pyridines, one carboxylate and an sp^3 nitrogen donor [91]. The pentadentate ligand is to mimic the co-facial 2-His-1-COOH motif commonly found in non-heme iron oxygenases. Upon Fe^{2+} coordination to the ligand and dioxygen activation, the benzylic ether linker between the ligand and the fluorophore will be oxidatively cleaved to release the emissive reporter. Using also an oxidation strategy, the same research group has reported the use of endoperoxide as a caging motif in fluorescent Fe^{2+} probes [92, 93]. With a Fenton-like reaction with Fe^{2+}, the endoperoxide cage is removed to release the emissive fluorophore. These probes have been applied in the imaging of LIP in various cellular models such as hepatic iron import [91], ferroptosis [92], and cancer [93]. A bioluminescent probe based on similar Fe^{2+}-mediated uncaging of endoperox-

ide has also been developed and applied in the *in vivo* imaging of labile iron levels in mice in a bacterial infection model [94]. Applicability of these Fe^{2+} probes in the study of neurodegenerative diseases will have to be further demonstrated.

2.3.2.   *Probes for Fe^{3+} Imaging*

Because of the effective fluorescence quenching effect of the paramagnetic d^5 Fe^{3+}, there have been only a few fluorescent turn-on probes for Fe^{3+}. Vice versa, few studies report fluorescent turn-off probes for Fe^{3+} that utilize a siderophore-like strong ligand for the metal ion [95–98].

Ring-opening of spirolactam in rhodamines is another commonly used strategy in the development of an Fe^{3+} probe. Upon Fe^{3+} coordination, the spirolactam ring of the rhodamine is opened and the absorption and emission of the probe are restored [99–101]. Imaging of exogenously added iron in cells by using these probes has also been demonstrated [100, 101].

3.   FLUORESCENT SENSING OF SMALL MOLECULE NEUROTRANSMITTERS

Neurotransmitters are messenger molecules that enable neural transmission in synapses. Misregulation of neurotransmitters is often associated with neurodegenerative diseases. For example, dopamine depletion in dopaminergic neurons is a major characteristic of Parkinson's disease [102, 103]. Imaging by fluorescent probes is the most direct method to study neurotransmitter dynamics for elucidating their physiological and pathological roles, as well as developing new diagnostics and drugs for related neurodegenerative diseases [104].

Developing fluorescent probes for small molecule neurotransmitters is highly challenging owing to the difficulty in the design of selective hosts that can bind strongly to the small molecules. One strategy is to fuse a receptor protein for the target neurotransmitter with a fluorescent protein, such that neurotransmitter binding will lead to a conformational change of the fused protein and generate a fluorescent signal [105–107]. Although the engineered proteins offer a good selectivity and sensitivity, their uses are limited by the need of cell transfection and thus cannot be applied in primary tissues or cells. On the other hand, there are also fluorescent false neurotransmitters that are fluorescent compounds with structures highly similar to the native neurotransmitters. Neuronal activity such as uptake, storage, and release of neurotransmitters can be indirectly visualized by using these fluorescent analogues [108, 109].

In this section, fluorescent probes for small molecule neurotransmitters will be discussed. In particular, examples of small molecule probes for amino acids and catecholamines will be highlighted. Fluorescent probes for gaseous neurotransmitters such as NO, CO and H_2S are relatively better developed and readers are referred to related review papers for more information [110–116].

3.1.   Fluorescent Probes for Amino Acid Neurotransmitters

In addition to being fundamental building blocks for proteins, some amino acids such as glycine, aspartate, glutamate, and γ-aminobutyric acid (GABA) are also important small molecule neurotransmitters in the central nervous system. Glutamate and aspartate are excitatory neurotransmitters that stimulate the firing of an action potential of the neurons, while glycine and GABA are inhibitory neurotransmitters that decrease the chance of the neurons to produce an action potential [104, 117].

The use of metal coordination is an early developed strategy for the detection of amino acids. Fabbrizzi and coworkers have reported a rhodamine-complexed dicopper cage as a fluorescent displacement indicator for glutamate [118]. The quenched fluorescence of the rhodamine-copper(II) complex is restored upon competitive coordination of glutamate to the two copper ions. The fluorescent response selectivity of the glutamate is determined by the size of the cage such that other amino acids and competitive ligands are not able to displace the complexed rhodamine. Using a similar concept, a zinc complex coordinated to a terpyridine-based bis(guanidinium) ligand has been developed for the selective sensing of aspartate [119]. Upon aspartate binding, a pyrocatechol violet is displaced to give a colorimetric response. Even though these probes show a good selectivity and sensitivity to the amino acid neurotransmitters, no application in biological samples has been demonstrated.

Another strategy for amino acid sensing has been centered on imine/iminium formation between the amino group of the neurotransmitter and a carbonyl group of the fluorescent probe. Feuster and Glass have reported a first example of an amino acid probe featuring coumarins that are functionalized with an aldehyde [120]. Iminium formation between the aldehyde and a primary amine (Figure 5) changes the fluorescent quantum yield of the coumarin and results in a fluorescent signal. A fluorescent enhancement was observed upon treating the aldehyde-containing coumarins with glutamate, aspartate or glycine in water, and the fluorescent response is selective to primary amines against secondary amines and hydroxyl acids. Some of these probes have been demonstrated to be applicable in the imaging of neurotransmitter release from an acidic secretory vesicle to a synaptic cleft. Other primary amine-containing compounds such as dopamine and noradrenaline also showed a fluorescent response which may limit the specific type of neurons to which the probes can be applied [121].
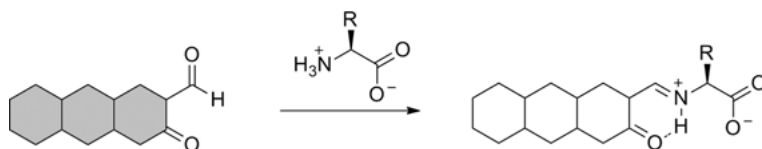
Figure 5.   Amino acid probes based on imine/iminium formation.

3.2. Fluorescent Probes for Catecholamines

Catecholamines are small molecule neurotransmitters that contain both amine and catechol functional groups and include dopamine, adrenaline, and noradrenaline. Catecholamines are involved in a wide variety of functions such as learning, memory, motor control, attention and alert, as well as modulation of heart rate and vasocontraction [122]. Various psychiatric and neurological disorders such as hypertension, schizophrenia, psychosis, hyperactivity, anxiety, sleep disorder, and Parkinson's disease are associated with an imbalance of catecholamines [103].

Imine/iminium formation has also been employed to target the amine group, in conjunction with boronate ester formation with the catechol using boronic acid, in designing fluorescent catecholamine probes [123]. Not only the relative positions of the aldehyde and boronic acid have to be optimal for the simultaneous binding of the amine and catechol groups, but also the fluorescent quenching by the aromatic moiety of the catecholamine adds further challenges in the design of a fluorescent catecholamine probe. A modified coumarin aldehyde, **NS521**, that contains an electron rich *p*-methoxyphenyl substituent has been reported by the Glass group [124]. Fluorescent measurement with **NS521** showed that the probe has a better binding affinity towards dopamine and noradrenaline over adrenaline and amino acids such as glycine, lysine, and glutamate. The probe has also been applied in noradrenaline imaging in chromaffin cells that synthesize the neurotransmitter.

Later, the quinolone-based **NS510** has been reported, which showed a stronger fluorescent response, and hence better sensitivity, towards noradrenaline and dopamine (log $K \sim 4$) when compared with **NS521** (log $K \sim 2$) [125]. The better fluorescent response from NS521 is explained by the use of the more electron-rich quinolone that results in a less efficient fluorescent quenching by the bound catechol. The probe has been demonstrated in the monitoring of noradrenaline exocytosis in chromaffin cells.

It is worth noting that the binding of catecholamine to these probes is reversible and thus could be applied for tracking changes in catecholamine levels over time. Yet, the reversible nature of the probe-catecholamine interactions also limits the applicability of the probe to samples that have a relatively high catecholamine content, because of the inherently weak equilibrium constants of imine and boronate ester formation (log $K \sim 2$–4) [126, 127] (Figure 6).

To further improve the sensitivity of catecholamine probes, our group has exploited an irreversible bond cleavage strategy for the development of fluorescent catecholamine probes [128] (Figure 6). Sensitivity of the reaction-based probes is independent of the binding equilibrium and is determined by the extent of the reaction and mechanism of fluorescent signal generation. Inspired by the selective dopamine oxidation of noradrenaline by dopamine β-hydroxylase, a copper(II) complex supported by a tripodal ligand containing two pyridine and one thioether donor was developed as a selective trigger, and catecholamine fluorescent probes were successfully prepared by linking the copper(II) complex to a fluorophore via an ether bond that renders the fluorophore non-emissive [128]. Upon reaction with catecholamine, dioxygen activation at the copper will gener-
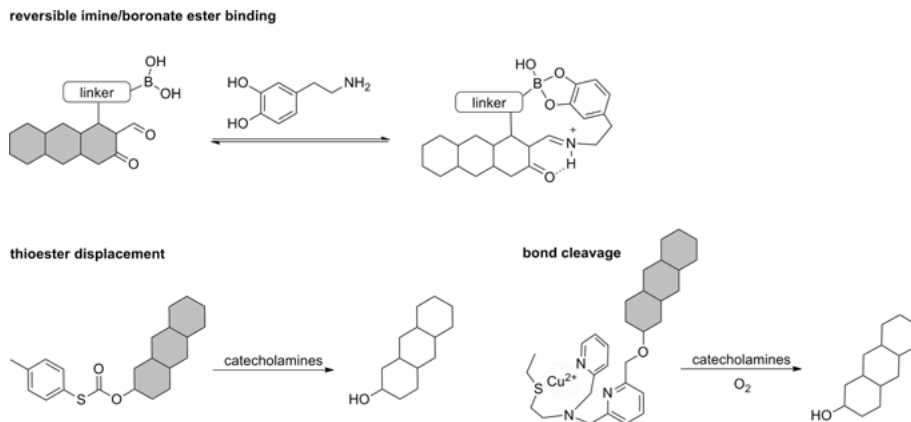
Figure 6. Strategies for catecholamine fluorescent probes.

ate an active oxidant, cleave the ether bond, and release the caged fluorophore to result in a fluorescent turn-on signal. The probes are highly selective to catecholamines against other biological amines, diols, and reductants. **CAP488**, a cyan-emitting member of the series, has been applied [128] in visualizing dopamine accumulation in a PC12 neuron differentiation model and also dopamine depletion in a cellular Parkinson's disease model, providing molecular information on dopamine levels that complements well with morphological assessment of the corresponding neuronal processes in a single imaging experiment.

Nucleophilic displacement of a thioester by 2-aminoethanol has been exploited by Yin and coworkers to develop a fluorescent probe for noradrenaline which has been applied in labelling noradrenergic neurons in brain tissues [129] (Figure 6).

3.3. Fluorescent Probes for Other Small Molecule Neurotransmitters

In addition to fluorescent probes for amino acids and catecholamines, there are also a few examples of fluorescent probes for other small molecule neurotransmitters. For example, Hettie and Glass have reported **NS715** which is an aldehyde-containing 1,2,3,4-tetrahydroquinoxaline that can engage in reversible imine formation with primary amines [130] (Figure 7). **NS715** was found to exhibit a strong fluorescent enhancement in the NIR region and selectivity to serotonin against other biological amines including dopamine, noradrenaline, and glutamate. Although **NS715** can be applied in noradrenaline imaging in chromaffin cells, its use in the study of serotonin in biological samples has to be demonstrated.

There are also few examples of fluorescent histamine probes (Figure 7). Imato and coworkers have reported a fluorescein-based nickel(II) iminodiacetate complex in which the paramagnetic metal ion quencher can be selectively displaced
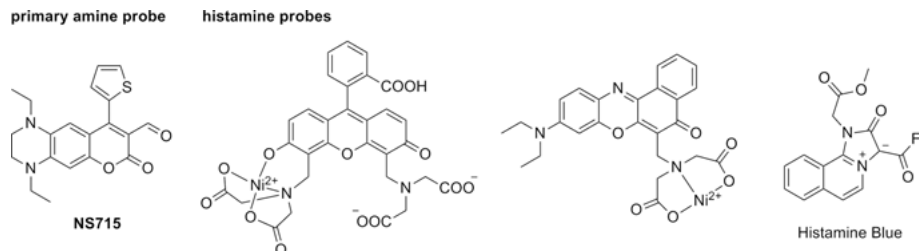
Figure 7. Fluorescent probes for detecting primary amines.

by forming a stable complex with histamine [131]. A similar nickel(II) complex derived from Nile Red has been applied in histamine imaging in RAW263 cells [132]. There is also Histamine Blue which is a mesoionic acid fluoride in which the quenched fluorescence is restored upon amide formation with histamine [133].

4.   METALS AND ALZHEIMER'S DISEASE

4.1.   Aggregated Proteins in Alzheimer's Disease

Alzheimer's disease (AD) is a common cause of dementia and is characterized by aggregation of misfolded proteins such as amyloid-β (Aβ) and tau proteins. High levels of iron, copper, and zinc have been found in the brains of patients with AD, and the transition metals have been shown to play important roles in the aggregation of Aβ and tau proteins during AD progression [4, 5]. In the following, fluorescent probes for imaging aggregated Aβ and tau proteins, as well as metals as parts of the aggregates will be highlighted.

4.2.   Fluorescent Probes for Amyloid-β Aggregates

In general, aggregated Aβ adopts a parallel, cross-β sheet structure with a hydrophobic interior [134]. Thus, probes for Aβ aggregates are usually designed to display a change in fluorescence in response to a change in the polarity of the environment. Useful probes for studying Aβ aggregates in brain tissue should also be able to pass through the blood-brain barrier, display a low toxicity and have a long emission wavelength for a lower background fluorescence and better tissue penetration [135, 136].

  Thioflavin-T (ThT) forms a series of fluorescent probes for staining amyloid fibrils [137, 138]. Upon binding to Aβ, rotation of the single bond that links the benzothiazole acceptor and benzylamine donor will be hindered and the emission is restored to result in a fluorescent enhancement. For example, **PP-BTA-1** and **PP-BTA-2** are two probes in the series that have a strong binding affinity
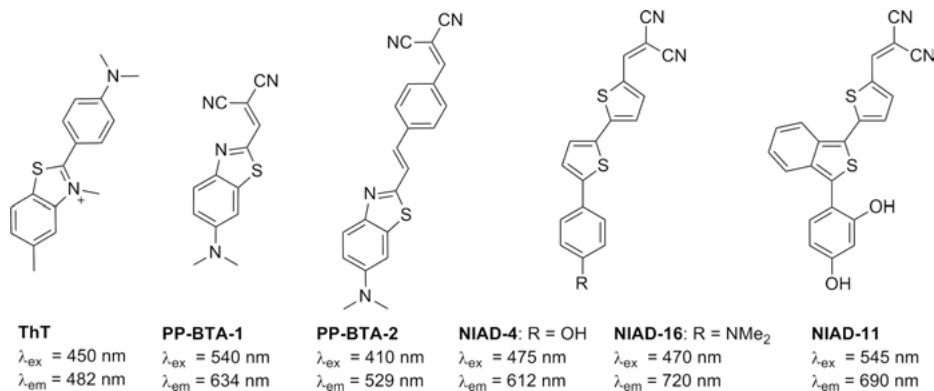
Figure 8. Fluorescent probes for detecting amyloid-β aggregates.

for Aβ with emissions at 500 nm to 600 nm, and are applicable in labelling Aβ plaques in human and mouse brain tissues [139] (Figure 8).

NIAD is another family of fluorescent Aβ probes. In particular, **NIAD-4** has a strong binding affinity to Aβ (K_d ~ 10 nM) and can be applied in labelling Aβ plaques in the brain. **NIAD-11** and **NIAD-16** feature emissions at 650 nm–900 nm which is suitable for *in vivo* imaging, and the latter has been demonstrated to distinguish vascular and non-vascular Aβ plaques through fluorescence lifetime imaging [140]. There are other Aβ probes of different photophysical properties and affinities for the aggregated proteins [136, 141, 142].

4.3. Fluorescent Probes for Aggregated Tau Proteins

Developing a fluorescent probe for aggregated tau proteins is in general more challenging due to the lack of a well-defined binding site, and some probes for tau proteins are also responsive to Aβ. Thioflavin-S, curcumin, **Tau-1** and **BD-tau** (Figure 9) are few examples of fluorescent probes developed for the fluorescent imaging of tau proteins, and some of these probes have been applied in imaging tau aggregates in live hippocampal neurons, brain tissues, and transgenic mice [143–147]. Electrostatic binding using a Zn^{2+} complex has also been exploited for developing probes for aggregated tau proteins [148, 149].

4.4. Fluorescent Probes for Studying Metals in Amyloid-β Aggregation

To study the role of transition metal ions in the aggregation of Aβ, moieties that are known to target Aβ are modified with coordination donors for the simultaneous interactions with metals and Aβ. Interactions of the bifunctional compounds with Cu^{2+}- and Zn^{2+}-associated Aβ have been studied [143, 150, 151]. In addi-
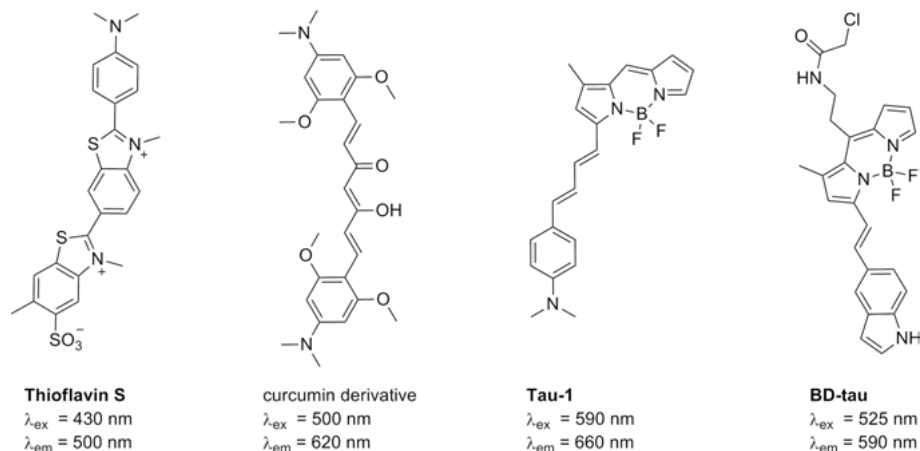
Figure 9.   Fluorescent probes for detecting tau aggregates.

tion to the detection of the metal-bound aggregated Aβ, these compounds are also able to inhibit the metal-induced Aβ aggregation and thus modulate the metal-induced Aβ activity and neurotoxicity.

5.   CONCLUDING REMARKS

In summary, fluorescent probes for studying transition metal ions and the use of chemical reactivity of metals in designing probes for neurotransmitters and protein aggregates are discussed. These fluorescent probes not only are important bioanalytical tools for basic studies of neurobiology and neurodegenerative diseases, but also highlight the diverse roles and importance of transition metal chemistry in processes that are fundamental to human health. With innovative designs of novel chemical probes, a deeper understanding of metals in neurobiology and new strategies for diagnosis and treatments of neurodegenerative diseases can be anticipated.

ACKNOWLEDGMENTS

ABBREVIATIONS AND DEFINITIONS

Aβ	amyloid-β
AD	Alzheimer's disease
BODIPY	boron-dipyrromethane
CAP	catecholamine probe
CS	copper sensor
CTAP	copper-responsive triarylpyrazoline
DCF	2',7'-dichlorofluorescein
DPA	di-(2-picoyl)amine
FRET	fluorescence resonance energy transfer
GABA	γ-aminobutyric acid
IP1	Iron Probe 1
LIP	labile iron pool
NG	Newport Green
NIAD	near-infrared Alzheimer's dye
NIR	near infrared
NS	neurosensor
PET	photoinduced electron transfer
PD	Parkinson's disease
PP-BTA	push-pull benzothiazole
TEMPO	(2,2,6,6-tetramethylpiperidin-1-yl)oxy
ThT	thioflavin-T
ZnAF	aminofluorescein-based zinc sensor
ZP	Zinpyr

REFERENCES

1. M. E. Götz, G. Künig, P. Riederer, M. B. H. Youdim, *Pharmac. Ther.* **1994**, *63*, 37–122.
2. A. I. Bush, *Curr. Opin. Chem. Biol.* **2000**, *4*, 184–191.
3. X. Huang, M. P. Cuajungco, C. S. Atwood, R. D. Moir, R. E. Tanzi, A. I. Bush, *J. Nutr.* **2000**, *130*, 1488S–1492S.
4. H. Kozlowski, M. Luczkowski, M. Remelli, D. Valensin, *Coord. Chem. Rev.* **2012**, *256*, 2129–2141.
5. K. J. Barnham, A. I. Bush, *Curr. Opin. Chem. Biol.* **2008**, *12*, 222–228.
6. C. J. Chang, *Nat. Chem. Biol.* **2015**, *11*, 744–747.
7. J. T. Rubino, K. J. Franz, *J. Inorg. Biochem.* **2011**, *107*, 129–147.
8. H. M. Baker, B. F. Anderson, E. N. Baker, *Proc. Natl. Acad. Sci. USA* **2003**, *199*, 3579–3583.
9. A. Lothian, D. J. Hare, R. Grimm, T. M. Ryan, C. L. Masters, B. R. Roberts, *Front. Aging Neurosci.* **2013**, *5*, 35.
10. D. R. Brown, *Metallomics* **2010**, *2*, 186–194.
11. C. M. Ackerman, S. Lee, C. J. Chang, *Anal. Chem.* **2017**, *89*, 22–41.
12. C. J. Chang, *Acc. Chem. Res.* **2017**, *50*, 535–538.
13. K. P. Carter, A. M. Young, A. E. Palmer, *Chem. Rev.* **2014**, *114*, 4564–4601.
14. E. L. Que, D. W. Domaille, C. J. Chang, *Chem. Rev.* **2008**, *108*, 1517–1549.

15. E. M. Nolan, S. J. Lippard, *Acc. Chem. Res.* **2009**, *42*, 193–203.

16. Y. Chen, Y. Bai, Z. Han, W. He, Z. Guo, *Chem. Soc. Rev.* **2015**, *44*, 4517–4546.

17. G. K. Walkup, S. C. Burdette, S. J. Lippard, R. Y. Tsien, *J. Am. Chem. Soc.* **2000**, *122*, 5644–5645.

18. S. C. Burdette, G. K. Walkup, B. Spingler, R. Y. Tsien, S. J. Lippard, *J. Am. Chem. Soc.* **2001**, *123*, 7831–7841.

19. C. Frederickson, *Sci. STKE* **2003**, *2003*, pe18.

20. M. L. Zastrow, R. J. Radford, W. Chyan, C. T. Anderson, D. Y. Zhang, A. Loas, T. Tzounopoulos, S. J. Lippard, *ACS Sens.* **2015**, *1*, 32–39.

21. C. J. Chang, E. M. Nolan, J. Jaworski, S. C. Burdette, M. Sheng, S. J. Lippard, *Chem. Biol.* **2004**, *11*, 203–210.

22. T. Hirano, K. Kikuchi, Y. Urano, T. Higuchi, T. Nagano, *J. Am. Chem. Soc.* **2000**, *122*, 12399–12400.

23. A. Takeda, K. Yamada, A. Minami, T. Nagano, N. Oku, *Epilepsy Res.* **2005**, *63*, 77–84.

24. T. Hirano, K. Kikuchi, Y. Urano, T. Nagano, *J. Am. Chem. Soc.* **2002**, *124*, 6555–6562.

25. S. Wuertz, E. Müller, R. Spaeth, P. Pfleiderer, H. C. Flemming, *J. Ind. Microbiol. Biotechnol.* **2000**, *24*, 116–123.

26. K. R. Gee, Z. L. Zhou, D. Ton-That, S. L. Sensi, J. H. Weiss, *Cell Calcium* **2002**, *31*, 245–251.

27. E. M. Nolan, S. J. Lippard, *Inorg. Chem.* **2004**, *43*, 8310–8317.

28. E. M. Nolan, J. W. Ryu, J. Jaworski, R. P. Feazell, M. Sheng, S. J. Lippard, *J. Am. Chem. Soc.* **2006**, *128*, 15517–15528.

29. K. Komatsu, K. Kikichi, H. Kojima, Y. Urano, T. Nagano, *J. Am. Chem. Soc.* **2005**, *127*, 10197–10204.

30. M. Khan, C. R. Goldsmith, Z. Huang, J. Georgiou, T. T. Luyben, J. C. Order, S. J. Lippard, K. Okamoto, *Proc. Natl. Acad. Sci. USA* **2014**, *111*, 6786–6791.

31. Y. Wu, X. Peng, B. Guo, J. Fan, Z. Zhang, J. Wang, A. Cui, Y. Gao, *Org. Biomol. Chem.* **2005**, *3*, 1387–1392.

32. B. Tang, H. Huang, K. Xu, L. Tong, G. Yang, X. Liu, L. An, *Chem. Commun.* **2006**, 3609–3611.

33. Z. Guo, G. H. Kim, J. Yoon, I. Shin, *Nat. Protoc.* **2014**, *9*, 1245–1254.

34. Z. Guo, G. H. Kim, I. Shin, J. Yoon, *Biomaterials* **2012**, *33*, 7818–7827.

35. P. Du, S. J. Lippard, *Inorg. Chem.* **2010**, *49*, 10753–10755.

36. Y. Koide, Y. Urano, K. Hanaoka, T. Terai, T. Nagano, *ACS Chem. Biol.* **2011**, *6*, 600–608.

37. N. C. Lim, C. Brückner, *Chem. Commun.* **2004**, 1094–1095.

38. C. J. Chang, J. Jaworski, E. M. Nolan, M. Sheng, S. J. Lippard, *Proc. Natl. Acad. Sci. U.S.A.* **2004**, *101*, 1129–1134.

39. J. Wang, Y. Xiao, Z. Zhang, X. Qian, Y. Yang, Q. Xu, *J. Mater. Chem.* **2005**, *15*, 2836–2839.

40. H. Y. Au-Yeung, C. Y. Chan, K. Y. Tong, Z. H. Yu, *J. Inorg. Biochem.* **2017**, *177*, 300–312.

41. E. Gaggelli, H. Kozlowski, D. Valensin, G. Valensin, *Chem. Rev.* **2006**, *106*, 1995–2044.

42. J. A. Cotruvo, Jr, A. T. Aron, K. M. Ramos-Torres, C. J. Chang, *Chem. Soc. Rev.* **2015**, *44*, 4400–4414.

43. K. M. Ramos-Torres, S. Kolemen, C. J. Chang, *Isr. J. Chem.* **2016**, *56*, 724–737.

44. L. Yang, R. McRae, M. M. Henary, R. Patel, B. Lai, S. Vogt, C. J. Fahrni, *Proc. Natl. Acad. Sci. USA* **2005**, *102*, 11179–11184.

45. M. T. Morgan, P. Bagchi, C. J. Fahrni, *J. Am. Chem. Soc.* **2011**, *133*, 15906–15909.

46. L. Zeng, E. W. Miller, E. Y. Pralle, E. Y. Isacoff, C. J. Chang, *J. Am. Chem. Soc.* **2006**, *128*, 10–11.

47. S. C. Dodani, D. W. Domaille, C. I. Nam, E. W. Miller, L. A. Finney, S. Vogt, C. J. Chang, *Proc. Natl. Acad. Sci. USA* **2011**, *108*, 5980–5985.

48. S. C. Dodani, A. Firl, J. Chan, C. I. Nam, A. T. Aron, C. S. Onak, K. M. Ramos-Torres, J. Paek, C. M. Webster, M. B. Feller, C. J. Chang, *Proc. Natl. Acad. Sci. USA* **2014**, *111*, 16280–16285.

49. D. W. Domaille, L. Zeng, C. J. Chang, *J. Am. Chem. Soc.* **2010**, *132*, 1194–1195.

50. C. Satriano, G. T. Sfrazzetto, M. E. Amato, F. P. Ballistreri, A. Copani, M. L. Giuffrida, G. Grasso, A. Pappalardo, E. Rizzarelli, G. A. Tomaselli, R. M. Toscano, *Chem. Commun.* **2013**, *49*, 5565–5567.

51. S. C. Dodani, S. C. Leary, P. A. Cobine, D. R. Winge, C. J. Chang, *J. Am. Chem. Soc.* **2011**, *133*, 8606–8616.

52. X. Cao, W. Lin, W. Wan, *Chem. Commun.* **2012**, *48*, 6247–6249.

53. T. Hirayama, G. C. Van de Bittner, L. W. Gray, S. Lutsenko, C. J. Chang, *Proc. Natl. Acad. Sci. USA* **2012**, *109*, 2228–2233.

54. C. S. Lim, J. H. Han, C. W. Kim, M. Y. Kang, D. W. Kang, B. R. Cho, *Chem. Commun.* **2011**, *47*, 7146–7148.

55. M. Taki, S. Lyoshi, A. Ojida, I. Hamachi, Y. Yamamoto, *J. Am. Chem. Soc.* **2010**, *132*, 5938–5939.

56. M. Taki, K. Akaoka, K. Mitsui, Y. Yamamoto, *Org. Biomol. Chem.* **2014**, *12*, 4999–5005.

57. C. Y. S. Chung, J. M. Posimo, S. Lee, T. Tsang, J. M. Davis, D. C. Brady, C. J. Chang, *Proc. Natl. Acad. Sci. USA* **2019**, *116*, 18285–18294.

58. M. C. Heffern, H. M. Park, H. Y. Au-Yeung, G. C. Van de Bittner, C. M. Ackerman, A. Stahl, C. J. Chang, *Proc. Natl. Acad. Sci. USA* **2016**, *113*, 14219–14224.

59. Z. Xu, Y. Xiao, X. Qian, J. Cui, D. Cui, *Org. Lett.* **2005**, *7*, 889–892.

60. M. L. Giuffrida, G. T. Sfrazzetto, C. Satriano, S. Zimbone, G. A. Tomaselli, A. Copani, E. Rizzarelli, *Inorg. Chem.* **2018**, *57*, 2365–2368.

61. S. Wang, Z. Sheng, Z. Yang, D. Hu, X. Long, G. Feng, Y. Liu, Z. Yuan, J. Zhang, H. Zheng, X. Zhang, *Angew. Chem. Int. Ed.* **2019**, *58*, 12415–12419.

62. P. Li, X. Duan, Z. Chen, Y. Liu, T. Xie, L. Fang, X. Li, M. Yin, B. Tang, *Chem. Commun.* **2011**, *47*, 7755–7757.

63. S. Y. Park, W. Kim, S. H. Park, J. Han, J. Lee, C. Kang, M. H. Lee, *Chem. Commun.* **2017**, *53*, 4457–4460.

64. J. Kovács, A. Mokhir, *Inorg. Chem.* **2008**, *47*, 1880–1882.

65. J. Wang, Q. Zong, *Sens. Actuators B Chem.* **2015**, *216*, 572–577.

66. H. Li, P. Zhang, L. P. Smaga, R. A. Hoffman, J. Chan, *J. Am. Chem. Soc.* **2015**, *137*, 15628–15631.

67. N. Li, Y. Xiang, A. Tong, *Chem. Commun.* **2010**, *46*, 3363–3365.

68. V. Dujols, F. Ford, A. Czarnik, *J. Am. Chem. Soc.* **1997**, *119*, 7386–7387.

69. C. Yu, J. Zhang, J. Li, P. Liu, P. Wei, L. Chen, *Microchim. Acta* **2011**, *174*, 247–255.

70. K. M. K. Swamy, S. K. Ko, S. K. Kwon, H. N. Lee, C. Mao, J. M. Kim, K. H. Lee, J. Kim, I. Shin, j. Yoon, *Chem. Commun.* **2008**, 5915–5917.

71. D. Wang, Y. Shiraishi, T. Hirai, *Chem. Commun.* **2011**, *47*, 2673–2675.

72. W. Lin, L. Long, B. Chen, W. Tan, W. Gao, *Chem. Commun.* **2010**, *46*, 1311–1313.

73. Z. Shi, X. Tang, X. Zhou, J. Cheng, Q. Han, J. A. Zhou, B. Wang, Y. Yang, W. Liu, D. Bai, *Inorg. Chem.* **2013**, *52*, 12668–12673.

74. I. Bertini, H. B. Gray, S. J. Lippard, J. S. Valentine, *Bioinorganic Chemistry*, University Science Books, Mill Valley, California, **1994**.

75. G. Greeenberg, M. M. Wintrobe, *J. Biol. Chem.* **1946**, *165*, 397–398.

76. A. Jacobs, *Ciba Found. Symp.* **1977**, *51*, 91–106.

77. A. T. Aron, A. G. Reeves, C. J. Chang, *Curr. Opin. Chem. Biol.* **2018**, *42*, 113–118.

78. Y. Ma, V. Abbate, R. C. Hider, *Metallomics* **2015**, *7*, 212–222.

79. W. Breuer, S. Epsztejn, P. Millgram, I. Z. Cabantchik, *Am. J. Physiol.* **1995**, *268*, C1354–C1361.

80. F. Petrat, U. Rauen, H. de Groot, *Hepatology* **1999**, *29*, 1171–1179.

81. P. Li, L. Fang, H. Zhou, W. Zhang, X. Wang, N. Li, H. Zhong, B. Tang, *Chem. Eur. J.* **2011**, *17*, 10520–10523.

82. J. L. Chen, S. J. Zhuo, Y. Q. Wu, F. Fang, L. Li, C. Q. Zhu, *Spectrochim. Acta A Mol. Biomol. Spectrosc.* **2006**, *63*, 438–443.

83. S. Maiti, Z. Aydin, Y. Zhang, M. Guo, *Dalton Trans.* **2015**, *44*, 8942–8949.

84. T. Hirayama, *Acta Histochem. Cytochem.* **2018**, *51*, 137–143.

85. T. Hirayama, K. Okuda, H. Nagasawa, *Chem. Sci.* **2013**, *4*, 1250–1256.

86. F. Ito, T. Nishiyama, L. Shi, M. Mori, T. Hirayama, H. Nagasawa, H. Yasui, S. Toyokuni, *Biochem. Biophys. Res. Commun.* **2016**, *476*, 600–606.

87. Y. Ikeda, Y. Horinouchi, H. Hamano, T. Hirayama, S. Kishi, Y. Izawa-Ishizawa, M. Imanishi, Y. Zamami, K. Takechi, L. Miyamoto, K. Ishizawa, K. I. Aihara, H. Nagasawa, K. Tsuchiya, T. Tamaki, *Sci. Rep.* **2017**, *7*, 10621.

88. M. Niwa, T. Hirayama, K. Okuda, H. Nagasawa, *Org. Biomol. Chem.* **2014**, *12*, 6590–6597.

89. T. Hirayama, H. Tsuboi, M. Niwa, A. Miki, S. Kadota, Y. Ikeshita, K. Okuda, H. Nagasawa, *Chem. Sci.* **2017**, *8*, 4858–4866.

90. M. Niwa, T. Hirayama, I. Oomoto, D. O. Wang, H. Nagasawa, *ACS Chem. Biol.* **2018**, *13*, 1853–1861.

91. H. Y. Au-Yeung, J. Chan, T. Chantarojsiri, C. J. Chang, *J. Am. Chem. Soc.* **2013**, *135*, 15165–15173.

92. A. T. Aron, M. O. Loehr, J. Bogena, C. J. Chang, *J. Am. Chem. Soc.* **2016**, *138*, 14338–14346.

93. B. Spangler, C. W. Morgan, S. D. Fontaine, M. N. Vander Wal, C. J. Chang, J. A. Wells, A. R. Renslo, *Nat. Chem. Biol.* **2016**, *12*, 680–685.

94. A. T. Aron, M. C. Heffern, Z. R. Lonergan, M. N. Vander Wal, B. R. Blank, B. Spangler, Y. Zhang, H. M. Park, A. Stahl, A. R. Skaar, C. J. Chang, *Proc. Natl. Acad. Sci. USA* **2017**, *114*, 12669–12674.

95. S. D. Lytton, B. Mester, J. Libman, A. Shanzer, Z. I. Cabantchik, *Anal. Biochem.* **1992**, *205*, 326–333.

96. H. Ouchetto, M. Dias, R. Mornet, E. Lesuisse, J. M. Camadro, *Bioorg. Med. Chem.* **2005**, *13*, 1799–1803.

97. S. Noël, L. Guillon, I. J. Schalk, G. L. Mislin, *Org. Lett.* **2011**, *13*, 844–847.

98. S. Fakih, M. Podinovskaia, X. Kong, U. E. Schaible, H. L. Collins, R. C. Hider, *J. Pharm. Sci.* **2009**, *98*, 2212–2226.

99. Z. Yang, M. She, B. Yin, J. Cui, Y. Zhang, W. Sun, J. Li, Z. Shi, *J. Org. Chem.* **2011**, *77*, 1143–1147.

100. Y. Xiang, A. Tong, *Org. Lett.* **2006**, *8*, 1549–1552.

101. M. Zhang, Y. Gao, M. Li, M. Yu, F. Li, L. Li, M. Zhu, J. Zhang, T. Yi, C. Huang, *Tetrahedron Lett.* **2007**, *48*, 3709–3712.

102. S. J. Kish, K. Shannak, O. Hornykiewicz, *N. Engl. J. Med.* **1988**, *318*, 876–880.

103. J. H. Ko, A. P. Strafella, *Neuroscientist* **2012**, *18*, 149–168.

104. T. Pradhan, H. S. Jung, J. H. Jang, T. W. Kim, C. Kang, J. S. Kim, *Chem. Soc. Rev.* **2014**, *43*, 4684–4713.

105. J. S. Marvin, G. G. Borghuis, L. Tian, J. Cichon, M. T. Harnett, J. Akerboom, A. Gordus, S. L. Renninger, T. W. Chen, C. I. Bargmann, M. O. Orger, E. R. Schreiter, J. B. Demb, W. B. Gan, S. A. Hires, L. L. Looger, *Nat. Methods* **2013**, *10*, 162–170.

106. T. Patriarchi, J. R. Cho, K. Merten, M. W. Howe, A. Marley, W. H. Xiong, R. W. Folk, G. J. Broussard, R. Liang, M. J. Jang, H. Zhong, D. Dombeck, M. von Zastrow, A. Nimmerjahn, V. Gradinaru, J. T. Williams, L. Tian, *Science* **2018**, *360*, eaat4422.

107. F. Sun, J. Zeng, M. Jing, J. Zhou, J. Feng, S. F. Owen, Y. Luo, F. Li, H. Wang, T. Yamaguchi, Z. Yong, Y. Gao, W. Peng, L. Wang, S. Zhang, J. Du, D. Lin, M. Xu, A. C. Kreitzer, G. Cui, Y. Li, *Cell* **2018**, *174*, 481–496.

108. N. G. Gubernator, H. Zhang, R. G. Staal, E. V. Mosharov, D. B. Pereira, M. Yue, V. Balsanek, P. A. Vadola, B. Mukherjee, R. H. Edwards, D. Sulzer, D. Sames, *Science* **2009**, *324*, 1441–1444.

109. A. Henke, Y. Kovalyova, M. Dunn, D. Dreier, N. G. Dincheva, C. Hwu, P. Šebej, M. S. Ansorge, D. Sulzer, D. Sames, *ACS Chem. Neurosci.* **2018**, *9*, 925–934.

110. X. Chen, X. Tian, I. Shin, J. Yoon, *Chem. Soc. Rev.* **2011**, *40*, 4783–804.

111. X. Ye, S. S. Rubakhin, J. V. Sweedler, *Analyst* **2008**, *133*, 423–433.

112. V. S. Lin, C. J. Chang, *Curr. Opin. Chem. Biol.* **2012**, *16*, 595–601.

113. N. Kumar, V. Bhalla, M. Kumar, *Coord. Chem. Rev.* **2013**, *257*, 2335–2347.

114. M. Strianese, C. Pellecchia, *Coord. Chem. Rev.* **2016**, *318*, 16–28.

115. V. S. Lin, W. Chen, M. Xian, C. J. Chang, *Chem. Soc. Rev.* **2015**, *44*, 4596–4618.

116. X. Liu, N. Li, M. Li, H. Chen, N. Zhang, Y. Wang, K. Zheng, *Coord. Chem. Rev.* **2020**, *404*, doi: 10.1016/j.ccr.2019.213109.

117. Z. M. Sheffler, L. S. Pillarisetty, *Physiology, Neurotransmitters*, StatPearls Publishing, Treasure Land, Florida, **2019**.

118. M. Bonizzoni, L. Fabbrizzi, G. Piovani, A. Taglietti, *Tetrahedron* **2004**, *60*, 11159–11162.

119. H. Aït-Haddou, S. L. Wiskur, V. M. Lynch, E. V. Anslyn, *J. Am. Chem. Soc.* **2001**, *123*, 11296–11297.

120. E. K. Feuster, T. E. Glass, *J. Am. Chem. Soc.* **2003**, *125*, 16174–16175.

121. J. L. Klockow, K. S. Hettie, T. E. Glass, *ACS Chem. Neurosci.* **2013**, *4*, 1334–1338.

122. R. A. Webster, *Neurotransmitters, Drugs and Brain Function*, John Wiley & Sons, UK, **2001**.

123. K. E. Secor, T. E. Glass, *Org. Lett.* **2004**, *21*, 3727–3730.

124. K. S. Hettie, X. Liu, K. D. Gillis, T. E. Glass, *ACS Chem. Neurosci.* **2013**, *4*, 918–923.

125. L. Zhang, X. A. Liu, K. D. Gillis, T. E. Glass, *Angew. Chem. Int. Ed.* **2019**, *58*, 7611–7614.

126. J. Yan, G. Springsteen, S. Deeter, B. Wang, *Tetrahedron* **2004**, *60*, 11205–11209.

127. C. Godoy-Alcäntar, A. K. Yatsimirsky, J. M. Lehn, *J. Phys. Org. Chem.* **2005**, *18*, 979–985.

128. K. Y. Tong, J. Zhao, C. W. Tse, P. K. Wan, J. Rong, H. Y. Au-Yeung, *Chem. Sci.* **2019**, *10*, 8519–8526.

129. Y. Yue, F. Huo, C. Yin, *Anal. Chem.* **2018**, *91*, 2255–2259.

130. K. S. Hettie, T. E. Glass, *ACS Chem. Neurosci.* **2016**, *7*, 21–25.

131. D. Seto, N. Soh, K. Nakano, T. Imato, *Anal. Biochem.* **2010**, *404*, 135–139.

132. D. Seto, N. Soh, K. Nakano, T. Imato, *Bioorg. Med. Chem. Lett.* **2010**, *20*, 6708–6711.

133. N. Kielland, M. Vendrell, R. Lavilla, Y. T. Chang, *Chem. Commun.* **2012**, *48*, 7401–7403.

134. J. Nasica-Labouze, P. H. Nguyen, F. Sterpone, O. Berthoumieu, N. V. Buchete, S. Coté, A. De Simone, A. J. Doig, P. Faller, A. Garcia, A. Laio, M. S. Li, S. Melchionna, N. Mousseau, Y. Mu, A. Paravastu, S. Pasquali, D. J. Rosenman, B. Strodel, B. Tarus, J. H. Viles, T. Zhang, C. Wang, P. Derreumaux, *Chem. Rev.* **2015**, *115*, 3518–3163.

135. E. E. Nesterov, J. Skoch, B. T. Hyman, W. E. Klunk, B. J. Bacskai, T. M. Swager, *Angew. Chem. Int. Ed.* **2005**, *44*, 5452–5456.

136. M. M. Xu, W. M. Ren, X. C. Tang, Y. H. Hu, H. Y. Zhang, *Acta Pharmacol. Sin.* **2016**, *37*, 719–730.

137. W. E. Klunk, Y. Wang, G. F. Huang, M. L. Debnath, D. P. Holt, C. A. Mathis, *Life Sci.* **2001**, *69*, 1471–1484.

138. S. J. Jung, Y. D. Park, J. H. Park, S. D. Yang, M. G. Hur, K. H. Yu, *Med. Chem. Res.* **2013**, *22*, 4263–4268.

139. M. Ono, S. Hayashi, H. Kimura, H. Kawashima, M. Nakayama, *Bioorg. Med. Chem.* **2009**, *17*, 7002–7007.

140. S. B. Raymond, J. Skoch, I. D. Hills, E. E. Nesterov, T. M. Swager, B. J. Bacskai, *Eur. J. Nucl. Med. Mol. Imaging* **2008**, *35*, S93–S98.

141. H. Tong, K. Lou, W. Wang, *Acta Pharm. Sin. B.* **2015**, *5*, 25–33.

142. C. Peng, X. Wang, Y. Li, H. W. Li, M. S. Wong, *J. Mater. Chem. B.* **2019**, *7*, 1986–1995.

143. Y. W. Jun, S. W. Cho, J. Jung, Y. Huh, Y. Kim, D. Kim, K. H. Ahn, *ACS Cent. Sci.* **2019**, *5*, 209–217.

144. P. G. Vallet, R. Guntern, P. R. Hof, J. Golaz, A. Delacourte, N. K. Robakis, C. Bouras, *Acta Neuropathol.* **1992**, *83*, 170–178.

145. K. S. Park, Y. Seo, M. K. Kim, K. Kim, Y. K. Kim, H. Choo, Y. Chong, *Org. Biomol. Chem.* **2015**, *13*, 11194–11199.

146. P. Verwilst, H. R. Kim, J. Seo, N. W. Sohn, S. Y. Cha, Y. Kim, S. Maeng, J. W. Shin, J. H. Kwak, C. Kang, J. S. Kim, *J. Am. Chem. Soc.* **2017**, *139*, 13393–13403.

147. S. Lim, M. M. Haque, D. Su, D. Kim, J. S. Lee, Y. T. Chang, Y. K. Kim, *Chem. Commun.* **2017**, *53*, 1607–1610.

148. A. Ojida, T. Sakamoto, M. A. Inoue, S. H. Fujishima, G. Lippens, I. Hamachi, *J. Am. Chem. Soc.* **2009**, *131*, 6543–6548.

149. H. Y. Kim, U. Sengupta, P. Shao, M. J. Guerrero-Muñoz, R. Kayed, M. Bai, *Am. J. Nucl. Med. Mol. Imaging* **2013**, *3*, 102–117.

150. S. S. Hindo, A. M. Mancino, J. J. Braymer, Y. Liu, S. Vivekanandan, A. Ramamoorthy, M. H. Lim, *J. Am. Chem. Soc.* **2009**, *131*, 16663–16665.

151. J. S. Choi, J. J. Braymer, R. P. R. Nanga, A. Ramamoorthy, M. H. Lim, *Proc. Natl. Acad. Sci. USA* **2010**, *107*, 21990–21995.

17

Heavy Elements for X-Ray Contrast

Yuxi C. Dong and David P. Cormode

Departments of Radiology and Bioengineering, University of Pennsylvania,
Philadelphia, PA 19104, USA
<david.cormode@pennmedicine.upenn.edu>

Abstract: X-ray imaging is the oldest, but most important ionizing radiation-based technique. It provides information on the structural features of the human body, contributing to the diagnosis and treatment of numerous diseases. The success of X-ray imaging depends not only on the advances of diagnostic instruments (i.e., computed tomography (CT), mammography, etc.), but also on the development of contrast agents. The use of contrast agents in X-ray imaging can improve the visualization of target tissues and organs and provides anatomical information for disease diagnosis and treatment. X-ray contrast agents are usually small molecules or nanoparticles that contain high atomic number (Z) heavy elements, such as iodine, barium, gold, silver, and so forth. The current clinically approved contrast agents for X-ray imaging are iodinated small molecules or barium sulfate suspensions, although adverse events can result from these agents, and they have shortcomings in their specificity, as well as contrast generation. The development of alternative heavy element-based X-ray contrast agents has therefore become a key focus in the field of X-ray imaging. Tremendous progress has been made in the field over the past decade. In this chapter, we summarize the advances in the developments of heavy elements as contrast agents for X-ray imaging. Moreover, we describe their applications in molecular imaging, including targeted imaging, as well as CT cell tracking, and theranostics. Finally, the prospects and the challenges in clinical translation will be discussed.

Keywords: contrast agents · gold nanoparticles · heavy elements · nanoparticles · X-ray imaging

1. INTRODUCTION

The discovery of X-rays by the German physics professor Wilhelm Conrad Röntgen in 1895 marked the beginning of the medical physics and imaging revolution [1–3]. When operating with an electron-discharge tube, Röntgen inadvertently noticed that the tube produced a fluorescent glow on a screen several feet away, even though the tube was covered by heavy black cardboard. This previously undiscovered ray was then dubbed "X-ray" by Röntgen because of its unknown nature [4]. The iconic X-ray image of Mrs. Röntgen's hand that revealed her bones instantly aroused immense interest in the science community for X-ray's medical applications, and created a huge advance in medicine [1]. By 1930, X-ray was a routine part of hospital diagnosis and clinical care [5]. Nowadays, in the United States alone, more than 350 million medical X-ray based examinations and procedures are carried out each year, making X-ray imaging one of the most common imaging procedures [6].

While there has been enormous improvements in X-ray imaging over the last century in regard to X-ray generation and image quality, the fundamentals of X-ray contrast generation remain unchanged [7, 8]. Certain body tissues can be distinguished under X-ray imaging such as bone due to high mineralization [8, 9] However, being similar in terms of densities, some adjacent soft tissues are difficult to distinguish on the basis of the contrast produced by the tissue itself [9–11]. As a result, X-ray contrast agents are typically used for better differentiation and visualization of body tissues and their significance has been widely recognized.

Currently, barium sulfate suspensions and iodinated small molecules are the only FDA approved and commercially available X-ray contrast agents for human use [3, 12]. While visualizing tissues of interest effectively, both can potentially pose serious complications such as barium sulfate aspiration and contrast-induced nephropathy. These risks have created interest in developing safer and more efficient X-ray contrast agents [13–15]. Moreover, these agents are non-specific and are not well-suited to some newer multi-energy X-ray imaging techniques, such as photon counting CT or dual-energy mammography [16]. Recent progress in nanotechnology has created opportunities for nanoparticles based on heavy elements to be contrast agents for X-ray imaging [17–20]. Nanoparticles as contrast agents offer significant advantages in their design, such as coating material, shape and size, to match various imaging purposes [21–23].

In the following sections, we will first outline the basic physics of X-ray generation, principles of contrast enhancement from heavy elements, and various imaging modalities based on X-ray. In a study of historical and contemporary inquiries, we will then focus on the structural characteristics, contrast enhancement and safety of contrast agents based on heavy elements. In addition, the applications of these contrast agents in molecular imaging such as targeted imaging, cell tracking, and therapeutics will be described. Last, the obstacles and future prospects for these contrast agents will be discussed.

2. PHYSICS OF X-RAY CONTRAST GENERATION

2.1. Overview of X-Ray Production

X-rays are a form of electromagnetic radiation with wavelengths between 0.01 to 10 nm [24].
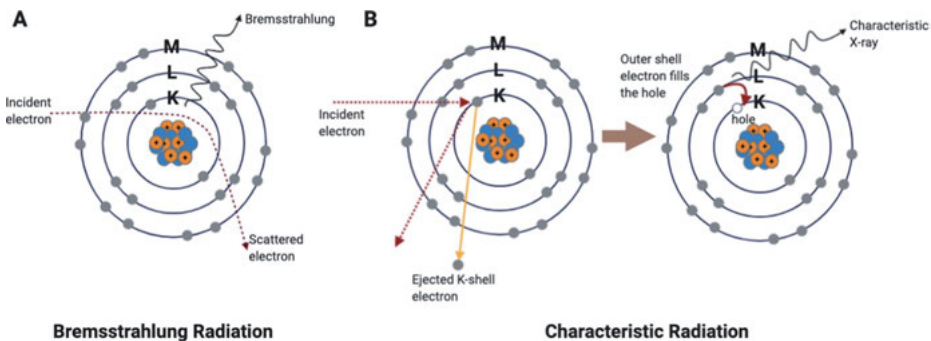
Figure 1. Schematic of X-ray production. (**A**) *Bremsstrahlung* radiation is produced when the incident electrons are diverted by the electric field of the nuclei of the anode. (**B**) Characteristic radiation is produced when the incident electrons collide with the electrons in the inner shell and knock out an electron on the K-shell, creating a vacancy, which is filled by an outer electron.

They are typically produced by two mechanisms, known as Bremsstrahlung radiation (braking radiation) and characteristic radiation. During the Bremsstrahlung process, the bombarding electrons penetrate into the target and approach to the nucleus due to the attraction of its positive charge. The electrons are then turned away by the nucleus' electrical field, and a part or all of their kinetic energy is lost. The energy lost from this process is released as X-ray photons, or Bremsstrahlung radiation (Figure 1A). Characteristic radiation is produced when a fast-moving bombarding electron ejects a K-shell electron leaving behind a 'hole' (Figure 1B). A higher shell electron then moves to fill the empty space and energy is released in the form of a single X-ray photon with a specific energy [25, 26]. An X-ray spectrum is formed that is the result of a combination of the Bremsstrahlung radiation and characteristic radiation. The X-ray spectrum can be altered by manipulating the X-ray tube current or potential, adding filtration, or changing the target material [27].

2.2.   Principles of Contrast Enhancement

X-ray attenuation is the reduction of an X-ray beam's intensity as it traverses matter [28]. It results from tissue absorption or scattering of X-rays. Air absorbs X-rays, for example, weakly, but bone intensely absorbs X-rays leading to substantial contrast between these substances. At standard pressure and temperature, water attenuation is defined as 0 HU, and while that of air is –1000 HU [29]. However, soft tissues do not tend to have significant differences in attenuation. Hence, contrast agents are often administered to better visualize and distinguish soft tissues. X-ray attenuation is defined in Hounsfield units (HU) for a given material X in Equation (1):

$$HU\ (X) = \frac{1000\left(\mu_X - \mu_{water}\right)}{\left(\mu_{air} - \mu_{water}\right)} \tag{1}$$

The linear X-ray mass attenuation coefficient characterizes the fraction of an X-ray beam that is absorbed or scattered by absorber's unit thickness, in a unit of cm^{-1}, or expressed in g/cm^2 after normalizing the linear attenuation coefficient per unit material density. Usually, the X-ray beam is easily attenuated by high attenuation coefficient materials. Contrary to this, low attenuation coefficients indicate that the material is somewhat transparent to the X-ray beam [28, 30]. Due to their different Z number and density, the elements have different characteristic, energy-dependent X-ray attenuation profiles. The probability of the occurrence of the photoelectric effect, one of the two fundamental mechanisms responsible for the attenuation of X-rays passing through a material, is proportional to Z^3 (above the K-edge of the element), suggesting that the photoelectric effect more likely occurs for heavier elements.

The K-edge energy is the minimum energy required for the photoelectric event to occur for a K-shell electron. Generally speaking, photoelectric events are most

likely to occur when the energy is just above the K-edge [31]. In soft tissues, the dominant elements (i.e., C, H, O, and N) have very low energy K-edges, thus only attenuating very low energy X-rays. However, heavy elements such as iodine and barium have K-edges closer in energy to X-ray beam spectra typically used in medical imaging, resulting in greater attenuation. Certain heavy elements such as gold, bismuth, tantalum, and ytterbium have K-edges between 50 kV and 100 kV and also attenuate strongly at clinically relevant energies [32].

On the other hand, the probability of the second major process of X-ray absorption, Compton scattering, is more dependent on the element's physical density. A photon strikes an atom in the Compton effect, ionizing a weakly bound electron. Then the photon scatters in a different direction with reduced energy, attenuating the X-ray beam. Since the Compton effect is the interaction between photons and outer electrons, the Compton scattering is nearly independent of the X-ray energy but depends on the electron density of the material. Therefore, heavy elements with high densities would generally have more Compton scattering [25, 33].

Taking into consideration both the photoelectric effect and Compton scattering, heavy elements, identified as elements with high Z number, high density, and high atomic weights, are typically considered as good candidates from which to form X-ray contrast agents [34].

2.3. X-Ray-Based Imaging Modalities

Planar X-ray imaging, i.e., conventional radiography, produces 2-dimensional images of objects. It provides an initial screening tool for both acute injuries such as bone fracture and chronic diseases such as gastrointestinal (GI) tract diseases [35]. Depending upon the results of an X-ray scan, a full 3D CT scan (or other type of imaging modality) may be requested for more detailed diagnosis. CT is a non-destructive imaging tool that uses computerized X-ray imaging techniques to produce detailed, cross-sectional and 3-dimensional images of anatomy. CT is a common imaging modality used routinely in clinics for a variety of diagnostic and therapeutic purposes [17, 36]. Unlike a conventional X-ray using a fixed X-ray tube, a CT scanner uses a motorized X-ray source that rotates on a ring around the patient, allowing data acquisition from every angle. X-rays emitted from the X-ray tube travel through the patient and then encounters the X-ray detector array system that measures the flux of X-rays. The CT scanner reconstructs images from the dataset using sophisticated algorithms each time the X-ray source completes a full rotation around the patients [37, 38]. Similarly, fluoroscopy uses a mobile X-ray source to obtain real-time moving images of anatomy in short intervals [39]. It is widely used in interventional radiology, and image-guided surgery [40]. X-ray CT imaging can also be combined with other imaging modalities to form a combined imaging modality, such as positron emission tomography-computed tomography (PET/CT) imaging. These combined scans can pinpoint abnormal metabolic activity by precisely co-reregistering functional and anatomic images [41].

Spectral photon-counting computed tomography (SPCCT) is an investigational X-ray imaging technique derived from conventional CT. A prominent advantage of SPCCT includes its material-specific K-edge imaging and the potential to identify the type of tissue based on their energy-dependent attenuation of X-rays [42–44]. SPCCT has a standard polychromatic X-ray source and energy-sensitive photon counting detectors that measure the energy of individual X-ray photons and can divide the absorbed photons into several energy bins. Thus, a material-specific map can be produced and specific information can be obtained on elements with K-edges in the region of CT X-ray beams with high photon flux (i.e., 40–100 keV) such as gadolinium (K-edge = 50.2 keV), gold (K-edge = 80.72 keV), or bismuth (K-edge = 90.53 keV) [23, 45, 46].

Mammography is a type of X-ray based, specialized medical imaging technique that uses low energy X-rays (e.g., 30 kV) to examine the breast for early detection of breast cancer, usually by detecting irregular structures or microcalcifications [47, 48]. However, for patients with dense breast tissue, which, unlike non-dense tissue, is bright in mammography images and looks similar to cancerous tissue, the sensitivity of mammography is low [49, 50]. To overcome this constraint, dual energy contrast-enhanced mammography (DEM) consisting of both high-energy and low-energy mammograms has been studied [51, 52]. The low-energy images provide maximal soft tissue contrast, while high-energy images are used for post-processing. The images are subtracted to cancel out the common soft tissue contrast and to isolate the contrast enhancement in the region of interest [53, 54]. Several heavy element-based contrast agents are being investigated for this technique due to the allergic reactions posed by iodinated contrast agents and iodine's suboptimal contrast generation. The best candidate materials for DEM have a Z number from 42 to 62 [55]. Molybdenum (Z = 42), rhodium (Z = 45), palladium (Z = 46), silver (Z = 47), and tellurium (Z = 52) are possible DEM contrast materials under investigation [19, 56].

3.   HEAVY ELEMENT-BASED CONTRAST AGENTS

3.1.   Current Clinically Used Contrast Agents

3.1.1.   *Barium Sulfate*

Barium sulfate suspensions are the standard contrast agent taken orally for opacification of the upper and lower GI tract in radiographic examinations [57, 58]. With a high Z number of 56, barium sulfate absorbs and scatters X-rays effectively, thereby rendering the structure of the GI radiopaque. Barium sulfate is commonly suspended as thick, chalky, cream like liquids with flavoring agents added, which are also referred to as barium shakes. While barium is a heavy metal, it is not absorbed by the digestive tract or metabolized in the body due to the poor solubility of barium sulfate in aqueous media [59, 60]. In addition, the high viscosity and insolubility of barium sulfate suspensions prevent them from diluting in the GI tract [61–63]. Using barium sulfate as a contrast agent

was generally thought to be a safe technique in GI examination. In addition to the common side effects of administering barium sulfate such as diarrhea, nausea and barium sulfate aspiration, however, a rare complication has been documented worldwide. High-density aspiration is potentially life-threatening and restricts the use of agents in patients with certain underlying conditions such as dysphagia [13, 14, 59].

3.1.2. *Iodinated Contrast Agents*

Iodinated contrast agents, first introduced into clinical practice in the 1950s, are still the most commonly used X-ray imaging intravenous radiocontrast agents [64]. Because it is a heavy element, with a Z number of 53, iodine imparts strong contrast to objects imaged with X-rays. Iodinated contrast agents are typically derivatives of tri-iodinated benzene rings with various hydrophilic functional groups appended to the ring. Their chemical compositions and structures provide them with advantageous properties for intravenous injection. For example, iohexol, a nonionic monomer-iodinated small molecule has three amide and six hydroxyl substituent groups that make it water-soluble. In addition, the covalent bonds between the iodine atoms and benzene rings reduce the risk of side effects that might occur from free iodine [37, 65]. Therefore, iodinated contrast agents are usually considered safe. Nonetheless, severe reactions may occur [66]. The most common adverse reactions in patients with iodinated contrast agent include contrast-induced nephropathy, hypersensitivity reactions, and renal impairment due to its high osmolarity and rapid kidney clearance [65–67]. In addition, short blood circulation and rapid contrast washout restrict post-injection imaging time [68]. In the past decades, significant attempts have been made to develop novel heavy element-based agents with comparable or better contrast generation, longer blood circulation times, and targeting capabilities.

3.2. Nanoparticle Contrast Agents

3.2.1. *Gold*

Gold nanoparticles (AuNP) have been extensively studied over the past fifteen years for X-ray imaging, following Hainfeld's report of a 1.9 nm AuNP formulation as a new X-ray contrast agent [69]. Gold has several desirable properties making it a promising candidate to be used as an X-ray contrast agent. For example, gold has a high Z number of 79 and high electron density, resulting in efficient X-ray absorption [70, 71]. The K-edge of gold is 80.7 kV, meaning that it strongly absorbs X-rays within the typical clinical tube voltage range (i.e., 80–140 kV) and provides more X-ray contrast at 120 kV than at 80 kV [37]. In fact, several studies have shown that gold produces more contrast than iodinated contrast agents when scanned at 120 kV [17, 72]. In addition, AuNP are bioinert and biocompatible, and several formulations have been in clinical trials for biomedical uses [73–76]. Besides, the surface modification of AuNP with different
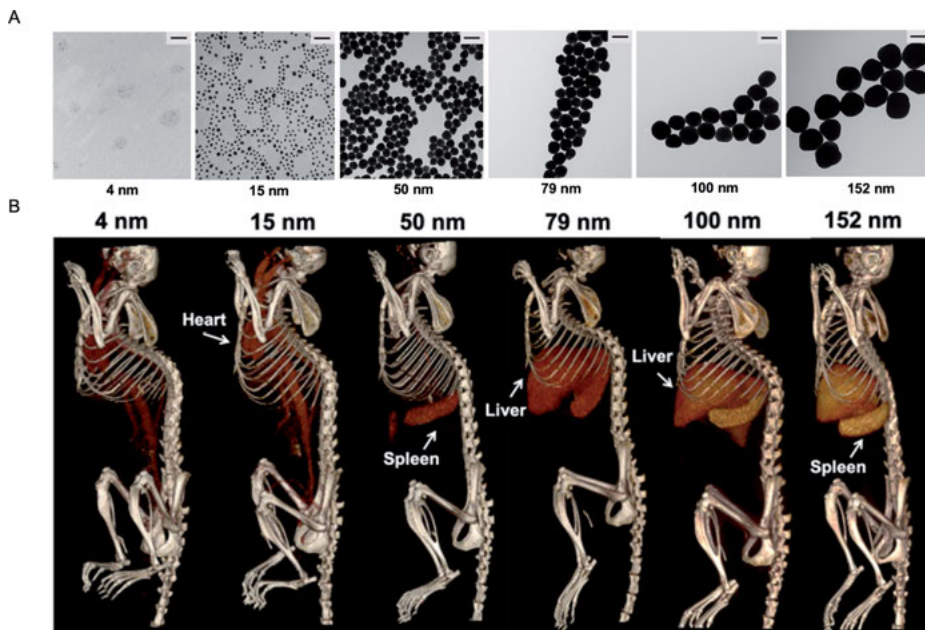
Figure 2. **(A)** TEM micrographs of 4–152 nm AuNP. The scale bars represent 100 nm in all panels. **(B)** 3D volume rendered CT images at 2 hours post-injection of AuNP of different sizes in mice. Reproduced by permission from Ref. [17]; copyright 2019, Springer Nature.

capping ligands is easy to achieve and synthetic techniques for AuNP of different shapes and sizes are widely available [71, 75]. AuNP's sizes and morphology can lead to different pharmacokinetics and biodistribution [77]. For example, small AuNP (i.e., 4 and 15 nm) have longer blood circulation times compared to the very short circulation half-lives of iodinated small molecules and sub-6 nm AuNP can be excreted by the kidneys, while large AuNP (i.e., 50 to 152 nm) are cleared from the blood more rapidly and have faster accumulation in liver and spleen (Figure 2), despite the fact that CT contrast generation is independent of AuNP size [17]. These physico-chemical properties of AuNP allow them to detect and image different tissues with the high temporal and spatial resolution of CT [36].

Meanwhile, AuNP have also been shown to be effective contrast agents for SPCCT [21, 43]. Phantom imaging studies with AuNP using an SPCCT prototype (Figure 3), illustrated that the scanner could specifically image AuNP in a milli-molar concentration range and could distinguish them from iodine. This shows the potential of SPCCT imaging to probe biological processes and diseases with more than one contrast agent simultaneously [78]. Studies have shown that gold high-density lipoprotein nanoparticles (Au-HDL) can be used to identify the macrophage-rich aortic plaques and calcifications in atherosclerosis from a single SPCCT scan [21, 42]. Furthermore, functionalized AuNP can enable targeted tumor CT imaging, which will be discussed in detail later in this chapter.
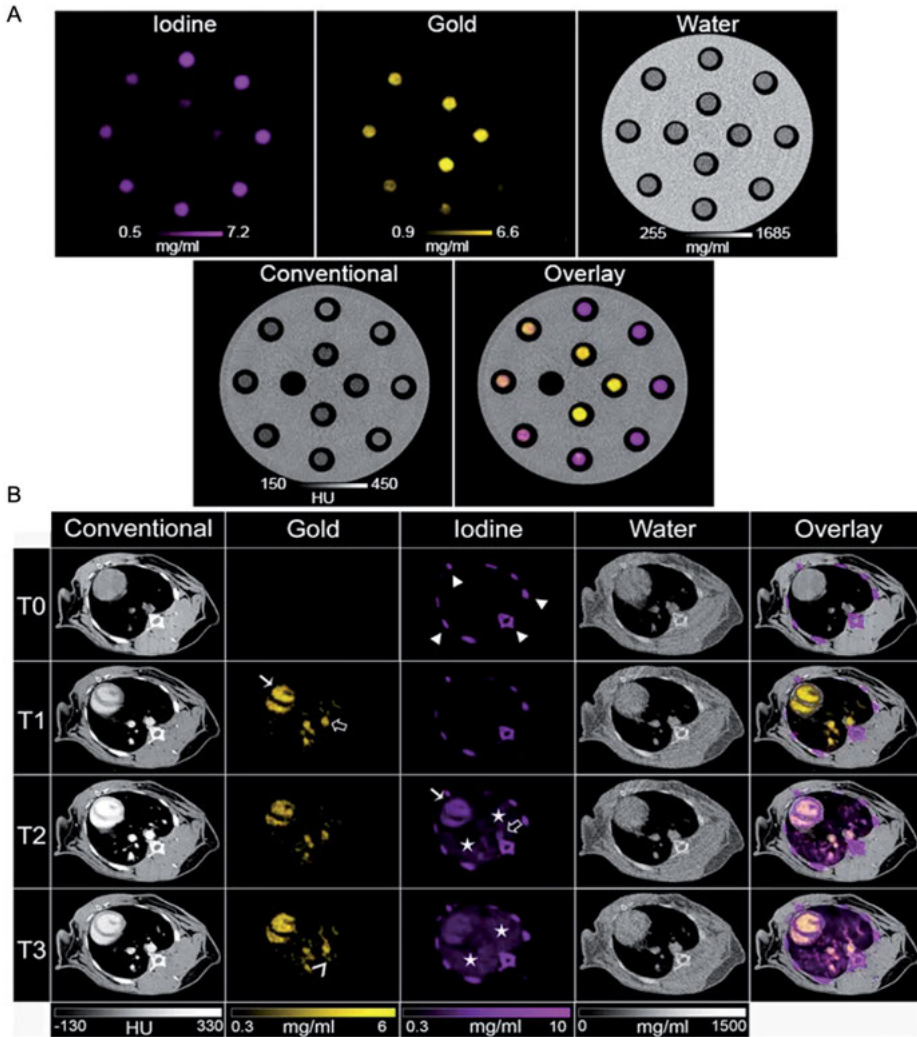
Figure 3. **(A)** Images derived from a SPCCT scan of a phantom that contained mixtures of AuNP and iodine in a range of concentrations. Iodine image, gold image, water image (top left to right), conventional CT equivalent image and overlay of gold and iodine images on the water image (bottom left to right). **(B)** SPCCT images of the chest of a rabbit at four time points. White arrows indicate the heart, arrowhead indicate bones, black arrows indicate the aorta, and stars indicate the lungs. Reproduced by permission from [78]; copyright 2017, Springer Nature.
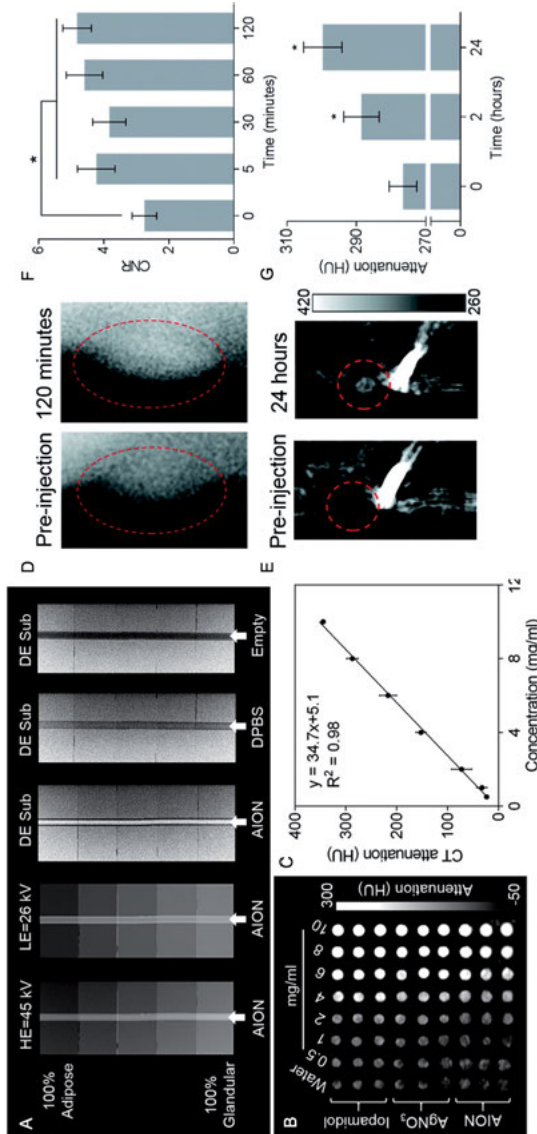
Figure 4. **(A)** DEM phantom images of AION (HE = high energy, LE = low energy, and DE Sub = dual energy subtraction). **(B)** CT phantom image. **(C)** Calculated CT attenuation of AION as a function of concentration with AION. **(D)** Representative DEM images of tumor-bearing mice at pre-injection and 2-hours post-injection with AION. **(E)** Representative CT images of tumor-bearing mice at pre-injection and 24-hours post-injection with AION. **(F)** DEM image-derived CNR in the tumor regions. **(G)** Average CT attenuation before and at 2- and 24-hours post injection. Reproduced by permission from [19]; copyright 2018, Royal Society of Chemistry.

3.2.2. Silver

Currently, contrast-enhanced mammography is done with the administration of iodinated small molecule contrast agents. Such contrast agents are rapidly filtered by kidneys and therefore require fast post-injection imaging and may result in contrast-media nephropathy in patients with renal insufficiency. These limitations may be resolved by nanoparticle contrast agents since they may have increased blood circulation times and can be targeted to tumors via appropriate surface modifications [79, 80]. Silver nanoparticles (AgNP) have been of tremendous scientific interest for biomedical applications including biosensing, as antimicrobial agents, catalysis, and biomedical imaging [55, 81–84]. In X-ray imaging, particularly in CT and DEM, AgNP have been investigated as alternatives to iodine. As mentioned above, breast images in DEM are acquired at both low and high tube voltages (e.g., 26 and 49 kV) [16, 85]. With its K-edge of 25.5 kV and Z number of 47, silver is well-matched to the energies used in DEM and is thus known as a possible DEM contrast agent [20]. Studies have shown that AgNP provide a 43 % higher signal difference-to-noise ratio (SDNR) than iodine with optimal DEM imaging parameters [55, 86]. Recently, Hsu et al. have developed an all-in-one nanoparticle (AION) formed by co-encapsulation of a near-infrared fluorophore (DiR), silver sulfide nanoparticles (Ag_2S-NP), and iron oxide nanoparticles (IO-NP) for DEM-CT-MRI and near-infrared fluorescence (NIRF) imaging for breast cancer screening. The safety and efficacy of AION as an X-ray imaging contrast agent was further demonstrated by *in vivo* tumor imaging of mice injected with AION with DEM and CT (Figure 4) [19].

In order to have higher chances for clinical translation as cancer imaging agents for DEM and CT, rapid renal excretion of contrast agents should be achieved. Hsu et al. reported Ag_2S-NP of 3.1 nm that can act as both DEM and CT contrast agents and have successful renal clearance [22]. In addition, another key for potential clinical translation of AgNP is avoiding the potential for silver ion-induced toxicity. Unlike elemental gold, elemental silver is not stable toward oxidation. Therefore, although AgNP have been widely used in many applications, the release of silver ions can be a safety concern [87, 88]. As a result, alternative silver chemistries are needed to achieve biocompatibility, especially given the high doses required in X-ray imaging. Strategies taken to address this issue have included forming gold-silver alloy nanoparticles or silver sulfide nanoparticles, with the latter resulting in at least 10-fold lower silver ion release in media over a span of 7 days compared to elemental silver nanoparticle controls [22].

3.2.3. Tantalum

Since the 1960s, powdered tantalum has been investigated as a contrast medium for X-ray examination of human airways [89]. Tantalum powder has subsequently been researched to provide contrast for inhalation bronchography, otolaryngology, liver imaging, and GI imaging [90–95]. Historical applications of tantalum in X-ray imaging are largely due to its high Z number of 73 and K-edge of 67 kV, as well as its nontoxicity and low cost compared to other contrast agents (i.e.,
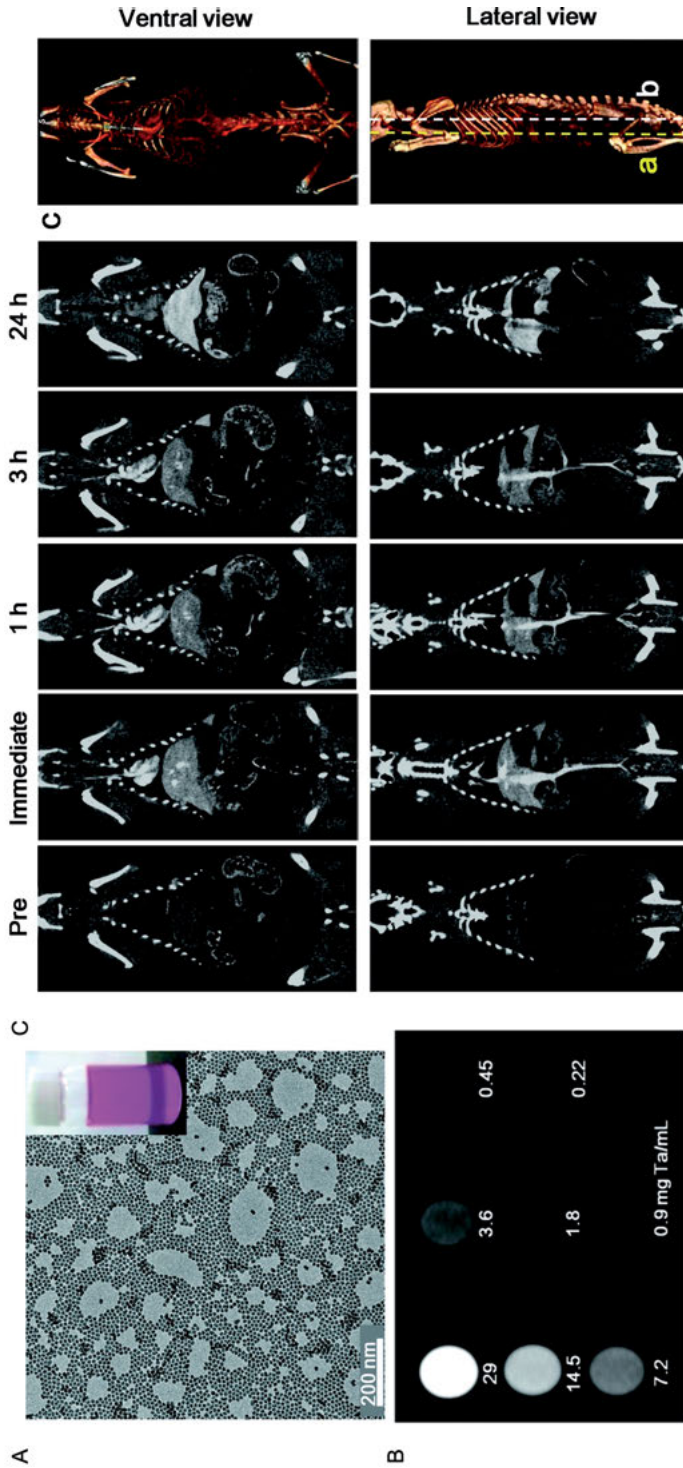
Figure 5. **(A)** TEM micrograph of TaONP dispersed in water. **(B)** CT phantom image of TaONP suspended in water in a range of concentrations. **(C)** *In vivo* X-ray CT imaging of a rat injected with 1 mL of TaONP (840 mg/kg) into the tail vein at different time points. Reproduced by permission from [99]; copyright 2011, American Chemical Society.

gold). For example, tantalum outperforms iodine in terms of CT contrast generation by 50 % at 120 kV [34].

Over the past ten years, some tantalum oxide nanoparticle (TaONP) formulations have been reported as X-ray contrast agents [96–99]. For example, Oh et al. reported large-scale syntheses of uniformly sized PEG-silane modified TaONP ranging from 5 to 15 nm. The nanoparticles are biocompatible and were effective in CT phantom imaging and *in vivo* CT angiography (Figure 5) [99]. The tolerable dosage levels of up to 1500 mg tantalum/kg with minimal side effects, and rapid elimination through renal clearance with low major organ retention in rat studies, show the potential clinical utility of TaONP as X-ray contrast agents [96, 98] In addition, TaONP have been proposed as potential contrast agents for SPCCT [43, 100, 101]. As a proof of concept SPCCT contrast agent, they showed excellent biocompatibility and strong contrast production [101].

TaONP have been reported as CT contrast agents for imaging articular cartilage with CT, as a drug-loading vehicle for synergetic chemoradiotherapy, and as a nanotheranostic agent for CT/photoacoustic biomodal imaging-guided cancer therapy [102–104], underscoring the versatility of this material.

3.2.4. *Bismuth*

Bismuth salts are noted for their low toxicity in medical applications such as treating gastrointestinal disorders and bacterial infections [105–107]. Moreover, bismuth is used in over-the-counter medicines (i.e., Pepto-Bismol) [108]. Thanks to its high Z number of 83 and high electron density, bismuth produces comparable contrast at 80 and 100 kV and greater contrast at 120 and 140 kV compared with conventional iodinated contrast agents [109, 110]. To date, several nanoparticle forms of bismuth, including elemental bismuth, bismuth sulfide (Bi_2S_3) or bismuth selenide (Bi_2Se_3), with various shapes and sizes have been investigated as X-ray contrast agents [110–114].

Bismuth can in particular be used as a radiosensitizer because of its high Z number. Meanwhile, some forms of bismuth nanoparticles can also be used in photoacoustic imaging (PA), making dual-modal CT/PA imaging and synergistic photothermal therapy (PTT)/radiotherapy (RT) treatment possible (Figure 6) [115]. Recently, additional efforts have been made to synthesize pure bismuth nanoparticles (i.e., 100 % bismuth content) to minimize the involvement of additional compounds (i.e., sulfides and selenides), which reduce the bismuth payload and maximize X-ray absorption efficiency [18, 116, 117]. Similar to other nanoparticles, further investigations on renal clearance and safety are needed for successful future clinical translation of these nanoparticles.

3.2.5. *Other Heavy Metals*

Some other heavy metals also possess strong X-ray attenuation, but have not yet been studied extensively as X-ray contrast agents in their nanoparticle forms. For instance, tungsten, with a Z number of 74 and K-edge of 69.5 kV, is known
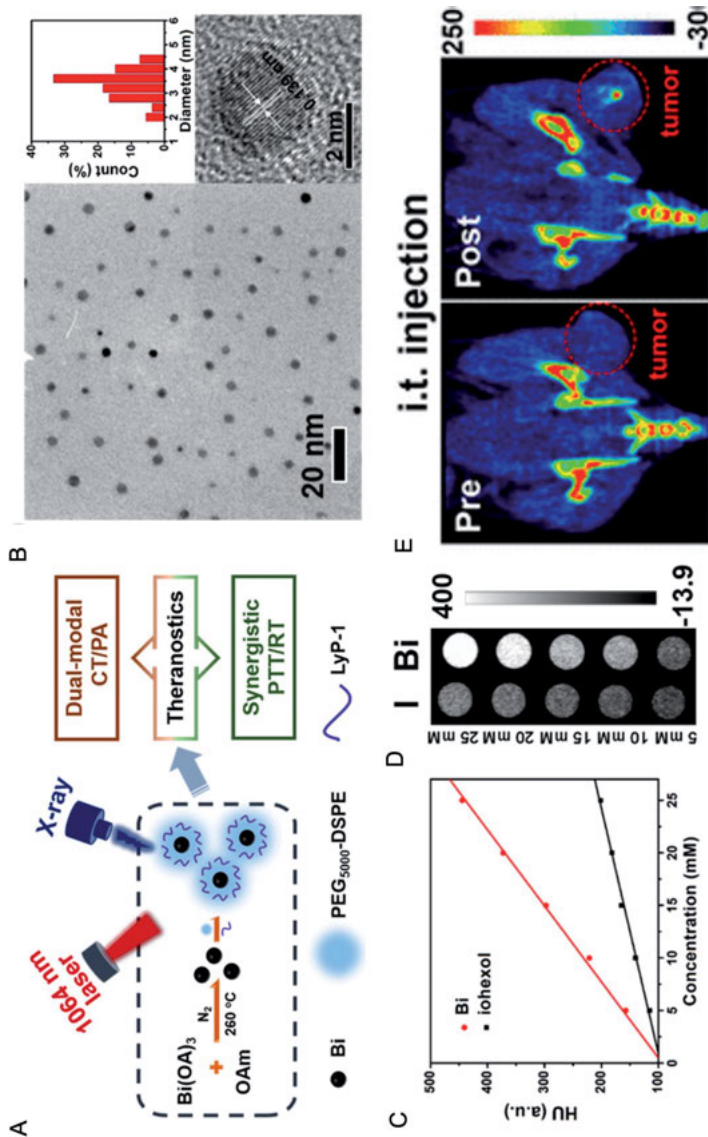
Figure 6. **(A)** Schematic depiction of bismuth nanoparticle synthesis and application. **(B)** A representative TEM micrograph and a HRTEM micrograph of bismuth nanoparticles. Inset histogram shows the measured diameter of bismuth nanoparticles. **(C)** Comparison of attenuation value between bismuth nanoparticles and iohexol. **(D)** A CT phantom image of iohexol and bismuth suspension in a range of concentrations. **(E)** Representative CT images of tumor obtained pre-injection and 5 minutes post-injection. Reproduced by permission from [115]; copyright 2017, American Chemical Society.

to be an X-ray contrast-generating element [3]. Tungsten clusters and tungsten powder have been studied *in vitro* and yielded strong contrast under CT [93, 118, 119]. However, significant decreases in attenuation between tantalum (Z = 73) and tungsten (Z = 74) when scanned by SPCCT may be due to the fact that the X-ray tube anode is made of tungsten and internal K-edge absorption occurred within the tube [101].

Tin with a Z number of 50 also shows potential of being a candidate as X-ray contrast agent. Tin(IV) oxide, also known as stannic oxide, has been proposed as a liver imaging agent. Preliminary animal studies showed that it can be given intravenously with repeated dosing without acute or delayed reaction [120]. Recently, syntheses of tin nanoparticles are developed for other applications [121, 122]. The use of these nanoparticles in X-ray imaging has great promise although their biocompatibility needs to be investigated.

3.3. Lanthanide-Based Contrast Agents

The lanthanides are a sequence of chemical elements with Z numbers of 57–71, ranging from lanthanum to lutetium [123]. Lanthanides typically have high atomic numbers, thereby fulfilling one of the basic requirements for being an X-ray contrast agent candidate. Considering the toxicity, cost and synthetic pathways available for these elements, gadolinium and ytterbium have been studied for their potential as X-ray contrast agents.

3.3.1. Gadolinium

Gadolinium is known for its use as an MRI contrast agent and several gadolinium-based contrast agents have been approved by the FDA since 1988 [124, 125]. In recent years, gadolinium has been investigated as an alternative to iodinated contrast agents for X-ray imaging, especially angiography, in patients with severe iodine allergies [126, 127]. Typically, 70 kV is used as the tube energy in digital angiography. Research has shown that gadolinium attenuation in X-rays at 70 kV is approximately the same as iodine attenuation. In comparison, the X-ray attenuation was observed to be nearly double that of iodine when tested at 120 kV, which is a commonly used tube energy in clinical CT [128]. Successful X-ray angiography with a gadolinium-based contrast agent (i.e., gadolinium-DTPA) was reported in the clinic for CT examinations of cancer patients [126, 129]. It is often acknowledged that information obtained from a single imaging modality cannot provide certainty in clinical diagnosis, so multi-modal imaging is sometimes required. Combining MRI and CT to achieve high sensitivity, resolution and soft tissue contrast with a single contrast agent injection would be possible with the high contrast properties that gadolinium possesses for both MRI and CT [130].

3.3.2. *Ytterbium*

Similar to other heavy elements, ytterbium has a high X-ray attenuation coefficient [131]. While scanned with CT, ytterbium substantially outperformed iodine at tube voltages between 100–140 kV [34]. The earliest study on the use of ytterbium for X-ray imaging can be traced back to 1986, when ytterbium-DTPA synthesized from ytterbium oxide and diethylene triamine penta-acetic acid (DTPA) for pulmonary angiography was evaluated *in vitro* and *in vivo* [132].

The first case of injectable ytterbium nanoparticles was reported in 2012, when oleic acid-stabilized ytterbium nanoparticles were doped with gadolinium and were encapsulated with DSPE-PEG2000 copolymer. The nanoparticles exhibited low cytotoxicity and strong CT contrast *in vivo* [133]. Meanwhile, an assessment of candidate elements as contrast agents for SPCCT suggested that ytterbium generated most contrast from the elements under evaluation (Figure 7) [101]. Indeed, an early investigation of ytterbium nanocolloids developed for SPCCT indicated the feasibility of using ytterbium as both CT and SPCCT contrast agents [134].
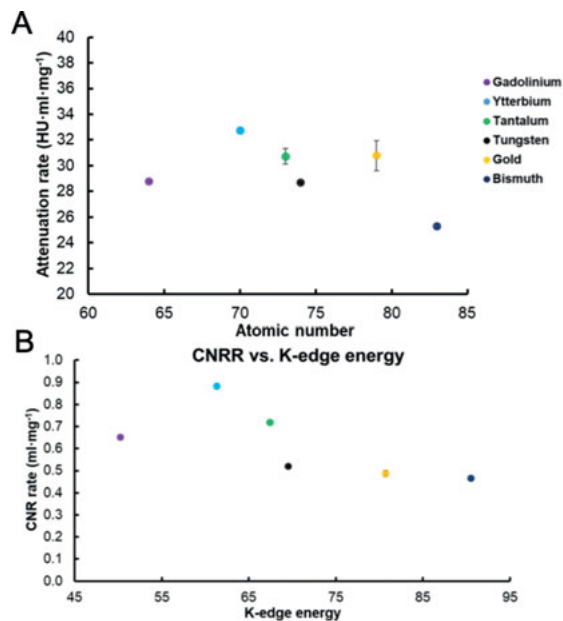
Figure 7. **(A)** Comparison of attenuation rates of different elements studied in conventional CT. **(B)** The CNRR of different elements compared with their K-edge energies. Reproduced by permission from [101]; copyright 2018, Springer Nature.

4. X-RAY CONTRAST AGENTS IN MOLECULAR IMAGING

4.1. Targeted Contrast Agents in Molecular Imaging

Developing targeted X-ray contrast agents for imaging specific sites of disease has recently attracted considerable attention, particularly with nanoparticle contrast agents such as AuNP [36]. For example, some disease sites such as tumor tissues or atherosclerotic plaques can be passively targeted due to enhanced permeability and retention (EPR) effects, which are largely due to "leaky" vasculature and impaired lymphatic drainage [135, 136]. On the other hand, active cell surface targeting can be achieved by functionalizing contrast agents via surface modification [137, 138].

Many targeted X-ray contrast agents have been evaluated in a wide range of molecular imaging applications, including cardiovascular disease and cancer. AuNP is one of the most popular contrast agents studied for active targeted CT imaging thanks to its easy surface functionalization by conjugating specific ligands to the nanoparticle surface and high density leading to high payloads [139]. AuNP, for example, have been used to visualize myocardial lesions by targeting collagen, atherosclerosis and cerebral thromboembolic imaging by targeting fibrin, lung tumor characteristics imaging by targeting epidermal growth factor receptor (EGFR), lymph nodes imaging by targeting CD4, and so on [140–144]. In fact, targeted CT/MR dual-mode imaging of hepatocellular carcinoma can be accomplished by coating AuNP with manganese chelates and using hyaluronic acid (HA) to target the CD44 receptor [145]. AuNP's passive targeting has also been studied extensively. The retention of AuNP in tumors can be tuned by adjusting sizes and coatings, which is advantageous for cancer imaging [146, 147].

Other heavy element-based nanoparticles have been used for targeted X-ray imaging as well. For instance, fibrin-targeted bismuth and ytterbium nanocolloids were used to detect ruptured atherosclerotic plaques by CT angiograms and SPCCT, iodinated polymeric nanoparticles were targeted to macrophages for evaluation of coronary arteries with CT, HA-modified tantalum oxide nanoparticles conjugated with doxorubicin were used for tumor-targeted CT imaging, and hybrid gold-gadolinium nanoclusters were applied for tumor CT imaging by passive targeting [104, 148–151]. The ongoing development of X-ray contrast agents for targeted imaging could improve imaging specificity and offer improved diagnoses for a wide range of diseases.

4.2. Nanoparticles for Cell Tracking

Cell-based treatments have made great strides over the past few decades. Recently, the FDA approval of chimeric antigen receptor (CAR) T-cell therapy has initiated a new era of immune cell therapies for cancer [152]. While the field of cancer immunotherapy is being reenergized, there are still some daunting challenges to tackle to achieve stable therapeutic outcomes, such as possibility of off-target effects, lack of ideal targets, and associated side effects [153]. These
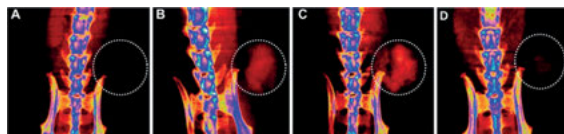
Figure 8. Time-dependent accumulation of targeted T-cells at the tumor visualized by micro-CT scans **(A)** before T-cell injection, **(B)** 24 hours post-injection, **C)** 48 hours post-injection, and **(D)** 72 hours post-injection. Reproduced by permission from [162]; copyright 2015, American Chemical Society.

issues may benefit from information derived from imaging transplanted cells from the point of administration to the end of the treatment. CT is an emerging method for cell tracking thanks to its high spatial resolution and wide availability. It allows comprehensive tracking of transplanted cells in patients, thus providing real-time information about the cells' migration, distribution, viability, differentiation, and fate [154, 155].

Recently, the development of novel X-ray contrast agents to enable cell visualization in CT through the labeling of transplanted cells has led to significant interest in their potential to evaluate and monitor cell-based therapies. In particular, *ex vivo* direct cell labeling using AuNP with CT imaging is one of the most commonly used methods. In this approach, pre-transplantation target cells are incubated with AuNP. The AuNP will be either internalized by the cells or attached to the cells' surface [23]. Numerous studies have evidenced the significance of AuNP size, shape, and surface properties in cellular uptake [156–158]. With the knowledge of AuNP uptake in different cell types, progress has been made in *in vivo* cell tracking [159–161]. For example, T cells expressing a melanoma-specific T-cell receptor were labeled with AuNP and injected intravenously into mice in the study by Meir et al. A full-body CT scan allowed the imaging of these T-cells' distribution, migration, and kinetics (Figure 8) [162].

Indirect cell labeling is an alternative way to label cells that can provide more information on cell viability and enable long-term tracking of labeled cells [163]. It is implemented by reporter genes in the cells in question [154]. However, this type of approach has yet to be implemented for CT.

4.3.   Theranostic X-Ray Agents

Multifunctional X-ray contrast agents are of interest for simultaneous imaging and therapy of a disease, which is also known as theranostics [164]. Theranostic X-ray agents would possess, at the minimum, the dual properties of contrast generation in X-ray imaging and be able to deliver drugs to the disease site or otherwise providing a therapeutic benefit. The recent advances in synthetic methods have opened a new era for nanoparticle agents in theranostics.

A significant amount of preclinical evidence has shown that nanocarriers can improve the therapeutic index of low molecular weight drugs [165]. The combination of CT imaging and drug delivery with nanoparticles allows for noninva-
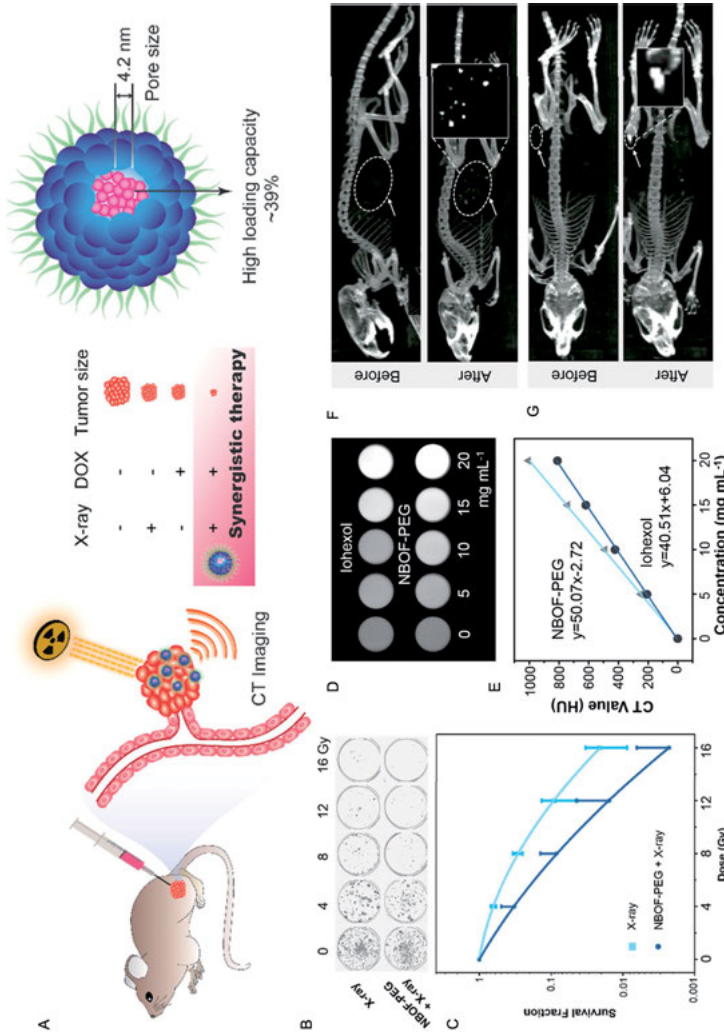
Figure 9. **(A)** A schematic illustration of bismuth nanoparticles for CT image-guided enhanced chemoradiotherapy of tumors. **(B)** Micrographs of 4T1.2 cells with or without incubation with bismuth nanoparticles, and then exposed to radiotherapy. **(C)** Survival fractions of 4T1.2 cells with or without bismuth nanoparticles incubation and treated with X-ray doses from 0–16 Gy. **(D)** A CT phantom image of bismuth nanoparticles and iohexol in a range of concentrations. **(E)** Quantification of the attenuation of bismuth nanoparticles and iohexol from the phantom in D. **(F)** CT images of tumor-bearing mice before and 1 hour after nanoparticle administration through intravenous injection and **(G)** through intratumoral injection. Reproduced by permission from [179]; copyright 2019, American Chemical Society.

sive assessment of drug accumulation at the disease site. A drug-loaded aptamer-AuNP bioconjugate was developed for CT imaging and therapy of prostate cancer, a Gd-doped Mg-Al-LDH/Au nanocomposite demonstrated effective CT/MR dual modal tumor imaging and drug delivery simultaneously, and a TPGS-stabilized $NaYbF_4$ exhibited X-ray imaging-guided drug delivery properties [166–168].

On the other hand, certain heavy element-based nanoparticles themselves may act as radiosensitizers or photosensitizers for radiotherapy or photothermal therapy, respectively, and at the same time act as contrast agents. AuNP can be engineered to have strong surface plasmon resonance in the near-infrared (NIR) region (i.e., $\lambda = 650–1350$ nm), where light can penetrate deeply into tissue and reach AuNP embedded within tumors [169]. Numerous studies have shown that plasmonic AuNP can be used as theranostic probes for tumor imaging [170–172]. Other contrast agent-based nanoplatforms for combined CT and PTT, such as tantalum sulfide nanosheets, bismuth nanoparticles, and molybdenum oxide nanostructures, are also being investigated [173–175]. Similarly, nanoparticle contrast agents usually can also serve as radiosensitizers and enable combined CT imaging and radiotherapy [176–178]. For example, doxorubicin-loaded bismuth nanoparticles provided CT-guided enhanced chemoradiotherapy (Figure 9) [179]. Overall, heavy element-based theranostic contrast agents have shown significant promise for integrated imaging and therapy of disease.

5. CONCLUDING REMARKS AND FUTURE DIRECTIONS

Overall, the development of heavy element-based X-ray contrast agents has been remarkable over the past decade. Given the high efficacy benchmarks presented by the existing iodinated small molecule contrast agents for blood pool imaging and barium sulfide for GI imaging that are widely used in clinics, progress towards more efficient, functional, and practical contrast agents is challenging. Nanoparticle contrast agents in particular are growing in usefulness in blood pool, cancer, and cell imaging, thanks to their size-dependent pharmacokinetics, high payloads, and ease of functionalization. Several new elements including silver, tantalum, bismuth and ytterbium, were introduced for CT, DEM, and SPCCT. There have also been extensive studies and reports of using X-ray contrast agents in targeted imaging, cell tracking, as well as in theranostic applications.

Although research on these contrast agents has bloomed over the period covered herein, only a limited number of new formulations are being investigated in clinical trials. The distance between research and commercialization of these contrast agents can be multifactorial. In order to be fully clinical translatable, more comparable information related to their biodistribution, degradability, systemic toxicity, renal clearance, and possible long-term accumulation in the body is needed [180]. Besides, the lack of scale-up synthesis of these nanoparticle contrast agents hinders their commercialization. In addition, contrast agents that play the sole role in providing image contrast have a much lower potential reve-

nue than drug codelivery or other therapeutic purposes [181]. Despite the fact that a growing amount of research has focused on theranostic agents, the clinical translation of these multifunctional contrast agents is in its infancy. Nonetheless, the rapid development of X-ray contrast agents that focus on numerous targeting options, being "smart", reduced toxicity, and comparable contrast generation to current products, has promised the potential of new X-ray contrast agents being approved. We believe that sufficient proof-of-concept research has been done to provide a foundation for more rapid progress in X-ray contrast agents to be made in the coming decade.

ACKNOWLEDGMENTS

ABBREVIATIONS

AgNP	silver nanoparticles
Ag_2S-NP	silver sulfide nanoparticles
AION	all-in-one nanoparticle
Au-HDL	gold high-density lipoprotein nanoparticle
AuNP	gold nanoparticle
Bi_2S_3	bismuth sulfide
Bi_2Se_3	bismuth selenide
CAR	chimeric antigen receptor
CD4	cluster of differentiation 4
CD44	cluster of differentiation 44
CEDM	contrast-enhanced digital mammography
CNR	contrast-to-noise ratio
CNRR	contrast-to-noise ratio rate
CT	computed tomography
DEM	dual energy contrast-enhanced mammography
DTPA	diethylene triamine pentaacetic acid
DiR	near-infrared fluorophore
EGFR	epidermal growth factor receptor
EPR	enhanced permeability and retention
FDA	Food and Drug Administration
GI	gastrointestinal
HA	hyaluronic acid
HRTEM	high-resolution transmission electron microscopy
HU	Hounsfield unit
IO-NP	iron oxide nanoparticles

LDH	layered double hydroxide
MoO_2	molybdenum oxide
MoS_2	molybdenum sulfide
MRI	magnetic resonance imaging
NIR	near-infrared
NIRF	near-infrared fluorescence
PA	photoacoustic imaging
PEG	polyethylene glycol
PET/CT	positron emission tomography-computed tomography
PTT	photothermal therapy
RT	radiotherapy
SDNR	signal difference-to-noise ratio
SPCCT	spectral photon-counting computed tomography
TaONP	tantalum oxide nanoparticles
TEM	transmission electron microscopy
TPGS	d-alpha-tocopheryl polyethylene glycol succinate
Z	atomic number

REFERENCES

1. W. C. Röntgen, *Science* **1896**, *3*, 227–231.
2. G. Sternbach, J. Varon, *J. Emerg. Med.* **1993**, *11*, 743–745.
3. S.–B. Yu, A. D. Watson, *Chem. Rev.* **1999**, *99*, 2353–2378.
4. M. Tubiana, *Bull. Acad. Natl. Med.* **1996**, *180*, 97–108.
5. J. D. Howell, *Trans. Am. Clin. Climatol. Assoc.* **2016**, *127*, 341–349.
6. J. Fred A. Mettler, M. Bhargavan, K. Faulkner, D. B. Gilley, J. E. Gray, G. S. Ibbott, J. A. Lipoti, M. Mahesh, J. L. McCrohan, M. G. Stabin, B. R. Thomadsen, T. T. Yoshizumi, *Radiology* **2009**, *253*, 520–531.
7. M. Endrizzi, *Nuclear Instruments and Methods in Physics Research. Section A: Accelerators, Spectrometers, Detectors and Associated Equipment* **2018**, *878*, 88–98.
8. Y. Liu, K. Ai, L. Lu, *Acc. Chem. Res.* **2012**, *45*, 1817–1827.
9. H. Lusic, M. W. Grinstaff, *Chem. Rev.* **2013**, *113*, 1641–1666.
10. A. Momose, T. Takeda, Y. Itai, K. Hirano, *Nat. Med.* **1996**, *2*, 473–475.
11. L. W. Goldman, *J. Nucl. Med. Technol.* **2007**, *35*, 115–128; quiz 129–130.
12. B. M. Yeh, P. F. FitzGerald, P. M. Edic, J. W. Lambert, R. E. Colborn, M. E. Marino, P. M. Evans, J. C. Roberts, Z. J. Wang, M. J. Wong, P. J. Bonitatibus, Jr., *Adv. Drug Deliv. Rev.* **2017**, *113*, 201–222.
13. C. Fuentes Santos, B. Steen, *Case Rep. Pulmonol.* **2014**, *2014*, 3.
14. G. L. Hundemer, V. Kumar, M. Vaduganathan, *Baylor Univ. Med. Center Proc.* **2015**, *28*, 183–184.
15. W. Bottinor, P. Polkampally, I. Jovin, *Int. J. Angiol.* **2013**, *22*, 149–154.
16. R. Karunamuni, P. C. Naha, K. C. Lau, A. Al-Zaki, A. V. Popov, E. J. Delikatny, A. Tsourkas, D. P. Cormode, A. D. A. Maidment, *Eur. Radiol.* **2016**, *26*, 3301–3309.
17. Y. C. Dong, M. Hajfathalian, P. S. N. Maidment, J. C. Hsu, P. C. Naha, S. Si-Mohamed, M. Breuilly, J. Kim, P. Chhour, P. Douek, H. I. Litt, D. P. Cormode, *Sci. Rep.* **2019**, *9*, 14912.
18. S. Chakravarty, J. Unold, D. D. Shuboni-Mulligan, B. Blanco-Fernandez, E. M. Shapiro, *Nanoscale* **2016**, *8*, 13217–13222.

19. J. C. Hsu, P. C. Naha, K. C. Lau, P. Chhour, R. Hastings, B. F. Moon, J. M. Stein, W. R. T. Witschey, E. S. McDonald, A. D. A. Maidment, D. P. Cormode, *Nanoscale* **2018**, *10*, 17236–17248.

20. P. C. Naha, K. C. Lau, J. C. Hsu, M. Hajfathalian, S. Mian, P. Chhour, L. Uppuluri, E. S. McDonald, A. D. A. Maidment, D. P. Cormode, *Nanoscale* **2016**, *8*, 13740–13754.

21. D. P. Cormode, T. Skajaa, M. M. van Schooneveld, R. Koole, P. Jarzyna, M. E. Lobatto, C. Calcagno, A. Barazza, R. E. Gordon, P. Zanzonico, E. A. Fisher, Z. A. Fayad, W. J. M. Mulder, *Nano Lett.* **2008**, *8*, 3715–3723.

22. J. C. Hsu, E. D. Cruz, K. C. Lau, M. Bouché, J. Kim, A. D. A. Maidment, D. P. Cormode, *Chem. Mater.* **2019**, *31*, 7845–7854.

23. J. Kim, P. Chhour, J. Hsu, H. I. Litt, V. A. Ferrari, R. Popovtzer, D. P. Cormode, *Bioconjug. Chem.* **2017**, *28*, 1581–1597.

24. J. M. Boone, *X-Ray Production, Interaction, and Detection in Diagnostic Imaging*, in *Handbook of Medical Imaging*, Vol. 1, Eds. R. L. V. Metter, J. Beutel, H. L. Kundel, SPIE, Bellingham, USA, **2000**, pp. 3–77.

25. R. Percuoco, *Plain Radiographic Imaging*, in *Clinical Imaging*, 3rd ed., Ed. D. M. Marchiori, Mosby, Saint Louis, **2014**, pp. 1–43.

26. W. J. Meredith, J. B. Massey, *The Production of X-Rays*, in *Fundamental Physics of Radiology*, 3rd ed., Eds. W. J. Meredith, J. B. Massey, Butterworth-Heinemann, Oxford, UK, **1977**, pp. 44–56.

27. E. L. Nickoloff, H. L. Berman, *Radiographics* **1993**, *13*, 1337–1348.

28. M. H. McKetty, *Radiographics* **1998**, *18*, 151–163.

29. J. Broder, *Imaging of Nontraumatic Abdominal Conditions*, in *Diagnostic Imaging for the Emergency Physician*, Ed. J. Broder, W. B. Saunders, Saint Louis, **2011**, pp. 445–577.

30. B. Akça, S. Z. Erzeneoğlu, *Sci. Technol. Nucl. Ins.* **2014**, *2014*, 8.

31. E. Roessl, R. Proksa, *Phys. Med. Biol.* **2007**, *52*, 4679–4696.

32. X-Ray Physics: X-Ray Interaction with Matter and Attenuation, **2014**. http://xrayphysics.com/attenuation.html (accessed May 9, 2020).

33. S. R. Cherry, J. A. Sorenson, M. E. Phelps, *Interaction of Radiation with Matter*, in *Physics in Nuclear Medicine*, 4th ed., Eds. S. R. Cherry, J. A. Sorenson, M. E. Phelps, W. B. Saunders, Philadelphia, **2012**, pp. 63–85.

34. P. F. FitzGerald, R. E. Colborn, P. M. Edic, J. W. Lambert, A. S. Torres, P. J. Bonitatibus, Jr., B. M. Yeh, *Radiology* **2016**, *278*, 723–733.

35. X. Ying, N. J. Barlow, M. H. Feuston, *Micro-CT and volumetric imaging in developmental toxicology*, in *Reproductive and Developmental Toxicology*, Ed. R. C. Gupta, Academic Press, San Diego, **2011**, pp. 983–1000.

36. M. Bouché, J. C. Hsu, Y. C. Dong, J. Kim, K. Taing, D. P. Cormode, *Bioconjug. Chem.* **2020**, *31*, 303–314.

37. D. P. Cormode, P. C. Naha, Z. A. Fayad, *Contrast Media Mol. Imaging* **2014**, *9*, 37–52.

38. N. Lee, S. H. Choi, T. Hyeon, *Adv. Mater.* **2013**, *25*, 2641–2660.

39. E. A. Jensen, D. A. Mong, D. M. Biko, K. L. Maschhoff, H. Kirpalani, *Imaging: Radiography, Lung Ultrasound, and Other Imaging Modalities*, in *Assisted Ventilation of the Neonate*, 6th ed., Eds. J. P. Goldsmith, E. H. Karotkin, M. Keszler, G. K. Suresh, Elsevier, Amsterdam, Netherlands, **2017**, pp. 67–79.e64.

40. E. K. Paulson, D. H. Sheafor, D. S. Enterline, H. P. McAdams, T. T. Yoshizumi, *Radiology* **2001**, *220*, 161–167.

41. V. Kapoor, B. M. McCook, F. S. Torok, *Radiographics* **2004**, *24*, 523–543.

42. D. P. Cormode, E. Roessl, A. Thran, T. Skajaa, R. E. Gordon, J.-P. Schlomka, V. Fuster, E. A. Fisher, W. J. M. Mulder, R. Proksa, Z. A. Fayad, *Radiology* **2010**, *256*, 774–782.

43. S. Si-Mohamed, D. P. Cormode, D. Bar-Ness, M. Sigovan, P. C. Naha, J.-B. Langlois, L. Chalabreysse, P. Coulon, I. Blevis, E. Roessl, K. Erhard, L. Boussel, P. Douek, *Nanoscale* **2017**, *9*, 18246–18257.

44. J. P. Schlomka, E. Roessl, R. Dorscheid, S. Dill, G. Martens, T. Istel, C. Baumer, C. Herrmann, R. Steadman, G. Zeitler, A. Livne, R. Proksa, *Phys. Med. Biol.* **2008**, *53*, 4031–4047.

45. S. Si-Mohamed, V. Tatard-Leitman, A. Laugerette, M. Sigovan, D. Pfeiffer, E. J. Rummeny, P. Coulon, Y. Yagil, P. Douek, L. Boussel, P. B. Noël, *Sci. Rep.* **2019**, *9*, 8458.

46. I. Riederer, D. Bar-Ness, M. A. Kimm, S. Si-Mohamed, P. B. Noël, E. J. Rummeny, P. Douek, D. Pfeiffer, *Sci. Rep.* **2019**, *9*, 5268.

47. M. S. Sabel, *Principles of Breast Cancer Screening*, in *Essentials of Breast Surgery*, Ed. M. S. Sabel, Mosby, Philadelphia, **2009**, pp. 19–40.

48. E. A. Sickles, *Am. J. Roentgenol.* **1982**, *139*, 913–918.

49. E. D. Pisano, C. Gatsonis, E. Hendrick, M. Yaffe, J. K. Baum, S. Acharyya, E. F. Conant, L. L. Fajardo, L. Bassett, C. D'Orsi, R. Jong, M. Rebner, *N. Engl. J. Med.* **2005**, *353*, 1773–1783.

50. P. E. Freer, *Radiographics* **2015**, *35*, 302–315.

51. M. A. Helvie, *Radiol. Clin. North Am.* **2010**, *48*, 917–929.

52. R. A. Jong, M. J. Yaffe, M. Skarpathiotakis, R. S. Shumak, N. M. Danjoux, A. Gunesekara, D. B. Plewes, *Radiology* **2003**, *228*, 842–850.

53. U. Lalji, M. Lobbes, *Womens Health* **2014**, *10*, 289–298.

54. A.-K. Carton, C. Ullberg, K. Lindman, R. Acciavatti, T. Francke, A. D. A. Maidment, *Med. Phys.* **2010**, *37*, 5896–5907.

55. R. Karunamuni, A. Tsourkas, A. D. A. Maidment, *Br. J. Radiol.* **2014**, *87*, 20140081.

56. R. Karunamuni, A. D. Maidment, *Phys. Med. Biol.* **2014**, *59*, 4311–4324.

57. L. K. Petrovich, E. S. Pretorius, *Introduction to Plain Film Radiography and Fluoroscopy*, in *Radiology Secrets Plus*, 3rd ed., Eds. E. S. Pretorius, J. A. Solomon, Mosby, Philadelphia, **2011**, pp. 9–12.

58. S. Hultzsch, *Diagnostic Agents*, in *Drugs During Pregnancy and Lactation*, 3rd ed., Eds. C. Schaefer, P. Peters, R. K. Miller, Academic Press, San Diego, **2015**, pp. 527–540.

59. M. Hamid, W. Ullah, M. Ur Rashid, W. Amjad, M. Mukhtar, A. Hurairah, *J. Investig. Med. High Impact Case Rep.* **2018**, *6*, 2324709618802872.

60. M. A. Périard, *Can. J. Med. Radiat. Technol.* **2003**, *34*, 3–9.

61. D. J. Ott, D. W. Gelfand, *J. Am. Med. Ass.* **1983**, *249*, 2380–2384.

62. J. S. Thompson, *Ann. Surg.* **2002**, *236*, 7–8.

63. S. E. Seltzer, B. Jones, G. C. McLaughlin, *CRC Crit. Rev. Diagn. Imaging* **1979**, *12*, 79–99.

64. C. Christiansen, *Toxicology* **2005**, *209*, 185–187.

65. J. J. Pasternak, E. E. Williamson, *Mayo Clin. Proc.* **2012**, *87*, 390–402.

66. J. Singh, A. Daftary, *J. Nucl. Med. Technol.* **2008**, *36*, 69–74; quiz 76–67.

67. S. K. Morcos, H. S. Thomsen, *Eur Radiol* **2001**, *11*, 1267–1275.

68. J. F. Hainfeld, S. M. Ridwan, Y. Stanishevskiy, N. R. Smilowitz, J. Davis, H. M. Smilowitz, *Sci. Rep.* **2018**, *8*, 13803.

69. J. F. Hainfeld, D. N. Slatkin, T. M. Focella, H. M. Smilowitz, *Br. J. Radiol.* **2006**, *79*, 248–253.

70. A. J. Mieszawska, W. J. M. Mulder, Z. A. Fayad, D. P. Cormode, *Mol. Pharm* **2013**, *10*, 831–847.

71. R. Cheheltani, R. M. Ezzibdeh, P. Chhour, K. Pulaparthi, J. Kim, M. Jurcova, J. C. Hsu, C. Blundell, H. I. Litt, V. A. Ferrari, H. R. Allcock, C. M. Sehgal, D. P. Cormode, *Biomaterials* **2016**, *102*, 87–97.

72. M. W. Galper, M. T. Saung, V. Fuster, E. Roessl, A. Thran, R. Proksa, Z. A. Fayad, D. P. Cormode, *Invest. Radiol.* **2012**, *47*, 475–481.

73. P. C. Naha, P. Chhour, D. P. Cormode, *Toxicol. In Vitro* **2015**, *29*, 1445–1453.

74. F. Hallouard, N. Anton, P. Choquet, A. Constantinesco, T. Vandamme, *Biomaterials* **2010**, *31*, 6249–6268.

75. A. S. Thakor, J. Jokerst, C. Zavaleta, T. F. Massoud, S. S. Gambhir, *Nano Lett.* **2011**, *11*, 4029–4036.

76. Nanocrystalline Gold to Treat Remyelination Failure in Chronic Optic Neuropathy In Multiple Sclerosis, https://ClinicalTrials.gov/show/NCT03536559 (accessed May 9, 2020).

77. M. Hajfathalian, A. Amirshaghaghi, P. C. Naha, P. Chhour, J. C. Hsu, K. Douglas, Y. Dong, C. M. Sehgal, A. Tsourkas, S. Neretina, D. P. Cormode, *Nanoscale* **2018**, *10*, 18749–18757.

78. D. P. Cormode, S. Si-Mohamed, D. Bar-Ness, M. Sigovan, P. C. Naha, J. Balegamire, F. Lavenne, P. Coulon, E. Roessl, M. Bartels, M. Rokni, I. Blevis, L. Boussel, P. Douek, *Sci. Rep.* **2017**, *7*, 4784.

79. M. Wang, M. Thanou, *Pharmacol. Res.* **2010**, *62*, 90–99.

80. X. Duan, Y. Li, *Small* **2013**, *9*, 1521–1532.

81. D. Graham, K. Faulds, W. E. Smith, *Chem. Commun.* **2006**, *42*, 4363–4371.

82. I. Sondi, B. Salopek-Sondi, *J. Colloid Interface Sci.* **2004**, *275*, 177–182.

83. J. S. Kim, E. Kuk, K. N. Yu, J.-H. Kim, S. J. Park, H. J. Lee, S. H. Kim, Y. K. Park, Y. H. Park, C.-Y. Hwang, Y.-K. Kim, Y.-S. Lee, D. H. Jeong, M.-H. Cho, *Nanomed.* **2007**, *3*, 95–101.

84. R. M. Crooks, M. Zhao, L. Sun, V. Chechik, L. K. Yeung, *Acc. Chem. Res.* **2001**, *34*, 181–190.

85. M. Jochelson, *Radiol. Clin. North Am.* **2014**, *52*, 609–616.

86. J. Zou, M. Hannula, S. Misra, H. Feng, R. H. Labrador, A. S. Aula, J. Hyttinen, I. Pyykkö, *J. Nanobiotechnol.* **2015**, *13*, 5.

87. C. Levard, E. M. Hotze, G. V. Lowry, G. E. Brown, *Environ. Sci. Technol.* **2012**, *46*, 6900–6914.

88. C. Beer, R. Foldbjerg, Y. Hayashi, D. S. Sutherland, H. Autrup, *Toxicol. Lett.* **2012**, *208*, 286–292.

89. J. A. Nadel, W. G. Wolfe, P. D. Graf, J. E. Youker, N. Zamel, J. H. M. Austin, W. A. Hinchcliffe, R. H. Greenspan, R. R. Wright, *N. Engl. J. Med.* **1970**, *283*, 281–286.

90. J. C. Smith, F. P. Stitik, D. L. Swift, *Am. Rev. Respir. Dis.* **1976**, *113*, 515–529.

91. G. Gamsu, A. R. Forbes, C. O. Ovenfors, *Am. J. Roentgenol.* **1981**, *136*, 317–322.

92. R. E. Pickard, *Arch. Otolaryngol.* **1971**, *94*, 202–207.

93. S. Rathnayake, J. Mongan, A. S. Torres, R. Colborn, D.-W. Gao, B. M. Yeh, Y. Fu, *Contrast Media Mol. Imaging* **2016**, *11*, 254–261.

94. A. R. Margulis, J. A. Stoughton, L. A. Stein, *Am. J. Roentgenol. Radium Ther. Nucl. Med.* **1975**, *125*, 244–250.

95. A. E. Dumont, A. Martelli, *Lymphology* **1969**, *2*, 91–95.

96. P. J. Bonitatibus, Jr., A. S. Torres, B. Kandapallil, B. D. Lee, G. D. Goddard, R. E. Colborn, M. E. Marino, *ACS Nano* **2012**, *6*, 6650–6658.

97. P. J. Bonitatibus, Jr., A. S. Torres, G. D. Goddard, P. F. FitzGerald, A. M. Kulkarni, *Chem. Commun.* **2010**, *46*, 8956–8958.

98. A. S. Torres, P. J. Bonitatibus, Jr., R. E. Colborn, G. D. Goddard, P. F. FitzGerald, B. D. Lee, M. E. Marino, *Invest. Radiol.* **2012**, *47*, 578–587.

99. M. H. Oh, N. Lee, H. Kim, S. P. Park, Y. Piao, J. Lee, S. W. Jun, W. K. Moon, S. H. Choi, T. Hyeon, *J. Am. Chem. Soc.* **2011**, *133*, 5508–5515.

100. I. Riederer, D. Bar-Ness, M. A. Kimm, S. Si-Mohamed, P. B. Noël, E. J. Rummeny, P. Douek, D. Pfeiffer, *Sci. Rep.* **2019**, *9*, 5268.

101. J. Kim, D. Bar-Ness, S. Si-Mohamed, P. Coulon, I. Blevis, P. Douek, D. P. Cormode, *Sci. Rep.* **2018**, *8*, 12119.

102. J. D. Freedman, H. Lusic, B. D. Snyder, M. W. Grinstaff, *Angew. Chem. Int. Ed.* **2014**, *53*, 8406–8410.

103. Y. Chen, G. Song, Z. Dong, X. Yi, Y. Chao, C. Liang, K. Yang, L. Cheng, Z. Liu, *Small* **2017**, *13*, 1602869.

104. Y. Jin, Y. Li, X. Ma, Z. Zha, L. Shi, J. Tian, Z. Dai, *Biomaterials* **2014**, *35*, 5795–5804.

105. D. M. Keogan, D. M. Griffith, *Molecules* **2014**, *19*, 15258–15297.

106. J. A. Salvador, S. A. Figueiredo, R. M. Pinto, S. M. Silvestre, *Future Med. Chem.* **2012**, *4*, 1495–1523.

107. D. W. Bierer, *Rev. Infect. Dis.* **1990**, *12, Suppl 1*, S3–8.

108. R. Mohan, *Nat. Chem.* **2010**, *2*, 336–336.

109. E. J. Rivera, L. A. Tran, M. Hernández-Rivera, D. Yoon, A. G. Mikos, I. A. Rusakova, B. Y. Cheong, M. d. G. Cabreira-Hansen, J. T. Willerson, E. C. Perin, L. J. Wilson, *J. Mater. Chem. B* **2013**, *1*, 10.1039/C1033TB20742K.

110. K. Ai, Y. Liu, J. Liu, Q. Yuan, Y. He, L. Lu, *Adv. Mater.* **2011**, *23*, 4886–4891.

111. Y. Wang, Y. Wu, Y. Liu, J. Shen, L. Lv, L. Li, L. Yang, J. Zeng, Y. Wang, L. W. Zhang, Z. Li, M. Gao, Z. Chai, *Adv. Funct. Mater.* **2016**, *26*, 5335–5344.

112. J. Chen, X.-Q. Yang, Y.-Z. Meng, H.-H. Huang, M.-Y. Qin, D.-M. Yan, Y.-D. Zhao, Z.-Y. Ma, *Nanotechnology* **2014**, *25*, 295103.

113. J. M. Kinsella, R. E. Jimenez, P. P. Karmali, A. M. Rush, V. R. Kotamraju, N. C. Gianneschi, E. Ruoslahti, D. Stupack, M. J. Sailor, *Angew. Chem. Int. Ed.* **2011**, *50*, 12308–12311.

114. J. Li, F. Jiang, B. Yang, X.-R. Song, Y. Liu, H.-H. Yang, D.-R. Cao, W.-R. Shi, G.-N. Chen, *Sci. Rep.* **2013**, *3*, 1998.

115. X. Yu, A. Li, C. Zhao, K. Yang, X. Chen, W. Li, *ACS Nano* **2017**, *11*, 3990–4001.

116. B. Wei, X. Zhang, C. Zhang, Y. Jiang, Y.-Y. Fu, C. Yu, S.-K. Sun, X.-P. Yan, *ACS Appl. Mater. Interfaces* **2016**, *8*, 12720–12726.

117. Z. Li, J. Liu, Y. Hu, Z. Li, X. Fan, Y. Sun, F. Besenbacher, C. Chen, M. Yu, *Biomaterials* **2017**, *141*, 284–295.

118. T. Nowak, M. Hupfer, R. Brauweiler, F. Eisa, W. A. Kalender, *Med. Phys.* **2011**, *38*, 6469–6482.

119. D. Sülzle, M. Bauser, T. Frenzel, G. Jost, H. Pietsch, M. Schäfer, M. Berger, J. Hassfeld, H. Schmitt-Willich, *J. Cluster Sci.* **2015**, *26*, 111–118.

120. H. W. Fischer, *Radiology* **1957**, *68*, 488–498.

121. S.-S. Chee, J.-H. Lee, *Transactions of Nonferrous Metals Society of China* **2012**, *22*, s707–s711.

122. O. Riedel, A. Düttmann, S. Dühnen, J. Kolny-Olesiak, C. Gutsche, J. Parisi, M. Winter, M. Knipper, T. Placke, *ACS Appl. Nano Mater.* **2019**, *2*, 3577–3589.

123. C. H. Evans, *Trends Biochem. Sci.* **1983**, *8*, 445–449.

124. M. Rogosnitzky, S. Branch, *Biometals* **2016**, *29*, 365–376.

125. V. C. Pierre, M. J. Allen, P. Caravan, *J. Biol. Inorg. Chem.* **2014**, *19*, 127–131.

126. K. Ose, T. Doue, K. Zen, M. Hadase, T. Sawada, A. Azuma, H. Matsubara, *Circ. J.* **2005**, *69*, 507–509.

127. H. S. Thomsen, T. Almèn, S. K. Morcos, and members of the *Contrast Media Safety Committee of the European Society of Urogenital, *Eur. Radiol.* **2002**, *12*, 2600–2605.

128. H. S. Thomsen, *Radiography with Gadolinium Contrast Agents*, in *Contrast Media*, Eds. H. S. Thomsen, J. A. W. Webb, Springer, Berlin, Heidelberg, **2009**, pp. 171–177.

129. T. Albrecht, P. Dawson, *Br. J. Radiol.* **2000**, *73*, 878–882.

130. L. Zhang, R. Liu, H. Peng, P. Li, Z. Xu, A. K. Whittaker, *Nanoscale* **2016**, *8*, 10491–10510.

131. Tables of X-Ray Mass Attenuation Coefficients and Mass Energy-Absorption Coefficients 1 keV to 20 MeV for Elements Z = 1 to 92 and 48 Additional Substances of Dosimetric Interest, **1995**, https://www.nist.gov/publications/tables-x-ray-mass-attenuation-coefficients-and-mass-energy-absorption-coefficients-1-0 (accesses May 9, 2020).

132. E. Unger, F. Gutierrez, *Invest. Radiol.* **1986**, *21*, 802–807.

133. Y. Liu, K. Ai, J. Liu, Q. Yuan, Y. He, L. Lu, *Angew. Chem. Int. Ed.* **2012**, *51*, 1437–1442.

134. D. Pan, C. O. Schirra, A. Senpan, A. H. Schmieder, A. J. Stacy, E. Roessl, A. Thran, S. A. Wickline, R. Proska, G. M. Lanza, *ACS Nano* **2012**, *6*, 3364–3370.

135. R. Bazak, M. Houri, S. E. Achy, W. Hussein, T. Refaat, *Mol. Clin. Oncol.* **2014**, *2*, 904–908.

136. Z. Cheng, A. Al Zaki, J. Z. Hui, V. R. Muzykantov, A. Tsourkas, *Science* **2012**, *338*, 903–910.

137. O. C. Farokhzad, R. Langer, *ACS Nano* **2009**, *3*, 16–20.

138. S. Kunjachan, R. Pola, F. Gremse, B. Theek, J. Ehling, D. Moeckel, B. Hermanns-Sachweh, M. Pechar, K. Ulbrich, W. E. Hennink, G. Storm, W. Lederle, F. Kiessling, T. Lammers, *Nano Lett.* **2014**, *14*, 972–981.

139. J. R. Ashton, J. L. West, C. T. Badea, *Front. Pharmacol.* **2015**, *6*.

140. D. Danila, E. Johnson, P. Kee, *Nanomed.* **2013**, *9*, 1067–1076.

141. P. M. Winter, H. P. Shukla, S. D. Caruthers, M. J. Scott, R. W. Fuhrhop, J. D. Robertson, P. J. Gaffney, S. A. Wickline, G. M. Lanza, *Acad. Radiol.* **2005**, *12*, S9–S13.

142. J. R. Ashton, E. B. Gottlin, E. F. Patz, Jr., J. L. West, C. T. Badea, *PLoS ONE* **2018**, *13*, e0206950.

143. J.-Y. Kim, J. H. Ryu, D. Schellingerhout, I.-C. Sun, S.-K. Lee, S. Jeon, J. Kim, I. C. Kwon, M. Nahrendorf, C.-H. Ahn, K. Kim, D.-E. Kim, *Theranostics* **2015**, *5*, 1098–1114.

144. W. Eck, A. I. Nicholson, H. Zentgraf, W. Semmler, S. Bartling, *Nano Lett.* **2010**, *10*, 2318–2322.

145. R. Wang, Y. Luo, S. Yang, J. Lin, D. Gao, Y. Zhao, J. Liu, X. Shi, X. Wang, *Sci. Rep.* **2016**, *6*, 33844.

146. I. Brigger, C. Dubernet, P. Couvreur, *Adv. Drug Deliv. Rev.* **2002**, *54*, 631–651.

147. M. Yu, J. Zheng, *ACS Nano* **2015**, *9*, 6655–6674.

148. D. Pan, E. Roessl, J.-P. Schlomka, S. D. Caruthers, A. Senpan, M. J. Scott, J. S. Allen, H. Zhang, G. Hu, P. J. Gaffney, E. T. Choi, V. Rasche, S. A. Wickline, R. Proksa, G. M. Lanza, *Angew. Chem. Int. Ed.* **2010**, *49*, 9635–9639.

149. D. Pan, C. O. Schirra, A. Senpan, A. H. Schmieder, A. J. Stacy, E. Roessl, A. Thran, S. A. Wickline, R. Proska, G. M. Lanza, *ACS Nano* **2012**, *6*, 3364–3370.

150. F. Hyafil, J. C. Cornily, J. E. Feig, R. Gordon, E. Vucic, V. Amirbekian, E. A. Fisher, V. Fuster, L. J. Feldman, Z. A. Fayad, *Nat. Med.* **2007**, *13*, 636–641.

151. D.-H. Hu, Z.-H. Sheng, P.-F. Zhang, D.-Z. Yang, S.-H. Liu, P. Gong, D.-Y. Gao, S.-T. Fang, Y.-F. Ma, L.-T. Cai, *Nanoscale* **2013**, *5*, 1624–1628.

152. K. Newick, S. O'Brien, E. Moon, S. M. Albelda, *Annu. Rev. Med.* **2017**, *68*, 139–152.

153. Z. Wang, W. Chen, X. Zhang, Z. Cai, W. Huang, *J. Cancer* **2019**, *10*, 3112–3123.

154. M. F. Kircher, S. S. Gambhir, J. Grimm, *Nat. Rev. Clin. Oncol.* **2011**, *8*, 677–688.

155. A. K. Srivastava, J. W. M. Bulte, *Stem Cell Rev. Rep.* **2014**, *10*, 127–144.

156. B. D. Chithrani, A. A. Ghazani, W. C. Chan, *Nano Lett.* **2006**, *6*, 662–668.
157. Y. Jiang, S. Huo, T. Mizuhara, R. Das, Y. W. Lee, S. Hou, D. F. Moyano, B. Duncan, X. J. Liang, V. M. Rotello, *ACS Nano* **2015**, *9*, 9986–9993.
158. P. Chhour, J. Kim, B. Benardo, A. Tovar, S. Mian, H. I. Litt, V. A. Ferrari, D. P. Cormode, *Bioconjug. Chem.* **2017**, *28*, 260–269.
159. A. Astolfo, F. Qie, A. Kibleur, X. Hao, R. H. Menk, F. Arfelli, L. Rigon, T. M. Hinton, M. Wickramaratna, T. Tan, T. C. Hughes, *Nanomed.* **2014**, *10*, 1821–1828.
160. O. Betzer, A. Shwartz, M. Motiei, G. Kazimirsky, I. Gispan, E. Damti, C. Brodie, G. Yadid, R. Popovtzer, *ACS Nano* **2014**, *8*, 9274–9285.
161. T. Kim, N. Lee, D. R. Arifin, I. Shats, M. Janowski, P. Walczak, T. Hyeon, J. W. M. Bulte, *Adv. Funct. Mater.* **2017**, *27*, 1604213.
162. R. Meir, K. Shamalov, O. Betzer, M. Motiei, M. Horovitz-Fried, R. Yehuda, A. Popovtzer, R. Popovtzer, C. J. Cohen, *ACS Nano* **2015**, *9*, 6363–6372.
163. J. W. M. Bulte, *Am. J. Roentgeneol.* **2009**, *193*, 314–325.
164. S. Walia, A. Acharya, *Theragnosis: Nanoparticles as a Tool for Simultaneous Therapy and Diagnosis*, in *Nanoscale Materials in Targeted Drug Delivery, Theragnosis and Tissue Regeneration*, Ed. S. K. Yadav, Springer Singapore, Singapore, **2016**, pp. 127–152.
165. T. Lammers, F. Kiessling, W. E. Hennink, G. Storm, *Mol. Pharm.* **2010**, *7*, 1899–1912.
166. D. Kim, Y. Y. Jeong, S. Jon, *ACS Nano* **2010**, *4*, 3689–3696.
167. L. Wang, H. Xing, S. Zhang, Q. Ren, L. Pan, K. Zhang, W. Bu, X. Zheng, L. Zhou, W. Peng, Y. Hua, J. Shi, *Biomaterials* **2013**, *34*, 3390–3401.
168. G. Tian, X. Zheng, X. Zhang, W. Yin, J. Yu, D. Wang, Z. Zhang, X. Yang, Z. Gu, Y. Zhao, *Biomaterials* **2015**, *40*, 107–116.
169. R. S. Riley, E. S. Day, *Wires Nanimed Nanobi* **2017**, *9*, e1449.
170. Y. Liu, J. R. Ashton, E. J. Moding, H. Yuan, J. K. Register, A. M. Fales, J. Choi, M. J. Whitley, X. Zhao, Y. Qi, Y. Ma, G. Vaidyanathan, M. R. Zalutsky, D. G. Kirsch, C. T. Badea, T. Vo-Dinh, *Theranostics* **2015**, *5*, 946–960.
171. D. Li, Y. Zhang, S. Wen, Y. Song, Y. Tang, X. Zhu, M. Shen, S. Mignani, J.-P. Majoral, Q. Zhao, X. Shi, *J. Mater. Chem. B* **2016**, *4*, 4216–4226.
172. H. Deng, Y. Zhong, M. Du, Q. Liu, Z. Fan, F. Dai, X. Zhang, *Theranostics* **2014**, *4*, 904–918.
173. Y. Liu, X. Ji, J. Liu, W. W. L. Tong, D. Askhatova, J. Shi, *Adv. Funct. Mater.* **2017**, *27*, 1703261.
174. C. Yang, C. Guo, W. Guo, X. Zhao, S. Liu, X. Han, *ACS Appl. Nano Mater.* **2018**, *1*, 820–830.
175. B. Li, X. Wang, X. Wu, G. He, R. Xu, X. Lu, F. R. Wang, I. P. Parkin, *Nanoscale* **2017**, *9*, 11012–11016.
176. J. F. Hainfeld, H. M. Smilowitz, M. J. O'Connor, F. A. Dilmanian, D. N. Slatkin, *Nanomed.* **2013**, *8*, 1601–1609.
177. J. R. Ashton, K. D. Castle, Y. Qi, D. G. Kirsch, J. L. West, C. T. Badea, *Theranostics* **2018**, *8*, 1782–1797.
178. A. Detappe, E. Thomas, M. W. Tibbitt, S. Kunjachan, O. Zavidij, N. Parnandi, E. Reznichenko, F. Lux, O. Tillement, R. Berbeco, *Nano Lett.* **2017**, *17*, 1733–1740.
179. J. Liu, Y. Deng, X. Qin, B. Li, J. Zhang, Y. Xu, R. Ouyang, Y. Li, Y. Miao, Y. Sun, *ACS Appl. Mater. Interfaces* **2019**, *11*, 42932–42942.
180. L. Mazzola, *Nat. Biotechnol.* **2003**, *21*, 1137–1143.
181. C. Li, *Nat. Mater.* **2014**, *13*, 110–115.

Subject Index

A

AAZTA (6-amino-6-methylperhydro-1,4-diazepinetetraacetic acid), 53, 54, 58, 77, 79, 86, 87, 114, 162, 174, 251, 261, 326–328, 330, 334
   structures, 54, 59, 173, 325
Aβ, *see* Amyloid-β
Actinium (Ac)
   ^{225}Ac, 176, 219, 321–323, 326, 336, 338
   ^{225}Ac/^{213}Bi generator, 322
   ^{225}Ac(DOTA-PSMA), 322
   ^{225}Ac-labeled antibody, 321
Acyclic chelators (contrast agents), 3, 125, 163, 168, 174, 324, 327, 328, 333
AD, *see* Alzheimer's disease
AdreView™, 316, 337
Affibodies, 171, 212, 338
Alexa dyes, 140
Alkali metals, *see* individual elements
Allysine, 7
AlphaMedix™, 336
Aluminum (Al), 228, 320
Alzheimer's disease (AD), 119, 209, 219–221, 319, 360, 406, 438, 440, 448
Amides, 13, 87, 110, 111, 115, 116, 119, 121, 125, 127, 128, 206, 207, 209, 221, 246, 248, 250, 251, 254, 255, 256, 448, 463
   acet-, 55, 114, 116, 128
   acetazole-, 6
   acryl-, 121
   benz-, 226
   bis-/di-, 61, 114, 259
   bismethyl-, 87
   diglycol-, 172
   gadodi- (Omniscan), 44, 46
   gadoverset-, 44

   mono-, 55, 60, 81, 114, 119, 250, 256, 259–262
   picolyl-, 128
   sulfon-, 56, 58, 60, 146, 226, 248, 388, 389
   tetra-, 107, 110, 112,–117, 119, 121, 128, 250, 252, 255, 259
   thio-, 220
   tri-, 119
Amines, 13, 85–87, 92, 113, 117, 119, 120, 125, 127, 128, 147, 168, 204, 207, 210, 228, 246, 331, 441, 445–448
   aliphatic, 207, 208
   benzyl-, 260, 448
   dipicolyl-, 94, 117, 205, 206, 427, 439
   hydroxyl-, 119
   trimethyl-, 275
   tetra-, 208, 324, 326
Amino acids (*see also* individual names), 5, 203, 205–208, 212, 213, 220, 303, 306, 317, 410, 444–447
   metabolism, 318
   neurotransmitters, 445
6-Amino-6-methylperhydro-1,4-diazepinetetraacetic acid, *see* AAZTA
4-Aminonaphthalimide, 440
Amino-polycarboxylate (APC), 41, 48, 56, 62
Amyloid-β (Aβ)
   Aβ$_{1–42}$ fibrils, 79, 80, 208, 209
   cerebral angiopathy, 360, 361
   plaques, 209, 220, 319, 360, 361, 438, 448–450
Angiography, 23, 44, 78, 282, 285, 287, 469, 471, 472
Animal experiments/models, 73, 119, 129, 174, 287, 320, 372, 426, 470
Annexin V, 214
Antibiotics, 427, 432